ICESAR 2007

Technical Assistance for the Deployment of Airborne SAR and Geophysical Measurements during the IceSAR 2007

Final Report - Part 1: Land Ice

Prepared for

European Space Agency

Prepared by

German Aerospace Center

Microwaves and Radar Institute (HR)

Oberpfaffenhofen

and

Alfred Wegner Institute for Polar and Marine Research

Climate Science Division

Bremerhaven

Primary Contractor:
Irena Hajnsek
German Aerospace Center
Microwaves and Radar Institute
PO BOX 1116, D-82234 Wessling
Phone: + 49/8153282363
Email: irena.hajnsek@dlr.de

Subcontractor:
Wolfgang Dierking
Alfred Wegener Institute for Polar & Marine Research
Climate Science Division
Bussestr. 24, D-27570 Bremerhaven
Phone: +49/4748311714
Email: wolfgang.dierking@awi.de

14. Nov 2008
Version 1.1

ESA STUDY CONTRACT REPORT -SPECIMEN

ESA Contract No.: **20655/07/NL/CB**	Subject: **Technical Assistance for the Deployment of Airborne SAR and Geophysical Measurements during the IceSAR 2007**	Contractor: **German Aerospace Center, Microwaves and Radar Institute**
ESA CR() No:	No.of Volume: 1 This is Volume No.: 1	Contractors References: Final Report

Abstract:

The ICESAR campaign was carried out in Svalbard in the period from March 8 to April 26, 2007 consisted of two parts, taking place over three weeks in March and over two and a half weeks in April, respectively. The main objectives of ICESAR were to acquire SAR images and complementary data over sea and land ice for preparation of the Sentinel-1 mission and for providing a basis for the assessment of potential applications of the Earth Explorer BIOMASS mission in the monitoring of the Polar Regions. The campaign was executed in collaboration between DLR, AWI, and ESA. Despite the rough Arctic environment and the highly variable weather conditions all data could be successfully acquired as planned and desribed in the Experimental Plan that was delivered to ESA. Furthermore, also additional flights could be carried out that were not included in the Experimental Plan, with data acquisitions over sea ice in the Frame Strait northwest of Svalbard, and over land ice with the P-band Sounder. All acquired SAR data over sea and land ice were processed and are of good quality for further analysis. The absolute radiometric accuracy lies within the ± 2 dB and the relative within ± 0.5 dB.

In this document first order analysis were carried out for the derivation of ice structure parameters and identification of bedrock. The main physical parameter describing ice structure is the extinction that was derived using polarimetric decomposition in combination with polarimetric SAR interferometry. Strong differences between the two test sites could be reported, as expected.

Further P-band sounder data were processed and analysed. The identification of bedrock and thus the thickness of the ice layer was the main objective. The best result was obtained with the identification of the bedrock up to 570 m.

Name of authors: Editor Irena Hajnsek (DLR) – Complete authors name next page!

Name of ESA study manager: Malcolm Davidson Div: Mission Science Division Directorate: Earth Observation Program	ESA Budget Heading:

Contract:

ESA contract No.: 20655/07/NL/CB

ESA study manager:

Malcolm Davidson

Part- 1 Prepared by:

Irena Hajnsek, Ralf Horn, Rolf Scheiber,

Martin Keller, Jayanti Sharma

German Aerospace Centre, Microwaves and Radar Institute

Version date changes:

1.0	03/10/2008	Draft version
1.1	14/11/2008	Final version

The authorship of this report is listed in the table below:

Chapter	Authors
2. Introduction	Irena Hajnsek
3. Description of the Study Area	Irena Hajnsek
4. IceSAR Campaign Schedule	Irena Hajnsek
5. Airborne Data Acquisition	Irena Hajnsek, Ralf Horn
6. SAR Processing	Rolf Scheiber, Martin Keller, Irena Hajnsek
7. Data Analysis Land Ice	Jayanti Sharma, Irena Hajnsek
8. Sattelite Data Acquistion	Irena Hajnsek
9. IceSAR Data Base	Irena Hajnsek
10. Summary & Recommendation	Irena Hajnsek, Jayanti Sharma, Rolf Scheiber

1 CONTENTS

2 INTRODUCTION

This document describes the IceSAR campaign that was carried out in winter 2007 in the vicinity of Svalbard, Norway, the data collected over sea and land ice during the two main campaign periods in March and April 2007, the acquired and processed SAR data and their qualtity and the results obtained from a first order analysis over land ice.

In a second part first order analysis over sea ice are presented, that was compiled by the Alfred Wegner Institute for Polar & Marine Research.

In this project we extended the data base that has already been acquired during the SVALEX campaign in 2005. The data consitst of SAR imagery gathered over sea and land ice, utilizing different radar frequencies and polarisations. The airborne imaging was complemented by in situ measurements on a glacier, and airborne optical imaging togther with measurements of atmospheric turbulence over sea ice. These activities will provide valuable data for the analysis of SAR images and the development of new applications for the use of satellite radar data. Airborne SAR data that were acquired at C-band are of fundamental importance for assessing the technical design of ESA's Sentinel-1 SAR mission with regard to sea and land ice monitoring. Gathering airborne data at P-band will help to develop further measurement strategies and methodologies for land ice applications employing data of the BIOMASS Earth Explorer Mission.

2.1 Background

In the framework of its Earth Observation Envelope Programme, the European Space Agency (ESA) coordinated a number of ground-based and airborne campaigns in Scandinavia to support geophysical algorithm development, calibration/validation and the simulation of future spaceborne earth observation missions during spring 2007 in support of the forthcoming GMES and Earth Explorer Missions.

CryoVEx 2007 (CryoSat Validation Experiment) continued the preparatory activities related to the CryoSat-2 validation objectives with a programme of airborne laser/radar altimeter acquisitions in conjunction with ground measurements on the Austfonna ice cap, Svalbard.

IceSAR 2007 supported the on-going preparation of two ESA Earth Observation programmes, the GMES Sentinel-1 mission and the Candidate Earth Explorer Mission, BIOMASS, with airborne multi-polarimetric SAR acquisitions over sea ice close to Svalbard as well as on the Austfonna ice cap.

BioSAR 2007 supported the Candidate Earth Explorer Mission, BIOMASS, providing airborne P- and L-band SAR measurements over a boreal forest site Remmingstrop in southern Sweden. The main objective of BIOMASS is to measure forest biomass at a global level to support carbon modelling.

The three campaigns were carried out in two periods during mid-March and mid-April 2007. Operations were focussed on Svalbard, Norway. The boreal forest site located in Sweden was flown during transit flights between Germany and Svalbard.

In the beginning of March 2007, the International Polar Year 2007-8 provided additional context for the activities of the ESA Spring 2007 Campaigns. Several of the participating teams have funding associated with the initiative.

2.2 IceSAR Objectives

The overall objective of the IceSAR campaign is to provide feedback to ESA on Sentinel-1 and BIOMASS mission concepts (through the collection and analysis of airborne data), including:

- The verification of the Sentinel-1 technical concept for ice services;
- An assessment of the potential of BIOMASS to measure ice thickness and bedrock topography;
- Assessment of the potential for SAR constellation observations at different frequencies and polarisations.

Specific IceSAR tasks include:

- Verifying suitability of Sentinel-1 operational modes for ice monitoring, including the added value of the Interferometric Wide Swath (IW) dual-polarisation mode with respect to single-polarisation and Extra Wide Swath (EW) modes [R-1];
- Simulating the impact of Sentinel-1 degraded observations on Ice Services, including quantification of impact of choice of NESN, resolution and calibration on product quality;
- Generating prototype Sentinel-1 image products for sea ice mapping;
- Assessing potential of P-Band SAR to measure ice thickness and bedrock topography;
- Assessing information content and observation requirements for land ice at P-Band;
- Assessing impact of choice of frequency (P-band and L-Band) and polarisation for land and sea ice.

In order to address these objectives, the campaign will provide quality datasets over sea and land ice that enable the following experiments and measurements to be carried out.

Over sea ice (data acquired in March):

- Retrieval of deformation characteristics of sea ice from SAR images for evaluation of atmospheric drag and application to modelling of atmosphere-ice interactions;
- For Sentinel-1, assessment of potential for separating ice classes dependent on system parameters (polarisation, noise level) and simulation of Sentinel-1 Level-1b products using E-SAR imagery as starting point;
- Assessment of information content in SAR images of different frequencies – which frequency is optimal for a certain mapping task?

Over land ice (data acquired in March and April):

- Change detection for a period of two years (2005-2007) & one month (March-April 2007);
- Land ice structure characterisation in the ice volume using L- and P- band;

- Complementarity with C-band (dual/repeat pass) data acquisition for Sentinel-1;
- P-band sounder experiment to be performed with a new antenna and new modes.

2.3 Campaign Participants

IceSAR involved in total approximately 20 people coming from mainly three institutions in Germany.

AIR OPERATIONS TEAM:

German Aerospace Center (DLR), Microwaves and Radar Institute (HR)

P.O. Box 11 16, D-82230 Wessling, Germany
in the following referred to as **DLR-HR**

German Aerospace Center (DLR), Flight Operations (FB)

P.O. Box 11 16, D-82230 Wessling, Germany
in the following referred to as **DLR-FB**

Alfred Wegner Institute for Polar and Marine Research (AWI)

Bussestr. 24, D-27570 Bremerhaven

In the following referred to as **AWI**

Optimare Sensor Systems

Am Luneort 15a, D-27572 Bremerhaven

In the following referred to as **Optimare**

GROUND TEAM:

German Aerospace Center (DLR), Microwaves and Radar Institute (HR)

P.O. Box 11 16, D-82230 Wessling, Germany
in the following referred to as **DLR-HR**

PROCESSING TEAM:

German Aerospace Center (DLR), Microwaves and Radar Institute (HR)

P.O. Box 11 16, D-82230 Wessling, Germany
in the following referred to as **DLR-HR**

Fig. 2.1: IceSAR team at the first part of the IceSAR campaign in March 2007 in front of the DLR's Do228 at the airport of Longyerbyen, Svalbard.

Fig. 2.2: IceSAR team at the second part of the IceSAR campaign in April 2007 infront of the DLR's Do228 at the airport of Longyerbyen, Svalbard.

ORGANISATION Team:

ESA Technical Officer	Malcolm Davidson
RSAC Assistant	Mike Wooding
DLR-HR Primary Contracter	Irena Hajnsek
AWI Subcontractor	Wolfgang Dierking

AIRBORNE Team:

DLR-FB	Heinz Finkenzeller Philip Weber Stefan Grillenbeck Klaus Dietl Roland Welser Michael Grossrubatscher Emil Sauer Siegfried Judt Roman Koch Andreas Hahn Jens Heider Jens Hammer
DLR-HR	Ralf Horn Bernd Gabler Markus Limbach Peter Hackenberg
AWI	Christof Lüpkes Wolfgang Dieking
Optimare	Thomas Garbrecht

Ground Team:

DLR-HR	Florian Kugler Stefan Baumgartner
AWI	Jörg Hartmann
Optimare	Axel Bochert

Processing Team:

DLR-HR	Rolf Scheiber Christian Andres Jayanti Sharma

3 DESCRIPTION OF THE STUDY AREA

The main research interest during the IceSAR campaign was focused on two application areas: sea ice and land ice. For these two ice categories different test sites were chosen. ESA, DLR, and AWI already agreed in preparation of the study on the test site selection.

3.1 Sea Ice

The test sites for the sea ice measurements needed to fulfil certain conditions with regard to the position of different sea ice types.

The main strategy of data acquisition was to collect close simultaneously the data over the same sea ice are with two aircraft carrying different instruments on board. The main idea was to combine airborne measurements of the atmospheric turbulence and of ice surface characteristics with airborne SAR imaging.

The following criteria were applied for the choice of the respective sea ice test site:

1. The atmospheric measurements require that the test site is undisturbed by the air flow around any obstacle (coastlines, islands).
2. Because an optical scanner was utilized, the visibility conditions had to be considered.
3. Different ice conditions had to be imaged.
4. Areas with high ice concentrations had a higher priority.

Decisions were based on meteorological data and forecasts and on imagery over sea ice from spaceborne optical and SAR sensors. The typical measurement strategy for the atmospheric measurements was to fly at low altitude (30-50 m) along a profile parallel to the wind direction, preferably more often in order to get a reliable statistics for the turbulence data. One profile was flown at higher altitude (500-1500 m) for acquiring optical imagery over a wider swath. This had also an impact of the maximum distance that can be covered between the airport base and the test site. During IceSAR (same test areas were also chosen at the Svalbard Experiment in 2005), test sites were located in the Barents Sea east of Barentsøya and Edgeøya, in the Storfjord between Spitsbergen and Edgeøya and in the Frame strait.

3.2 Land Ice

The area of interest for land ice data acquisition is Nordauslandet, located North-East of Svalbard. On this island several ice caps and glaciers cover an area of 11.150 km² and represent one of the largest land ice masses outside of the Antarctic and Greenland ice sheets. They are of sub-polar thermal regime, and are of particular interest because several glaciers in drainage basins have been observed to surge. In addition, the ice-covered area is of logistically manageable extent, which can be used as an analogue for studies of the dynamic of large ice masses. This was the main reason why this island has been chosen for long-term investigations.

One of the first field campaigns for collecting glaciological information was the Swedish IGY Expedition 1957 and 1958, published by Schytt 1964.

In April 2005, in the frame of SVALEX 2005, three flight lines were fixed in accordance with the test site of the University of Oslo and the Norwegian Polar Institute (Taurisano 2005). During Svalex 2005, carried out in cooperation with AWI, experience was gained with the test site logistics and the ice cap characteristics. Therefore the DLR team suggests using the same test site and same flight lines in order to be able to compare the results obtained from both campaigns.

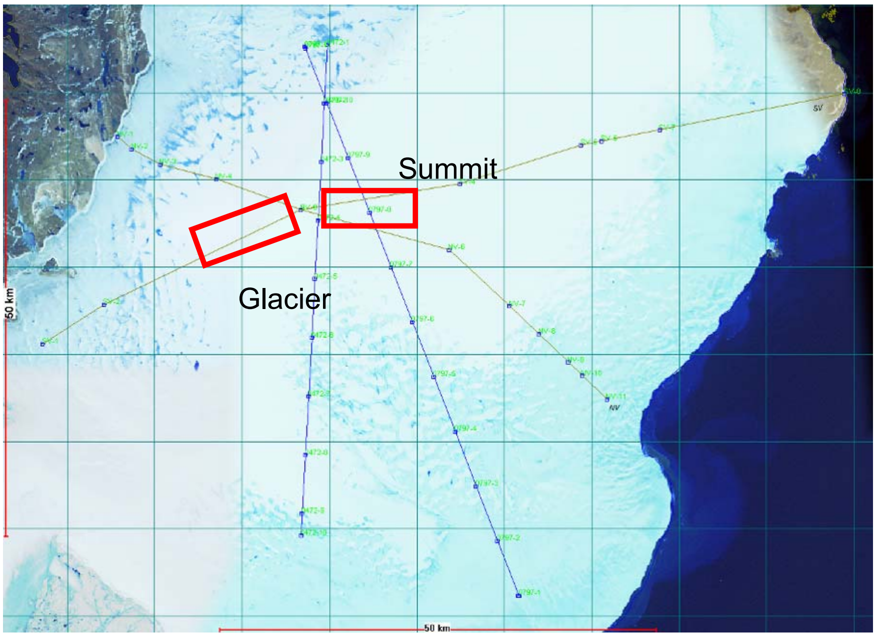

Fig. 3.1: Location of land ice measurement locations at Nordauslandet on the Austfonna cap with a length of 10km and 3km wide stripe (red boxes)

4 ICESAR CAMPAIGN SCHEDULE

The IceSAR campaign started on March 08/03/2007 when DLR's E-SAR system was first flown from Oberpfaffenhofen to Sweden for the BIOSAR campaign and afterwards to Svalbard to the airport of Longyerbyen. After instrument installation the main measurements campaign started over different sea ice regions together with the AWI's Polar-2 aircraft on which optical and meteorological instruments were installed. After four sea ice flights, measurements over the Austfonna cap were performed solely with the E-SAR system. Simultanously with the land ice flights over Austfonna a ground team were installing corner reflectors. After several Pol-InSAR and one 2 P-band sounder flights the system was flown back to Oberpfaffenhofen. In the beginning of April the second IceSAR campaign started, during which the E-SAR was flying used to acquire Pol-InSAR as well as P-band sounder data. Not simultanoulsy but in the same period also the AWI's Polar-2 was carrying out measurements over the land ice area of Austfonna with the ASIRAS system as part of the CryoVex project. Simultanously ground measurements were taken from a Norwegian team. The IceSAR campaign was completed on the 25th of April. The aircraft was back in Oberpfaffenhofen at the 3rd of May 2007. In Table 4.1 the time schedule for the different task and activities is shown.

Month	*MARCH 2007*				*APRIL 2007*			
Days	*08/03-11/03*	*12/03-18/03*	*19/03-25/03*	*26/03-31/03*	*02/04-08/04*	*09/04-15/04*	*16/04-22/04*	*23/04-29/04*
Topic								
IceSAR Campaign	*1. Campaign*				*2. Camapaign*			
Arrival	X					X		
Departure				X				X
Instrument installation		X				X		
Measurement campaign		X	X			X	X	X
Ground Campaign (DLR)	X	X	X	X	X			
Ground campaign (CryoVex)						X	X	X

Table 4.1: IceSAR camapign schedule from March to April at Svalbard.

5 AIRBORNE DATA ACQUISITION

In this section the two airborne campaigns with the different instruments and the data acquired are described. One major challenge for the IceSAR campaign was the unpredictable weather situation in the Arctic that are difficult to forecast. This means that the planning of the flight schedule has to be very flexible. Twice a day a common briefing took place in the facilties of the University of Svalbard or at the rooms of the main hall of Longyerbyen. In the morning the weather situation was checked and necessary actions and flight plans were discussed, in the evening flight crews and scientists reported about the day's flights and activities and set up a preliminary schedule for the next day.

Fig. 5.1: Morning briefing of the DLR and AWI team in March 2007

5.1 Synthetic Aperture Radar Data Acquisition

Already the proposal and experimental plan described the DLR's E-SAR system, the main instrument on board the DLR's aircraft Do228 for operation and radar data acquisition.

5.1.1 Mission Logistics

In support of the radar operation during the 2007 ICESAR campaign material and equipment of up to 2t gross weight had to be shipped to Longyearbyen and back. All arrived timely before the start of the campaign, thanks to LSI logistics in Germany and Scandinavian Airlines in Norway.

The shipment contained:

- E-SAR X- and C-band radar segments, leaving only L- and P-band operational onboard the DLR DO228. This was due to transport capacity limitations on the leg from Tromsø to Longyearbyen.

- GPS monitoring and DGPS data link equipment to be used at the airport (LYR) and at the NPI depot on Oxford peninsula next to the western skirts of the Austfonna ice field.
- RF measurement equipment to check and maintain radar performance during the campaign.
- Six foldable trihedral radar reflectors (4 of of 150cm and 2 of 90cm leg length) to be deployed as ground control points on Austfonna.
- An aircraft heater to heat up the radar installation prior to power on.


Fig. 5.2: Campaign preparation: Instrument (left) and corner reflector (right) shipment to Longyearbyen

The operation base was located at Longyearbyen airport. Offices and briefing room were rented at the Nybygget in the town centre.

Air operation around the Svalbard archipelago is subject to special air safety regulations. It is required to carry sea and ice survival equipment sufficient for the aircrew on board. A fuel reserve equivalent to 1.5h flight time has to be kept for emergency situations. Due to the limited payload capacity of the DO228-212 and the need for a minimum flight time of 2.75h it was necessary to operate the E-SAR system in a minimum configuration for each sortie. This had strong impact on the radar measurement programme. In the time table of the campaign sufficiently long periods for system modifications had to be carefully planned taking also into account airport operation hours and other constraints (see Tables 5.2 and 5.3). In the time table not only the installation, deinstallation and reinstallations are listed but also the time table for the main arrival of the SAS is listed. The main reason for it was that we needed to arrange our flight schedule and usage of the hanger around the arrival and departure of the SAS. In the table also the briefing in the morning and evenings are listed.

Due to the deep temperatures during day and night a hanger was mandatory to intall the E-SAR system. Unfortunaltely only one hanger was available that needed to be shared with three other aircrafts. It was a challenge to coordinate the work on the aircraft that lasted sometimes until midnight (Figure 5.3).

Fig. 5.3: Preparation for the first E-SAR flight: Upper left: Storage of the equipment in the hanger; Lower left: airport tower and hangar were the Do228 is parked; Right: installation of the E-SAR system on board the Do228

The equipment that has been shipped by containers on a ship was placed close to the hanger at the airport of Longyearbyen. The corner reflector box could not be lifted by 3 men as it had a weight of 168 kg and was therefore transported on a small trolley to the hanger. The corner reflectors were needed for the positioning and coregistration for the SAR processing.

Fig. 5.4: Preparation for the first E-SAR flight: Left: container where the corner reflector and a part of the E-SAR system were transported; Left: DLR Do228 and AWI's Polar-2 together in the hangar.

5.1.2 Calibration of the E-SAR system

For the DLR E-SAR system it is recommended to perform at least one measurement flight over a calibration site to test the system and check its performance after it has been installed as preparatory measure well ahead of any SAR campaign. For the 2007 ICESAR campaign we set up a calibration site near the town of Mindelheim, located about 60km west of the DLR Oberpfaffenhofen research centre. The cal flight was performed on February 16, 2007. A number of seven radar reflectors, trihedral corner reflectors of 150cm leg length, large enough for frequencies from L- to X-band, were set up. The P-band had to be calibrated at Remningstorp, Sweden, where FOI provided three trihedral reflectors of 5m leg length in the frame of the BIOSAR campaign. Two reflectors were used for this analysis. The flight was performed on March 9, 2007. The results (normalized to the 60dB calibration constant of E-SAR data) are summarised in the table below.

Test Site	Frequency	Polarisation VV	Polarisation HH
Mindelheim (Germany) (7 reflectors)	**X-band** XTI mode Image channel Calibration 60dB +/- 0.5dB	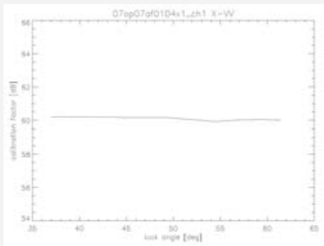	
Mindelheim	**C-band** Co-polar channels C-VV calibration 60.5dB +/- 0.5dB C-HH calibration 60dB +/- 0.5dB	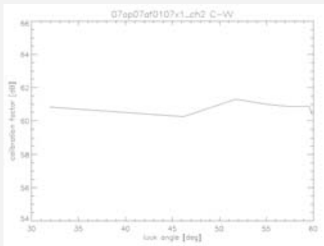	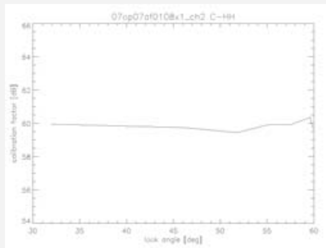
Mindelheim	**L-band** Co-polar channels L-VV calibration 60dB +/- 0.5dB L-HH calibration 60dB +/- 0.5dB	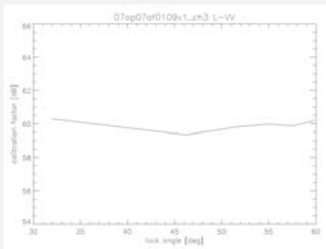	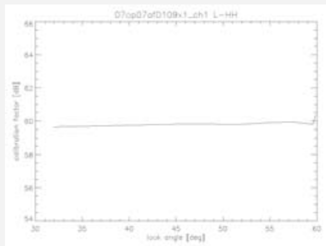
Remningstorp (Sweden) (2 reflectors, the one in near range is slightly misaligned)	**P-band** Co-polar channels P-VV calibration 59dB +/- 1dB P-HH calibration 59dB +/- 1dB	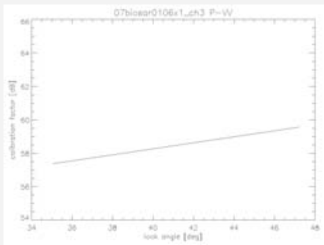	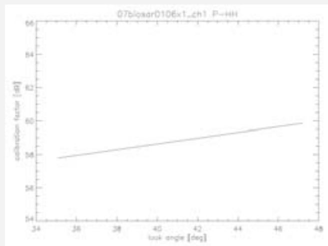

Table 5.1: E-SAR calibration analysis at different frequencies and polarisation

Table 5.2: Time table of ICESAR 2007 campaign – campaign 1 (March 2007)

Day	**1**	**2**	**3**	**4**	**5**	**6**	**7**	**8**	**9**	**10**	**11**
Date	**15.03.07**	**16.03.07**	**17.03.07**	**18.03.07**	**19.03.07**	**20.03.07**	**21.03.07**	**22.03.07**	**23.03.07**	**24.03.07**	**25.03.07**
System Configuration											
Sea Ice											
C-/L-band	Test flight	**1x**		**1x**	**1x**						
Land Ice											
X-Band							**1x**				
C-Band							**1x**				
L-Band						**2x**					
P-Band										**2x**	
P-Sounder								**2x**			
Ground Activities			P-Sounder ready for installation **2:00 h**		After flight: removal of sea survival equipment. **0:30 h**	After flights: L-b de-installation, X-TWTA installation. **2:30 h**	After flights: rack D de-installation, take out C-b, radome de-installation, take out C-, P-sounder integration. **6:00 h**		P-Side-Looking reconfiguration and installation. **4:00**	Rack D integration (no C-b!), radome only integration. **2:00 h**	
SAS arrival (LYR)					01:30				01:30		
SAS departure (LYR)					05:05				05:05		
SAS arrival (LYR)	13:55	13:55		13:55	13:55	13:55	13:55	13:55	13:55		13:55
SAS departure (LYR)	14:55	14:55		14:55	14:55	14:55	14:55	14:55	14:55		14:55
Briefing	09:00	09:00	09:00	09:00	09:00	09:00	09:00	09:00	09:00	09:00	
Debriefing	12:30			18:00	18:00	18:00	18:00	18:00	18:00	18:00	

Table 5.3: Time table of ICESAR 2007 campaign – camapign 2 (April 2007)

Day	2	4	6	7	8	9	10	11	13	14	15	16
Date	11.04.07	13.04.07	15.04.07	16.04.07	17.04.07	18.04.07	19.04.07	20.04.07	22.04.07	23.04.07	24.04.07	25.04.07
System Configuration												
Land Ice												
X-Band										**1x**		
C-Band					**2x**					**1x**		
L-Band						**1x**	**1x**					
P-Band			**1x**	**1x**								
P-Sounder								**1x**				
Ground Activities	*Intro of the GPS-Link to the NPI ground team; Coord. of communication link; intro to the CR install.*	*Pre-flight: remove Rack D and C-band radome, install P-band antenna,* ***2:00 h***	*Pre-flight: System warm up and test,* ***2:00 h***	*Pre-flight: System warm up and test,* ***2:00 h*** *Remove P-band, install C- and L-b,* ***6:00 h***	*Pre-flight: System warm up and test,* ***2:00 h***	*Pre-flight: System warm up and test,* ***2:00 h***	*Pre-flight: System warm up and test,* ***2:00 h*** *Post-flight: remove Rack D and C-b radome, install P-sounder,* ***2:00 h***	*Pre-flight: System warm up and test,* ***2:00 h*** *Post-flight: remove P-band, install Rack D and C-b with radome,* ***3:00 h***		*Pre-flight: System warm up and test,* ***2:00 h*** *After first flight remove C-b, install X-TWTA and test,* ***2:00 h***	*Prepare for ferry to Tromso, configuration as for BIOSAR and test,* ***3:00 h***	
SAS arrival (LYR)		01:30		01:30				01:30		01:30		
SAS departure (LYR)		05:05		05:05				05:05		05:05		
SAS arrival (LYR)	13:55	13:55	13:55	13:55	13:55	13:55	13:55	13:55	13:55	13:55	13:55	13:55
SAS departure (LYR)	14:55	14:55	14:55	14:55	14:55	14:55	14:55	14:55	14:55	14:55	14:55	14:55
Briefing		18:00	09:00	09:00	09:00	09:00	09:00	09:00	09:00	09:00	09:00	
Debriefing			18:00	18:00	18:00	18:00	18:00	18:00		18:00		

5.1.3 Radar Data Acquisition

Radar data acquisition flights commenced on March 16, 2007 with a series of flights over sea ice in the areas ‘Storfjorden’, ‘Barent Sea’ and ‘Fram Strait’. The first flight overhead the ‘Austfonna’ area, which is split into two sub-areas named ‘Summit’ and ‘Glacier’, could be carried out on March 21, 2007. The last was executed on April 22, 2007.

Table 5.4: campaign 1 – March 2007

Subject	Date	Area	Flight	Pass	Track	Band	Polarisation	Mode
Sea Ice	16.3.07	**Storfjorden**	2	1	2	C	DP	VH-VV
				2	3	L	PM	
				3	2	C	DP	HV-HH
	18.3.07	**Barents Sea**	3	1	5	C	DP	VH-VV
				2	6	L	PM	
				3	5	C	DP	HV-HH
	19.3.07	**Fram Strait**	4	1	2	C	DP	VH-VV
				2	3	C	DP	HV-HH
	20.3.07	**Fram Strait**	5	1	2	C	DP	VH-VV
				2	3	L	PM	
Land Ice	21.3.07	**A. - Summit**	6	1	10	L	PM	Master - North
Pol-InSAR				2	20	L	PM	Master - South
				3	11	L	PM	Slave 5m - North
				4	21	L	PM	Slave 7m - South
				5	12	L	PM	Slave 10m - North
				6	22	L	PM	Slave 14m - South
				7	13	L	PM	Slave -10m - North
				8	24	L	PM	Slave -8m - South
				9	10	L	PM	Slave 0m - North
Pol-InSAR	23.3.07	**A. - Glacier**	7	1	10	L	PM	Master - North
				2	11	L	PM	Slave 5m - North
				3	12	L	PM	Slave 10m - North
				4	13	L	PM	Slave -10m - North
P-Sounder	25.3.07	**A. - Summit**	8	1	40	P	PM	25MHz, Master
				2	-40	P	PM	94MHz, Master
				3	41	P	PM	25MHz, Slave 5m
				4	-41	P	PM	94MHz, Slave 5m
				5	43	P	PM	25MHz, Slave -5m
				6	-43	P	PM	94MHz, Slave -5m
Pol-InSAR	26.3.07	**A. - Summit**	9	1	20	P	PM	Master - South
				2	10	P	PM	Master - North
				3	21	P	PM	Slave 15m - South
				4	11	P	PM	Slave 10m - North
				5	22	P	PM	Slave 25m - South

Subject	Date	Area	Flight	Pass	Track	Band	Polarisation	Mode
				6	12	P	PM	Slave 20m - North
				7	24	P	PM	Slave -20m - -South
				8	13	P	PM	Slave -20m - North
		A. - Glacier	9	9	10	P	PM	Master - North
DEM	26.3.07	**A. - Summit**	10	1	10	X	VV	XTI full base - North
				2	20	X	VV	XTI full base - South
				3	11	X	VV	XTI half base - North
				4	21	X	VV	XTI half base - South
		A. - Glacier		5	20	X	VV	XTI full base - South
				6	10	X	VV	XTI full base - North
				7	21	X	VV	XTI half base - South
				8	11	X	VV	XTI half base - North
Pol-InSAR	27.3.07	**A. - Glacier**	11	1	20	P	PM	Master - South
				2	10	P	PM	Master - North
				3	21	P	PM	Slave 15m - South
				4	11	P	PM	Slave 10m - North
				5	22	P	PM	Slave 25m - South
				6	12	P	PM	Slave 20m - North
				7	24	P	PM	Slave -20m - -South
				8	13	P	PM	Slave -20m - North

Table 5.5: campaign 2 – April 2007

Subject	Date	Area	Flight	Pass	Track	Band	Polarisation	Mode
Land Ice	16.4.07	**A. - Glacier**	12	1	10	P	PM	Master - North
Pol-InSAR				2	20	P	PM	Master - South
				3	11	P	PM	Slave 10m - North
				4	21	P	PM	Slave 15m - South
				5	12	P	PM	Slave 20m - North
				6	22	P	PM	Slave 25m - South
				7	13	P	PM	Slave -20m - North
				8	24	P	PM	Slave -20m - South
				9	10	P	PM	Slave 0m - North
Pol-InSAR	16.4.07	**A. - Summit**	13	1	20	P	PM	Master - South
				2	10	P	PM	Master - North
				3	21	P	PM	Slave 15m - South
				4	11	P	PM	Slave 10m - North
				5	22	P	PM	Slave 35m - South
				6	12	P	PM	Slave 20m - North
repeated				7	22	P	PM	Slave 35m - South
				8	13	P	PM	Slave -20m - North
Pol-InSAR	17.4.07	**A. - Summit**	14	1	20	L	PM	Master - South
				2	10	L	PM	Master - North
				3	21	L	PM	Slave 7m - South
				4	11	L	PM	Slave 5m - North

Subject	Date	Area	Flight	Pass	Track	Band	Polarisation	Mode
				5	22	L	PM	Slave 19m - South
				6	12	L	PM	Slave 10m - North
				7	24	L	PM	Slave -8m - South
				8	13	L	PM	Slave -10m - North
Pol-InSAR	18.4.07	**A. - Glacier**	15	1	10	C	DP/VH-VV	Master - North
				2	20	C	DP/VH-VV	Master - South
				3	10	C	DP/HV-HH	Master - North
				4	20	C	DP/HV-HH	Master - South
				5	11	C	DP/HV-HH	Slave 5m - North
				6	21	C	DP/HV-HH	Slave 7m - South
				7	11	C	DP/VH-VV	Slave 5m - North
				8	21	C	DP/VH-VV	Slave 7m - South
Pol-InSAR	19.4.07	**A. - Glacier**	16	1	10	L	PM	Master - North
				2	20	L	PM	Master - South
				3	11	L	PM	Slave 5m - North
				4	21	L	PM	Slave 7m - South
				5	12	L	PM	Slave 10m - North
				6	22	L	PM	Slave 14m - South
				7	13	L	PM	Slave -10m - North
				8	24	L	PM	Slave -8m - South
				9	10	L	PM	Slave 0m - North
Pol-InSAR	19.4.07	**A. - Summit**	17	1	20	C	DP/VH-VV	Master - South
				2	10	C	DP/VH-VV	Master - North
				3	20	C	DP/HV-HH	Master - South
				4	10	C	DP/HV-HH	Master - North
				5	21	C	DP/HV-HH	Slave 7m - South
				6	11	C	DP/HV-HH	Slave 5m - North
				7	21	C	DP/VH-VV	Slave 7m - South
				8	11	C	DP/VH-VV	Slave 5m - North
P-Sounder	20.4.07	**A. - Glacier**	18	1	30	P	PM	94MHz, Master
				2	-30	P	PM	25MHz, Master
				3	31	P	PM	94MHz, Slave 5m
				4	-31	P	PM	25MHz, Slave 5m
repeated				5	30	P	PM	94MHz, Master
				6	-32	P	PM	94MHz, Slave -5m
repeated				7	31	P	PM	94MHz, Slave 5m
				8	-33	P	PM	94MHz, Slave 10m
				9	34	P	PM	94MHz, Master, low
DEM	22.4.07	**A. - Summit**	19	1	10	X	VV	XTI full base - North
				2	20	X	VV	XTI full base - South
				3	11	X	VV	XTI half base - North
				4	21	X	VV	XTI half base - South
		A. - Glacier		5	20	X	VV	XTI full base - South
				6	10	X	VV	XTI full base - North

Subject	Date	Area	Flight	Pass	Track	Band	Polarisation	Mode
				7	21	X	VV	XTI half base - South
				8	11	X	VV	XTI half base - North
repeated				9	20	X	VV	XTI full base - South
Pol-InSAR	22.4.07	**A. - Glacier**	20	1	10	C	DP/VH-VV	Slave 0m, 4d, North
				2	20	C	DP/VH-VV	Slave 0m, 4d, South
				3	10	C	DP/HV-HH	Slave 0m, 4d, North
				4	20	C	DP/HV-HH	Slave 0m, 4d, South
repeated				5	10	C	DP/VH-VV	Slave 0m, 4d+, North
repeated				6	20	C	DP/VH-VV	Slave 0m, 4d+, South

5.1.4 Flight Overview

Three test areas were selected for the campaign for the sea ice part on a daily basis and for the land ice part the test site was already fixed before the project proposal. Operations base was the airport of Lonyearbyen. The following plots show the locations of the test areas on the map (Google Earth). The distances to the areas were ranging from 120nm ('Storfjorden') to 150nm ('Austfonna-Summit') up to 208nm ('Fram Strait').

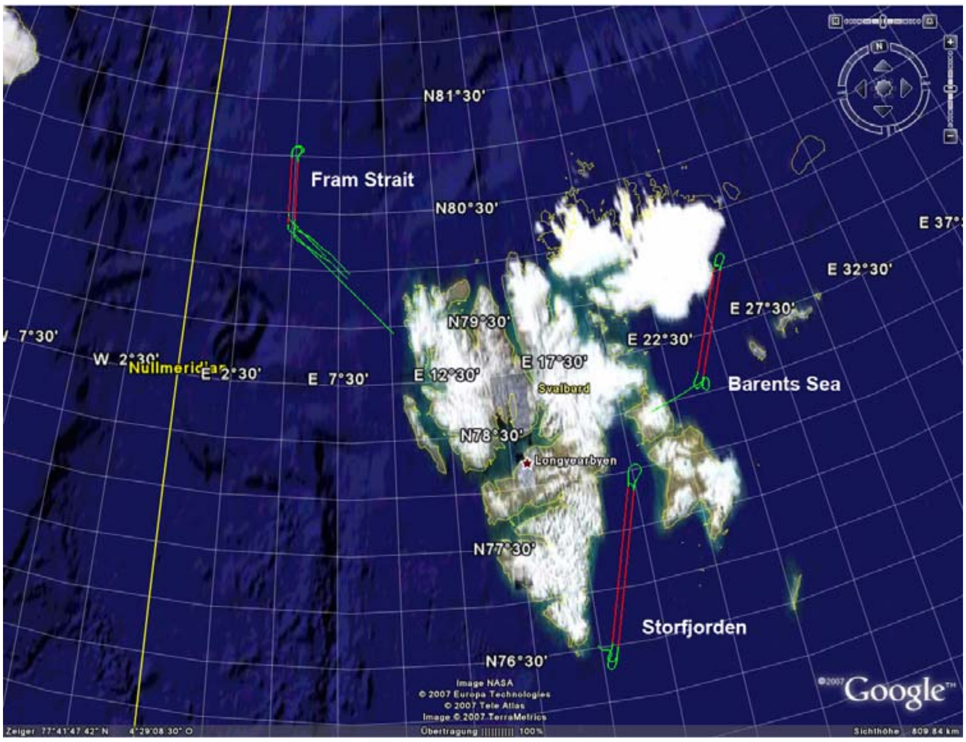

Fig. 5.5: Flight overview: Sea Ice measurement flights. Locations 'Storfjorden', 'Barents Sea' and 'Fram Strait'.

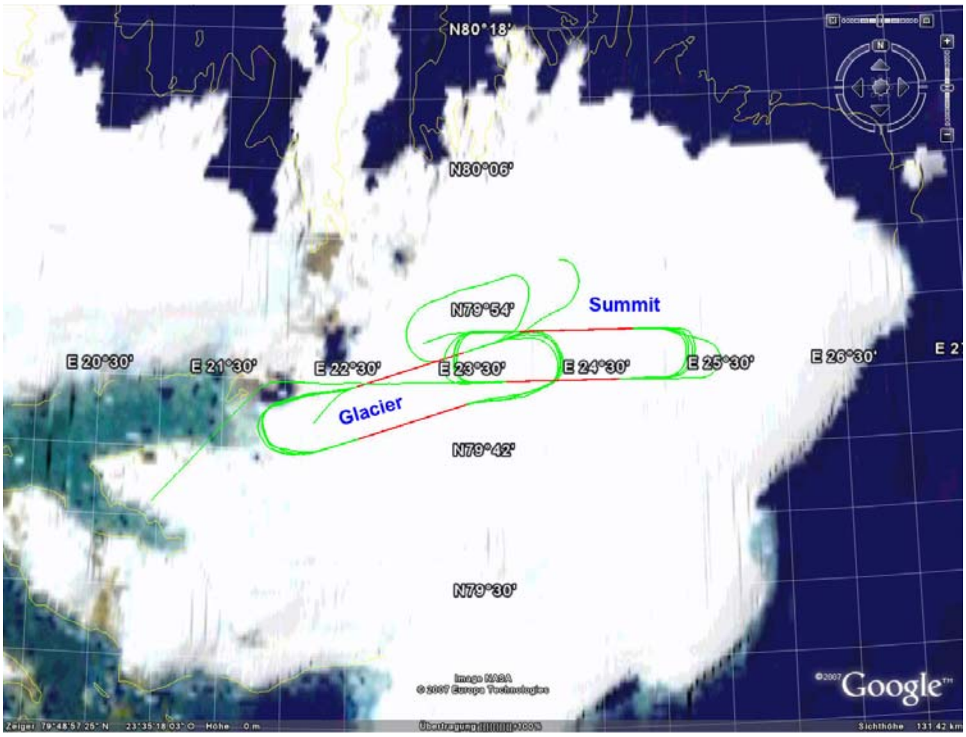

Fig. 5.6: Flight overview: Land Ice measurement flights. Locations 'Summit' and 'Glacier'.

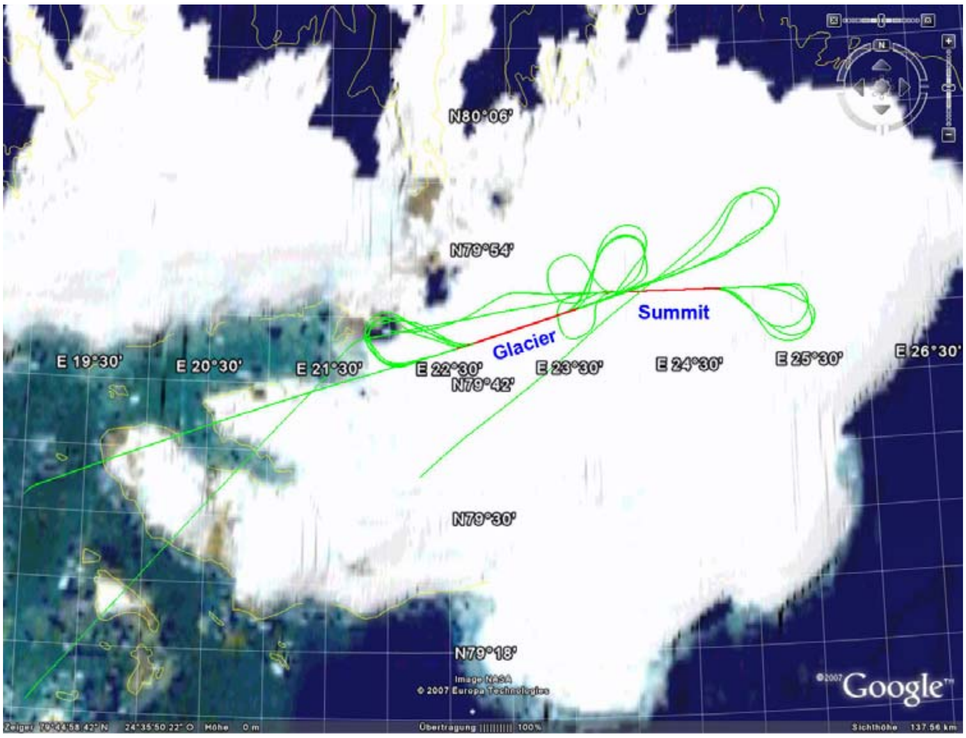

Fig. 5.7: Flight overview: Land Ice measurement flights. P-Band ice sounder mode. Locations 'Summit' and 'Glacier'.

In all figures radar data acquisition on line is indicated in red. Flight planning of the P-band ice sounder experiments foresaw the tracks to be located in the centre of a test area, at 'Summit' as well as 'Glacier'.

5.1.5 GPS Data Acquisition

GPS data acquisition is essential for E-SAR operation. SAR focussing requires sufficiently good motion compensation. Due to the large distances to the test areas GPS monitoring stations at known geographical positions are required at the airport and close to or in the test areas at the same time during a flight. This requirement could be fulfilled for the land ice measurements only for obvious reasons.

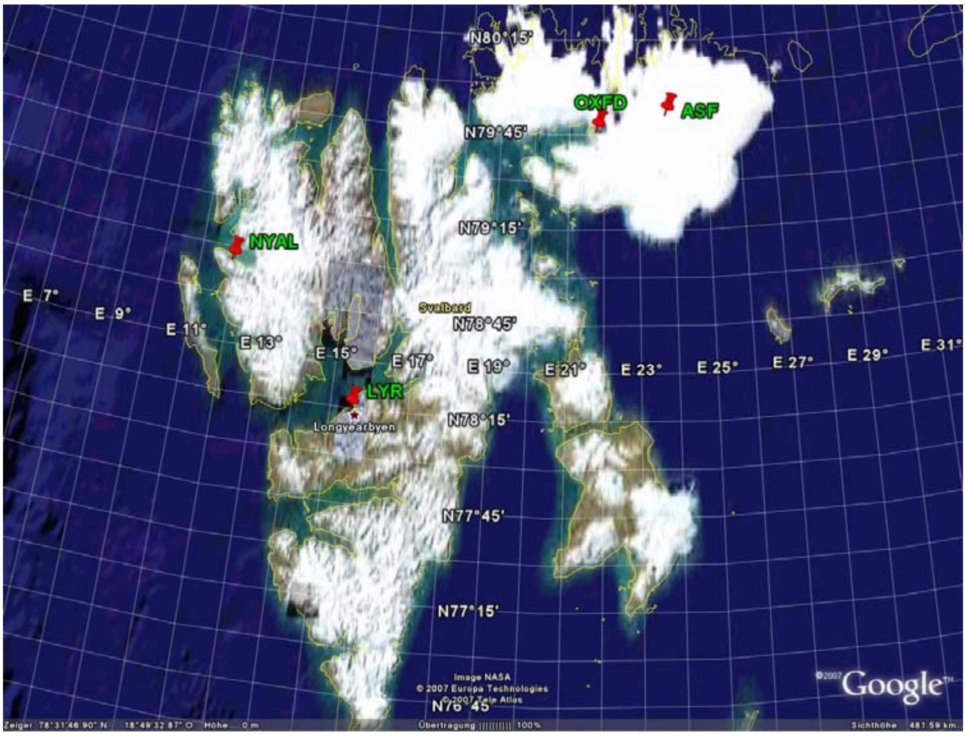

Fig. 5.8: GPS reference and monitoring stations used during ICESAR 2007.

NYAL: EUREF network, GPS reference.

LYR: DLR GPS monitoring station at the airport.

OXFD: DLR GPS monitoring station on Oxford peninsula on Nordaustlandet (NPI depot) used during first session.

ASF: DLR GPS monitoring station on Austfonna ('Summit') operated by NPI during second session.

We have used the EUREF/IGS reference station at Ny Alesund as GPS reference for all our measurements. The data is available on the internet at 30sec data rate. The positions of all monitoring stations were obtained by means of differential GPS processing referring them to the Ny Alesund station. All GPS antenna positions were kept as stable as possible during the campaign sessions.

NYAL	78° 55'46.4959''N	11° 51'54.2900''E	78.413 m
LYR	78° 14'45.2005''N	15° 30'14.8200''E	54.560 m
OXFD	79° 46'01.8675''N	21° 45'28.0463''E	83.321 m
ASF	79° 51'09.5430''N	23° 47'51.5588''E	801.446 m

All aircraft positions were precision DGPS corrected in post-processing using data of the available monitoring stations. Session1: for sea ice LYR only, for land ice LYR and OXFD. Session2: LYR and ASF.

In all cases good to excellent post-processing results were obtained.

For the land ice measurements precise navigation was required on top. Hence, DGPS corrections had to be transmitted to the DLR aircraft overhead the Austfonna. Services on geostationary satellites, like Omni-Star, are not reliable at latitudes above 78° north. Therefore it was necessary to operate a ground based data link together with the GPS monitoring station in the field. The DGPS corrections were based on GPS L1 (in RTCM format). They allow platform positioning with a precision of about 1m (3D), which is sufficient for the purpose.

For imaging sea ice the requirements on absolute aircraft position accuracy were less stringent. It was important to have a good relative measurement quality. This could be achieved with a single monitoring station, LYR, located at the airport.

5.1.6 SAR processing facility

From the experience of the previous ice campaign at SVALBARD in 2005 we installed also a small processing unit at an office in Longyearbyen. The data that were collected during the flight, were transcribed during the night and processed the next day whileother flights were ongoing. The main reason for it was to check

- the area where data were acquired especially for the sea ice, as two aircraft needed to cover the same area
- the SAR data quality
- the repeat pass quality and flight line robustness in order to have stable baselines for parameter inversion
- the stability of the hardware

Fig. 5.9: SAR processing facility at Longyerbyen. On the screen first sea ice images are displayed (Rolf Scheiber).

In the artic region the main problem are caused due to very low temperature and strong winds for the stability of the hardware system and the baseline. Before take-off to the measurement flight the E-SAR system was heated up with a special airheater at least for one hour. Then the hardware system was operating stable until the test site was reached and data could be recorded.

5.1.6.1 Ground Campaign

The ground campaign was performed for the first campaign in March from DLR personal. The ground campaign was only needed for the land ice part of the whole IceSAR project. There was a team out on Austfonna to set up radar reflectors and operate a GPS monitoring station including a DGPS data link. The DLR scientists managed to set up the planned six reflectors and operate the GPS equipment successfully under odd weather conditions. For the second campaign in April, that was about land ice only, scientists from Norwegian Polar Institute (NPI) were engaged for this task. They removed the material after the completion of the campaign.

Fig. 5.10: DLR scientists before (left) the flight to the Austfonna ice cap and after (right) their return (Florian Kugler (left) and Stefan Baumgartner (right)).

Corner reflectors for E-SAR are inclined to match the instrument viewing angle (see Figure 5.11). Six corner reflectors (four 1.5m type and two 90cm type) were installed at the land ice measurement locations in March by a field party of two DLR personnel. They were left in place for the whole campaign period. For the second campaign in April the corner reflectors were relocated by the CryoVEx field party, dug out and cleaned of snow and ice.

Fig. 5.11: Ground campaign organised by DLR scientists at the Austfonna ice cap; Left airview from the aircraft; Upper right: base station of the DLR scientist Oxford; Lower right: corner reflector at the summit of the Austfonna ice cap.

During the March measurement period, a DGPS base station was located at the 'Depot'. In April, the NPI/UiO field party the main base camp was at the ice cap and Trond Eiken was taken responsibility to operate the DGPS base station at the 'Summit'. Training was provided in Longyearbyen on 12-13 April 2007. A team of 8 persons were flown out to the base station at Oxford from where they travelled to the summit of the ice cap and installed there a camp (Figure 5.12).

Fig. 5.12: The CryoVEX team during the IceSAR campaign in April. From left to right Jens Abbild – NPI, Jon Ove Hagen – Uni Oslo, Geir Mohold – Uni Svalbard, Irena Hajnsek – DLR (not part of the team), Trond Eiken – Uni Oslo, Liz Morris – SPRI, Thorben Dunse – AWI, Ola Brandt – NPI, Martin Hignell – BAS.

The position of the corner reflectors on the Austfonna ice cap and Etonbreen glacier area were defined with respect to near and far range distance and the north and south flights over the same test area. In order to save flight time each of the two test sites data acquisitions were made from north and south. According to the flight acquisition two corner reflector were positioned to north in near and far range with the preference to position them in the middle of a whole azimuth flight track and for the south data acquisition only one corner reflector were positioned in the middle in elevation and 2.5 km away from the north looking corner reflector in azimuth direction. In Figure 5.13 the position of the corner reflectors are dispayed for both test sites.

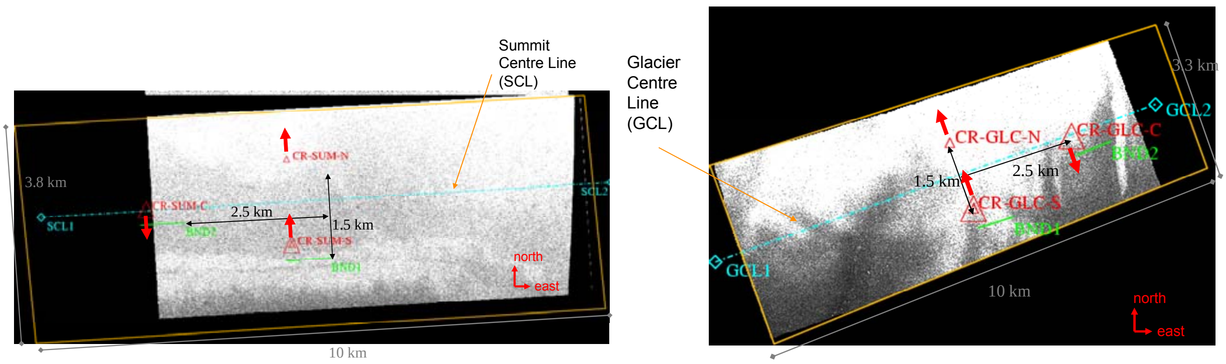

Fig. 5.13: Corner reflector position: left summit of the Austfonna cap, right Etonbreen glacier. Two corner reflectors looking north and one looking south.

6 SAR PROCESSING

This section describes the SAR processing applied to the data of the ICESAR campaign carried out in March and April 2007 on Svalbard. The test sites selected for data acquisition were described in section 3 and are summarized below:

Sea Ice (see indication on map):

- Storfjorden (SE of Spitzbergen island) (flight track length 150 km)
- Barentssea (NE) (flight track length 60 km)
- Framstrait (NW) (flight track length 50 km)

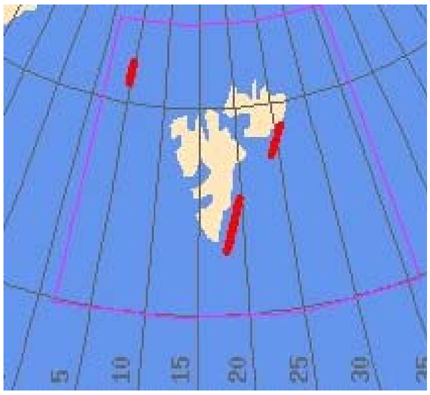

Land Ice:

- Summit area on Nordaustlandet (flight track length 15 km)
- Etonbreen glacier on Nordaustlandet (flight track length 15 km)

6.1 SAR Data Overview

An overview of the acquired E-SAR data and their correspondence to flight numbers (mission) is given in the table below. It indicates already the different type of processing applied to each type of data. Details on processing and selected processing parameters are given in the following sections.

	Mission	01	02	03	04	05	06	07	08	09	10	11	12	13	14	15	16	17	18	19	20
X-band Processing	Xvv XTI RGI	Testflight									x									x	
C-band Processing	Cvh/vv RGI		x	x	x	x										x		x			x
	Chv/hh RGI		x	x	x											x		x			x
	C synth.pol RGI															x		x			x
	C Sentinel Sim. RGI		x	x	x	x															
L-band Processing	Lpol RGI		x	x		x	x	x							x		x				
P-band Processing	Ppol RGI									x		x	x	x							
	Ppol Sounder								x										x		
Geocoding	Xvv XTI GTC										x									x	
	Cvh/vv GTC															x		x			x
	Chv/hh GTC															x		x			x
	C synth.pol GTC															x		x			x
	Lpol GTC						x	x							x		x				
	Ppol GTC									x		x	x	x							
Testsite:	Storfjorden		x																		
	Barentssea			x																	
	Framstrait				x	x															
	Glacier							x		x	x	x	x			x	x		x	x	x
	Summit						x		x	x	x			x	x			x		x	

Fig. 6.1: ICESAR data overview and associated processing.

6.2 E-SAR Processing Strategy

DLR-HR has defined different E-SAR data products to be able to serve the needs of different SAR data users and also to ease the data archiving. Therefore one distinguishes between RAW, RGI (radar geometry image) and GTC (geocoded terrain corrected) data. Usually, one obtains the image data (and auxiliary data) of one product type form the components of the preceding data type. This is summarized in the E-SAR data processing flow of Figure 6.2.

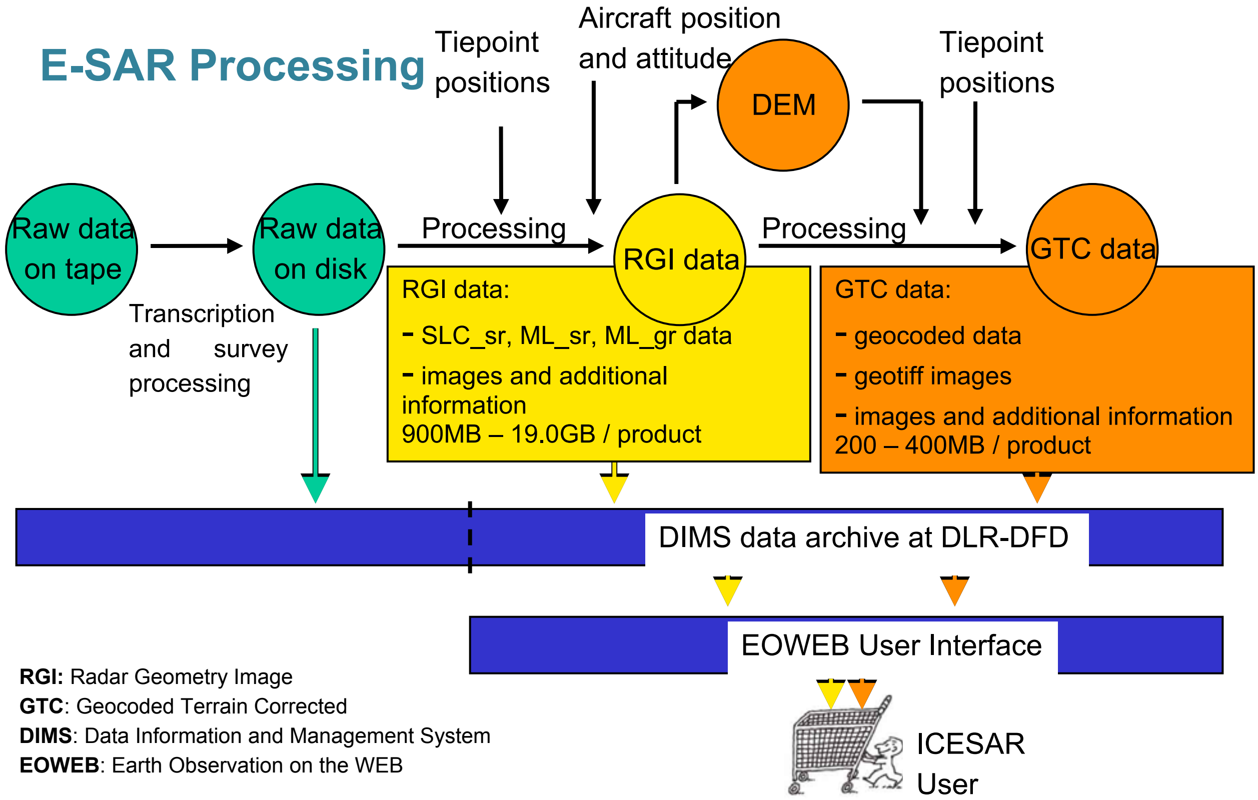

Fig. 6.2: E-SAR data processing overview.

DEMs are used as auxiliary data were applicable and can be generated also from RGI data acquired in X-band single-pass interferometric mode. Corner reflectors are used as geometric and radiometric calibration targets, if available. Repeat-pass interferometric data are generated and archived within a special RGI product component. They include resampled, co-registered SLC data to a common master, interferometric phase and coherence maps as well as track information. Details on individual file contents and format description are included in a special README-file for each product.

E-SAR data are archived within DIMS (Data Information and Management System of the German Remote Sensing Data Center, DLR-DFD). Access to users is granted via the EOWEB interface (http://taurus.caf.dlr.de:8080/servlets/template/welcome/entryPage.vm).

6.2.1 SAR Data Specification

The parameters selected for the regular processing of the ICESAR data are summarized in the Table 6.1 below:

Resolution	SLC image		Multilook image		
	slant range	azimuth	No. of looks (50% overlap)	slant range	azimuth
X-band	2.1m	0.6m	16	2.1m	5m
C-band	2.1m	0.7m	8	2.1m	3m
L- & P-band	2.1m	1.0m	8	2.1m	4.5m
Posting GTC	5m x 5m				
UTM zone	31: Framstrait, 33: Glacier, Summit, 34: Storfjorden, Barentssea				

Tab. 6.1: E-SAR data processing parameters for ICESAR.

For the Etonbreen Glacier and Summit data the UTM zone is used to generate the DEM and geocode the data (GTC product), whereas for the sea ice testsites it is used to perform the segmentation.

6.3 Processing of Sea Ice Data Takes

Sea ice data takes were acquired on 4 E-SAR flights (see table below).

Flight no.	Test site	Freq.-bands & polarisations of individual data takes	Date of acquisition	No of segments for processing
02	Storfjorden	C-VH/VV, L-PM, C-HV/HH	15.03.07	9
03	Barentssea	C-VH/VV, L-PM, C-HV/HH	18.03.07	8
04	Framstrait	C-VH/VV, L-PM	19.03.07	4
05	Framstrait	C-VH/VV, L-PM	20.03.07	5

The processing was performed for each segment separately to generate output products of limited data size of 15 km length, which ensures better selection of the reference track for motion compensation and to account for the variation of the Doppler centroid along the flight path. Nevertheless, the full strips were processed also as single data set. They may be used for browsing the areas of interest, but should not be used for quantitative data analysis.

6.3.1 Segmentation of Long Data Takes

The segmentation is performed according to predefined geographic areas. In this way, data acquired on subsequent tracks, some of them also in opposite directions, will be assigned to the same segment. This allows for finding the correspondence to AWI sensor data which were also acquired during ICESAR along the same tracks.

In the following we present examples of data acquired in C- and L-band for the three different acquisition areas. An overlap of about 500m between adjacent segments ensures that there is no gap between them.

Test site: Strofjorden

Fig. 6.3: Segments for processing Storfjorden data takes (E-SAR flight icesar02)

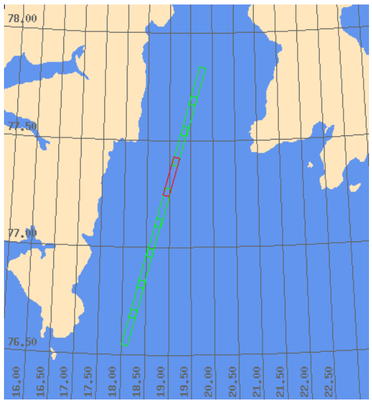

The segments for Storfjorden data takes are shown in the Figure 6.3 above. The polarimetric composite images for C- and L-band are presented in the Figure 6.4 below for the 4-th segment (numbered from North to South). Near range is on the top for C-band and on the bottom for L-band.

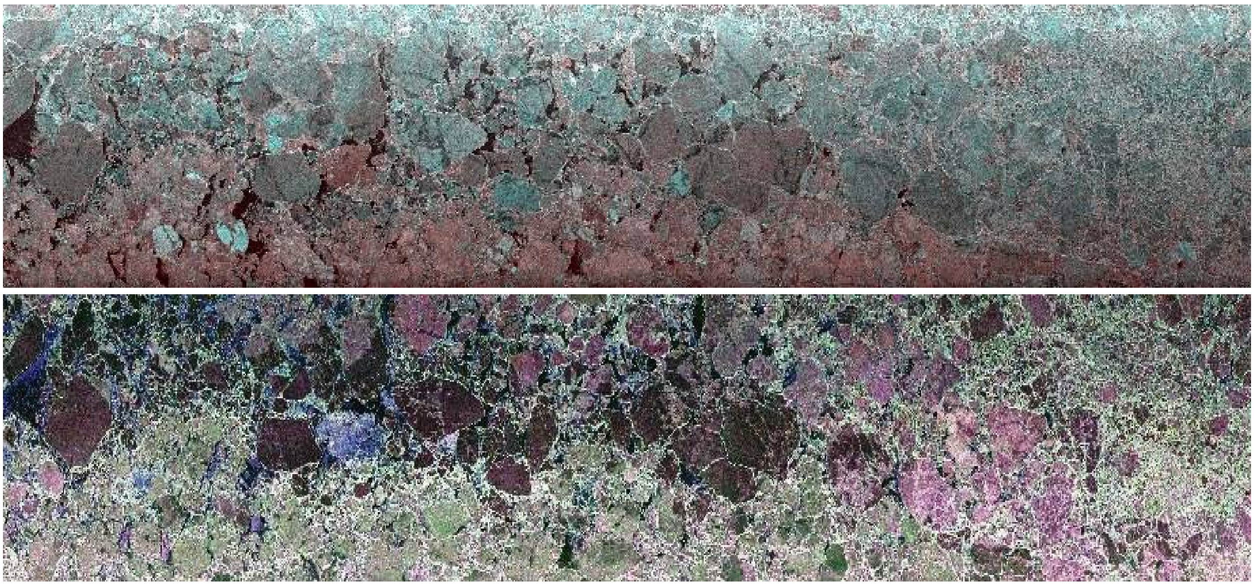

Fig. 6.4: Storfjorden polarimetric data corresponding to segment t04. C-band (top, sceneID=0203, RGB=HV-HH-HH) and L-band (bottom, scene_id=0202, RGB=HH-HV-VV). Scene dimension is 15km by 3km.

Test Site: Barentssea

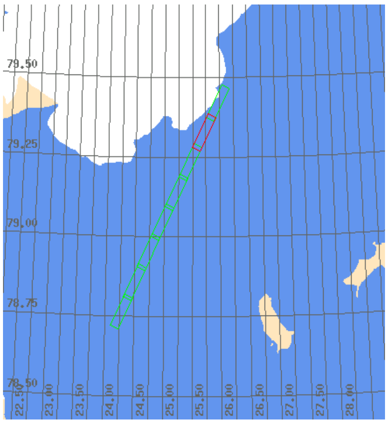

Fig. 6.5: Segments for processing Barentssea data takes (E-SAR flight icesar03)

The segments for Barentssea data takes are shown in the Figure 6.5 above. The polarimetric composite images for C- and L-band are presented in the Figure 6.6 below for the 7-th segment (numbered from South to North). Near range is on the top for C-band and on the bottom for L-band.

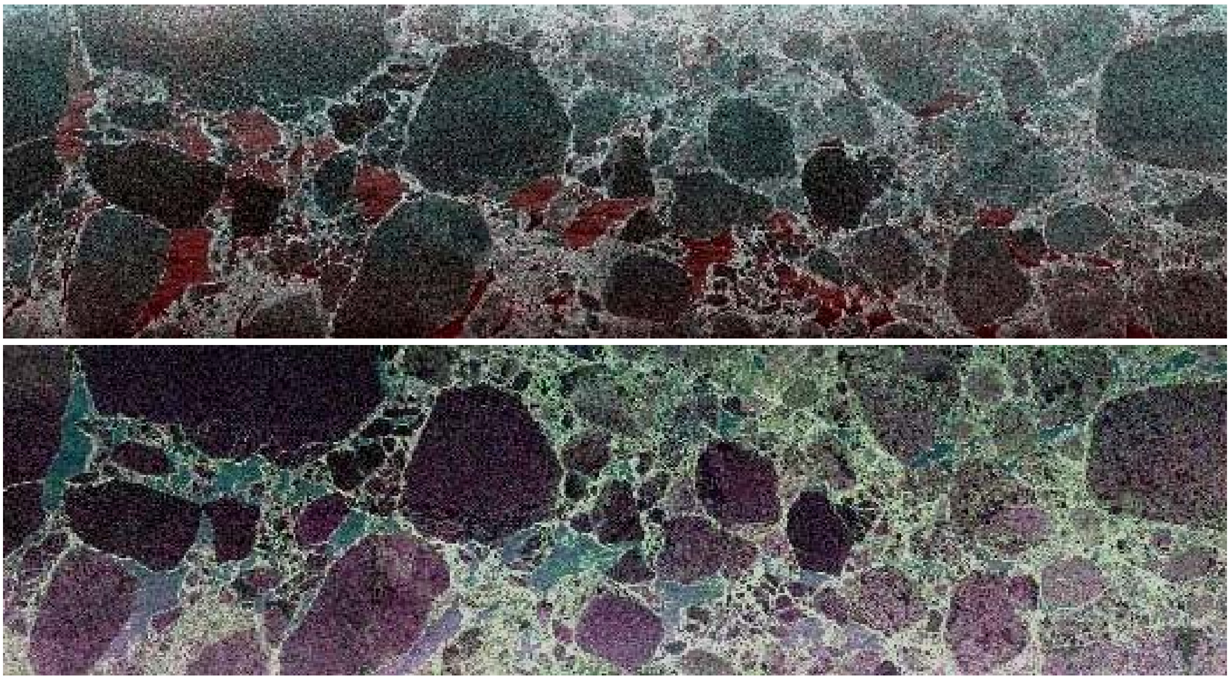

Fig. 6.6: Barentssea polarimetric data corresponding to segment t07. C-band (top, sceneID=0303, RGB=HV-HH-HH) and L-band (bottom, scene_id=0302, RGB=HH-HV-VV). Scene dimension is 10km by 3km.

Test Site: Framstrait

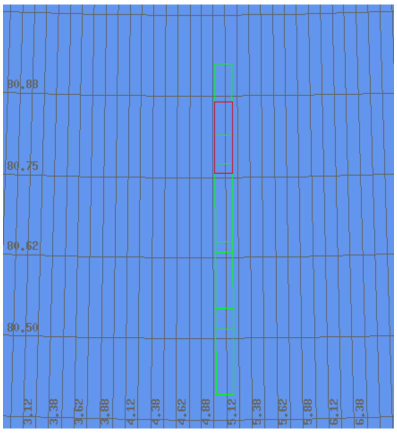

Fig. 6.7: Segments for processing Framstrait data takes (E-SAR flights icesar04 and icesar05)

The segments for Framstrait data takes are shown in the Figure 6.7 above. The polarimetric composite images for C- and L-band are presented in the Figure 6.8 below for the 4-th segment (numbered from South to North). Near range is on the top for C-band and on the bottom for L-band.

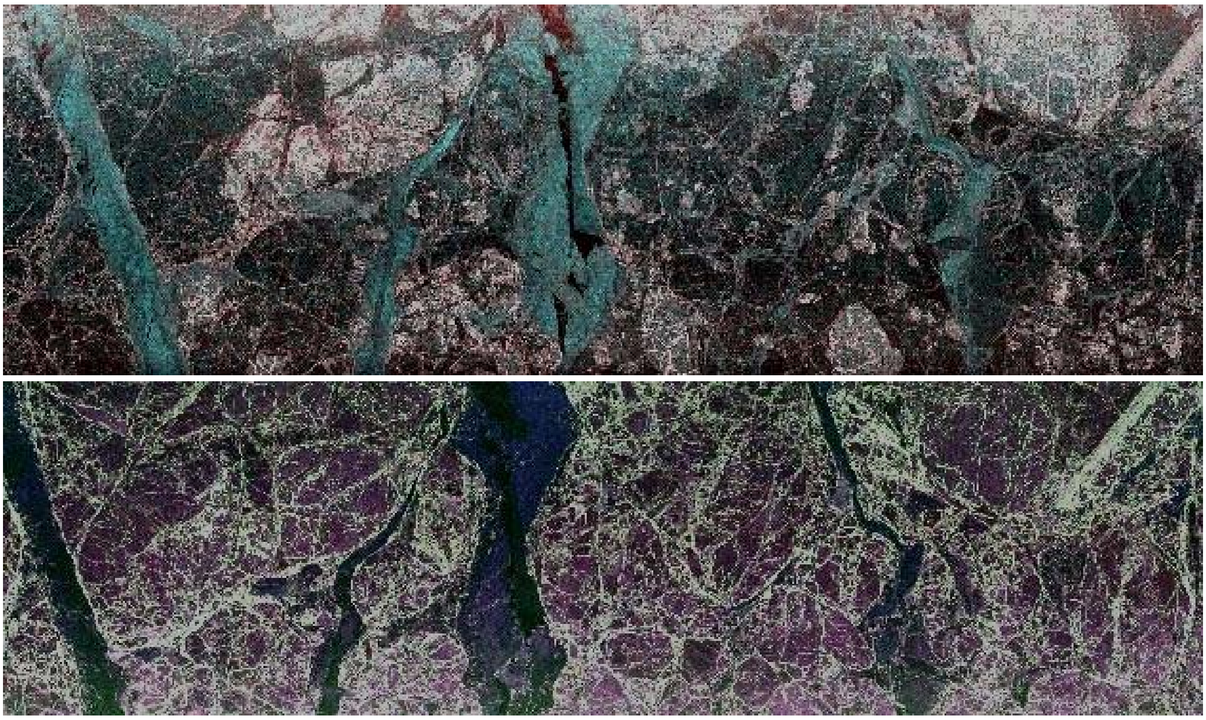

Fig. 6.8: Framstrait polarimetric data corresponding to segment t04. C-band (top, sceneID=0501, RGB=VH-VV-VV) and L-band (bottom, scene_id=0502, RGB=HH-HV-VV). Scene dimension is 10km by 3km.

6.3.2 Sentinel-1 Simulation

A limited amount of data sets have been processed also with degraded resolution and with enhanced noise level anticipating the data quality of future Sentinel-1 IWS mode data. The degradation was performed using the following parameters:

- azimuth resolution: 20 m
- range resolution: 5m
- number of looks: 1
- noise equivalent sigma zero (NESZ): -22dB
- distributed signal to ambiguity ratio (DTAR): 20dB

The following segments have been processed as Sentinel-1 simulation (all data VH-VV polarisation):

- Storfjorden, SceneID 0201, segment 3, try/revision number 13
- Barentssea, SceneID 0301, segment 7, try/revision number 17
- Framstrait, SceneID 0401, segment 02, try/revision number 12
- Framstrait, SceneID 0501, completes scene, try/revision number 20

A comparison of full resolution E-SAR images (2-3m resolution) and Sentinel IWS simulation is shown in the Figures 6.9 - 6.11. For the displayed IWS images a multilooking of 4 has been applied to the range direction for Speckle reduction purposes.

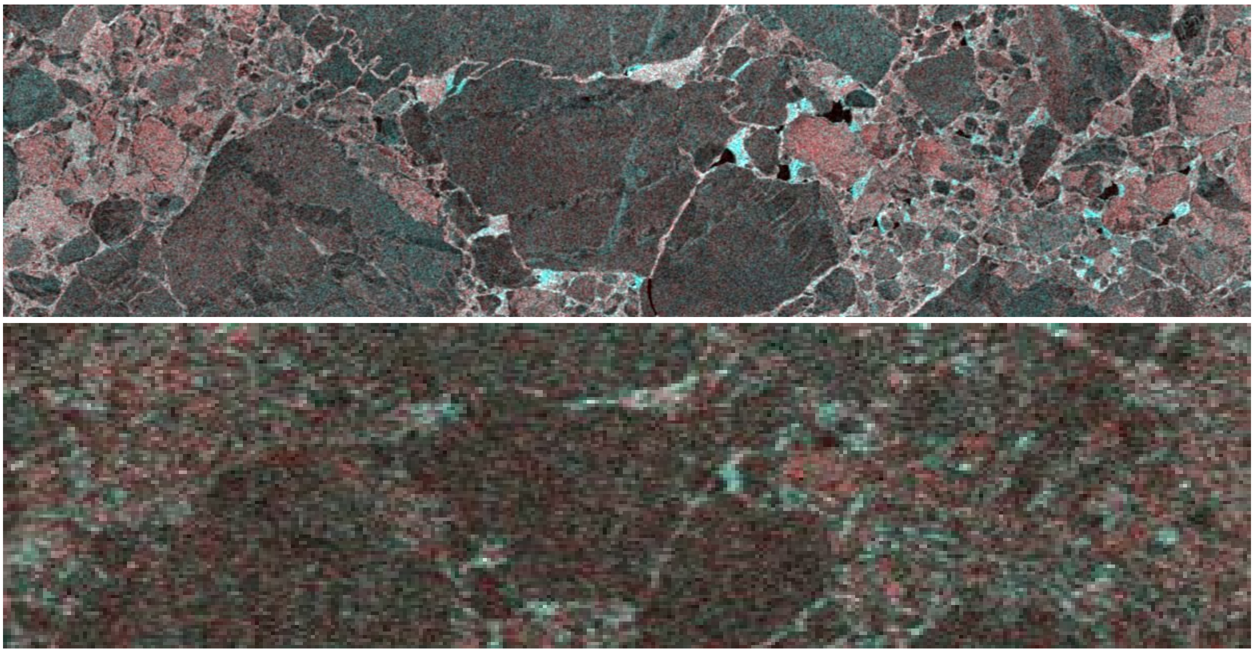

Fig. 6.9: Storfjorden polarimetric data corresponding to segment t04. C-band (top, sceneID=0201, RGB=VH-VV-VV) and C-band Sentinel-1 IWS simulation (bottom, sceneID=0201, RGB=HH-HV-VV). Scene dimension is 15km by 3km.

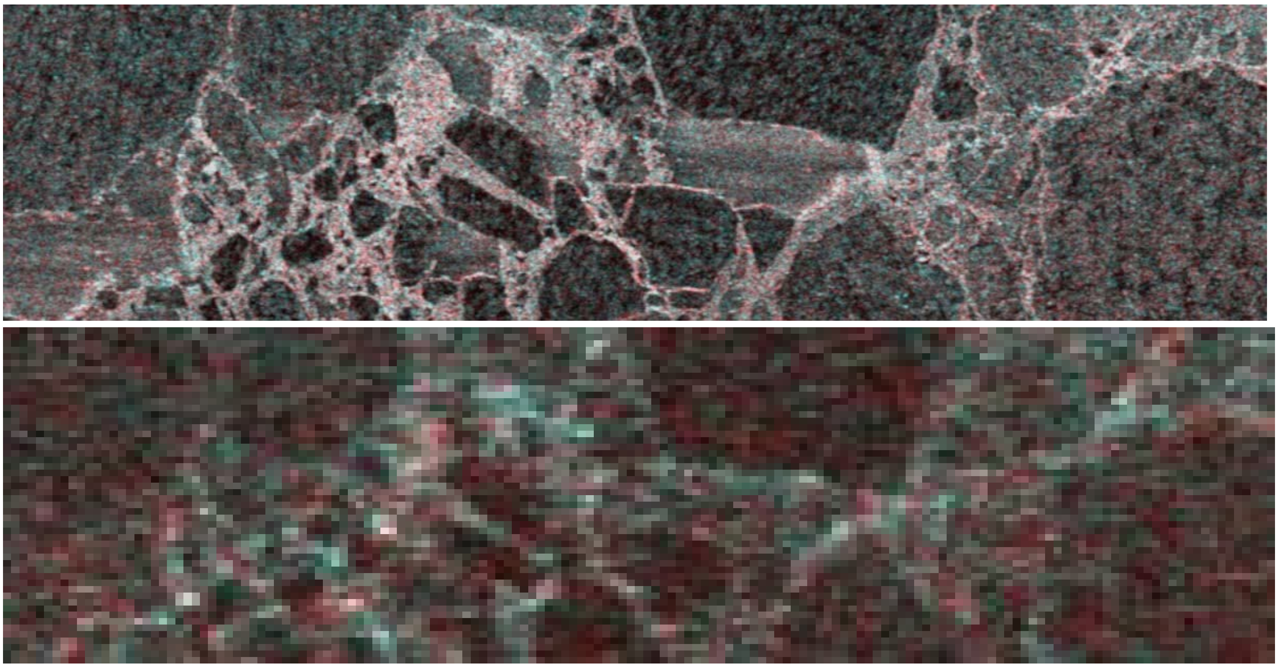

Fig. 6.10: Barentssea polarimetric data corresponding to segment t04. C-band (top, sceneID=0201, RGB=VH-VV-VV) and C-band Sentinel-1 IWS simulation (bottom, sceneID=0201, RGB=HH-HV-VV). Scene dimension is 15km by 3km.

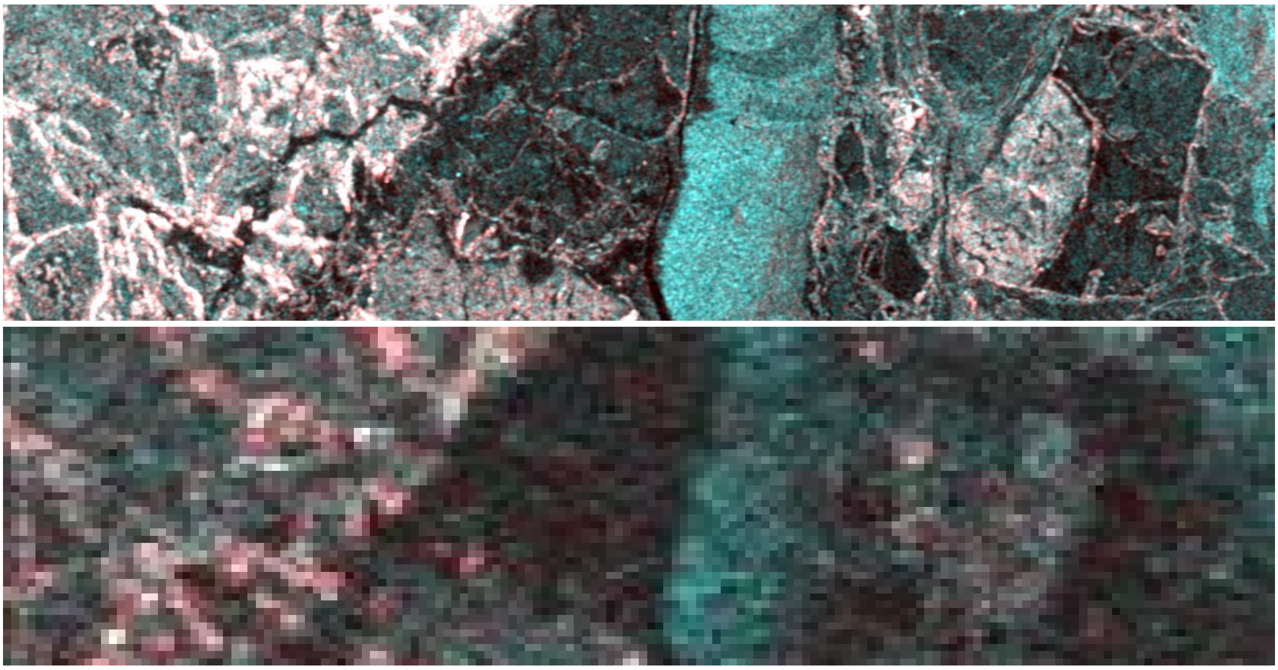

Fig. 6.11: Barentssea polarimetric data corresponding to segment t04. C-band (top, sceneID=0201, RGB=VH-VV-VV) and C-band Sentinel-1 IWS simulation (bottom, sceneID=0201, RGB=HH-HV-VV). Scene dimension is 15km by 3km.

Further Sentinel-1 simulations and evaluation of these data for ice type classification has been perfomed by AWI (see part 1 of ICESAR final report). There are small differenes of the simulations performed by AWI and those shown here, which can be summarized as follows:

- slant range resolution constant (DLR), ground range resolution constant (AWI).
- constant noise floor in SLC image (i.e. noise constant for backscatter β^0, range dependent for σ^0 and γ^0) (DLR), constant noise floor for σ^0 images (i.e. range dependent for β^0 and γ^0)(AWI).

AWI investigations revealed partly reduced classification possibilities mainly because of the increased noise floor of the Sentinel-1 IWS product (see part 1 of ICESAR final report).

6.3.3 Sea Ice Drift Effects in Repeat Pass Tracks

The E-SAR data covering the sea ice test sites have not been geocoded (map projection, oriented towards north), as there will not be much benefit. This is due to the sea ice drift which avoids individual features to overlap because of the time interval between the different acquisitions, which causes mis-registration. This is also the reason to fail, for any attempt to perform repeat-pass interferometry. Instead relative displacements could be found by feature tracking or for small displacements by cross-correlations of small patches (has not been attempted). An example of sea ice drift is shown in Figure 6.12 for two successive data sets. The time interval between the acquisitions is 25 min and the measured relative displacement is in the order of 400m. (The two data sets were acquired from opposite flight directions.)

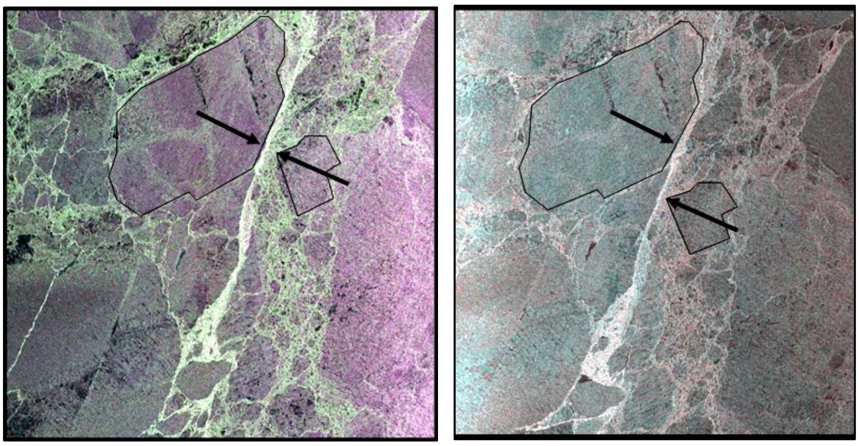

Fig. 6.12: Feature tracking of sea ice drift. Polarimetric L-band image (left, sceneID 0302 t04) acquired 25 minutes before the C-band image (right, sceneID 0303 t04).

6.3.4 Sea Ice Data Quality Checks

The radiometric quality has been also assessed based on the post campaign calibration flight of the E-SAR system performed on May, 16, after the equipment was returned to DLR facilities in Oberpfaffenhofen. For C-band a calibration offset of +2 dB has been found for VV polarisation (and 1 dB for the cross-polarisations) whereas precise calibration was confirmed for C-HH and L-band data. As pre campaign calibration indicated nominal calibration constants, there remains an uncertainty for the C-band radiometric accuracy in the ICESAR C-VV, C-VH/HV data.

Inspection of the processed data revealed some antenna calibration inaccuracies in the near near range of Storfjorden data takes (C-band, 0201 & 0203). These are attributed to high squint & motion errors. Attempts to better correct the antenna pattern failed.

Finally, a naming convention violation should be mentioned. The Storfjorden data take 0201 (7 segments) is shorter than 0202 and 0203 data takes (9 segments). Segment x (in data take 0201) corresponds to segment x+2 (in 0202 and 0203) data takes.

6.4 Processing of Land Ice Data Takes

Dependent on the frequency band, different processing had to be performed to E-SAR data acquired on Nordaustlandet for the two campaigns in March and April 2007. First X-band data were processed to generate digital elevation models (DEMs) for the two test sites Summit and Etonbreen Glacier. For this purpose the precise positions of Corner reflectors have been computed using static differential GPS measurements of the reference station Oxford the measurements performed by the ground team on top of the glacier.

The coordinates of the deployed corner reflectors are summarized in Table 6.2.

Corner reflectors on SUMMIT test site:

CR name	pointing	elevation	leg length	Longitude	Latitude	Ell. height
CR-SUM-S	2	10	150,00	N 79° 49' 32,4337"	E 24° 13' 55,6999"	812,080
CR-SUM-C	182	15	150,00	N 79° 49' 56,3876"	E 24° 06' 16,3240"	804,240
CR-SUM-N	2	20	90,00	N 79° 50' 20,5983"	E 24° 13' 56,9776"	802,670

Corner reflectors on Etonbreen GLACIER test site:

CR name	pointing	elevation	Leg length	Longitude	Latitude	Ell. height
CR-GLC-S	340	10	150,00	N 79° 46' 26,1867"	E 23° 04' 36,3001"	646,660
CR-GLC-C	160	15	150,00	N 79° 47' 13,8700"	E 23° 11' 08,4510"	680,900
CR-GLC-N	340	20	90,00	N 79° 47' 12,0868"	E 23° 03' 13,3906"	646,260

6.4.1 X-band Processing for DEM Generation

DEMs were processed from single-pass interferometric data in X-band. For this purpose, the data acquired from opposite look directions were used for interferometric processing followed by a mosaicking step, which overlayed the two scenes to enhance spatial coverage and reduce phase noise.

Figure 6.13 presents the DEM for the Etonbreen Glacier testsite which includes the assessment of the final height errors at the position of the corner reflectors, which is found to be 1-2m. A considerable slope is noted along the azimuth direction of the image. Some border effects are notred at the edges of the imaged swath. For this purpose the data takes 1005 (looking from south) and 1006 (looking from North) were used, both acquired in full baseline mode on March, 23 during the first campaign.

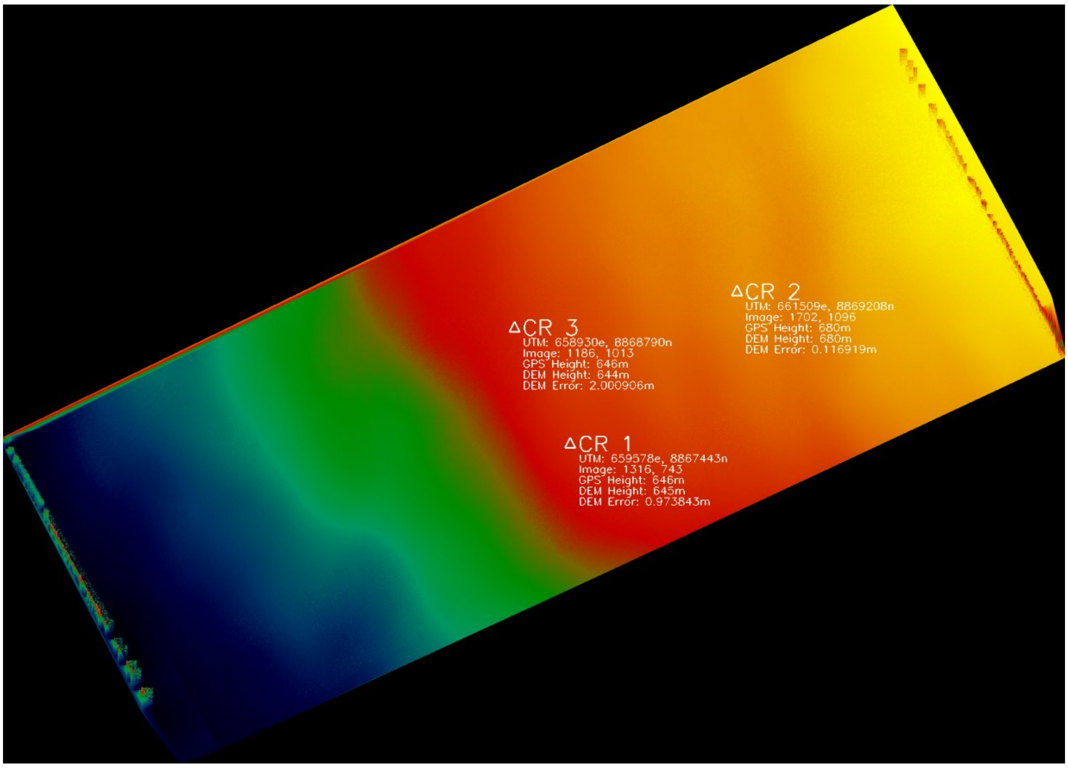

Fig. 6.13: DEM of Etonbreen glacier test-site (grid dimensions 12km by 9km).

Figure 6.14 presents the DEM for the Summit testsite which also includes the assessment of the final height errors at the position of the corner reflectors. It is found to be in the order of 1m for CR1 and CR2, but for CR3 a considerable bias of 5m is found. This is due to an approximately linear bias along the range dimension, which unfortunately could not be calibrated. The reason is the lack of visibility of CR3 in the data. Therefore only one CR was used for phase offset estimation. Mosaicking effects are noted in areas where the test-site is covered by only one observation. For this DEM the data takes 1002 (looking from south) and 1001 (looking from North) were used, both acquired in full baseline mode on March, 23 during the first campaign.

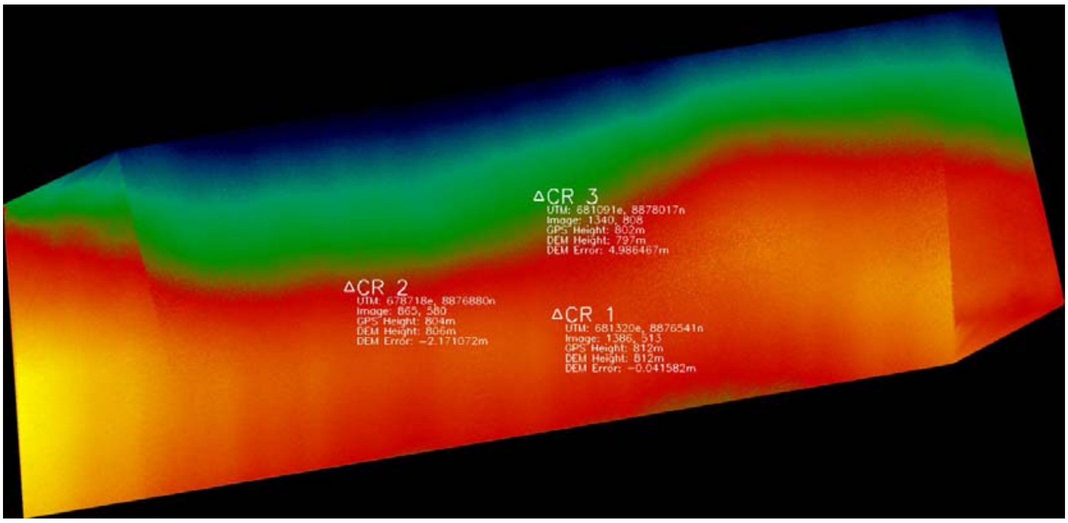

Fig. 6.14: DEM of Summit test-site (grid dimensions 13km by 6km).

Both DEMs were used for the subsequent processing of repeat-pass interferometric data in L-, P-, and C-band. In addition, all other X-band data were also processed as single-pass interferometric pairs, providing coherence information for two different spatial baselines.

Finally, for each acquisition the image data are also geocoded to allow the comparison with ground measurements. X-band data of the April campaign (mission 19) could not be processed successfully because of strong squint and motion errors.

6.4.2 Corner Reflector Analysis

Six corner reflectors were mounted in the test sites, three in the Etonbreen Glacier test site and three in the Summit test site. For each test site in one look direction one reflector with 1,50 m edge length was mounted, whereas in the other look direction one 1,50 m reflector and one 90 cm reflector were installed.

Tables of the corner reflector analysis results can be found in the appendix of this document. For each data set and each visible reflector the resolutions in range and azimuth, the difference between theoretical and observed RCS and the signal to background ratio can be seen in hh and vv polarisation. For the polarimetric data sets, the cannel amplitude and phase imbalance is shown. The sceneID of master scenes is written in bold. For X- and C-band multilook amplitude data have been checked while for the polarimetric L- and P-band the complex SLC data were used. Therefore the observed resolution in L- and P-band is higher than in X- and C-band.

In the following the main information content of the tables is summarised:

Test site Etonbreen Glacier, look direction North:

- CR 3 is a small 90cm reflector and has a very low signal to background ratio. Therefore it can not be used for L- and P-band.
- For C- and X-band the strong reflection from snow leads to a low signal to background ratio. The RCS evaluation provided strongly biased and thus non reliable results.
- L-Band data of April (Mission 16) show a very low signal when processed as a temporal repeat pass scene with master 0701_t01. This is due to about 10 degrees difference in the squint angle between mission 07 and mission 16.
  When it is processed with master 1601_t01 of the same flight, the ΔRCS is about 8-10dB, similar to the March data (Mission 7). This deviation is attributed to the non ideal properties of the foldable corner reflector. The April L-band data processed as t02 should not be used for radiometric analyis.
- CR 1 is below the expected RCS value also in the March data. In X-band the difference is about 3dBm^2, in L-band 8-10dBm^2, and in P-band 1-3dBm^2.
- The polarimetric behaviour of CR1 shows +/- 1dB amplitude imbalance and +/-15° phase imbalance for L-band t01 data. In P-band the amplitude imbalance is about +/- 3dB and the phase imbalance can be as high as 35°. These less accurate values are attributed to coarse accuracy for the relative small size of 1,50m of the corner reflector. The temporal interferometric L-band slaves 12xx_t02 show a slight degradation in phase imbalance whereas in P-band the temporal baseline doesn't affect the polarimetric calibration.

Test site Etonbreen Glacier, look direction South:

- For C- and X-band the strong reflection from snow leads to low signal to background ratio. The RCS evaluation provided strongly biased and thus non reliable results.
- In contrast to the data of look direction North the April P-band data (mission 12) show the same ΔRCS as the March (mission 11) data. The orientation of the corner reflector seems to be unchanged. In average the observed RCS is about 5dBm^2 lower than the theoretical value. This can be explained by imperfections of the foldable reflector and presence of snow and ice inside the reflector.
- The polarimetric behaviour of CR1 shows +/- 1dB amplitude imbalance and +/-15° phase imbalance for L- and P-band data, when processed as interferometric as well as temporal interferometric data.

Test site Summit, look direction North:

- CR 3 is a small 90cm reflector and has a very low signal to background ratio. Therefore it can not be used for L- and P-band.
- For X-band the strong reflection from snow leads to a low signal to background ratio. Thus the RCS could not be checked. In C-Band the signal to background ratio is much higher than at the Etonbreen Glacier test site so that at least CR 1 is usable. The C-band the RCS is approx. 5dBm^2 lower than the theoretical value.
- In L-band the ΔRCS is nearly 0 dBm^2 while in P-band the observed signal is about 5 dBm^2 lower than the theoretical value.
- The April data are of the same quality as the March data. The reflectors seem to be untouched.
- Temporal processing of the L- and P-band data has no negative effect on the quality of the corner reflector signals. The squint angles of the March and April data are more or less similar.
- The polarimetric behaviour of CR1 shows +/- 1dB amplitude imbalance and +/-10° phase imbalance for L-band t01 data. In P-band the amplitude imbalance is about +/- 2dB and the phase imbalance about 35°. The temporal interferometric L-band slaves 14xx_t02 show a slight degradation in amplitude and phase imbalance whereas in P-band the temporal baseline doesn't affect the polarimetric calibration.

Test site Summit, look direction South:

- For C- and X-band the strong reflection from snow leads to a very low signal to background ratio. Thus the RCS could not be checked.
- In L-band the ΔRCS is about 3 dBm^2, in P-band about 5 dBm^2.
- The April data are of the same quality as the March data. The reflectors seem to be untouched.
- Temporal processing of the L- and P-band data has no negative effect on the quality of the corner reflector signals. The squint angles of the March and April data are more or less similar.
- The polarimetric behaviour of CR1 shows +/- 1dB amplitude imbalance and +/-10° phase imbalance for L- and P- band t01 data. The temporal interferometric L-band slaves 14xx_t02 show a slight degradation in phase imbalance whereas in P-band the temporal baseline doesn't affect the polarimetric calibration.

Although not every corner reflector provided useful information, it can be conclude from their evaluation:

- The E-SAR system was stable throughout the acquisitions allowing to acquire data of comparable quality for the March and April missions. A drawback is the different squint for Etonbreen glacier during L-band data takes.

- The polarimetric calibration quality could be shown to be very good, both in L- and P-band.
- The strong background reflection from snow together with the relatively small size of the corner reflectors, does not allow concluding for the absolute radiometric calibration accuracy, especially for X- and C-band. However, the system was calibrated before the campaign at DLR premises and radiometric accuracy was found within specifications (+/-2dB).

6.4.3 Repeat-Pass InSAR Processing

The repeat-pass interferometric processing was conducted with a single Master for all data takes from the same look direction.

The particularities of the E-SAR repeat-pass processing can be summarized as follows:

- topography dependent motion compensation
- estimation and correction of residual motion errors
- RFI filter for P-band
- Generation of quad-pol data products at C-band from 2 complementary dual-pol data.

The following tables summarize which were selected as Master or Slave. If available, a general Master was selected from the March campaign:

Test-Site	Sensor look Direction	Freq-Band	Master – SceneIDs	Slave – SceneIDs	Comment
Glacier	S	L	1602	1604,1606,1608	None in March
Glacier	S	P	1101	1103,1105,1107, 1202*,1204*,1206*,1208*	-
			1202	1204,1206,1208	
Glacier	S	C	1502	1504,1506,1508, 2002*,2004*,2006*	None in March (∗) ΔSquint of 5deg
			2002	2004,2006	
Glacier	N	L	0701	0702,0703,0704, 1601*,1603*,1605*,1607*, 1609*	(∗) ΔSquint of 10deg wrt: 0701
			1601	1603,1605,1607,1609	
Glacier	N	P	1102	1104,1106,1108,0909 1201*,1203*,1205*,1207*, 1209*	-
			1201	1203,1205,1207,1209	
Glacier	N	C	1501	1503,1505,1507 2001*,2003*,2005*	None in March (∗) ΔSquint of 5deg
			2001	2003,2005	

Test-Site	Sensor look Direction	Freq-Band	Master – SceneIDs	Slave – SceneIDs	Comment
Summit	S	L	0602	0604,0606,0608, 1401*,1403*,1405*,1407*	-
			1401	1403,1405,1407	
Summit	S	P	0901	0903,0905,0907, 1303*,1305*,1307*	1301 corrupt
			1307	1303,1305	
Summit	S	C	1701	1703,1705,1707	None in March
Summit	N	L	0601	0603,0605,0607,0609, 1402*,1404*,1406*,1408*	-
			1402	1404,1406,1408	
Summit	N	P	0902	0904,0906,0908, 1302*,1304*	-
			1302	1304, 1306, 1308	
Summit	N	C	1702	1704,1706,1708	None in March

As the environmental conditions in arctic regions change very fast, it cannot be assumed that data acquisition on different days is performed with similar squint angles and forward velocity of the aircraft. Therefore dedicated Master scenes have been selected for processing the April acquisitions. These are also included in the tables. Note that all Master scenes come with the “t01” revision number.

For the slave scenes, revision numbers “t01” have been selected in case the associated master is from the same flight period and “t02” if the slave acquisition is from April but the Master from March.

All master scenes were finally geocoded onto the DEM grid computed from X-band data. In the following some image results are presented for the different frequency bands as well as some specific remarks.

6.4.4 Processing Quality for the Austfona Ice Cap

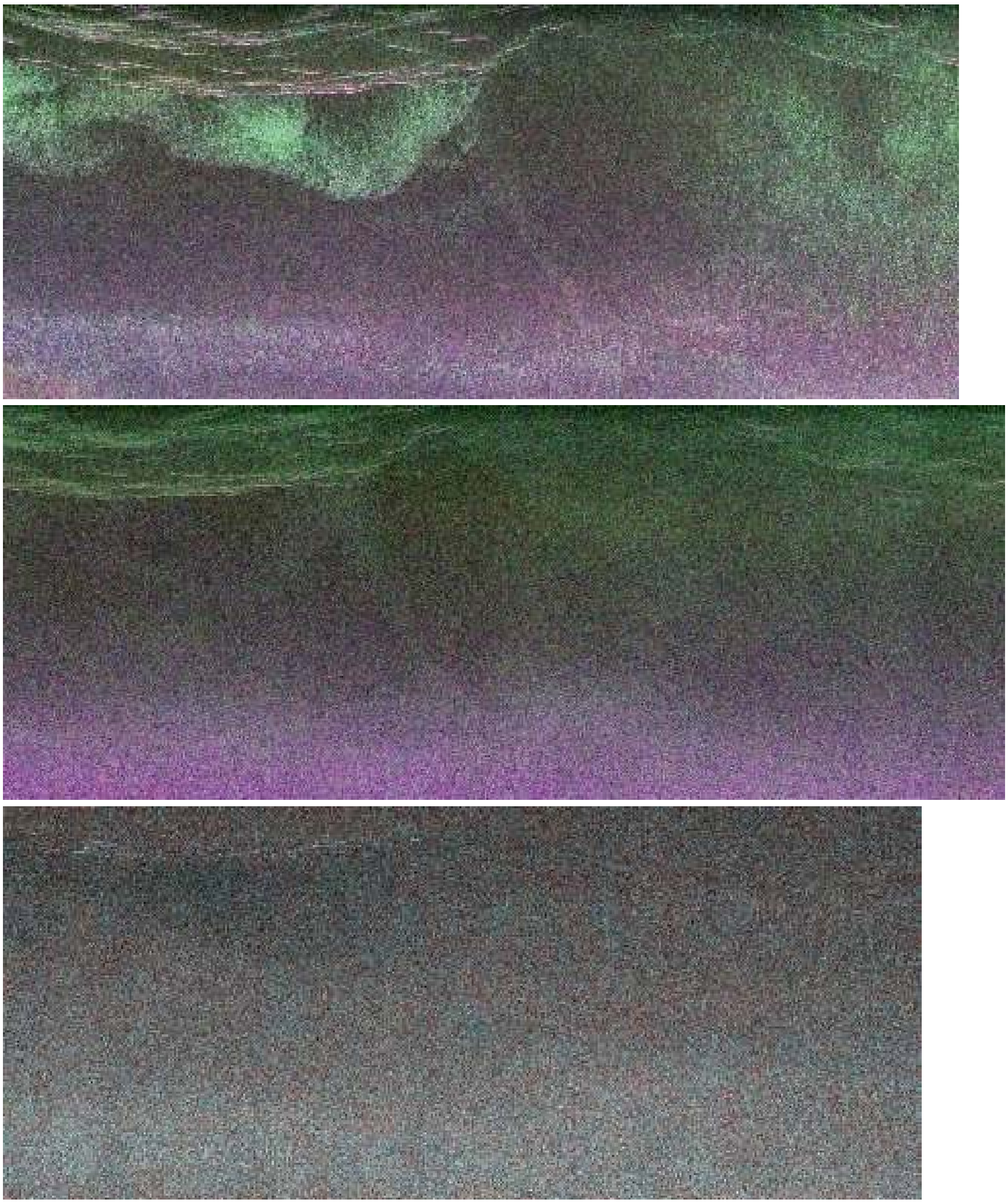

Fig. 6.15: Polarimetric images for Summit test site acquired during ICESAR campaign: P-band (top, sceneID=1303, RGB=HH-HV-VV), L-band (middle, sceneID=0604, RGB=HH-HV-VV), and C-band (bottom, sceneID=1703, RGB=VH-VV-VV). Flight direction is from top.

From the comparison of the three different frequencies, it is obvious that the ice surface presents itself quite homogeneous for small wavelength (C-band) but volume structures can be identified already at L-band and much better in P-band.

Some processing related remarks:

C-band:

- Synthetic quad-pol data products have been generated (sceneID 1741 from S and 1742 from N). (Not displayed here).

L-band:

- The processing of the April slaves (sceneID 14xx) onto the March-Master (sceneID 0601 and 0602) was not fully successful in terms of residual motion error computation. Obvious residual errors can be noted in some of the repeat-pass interferometric phase images for these data sets. This is because residual motion error estimation is assuming good coherence in large parts of the image, which was not the case for L-band (see temporal coherence evaluations in Section 6.6.2).

P-band:

- Residual RFI is present in the HV (ch2) data. This can be noted in the range spectra.
- The +/-20m baseline data form the N direction (1306 and 1308) could not be processed because the data acquisition stopped too early.
- Also the data form sceneID 1301 (intended MASTER for April South) could not be processed. Instead 1307 was used as master and a 0m and 20m baseline are associated to it (sceneIDs 1305 and 1303).

The summary of the repeat-pass pairs with temporal baseline is given in the table below.

Testsite Summit													
Master	Slave	Pol. Master	Pol. Slave	Spatial baseline	Temporal baseline	Illuminated from	Average coh hh-hh	Average coh hv-hv	Average coh vv-vv	Average coh vh-vh	Average coh vv-hh	Average coh vh-hv	Remarks
C-band													
no temporal RP IF data at C-band													
L-band													
0601_t01	1402_t02	pol.	pol.	0 m	27 days	North	0.29	0.22	0.29	0.22	---	---	Low coherence
0601_t01	1404_t02	pol.	pol.	5 m	27 days	North	0.25	0.20	0.25	0.20	---	---	Low coherence
0601_t01	1406_t02	pol.	pol.	10 m	27 days	North	0.24	0.19	0.24	0.19	---	---	Low coherence
0601_t01	1408_t02	pol.	pol.	-10 m	27 days	North	0.32	0.27	0.31	0.27	---	---	Low coherence
0602_t01	1401_t02	pol.	pol.	0 m	27 days	South	0.28	0.21	0.28	0.21	---	---	Low coherence
0602_t01	1403_t02	pol.	pol.	7 m	27 days	South	0.14	0.14	0.14	0.14	---	---	Very low coherence
0602_t01	1405_t02	pol.	pol.	19 m	27 days	South	0.17	0.15	0.18	0.15	---	---	Very low coherence
0602_t01	1407_t02	pol.	pol.	-8m	27 days	South	0.23	0.19	0.22	0.19	---	---	Low coherence
P-band													
0902_t01	1302_t02	pol.	pol.	0 m	21 days	North	0.50	0.35	0.46	0.35	---	---	
0902_t01	1304_t02	pol.	pol.	10 m	21 days	North	0.47	0.31	0.43	0.31	---	---	
0902_t01	1306_t02	pol.	pol.	20 m	21 days	North	---	---	---	---	---	---	Insufficient coverage
0902_t01	1308_t02	pol.	pol.	-20 m	21 days	North	---	---	---	---	---	---	Insufficient coverage
0901_t01	1301_t02	pol.	pol.	0 m	21 days	South	---	---	---	---	---	---	Data corrupt
0901_t01	1303_t02	pol.	pol.	15 m	21 days	South	0.47	0.31	0.45	0.31	---	---	
0901_t01	1305_t02	pol.	pol.	35 m	21 days	South	0.41	0.25	0.39	0.25	---	---	
0901_t01	1307_t02	pol.	pol.	35 m	21 days	South	0.41	0.24	0.39	0.25	---	---	

6.4.5 Processing Quality for the Etonbreen Glacier

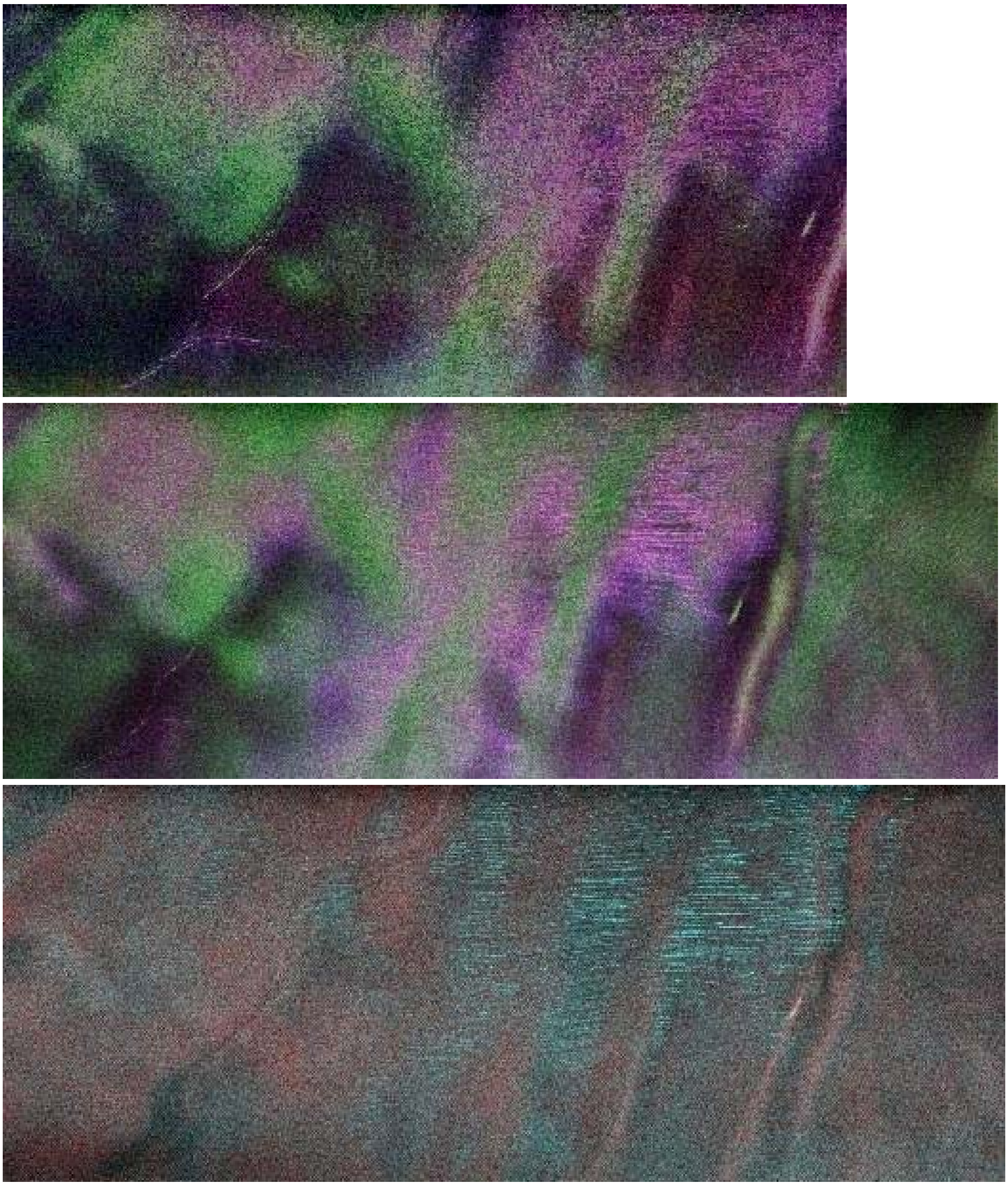

Fig. 6.16: Polarimetric images for Etonbreen Glacier test site acquired during ICESAR campaign: P-band (top, sceneID=1101, RGB=HH-HV-VV), L-band (middle, sceneID=1604 ,RGB=HH-HV-VV), and C-band (bottom, sceneID=1504, RGB=HV-HH-HH). Flight direction is from top.

When compared to Summit test site, the additional presence of ice surface features is C-band is the most prominent difference. Due to their orientation parallel to the flight track they become even more distinct than in L- and P-band.

Some processing related remarks:

C-band:

- Synthetic quad-pol data products have been generated (sceneID 1541, 1545, and 2041 from N and 1542, 1546 and 2042 from S). (see Figure 6.17 below)
- A discussion on the difficulties to apply repeas-pass processing to C-band data of land ice is found in the following subsections. The effects of temporal decorrelation are also discussed there.

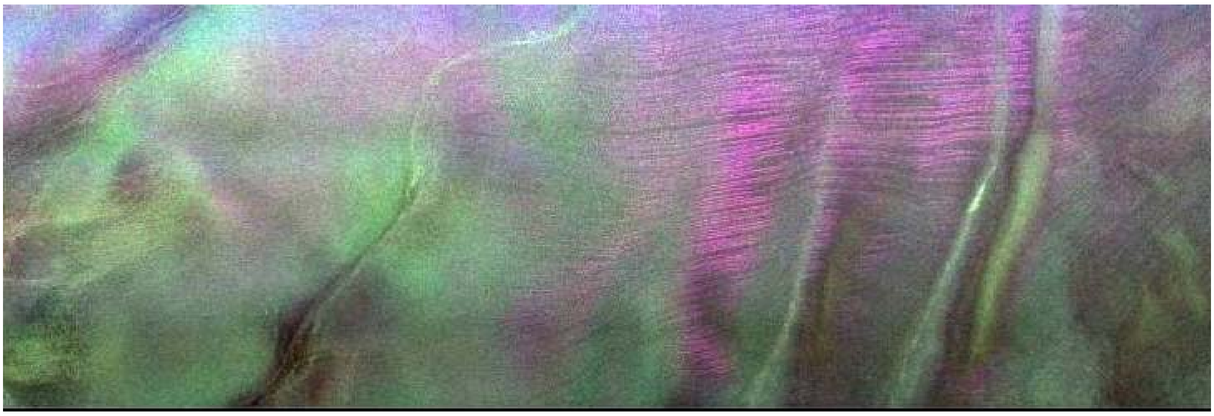

Fig. 6.17: Synthetic quad-pol image generated from two dual-polarized data sets (C-VH-VV and C-HV-HH). RGB=HH-HV-VV

L-band:

- same comment as for Summit test site

P-band:

- good temporal coherence behaviour. An evaluation is presented in the next subsection.

The summary of the repeat-pass pairs with temporal baseline is given in the table below.

Testsite Glacier													
Master	Slave	Pol. Master	Pol. Slave	Spatial baseline	Temporal baseline	Illuminated from	Average coh hh-hh	Average coh hv-hv	Average coh vv-vv	Average coh vh-vh	Average coh vv-hh	Average coh vh-hv	Remarks
C-band													
1501_t01	2001_t02	vh/vv	vh/vv	0 m	4 days	North	---	---	0.14	0.15	---	---	Very low coherence
1501_t01	2003_t02	vh/vv	hv/hh	0 m	4 days	North	---	---	---	---	0.14	0.14	Very low coherence
1501_t01	2005_t02	vh/vv	vh/vv	0 m	4 days	North	---	---	0.15	0.14	---	---	Very low coherence
1502_t01	2002_t02	vh/vv	vh/vv	0 m	4 days	South	---	---	0.18	0.16	---	---	Very low coherence
1502_t01	2004_t02	vh/vv	hv/hh	0 m	4 days	South	---	---	---	---	0.16	0.16	Very low coherence
1502_t01	2006_t02	vh/vv	vh/vv	0 m	4 days	South	---	---	0.17	0.15	---	---	Very low coherence
L-band													
0701_t01	1601_t02	pol.	pol.	0 m	27 days	North	0.23	0.19	0.25	0.19	---	---	Low coherence
0701_t01	1603_t02	pol.	pol.	5 m	27 days	North	0.19	0.16	0.19	0.16	---	---	Low coherence
0701_t01	1605_t02	pol.	pol.	10 m	27 days	North	0.18	0.16	0.18	0.16	---	---	Low coherence
0701_t01	1607_t02	pol.	pol.	-10 m	27 days	North	0.35	0.27	0.39	0.27	---	---	Low coherence
0701_t01	1609_t02	pol.	pol.	0 m	27 days	North	0.21	0.17	0.22	0.17	---	---	Low coherence
P-band													
1102_t01	0909_t02	pol.	pol.	0 m	1 day	North	0.38	0.25	0.40	0.26	---	---	SNR problem
1102_t01	1201_t02	pol.	pol.	0 m	20 days	North	0.73	0.52	0.74	0.54	---	---	
1102_t01	1203_t02	pol.	pol.	10 m	20 days	North	0.64	0.44	0.64	0.46	---	---	
1102_t01	1205_t02	pol.	pol.	20 m	20 days	North	0.49	0.34	0.50	0.35	---	---	
1102_t01	1207_t02	pol.	pol.	-20 m	20 days	North	0.59	0.40	0.59	0.41	---	---	
1102_t01	1209_t02	pol.	pol.	0 m	20 days	North	0.76	0.54	0.77	0.56	---	---	
1101_t01	1202_t02	pol.	pol.	0 m	20 days	South	0.78	0.59	0.79	0.60	---	---	
1101_t01	1204_t02	pol.	pol.	15 m	20 days	South	0.55	0.42	0.56	0.43	---	---	
1101_t01	1206_t02	pol.	pol.	25 m	20 days	South	0.51	0.40	0.52	0.41	---	---	
1101_t01	1208_t02	pol.	pol.	-20 m	20 days	South	0.63	0.48	0.63	0.49	---	---	

6.4.6 P-band temporal decorrelation assessment

The interferometric coherence is a good indicator for the temporal stability. However, coherence is also affected by volume scattering and by SNR decorrelation. As absolute coherence levels may be misleading, a comparative analysis is presented, which uses data acquired on the same day (1201,1203, and 1209) and compares coherence levels with data acquired 3 weeks before (1102).

The data sets summarized in the table below were used for this purpose. All data sets were flown on the Etonbreen glacier area of Nordaustlandet. Unfortunately, no data with nearly zero spatial baseline are available to exclude volume decorrelation.

Scene ID	Acquisition Date & Time	Mean effective baseline
07icesar1201x1	16-Apr-07 18:16:32	MASTER
07icesar1203x1	16-Apr-07 18:35:05	7m
07icesar1209x1	16-Apr-07 19:26:40	3m
07icesar1102x1	27-Mar-07 12:10:45	5m

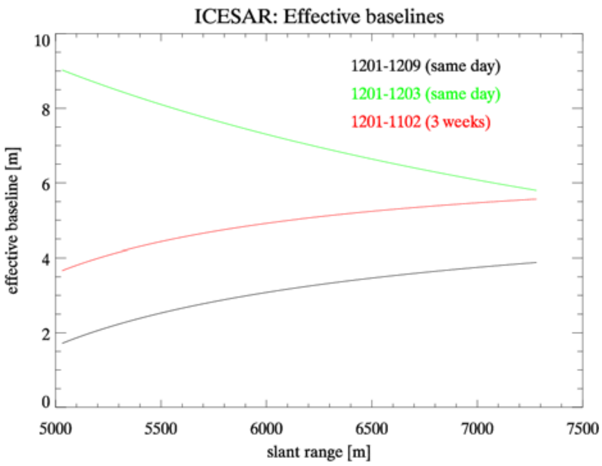

Figure 6-18: Effective baselines of P-band interferometric SAR data used for analysis of temporal decorrelation

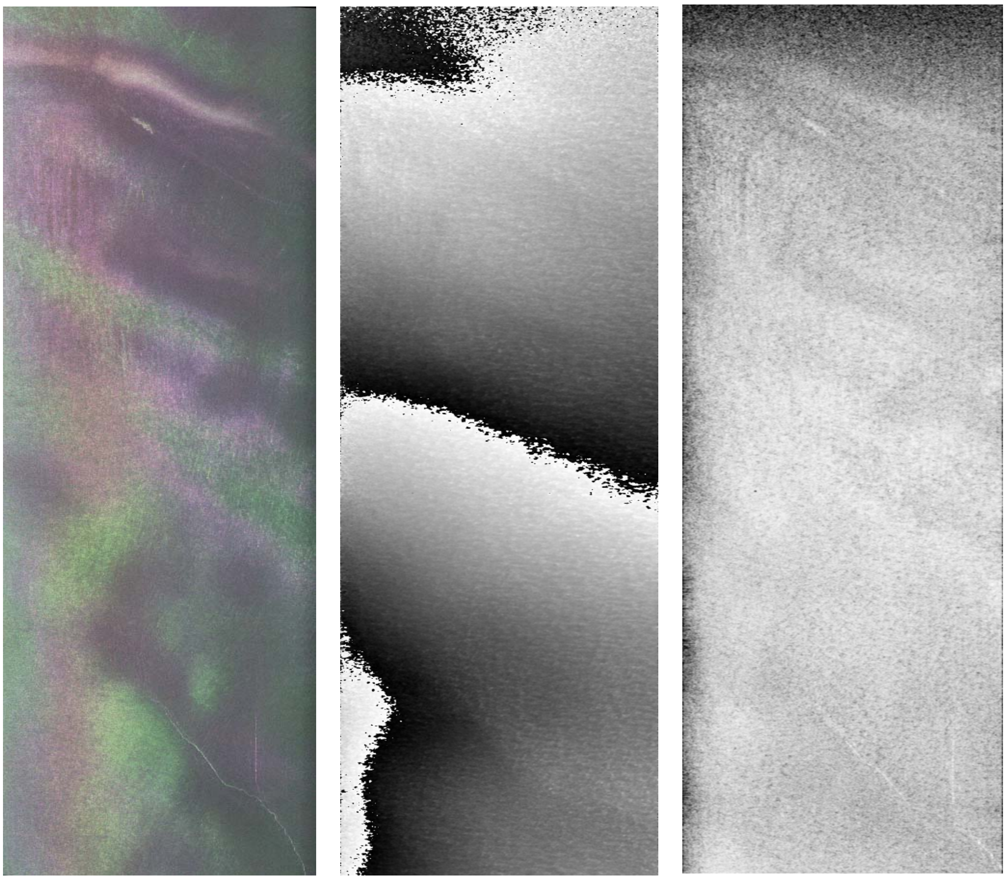

Figure 6-19: P-band interferometric SAR data acquired with 3 weeks temporal baseline. Polarimetric composite(left, RGB=HH-HV-VV), interferometric phase(middle), and coherence (right).

Figure 6-18 above presents the effective baseline as a function of the slant-range, which relates to incidence angles from 25-55 deg. Comparable effective baselines are only found for the far range of the 1201-1203 and 1201-1102 pairs. However, there is also a variation along azimuth due to the motion deviation from the nominal track. Therefore, this figure gives only a rough overview.

Figure 6-19 presents the polarimetric SAR image, which shows that the ice surface cannot be considered perfectly homogeneous. The interferometric phase and coherence correspond to the 3 weeks temporal baseline between the acquisitions 1201 and 1102. The first impression is that the coherence is quite high, but there is also a decorrelation component. However, it is not clear to which source of decorrelation it must be attributed to. Therefore, coherences of data acquired on the same day are also analysed. Their information is concentrated in the histograms of Figure 6-20. Only the far range region (range larger than 7000m) has been analysed.

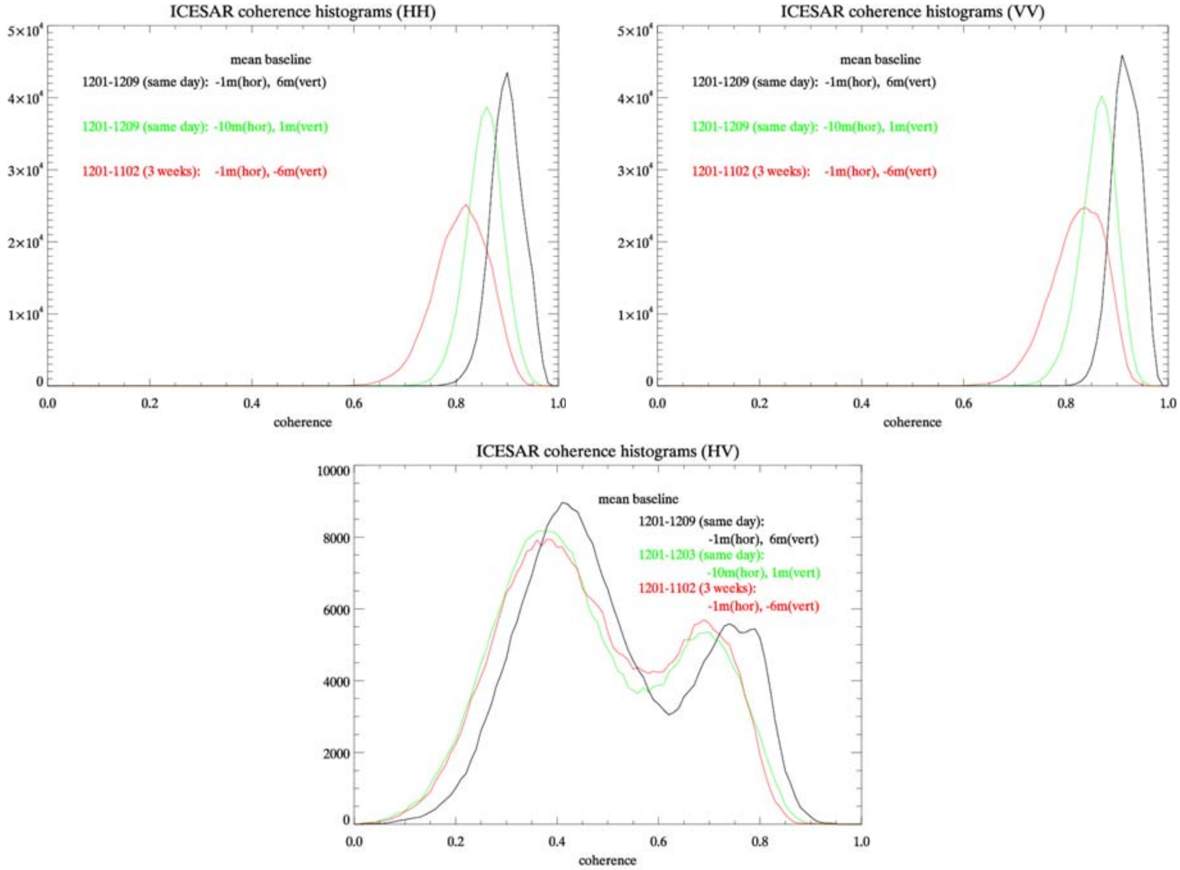

Figure 6-20: P-band coherence histograms for interferometric acquisitions on Nordaustlandet, Svalbard, 2007.

This analysis allows the following conclusions:

- The main decorrelation factor is due to volume scattering (baseline dependent decorrelation for same day acquisitions).
- Temporal decorrelation is present in the 1201-1102 pair, which leads to a coherence loss of ~0.05 compared to the same day baseline pair. Only the like polarisations (HH and VV) are affected, whereas for the HV there is no impact of temporal effects. This might be an indication that changes are mostly occurring on surface layers (close to the ice surface?), rather than within the volume (which is expected).

It appears that the ice surface is sufficiently stable within a couple of days (and even weeks), which would allow (to a certain amount) also repeat-pass techniques like differential SAR interferometry. For this purpose however, the limiting effect of the ionosphere must also be considered.

6.4.7 C-band Repeat-Pass Processing for Synthetic Quad-Pol Products

The first discussion with respect to repeat-pass processing of C-band data relates to the combination of subsequent tracks (acquired on the same day) for generating synthetic quad-pol products. For this purpose it is assumed that the complementary polarisations were acquired form the same track, which is not perfectly true. In fact the spatial baseline is not zero and varies with azimuth as can be seen from Figure 6.18.

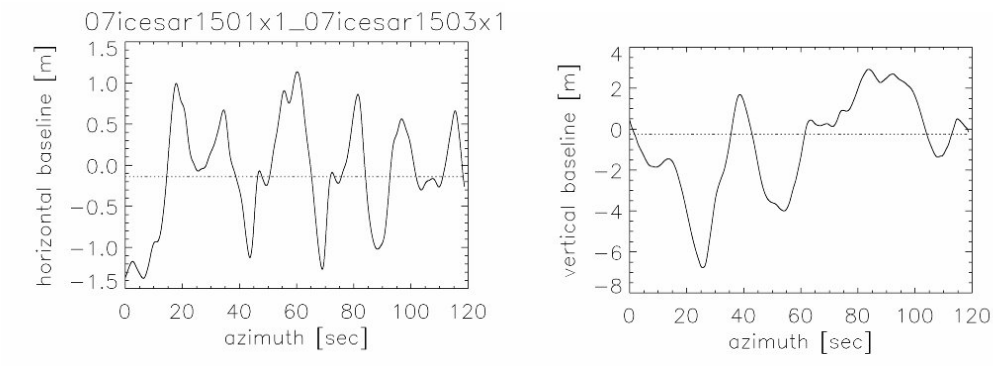

Fig. 6.18: Spatial baselines of complementary C-band acquisitions (1501 - VH-VV and 1503 – HV-HH)

The associated vertical wavenumber kz is computed via:

$$k_z = \frac{4 \cdot \pi \cdot B_\perp}{\lambda \cdot r \cdot \sin\theta}$$

where r is slant range, λ is wavelength, θ is the incidence angle and B is the baseline projection perpendicular to the line of sight, Kz is displayed in the 3rd image from top in Figure 6.19. From the same Figure we also note the presence of correlated coherence behaviour (especially for the HV-VH combination), which is an indication of the presence of strong volume scattering (the coherence decreases with an increase in absolute kz value). However, the interferometric phase appears as if we have to deal with a relatively smooth surface corresponding to the mean scattering center.

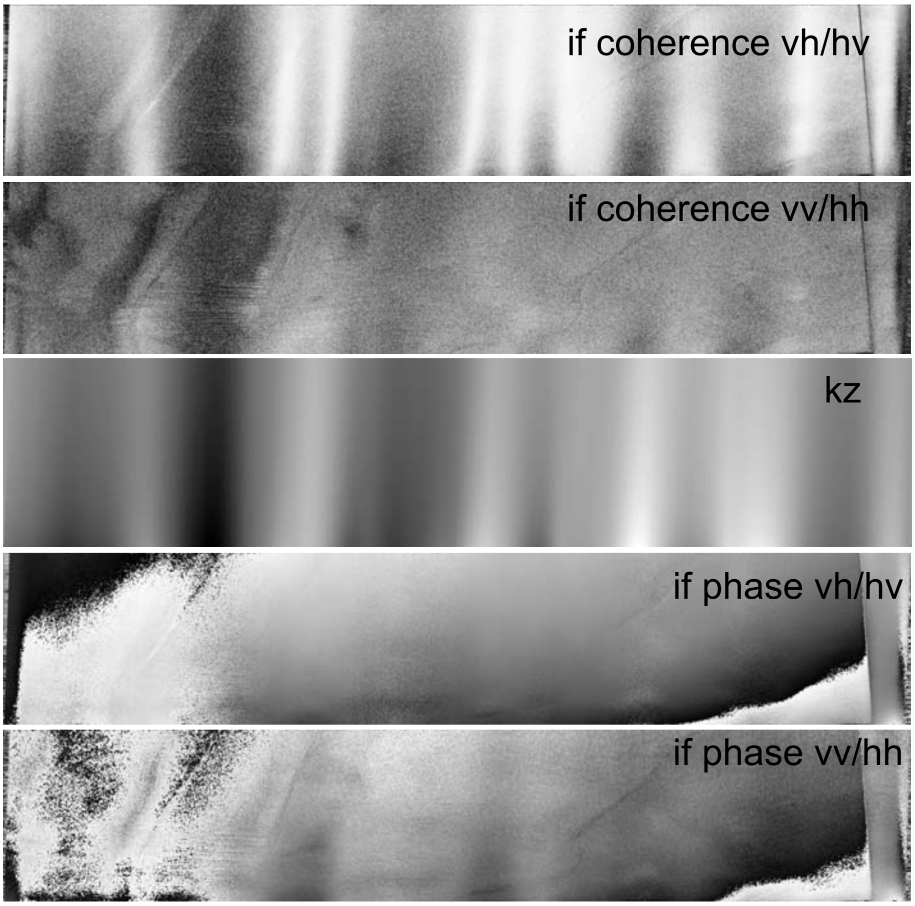

Fig. 6.19: Interferometric coherence and phase for two complementary C-band acquisitions (1501 - VH-VV and 1503 – HV-HH)

Two conclusions can be drawn from this observation: The data can be used for the assessment of the amount of volume scattering but the interpretation of the complex polarimetric data must be handled very carefully due to the simultaneous presence of considerable volume and non-zero baseline. From the processing point of view, the generation of repeat-pass C-band products with data acquired on the same day was successful, especially for the zero baseline acquisitions, where the residual motion errors could be estimated quite well.

6.4.8 C-band Repeat-Pass Processing for Temporal Decorrelation

The following second discussion is with respect to the evaluation of temporal image pairs. The only available data sets with nominal zero baseline are from the Etonbreen Glacier test site and have acquisition times separated by 4 days. Strong temporal decorrelation has been encountered and the mandatory estimation of residual motion errors could not be performed.
In addition, the squint angle also differs by 5 deg due to different wind conditions for the different acquisition dates. (This is the case for both look directions.) Thus the common Doppler bandwidth does not correspond to the highest SNR for these slave images. However, the associated degradation is nearly degligible (decrease of coherence values in the order of 0.01) when compared to a case of squint angle matching (good SNR).

Therefore the low coherence presented in Figure 6.20 must be attributed primarily to temporal decorrelation. Volume effects contribute in a variable manner similar to the example pair discussed in the first part of this subsection. As the temporal decorrelation is nearly complete, further quantification of the individual components has not been attempted. Mean coherence values are listed in the tables summarizing the temporal repeat-pass products at the end of the previous subsection.

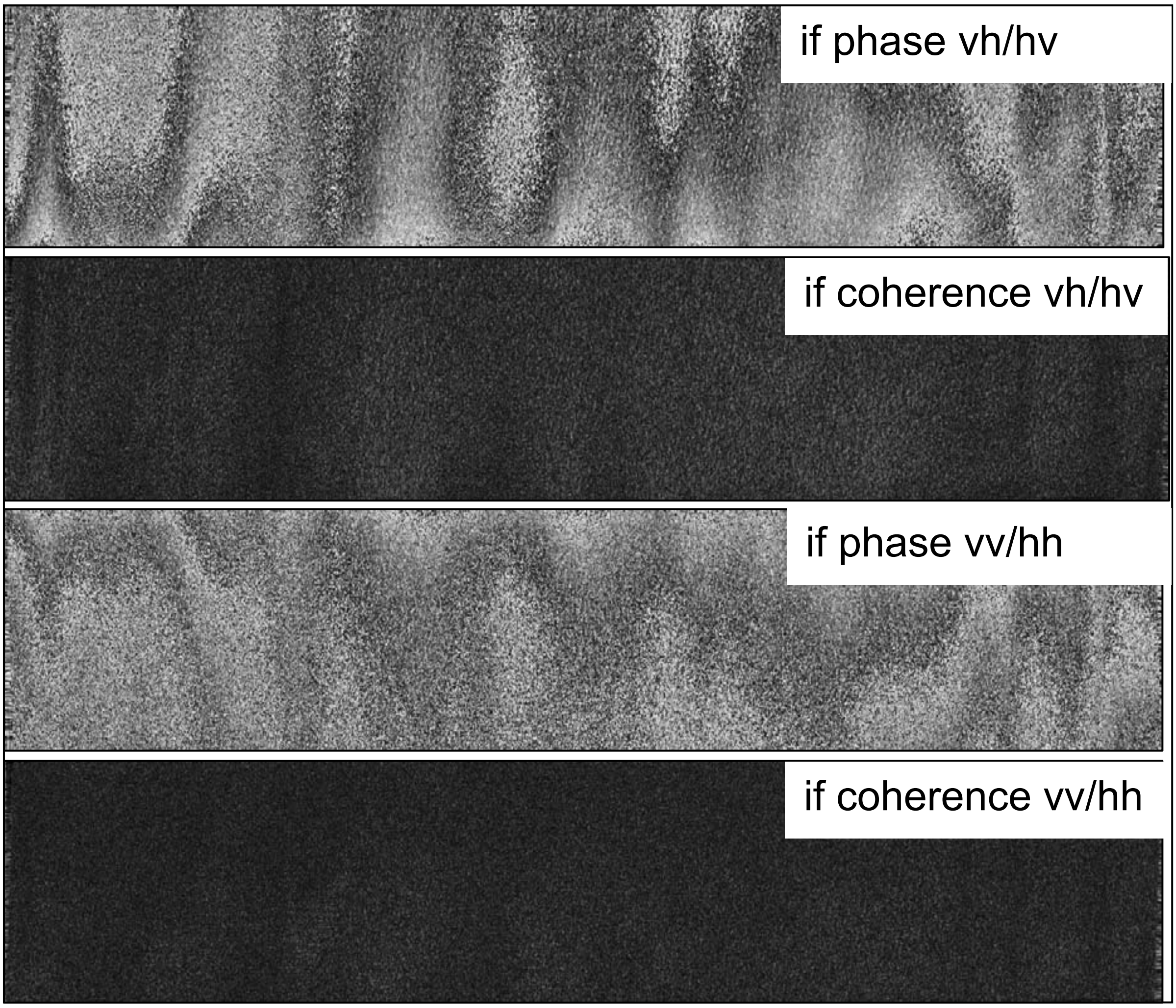

Fig. 6.20: Interferometric coherence and phase for two complementary C-band acquisitions (1501 - VH-VV and 2003 – HV-HH)

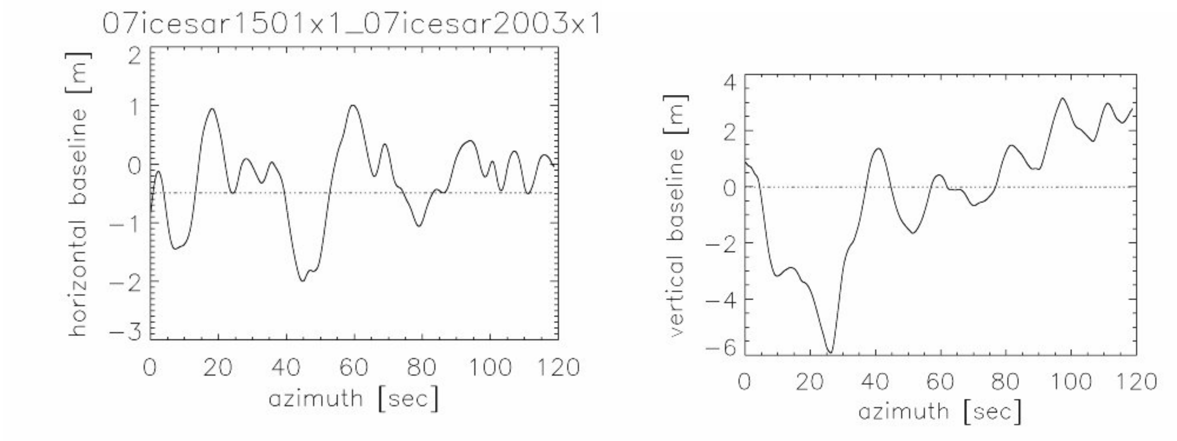

Fig. 6.21: Spatial baselines of complementary C-band acquisitions (1501 - VH-VV and 2003 – HV-HH)

6.4.9 Data Quality: SAR Polarimetry

The polarimetric properties of the SAR data collected at both the Summit and Etonbreen test sites and L- and P-band frequencies are outlined below. At X-band only backscattering coefficients are presented since data were collected at a single-polarisation (VV). Properties including backscattering coefficients (in lexicographic, Pauli and circular bases), and entropy, anisotropy and alpha angle (HAα) from eigenvector decomposition are examined. The properties are compared and contrasted at the two different test sites and at the two frequencies, and efforts are made to identify whether surface, volumetric, or both types of scattering mechanisms are involved.

Both North and South passes over the two test sites were flown in March and April. Due to the large amount of data and because March/April and North/South passes were very similar, here we concentrate on results from March, for the North passes. For reference Figure 22 presents backscattering coefficients at X-, L- and P-band averaged through azimuth for both North and South passes. North and South passes are especially similar for the Summit test site which is very homogeneous; such that the dominant trends in backscatter at all polarisations are due to incidence angle effects rather than ice structure. Etonbreen is more heterogeneous, which is seen in the differences between North and South trends.

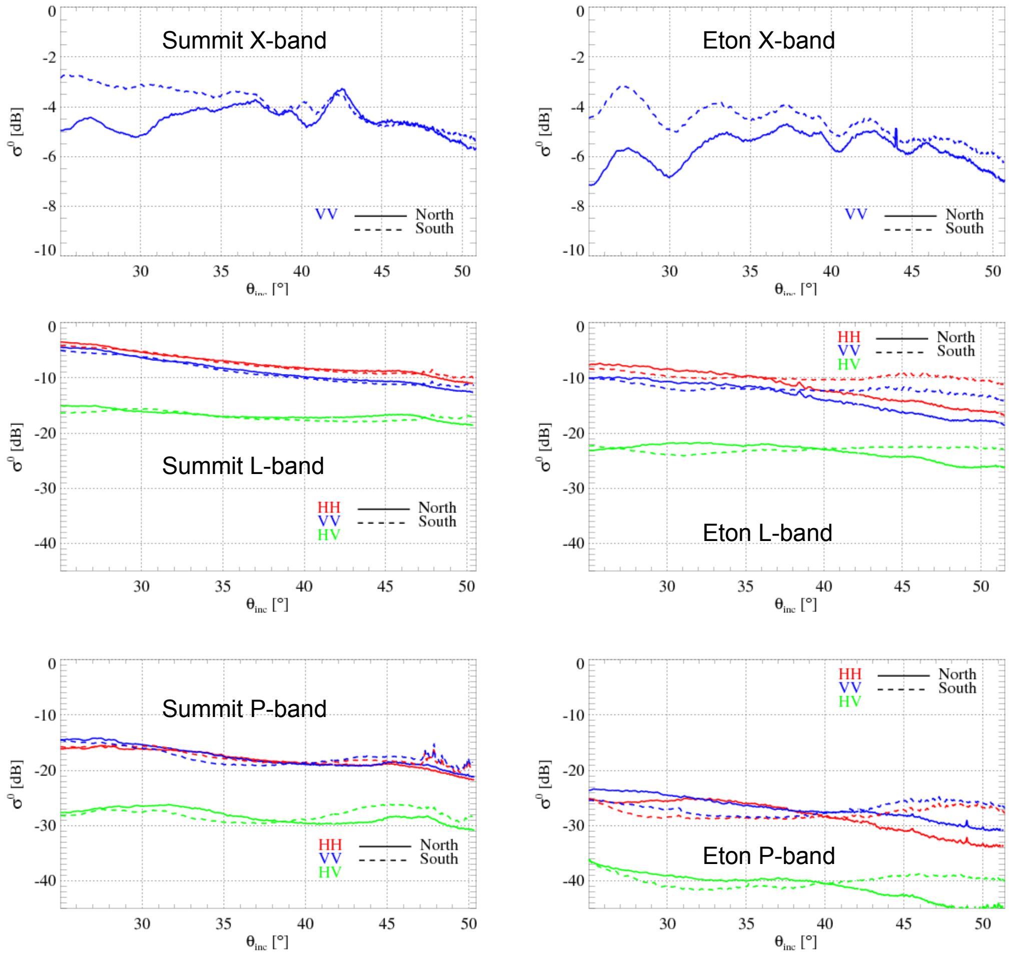

Fig. 6.22: Backscattering coefficients versus incidence angle averaged through azimuth for X-, L- and P-band data for both North (solid) and South (dashed) passes for both Summit and Etonbreen.

Fig. 6.23 and Fig. 6.24 present the backscattering coefficients at X-band for two sample passes. Some artifacts are present in the data, especially noticeable for Etonbreen, due to multipath reflections which have a strong impact on the antenna gain pattern. Nevertheless, one sees that the Summit test site is very homogeneous for X-band frequencies. Some ridge-like structure is visible for Etonbreen, although the data are still fairly homogeneous. There is relatively little variation in the backscattering coefficient with incidence angle, with only a slight decreasing trend, indicating strong volume scattering from the snow and ice crystals and a potentially smaller component from the snow-ice interface.

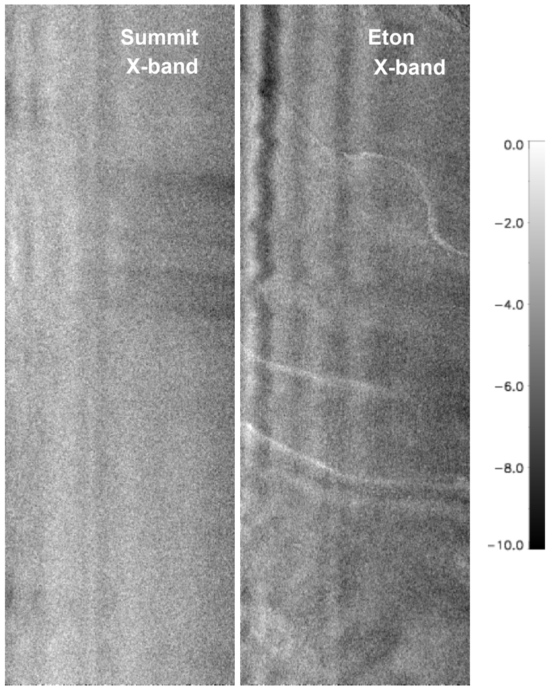

Fig. 6.23: X-band backscattering coefficients (in dB) for Summit April North (left) and Etonbreen March South (right).

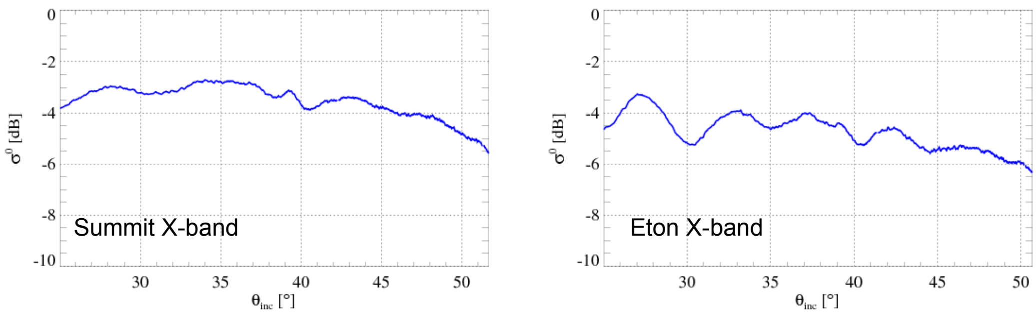

Fig. 6.24: X-band backscattering coefficients versus incidence angle averaged through azimuth from Fig. 6.23

Pauli decomposition of L- and P-band data, for both Summit and Etonbreen test sites are shown in Fig. 6.25 where blue (HH + VV) represents surface scattering, red (HH- VV) double bounce and green (2HV) volume scattering. The Summit L-band image is relatively homogeneous with slightly more surface scattering (blue) in near-range. P-band Summit, with deeper penetration depths and less scattering from snow and ice grain crystals, reveals the presence of multiple ice features including double bounce scattering from buried crevasses in near-range, and volume scattering (green) from a well-defined area of possible melt features in near-range and a long ridge-like feature in far-range. For the Etonbreen test site both L- and P-band show similar features, with areas of increased volume scattering and double bounce scattering.

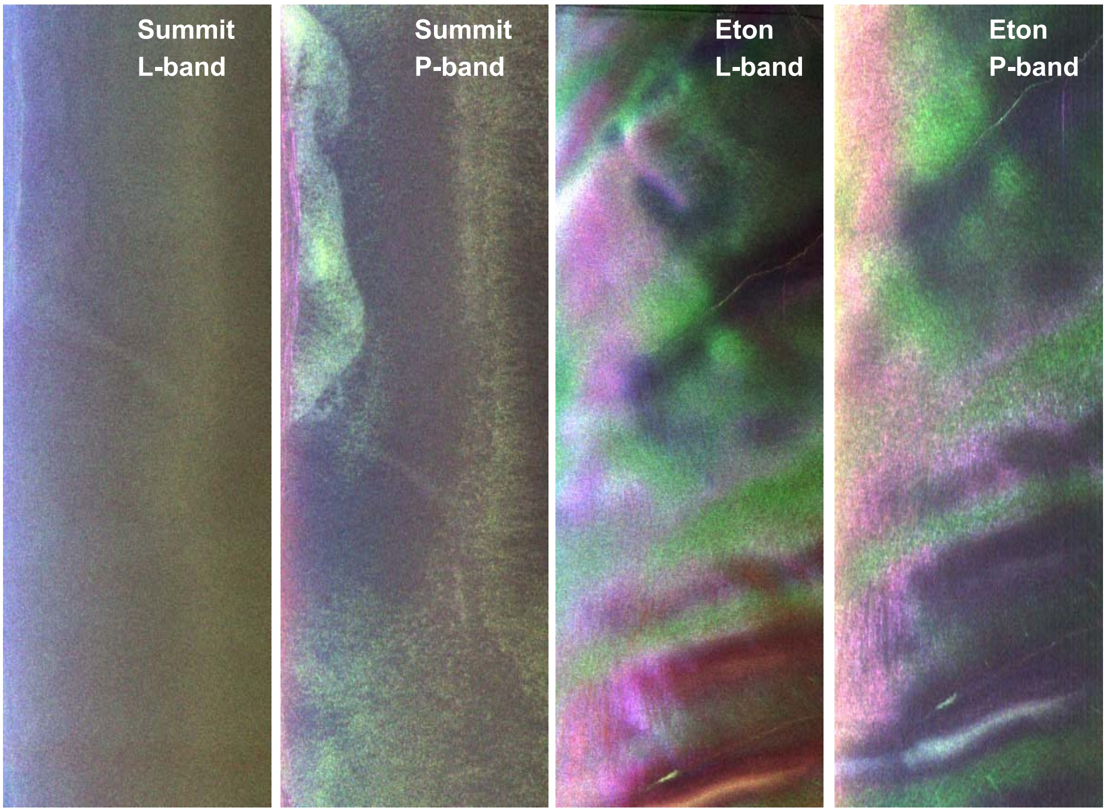

Fig. 6.25: Pauli decomposition for L-/P-band at both Summit and Etonbreen test sites for March, North flight line.

Fig. 6. shows the backscattering coefficients averaged through azimuth to reveal trends with range for L- and P-band. Decreasing trends of σ^o with incidence angle are seen for both test sites, particularly for the co-polarisations which are expected to have significant surface scatter from the snow-ice interface and potentially other stratified layers in the ice. These results are in agreement with the small perturbation model for slightly rough surfaces, where a decrease in σ^o is predicted with increasing incidence angle. The cross-polarisation, on the other hand, is expected to be dominated by volume scattering, which is less sensitive to the angle of incidence. L-band Summit backscattering coefficients are approximately 5 dB larger than at Etonbreen, likely due to increased volume scatter and a possibly rougher snow-ice interface. P-band Summit values are approximately 10 dB larger than at Etonbreen, which again could be attributed to increased volume scattering at Summit as well as to smoother ice layers at Etonbreen, decreasing the amount of backscattered energy.

Histogram distributions for linear (HH, VV, HV) and circular (RR, LL, RL) polarisations are shown in Fig. 6.26 and Fig. 6.27 respectively. In all instances normalised histograms are presented in which the y-axis is scaled between zero and one. Co-polarisations HH and VV are very similar, while HV backscattering values are approximately 10 dB less than co-polar values, likely due to a reduced surface contribution. In the circular basis, like-polarisations RR and LL are very similar and (except for Summit L-band) RL backscatter has a mean value approximately 5 dB higher than like-circular polarisations. Each reflection reverses the helicity of the polarisation, and therefore high σ^o_{RL} and low σ^o_{RR} and σ^o_{LL} are characteristic of dominant odd-bounce scattering, such as single-bounce surface scattering.

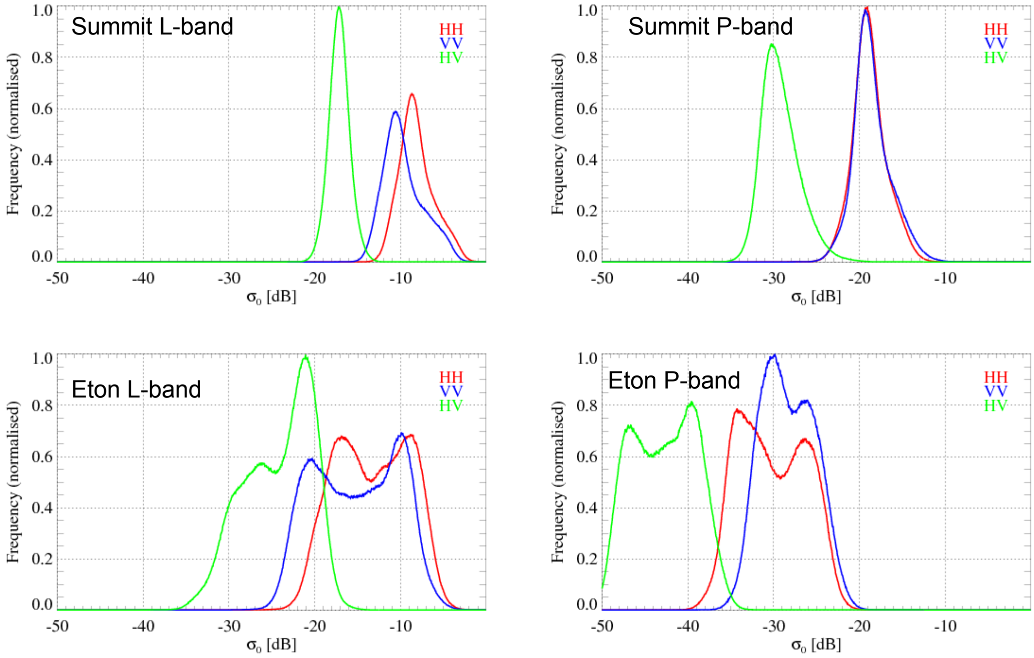

Fig. 6.26: Histograms of backscattering coefficients for linear polarisations (HH, VV, HV) for March, North.

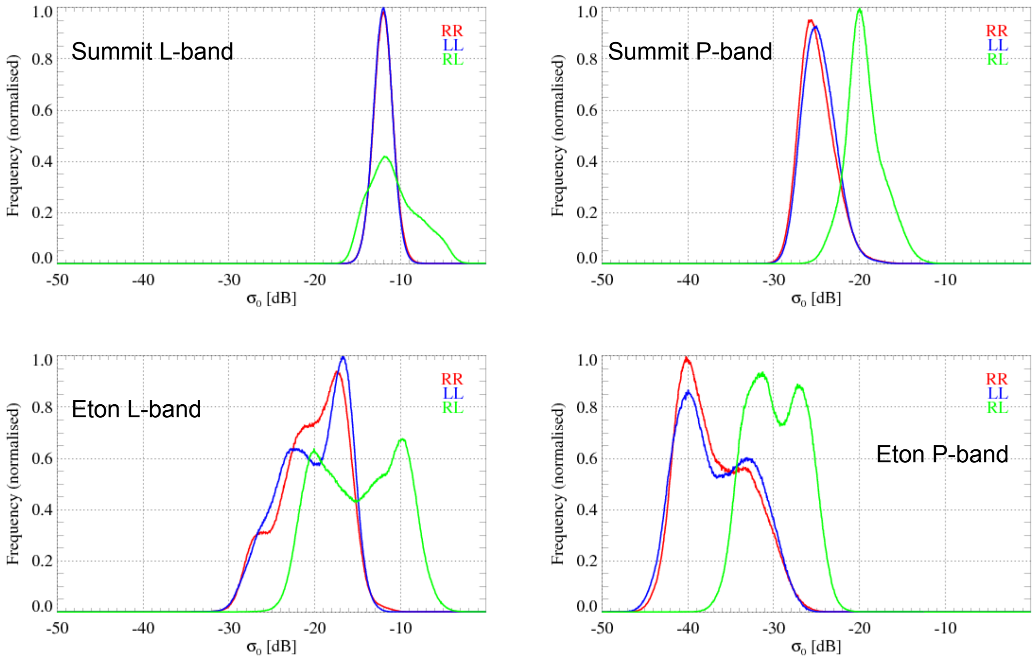

Fig. 6.27: Histograms of backscattering coefficients for circular polarisations (RR, LL, RL) for March, North.

Mean backscatter values for the linear polarisations averaged over an incidence angle of 40º ± 0.5º are shown in Table 6.3. A value of 40º was chosen because it is often referenced in the literature, and a commonly-cited empirical backscatter model uses σº at 40º as the starting value from which incidence angle and azimuth dependencies can be introduced (Long and Drinkwater 94).

Table 6.3: Averaged backscattering coefficients in dB for an incidence angle of 40º ±0.5º for the March, North flight lines.

X-band	Summit	Eton	Δ(Sum-Etn)
VV	-4.6- ± 0.8	-5.6 ± 0.9	+1.0

L-band	Summit	Eton	Δ(Sum-Etn)
HH	-8.4 ± 0.9	-12.6 ± 2.9	+4.2
VV	-9.9 ± 0.9	-13.0 ± 3.1	+3.1
HV	-17.3 ± 0.9	-23.2 ± 3.1	+5.9

P-band	Summit	Eton	Δ(Sum-Etn)
HH	-19.0 ± 1.1	-29.3 ± 2.6	+10.3
VV	-19.1 ± 1.1	-28.2 ± 2.0	+9.2
HV	-30.1 ± 1.8	-41.7 ± 3.2	+11.6

Decomposition of the coherency matrix into entropy (H), anisotropy (A) and alpha angle (α) was also performed in order to better understand the dominant scattering mechanisms present in the data. Results are shown in Fig. 6.29 to Fig. 6.32. To aid in interpretation of α, a schematic representation is given in Fig. 6.28 after Cloude 1999.

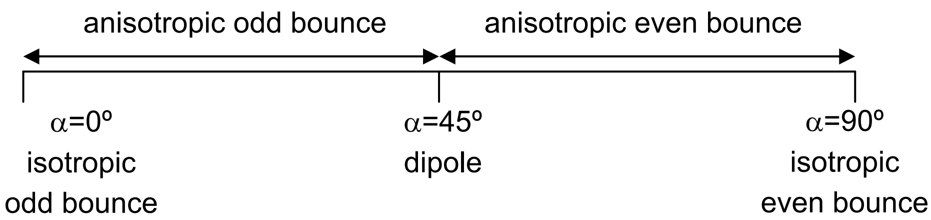

Fig. 6.28: Schematic illustration of the alpha angle and its interpretation.

At Summit L-band, there is a clear pattern of low entropy (indicating a single scattering mechanism) in near range, with entropy progressively increasing with range towards multiple scattering mechanisms. The low, noisy anisotropy indicates one dominant scattering mechanism (perhaps mostly surface scattering, based on interpretation of H and α) since the second and third eigenvalues are similar in magnitude. The α values also increase from near- to far-range, ranging from fairly low values of ~20 degrees at near-range indicating strong surface scattering to approximately 60 degrees at far-range indicating a possible mix of mechanisms (e.g. a mix of volume and surface scattering). This incidence angle behaviour is consistent with Bragg-type surface scattering theory.

Summit P-band shows similar results as for L-band, including an increase in entropy with incidence angle and relatively low anisotropy, although more detailed ice structure can be seen including increased entropy in areas of likely volume scattering such as the irregularly-shaped area in near-range and the long ridge-shaped feature in far-range. In addition, α for P-band is generally low throughout (~< 20º), although it increases slightly in far-range and for the aforementioned areas of likely volume scattering.

For Etonbreen, the swath is much more heterogeneous and trends with incidence angle are not as evident as for Summit. For L-band again we see slowly increasing entropy with incidence angle, although the anisotropy shows some structure, including a second scattering mechanism in near-range. However, the first scattering mechanism - which is characteristic of surface scattering - remains very dominant such that α angles are low throughout, although a little higher in far-range. For P-band we see high entropy in patches in near-range corresponding to possible volume scattering areas (these same patches have low anisotropy), although again the first eigenvalue is extremely dominant, corresponding to a strong odd-bounce surface scattering-type mechanism with very low α angles.

On average, at both test sites L-band shows increased entropies and higher alpha angles in comparison with P-band, this is to be expected given the shorter wavelength and thus increased sensitivity to small ice crystals.

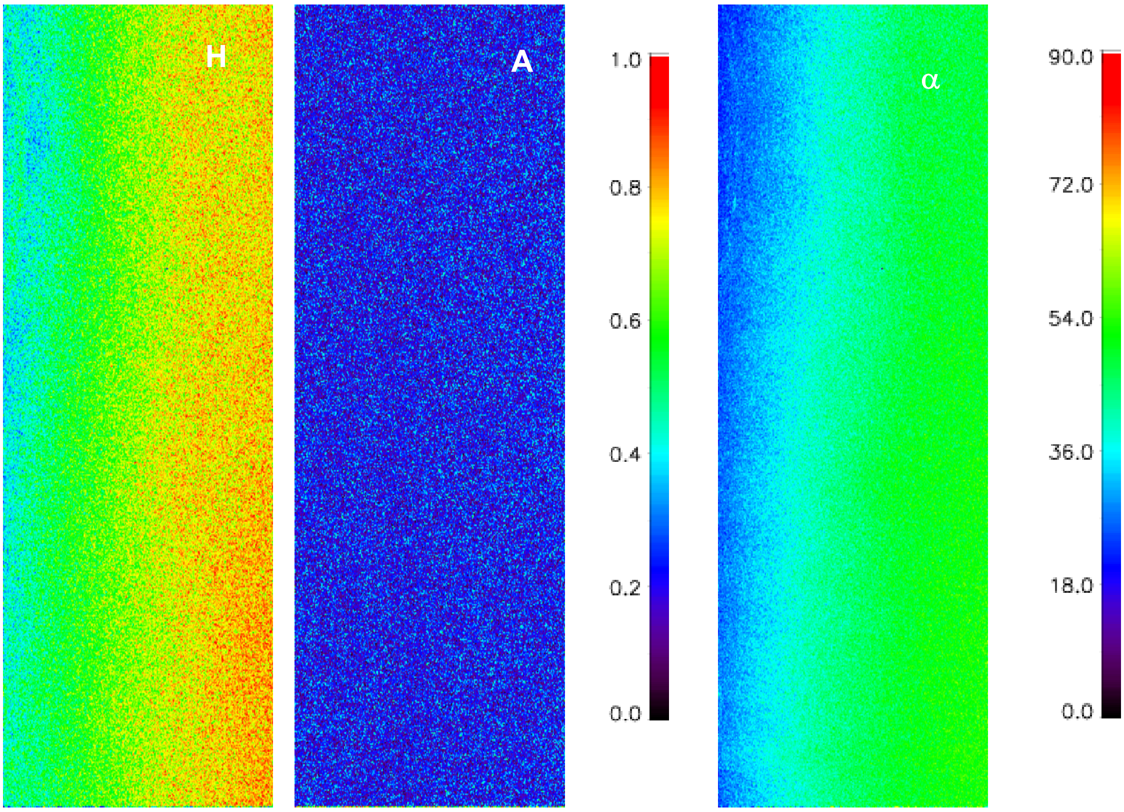

Fig. 6.29: Summit L-band H-A-alpha decomposition, March North.

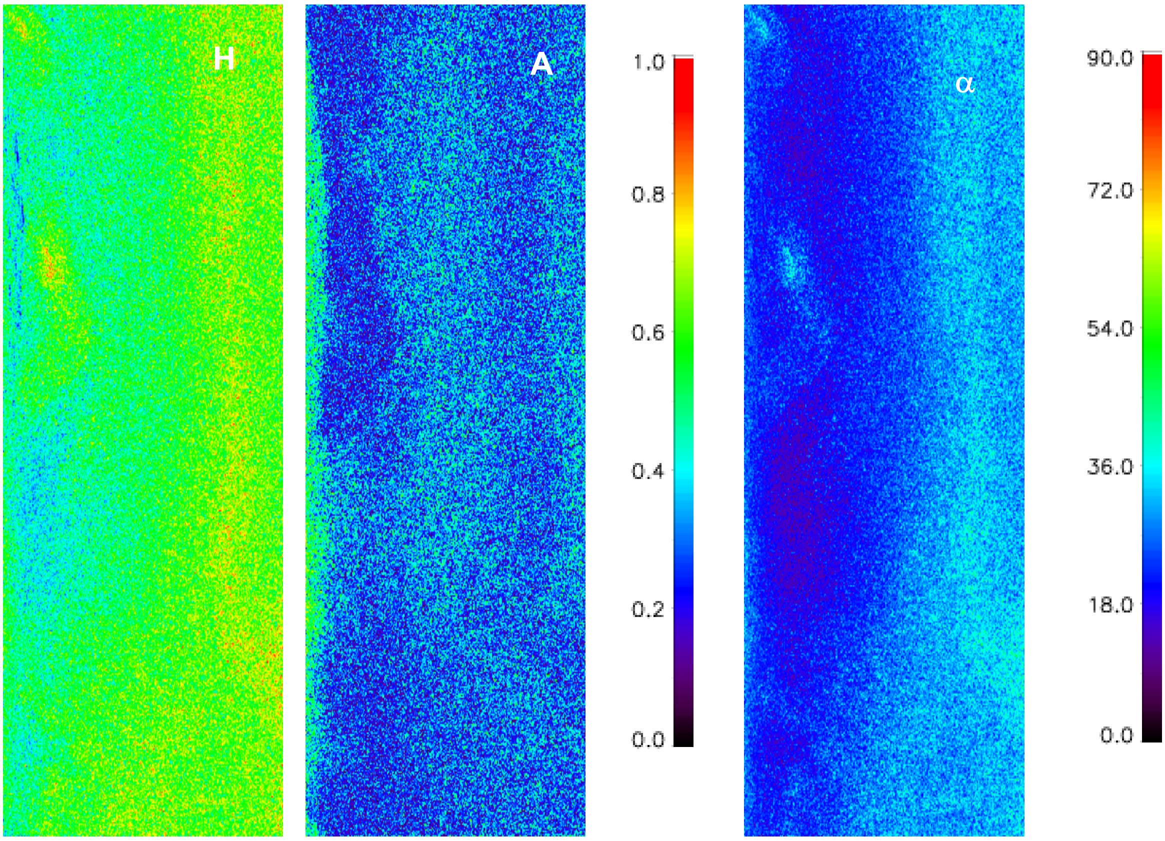

Fig. 6.30: Summit P-band H-A-alpha decomposition, March North.

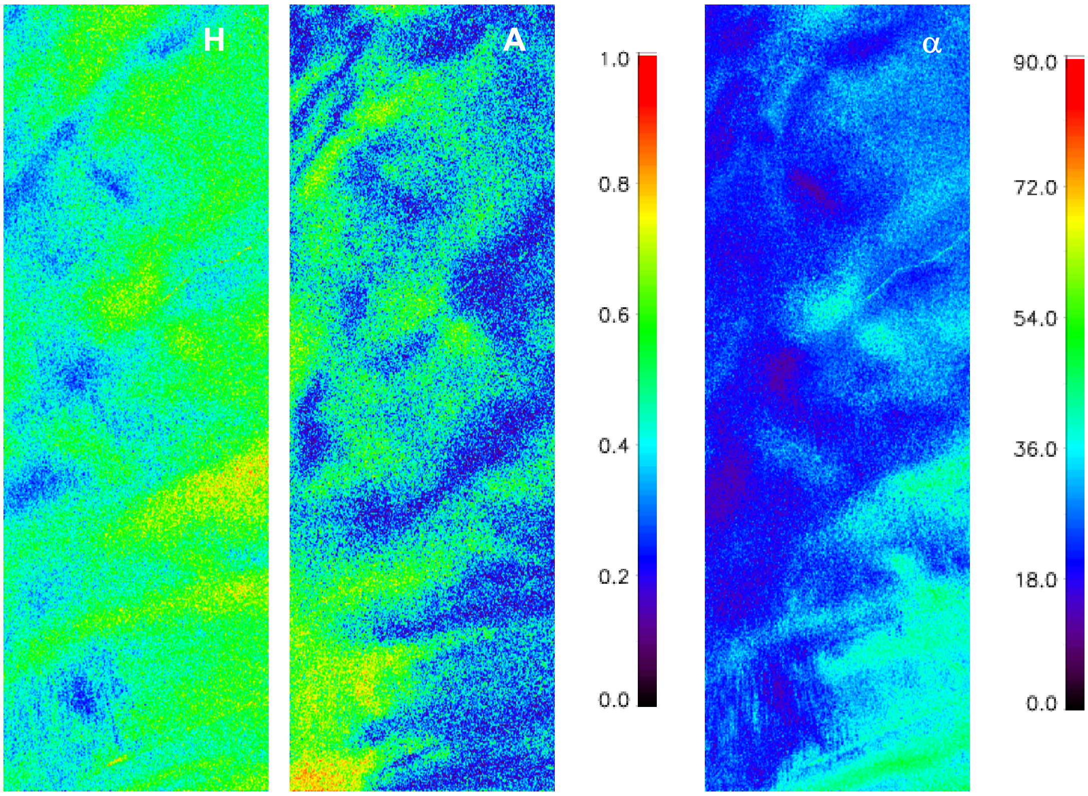

Fig. 6.31: Etonbreen L-band H-A-alpha decomposition, March North.

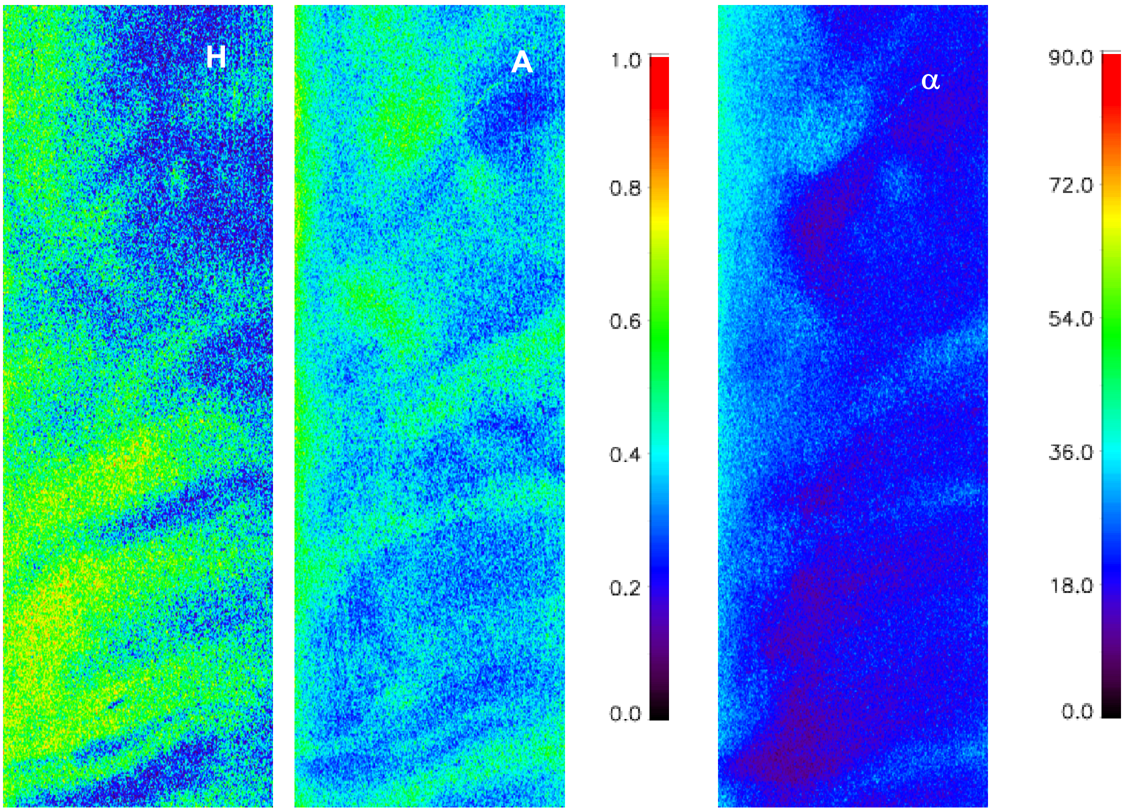

Fig. 6.32: Etonbreen P-band H-A-alpha decomposition, March North.

6.4.10 Data Quality: Polarimetric SAR Interferometry

As part of the interferometric analysis coherences were examined as a function of baseline and polarisation. Examples illustrating this coherence variation are given for Etonbreen, P-band, March North flight line in Fig. 6.33 to Fig. 6.36. As expected from volume scattering theory, the histograms show a decrease in coherence magnitude with increasing baseline (see Fig. 6.35 left). In Fig. 6.33 there is a progressive decrease in coherence with increasing baseline, although there are some areas which maintain a higher coherence, possibly indicating increased surface return. Co-polarisation coherences (HH and VV) are similar to one another whereas cross-polarised coherences (HV) are somewhat reduced due to the probable lack of a coherent ground contribution (see Fig. 6.34).

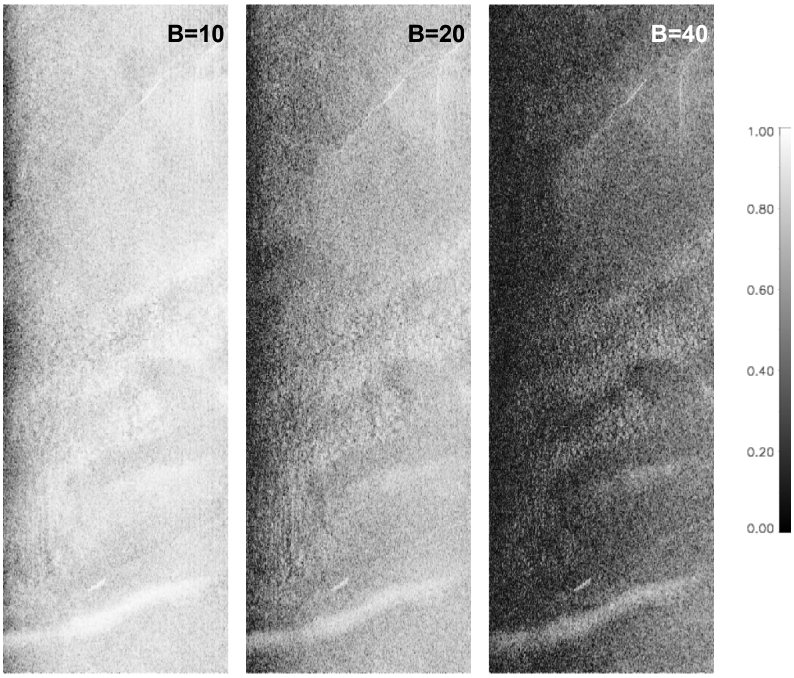

Fig. 6.33: Coherence magnitude variation with nominal horizontal baseline (in metres) for Etonbreen, P-band, March North, HH polarisation.

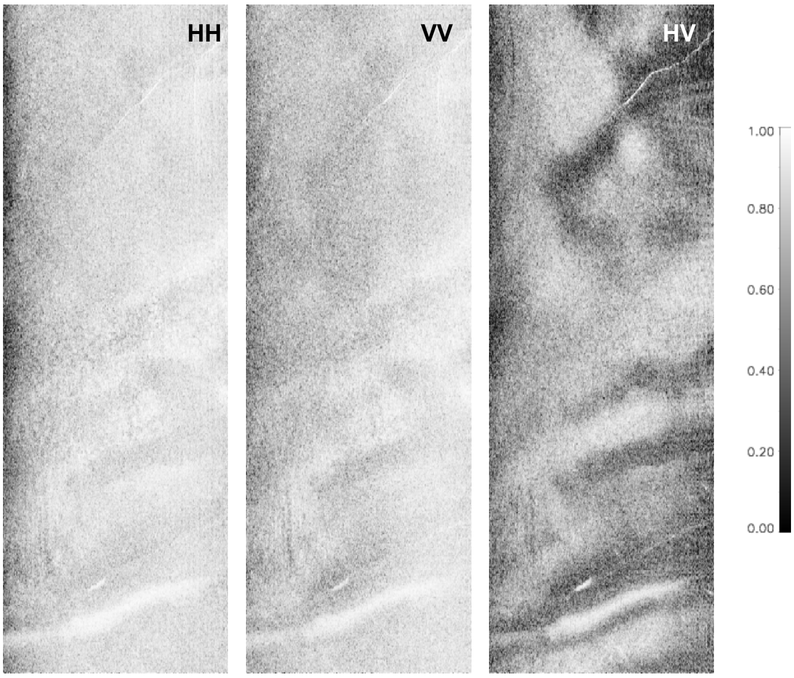

Fig. 6.34: Coherence magnitude variation with polarisation for Etonbreen, P-band, March North, 10 m nominal horizontal baseline.

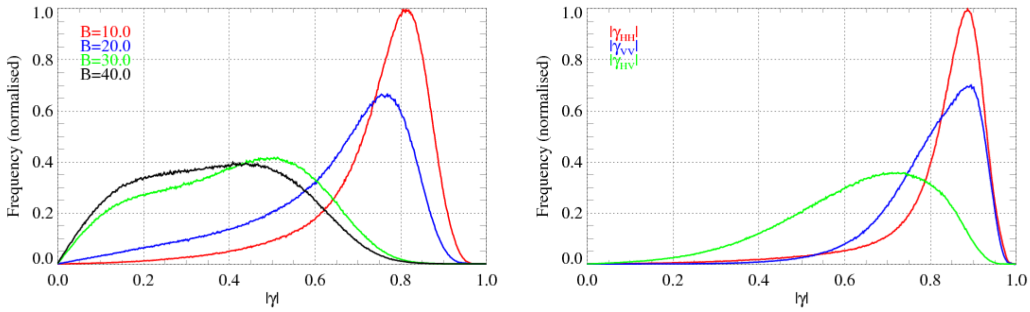

Fig. 6.35: Histograms showing variation of coherence magnitude with baseline for HH polarisation (left) and variation of coherence magnitude with polarisation at a nominal 10 m baseline (right) for Etonbreen, P-band, March North.

Further analysis was conducted using corner reflectors deployed on the ice's surface as a reference to help determine the average penetration depth. Phase centres were computed using the difference between the interferometric phase at the reflector and the ice in the immediate vicinity. An example of the amplitude image, coherence magnitude and coherence phase in a subset surrounding a reflector is shown in Fig. 6.36, where the red box identifies the location of the reflector whose pixels are excluded from the ice phase centre computation. Phase centre results which have been averaged over all baselines, North and South passes and March and April for each site are given in Table 6.4 and plotted in Fig. 6.37.

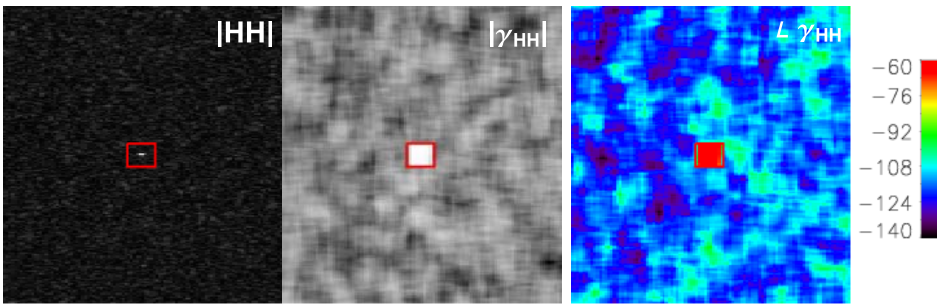

Fig. 6.36: Area surrounding corner reflector with subsets of magnitude image (left), coherence magnitude (centre), and coherence phase in degrees (right) for HH polarisation, Summit L-band, CR-SUM1 (150 cm) March North.

Tab. 6.4: Phase centre depths in metres relative to corner reflectors. Phase centres have been averaged over all baselines relative to 150 cm corners.

X-band	Summit	Eton	Δ(Sum-Etn)
VV	-4.4 ± 0.5	-2.9 ± 0.7	-1.5

L-band	Summit	Eton	Δ(Sum-Etn)
HH	-6.8 ± 0.9	-11.5 ± 0.9	+4.7
VV	-7.1 ± 1.0	-11.9 ± 1.0	+4.8
HV	-10.0 ± 1.5	-13.9 ± 0.6	+3.9

P-band	Summit	Eton	Δ(Sum-Etn)
HH	-7.6 ± 0.8	-12.9 ± 3.0	+5.3
VV	-7.2 ± 0.8	-12.6 ± 2.6	+5.4
HV	-12.3 ± 1.1	-16.8 ± 1.1	+4.5

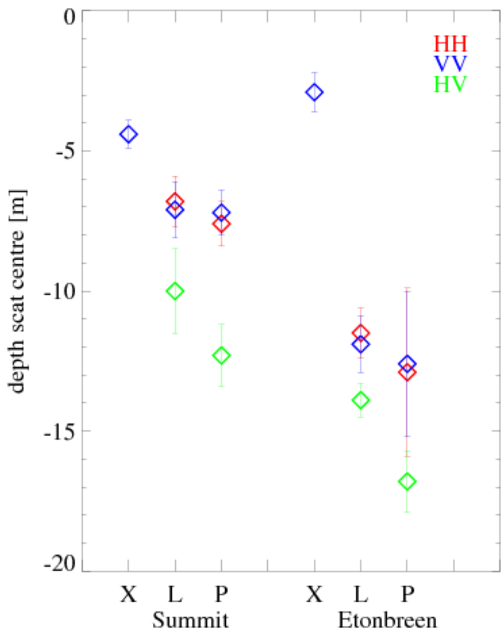

Fig. 6.37: Depths of average scattering centres referenced to corner reflectors on the ice's surface for X-, L- and P-band.

Longer wavelengths (L- and P-band) experience less scattering and absorption loss and thus penetrate deeper into the ice than shorter wavelengths (X-band). The differences between polarisations are likely due to the different relative contributions of a ground component to the total phase, although it is seen that the co-pols are very similar to one another. At L- and P-band there are slightly deeper penetrations at Etonbreen than at Summit. This could be due to the presence of increased melt features in the percolation zone (Summit) increasing scattering attenuation in the upper layers compared to the more solid ice in the superimposed ice zone (Etonbreen).

6.4.11 Temporal Decorrelation

The influence of temporal decorrelation was also examined using a one month temporal baseline between March and April. Interpretation is hampered by the fact that squint angles were significantly different between acquisitions (decreasing SNR and signal quality) and that the acquired baselines were not precisely zero-baselines, requiring modelling of the volume decorrelation. However, conservative estimates of the temporal decorrelation (due to, for instance wind and precipitation influences) are 0.4 at L-band and 0.7 at P-band for the Summit area and 0.5 (L-band) and 0.9 (P-band) for Etonbreen.

The volume decorrelation was estimated using a simple uniform infinite volume model (Sharma et al. 2007). In each case one baseline from the repeat-pass March data (with a temporal baseline of less than one hour) best matching the 1-month spatial baseline was chosen to model the extinction. This 2-D extinction map was then used in combination with the actual flown tracks from the 1-month baseline to estimate the expected volume decorrelation on a pixel-by-pixel basis, enabling the isolation of the temporal decorrelation component.

Fig. 6.38 presents the L- and P-band estimated temporal decorrelations after removal of volume decorrelation for both test sites at HH polarisation. Histograms of temporal decorrelation for all polarisations are presented in Fig. 6.39. L-band shows a near complete loss of coherence in the one month interval, with very noisy results, particularly at Etonbreen. P-band generally has higher coherence after the 1-month time interval than L-band, likely due to decreased sensitivity to changes in snow crystal structure and snow depth in the uppermost layer.

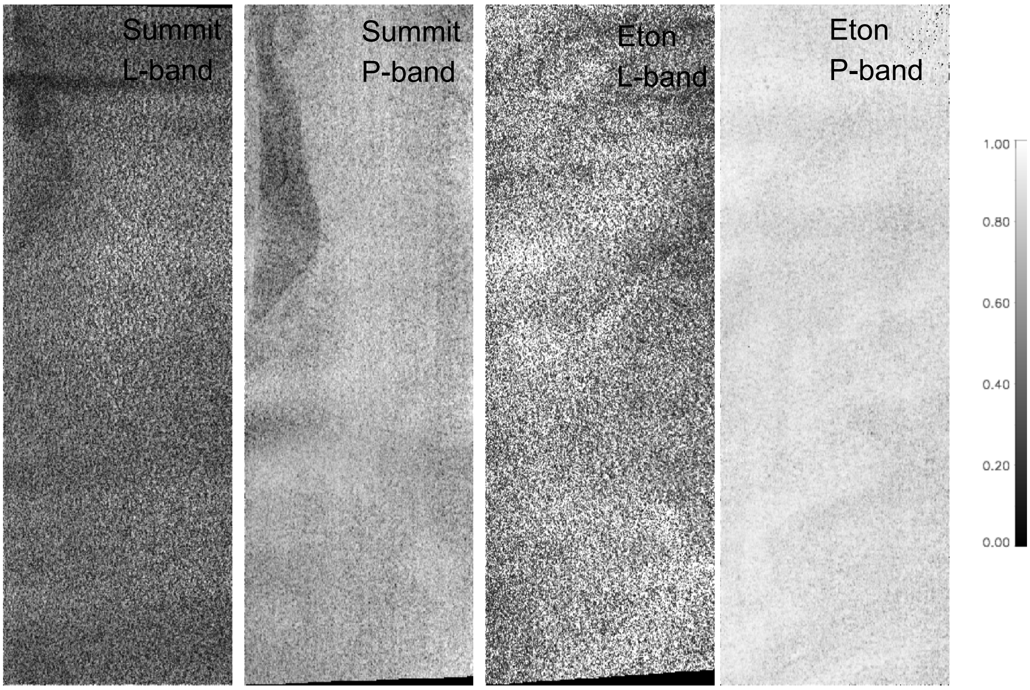

Fig. 6.38: Coherence magnitudes with a temporal baseline of 1 month (March-April) for HH polarisation, North after correction for volume decorrelation.

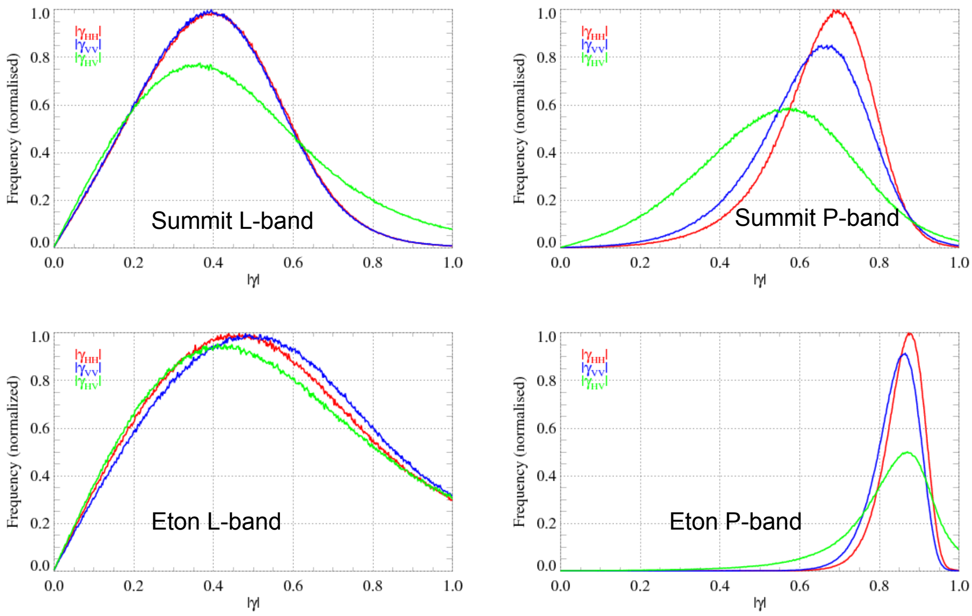

Fig. 6.39: Histograms of coherence magnitudes with a temporal baseline of 1 month (March-April), North after correction for volume decorrelation.

6.5 Processing of Sounder Data

During ICESAR 2007 two flights were dedicated to the acquisition of nadir looking P-band data (center frequency: 350 MHz) in ice sounding mode.

The details of these flights are summarized in Table 6.5 below:

Table 6.5: Summary of E-SAR data takes in Ice sounding mode.

Flight ID	Flight Date	Testsite	Flight Altitude above MSL	Tracks East to West	Tracks West to East	Comments
icesar08	25.03.07	Summit	~2660m	0802; 0804; 0806; (with 94 MHz bandwidth)	0801; 0803; 0805; (with 25 MHz bandwidth)	track 0806 has been extended towards the margins of the ice sheet
icesar18	20.04.07	Etonbreen Glacier	~5200m	1801; 1803; 1805; 1807; 1809 (with 94 MHz bandwidth)	1802; 1804; (with 25 MHz bandwidth) 1806; 1808; (with 94 MHz bandwidth)	Flight altitude offset of 20 m for data takes 1804-1809 due to temporary loss of GPS link

In the initial planning, at least 2 additional flights were scheduled, but had to be cancelled due to low priority of this data acquisition mode. Nevertheless, the data acquired during the March campaign were evaluated immediately after the campaign. It was found that no bedrock could be observed at the Summit test-site region. However, the processing of the prolongated last track indicated increased bedrock reflections from the outer areas of the ice cap. Therefore the sounder acquisition for the April campaign was scheduled for the Etonbreen glacier test-site.

In Figure 6.40 the results of the processing of the 3 West to East tracks of the Summit test site are shown for HH and VV polarisations and Figure 6.41 the corresponding baselines:

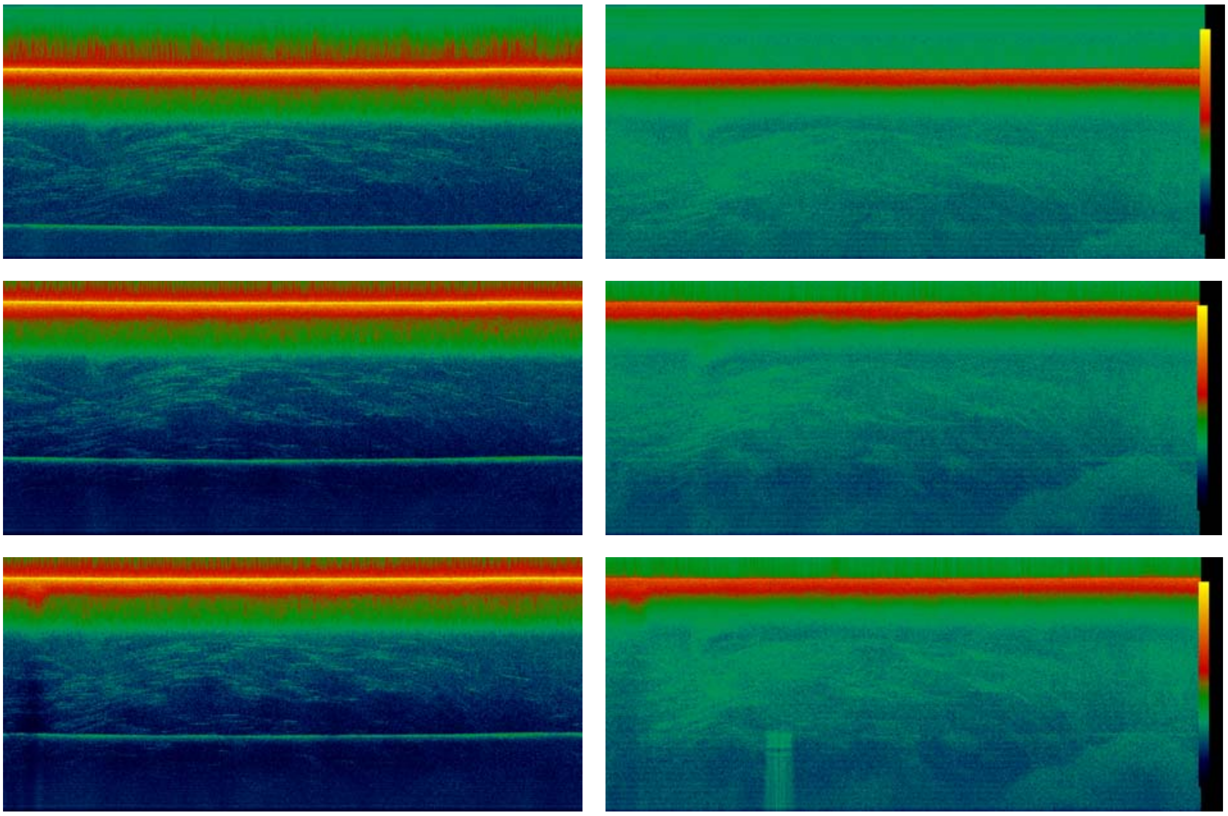

Fig. 6.40: Sounder profiles of 3 parallel tracks (0801, 0803, and 0805) acquired at Summit testsite. Polarisations: HH (left) and HV (right). Logarithmic scale with 50 dB dynamic range.

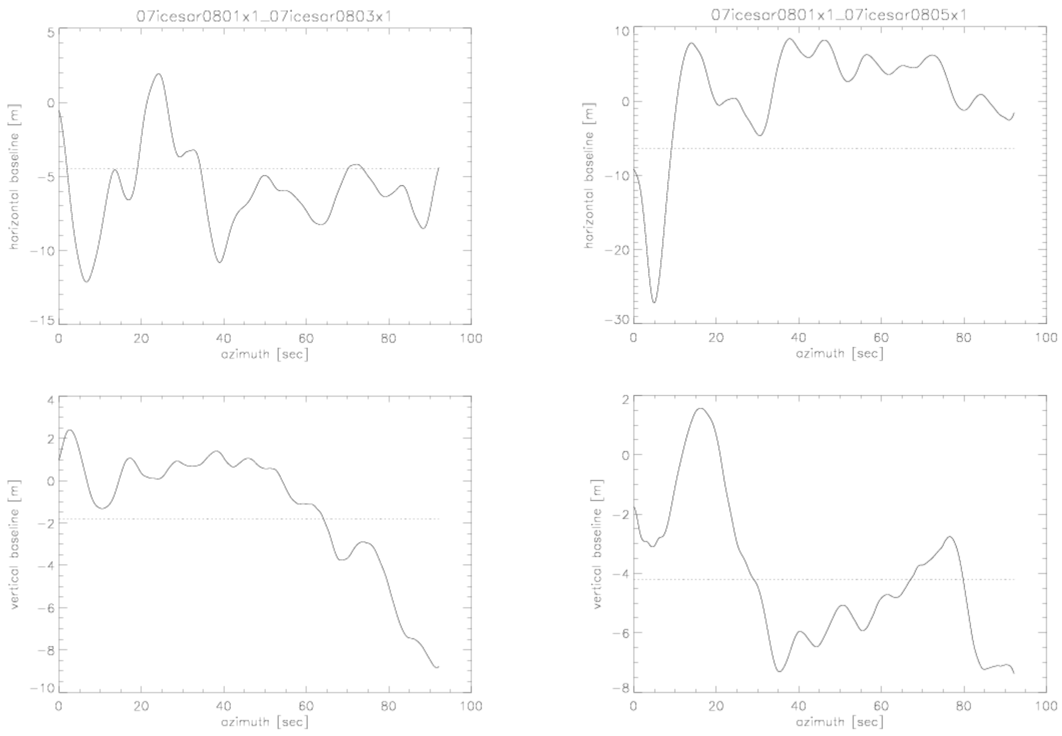

Fig. 6.41: Baselines of sounder data acquired with 94 MHz at Summit location.

The following observations are made for Summit area:

1. For HH polarisation the ice surface reflection is very strong, partially saturating the receiver. This is not the case for HV. The radar settings (receiver gain and range delay) were not ideal for the first acquisition (0801) and have been changed for the subsequent flights.
2. There is a second strong reflection in case of HH polarised data. It corresponds to the second reflection at the ice surface (corresponding travel path: Antenna-Ice Surface – Aircraft fuselage –Ice Surface – Antenna).
3. Limitations of HW (receiver amplifier) can be observed as horizontal lines in the deep areas of the HV polarised radargrams.
4. No indication of bedrock reflection has been found. Measurement of ice thickness at this location was thus not possible.
5. Surface and most likely also subsurface clutter is observed to be very much correlated within the three acquisitions.

Figure 6.42 presents the results of processing the prolongated track 0806 covering parts of the Etonbreen glacier area. Similar results were obtained for the Etonbreen glacier flights, acquired during 2nd campaign in April.

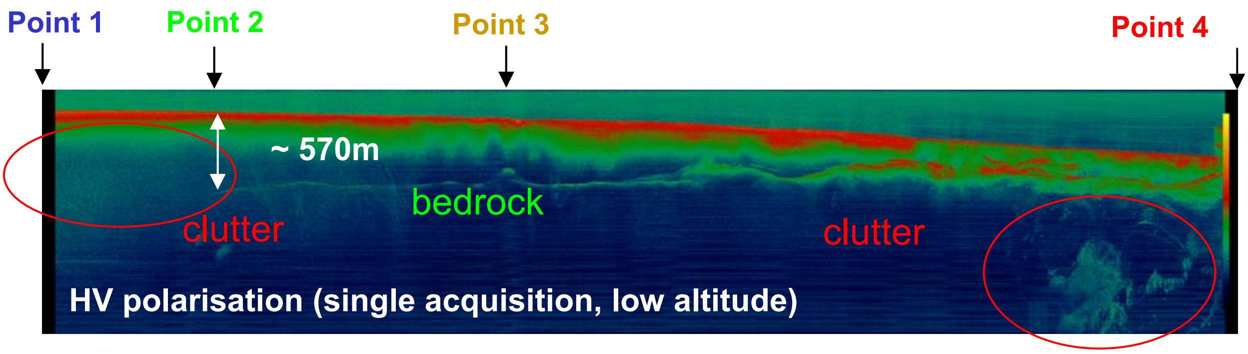

Figure 6.42: Sounder profile (length of 32km) Etonbreen area and outlets of Nordaustlandet icecap. Track 0806 data were used.

The coordinates indicated in the Figure are summarized below:

- Point1 – start of track (lat, lon [deg]: 79.833533, 23.866352)
- Point 2 – point of bedrock disappearance detected at an ice thickness of ~570m: (lat, lon [deg]: 79.826974, 23.634334)
- Point 3 – bedrock ridge (with height of ~116m); less ice thickness of ~345m: : (lat, lon [deg]: 79.815578, 23.244858)
- Point4 – end of track (lat, lon [deg]: 79.785241, 22.279962)

It is assumed that the bedrock reflection is disappearing at Point 2 because of changing bedrock conditions. This would be in line with a paper of Bamber which found about 10 dB less bedrock reflection for the inner part of Nordaustlandet, concluding that there is no water and lower temperatures at bedrock level at these locations (Bamber 1989).

Additional processing has been performed with respect to investigations in the frame of the ACRAS project:

- test of subsurface focussing algorithm.
- investigation of surface clutter decay with increasing off-nadir angle (using data of both test sites)
- coherent combination of repeated tracks (first attempts, using April campaign data)
- first polarimetric investigations of sounder data concerning properties of ice sheets.

The results are summarized in ACRAS WP430 report (ACRAS 2008).

The acquired E-SAR data are the first polarimetric sounder data acquired at P-band. It's information content is not yet exploited.

6.6 Data Product Summary

The summary of all processed a delivered E-SAR data products are given in the tables below, according to the different test sites and frequency bands.

(A table with listed products will be included)

6.7 Summary

In summary the data processing and the quality analysis provided an insight into the SAR data quality of the ICESAR data.

An in-depth polarimetric and interferometric analysis has been carried out. Polarimetric properties examined include the linear polarisation and Pauli backscattering components, eigenvector analysis and entropy-alpha-anisotropy decompositions.

- Backscattering coefficients are much lower for the Etonbreen test site than at Summit (5 dB lower at L-band, 10 dB lower at P-band), which could be due to percolation structures such as ice lenses and ice pipes only present at Summit as well as to smoother ice surfaces at Etonbreen. At X-band σ^o is similar at both test sites, varying from approximately -4 to -6 dB.
- On average, at both test sites L-band shows increased entropies and higher alpha angles in comparison with P-band, this is to be expected given the shorter wavelength and thus increased sensitivity to ice crystals.

As part of the interferometric analysis coherences were examined as a function of spatial baseline, polarisation, and temporal baseline.

- As predicted by volume scattering theory, histograms show decreasing coherence magnitudes with increasing baseline.
- Co-polarisation coherences (HH and VV) are similar to one another whereas cross-pol coherences (HV) are somewhat reduced due to the probable lack of a highly-coherent ground contribution.
- The influence of temporal decorrelation was also examined using a one month temporal baseline between March and April. Interpretation is hampered by the fact that squint angles were significantly different between acquisitions and the acquired baselines were not exactly zero-baselines, requiring modelling of the volume decorrelation. However, conservative estimates of the temporal decorrelation (due to, for instance wind and precipitation effects) are 0.4 at L-band and 0.7 at P-band for the Summit area and 0.5 (L-band) and 0.9 (P-band) for Etonbreen.

Further interferometric analysis was conducted using corner reflectors deployed on the ice's surface as a reference to help determine the average penetration depth.

- Phase centres were computed using the difference between the interferometric phase at the reflector and the ice in the immediate vicinity yielding:
    - X-band: depths of ~ 4 m for both test sites
    - L-band: depths of 7-10 m at Summit, 12-14 m at Etonbreen
    - P-band: depths of ~7-12 at Summit, 13 -17 m (cross-pol) at Etonbreen

The differences between polarisations are likely due to the different relative contributions of a ground component to the total phase.

The P-band sounder data were processed and an intensive study is performed in the frame of the ACRAS project. Sounder data acquisitions were made over the Austfonna ice cap and the Etonbreen glacier. The most promising results were obtained over the Etonbreen glacier, were data are acquired over bedrock with increasing ice layer thickness during the flight track. Ice layer thickness up to 570 m could be identified. One important result of the first order analysis is that the choise of the polarizations for bedrock identification plays a role.

7 DATA ANALYSIS LAND ICE

7.1 Introduction

This section describes the estimation of ice volume extinctions through modelling of Pol-InSAR coherences. Extinction is a relevant parameter for glaciologists since it is related to the density and internal structure of the ice.

Extinction (conventionally represented as κ_e) accounts for the combined effect of absorption and scattering in the medium and may be expressed in terms of the penetration depth d_{pen} at which the one-way backscattered power falls to $1/e^{-1}$ (approximately 38%) (Ulaby 82):

$$\kappa_e = \frac{-\cos\theta_r}{d_{pen}} \tag{1}$$

Where θ_r is the refracted incidence angle in the ice volume and the cos θ_r factor accounts for the off-vertical travel distance of the wave within the medium. κ_e is the 1-way power extinction coefficient in units of Nepers per meter (Npm^{-1}), although it is conventionally quoted as a two-way extinction: $20\log_{10}e^{\kappa e} \simeq 8.686\,\kappa_e$ in units of dB/m.

Knowledge of κ_e may be useful for characterizing regions of greater or lesser volume scatter, and in turn increasing the accuracy of facie delineation and classification. Monitoring the extent of the various melt zones (facies) is a key requirement for detecting any fluctuations that may be occurring in the polar and subpolar regions as a result of climatic changes. With *a priori* knowledge extinction can further help in determination of grain sizes and/or temperature regime (Hoen 2001).

The SAR observables are modelled as a combination of a surface contribution from the snow-ice interface and a volume response. Separation of the ground and volume contributions is obtained through decomposition of the polarimetric covariance and coherency matrices. Both model-based Freeman 2- and 3-component and eigenvector decompositions are examined. Ground-to-volume scattering ratios derived from polarimetry are used in conjunction with Pol-InSAR interferometric coherences to invert the extinction of the ice volume. Validation is performed with airborne Pol-InSAR data at L- and P-band collected from the ICESAR and SVALEX campaigns.

7.2 Methodology for the Derivation of Ice Structure

The methodology section is split into two parts. First we use polarimetric decompositions techniques to separate the volume and surface responses, considering all polarisations together. Information on the ground-to-volume scattering ratio for each polarisation is then used in the subsequent section in combination with interferometric coherences to obtain an estimate of extinction, a parameter which is related to ice structure.

7.2.1 Decomposition Approach

To estimate the extinction of ice volumes, it is necessary to separate the ground and volume contributions. Here we estimate the ground-to-volume scattering ratios through decomposition of the polarimetric covariance and coherency matrices. Eigenvector decompositions (Cloude and Pottier 1996) separating dominant scattering mechanisms as well as the model-based Freeman 3-component (Freeman and Durden 1998) and Freeman 2-component (Freeman 2007) decompositions yield estimates of the ground-to-volume scattering ratio at each polarisation. Each of these decompositions is briefly outlined below.

Eigenvector decomposition:
This class of decomposition theorems is those based on the eigenvector decompositions of the coherency matrix. Cloude and Pottier were the first to consider such a decomposition to identify the dominant scattering mechanism via extraction of the largest eigenvalue.

The eigenvalue problem can be used to generate a diagonal form of the coherency matrix *[T]*, which we can physically interpret as statistical independence between a set of target vectors, yielding a general decomposition into three independent scattering processes:

$$\begin{aligned}[T] &= [T_1]+[T_2]+[T_3] \\ &= [U_3][\Lambda][U_3]^{-1}\end{aligned} \qquad (2)$$

Where $[\Lambda]$ is the diagonal eigenvalue matrix with elements ($\lambda_1 \geq \lambda_2 \geq \lambda_3 \geq 0$) and $[U_3] = [e_1, e_2, e_3]^T$ is the unitary eigenvector matrix with columns corresponding to the orthonormal eigenvectors. We assume that the dominant scattering mechanism yielding coherency matrix $[T_1] = \lambda_1 (e_1 e_1^{*T})$ is due to surface scattering and that the other two scattering mechanisms are volume-type scattering. These assumptions can be verified by examining the polarimetric properties of $[T_1]$, $[T_2]$ and $[T_3]$. The eigenvector decomposition has the advantage in that no underlying model is assumed.

Although traditionally the decomposition has been performed on the coherency matrix since the Pauli basis enables a more straightforward interpretation in terms of elementary scattering mechanisms (Hajnsek 2001), eigenvector decomposition is basis invariant, i.e. the same result is obtained for any polarisation basis. For consistency with subsequent model-based decomposition we may also perform eigenvector decomposition on the covariance matrix, yielding:

$$[C] = [C_1]+[C_2]+[C_3] \qquad (3)$$

Freeman 3-component decomposition

The Freeman 3-component decomposition (abbreviated Freeman-3) assumes that the signal consists of three components: surface and dihedral returns from reflection-symmetric media, and a volume component from a cloud of randomly-oriented dipoles. Combined, this gives the following reflection-symmetric covariance matrix:

$$[C]=[C_s]+[C_d]+[C_v]$$
$$= f_s\begin{bmatrix} |\beta|^2 & 0 & \beta \\ 0 & 0 & 0 \\ \beta^* & 0 & 1 \end{bmatrix} + f_d\begin{bmatrix} |\alpha|^2 & 0 & \alpha \\ 0 & 0 & 0 \\ \alpha^* & 0 & 1 \end{bmatrix} + f_v\begin{bmatrix} T_S^4 & 0 & T_S^2 T_P^2 \frac{1}{3} \\ 0 & T_S^2 T_P^2 \frac{2}{3} & 0 \\ T_S^2 T_P^2 \frac{1}{3} & 0 & T_P^4 \end{bmatrix} \quad (4)$$

Where *s* is surface, *d* is dihedral and *v* is volume, and f_s, f_d, f_v, α and β are parameters inverted from the model used to reconstruct *[C_s], [C_d]* and *[C_v]*. Here the volume component *[C_v]* has been adjusted to take into account snow-firn transmissivities using the Fresnel transmission power coefficients T_s (for horizontal polarisation) and T_p (for vertical polarisation) which may be determined given approximate knowledge of the dielectric constants of the overlying snow ($\varepsilon_r \simeq 1.7$), the underlying firn ($\varepsilon_r \simeq 2.8$) and the refracted incidence angle from Snell's law (Ulaby 1982).

Additional assumptions of this decomposition are that the radar backscatter is reciprocal (as for all monostatic systems, i.e. HV = VH), that like- and cross-polarised returns are uncorrelated ($\langle S_{HH}\ S_{HV}^*\rangle = \langle S_{VV}\ S_{HV}^*\rangle = 0$), and that the volume, double-bounce and surface scatter components are uncorrelated, such that the combined covariance matrix is the sum of the matrices for the individual mechanisms.

Freeman 2-component decomposition

Freeman developed a second polarimetric decomposition technique in which two scattering mechanisms are fitted to PolSAR data. The two mechanisms are volume scatter from a medium with azimuthal symmetry and a ground scatter term that can represent *either* double-bounce scatter or slightly rough surface scatter. It is assumed that one of these two mechanisms is dominant and that the other can be neglected. The surface or double-bounce term is modelled in the same way as for the Freeman-3 component decomposition. The 2-component model also has an additional degree of freedom in the volume scattering term which allows a broader range of volumes to be modelled in contrast with the 3-component model in which the volume scatter is assumed to be from randomly-oriented dipoles.

For glacier scenarios, in which the dihedral component is expected to be very low, we assume that the surface component dominates, such that the returns are from a reflection-symmetric surface and a random volume of particles. Combined, this gives:

$$[C]=[C_s]+[C_v]$$

$$= f_s\begin{bmatrix} 1 & 0 & \beta \\ 0 & 0 & 0 \\ \beta^* & 0 & |\beta|^2 \end{bmatrix} + f_v\begin{bmatrix} T_S^4 & 0 & T_S^2T_P^2\rho \\ 0 & T_S^2T_P^2(1-\rho) & 0 \\ T_S^2T_P^2\rho & 0 & T_P^4 \end{bmatrix} \qquad (5)$$

Where ρ is related to the shape and orientation of particles in the volume. For random volumes ρ is a real quantity and $1/3 \leq \rho \leq 1$, where ρ = 1/3 represents a dipole scatterer and ρ = 1 is a sphere. Inverted values of ρ outside this validity range indicate either deficiencies in the surface and/or volume model for describing the scattering physics or indicate excessive noise in the data.

Ground-to-volume scattering ratios

In the previous step we have separated the power contributions from the surface and from other scattering mechanisms for each linear polarisation using various polarimetric decompositions. In order to use this information to compute extinction values, ground-to-volume scattering ratios must be determined for input into a separate model. Ground-to-volume scattering ratios m = [m_{HH}, m_{HV}, m_{VV},] are computed using the powers along the diagonals of the covariance matrices:

Eigenvector: $m_{eigen}=\dfrac{diag([C_1])}{diag([C_2])+diag([C_3])}$

Freeman-3: $m_{F-3}=\dfrac{diag([C_s])}{diag([C_v])}$

Freeman-2: $m_{F-2}=\dfrac{diag([C_s])}{diag([C_v])}$. (6)

Note that both Freeman-3 and Freeman-2 models assume the surface power contributed by the cross-pol to be zero and thus $m_{HV} = 0$. As well, for the Freeman-3 decomposition we disregard the dihedral power contribution to the ground-to-volume scattering ratio since it is neither a clearly-interpretable volume nor surface contribution.

7.2.2 Polarimetric SAR Interferometry Approach

The ground-to-volume scattering ratios estimated in the previous step are used in combination with Pol-InSAR interferometric coherences and an infinite-uniform-volume-under-ground model for determination of the ice extinction coefficient.

In modelling the extinction, we use an adaptation of the Random Volume over Ground model (Cloude and Papathanassiou 2003). Let γ_z represent the coherence from a combination of volume scattering with complex coherence γ_{vol} and a surface scattering component at the snow-ice interface whose strength is determined by the positive scalar *m*. After correction of SNR and range spectral decorrelation the coherence magnitude is given as (Sharma et al. 2007):

$$|\gamma_z| = \left| \frac{\gamma_{vol} + m}{1+m} \right| \tag{7}$$

Where, assuming an infinite, uniform volume γ_{vol} can be represented by

$$\gamma_{vol} = \frac{1}{1 + \dfrac{j\cos\theta_r k_{zvol}}{2\ \kappa_e}} \qquad k_{zvol} = \frac{4\pi\sqrt{\varepsilon}}{\lambda}\frac{\Delta\theta_r}{\sin\theta_r} \ . \tag{8}$$

In (8) *j* is the imaginary number and k_{zvol} is the vertical wave number in the volume; λ is the wavelength in free space, ε the firn permittivity and $\Delta\theta_r$ the difference in look angles from each antenna as refracted in the volume.

With knowledge of *m* from the polarimetric decompositions of section 7.2.1, we can solve for κ_e using (7) and (8) at each polarisation and each pixel independently:

$$\kappa_e = \frac{\cos\theta_r |k_{zvol}|}{2(1+m)} \sqrt{\frac{|\gamma|^2 (1+m)^2 - m^2}{1 - |\gamma|^2}} \ . \tag{9}$$

Multiple baselines offer additional estimates of κ_e which may be combined for more robust extinction estimation. However, although longer baselines offer increased sensitivity to volume structure, they are also increasingly sensitive to shortcomings in the coherence model and to errors in the estimates of *m*. It is plausible that the 'surface' response modelled in (7) is not a single snow-firn interface at depth $z_{surf} = 0$, rather the return from multiple stratified layers in the upper few metres with effective depth $z_{surf\ eff} < 0$. In practice this effective depth is difficult if not impossible to measure and adds an additional unknown to the inversion resulting in effective coherence magnitude:

$$|\gamma_z| = \left| \frac{\gamma_{vol} + m e^{j z_{surf} k_{zvol}}}{1+m} \right| \ . \tag{10}$$

For an effective depth $z_{surf\ eff}$ = -0.5 m the resulting errors in estimated κ_e at L-band using (9) for a true value of κ_e=0.3 dB/m are given in Fig. 7.1 errors in estimated extinction are plotted both as a function of baseline and ground-to-volume scattering ratio magnitude. Since the baselines flown in the ICESAR campaign have larger baseline to wavelength ratios for L- than for P-band, L-band is more sensitive to these effects, and for conciseness plots are only shown at this frequency.

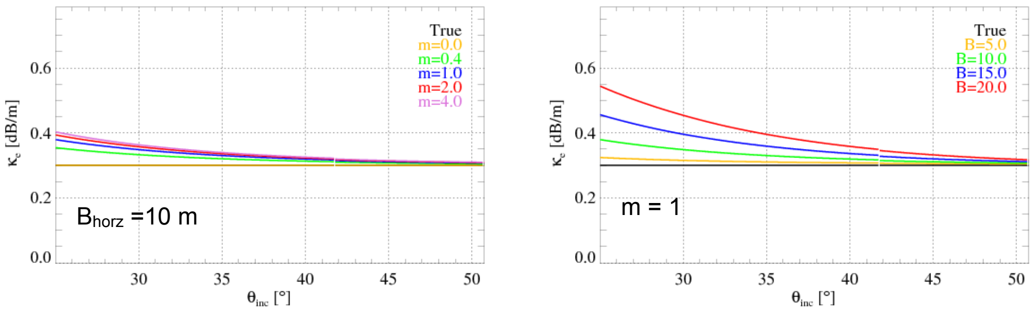

Fig. 7.1: Simulated κe inversions versus incidence angle in the presence of an error in the effective depth of the surface layer zsurf eff =-0.5 m. Results are shown for L-band and a true extinction of 0.3 dB/m.

One can also estimate the effect of an error in m of $m = m_{true} + \Delta m$ on inverted extinctions, which are plotted in Fig. 7.2 for $\Delta m = \pm 0.1$ as a function of baseline and m_{true}. It is seen that an overestimation of m (positive Δm) underestimates κ_e, whereas an underestimation of m (negative Δm) overestimates extinction.

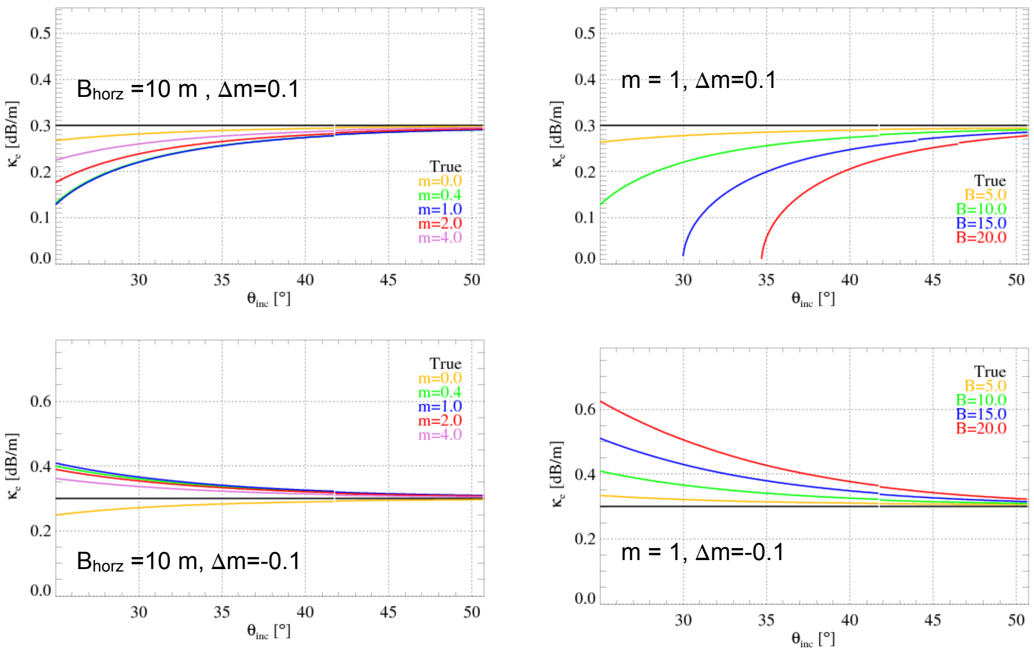

Fig. 7.2: Simulated κe inversions versus incidence angle in the presence of an error in m of ± 0.1. Results are shown for L-band and a true extinction of 0.3 dB/m.

In the above plots some combinations of m, B, Δm, and $z_{\mathrm{surf\ eff}}$ result in a negative square root in (9) such that there is no solution for κ_e (e.g. Fig. 7.2, upper right, B=20). In all cases, errors in estimated extinction are greatest in near-range since near-range has larger effective baselines, i.e. larger k_z. The error in κ_e is a non-linear function of m_{true}, B_{horz}, Δm, θ, $z_{\mathrm{surf\ eff}}$ and the true value of κ_e itself, and without knowledge of these parameters it is difficult to select B to achieve a certain maximum error of, for instance, $\Delta\kappa_e$ = 0.1 dB/m. However, when combining our baselines for a best approximation of κ_e we give additional weight to smaller baselines, masking out those baselines which are very large or which deliver no valid solution.

7.3 Preliminary Results of Ice Structure Estimation

7.3.1 Decomposition Approach

The three polarimetric decompositions from section 7.2.1 were applied to determine the dominant scattering mechanisms and their relative powers on a pixel-by-pixel basis for experimental airborne SAR data over the Austfonna ice cap. Ratios of these powers yield estimated ground-to-volume scattering ratios, which are subsequently used for extinction estimation in section 7.3.2

Eigenvector Decomposition

Results at both the Summit and Etonbreen sites and at L- and P-band for the eigenvector decomposition are shown in Fig. 7.3 to Fig. 7.6. In all instances normalised relative powers are shown for each pixel.

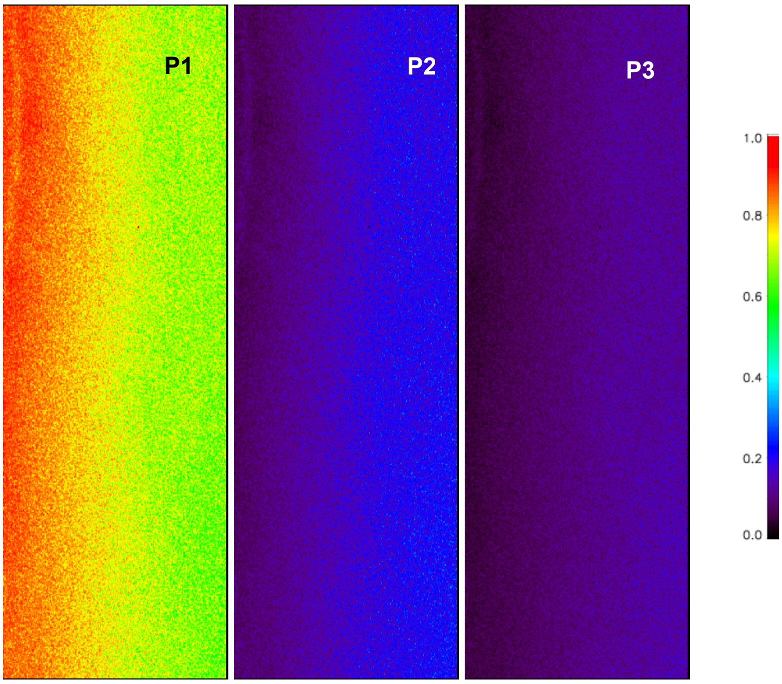

Fig. 7.3: Powers from eigenvector decomposition for L-band Summit, March, North. P1, P2 and P3 represent the normalised powers from the first, second and third scattering mechanisms, respectively.

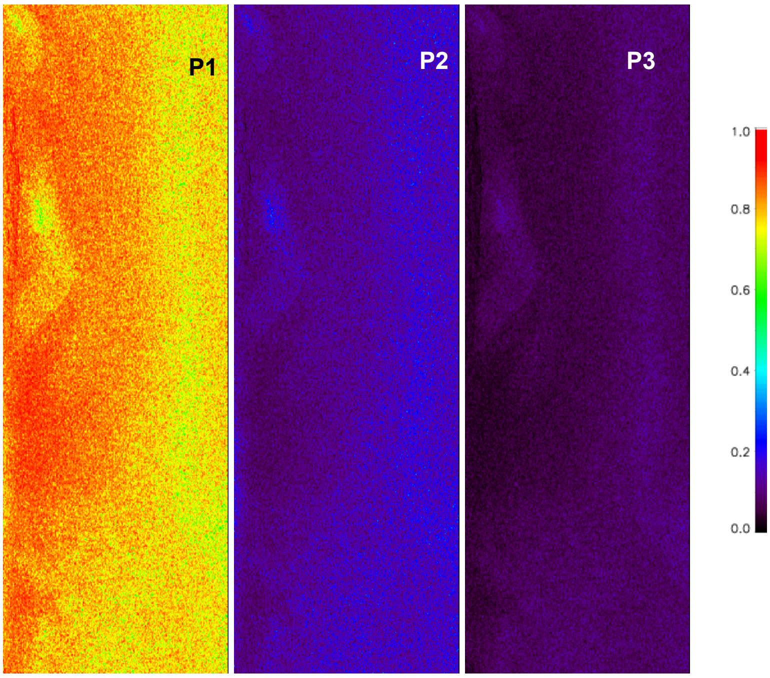

Fig. 7.4: Powers from eigenvector decomposition for P-band Summit, March, North.

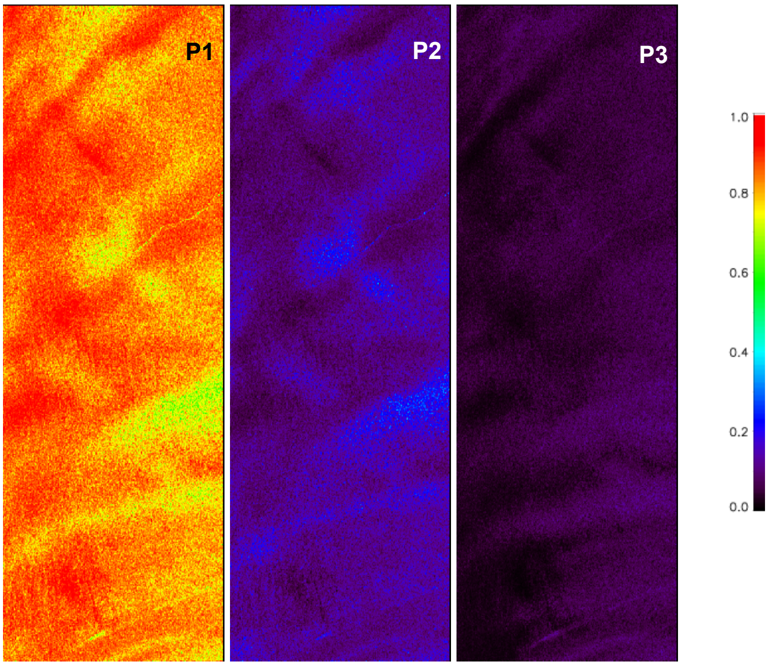

Fig. 7.5: Powers from eigenvector decomposition for L-band Etonbreen, March, North.

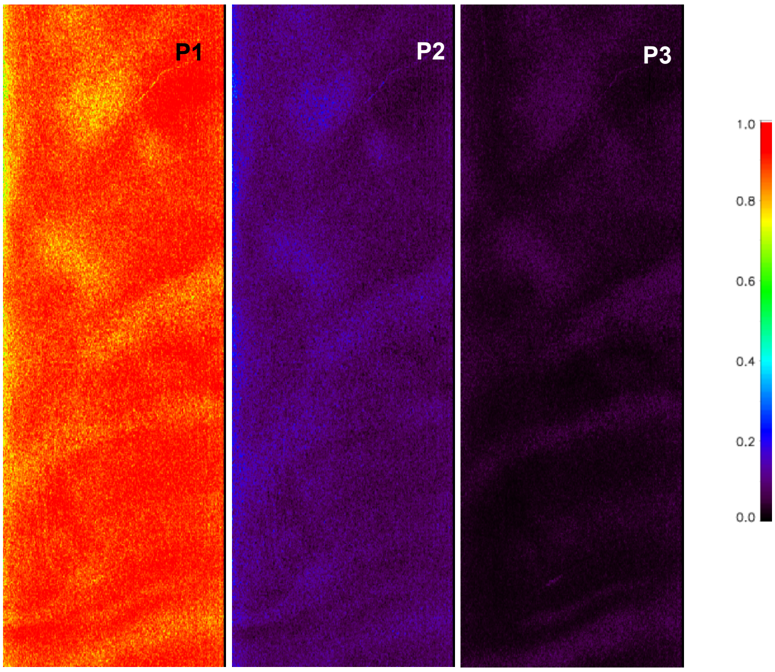

Fig. 7.6: Powers from eigenvector decomposition for P-band Etonbreen, March, North.

For Summit L-band (Fig. 7.3), it is seen that $[C_1]$ is most dominant in near-range, with power P_1 decreasing with increasing incidence angle as would be expected for a surface-type return. The presence of predominant surface scattering is confirmed by α_1 values, which in near-range are approximately 20°, corresponding to anisotropic odd-bounced scattering. In far-range the relative amount of power from the first component decreases and α_1 is closer to 50° suggesting a dipole mechanism. The second and third scattering mechanisms are more difficult to interpret ($\alpha_2 \simeq \alpha_3$

$\simeq$ 70º) although in far range all three mechanisms have closer values, suggesting volume scatter. The trends are similar at Summit P-band (Fig. 7.4), although *[C1]* is even more dominant than at L-band, with an average normalised P_1 over the entire image of 0.8. Again, α_1 corresponds to a surface-type scattering mechanism slowly increasing from ~ 5º in near-range to 20º in far-range. α_2 and α_3 are extremely high (~80º), suggesting double-bounce and/or volume mechanisms. Some ice structure is visible at P-band for which P_1 is decreased in comparison to the surrounding areas.

Eigenvector decompositions for Etonbreen generally display the same trends, although often even more exaggerated than at Summit. At L-band (Fig. 7.5) P_1 is even more dominant, accounting for an average of 83% of the total power and α_1 is generally < 20º, corresponding to predominantly surface scatter. Similarly for P-band (Fig. 7.6) P_1 has a mean value of 0.88 and typically also has $\alpha_1 < 20$. Again α_2 and α_3 are extremely high at ~ 80º for both L- and P-band. There are no clear trends with incidence angle and ice structure is visible at Etonbreen as patches of variable P_1 power.

In summary, the first scattering mechanism corresponds to a surface-like scattering and is very dominant, with the second mechanism P_2 -7 to -10 dB lower than P_1 and the third mechanism P_3 -9 to -14 dB lower than P_1.

Freeman 3-component

Freeman decomposition into 3-components (surface, dihedral, volume) was carried out for both test sites and frequencies. Normalised powers are plotted in Fig. 7.7 to Fig. 7.10. Average co- and cross-pol correlation components $\langle S_{HH} S_{HV}^* \rangle$ and $\langle S_{VV} S_{HV}^* \rangle$ are nearly negligible compared with co-pol components $|S_{HH}|^2$ and $|S_{VV}|^2$ (average values are < 5% of the dominant *[C]* components) fulfilling the Freeman assumption of $\langle S_{HH} S_{HV}^* \rangle \simeq \langle S_{VV} S_{HV}^* \rangle \simeq 0$.

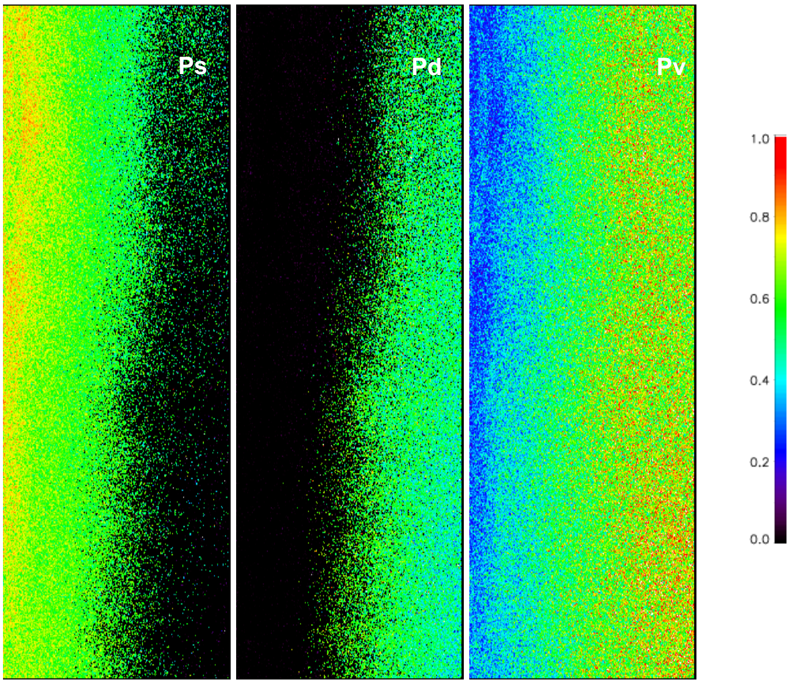

Fig. 7.7: Powers from Freeman 3-component decomposition for L-band Summit, March, North. Ps, Pd and Pv represent the normalised surface, dihedral and volumetric powers, respectively.

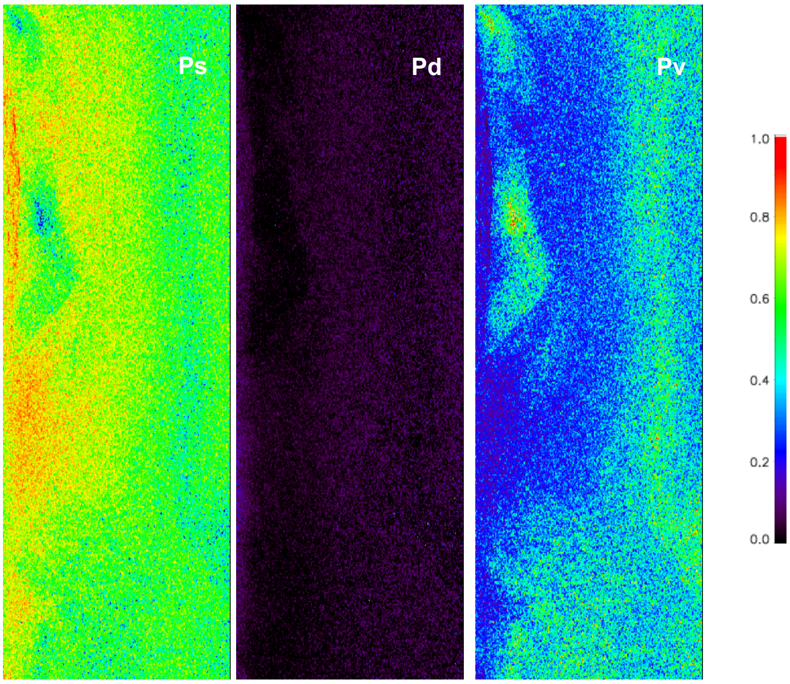

Fig. 7.8: Powers from Freeman 3-component decomposition for P-band Summit, March, North.

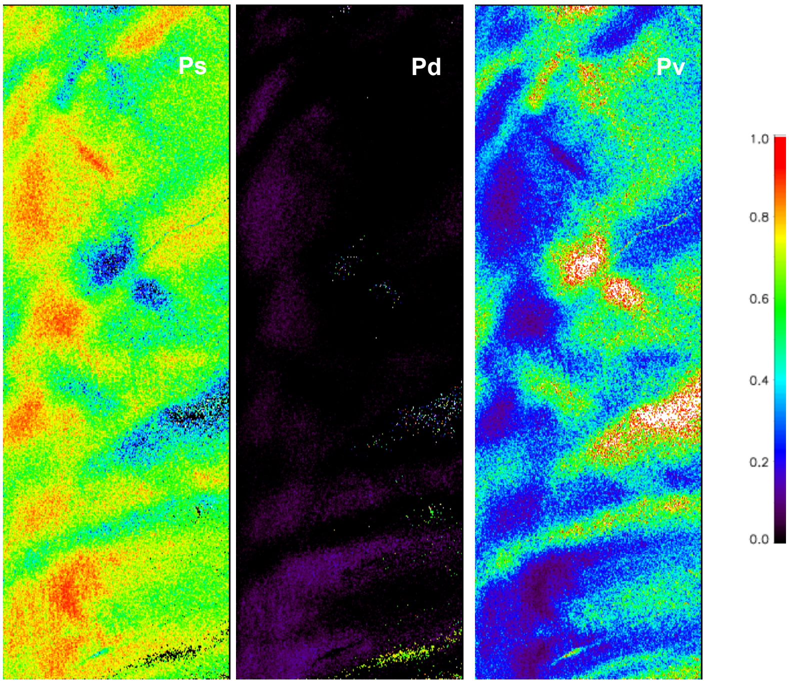

Fig. 7.9: Powers from Freeman 3-component decomposition for L-band Etonbreen, March, North.

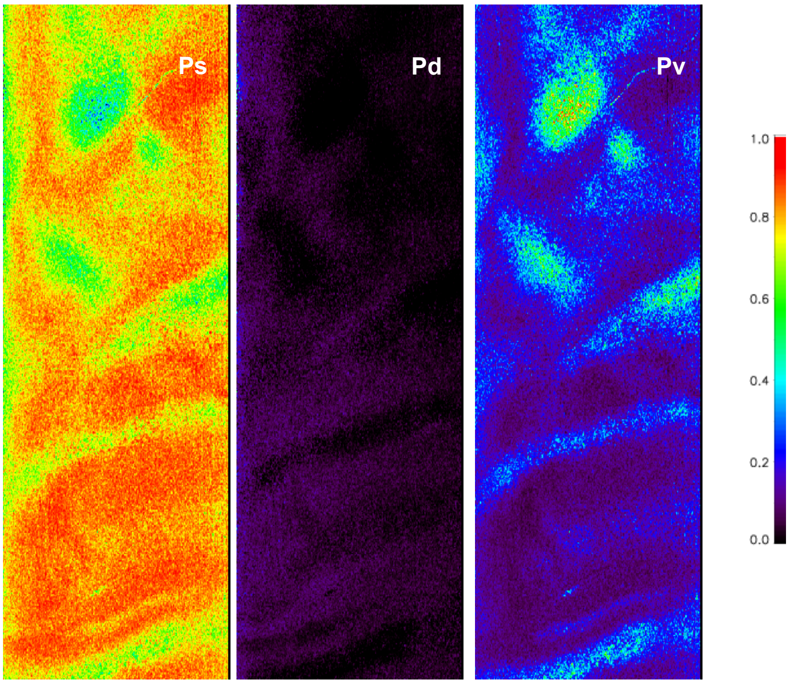

Fig. 7.10: Powers from Freeman 3-component decomposition for P-band Etonbreen, March, North.

For the Freeman 3-component decomposition at L-band (Fig. 7.7) we see dominant surface in near-range, slowly decreasing with incidence angle. At incidence angles of approximately $\theta \geq 45°$, the phase difference between HH and VV polarisations exceeds $\pi/2$ such that dihedral scattering is identified as being dominant. As surface/dihedral scatter decreases, we see a corresponding increase in the relative amount of volume scatter. In extreme near-range on the upper portion of the image some light crevassing is visible, but otherwise few ice features are discernible. At L-band the ice volume appears very homogeneous, and the Freeman-3 component powers are dominated by trends with incidence angle, enabling some insight into the scattering mechanisms present in the data.

At P-band (Fig. 7.8) there is strong surface scatter which decreases somewhat with increasing range, very weak dihedral scatter, and significant volume scatter. As at L-band there are trends in P_s and P_v with incidence angle, although at this longer wavelength more ice structure is visible, with increased volume scatter in an irregularly-shaped area in the upper-left and along a ridge-type feature in far-range. Summit lies in the percolation zone and these areas could correspond to areas of enhanced melt features such as ice pipes and lenses. Note that these areas are also consistent with regions of decreased P_1 power from the eigenvector decomposition.

There are some similarities between the Freeman-3 component decomposition for Summit and Etonbreen. For Etonbreen at L-band (Fig. 7.9), as before, we see strong relative surface power P_s in near-range decreasing with increasing incidence angle. Apart from a possible artifact due to missing DEM information during processing at the bottom of the image, dihedral contributions are minimal. However, compared to Summit, Etonbreen is more inhomogeneous and we can see ice features such as a possible drainage channel in the mid-upper right hand side as well as other patterns perhaps due to wind, melt and accumulation patterns.

For Etonbreen P-band (Fig. 7.10), again we see similarities to Summit with dominant surface scatter and negligible dihedral scatter, with similar ice features visible as for L-band Etonbreen. However, in this case surface scatter is even more dominant (normalised P_s = 0.63 for Summit compared with P_s = 0.78 for Etonbreen), perhaps due to the strong summer surface and relatively solid ice in the superimposed ice zone due to increased melting in comparison to the Summit test site.

The Freeman 3-component decomposition seems to generally deliver reasonable results with decreasing surface contributions with increasing incidence angle as expected from scattering theory and nearly negligible dihedral contribution. These trends are consistent with results from the eigenvector decomposition, although the relative surface scatter power contributions from Freeman-3 are not as strong as seen for the eigenvector decompositions.

Freeman 2-component

Results for Freeman decomposition into 2-components (surface and volume) are shown in Fig. 7.11 to Fig. 7.14. As seen from Freeman 3-component decomposition, the dihedral component is generally negligibly small (except for L-band Summit, although that may be due to a misinterpretation by the model of the HH-VV phase difference in far-range), such that our assumption that P_s is dominant over P_d is justified.

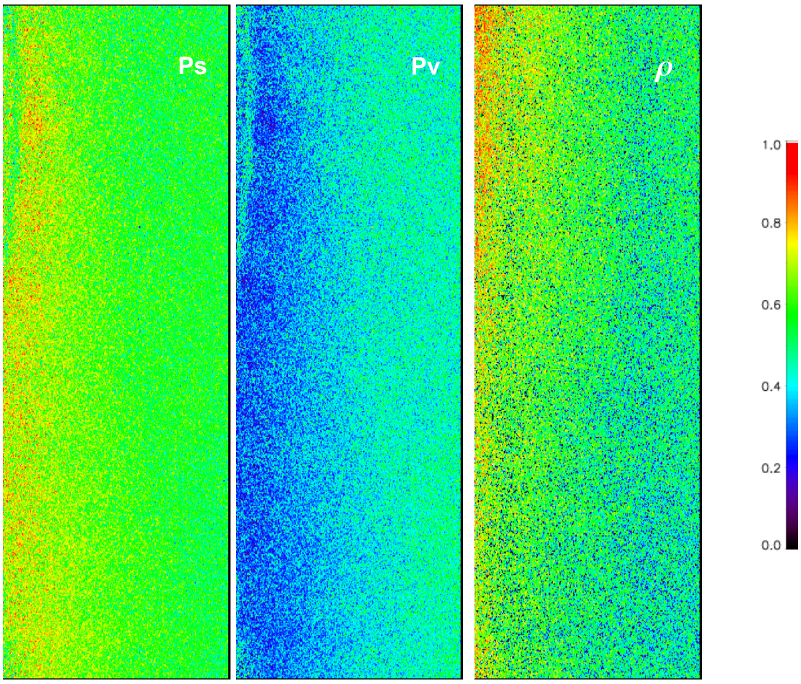

Fig. 7.11: Powers and shape from Freeman 2-component decomposition for L-band Summit, March, North. Ps, Pv and ρ represent the surface power, volumetric power, and shape parameter respectively

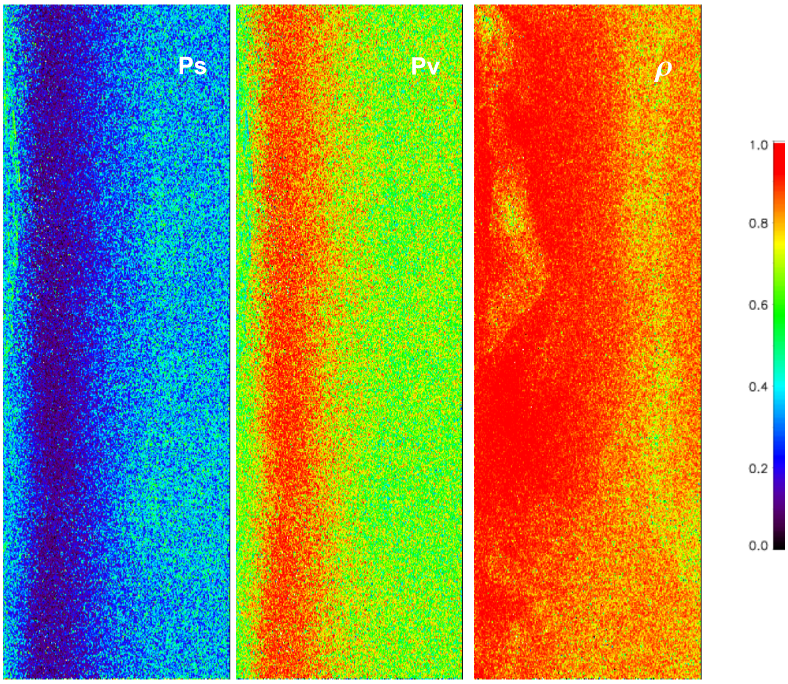

Fig. 7.12: Powers and shape from Freeman 2-component decomposition for P-band Summit, March, North.

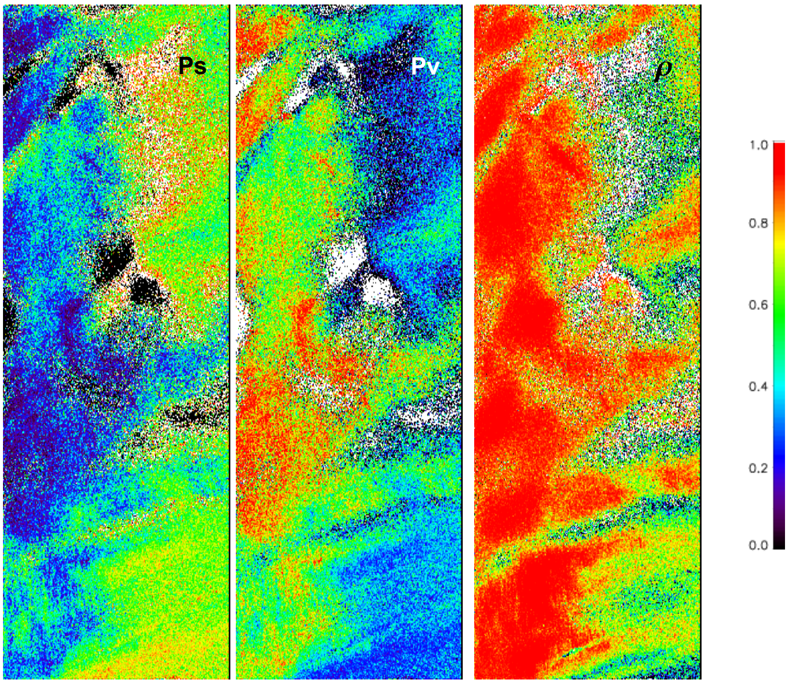

Fig. 7.13: Powers and shape from Freeman 2-component decomposition for L-band Etonbreen, March, North.

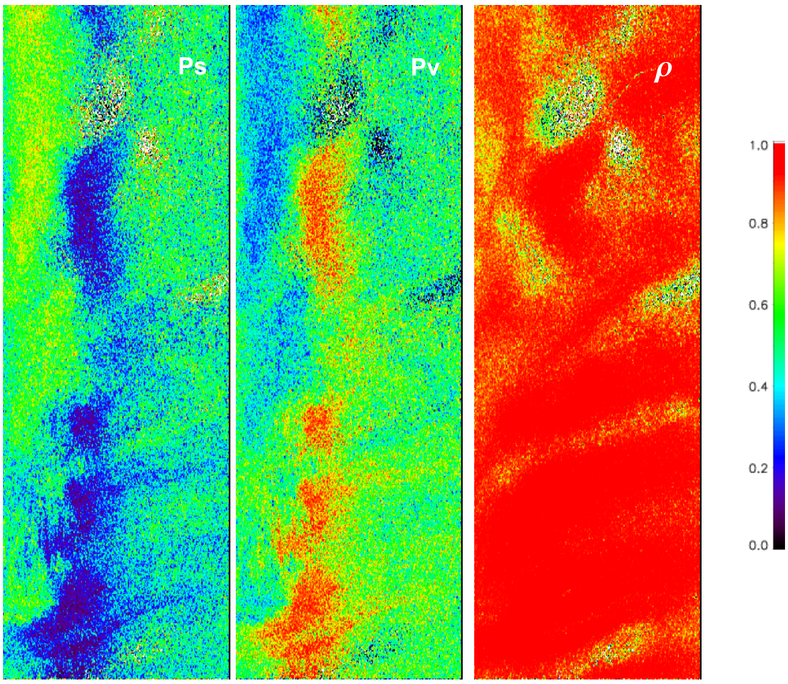

Fig. 7.14: Powers and shape from Freeman 2-component decomposition for P-band Etonbreen, March, North.

The Freeman-2 component decomposition for L-band Summit (Fig. 7.11) shows slightly more power from surface scattering than from volume scattering. As previously for the 3-component decomposition we see decreasing surface backscattering power with increasing incidence angle, although because the dihedral contribution is assumed to be zero, we see continuous results in the inversion even in far range. The shape parameter ρ shows maximum values in near-range corresponding to sphere-like particles and decreases with increasing incidence angle towards 1/3 representing dipoles. This behaviour is difficult to explain physically, as it is expected that the particle shape does not change with incidence angle. Again, as before, little in the way of ice structure is identifiable for Summit L-band.

Summit P-band (Fig. 7.12) shows larger relative volume scatter in comparison to L-band. Apart from a wide band close to near-range, relative volume and surface power do not show trends with incidence angle, rather the shape parameter ρ gradually decreases, which again is probably physically unrealistic. Areas of significant structure, corresponding to pixels with relatively high HV, are characterised by dipole-like particles, otherwise particles are relatively sphere-like with $\rho \simeq 1$, since spheres return no HV component.

For Etonbreen L-band Freeman-2 decomposition (Fig. 7.13) the surface and volume scattering powers vary strongly with incidence angle and ice structure. Results are noisier than at Summit and we see large salt-and-pepper-like areas characterised by highly varying surface and volume powers, likely due to a poor fit with the model. We see the opposite trend as one would expect from scattering theory, with increasing relative surface response with increasing incidence angle and decreasing relative volume response, also pointing to a likely-poor fit to the physical-scattering process. Although some deviations from this trend could be expected due to variation in ice structure over the swath, deviations of this magnitude are likely caused by other factors. For Etonbreen P-band (Fig. 7.14), surface and volume powers are similar except for a strip in near-range with strong volume scatter. The majority of $\rho > 1$, which is non-physical for a random volume, again suggesting a poor fit to the data.

Considering these results together, it seems that the Freeman-2 decomposition is not generally appropriate for modelling glacier ice since many of the results of the decomposition are non-physical or are not consistent with physical scattering behaviour such as decreasing surface power with incidence angle. Problematic seems to be modelling of the volume through the shape parameter ρ, which often takes on non-physical values outside of its validity range of 1/3 to 1 and seems to vary considerably with incidence angle.

Ground-to-volume scattering ratios

With the scattering powers for each scattering mechanism at each polarisation from the above decompositions, we use (6) to compute the ground-to-volume scattering ratios. Assumptions of the eigenvector decomposition were that $[T_1]$ (or equivalently $[C_1]$) corresponds to a surface scattering mechanism. This was verified by examining the α angle of $[T_1]$ which was generally < 20º except for L-band Summit far-range in which it climbed to approximately 50º. For the Freeman-2 component decomposition, it was assumed that $P_d \simeq 0$, which was also confirmed by the very low P_d powers from the Freeman-3 component decomposition. For conciseness and to examine trends through incidence angle, the mean m (ground-to-volume scattering ratios) for a subset 50 azimuth pixels wide in a relatively homogeneous area for each polarisation and decomposition are shown in Fig. 7.15 for Summit and Fig. 7.16 for Etonbreen. For reference the location of these subsets are shown in Fig. 7.17 to Fig. 7.20.

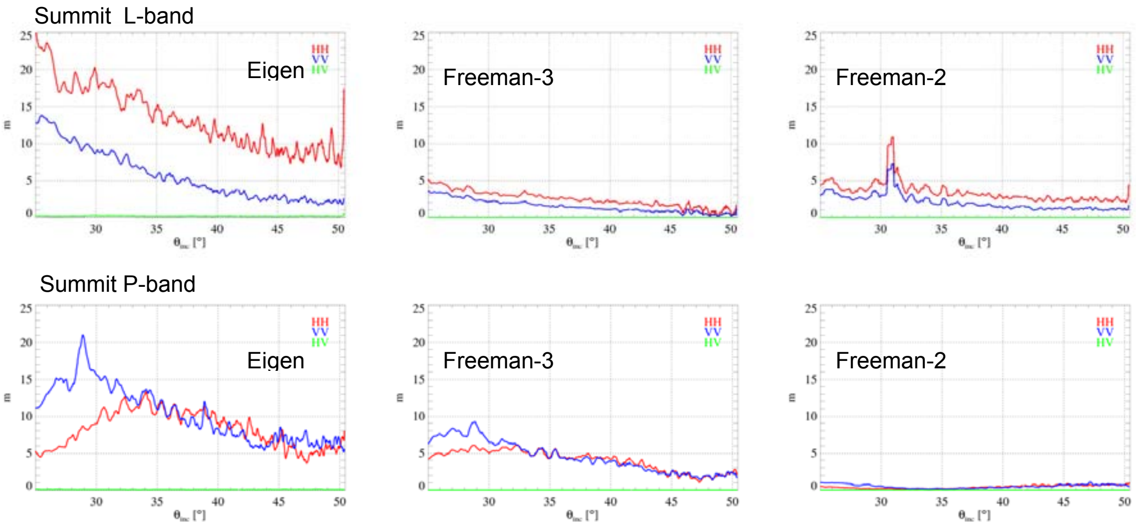

Fig. 7.15: Ground-to-volume scattering ratios for a homogeneous subset averaged through azimuth for Summit, March, North.

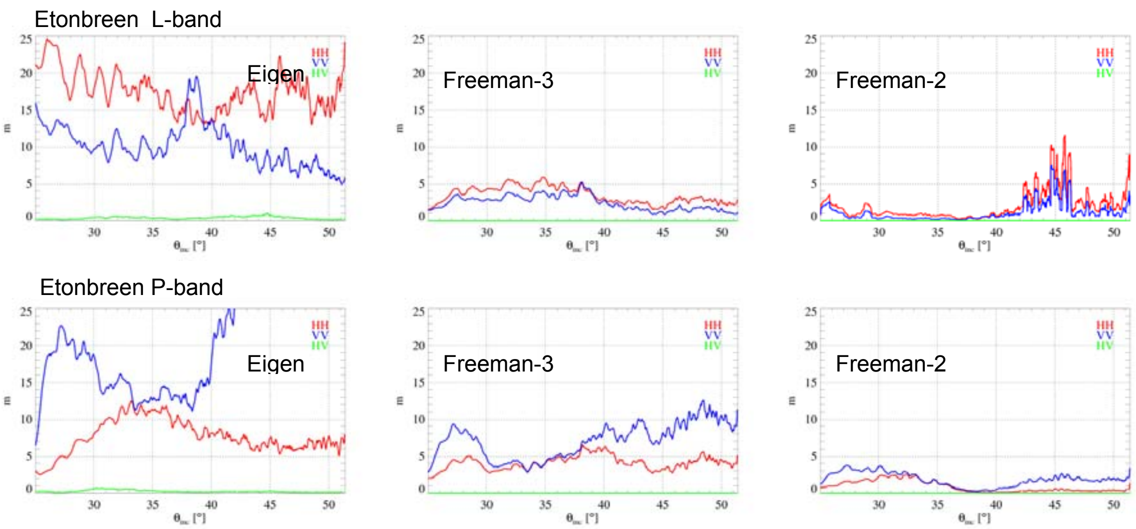

Fig. 7.16: Ground-to-volume scattering ratios for a homogeneous subset averaged through azimuth for Etonbreen, March, North.

It is seen that m_{HV} is negligible for the eigenvector decompositions, and thus the assumption of Freeman-2 and Freeman-3 that m_{HV} = 0 can be considered reasonable. In all instances, the eigenvector decompositions have much higher m values than the Freeman-2 and 3-component decompositions due to the extreme dominance of the 1st scattering mechanism and lack of HH and VV power in the *[C₂]* and *[C₃]* matrices. The Freeman-3 component decompositions show the same trends in *m* as the eigenvector decompositions although absolute *m* values are much lower (generally < 5 at L-band and < 10 at P-band). Freeman-2 component decompositions show very low *m* values and for L-band values are somewhat noisy.

Looking at the overall trends, for the homogeneous Summit L-band data and to a lesser extent the Summit P-band data, there is a clear decreasing trend in *m* with increasing incidence angle, which would be expected of Bragg-type scattering as predicted using the Small Perturbation Model (SPM). Etonbreen is more heterogeneous and ice structure plays a more dominant role than incidence angle in determining *m*. For both test sites at L-band in Fig. 7.15 and Fig. 7.16, m_{HH} is larger than m_{VV}, whereas Bragg scattering predicts the opposite polarisation relationship. We speculate that the increased HH backscatter (also visible in σ^o in Figure 6.22) is due to contributions from horizontal stratification layers and ice inclusions to the 'surface' response.

7.3.2 Polarimetric SAR Interferometry Approach

Given *m* from the various polarimetric decompositions, we use (9) to compute κ_e at each polarisation, baseline, frequency and test site. Results from multiple baselines are combined by first applying a mask of $0.01 < k_z < 0.1$ to eliminate solutions from extremely small baselines (which have virtually no interferometric sensitivity) and from longer baselines more susceptible to insufficiencies in modelling and to small errors in *m*. Results are then averaged from the remaining valid baselines on a pixel-by-pixel basis. If one polarisation does not have a solution, all polarisations for that pixel are set to undefined for consistency. Fig. 7.17 to Fig. 7.20 show inversion results at L- and P-band for the eigenvector, Freeman-3 and Freeman-2 component decompositions at HH. Due to the restrictions on k_z, not all pixels have a solution, evident in Fig. 7.17 by the dark patches, particularly in near-range where k_z is larger. As well, for eigenvector decomposition with very high *m* values, many pixels do not have a solution for κ_e although they do for Freeman-2 and Freeman-3 decompositions. For this reason the eigenvector decompositions in Fig. 7.17 and Fig. 7.19 show fewer valid areas and display this k_z-mask effect to a greater extent than for the Freeman decompositions, since oftentimes fewer baselines have valid pixels to be averaged.

Note that L- and P-band data are not coregistered and a different colour scale is used in each plot to better visualise the entire variation of κ_e within each scene. Relatively homogeneous subsets (each 50 azimuth pixels wide) are outlined in red, which are used in subsequent analysis to compare the various polarimetric decomposition methods through range.

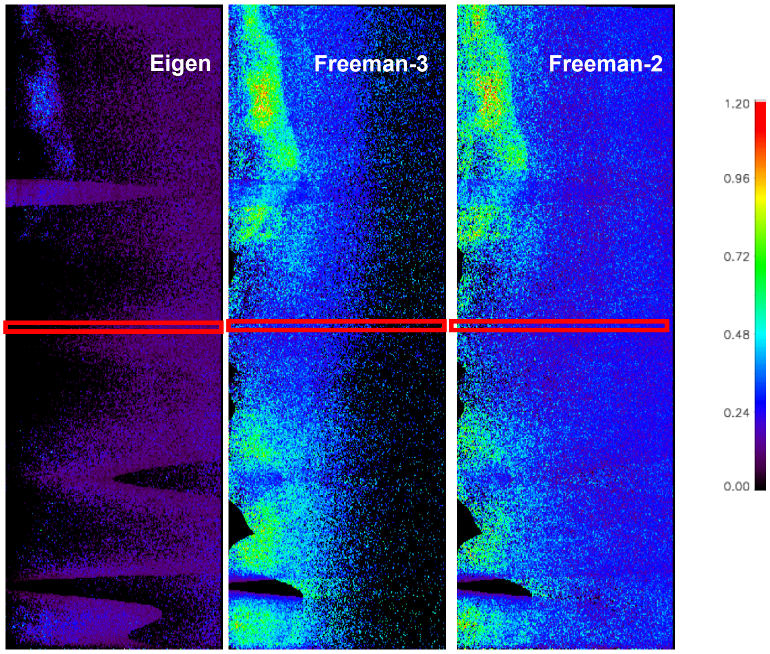

Fig. 7.17: Inverted extinctions for HH L-band Summit, March, North combining all baselines. Units are dB/m.

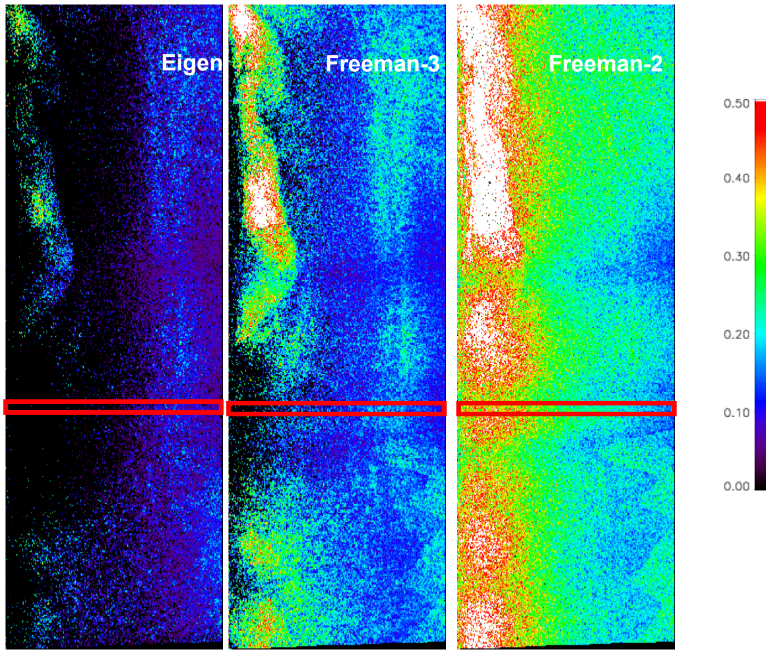

Fig. 7.18: Inverted extinctions for HH P-band Summit, March, North combining all baselines.

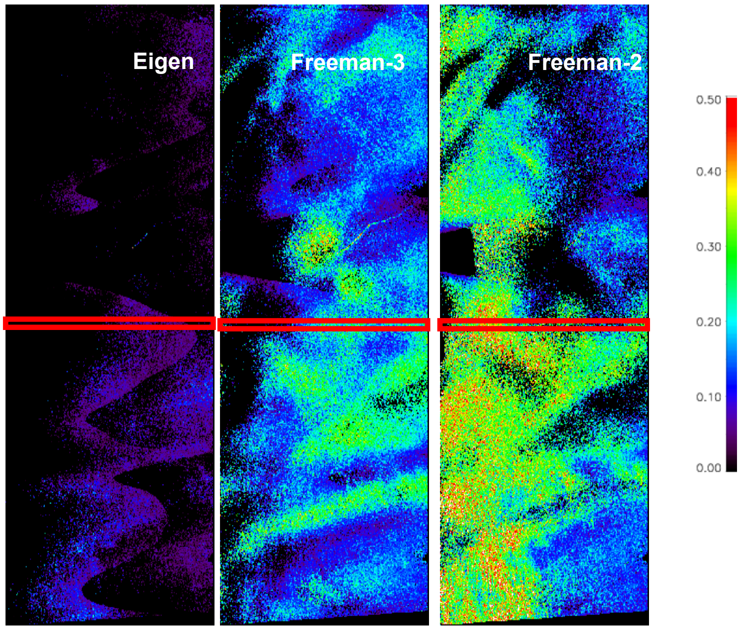

Fig. 7.19: Inverted extinctions for HH L-band Etonbreen, March, North combining all baselines.

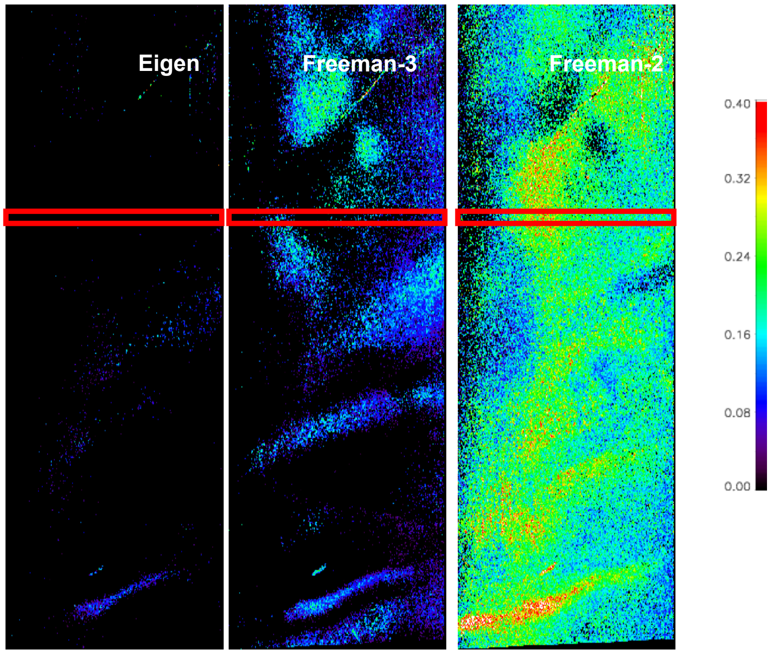

Fig. 7.20: Inverted extinctions for HH P-band Etonbreen, March, North combining all baselines.

Extinctions have been averaged through azimuth and smoothed through range within the subsets outlined in red above to reduce noise, and are plotted versus incidence angle in Fig. 7.21 and Fig. 7.22 to reveal the existence of any trends with range.

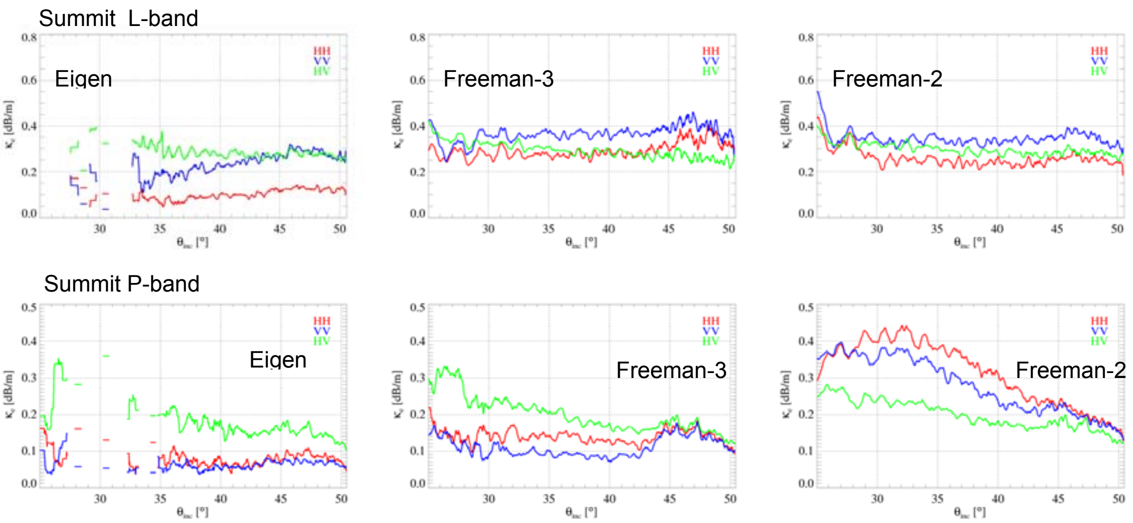

Fig. 7.21: Extinctions for a homogeneous subset averaged through azimuth for Summit, March, North

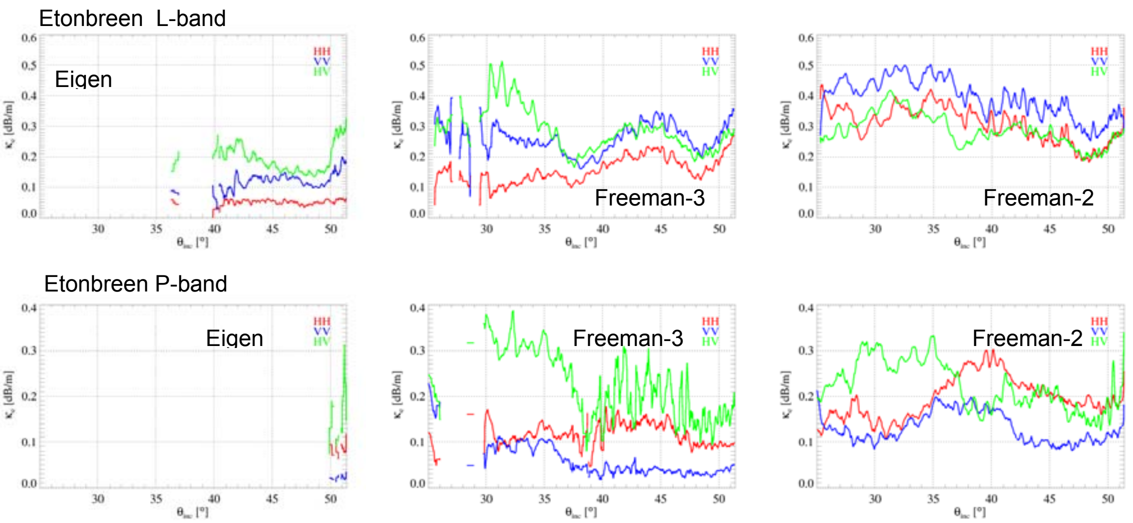

Fig. 7.22: Extinctions for a (relatively) homogeneous subset averaged through azimuth for Etonbreen, March, North.

It is constructive in the evaluation of all inversion methods to look at the HV extinctions since this polarisation displays a weaker incidence-angle dependency than the co-polar channels at P-band, and virtually no range-dependency at L-band. Conventional surface scattering models such as the SPM predict (to 1st order) an HV surface backscatter contribution of zero (i.e. m_{HV} = 0). Thus, we can assume that when the ground has been correctly removed, HH and VV extinctions should resemble those of HV, although the presence of an oriented volume component would result in differential extinctions between polarisations

For the eigenvector decomposition, inverted extinctions are very low if available at all for both L- and P-band at both test sites. In many cases the combination of a relatively low coherence magnitude $|\gamma_Z|$ and very large m results in a negative square root in (9) for which there is no solution. In addition, where inversion is possible, there is a likely over-estimation of the surface component since $\kappa_{e\,HV}$ is generally larger than both co-pol extinctions. Although the eigenvector decomposition mathematically rigorous, its relation to scattering physics is not straightforward, and it is possible that the assumption of $[C_1]$ and $[C_2]+[C_3]$ as surface and volume scattering mechanisms, respectively, is not accurate.

For the Freeman-3 component decomposition at Summit L-band the extinctions for all three linear polarisations are approximately equal and there is no distinguishable trend with range, consistent with a random volume and the correct removal of surface contributions. At Summit P-band the range trend has been removed using Freeman-3, although there exist differential extinctions between HH, VV and HV which may be due to oriented scatterers in the ice or due to inadequacies in the model such as unmodelled surface components at HV (since $\kappa_{e\,HV}$ resembles the result of a slightly underestimated *m* from Fig. 7.2). At Etonbreen, this subset is more inhomogeneous and extinction results are noisier, although the same general trends are apparent, with Freeman-3 L-band displaying similar κ_e in far-range (although some differential extinction in near-range) and P-band displaying similar co-pol κ_e and elevated $\kappa_{e\,HV}$.

Examining results over the entire image, the extinction results using Freeman-3 are generally satisfactory in that extinctions are very homogeneous throughout, with clearly defined area of high extinctions corresponding to potential percolation features such as ice lenses and ice pipes at Summit (see upper-left of images) and to potential enhanced layering and drainage-type features at Etonbreen.

Moving to the Freeman-2 component decomposition, that many of the trends in surface and volume powers from this decomposition were non-physical and therefore it is not expected to deliver valid extinctions. Although Summit L-band Freeman-2 gives reasonable results for κ_e which are in good agreement with Freeman-3, for Freeman-2 Summit P-band and Etonbreen, *m* appears to be underestimated, giving a strong decreasing trend in κ_e with range, likely due to an uncompensated surface contribution. This effect is particularly evident for P-band Summit in Fig. 7.18.

Overall, extinctions inverted using ground-to-volume scattering ratios m derived from Freeman 3-component decomposition were the most consistent with cross-pol data and displayed the least amount of incidence-angle dependency. Tab 7.1 summarizes these findings, where eigenvector decomposition and Freeman-2 decomposition often deliver physically invalid/inconsistent results. Freeman-3 for Etonbreen P-band was rated satisfactory since large areas had undefined extinctions. However, as seen in Fig. 6.32, the low entropy and alpha values for Etonbreen P-band suggest minimal volume contribution, and thus it is difficult to expect complete and accurate characterisation of volume scattering in such instances.

Tab 7.1 Summary of extinction estimation methods using various polarimetric decompositions.

	Eigen	Freeman-3	Freeman-2
Summit L-band	invalid	good	good
Summit P-band	invalid	good	invalid
Eton L-band	invalid	good	invalid
Eton P-band	invalid	satisfactory	invalid

7.4 Comparision between 2005 and 2007

To assess temporal change in the ice structure of the Austfonna ice cap, we compare extinctions inverted from ICESAR to those inverted using data from the SVALEX campaign in 2005 over the same test sites. Only the Southern passes from Summit SVALEX had small baselines appropriate for extinction inversion and so only ICESAR Summit South pass results are displayed for comparison. Extinctions inverted using *m* from Freeman-3 component decomposition for HH polarisation at Summit for both L- and P-band are shown for both campaigns in Fig. 7.23 and for Etonbreen in Fig. 7.24.

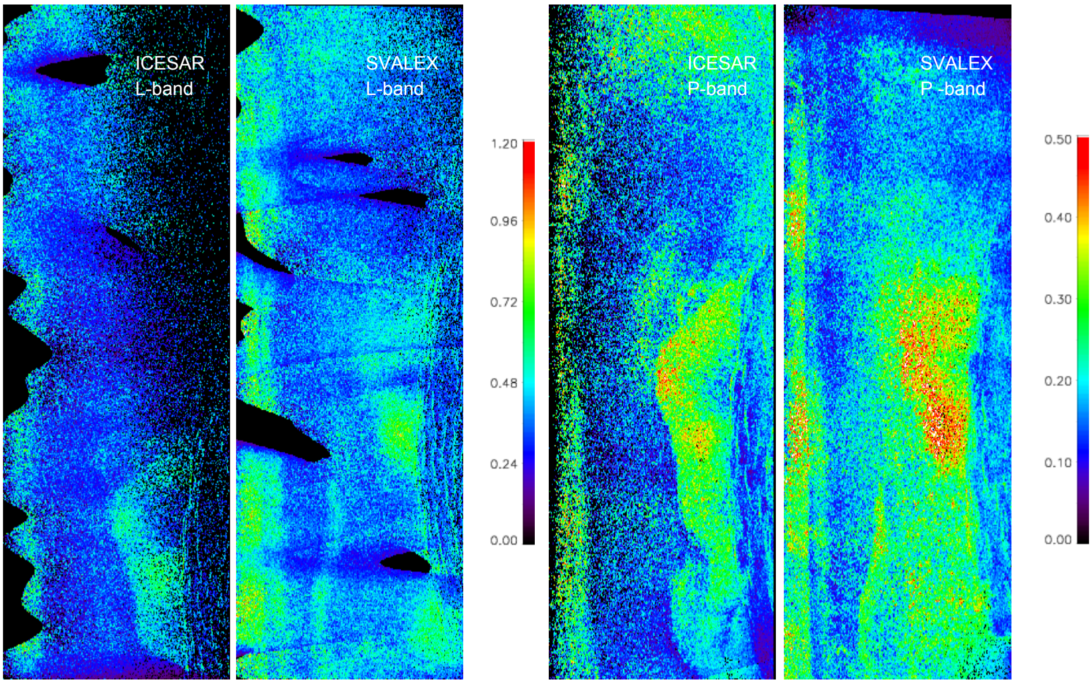

Fig. 7.23: Comparison of extinctions between ICESAR (2007) and SVALEX (2005) campaigns for HH polarisation, Summit, South.

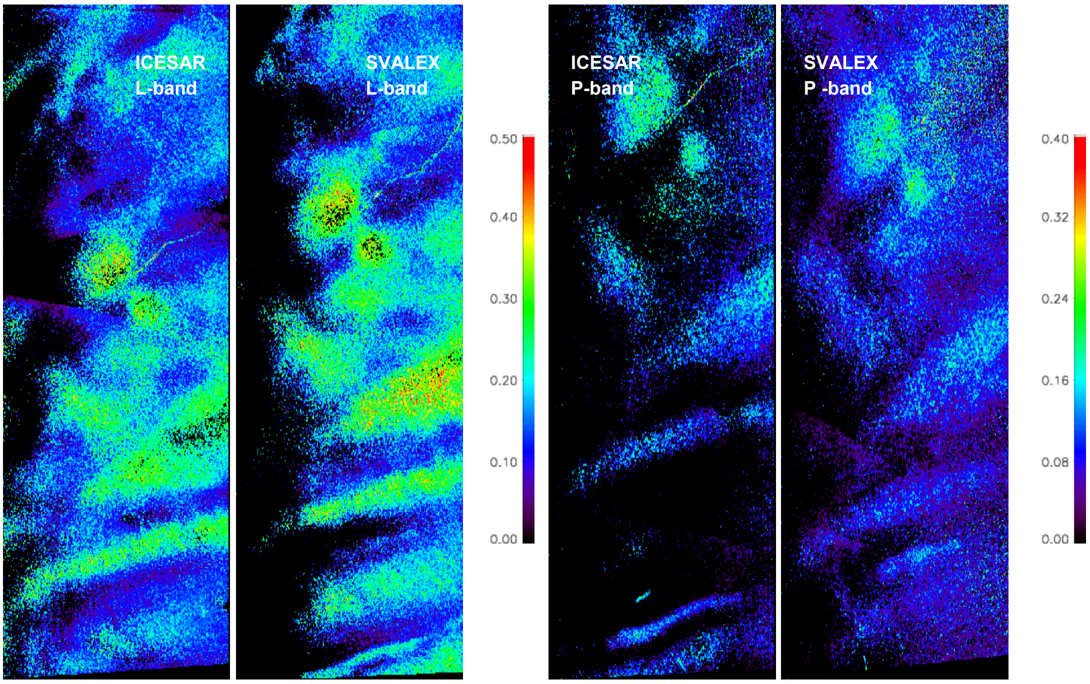

Fig. 7.24: Comparison of extinctions between ICESAR (2007) and SVALEX (2005) campaigns for HH polarisation, Etonbreen, North.

Note that the SVALEX and ICESAR results are not coregistered, but common features are easily identified between images from both campaigns. The evolvement and change in features characterised by high-extinction at Summit reveal never-before-seen temporal changes which may be a reflection of intervening snowfall and melt events. Boundaries of the percolation features at Summit are distinct in 2007 but are not yet distinguishable in 2005 (see P-band, Fig. 7.23). The near-range ridge feature on the other hand, remains relatively similar between 2005 and 2007. At Etonbreen, extinctions remain fairly constant between 2005 and 2007. At L-band the only discernible differences are slightly higher (speckled red) extinctions in a confined area in 2005, and a slightly different curving of the potential drainage-channel. At P-band extinctions are again very similar between campaigns, although the drainage-feature is only faintly visible in 2005.

7.5 Summary and Conclusion

An analysis of the extensive data set of the ICESAR campaign has been completed across test site (at both Summit and Etonbreen), through time (March and April acquisitions) and for various incidence angles. Single-polarisation, single-pass data are available for analysis at X-band and fully-polarised repeat-pass data at L- and P-band.

Extinctions of glacier ice have been inverted using Pol-InSAR observables by adapting existing PolSAR decompositions and a Pol-InSAR coherence model originally developed for vegetation applications to a glacier scenario. Separation of the ground and volume contributions was obtained through decomposition of the polarimetric covariance matrix using both eigenvector and model-based Freeman-3 component and Freeman-2 component decompositions, adjusted for the effective transmissivities of the radar signal into the ice volume. Ground-to-volume scattering ratios from polarimetry were then used in conjunction with Pol-InSAR coherences to estimate the extinction of the volume assuming an infinite-volume-under-ground model.

Best performance was achieved using ground-to-volume scattering ratios derived from the Freeman-3 component decomposition, yielding physically-plausible m and co-pol extinctions relatively independent of incidence angle and close to extinction magnitudes at HV. Results appear promising at both L- and P-band, particularly for short baselines which minimise the influence of slight inaccuracies and model deficiencies in the ground-to-volume scattering ratio.

Two-dimensional extinctions maps have been generated which may provide insight into the densities and internal structure of the ice, including the presence of melt features such as ice pipes and ice lenses. Future work will concentrate on further modelling improvements including investigation into the possibilities of an oriented volume and the estimation of differential extinctions, which may provide further information regarding the degree of horizontal stratification in the ice volume.

8 SATELLITE DATA ACQUISITION

On the basis of ice conditions observed during the Svalex Campaign in 2005 (with similar objectives as ICESAR) and monitored by satellite in the following year, the probability that flights over sea ice northwest of Svalbard would be carried out together with the DLR airplane were regarded as low, since the ice edge was relatively far from the northwest tip of Svalbard (the main island), and the maximum distance that can be flown by the DLR airplane with full radar equipment is shorter than for Polar-2. Therefore, higher-resolution APP-products from ENVISAT ASAR were ordered only over Storfjord and the Barents Sea. Wide-swath mode imagery from ASAR (swath width 400 km, spatial resolution 150 m) and WB1-images from ALOS PALSAR (swath width 250-350 km, resolution 100 m) are available over all test sites visited during ICESAR. Image properties are listed in Table 8.1.

Most of the ASAR data are already received. It was recognized; however, that some of the delivered ASAR data products did not cover the same strip length as the images shown in EOLISA (ESA's catalogue and ordering system) (although larger lengths were ordered). On the following pages, ASAR browse images from EOLISA are shown together with the position of corresponding swath in the Svalbard region. For PALSAR frames, no browse images are available. Data have not been ordered yet (status September 2007). One possibility is to receive data from the quota of an accepted ALOS Aden project proposal.

The satellite SAR images reveal variable signatures characteristics dependent on ice and weather conditions ("wet" and "dry"). For open water surfaces, the backscattered intensity varies with wind speed and wind direction relative to the radar look direction. The ASAR APP images are acquired at different incidence angle ranges. The angle change over the swath width is about 8 deg at mode IS1 (15.0-22.9 deg) and about 3 deg at mode IS7 (42.5-45.2 deg). The WSM images cover a much broader incidence angle range (17-43 deg). At larger incidence angles, the contrast between ice types is enhancd, and leads and deformation structures such as ridges are easier to identify.

Table 8.1a: Satellite Data

Date	Area	Imaging Mode	Start	Stop	Remark
13.03.	Svalbard East	ASAR WSM HH	09:30:48	09:32:25	Overview of ice conditions
13.03.	Svalbard West	ASAR WSM HH	19:28:26	19:30:13	
14.03.	Storfjord	ASAR APP HH/HV, IS1	10:40:12	10:40:51	initial conditions in Storfjord for flight on 1603; PALSAR frame same area
14.03.	Storfjord & Barents Sea	ALOS PALSAR WB1, HH	10:12:34	10:13:24	
14.03.	Barents Sea	ASAR APP HH/HV, IS4	18:56:57	18:57:37	
16.03.	Storfjord	ASAR APP HH/VV, IS6	09:37:23	09:38:02	joint flight over same area, a few hours later
17.03.	Barents Sea	ASAR APP HH/HV, IS1	10:45:27	10:46:08	
17.03.	Barents Sea & Fram Strait	ASAR WSM HH	19:02:36	19:04:30	flights in the Barents Sea on 1803 & north of Svalbard on 1903, overlap with PALSAR frame
17.03.	Barents Sea, Storfjord	ALOS PALSAR WB1, HH	10:35:30	10:36:21	

18.03.	Storfjord	ASAR APP HH/HV, IS1	10:14:31	10:15:10	northeast part of strip includes starting point of profile of Barents Sea flight
18.03	Barents Sea	ASAR WSM HH	18:30:59	18:32:02	

Table 8.1b: Satellite Data

Date	Area	Imaging Mode	Start	Stop	Remark
19.03.	Barents Sea	ASAR APP HH/VV, I4	9:42:37	9:43:17	includes parts of profile from Barents Sea flight on 1803
19.03.	Fram Strait	ASAR WSM HH	11:22:12	11:23:48	covers flight north of Svalbard
19.03.	Barents Sea	ASAR APP HH/HV, I1	17:59:53	18:00:27	
20.03.	Barents Sea	ASAR APP HH/HV, I7	9:11:08	9:11:47	
21.03.	Barents Sea	ASAR APP HH/HV, I2	10:19:46	10:20:25	overlap with PALSAR frames, meteoro-logical flight over Storfjord
21.03.	Fram Strait	ASAR WSM	11:59:56	12:00:39	covers flight profile 2003 in the north, overlap with PALSAR frames
21.03.	Storfjord	ASAR APP HH/HV, I1	18:36:58	18:37:36	
21.03.	Barents Sea	ALOS PALSAR WB1 HH	10:01:10	10:02:01	
21.03.	Fram Strait	ALOS PALSAR WB1, HH	11:39:12	11:40:03	
21.03.	Fram Strait	ALOS PALSAR WB1, HH	11:39:53	11:40:44	
21.03.	Storfjord	ALOS PALSAR WB1 HH	19:47:19	19:48:10	
22.03.	Barents Sea & Storfjord	ASAR WSM HH	9:48:33	9:49:39	overlap of ASAR APP and WSM, also overlap with PALSAR frames
22.03.	Barents Sea	ASAR APP HH/HV I1	18:05:30	18:06:09	
22.03.	Storfjord	ASAR APP HH/VV I6	19:45:38	19:46:11	
22.03.	Barents Sea & Storfjord	ALOS PALSAR WB1 HH	10:41:57	10:42:47	
22.03.	Storfjord	ALOS PALSAR WB1 HH	10:42:38	10:43:28	
22.03.	Fram Strait	ALOS PALSAR WB1 HH	12:19:59	12:20:50	
23.03.	Fram Strait	ASAR WSM	10:56:31	10:57:32	
23.03.	Barents Sea	ASAR APP HH/HV I6	19:14:06	19:14:45	
23.03.	Barents Sea	ALOS PALSAR WB1 HH	9:44:41	9:45:32	
23.03	Fram Strait	ALOS PALSAR WB1 HH	11:22:02	11:22:53	

A check on the JAXA web site (https://auig.eoc.jaxa.jp/auigs/en/top/index.html) carried out in the beginning of February 2008 indicates that no PALSAR images were acquired around Svalbard during the period from March 11-25, 2007.

March 13, 2007

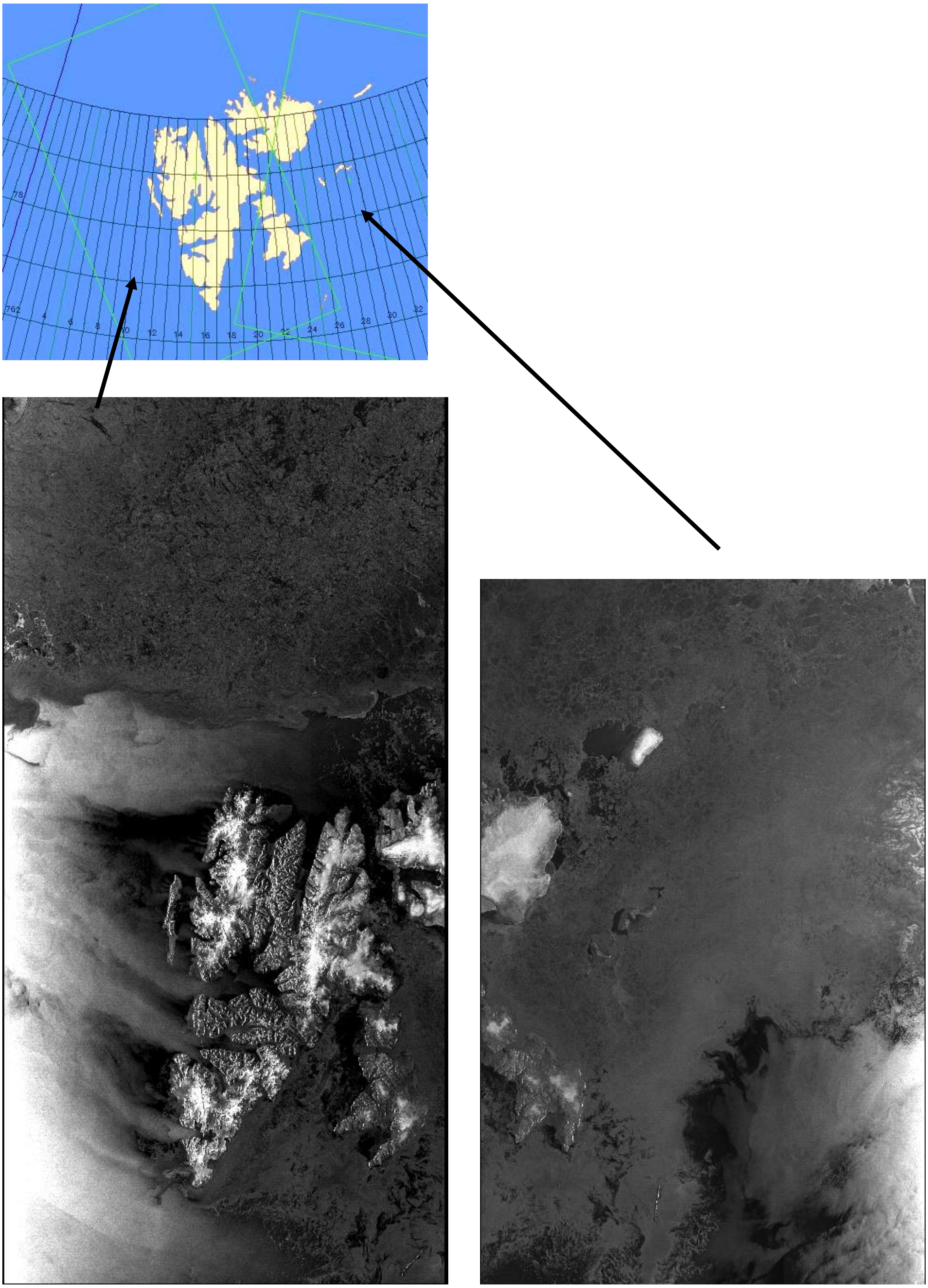

1303 1928

1303 0930

March 14, 2007

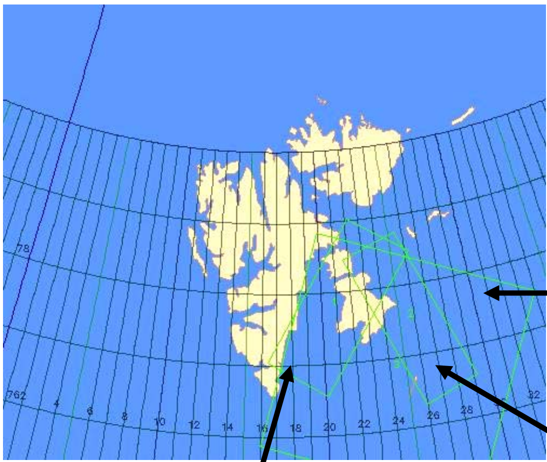

PALSAR WB1

1403 1040

1403 1856

March 16, 2007

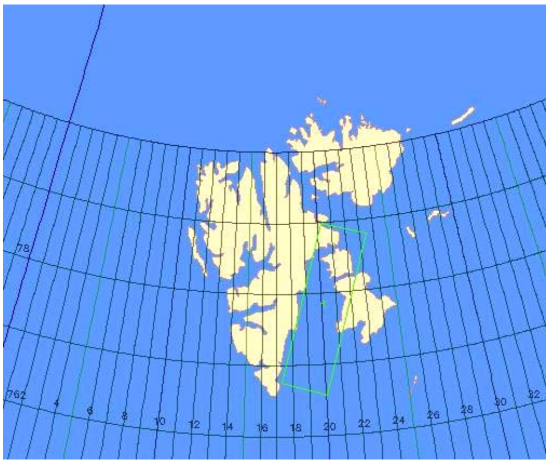

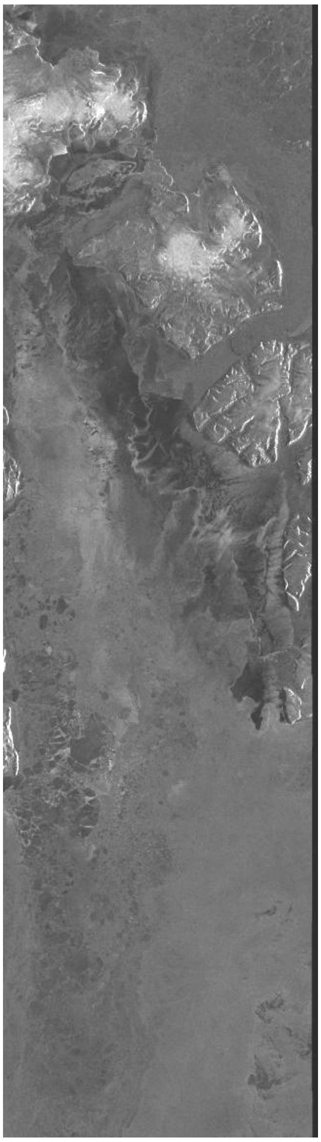

16030937

March 17, 2007

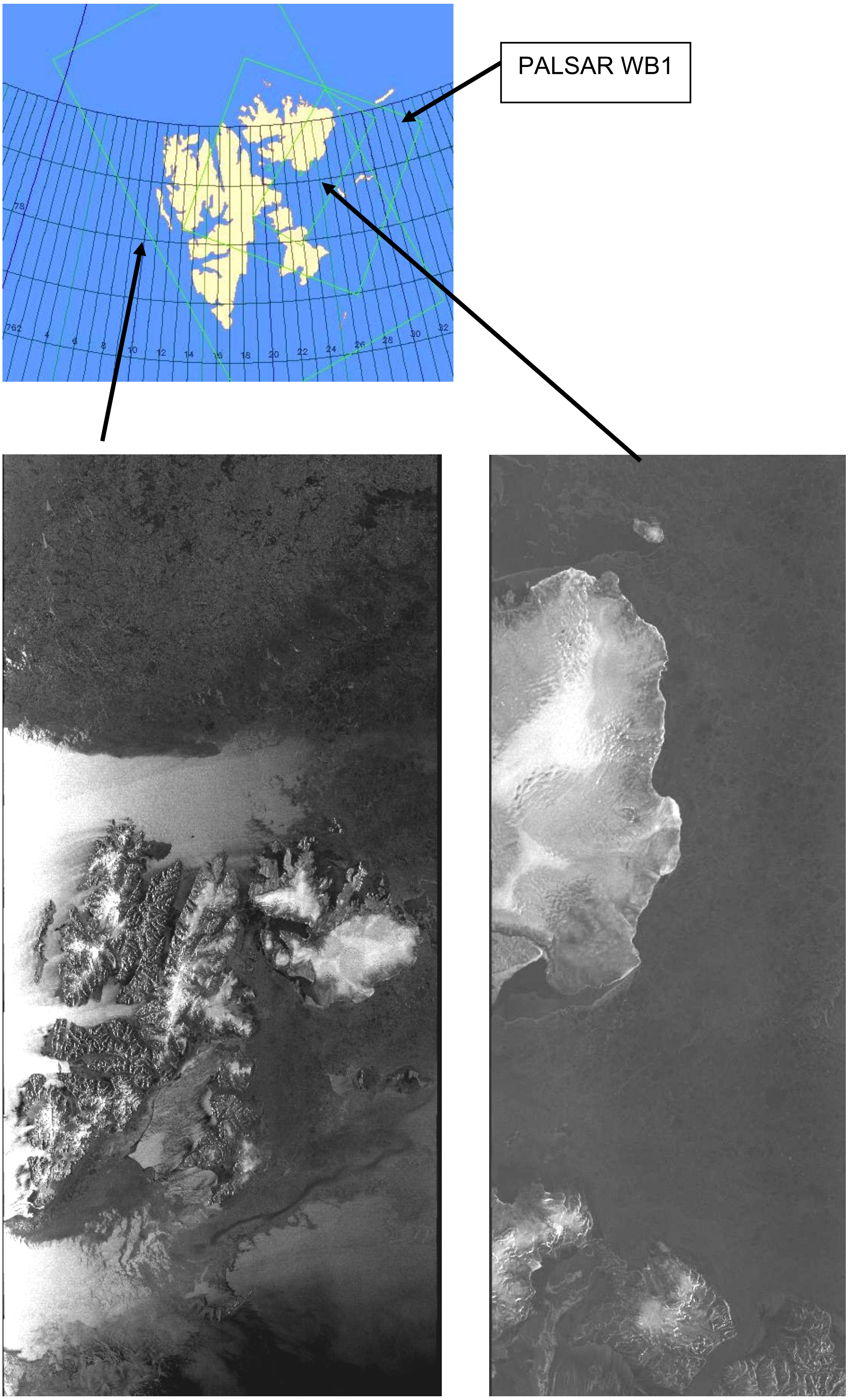

17031902

17031045

March 18, 2007

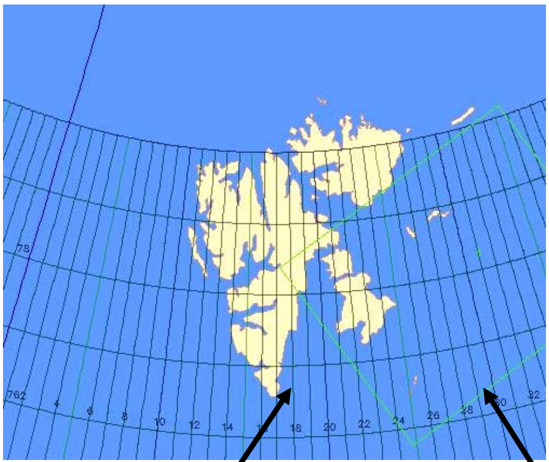

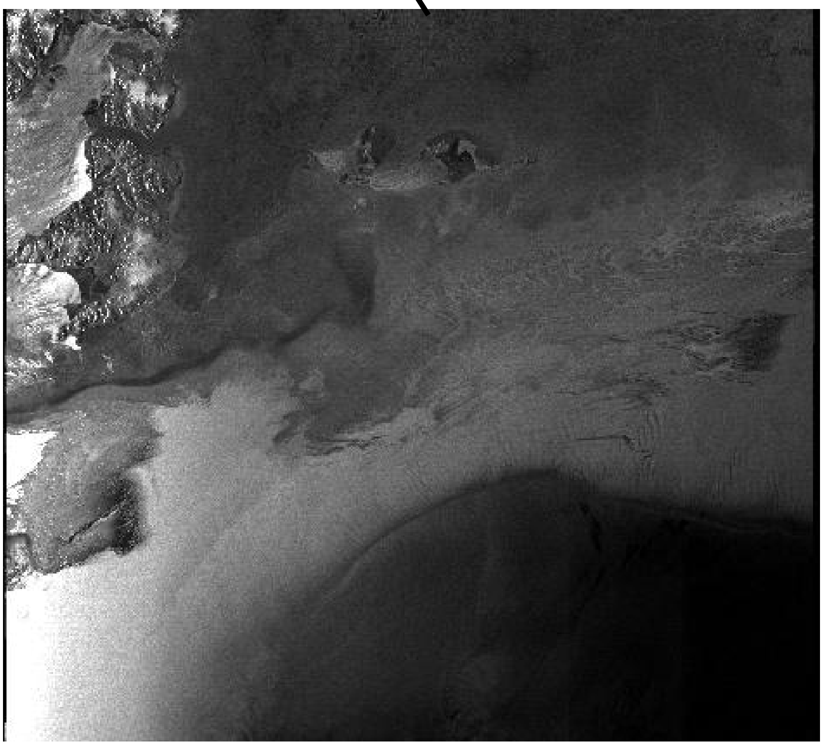

18031014

18031831

March 19, 2007

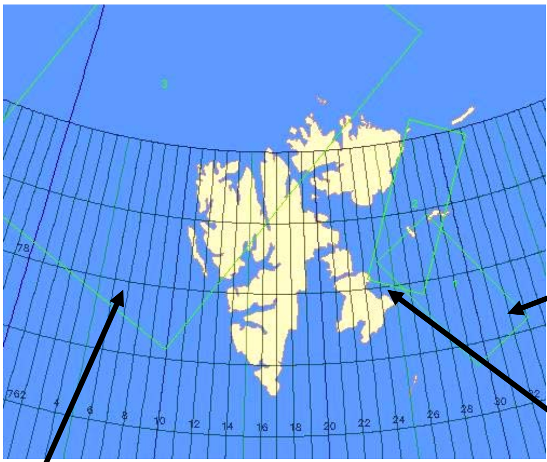

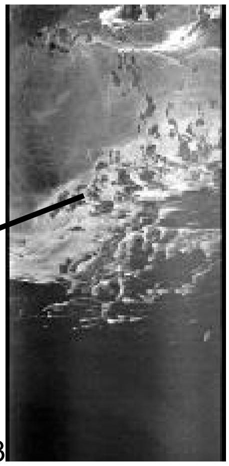

1903

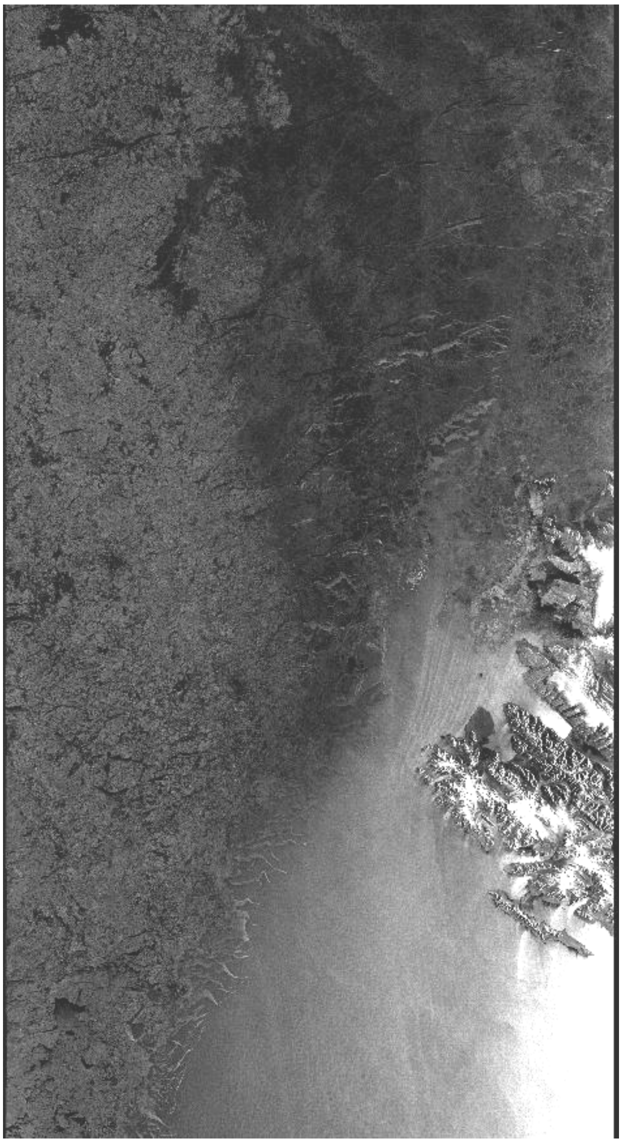

19031122

19030942

9 ICESAR DATA BASE

The web interface for the users is displayed in Figure 9.1. The interface named as EOWEB is an operational system used also for an easy access for satellite and shuttle data and has been developed by the Germany data archive center (DLR-DFD). Each data set of the ICESAR campaign is displayed and a quick look added for a first look. The data can be directly ordered through this interface and the data are provided over an ftp site. For ESA and for the IceSAR partner AWI a login and password have been provided in order to be able to check the data quality and to analyse the data.

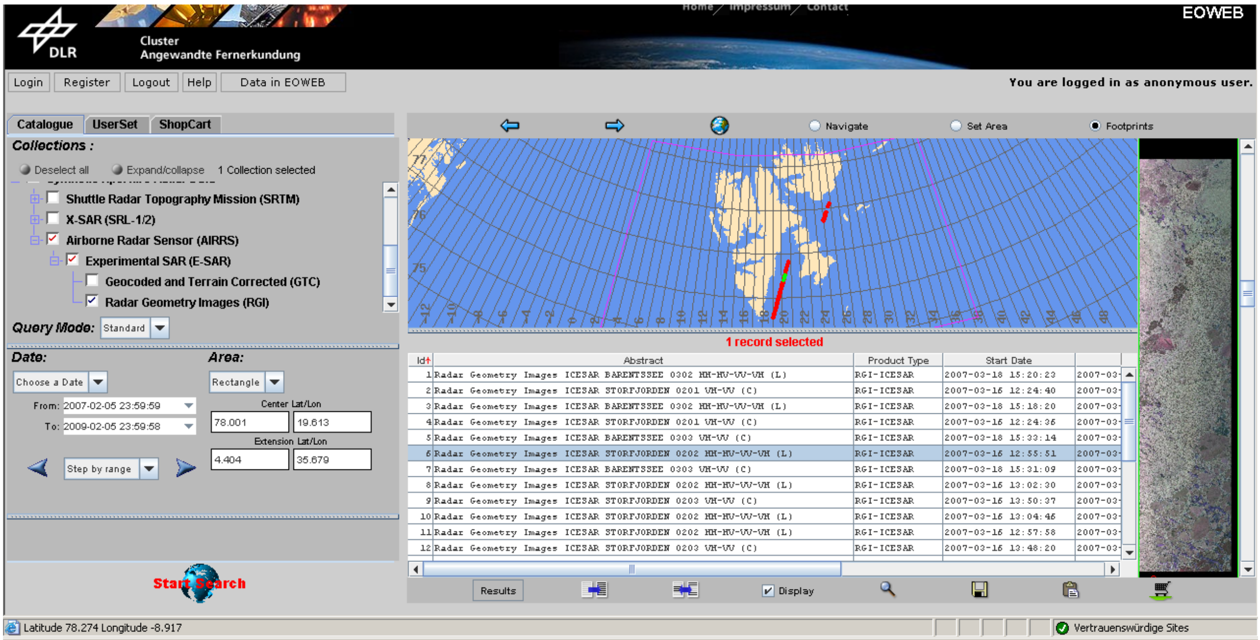

Fig. 9.1: The DLR's EOWEB portal for IceSAR radar data downloads

10 SUMMARY AND RECOMMENDATIONS

The ICESAR campaign was carried out in the vicinity of and on an island of Svalbard in the period from March 8 to April 26, 2007 consisted of two parts, taking place over three weeks in March and over two and a half weeks in April, respectively. The main objectives of ICESAR were to acquire SAR images and complementary data over sea and land ice for preparation of the Sentinel-1 mission and for providing a basis for the assessment of potential applications of the Earth Explorer BIOMASS mission in the monitoring of the Polar Regions. The campaign was executed in collaboration between DLR, AWI, and ESA.

Despite the rough Arctic environment and the highly variable weather conditions all data could be successfully acquired as planned and desribed in the Experimental Plan that was delivered to ESA. Furthermore, also additional flights could be carried out that were not included in the Experimental Plan, with data acquisitions over sea ice in the Frame Strait northwest of Svalbard, and over land ice with the P-band Sounder.

All acquired SAR data over sea and land ice were processed and are of good quality for further analysis. The absolute radiometric accuracy lies within the ± 2 dB and the relative within ± 0.5 dB. In summary the following SAR data were acquired and processed:

- Over sea ice dual polarimetric C-band and fully polarimetric L-band data over three defined test areas were processed. The main characteristic of these SAR data are the long flight tracks with 40 to 150 km length.
- Over land ice single-pass InSAR and single polarisation X-band, dual polarisation repeat-pass InSAR C-band, fully polarised repeat-pass InSAR in L-band and P-band with flight track lengths of 15 km was processed.
- In addition P-band sounder data over the same test areas of the land ice were processed.

One of the ICESAR objectives was to simulate Sentinel-1 wide swath products from the E-SAR C-band data for the sea ice test sites. The degradation in terms of resolution and noise equivalent sigma zero to 20 m azimuth resolution and 5 m range resolution with NESZ of -22 dB shows that large ice features could be distinguished but small and thin features are not recognisable. Another investigation with C-band over land ice was made were the main question was how fast and strong in time changes over snow/ice areas appear in terms of temporal decorrelation. As a result it can be summarised, that already after 4 days a strong decorrelation over the test areas appered, such that no interferometric evaluation of the data are possible. Unfortunately, at the acquisition of the C-band data strong wind introduced a squint of 5 degrees that also contributes to the interferometric coherence decorrelation.

Further C-band data were syntheticaly processed to fully polarimetric data. The C-band data are dual polarised and are combined in a repeat-pass acquisition with zero baseline. These data are also available for investigation but it should be noted that volume decorrelation and the movement of the aircraft with a deviation from the zero baseline could cause some effects.

The main interest in first order analysis over land ice is the physical parameter of the extinction. The extinction is a valuable parameter for ice structure cahracterisation. In this study extinctions of glacier ice have been inverted using Pol-InSAR observables by adapting existing PolSAR decompositions and a Pol-InSAR coherence model originally developed for vegetation applications to a glacier scenario. Best performance was achieved using ground-to-volume scattering ratios derived from the Freeman-3 component decomposition, yielding physically-plausible *m* and co-pol extinctions relatively independent of incidence angle and close to extinction magnitudes at HV. Results appear promising at both L- and P-band, particularly for short baselines which minimise the influence of slight inaccuracies and model deficiencies in the ground-to-volume scattering ratio. For both test sites extinction maps were derived.

Finaly, first results were shown with the P-band sounder were data are acquired over the two land ice test site. The most promising results were obtained over the Etonbreen glacier, were data are acquired over bedrock with increasing ice layer thickness during the flight track. Ice layer thickness up to 570 m could be identified. One important result of the first order analysis is that the choise of the polarizations for bedrock identification plays a role.

Recommendation for derivation of land ice parameters:

In recent years there has been increased interest in using SAR to study and monitor glaciers and ice sheets for glaciological and climate change research. SAR is sensitive to both surface and near-surface structures (up to tens of metres) related to accumulation, ablation and metamorphism of snow and firn. Thus, SAR-derived glacier properties could be used as proxy indicators of changes in glacier mass balance and regional climate (Engeset et al. 2002). In this study the Pol-InSAR signatures over parts of the Austfonna ice cap spanning two glacier zones, the percolation zone (Summit) and super-imposed ice zone (Etonbreen) were investigated. To further explore the extended observation space offered by Pol-InSAR for monitoring the cryosphere, it is recommended that additional campaigns should be carried out covering the remaining glacial zones, including the dry snow zone, wet snow zone, and ablation zone. More detailed relationships between SAR-derived parameters such as extinction and physical ice properties could then be established for each glacier zone.

Extinction consists of the combined effects of both absorption and scattering in the form $\kappa_e = \kappa_a + \kappa_s$ (Ulaby 1982). The absorption component (κ_a) is relatively well documented in the literature from laboratory experiments with pure ice including its dependencies on temperature and frequency (Hallikainen 1992, Warren1984). However, virtually no controlled experiments involving measurement of κ_s and κ_e have been conducted, particularly not at longer wavelengths, preventing validation of the inverted extinctions from this study. Rigorous measurements of extinction scattering coefficient κ_s are impractical because of the requirement for undisturbed ice samples much larger than the wavelength of interest to be transported to a controlled environment. Because scatterers and layers within the ice may be preferentially oriented, κ_s may also be dependent on incidence and azimuth angles, adding further complexity to its complete description.

Given these difficulties in a rigorous approach, we propose the use of radar sounder data to derive approximate estimates of κ_e. Flying along the glacier centre-line from the terminus over increasingly greater ice thicknesses, the radar return from the bedrock can be tracked until it eventually disappears altogether, falling below the noise floor, at which point it is assumed that the signal is completely attenuated by the ice. Given *a priori* knowledge of the ice-thickness from, e.g. GPR or seismic data, and assuming relatively smooth bedrock topography and bedrock surface roughness, an approximate ice volume extinction κ_e could be computed for validation purposes.

As evident in the P-band Summit comparisons between the 2005 SVALEX and 2007 ICESAR campaigns, changes in the ice structure are occurring over time. On-going monitoring of the Austfonna Summit percolation zone is recommended in order to continue to build up a long-term time series of long-wavelength SAR data for change detection in ice structure development and long-term accumulation, wind, and melt patterns. As well, supplemental flight lines in the across-track direction could help identify and characterise preferential orientation of the ice scattering bodies. Azimuth angle backscattering modulations of up to 3 dB have been shown to exist on the Greenland ice sheet at C-band (Ashcraft 2003). Further research on azimuth angle dependencies are recommended for additional test sites such as the Austfonna ice cap (using either airborne or spaceborne imagery), particularly at longer wavelengths, to help identify the presence of large-scale oriented backscatterers such as wind slabs, hoar layers, and wind-driven snow deposition features such as sastrugi.

A further recommendation is for the simultaneous collection of field measurements to supplement SAR acquisitions. GPR (Ground Penetrating Radar) data at the same centre frequencies as the SAR should be acquired for a meaningful comparison, since scattering is very sensitive to wavelength. GPR profiles integrated along depth could be compared to SAR backscattering coefficients and inverted extinctions as a means of validation. Additionally, acquiring both along- and across-track GPR profiles would allow insight into potential orientation effects of the ice volume scattering bodies

Scattering in low-loss layered media such as glacier ice is a complex process. Although the simple polarimetric decompositions and extinction models described in this study yield reasonable first results, they are adaptations of methods originally developed for vegetation applications, and thus cannot faithfully model all the realities of glacier geometries. Further research making use of more sophisticated electromagnetic models could provide additional insight into the expected backscatter and coherences of SAR returns from glacier ice. Resonance effects, coherent or weak localisation scattering theory and multiple scattering are potential topics of investigation to achieve improved modelling results. However, although such models could significantly improve our understanding of the scattering physics involved, complex scattering models often lead to underestimated inversion problems due to an increased number of parameters. Such inversion problems can be solved unambiguously only under simplifying assumptions or *a priori* information (requiring additional and detailed field measurements) and can have constrained applicability (Papathanassiou 2001).

Radar techniques already play an important role in monitoring glaciers and ice sheets on a global scale, and Pol-InSAR offers an even greater potential with its extended observation space. Polarimetry yields information regarding the separation of scattering mechanisms, and interferometry can deliver estimates of their distribution with depth. Further research on the use of Pol-InSAR for glaciological applications is recommended. In addition, studies such as ICESAR investigating the use of longer-wavelength Pol-InSAR observables are important for future spaceborne concepts. Potential satellite missions including the BIOMASS earth observation proposal would benefit from an increased understanding of SAR observables over glaciers and ice caps.

In summary, the following recommendations have been presented regarding future study of the cryosphere using multi-parametric SAR observations:

- Additional studies should be carried out in order to validate estimates of κe for glacier ice, with for instance, carefully-designed sounder experiments.
- On-going monitoring of Austfonna Summit is recommended to build-up a time series of data to track changes in ice structure, which could in turn reveal changes in long-term accumulation, wind, and melt patterns.
- Cross-track passes perpendicular to the glacier centre line should be flown for additional insight into possible orientation effects of the ice scattering bodies.
- GPR data collected nearly simultaneously to the SAR data and at the same centre frequencies is recommended for a meaningful comparison. The acquisition of profiles both parallel and perpendicular to the glacier the centre line might aid in interpretation of ice structures.
- Investigation into more complex electromagnetic models incorporating, e.g. resonance effects and multiple scattering, may improve our understanding of the scattering physics involved.

Recommendation for the P-band sounder

The limited dynamic range of the E-SAR system did not allow the detection of the bedrock at the Summit test-site. Also the timing restrictions did not allow for flights in low altitudes (usually few hundred meters) above the ice surface. A dedicated radar system (P-band sounders are operated by University of Kansas and recently also by ESA) would allow for better quality data.

During ICESAR the acquisition of parallel repeated tracks has been performed for purposes of across-track clutter suppression. Due to the limited number and partly turbulent motion of parallel tracks available, this approach could not be demonstrated. Since ESA ownes a radar sounder with multiple apertures antennas, it is recommended to evaluate cross-track clutter suppression techniques with this sensor first, before attempting the recombination of multiple tracks affected by severe uncorrelated motion.

11 REFERENCES

ACRAS: Advanced Concept for Radar Sounder; WP430:"", ESA-ESTEC project no.19961/06/NL/HE

Ashcraft, I.S. and Long, D.G. Relating microwave backscatter azimuth modulation to surface properties of the Greenland ice sheet. Proc. of the IEEE International Geoscience and Remote Sensing Symposium (IGARSS'03), July 2003, vol. 3, 1610-1612.

Bamber, J.L.: "Ice/bed interface and englacial properties of Svalbard Ice Masses deduced from Airborne Radio Echo-Sounding Data", Jopurnal of Glaciology, vol. 35, no. 119, 1989

Cloude, S.R. and Papathanssiou, K.P. Three-stage inversion process for polarimetric SAR interferometry. IEE Proc.-Radar Sonar Navig., 2003, vol. 150, no. 3, 125-134

Cloude, S.R. and Pottier, E. A review of target decomposition theorems in radar polarimetry. IEEE Trans. Geosci. and Remote Sens. March 1996, vol. 34, no. 2, 498-518

Cloude, S.R., Fortuny, J., Lopez-Sanchez, J.M. and Sieber, A.J. Wide-band polarimetric radar inversion studies for vegetation layer. IEEE Trans. Geosci. and Remote Sens. September, 1999, vol. 37, no. 5, 2430-2441

Engeset, R. V. and Kohler, J. and Melvold, K. amd Lundén, B. Change detection and monitoring of glacier mass balance and facies using ERS SAR winter images over Svalbard. International Journal of Remote Sensing, May 2002, vol. 23, no. 10, 2023-2050.

ESA Spring 2007 Campaigns CryoVEx – ICESAR - BIOSAR: Experiment Plan, ESA Dokuments, p. 40, 2007

Freeman, A. and Durden, S.L. A three-component scattering model for polarimetric SAR data. IEEE Trans. Geosci. Remote Sens., May 1998, vol. 36 no. 3, 963-973

Freeman, A. Fitting a two-component scattering model to polarimetric SAR data from forests. IEEE Trans. Geosci. Remote Sens., August 2007, vol. 45, no. 8, 2583-2592

Hajnsek, I. Inversion of Surface Parameters using Polarimetric SAR. Dissertation, 2001, Friedrich-Schiller Universität at Jena

Hallikainen, M. Review of the Microwave Dielectric and Extinction Properties of Sea Ice and Snow. Proc. of the IEEE International Geoscience and Remote Sensing Symposium (IGARSS'92), July 1992, vol. 2, 961-965, 1992.

Hoen, W. A correlation-based approach to modeling interferometric radar observations of the Greenland ice sheet. Phd Thesis, 2001, Stanford University

Long, D.G. and Drinkwater, Mark R. Greenland ice sheet surface properties observed by the Seasat-A scatterometer at enhanced resolution. Journal of Glaciology, 1994, 40(135), 213-230

Papathanassiou, K. P. and Cloude, S.R. Single-baseline polarimetric SAR interferometry. IEEE Transactions on Geoscience and Remote Sensing. November 2001, vol. 39, no. 11, 2352-2363.

Sharma, J. J., Hajnsek, I. and Papathanassiou, K.P. Multi-frequency Pol-InSAR signatures of a subpolar glacier in 3rd Intl. Workshop on Sci. and Appl. of SAR Polarimetry and Polarimetric Interferometry (Pol-InSAR), Frascati, Italy, 22-26 January 2007

Schytt, V, 'Scientific results of the Swedish galaciological expedition to Nordauslandet, Spitsbergen, 1957 and 1958', Geografiska Annaler, 1964, vol. 46, issues 3, pp. 243-281

Taurisano, A., Kohler, J., Hagen, J. O., Eiken, T., Loe, E., ‚Final report: Cryosat Calibration and validation on Austfonna Svalbard', ESA PRODEX, Feb. 2005, p. 39

Ulaby, F., Moore, R. and Fung, A. Microwave Remote Sensing, Active and Passive, Volume II: Radar Remote Sensing and Surface Scattering and Emission Theory. Addison-Wesley, Norwood MA,1982.

Warren, S.G. Optical constants of ice from the ultraviolet to the microwave. Applied Optics, April 1984, vol. 23, no. 8, 1206-1225.

12 APPENDIX A

Corner Reflector Analysis

Testsite Summit — **Illumination from South**

SceneID	CR #	Res rg hh [m]	Res az hh [m]	Δ RCS hh [dB*m^2]	Signal to background ratio hh	Res rg vv [m]	Res az vv [m]	Δ RCS vv [dB*m^2]	Signal to background ratio vv	Channel amplitude imbalance [dB]	Channel phase imbalance [°]
X-band											
1002_t01	1					2.72	5.22	16.9	xxx		
1004_t01	1					2.53	5.19	16.5	xxx		
1902_t01	1					2.53	5.01	10.8	2.2		
1904_t01	1					2.53	5.00	11.5	1.1		
C-band											
1701_t01	1					2.53	3.13	12.5	0.0		
1703_t01	1	2.34	3.22	17.7	xxx						
1705_t01	1	2.72	3.50	19.8	xxx						
1707_t01	1					2.62	3.13	17.5	xxx		

Corner Reflector Analysis

Testsite Summit — **Illumination from North**

SceneID	CR #	Res rg hh [m]	Res az hh [m]	Δ RCS hh [dB*m^2]	Signal to background ratio hh	Res rg vv [m]	Res az vv [m]	Δ RCS vv [dB*m^2]	Signal to background ratio vv	Channel amplitude imbalance [dB]	Channel phase imbalance [°]
X-band											
1001_t01	1					4.12	6.54	21.1	xxx		
	2					2.62	5.23	11.6	xxx		
1003_t01	1					3.00	6.02	22.6	xxx		
	2					2.44	5.01	8.9	xxx		
1901_t01	1					2.62	5.91	20.3	xxx		
	2					23.51	21.88	4.3	xxx		
1903_t01	1					2.90	6.05	20.1	xxx		
	2					3.37	8.01	7.6	xxx		
C-band											
1702_t01	1					2.53	3.09	3.3	10.7		
	2					2.62	3.18	6.1	xxx		
1704_t01	1	2.53	3.00	2.5	10.9						
	2	2.62	3.18	2.8	xxx						
1706_t01	1	2.44	3.09	5.7	12.4						
	2	2.44	3.09	5.1	0.4						
1708_t01	1					2.62	3.00	4.8	10.4		
	2					2.34	3.09	5.2	0.3		

Corner Reflector Analysis

Testsite Summit

Illumination from South

SceneID	CR #	Res rg hh [m]	Res az hh [m]	Δ RCS hh [dB*m^2]	Signal to background ratio hh	Res rg vv [m]	Res az vv [m]	Δ RCS vv [dB*m^2]	Signal to background ratio vv	Channel amplitude imbalance [dB]	Channel phase imbalance [°]
L-band											
0602_t01	1	2.15	1.15	-0.8	14.4	2.25	1.18	0.1	14.2	0.9	-4.4
0604_t01	1	2.25	1.15	-1.1	13.3	2.15	1.15	-0.5	14.8	0.6	-7.4
0606_t01	1	2.15	1.12	-1.1	15.0	2.15	1.12	0.3	14.9	1.4	-4.5
0608_t01	1	2.15	1.12	-1.3	14.6	2.15	1.15	-0.5	14.7	0.8	-8.1
1401_t02	1	2.25	1.10	3.8	7.9	2.44	1.12	2.8	11.0	-0.9	-18.7
1403_t02	1	2.15	1.18	3.2	9.7	2.25	1.10	3.6	12.7	0.4	-19.8
1405_t02	1	2.06	1.18	3.6	10.1	2.15	1.12	0.1	-14.1	0.1	-14.1
1407_t02	1	2.25	1.07	4.5	8.0	2.34	1.12	3.2	11.6	-1.3	-7.5
1401_t01	1	2.34	1.19	2.9	8.1	2.44	1.16	3.3	11.3	0.4	-8.1
1403_t01	1	2.06	1.19	2.9	9.2	2.25	1.13	4.4	11.5	1.5	-9.0
1405_t01	1	2.06	1.13	3.8	9.1	2.15	1.16	4.3	12.7	0.5	-3.1
1407_t01	1	2.25	1.16	3.6	9.0	2.34	1.16	3.5	12.0	-0.2	-2.1
P-band											
0901_t01	1	2.15	1.22	5.4	6.9	2.15	1.25	5.4	8.2	-0.1	-1.7
0903_t01	1	2.15	1.17	5.2	7.9	2.15	1.25	4.3	8.9	-0.8	1.5
0905_t01	1	2.15	1.25	4.9	7.0	2.15	1.22	4.9	8.2	-0.5	-5.3
0907_t01	1	2.15	1.17	5.0	7.6	2.15	1.30	4.5	7.7	-0.5	-4.2
1303_t02	1	2.15	1.30	4.0	8.0	2.34	1.30	3.9	8.6	-0.1	-9.6
1305_t02	1	2.25	1.38	4.0	6.9	2.44	1.45	3.1	7.8	-0.9	-6.5
1307_t02	1	2.34	1.35	3.3	7.4	2.62	1.50	2.7	8.9	-0.6	-5.7
1307_t01	1	2.34	1.35	3.1	7.8	2.53	1.43	2.7	9.1	-0.4	-5.6
1305_t01	1	2.25	1.38	3.6	7.4	2.44	1.40	3.2	8.0	-0.5	-8.0
1303_t01	1	2.15	1.33	3.7	8.2	2.44	1.30	3.7	9.1	0.0	-10.3

Corner Reflector Analysis

Testsite Summit

Illumination from North

SceneID	CR #	Res rg hh [m]	Res az hh [m]	Δ RCS hh [dB*m^2]	Signal to background ratio hh	Res rg vv [m]	Res az vv [m]	Δ RCS vv [dB*m^2]	Signal to background ratio vv	Channel amplitude imbalance [dB]	Channel phase imbalance [°]
L-band											
0601_t01	1	2.15	1.12	-0.5	14.0	2.12	1.15	0.4	14.5	0.9	1.3
	2	2.15	1.15	-4.5	4.4	2.15	1.15	-3.7	5.8	0.8	8.1
0603_t01	1	2.25	1.12	-0.6	13.8	2.15	1.12	0.3	15.7	1.0	0.0
	2	2.25	1.12	-4.8	5.4	2.25	1.15	-3.5	5.0	1.4	4.3
0605_t01	1	2.25	1.12	-0.9	14.5	2.15	1.10	-0.2	15.3	0.7	-0.9
	2	2.44	1.10	-5.7	6.3	2.34	1.12	-4.5	5.5	1.2	1.7
0607_t01	1	2.15	1.12	-0.8	13.6	2.15	1.12	0.3	14.8	1.1	0.2
	2	2.15	1.01	-2.8	5.2	2.06	0.98	-0.5	3.9	2.3	8.2
0609_t01	1	2.25	1.12	-0.5	13.8	2.15	1.12	0.3	14.4	0.8	2.1
	2	2.06	1.15	-4.8	3.8	2.06	1.12	-3.9	5.4	1.0	7.8
1402_t02	1	2.25	1.15	-0.3	14.5	2.25	1.12	2.9	15.7	3.2	13.8
	2	2.34	1.07	-2.7	2.5	2.25	1.10	0.7	3.4	3.3	2.8
1404_t02	1	2.25	1.18	-0.2	14.2	2.15	1.18	2.8	15.6	2.9	14.1
	2	2.34	1.12	-1.2	2.7	2.25	1.10	1.4	3.8	2.6	3.8
1406_t02	1	2.15	1.18	0.2	14.1	2.15	1.18	2.9	16.1	2.6	10.2
	2	2.34	1.15	-1.9	1.0	2.25	1.10	1.6	1.6	3.5	5.7
1408_t02	1	2.25	1.15	-0.6	15.4	2.25	1.15	2.3	15.8	3.0	11.0
	2	2.15	1.07	-2.0	1.7	2.15	1.10	0.2	4.1	2.2	-0.2
1402_t01	1	2.25	1.12	-0.9	15.2	2.25	1.19	0.5	15.4	1.4	10.3
	2	2.53	1.22	-3.2	4.3	2.34	1.19	-2.0	6.0	1.2	-1.5
1404_t01	1	2.25	1.12	-0.7	14.5	2.25	1.12	0.5	15.6	1.2	5.1
	2	2.53	1.22	-3.1	4.8	2.44	1.25	-2.3	6.2	0.8	16.8
1406_t01	1	2.25	1.12	-0.3	13.0	2.25	1.16	1.0	15.2	1.2	6.4
	2	2.15	1.16	-0.2	2.0	2.25	1.19	-0.7	4.5	-0.5	2.2
1408_t01	1	2.15	1.16	-0.7	15.3	2.15	1.16	0.6	16.0	1.3	6.3
	2	2.15	1.16	-2.1	4.1	2.15	1.19	-2.4	6.1	-0.3	-2.4

Corner Reflector Analysis

Testsite Summit

Illumination from North

SceneID	CR #	Res rg hh [m]	Res az hh [m]	Δ RCS hh [dB*m^2]	Signal to background ratio hh	Res rg vv [m]	Res az vv [m]	Δ RCS vv [dB*m^2]	Signal to background ratio vv	Channel amplitude imbalance [dB]	Channel phase imbalance [°]
P-band											
0902_t01	1	2.15	1.20	5.6	6.4	2.15	1.33	4.7	7.5	-0.9	32.3
	2	2.15	1.68	-3.6	1.2	1.87	2.24	-2.9	0.7	0.7	2.2
0904_t01	1	2.15	1.20	5.6	1.2	2.25	1.33	4.4	7.7	-1.2	32.3
	2	2.34	1.81	-3.1	0.2	2.06	1.72	-3.6	xxx	-0.4	4.7
0906_t01	1	2.15	1.16	6.0	5.4	2.15	1.29	4.5	8.4	-1.5	32.0
	2	2.15	1.29	-3.6	2.8	2.06	1.46	-1.5	0.0	2.1	-8.3
0908_t01	1			no information				no information		no information	no information
	2			no information				no information		no information	no information
1302_t02	1	2.15	1.25	5.8	4.8	2.25	1.38	4.7	8.1	-1.2	5.5
	2	2.34	1.33	-4.1	1.1	2.44	2.62	-5.4	0.8	-1.4	-6.9
1304_t02	1	2.15	1.29	6.1	4.1	2.34	1.46	4.6	8.0	-1.5	9.0
	2	2.25	1.42	-1.4	xxx	2.62	1.46	2.3	xxx	3.7	0.8
1302_t01	1	2.15	1.26	6.0	5.1	2.25	1.39	4.8	7.8	-1.2	8.3
	2	2.34	1.35	-3.7	1.1	2.53	1.63	-4.1	1.5	-0.4	-5.3
1304_t01	1	2.06	1.16	6.3	4.3	2.34	1.30	4.9	7.8	-1.4	9.2
	2	2.34	1.39	-2.2	xxx	2.53	2.37	2.7	xxx	4.9	-0.7
1306_t01	1	2.06	1.16	7.8	2.4	2.25	1.30	5.5	7.3	-2.3	-1.1
	2	2.25	1.63	-3.4	0.7	3.47	1.58	-0.5	xxx	2.9	12.0
1308_t01	1			no information				no information		no information	no information
	2			no information				no information		no information	no information

Corner Reflector Analysis

Testsite Etonbreen Glacier

Illumination from South

SceneID	CR #	Res rg hh [m]	Res az hh [m]	Δ RCS hh [dB*m^2]	Signal to background ratio hh	Res rg vv [m]	Res az vv [m]	Δ RCS vv [dB*m^2]	Signal to background ratio vv	Channel amplitude imbalance [dB]	Channel phase imbalance [°]
X-band											
1005_t01	1					2.62	5.27	20.4	xxx		
1007_t01	1					2.25	5.34	20.2	xxx		
1905_t01	1					4.12	19.93	15.2	xxx		
1907_t01	1					2.72	5.98	20.6	xxx		
1909_t01	1					3.00	6.13	19.8	xxx		
C-band											
1502_t01	1					5.81	9.10	15.5	xxx		
1504_t01	1	2.53	3.18	20.4	xxx						
1506_t01	1	2.62	3.09	19.1	xxx						
1508_t01	1					3.47	6.73	13.4	xxx		
2002_t02	1					3.47	5.46	16.9	xxx		
2004_t02	1	3.28	3.64	20.2	xxx						
2006_t02	1					2.81	4.00	19.3	xxx		
2002_t01	1					3.00	3.64	17.0	xxx		
2004_t01	1	3.37	5.01	19.3	xxx						
2006_t01	1					2.72	3.55	16.5	xxx		

Corner Reflector Analysis

Testsite Etonbreen Glacier — Illumination from North

SceneID	CR #	Res rg hh [m]	Res az hh [m]	Δ RCS hh [dB*m^2]	Signal to background ratio hh	Res rg vv [m]	Res az vv [m]	Δ RCS vv [dB*m^2]	Signal to background ratio vv	Channel amplitude imbalance [dB]	Channel phase imbalance [°]
X-band											
1006_t01	1					2.25	5.02	3.0	14.1		
	2					2.72	5.70	13.4	xxx		
1008_t01	1					2.44	5.13	2.6	14.3		
	2					2.53	5.32	12.7	xxx		
1906_t01	1					3.37	15.75	22.1	xxx		
	2					8.99	6.76	9.5	xxx		
1908_t01	1					3.56	6.86	22.4	xxx		
	2					3.75	7.23	11.5	xxx		
C-band											
1501_t01	1					3.18	3.46	20.0	xxx		
	2					2.72	3.18	8.0	xxx		
1503_t01	1	2.62	3.18	19.2	xxx						
	2	2.62	3.18	8.7	xxx						
1505_t01	1	2.34	3.18	19.8	xxx						
	2	2.62	8.48	8.5	xxx						
1507_t01	1					2.34	3.09	19.8	xxx		
	2					2.44	3.18	6.2	xxx		
2001_t02	1					2.25	3.18	23.2	xxx		
	2					2.44	3.46	12.6	xxx		
2003_t02	1	2.44	3.18	21.4	xxx						
	2	2.81	3.37	10.9	xxx						
2005_t02	1					2.44	3.18	21.7	xxx		
	2					2.53	3.37	11.7	xxx		
2001_t01	1					2.44	3.09	17.8	xxx		
	2					2.62	3.46	6.4	xxx		
2003_t01	1	2.62	3.28	20.3	xxx						
	2	2.81	3.82	10.2	xxx						
2005_t01	1					2.62	3.18	18.1	xxx		
	2					2.72	3.55	7.9	xxx		

Corner Reflector Analysis

Testsite Etonbreen Glacier

Illumination from South

SceneID	CR #	Res rg hh [m]	Res az hh [m]	Δ RCS hh [dB*m^2]	Signal to background ratio hh	Res rg vv [m]	Res az vv [m]	Δ RCS vv [dB*m^2]	Signal to background ratio vv	Channel amplitude imbalance [dB]	Channel phase imbalance [°]
L-band											
1602_t01	1	2.44	1.16	2.9	10.4	2.25	1.13	4.1	11.0	1.3	-9.0
1604_t01	1	2.44	1.07	5.5	9.9	2.44	1.10	5.7	9.8	0.2	-13.5
1606_t01	1	2.34	1.10	5.4	11.2	2.25	1.10	7.0	9.9	1.6	9.9
1608_t01	1	2.34	1.10	6.2	8.1	2.25	1.13	6.0	11.0	-0.2	-13.1
P-band											
1101_t01	1	2.25	1.28	6.0	17.7	2.15	1.34	6.9	16.9	0.9	4.4
1103_t01	1	2.25	1.28	5.8	19.2	2.15	1.34	5.8	17.4	0.0	7.0
1105_t01	1	2.25	1.28	5.8	17.7	2.06	1.34	5.4	16.8	-0.4	7.6
1107_t01	1	2.25	1.28	5.3	18.4	2.15	1.36	4.8	17.3	-0.4	7.8
1202_t02	1	2.15	2.51	14.7	3.7	3.93	1.71	16.0	0.5	1.2	-43.4
1204_t02	1	2.25	1.31	4.3	16.8	2.44	1.50	4.4	17.4	0.1	12.3
1206_t02	1	2.25	1.34	4.2	17.2	2.44	1.47	4.3	17.0	0.0	12.1
1208_t02	1	2.25	1.34	4.7	17.2	2.44	1.47	4.8	17.2	0.1	12.3
1202_t01	1	2.25	2.54	13.4	5.0	3.75	1.70	17.3	2.1	4.0	-52.3
1204_t01	1	2.15	1.32	4.7	15.6	2.34	1.32	4.5	17.3	-0.2	9.0
1206_t01	1	2.25	1.33	4.4	17.3	2.44	1.46	4.3	16.6	-0.1	12.6
1208_t01	1	2.15	1.25	4.8	17.2	2.44	1.35	4.7	17.5	-0.1	12.8

Corner Reflector Analysis

Testsite Etonbreen Glacier

Illumination from North

SceneID	CR #	Res rg hh [m]	Res az hh [m]	Δ RCS hh [dB*m^2]	Signal to background ratio hh	Res rg vv [m]	Res az vv [m]	Δ RCS vv [dB*m^2]	Signal to background ratio vv	Channel amplitude imbalance [dB]	Channel phase imbalance [°]
L-band											
0701_t01	1	2.15	1.15	10.4	10.9	2.15	1.12	10.8	11.5	0.4	7.5
	2	2.25	1.24	0.1	2.7	2.34	1.24	1.0	2.1	0.9	13.5
0702_t01	1	2.15	1.15	8.1	10.8	2.25	1.15	9.0	11.4	0.9	5.8
	2	2.25	1.24	-1.9	3.9	2.34	1.21	0.1	1.9	2.0	12.6
0703_t01	1	2.06	1.18	8.8	10.7	2.15	1.15	9.1	11.4	0.3	5.2
	2	2.25	1.15	0.2	1.8	2.34	1.12	1.0	1.4	0.8	7.0
0704_t01	1	2.15	1.07	10.7	8.5	2.15	1.07	11.8	9.4	1.0	2.7
	2	2.25	1.07	-1.8	5.7	2.34	1.07	-1.4	6.2	0.3	2.1
1601_t02	1	2.44	1.24	19.2	6.1	2.25	1.27	15.1	9.9	-4.1	-18.7
	2	2.15	1.35	4.5	5.5	2.15	1.27	2.8	4.0	-1.7	-20.9
1603_t02	1	2.34	1.12	20.9	6.5	2.25	1.15	16.7	10.5	-4.3	-20.0
	2	2.15	1.15	7.9	2.0	2.34	1.10	4.7	4.2	-3.3	-17.8
1605_t02	1	2.25	1.12	21.3	6.9	2.34	1.18	15.5	12.3	-5.8	-27.4
	2	2.25	1.18	7.0	3.3	2.34	1.29	4.1	4.3	-2.9	-23.6
1607_t02	1	2.34	1.27	20.9	7.3	2.25	1.24	16.1	13.0	-4.8	-24.2
	2	2.34	1.07	6.6	5.8	2.44	1.10	4.0	6.1	-2.6	-31.1
1609_t02	1	2.34	2.62	16.3	6.2	2.25	2.45	13.3	8.7	-3.0	-13.6
	2	2.53	1.12	10.8	xxx	2.44	1.32	7.7	1.0	-3.1	-31.7
1601_t01	1	2.25	1.17	10.1	6.8	2.15	1.26	9.1	10.3	-1.0	9.6
	2	2.25	1.20	-0.1	2.5	2.06	1.23	0.9	4.2	1.0	2.4
1603_t01	1	2.34	1.20	8.7	8.3	2.25	1.26	8.6	10.7	-0.1	20.5
	2	2.25	1.23	-1.4	4.0	2.15	1.26	-0.4	6.6	1.0	32.1
1605_t01	1	2.25	1.26	8.1	8.5	2.25	1.23	8.4	11.0	0.3	-14.0
	2	2.15	1.26	-1.2	5.9	2.15	1.23	-0.3	7.6	0.9	-18.8
1607_t01	1	2.15	1.20	10.2	7.1	2.15	1.20	8.2	11.1	-2.0	28.4
	2	2.15	1.33	-1.8	5.2	2.25	1.29	-0.6	5.5	1.2	19.5
1609_t01	1	2.25	1.20	8.6	8.0	2.25	1.23	7.4	12.3	-1.2	7.8
	2	2.15	1.67	-0.8	2.7	2.15	1.29	0.3	4.3	1.1	8.6

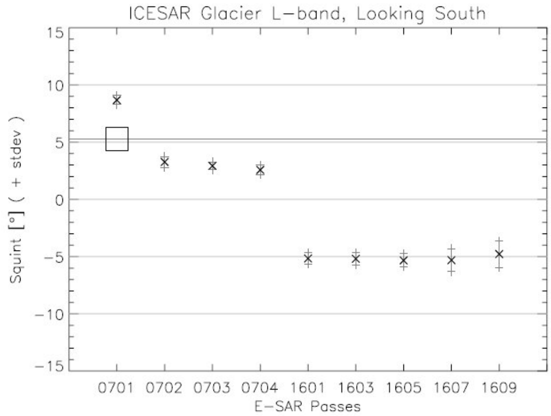

Corner Reflector Analysis

Testsite Etonbreen Glacier

Illumination from North

SceneID	CR #	Res rg hh [m]	Res az hh [m]	Δ RCS hh [dB*m^2]	Signal to background ratio hh	Res rg vv [m]	Res az vv [m]	Δ RCS vv [dB*m^2]	Signal to background ratio vv	Channel amplitude imbalance [dB]	Channel phase imbalance [°]
P-band											
1102_t01	1	2.34	1.29	3.5	18.7	2.25	1.29	1.0	18.7	-2.5	-36.9
	2	2.25	1.29	5.2	2.6	3.75	1.25	4.9	2.4	-0.3	-49.7
1104_t01	1	2.25	1.29	3.3	20.3	2.25	1.29	0.9	19.1	-2.4	-36.4
	2	2.72	2.02	4.1	0.2	2.62	1.68	6.0	xxx	1.9	-48.8
1106_t01	1	2.25	1.29	3.3	19.3	2.25	1.33	0.6	18.5	-2.7	-36.9
	2	2.15	1.20	6.4	0.6	2.15	1.59	9.4	xxx	3.1	-57.0
1108_t01	1	2.62	1.20	3.0	19.1	2.62	1.25	1.0	17.9	-2.0	-35.8
	2	2.44	1.08	5.3	2.1			no information		no information	no information
0909_t02	1	2.15	1.20	2.2	19.6	2.25	1.29	-0.9	19.5	-3.1	-38.6
	2	2.25	1.12	4.3	1.9	3.09	1.25	1.1	0.9	-3.2	-65.6
1201_t02	1	2.34	1.29	4.8	16.7	2.34	1.33	3.4	17.2	-1.4	-5.3
	2	2.25	1.42	0.6	4.7	2.15	2.49	3.2	1.4	2.6	-33.1
1203_t02	1	2.34	1.33	5.3	15.2	2.34	1.38	3.2	16.8	-2.1	-5.3
	2	2.53	1.51	-1.9	6.9	2.34	1.72	3.8	5.8	3.8	-26.1
1205_t02	1	2.34	1.38	5.5	14.4	2.34	1.42	3.5	16.2	-2.0	-7.8
	2	2.53	1.38	0.5	4.7	2.25	1.81	3.8	3.0	3.3	-28.7
1207_t02	1	2.34	1.25	5.0	15.8	2.34	1.29	3.4	17.2	-1.6	-8.4
	2	2.25	1.33	0.8	4.1	1.97	1.46	4.3	3.4	3.4	-36.3
1209_t02	1	2.34	1.25	5.4	15.8	2.34	1.29	3.5	17.1	-1.8	-8.3
	2	2.44	1.38	1.0	4.6	2.15	1.55	4.5	2.5	3.5	-27.1
1201_t01	1	2.44	1.24	4.9	17.1	2.34	1.29	3.5	17.4	-1.3	-5.3
	2	2.25	1.38	0.9	4.8	2.06	2.35	3.6	1.6	2.7	-30.9
1203_t01	1	2.34	1.24	5.4	15.4	2.34	1.29	3.4	17.2	-2.1	-6.2
	2	2.44	1.43	-1.6	7.3	2.25	1.66	2.1	5.7	3.7	-27.5
1205_t01	1	2.34	1.29	5.6	14.7	2.34	1.29	3.6	17.0	-1.9	-8.6
	2	2.53	1.29	0.7	4.9	2.25	1.52	4.3	3.7	3.6	-29.5
1207_t01	1	2.34	1.24	5.0	16.5	2.34	1.24	3.6	18.2	-1.4	-9.2
	2	2.34	1.29	0.6	4.3	2.06	1.29	5.3	2.7	4.8	-34.7
1209_t01	1	2.44	1.24	5.5	16.2	2.34	1.24	3.7	17.4	-1.8	-8.4
	2	2.34	1.24	1.1	5.5	1.97	1.61	4.8	3.0	3.6	-30.2

13 APPENDIX B

Available Data Products (SAR)

Two hard disks are delivered containing RGI (radar geometry image) and GTC (geocoded terrain corrected) data sets of the ICESAR 2007 measurement campaign.

Storfjorden	RGI data	Hard disk 1
Barentssea	RGI data	Hard disk 1
Framstrait	RGI data	Hard disk 1
Etonbreen Glacier	RGI data	Hard disk 1
Summit	RGI data	Hard disk 1
Sentinel Simulation	RGI data	Hard disk 2
Etonbreen Glacier	GTC data	Hard disk 2
Summit	GTC data	Hard disk 2

Data Products

SceneID	Band	Pol.	Flight date	View from	Resol. azim. [m]	Looks	Master / Slave to	spatial baseline [m]	temporal baseline [d]	Geocoding	Remarks
Testsite Storfjorden											
0201_t01	C	vh/vv	16-MAR-2007	East	4	8				no	
0201_t02	C	vh/vv	16-MAR-2007	East	4	8				no	
0201_t03	C	vh/vv	16-MAR-2007	East	4	8				no	
0201_t04	C	vh/vv	16-MAR-2007	East	4	8				no	
0201_t05	C	vh/vv	16-MAR-2007	East	4	8				no	
0201_t06	C	vh/vv	16-MAR-2007	East	4	8				no	
0201_t07	C	vh/vv	16-MAR-2007	East	4	8				no	
0201_t10	C	vh/vv	16-MAR-2007	East	4	8				no	Whole scene
0201_t13	C	vh/vv	16-MAR-2007	East	20	1				no	Sentinel IWS simulation of t03
0202_t01	L	pol.	16-MAR-2007	West	4	8				no	
0202_t02	L	pol.	16-MAR-2007	West	4	8				no	
0202_t03	L	pol.	16-MAR-2007	West	4	8				no	
0202_t04	L	pol.	16-MAR-2007	West	4	8				no	
0202_t05	L	pol.	16-MAR-2007	West	4	8				no	
0202_t06	L	pol.	16-MAR-2007	West	4	8				no	
0202_t07	L	pol.	16-MAR-2007	West	4	8				no	
0202_t08	L	pol.	16-MAR-2007	West	4	8				no	
0202_t09	L	pol.	16-MAR-2007	West	4	8				no	
0202_t10	L	pol.	16-MAR-2007	West	4	8				no	Whole scene
0203_t01	C	vh/vv	16-MAR-2007	East	4	8				no	
0203_t02	C	vh/vv	16-MAR-2007	East	4	8				no	
0203_t03	C	vh/vv	16-MAR-2007	East	4	8				no	
0203_t04	C	vh/vv	16-MAR-2007	East	4	8				no	
0203_t05	C	vh/vv	16-MAR-2007	East	4	8				no	
0203_t06	C	vh/vv	16-MAR-2007	East	4	8				no	
0203_t07	C	vh/vv	16-MAR-2007	East	4	8				no	
0203_t08	C	vh/vv	16-MAR-2007	East	4	8				no	
0203_t09	C	vh/vv	16-MAR-2007	East	4	8				no	
0203_t10	C	vh/vv	16-MAR-2007	East	4	8				no	Whole scene

Data Products

SceneID	Band	Pol.	Flight date	View from	Resol. azim. [m]	Looks	Master / Slave to	spatial baseline [m]	temporal baseline [d]	Geocoding	Remarks
Testsite Barentssea											
0301_t01	C	vh/vv	18-MAR-2007	East	4	8				no	
0301_t02	C	vh/vv	18-MAR-2007	East	4	8				no	
0301_t03	C	vh/vv	18-MAR-2007	East	4	8				no	
0301_t04	C	vh/vv	18-MAR-2007	East	4	8				no	
0301_t05	C	vh/vv	18-MAR-2007	East	4	8				no	
0301_t06	C	vh/vv	18-MAR-2007	East	4	8				no	
0301_t07	C	vh/vv	18-MAR-2007	East	4	8				no	
0301_t08	C	vh/vv	18-MAR-2007	East	4	8				no	
0301_t10	C	vh/vv	18-MAR-2007	East	4	8				no	Whole scene
0301_t17	C	vh/vv	18-MAR-2007	East	20	1				no	Sentinel IWS simulation of t07
0302_t01	L	pol.	18-MAR-2007	West	4	8				no	
0302_t02	L	pol.	18-MAR-2007	West	4	8				no	
0302_t03	L	pol.	18-MAR-2007	West	4	8				no	
0302_t04	L	pol.	18-MAR-2007	West	4	8				no	
0302_t05	L	pol.	18-MAR-2007	West	4	8				no	
0302_t06	L	pol.	18-MAR-2007	West	4	8				no	
0302_t07	L	pol.	18-MAR-2007	West	4	8				no	
0302_t08	L	pol.	18-MAR-2007	West	4	8				no	
0302_t10	L	pol.	18-MAR-2007	West	4	8				no	Whole scene
0303_t01	C	vh/vv	18-MAR-2007	East	4	8				no	
0303_t02	C	vh/vv	18-MAR-2007	East	4	8				no	
0303_t03	C	vh/vv	18-MAR-2007	East	4	8				no	
0303_t04	C	vh/vv	18-MAR-2007	East	4	8				no	
0303_t05	C	vh/vv	18-MAR-2007	East	4	8				no	
0303_t06	C	vh/vv	18-MAR-2007	East	4	8				no	
0303_t07	C	vh/vv	18-MAR-2007	East	4	8				no	
0303_t08	C	vh/vv	18-MAR-2007	East	4	8				no	
0303_t10	C	vh/vv	18-MAR-2007	East	4	8				no	Whole scene

Data Products

SceneID	Band	Pol.	Flight date	View from	Resol. azim. [m]	Looks	Master / Slave to	spatial baseline [m]	temporal baseline [d]	Geocoding	Remarks
Testsite Framstrait											
0401_t01	C	vh/vv	19-MAR-2007	East	4	8				no	
0401_t02	C	vh/vv	19-MAR-2007	East	4	8				no	
0401_t03	C	vh/vv	19-MAR-2007	East	4	8				no	
0401_t04	C	vh/vv	19-MAR-2007	East	4	8				no	
0401_t10	C	vh/vv	19-MAR-2007	East	4	8				no	Whole scene
0401_t12	C	vh/vv	19-MAR-2007	East	20	1				no	Sentinel IWS simulation of t02
0402_t01	C	hv/hh	19-MAR-2007	West	4	8				no	
0402_t02	C	hv/hh	19-MAR-2007	West	4	8				no	
0402_t03	C	hv/hh	19-MAR-2007	West	4	8				no	
0402_t04	C	hv/hh	19-MAR-2007	West	4	8				no	
0402_t10	C	hv/hh	19-MAR-2007	West	4	8				no	Whole scene
0501_t01	C	vh/vv	19-MAR-2007	East	4	8				no	
0501_t02	C	vh/vv	19-MAR-2007	East	4	8				no	
0501_t03	C	vh/vv	19-MAR-2007	East	4	8				no	
0501_t04	C	vh/vv	19-MAR-2007	East	4	8				no	
0501_t05	C	vh/vv	19-MAR-2007	East	4	8				no	
0501_t10	C	vh/vv	19-MAR-2007	East	4	8				no	Whole scene
0501_t20	C	vh/vv	19-MAR-2007	East	20	1				no	Whole scene, Sentinel IWS simulation of t10
0502_t01	L	pol.	20-MAR-2007	West	4	8				no	
0502_t02	L	pol.	20-MAR-2007	West	4	8				no	
0502_t03	L	pol.	20-MAR-2007	West	4	8				no	
0502_t04	L	pol.	20-MAR-2007	West	4	8				no	
0502_t05	L	pol.	20-MAR-2007	West	4	8				no	
0502_t10	L	pol.	20-MAR-2007	West	4	8				no	Whole scene

Data Products

SceneID	Band	Pol.	Flight date	View from	Resol. azim. [m]	Looks	Master / Slave to	spatial baseline [m]	temporal baseline [d]	Geocoding	Remarks
Testsite Etonbreen Glacier											
0701_t01	L	pol.	23-MAR-2007	North	4.5	8	Master			yes	
0702_t01	L	pol.	23-MAR-2007	North	4.5	8	0701_t01	5	0	no	
0703_t01	L	pol.	23-MAR-2007	North	4.5	8	0701_t01	10	0	no	
0704_t01	L	pol.	23-MAR-2007	North	4.5	8	0701_t01	-10	0	no	
0909_t01	P	pol.	26-MAR-2007	North	4.5	8				yes	RFI-Filter
0909_t02	P	pol.	26-MAR-2007	North	4.5	8	1102_t01	0	1	no	RFI-Filter
1005_t01	X	vv	26-MAR-2007	South	5	16	SP-IF			yes	Full baseline
1006_t01	X	vv	26-MAR-2007	North	5	16	SP-IF			yes	Full baseline
1007_t01	X	vv	26-MAR-2007	South	5	16	SP-IF			yes	Half baseline
1008_t01	X	vv	26-MAR-2007	North	5	16	SP-IF			yes	Half baseline
1101_t01	P	pol.	27-MAR-2007	South	4.5	8	Master			yes	RFI-Filter
1102_t01	P	pol.	27-MAR-2007	North	4.5	8	Master			yes	RFI-Filter
1103_t01	P	pol.	27-MAR-2007	South	4.5	8	1101_t01	15	0	no	RFI-Filter
1104_t01	P	pol.	27-MAR-2007	North	4.5	8	1102_t01	10	0	no	RFI-Filter
1105_t01	P	pol.	27-MAR-2007	South	4.5	8	1101_t01	25	0	no	RFI-Filter
1106_t01	P	pol.	27-MAR-2007	North	4.5	8	1102_t01	20	0	no	RFI-Filter
1107_t01	P	pol.	27-MAR-2007	South	4.5	8	1101_t01	-20	0	no	RFI-Filter
1108_t01	P	pol.	27-MAR-2007	North	4.5	8	1102_t01	-20	0	no	RFI-Filter
1201_t01	P	pol.	16-APR-2007	North	4.5	8	Master			yes	RFI-Filter
1202_t01	P	pol.	16-APR-2007	South	4.5	8	Master			yes	RFI-Filter
1203_t01	P	pol.	16-APR-2007	North	4.5	8	1201_t01	10	0	no	RFI-Filter
1204_t01	P	pol.	16-APR-2007	South	4.5	8	1202_t01	15	0	no	RFI-Filter
1205_t01	P	pol.	16-APR-2007	North	4.5	8	1201_t01	20	0	no	RFI-Filter
1206_t01	P	pol.	16-APR-2007	South	4.5	8	1202_t01	25	0	no	RFI-Filter
1207_t01	P	pol.	16-APR-2007	North	4.5	8	1201_t01	-20	0	no	RFI-Filter
1208_t01	P	pol.	16-APR-2007	South	4.5	8	1202_t01	-20	0	no	RFI-Filter
1209_t01	P	pol.	16-APR-2007	North	4.5	8	1201_t01	0	0	no	RFI-Filter

Data Products

SceneID	Band	Pol.	Flight date	View from	Resol. azim. [m]	Looks	Master / Slave to	spatial baseline [m]	temporal baseline [d]	Geocoding	Remarks
1201_t02	P	pol.	16-APR-2007	North	4.5	8	1102_t01	0	21	no	RFI-Filter
1202_t02	P	pol.	16-APR-2007	South	4.5	8	1101_t01	0	21	no	RFI-Filter
1203_t02	P	pol.	16-APR-2007	North	4.5	8	1102_t01	10	21	no	RFI-Filter
1204_t02	P	pol.	16-APR-2007	South	4.5	8	1101_t01	15	21	no	RFI-Filter
1205_t02	P	pol.	16-APR-2007	North	4.5	8	1102_t01	20	21	no	RFI-Filter
1206_t02	P	pol.	16-APR-2007	South	4.5	8	1101_t01	25	21	no	RFI-Filter
1207_t02	P	pol.	16-APR-2007	North	4.5	8	1102_t01	-20	21	no	RFI-Filter
1208_t02	P	pol.	16-APR-2007	South	4.5	8	1101_t01	-20	21	no	RFI-Filter
1209_t02	P	pol.	16-APR-2007	North	4.5	8	1102_t01	0	21	no	RFI-Filter
1501_t01	C	vh/vv	18-APR-2007	North	3	8	Master	0	0	yes	
1502_t01	C	vh/vv	18-APR-2007	South	3	8	Master	0	0	yes	
1503_t01	C	hv/hh	18-APR-2007	North	3	8	1501_t01	0	0	no	
1504_t01	C	hv/hh	18-APR-2007	South	3	8	1502_t01	0	0	no	
1505_t01	C	hv/hh	18-APR-2007	North	3	8	1501_t01	5	0	no	
1506_t01	C	hv/hh	18-APR-2007	South	3	8	1502_t01	7	0	no	
1507_t01	C	vh/vv	18-APR-2007	North	3	8	1501_t01	5	0	no	
1508_t01	C	vh/vv	18-APR-2007	South	3	8	1502_t01	7	0	no	
1541_t01	C	pol.	18-APR-2007	North	3	8				yes	Synthetic quad-pol data of 1501 and 1503
1542_t01	C	pol.	18-APR-2007	South	3	8				yes	Synthetic quad-pol data of 1502 and 1504
1545_t01	C	pol.	18-APR-2007	North	3	8				yes	Synthetic quad-pol data of 1505 and 1507
1546_t01	C	pol.	18-APR-2007	South	3	8				yes	Synthetic quad-pol data of 1506 and 1508
1601_t01	L	pol.	19-APR-2007	North	4.5	8	Master	0	0	yes	
1602_t01	L	pol.	19-APR-2007	South	4.5	8	Master	0	0	yes	
1603_t01	L	pol.	19-APR-2007	North	4.5	8	1601_t01	5	0	no	
1604_t01	L	pol.	19-APR-2007	South	4.5	8	1602_t01	7	0	no	
1605_t01	L	pol.	19-APR-2007	North	4.5	8	1601_t01	10	0	no	
1606_t01	L	pol.	19-APR-2007	South	4.5	8	1602_t01	14	0	no	
1607_t01	L	pol.	19-APR-2007	North	4.5	8	1601_t01	-10	0	no	
1608_t01	L	pol.	19-APR-2007	South	4.5	8	1602_t01	-8	0	no	
1609_t01	L	pol.	19-APR-2007	North	4.5	8	1601_t01	0	0	no	
1601_t02	L	pol.	19-APR-2007	North	4.5	8	0701_t01	0	27	no	
1603_t02	L	pol.	19-APR-2007	North	4.5	8	0701_t01	5	27	no	
1605_t02	L	pol.	19-APR-2007	North	4.5	8	0701_t01	10	27	no	
1607_t02	L	pol.	19-APR-2007	North	4.5	8	0701_t01	-10	27	no	
1609_t02	L	pol.	19-APR-2007	North	4.5	8	0701_t01	0	27	no	

Data Products

SceneID	Band	Pol.	Flight date	View from	Resol. azim. [m]	Looks	Master / Slave to	spatial baseline [m]	temporal baseline [d]	Geocoding	Remarks
1905_t01	X	vv	22-APR-2007	South	5	16	SP-IF			yes	Full baseline
1906_t01	X	vv	22-APR-2007	North	5	16	SP-IF			yes	Full baseline
1907_t01	X	vv	22-APR-2007	South	5	16	SP-IF			yes	Half baseline
1908_t01	X	vv	22-APR-2007	North	5	16	SP-IF			yes	Half baseline
1909_t01	X	vv	22-APR-2007	South	5	16	SP-IF			yes	Full baseline
2001_t01	C	vh/vv	22-APR-2007	North	3	8	Master	0	0	yes	
2002_t01	C	vh/vv	22-APR-2007	South	3	8	Master	0	0	yes	
2003_t01	C	hv/hh	22-APR-2007	North	3	8	2001_t01	0	0	no	
2004_t01	C	hv/hh	22-APR-2007	South	3	8	2002_t01	0	0	no	
2005_t01	C	vh/vv	22-APR-2007	North	3	8	2001_t01	0	0	no	
2006_t01	C	vh/vv	22-APR-2007	South	3	8	2002_t01	0	0	no	
2041_t01	C	pol	22-APR-2007	North	3	8				yes	Synthetic quad-pol data of 2001 and 2003
2042_t01	C	pol	22-APR-2007	North	3	8				yes	Synthetic quad-pol data of 2002 and 2004
2001_t02	C	vh/vv	22-APR-2007	North	3	8	1501_t01	0	4	no	
2002_t02	C	vh/vv	22-APR-2007	South	3	8	1502_t01	0	4	no	
2003_t02	C	hv/hh	22-APR-2007	North	3	8	1501_t01	0	4	no	
2004_t02	C	hv/hh	22-APR-2007	South	3	8	1502_t01	0	4	no	
2005_t02	C	vh/vv	22-APR-2007	North	3	8	1501_t01	0	4	no	
2006_t02	C	vh/vv	22-APR-2007	South	3	8	1502_t01	0	4	no	

Data Products

Testsite Summit

SceneID	Band	Pol.	Flight date	View from	Resol. azim. [m]	Looks	Master / Slave to	spatial baseline [m]	temporal baseline [d]	Geocoding	Remarks
0601_t01	L	pol.	21-MAR-2007	North	4.5	8	Master	0	0	yes	
0602_t01	L	pol.	21-MAR-2007	South	4.5	8	Master	0	0	yes	
0603_t01	L	pol.	21-MAR-2007	North	4.5	8	0601_t01	5	0	no	
0604_t01	L	pol.	21-MAR-2007	South	4.5	8	0602_t01	7	0	no	
0605_t01	L	pol.	21-MAR-2007	North	4.5	8	0601_t01	10	0	no	
0606_t01	L	pol.	21-MAR-2007	South	4.5	8	0602_t01	10	0	no	
0607_t01	L	pol.	21-MAR-2007	North	4.5	8	0601_t01	-10	0	no	
0608_t01	L	pol.	21-MAR-2007	South	4.5	8	0602_t01	-8	0	no	
0609_t01	L	pol.	21-MAR-2007	North	4.5	8	0601_t01	0	0	no	
0901_t01	P	pol.	26-MAR-2007	South	4.5	8	Master	0	0	yes	RFI-Filter
0902_t01	P	pol.	26-MAR-2007	North	4.5	8	Master	0	0	yes	RFI-Filter
0903_t01	P	pol.	26-MAR-2007	South	4.5	8	0901_t01	15	0	no	RFI-Filter
0904_t01	P	pol.	26-MAR-2007	North	4.5	8	0902_t01	10	0	no	RFI-Filter
0905_t01	P	pol.	26-MAR-2007	South	4.5	8	0901_t01	25	0	no	RFI-Filter
0906_t01	P	pol.	26-MAR-2007	North	4.5	8	0902_t01	20	0	no	RFI-Filter
0907_t01	P	pol.	26-MAR-2007	South	4.5	8	0901_t01	-20	0	no	RFI-Filter
0908_t01	P	pol.	26-MAR-2007	North	4.5	8	0902_t01	-20	0	no	RFI-Filter
1001_t01	X	w	26-MAR-2007	North	5	16	SP-IF			yes	Full baseline
1002_t01	X	w	26-MAR-2007	South	5	16	SP-IF			yes	Full baseline
1003_t01	X	w	26-MAR-2007	North	5	16	SP-IF			yes	Half baseline
1004_t01	X	w	26-MAR-2007	South	5	16	SP-IF			yes	Half baseline
1302_t01	P	pol.	26-MAR-2007	North	4.5	8	Master	0	0	yes	RFI-Filter
1303_t01	P	pol.	26-MAR-2007	South	4.5	8	1307_t01	15	0	no	RFI-Filter
1304_t01	P	pol.	26-MAR-2007	North	4.5	8	1302_t01	10	0	no	RFI-Filter
1305_t01	P	pol.	26-MAR-2007	South	4.5	8	1307_t01	35	0	no	RFI-Filter
1306_t01	P	pol.	26-MAR-2007	North	4.5	8	1302_t01	20	0	no	RFI-Filter
1307_t01	P	pol.	26-MAR-2007	South	4.5	8	Master	35	0	yes	RFI-Filter
1308_t01	P	pol.	26-MAR-2007	North	4.5	8	1302_t01	-20	0	no	RFI-Filter
1302_t02	P	pol.	16-APR-2007	North	4.5	8	0902_t01	0	21	no	RFI-Filter
1303_t02	P	pol.	16-APR-2007	South	4.5	8	0901_t01	15	21	no	RFI-Filter
1304_t02	P	pol.	16-APR-2007	North	4.5	8	0902_t01	10	21	no	RFI-Filter
1305_t02	P	pol.	16-APR-2007	South	4.5	8	0901_t01	35	21	no	RFI-Filter
1307_t02	P	pol.	16-APR-2007	South	4.5	8	0901_t01	35	21	no	RFI-Filter

Data Products

SceneID	Band	Pol.	Flight date	View from	Resol. azim. [m]	Looks	Master / Slave to	spatial baseline [m]	temporal baseline [d]	Geocoding	Remarks
1401_t01	L	pol.	17-APR-2007	South	4.5	8	Master	0	0	yes	
1402_t01	L	pol.	17-APR-2007	North	4.5	8	Master	0	0	yes	
1403_t01	L	pol.	17-APR-2007	South	4.5	8	1401_t01	7	0	no	
1404_t01	L	pol.	17-APR-2007	North	4.5	8	1402_t01	5	0	no	
1405_t01	L	pol.	17-APR-2007	South	4.5	8	1401_t01	19	0	no	
1406_t01	L	pol.	17-APR-2007	North	4.5	8	1402_t01	10	0	no	
1407_t01	L	pol.	17-APR-2007	South	4.5	8	1401_t01	-8	0	no	
1408_t01	L	pol.	17-APR-2007	North	4.5	8	1402_t01	-10	0	no	
1401_t02	L	pol.	17-APR-2007	South	4.5	8	0602_t01	0	27	no	
1402_t02	L	pol.	17-APR-2007	North	4.5	8	0601_t01	0	27	no	
1403_t02	L	pol.	17-APR-2007	South	4.5	8	0602_t01	7	27	no	
1404_t02	L	pol.	17-APR-2007	North	4.5	8	0601_t01	5	27	no	
1405_t02	L	pol.	17-APR-2007	South	4.5	8	0602_t01	19	27	no	
1406_t02	L	pol.	17-APR-2007	North	4.5	8	0601_t01	10	27	no	
1407_t02	L	pol.	17-APR-2007	South	4.5	8	0602_t01	-8	27	no	
1408_t02	L	pol.	17-APR-2007	North	4.5	8	0601_t01	-10	27	no	
1701_t01	C	vh/vv	19-APR-2007	South	3	8	Master	0	0	yes	
1702_t01	C	vh/vv	19-APR-2007	North	3	8	Master	0	0	yes	
1703_t01	C	hv/hh	19-APR-2007	South	3	8	1701_t02	0	0	no	
1704_t01	C	hv/hh	19-APR-2007	North	3	8	1702_t02	0	0	no	
1705_t01	C	hv/hh	19-APR-2007	South	3	8	1701_t02	7	0	no	
1706_t01	C	hv/hh	19-APR-2007	North	3	8	1702_t02	5	0	no	
1707_t01	C	vh/vv	19-APR-2007	South	3	8	1701_t02	7	0	no	
1708_t01	C	vh/vv	19-APR-2007	North	3	8	1702_t02	5	0	no	
1741_t01	C	pol.	19-APR-2007	South	3	8				yes	Synthetic quad-pol data of 1701 and 1703
1742_t01	C	pol.	19-APR-2007	North	3	8				yes	Synthetic quad-pol data of 1702 and 1704
1901_t01	X	vv	22-APR-2007	North	5	16	SP-IF			yes	Full baseline
1902_t01	X	vv	22-APR-2007	South	5	16	SP-IF			yes	Full baseline
1903_t01	X	vv	22-APR-2007	North	5	16	SP-IF			yes	Half baseline
1904_t01	X	vv	22-APR-2007	South	5	16	SP-IF			yes	Half baseline

ICESAR 2007

Technical Assistance for the Deployment of Airborne SAR and Geophysical Measurements during the IceSAR 2007

Final Report - Part 2: Sea Ice

Prepared for

European Space Agency

Prepared by

German Aerospace Center

Microwaves and Radar Institute (HR)

Oberpfaffenhofen

and

Alfred Wegner Institute for Polar and Marine Research

Climate Science Division

Bremerhaven

Primary Contractor:

Irena Hajnsek
German Aerospace Center
Microwaves and Radar Institute
PO BOX 1116, D-82234 Wessling
Phone: + 49/8153282363
Email: irena.hajnsek@dlr.de

Subcontractor:

Wolfgang Dierking
Alfred Wegener Institute for Polar & Marine Research
Climate Science Division
Bussestr. 24, D-27570 Bremerhaven
Phone: +49/4748311714
Email: wolfgang.dierking@awi.de

14. Nov 2008
Version 1.1

ICESAR 2007 – Sea Ice Image Analysis

Wolfgang Dierking
Alfred Wegener Institute for Polar and Marine Research
Bremerhaven, Germany

Introduction

The study presented here is part of the ICESAR campaign. The campaign took place in March 2007 on Svalbard, covering land and adjacent ocean areas. The objective was to provide high-resolution low-noise radar imagery of land and sea ice as a basis for investigations on the technical performance of ESA's Sentinel-1 mission. In the following sections, the focus is on sea ice. The major objectives of the sea ice study were:

- Assessment of the potential for separating different ice classes and identifying ice surface characteristics such as ridges and leads in radar imagery acquired with Sentinel-1 SAR system parameters (specifically noise level, spatial resolution, polarization).
- Simulation of Sentinel-1 Level 1b products using airborne SAR imagery as a starting point.
- Assessment of the different information content in C-band and L-band SAR images, respectively, regarding the retrieval of sea ice properties.

In the first section, the radar signatures of different ice types from three measurement sites representing different ice regimes are presented and discussed. The location of the test sites is shown in Fig. 1. The backscattering coefficients were calculated from images of the airborne ESAR-system. Ice types were identified through visual inspection by a sea ice expert, using C- and L-band SAR imagery, optical data, and photographs. The radar images are presented together with the corresponding optical images in Appendix 1. Details concerning data acquisitions over sea ice and environmental conditions during the measurements are provided in Appendix 2, together with selections of photographs taken with a hand-held camera during the measurement flights.

The second section deals with the effect of noise and spatial resolution on the perceptibility of ice cover characteristics in radar images. Images resembling the interferometric wide-swath mode (IWSM) of the Sentinel-1 SAR are simulated from the ESAR imagery. This imaging mode is of large interest for operational sea ice mapping. An alternative is the extra wide-swath mode (EWSM). The simulation of the latter from the data used in this study, however, does not make much sense since the across-track extension of the ESAR imagery is too narrow: the simulated product covers only a distance of roughly 70-80 times the extension of one EWSM resolution cell. In operational mapping, wide-swath images are typically utilized to characterize the large-scale ice conditions, i. e. spatial variations of the ice cover on the order of tens of kilometers.

During the ICESAR campaign, Envisat ASAR data were acquired. In cases for which the time difference between airborne measurements and satellite overpasses was not longer than a few hours, ESAR and ASAR images were jointly analyzed. A discussion of the results gained from ICESAR and an assessment of the Sentinel-1 system parameters in the context of operational sea ice mapping and sea ice science are provided in the third section. Results from other investigations on sea ice SAR signatures reported in the literature are also taken into account. Conclusions are summarized at the end of this report.

The SAR images gathered over sea ice during the ICESAR campaign extend and complement already existing data sets of past airborne C- and L-band campaigns, e. g. from the Danish EMISAR and the US AIRSAR. Unlike the SAR imagery from the former campaigns, the ICESAR radar images are supplemented by data that were acquired almost simultaneously from a second airplane flying at low altitude, including wide-swath optical images, information on the ice cover characteristics, and meteorological parameters. The data set covers the major ice regimes typical for the ocean regions around Svalbard.

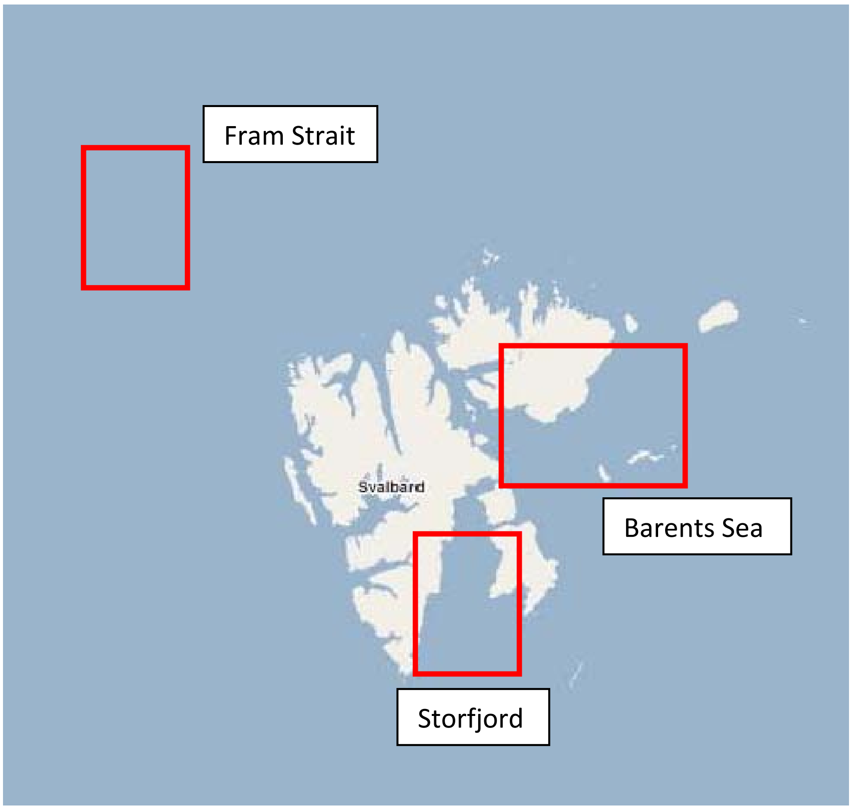

Figure 1. Positions of the three test sites for the ICESAR sea ice measurements.

Acknowledgment: I would like to thank my colleagues Irena Hajnsek, Rolf Scheiber, and Ralf Horn with their teams from DLR for the very fruitful and pleasant collaboration and the support I got through the course of ICESAR. I would also like to express my gratitude to Jörg Hartmann and Christof Lüpkes from AWI for their help and many useful advices. I have to thank Thomas Garbrecht and Axel Bochert from Optimare for their assistance in logistical and technical matters. Furthermore the pilots and technicians responsible for Polar-2 and the DLR airplane need also to be mentioned here. Finally, I thank Malcolm Davidson from ESA for his support and for making the ICESAR campaign possible.

Section 1: Sea Ice Classification

Satellite data play an important role in monitoring the ice-covered oceans on Earth. The goal of sea ice observation and mapping (either for science or for marine operations) is to retrieve certain sea ice properties and to document their status at a particular time, and to follow changes of the sea ice coverage over a certain period in time. Radar images are mostly used for separating different ice types from one another and from open water, for quantifying sea ice concentration (i. e. the fraction of a given area covered by ice), and for indicating the degree of sea ice deformation (mainly ridging and rafting). Sequences of images can be used for studying the ice drift. In any of these cases, it is essential that the characteristic features of an ice cover can be recognized in the imagery. The appearance of the ice in radar images depends on the frequency, polarization, incidence angle, noise level, and spatial resolution of the SAR.

This section deals with the discrimination of sea ice types in ESAR images. The spatial resolution (about 2 m) and the noise level (between about -30 and -35 dB) of the ESAR system make it possible to identify also narrow ice features such as ridges and elongated leads, small-scale variations of ice properties due to, e. g., small patches of young ice between older floes, and different stages of new ice growth. Hence, the ICESAR sea ice data can serve as an excellent reference for the judgment of satellite imaging radar systems. Ice types and features were classified by visual inspection which corresponds to the usual situation in operational sea ice mapping. The classification results are therefore to some degree “subjective”, which means that the assignment of a certain ice class to the observed radar signatures may vary between different sea ice analysts and/or may depend on the computational classification method that is used. The most appropriate classification schemes may also differ between ice regimes. The radar images from the Fram Strait (March 19 and 20), e. g., reveal clearly recognizable differences of the radar signature between lead ice, younger ice, older ice, and ridges. The task to define and distinguish ice classes in the images from Barents Sea and Storfjord is more difficult, since only younger ice types were present and large parts of the ice cover were broken and heavily deformed. This is, however, not critical for analyzing the utilization of the Sentinal-1 SAR image products for sea ice observation, since the major point is to assess whether information is lost by the imaging process. In this context, for example, it is not important whether a certain feature in a radar image is interpreted as bright nilas or grey ice, but rather if the radar intensity backscattered from this ice type is below or above the noise level of the SAR system.

The sea ice types that had to be considered for the ice regimes investigated in this study are listed in Table 1. Examples of their appearance in the C-band ESAR and the optical images are provided in Figs. 2 to 4. The ice thickness is one major criterion for the separation of ice types. This parameter could not be measured directly during the ICESAR campaign. It is thus difficult to distinguish, e. g. between thicker new ice and young ice, or between thicker young ice and thin FY ice. In addition, the sea ice was mostly snow-covered during data acquisitions. In such cases, ice types can only indirectly be separated in the optical imagery considering roughness characteristics and sizes of ice floes as well as shape (rounded or angular), provided that such properties are recognizable. In addition, the specific conditions of each test site were considered. Due to changing wind conditions, the ice was drifting back and forth in the Storfjord, and open-water areas developed in particular along the northern part of the track flown on March 16. In these zones of divergent ice motion, formation of new ice started because of the low air temperatures. In the Barents Sea, the occurrence of older ice floes (second-year ice or older) is a rare event, in particular in the region of the ICESAR test site. During the flights in Fram Strait, a few rounded floes with a thick snow cover and weathered ridges were observed for which it cannot be excluded that they were multi-year ice. However, considering the position of the test site (south of the summer ice edge in this area), the size and angular shape of many thicker ice floes and the cracks between the floes, it is highly probable that also the thicker ice was mostly first-year.

The visual classification was carried out using RGB-color composites of the dual-polarization radar images at C- band (R: cross-polarization, e. g. HV; G, B: like-polarization, e. g. G: HH, B: HH) together with the optical data and, when available, L-band imagery (R: cross-polarization, G: HH, B: VV). Besides the variations of the image color tone, identifiable features such as cracks, ridges, rafting zones, and floe shape were included in the classification. For example, rafting indicates new or young ice, ridges consisting of sharply edged ice blocks are typical for young and FY ice.

Table 1. Ice type terminology used in this study (after Armstrong et al., 1973)

New ice	General term for different types of recently formed ice. In this study, the term is mainly used for a thin elastic crust of ice up to 10 cm thick (nilas). Rafting is common when this ice type is under pressure.
Young ice	Transition between new and first-year ice, about 10-30 cm in thickness. Snow cover is normally moist and slushy.
First-year ice	Ice that grew in recent winter. Thickness from 30 cm to 2 m.
Ridges	On first-year ice, ridges are rough and sharply angular. More rounded on older ice.
Brash ice	Accumulation of ice fragments not more than 2 m across, the wreckage of other forms of ice.
Rafting	Pressure process by which one floe overrides another, most commonly found in new and young ice.
Broken ice	Ice cover with clearly identifiable open water cracks or a collection of ice floes between 2 m and about 10 m across with patches of open water, not separable in satellite imagery with moderate and coarse spatial resolution *(definition specifically for this study)*

Radar signatures were computed from "regions of interest" (ROIs) distributed over the images from the three sea ice sites over which flights were carried out. These measurement areas are shown in Fig. 1. The criterion for selecting an image for analysis was whether measurements at two or three different SAR configurations (C-HH+HV, C-VV+VH, L-HH+HV+VV+VH) were available for the given position. The images used in this study are shown in Appendix 1. All in all, more than 2300 ROIs were placed manually on the radar images available for the configurations listed above. For most of the ROI positions in one radar image, the corresponding ice floe / ice feature was also marked in the other radar image(s) that were taken over the same area, but usually at a different time. The images of different radar configurations were not registered to one another. ("Registration" in the sense used here is the process of making one image conform to another image without necessarily involving a map coordinate system). The reason is that the ice drifted between the respective data acquisitions, so that at certain positions, considerable changes of the ice cover were observed that required an individual placement of the ROIs in the respective images (see, e. g. image segments 6 from March 18, Appendix 1).

The size of the ROIs was variable. The number of looks for the 1.5 m pixel ESAR image product is about 5-8 (see below). For a 4-look image, the total spread between upper and lower standard deviation point around the mean backscattering coefficient is about 5 dB (Ulaby et al., 1982, chapter 7, page 485). In order to reduce the error of the estimated mean radar intensity for a certain ice type, a sufficient large number of pixels need to be averaged (also considering that neighboring pixels are correlated) (Oliver and Quegan, 1998, Chapter 4.8). The smallest ROI in the data set comprises more than 450 pixels so that the error due to speckle is negligible. In general, smaller ROIs (about 500-1000 pixels) were used for ice ridges and small patches of new or brash ice and open water (ridges: see, e. g. Fig. 4a, upper and middle row; small new ice or open water patches: Fig. 2a, upper and middle row; brash ice: Fig. 2a lower row, Fig. 3a, lower row). Larger ROIs had to be placed on broken ice consisting of floes on the order of a few meters (such as shown in Fig. 2a, upper and middle row) or on ice floes with an apparent textured radar signature (such as level ice floes in Fig. 3a, all rows, or Fig. 3b, middle row). Another motivation for using relatively large ROIs (a few thousand pixels) was that in satellite images with spatial resolutions of 30 m and coarser, the details of signature variations are not resolved.

The ESAR images were delivered as β-representation in single-look complex (SLC) format. The final products used in this study are in ground-range multi-look format and were stored as γ-values, in order to minimize the incidence angle sensitivity of the radar intensity. The relationships between γ, β, and the backscattering coefficient σ^0 are:

$$\sigma^0 = \beta \sin\theta_l, \quad \text{and} \quad \gamma = \beta \tan\theta_l = \sigma^0 / \cos\theta_l \tag{1}$$

where θ_l is the local incidence angle of the radar beam. The radar intensities at C-band (expressed as γ) for different ice types found over the three measurement sites are depicted in dual-polarization plots (like-polarization versus cross-polarization) in Figs. 5 to 7 for incidence angles ranging from 30° to 45° and 45° to 60°. The chosen angle intervals are relatively large, causing some overlap between the different ice classes due to the incidence angle sensitivity of the radar intensity. However, smaller intervals could not be used since the number of data points would have been too low in such a case. Also shown is the γ-value of a noise equivalent σ^0 (NESZ) of -22 dB at the mid-range of each incidence angle interval. On March 16, 18, and 20, measurements were also carried out at L-band quad-polarization, The L-band data corresponding to the results obtained for C-band are shown for comparison. With the Sentinel-1 SAR, data in dual polarization mode will be measured either as HH + HV or VV + VH, but not at HH + VV.

The dependence of γ on the incidence angle is shown in Figs. 9 to 12 for C- and L-band at different polarizations. Included is also a curve indicating the noise level γ_n corresponding to an NESZ of -22 dB constant over the whole incidence angle range. The calibration of the ESAR during the ICESAR campaign was carried out utilizing corner reflectors that were deployed on the land ice test site. The absolute accuracy of the C-band backscattering coefficient at HH-polarization, σ^0_{HH}, is better than 1 dB. The relative error is +2dB for σ^0_{VV} (i. e. σ^0_{VV} is too large) and +1dB for the cross-polarized channels. At L-band, differences between polarizations are between 0.5 and 1 dB (Rolf Scheiber, personnel communication).

In addition, plots of the variance-to-squared-mean ratio (VMR) at C- and L-band and different polarizations are shown in Figs. 9 to 12 as function of the incidence angle. The VMR is defined as

$$\frac{\sigma_P^2}{\langle P \rangle^2} = \frac{1}{L} + \left(1 + \frac{1}{L}\right)\left(1 + \frac{1}{SNR}\right)^{-2} \sigma_T^2 \qquad (2)$$

where σ_P^2 is the variance of the received power P, and $\langle\ \rangle$ denotes the expected value. The VMR depends on the number of independent looks, L, the texture variance, σ_T^2, and the signal-to-noise ratio, SNR. It is interesting to note that the VMR is independent of noise if the texture variance is zero. The image model from which equation (2) is derived assumes that system noise is modulated by image speckle in the same manner as the signal (Rignot and Kwok, 1993). The texture variance is a measure of the in-situ variability of the backscattering coefficient which would also be observed in the absence of speckle. It is hence related to spatial variations of the scattering ice surface and/or volume. In this analysis, the VMR values were calculated by taking the variance and the squared mean of each ROI. The minima of the calculated VMR-values are at about 0.20 to 0.25. This indicates that the images used had an ENL (estimated number of looks) of about 4 to 5. (Note that the original ESAR-data were re-processed for this sea ice study, see Section 2.) The ENL decreases slightly with increasing incidence angles.

Looking at Figs. 5 to 12, the radar signatures of open water at C- and L-band are rather variable, and the backscattering coefficient is higher at VV- than at HH-polarization, as expected. Sometimes, rather large values are observed for the VMR of open water, e. g. Fig. 9e or Fig. 10a. In such cases, the backscattered intensity is often close to the noise level of the ESAR.

In the Storfjord data from March 16, the radar intensities of broken and brash ice cannot be separated from one another both at C- and L-band (although the brash ice data cluster reveals clearly a different “center of mass” at L-band), see Figs. 5a to 5d. At C-band, the overlap between these two classes of deformed ice and the young/first-year level ice is large, whereas the signatures of both ice type groups can be well distinguished at L-band. The new ice radar intensities form separate clusters at C-band HH+HV (Fig. 5b) and L-band HH+HV (Fig. 5d) but overlap with level (young and first-year) ice signatures at C-VV+VH and L-VV+VH. For the separation of new ice from the other ice types, C- and L-band HH-polarization channels appear to be optimal (Figs. 9a, 9e). The VMR of broken ice at C-band is in most cases significantly larger than for the other ice types (Figs. 9a-9c). At L-band, the separation of broken ice is best at cross-polarization (Fig. 9f) but the VMR of the broken ice intensities is rather low (Figs. 9e-9g). For the Storfjord flight, both C-HV and C-VH intensities are shown in Figs. 9b and 9d, respectively. Since the measurements were taken separately (one way C-HH+HV, the way back on the same track C-VV+VH), the values differ slightly. The main reason is that the incidence angles are not the same for a given area on the ice because of the change of antenna look-direction relative to north on the way back. The conclusions that can be drawn from the analysis of the graphs for C-HV and C-VH are identical. Therefore, only one example is depicted for cross-polarization in case of the two other test sites. At L-band, data were taken in quad-pol mode, hence the relation $\gamma_{VH} = \gamma_{HV}$ holds.

In the Barents Sea imagery from March 18, the brash and broken ice signatures (here taken as one group) overlap strongly with the young/first-year ice signatures at C-band at incidence angles between 30 deg and 45 deg (Figs. 6a, 6b upper graphs). The overlap is rather small for incidence angles between 45 and 60 deg at C-band (Figs. 6a, 6b, lower graphs) and for all cases analyzed at L-band (Figs. 6c, 6d). It should be taken into account, however, that different incidence angle ranges mean different areas on the ice cover. Looking at Figs 10a to 10f, one recognizes that cross-polarization reveals a slight advantage compared to like-polarization concerning the separation of deformed (brash/broken) and level (young/first-year) ice. It is also worthwhile to emphasize that the signature contrast between deformed and level ice is similar at L- and C-band for this test site.

In the images from Barents Sea it was distinguished between “new” and “new/young” ice. Type “new” is the initial stage of ice formation. At C-band VV+VH (Fig.6a), the radar signatures of open water and new ice are similar. At C-band HH+HV, both intensity clusters can be well separated (Fig. 6b). This is also valid at L-band (Figs. 6c, 6d). At L-band, however, the “new” and “new/young” ice intensities cannot be separated from one another. The new/young ice intensity clusters overlap partly with young/first-year ice signatures both at C- and L-band. The VMR is not helpful for classifying different ice types (Figs. 10a-10f).

Over the test area of Fram Strait, the ice cover differed considerably from the conditions observed in the Storfjord or over the Barents Sea. Thicker ice floes and larger, elongated leads were present. The ice was not as heavily broken, and ridges stood out as distinct features. Figs. 7a, 7b, 8a, and 8b reveal that the radar intensities of “lead” ice are as high as of level ice at C-band like-polarization but lower at cross-polarization. At L-band (Fig. 8b) the intensity clusters of “lead” and “new” ice overlap completely. This could indicate the presence of frost flowers. Looking at the airborne imagery on the computer sreen and the hand-held photos (Appendix 2) from March 19 and 20, one recognizes that a number of leads were covered by a crust of hoar frost / frost flowers that increased the centimeter-scale roughness of the ice surface. Note that the structure of the lead iced surface is not well reproduced in the optical images printed in Appendix 1 because of the large contrast between the brightest and darkest part in the scenes. The radar intensity clusters of new/young, first-year/multi-year ice and ridges can be well distinguished both at C- and L-band (Figs. 7a, 7b, 8a, 8b). At smaller incidence angles (30-45 deg), an overlap between the new/young and first-year/multi-year ice types was found. Brash ice signatures are separated from ridge signatures at C- and L-band (Figs. 8a, 8b) but overlap with first-year/multi-year ice at C-band. The values of the VMR cover a larger range at L-band, single ice types cannot be distinguished.

The noise level of the Sentinel-1 SAR is also indicated in all graphs showing results for C-band. In Figs. 5 to 8, the mean values of the noise equivalent γ for the incidence angle intervals 30-45 deg and 45-60 deg were taken. In Figs. 9 to 12, the curve of γ corresponding to a constant NESZ (noise equivalent σ^o) of -22.0 dB is shown, as mentioned above. In the case of L-band, a value typical for ALOS-PALSAR (ScanSAR and Fine Resolution modes) was chosen. At C-band like-polarization, a NESZ of -22dB is only critical if different stages of newly formed ice shall be separated. The number of measured intensity values below the noise level are larger at HH- than at VV-polarization (which is expected, e. g., for slightly rough surfaces for which Bragg scattering theory is valid). In the case of cross-polarization, however, it may be even difficult to distinguish deformed and level ice as the examples from the Storfjord (Fig.9b, 9d, 10b) demonstrate. Hence, for sea ice mapping, the cross-polarized channel of the Sentinel-1 SAR may be useless in many cases. The only exception is given if ridges shall be separated from level ice which is clearly possible for certain ice regimes characterized by the conditions found in Fram Strait on March 19 and 20 (see Figs 11b, 12b). The same conclusion is also valid on the basis of the results at L-band cross-polarization, assuming a NESZ of -25dB (see Figs. 9f, 10e and 12d). At this noise level, it is also difficult to separate different types of new and young ice at L-band like-polarization (Figs. 9e, 9g, 10d, 10f, 12c, 12e).

It is important to note that the conclusions drawn above are based on data of high spatial resolution in which it is easier to distinguish ice types from one another. The images shown in Appendix 1 demonstrate that floes or patches of a certain ice type may cover relatively small areas. This means that at spatial scales typically used for operational sea ice mapping (effective spatial resolutions from 30 to 150 m) the radar signature for one resolution cell may be determined by a mixture of different ice types rather than one single ice type. Therefore, the optimal classification scheme depends also on the spatial resolution of a SAR system. The results shown in this section reveal as well that the VMR is in general not very useful for sea ice classification.

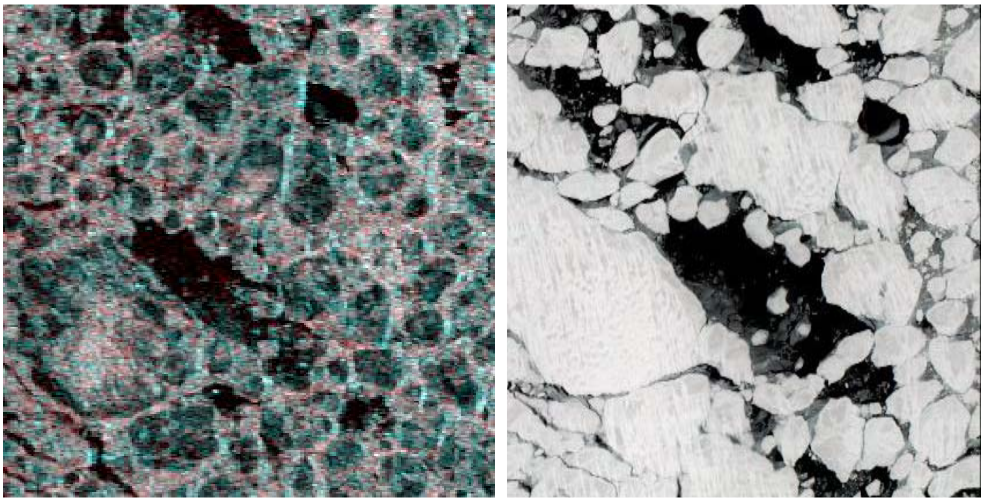

Broken ice, image width 375 m

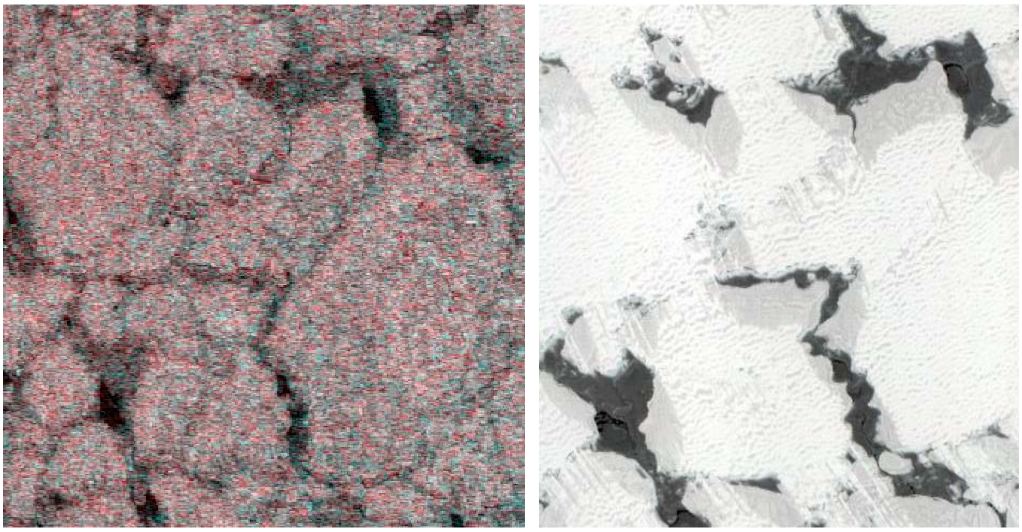

Broken ice and small patches of new ice, image width 525 m

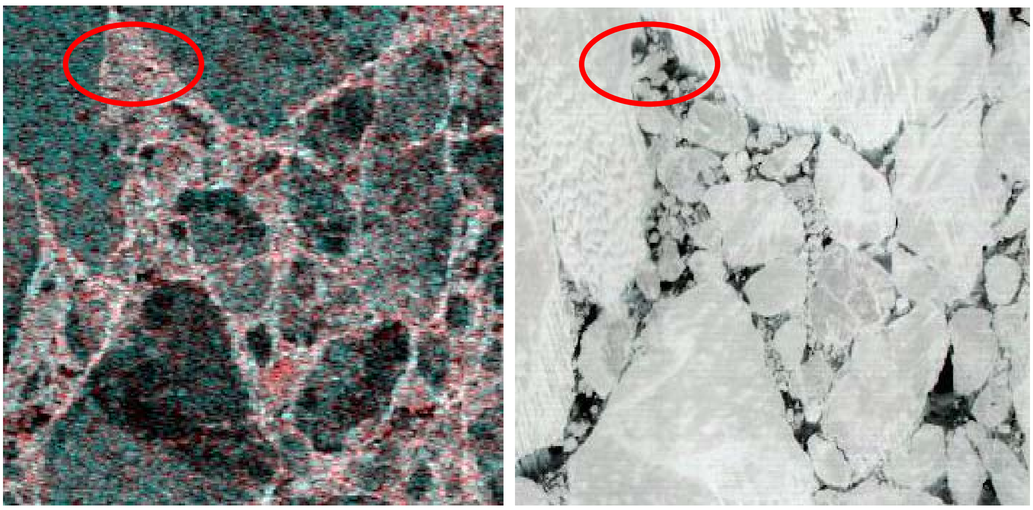

Brash and broken ice, image width 375 m

Figure 2a. Different ice types observed in the area of Storfjord on March 16. Radar images are C-band data (R:HV, G: HH, B:HH).

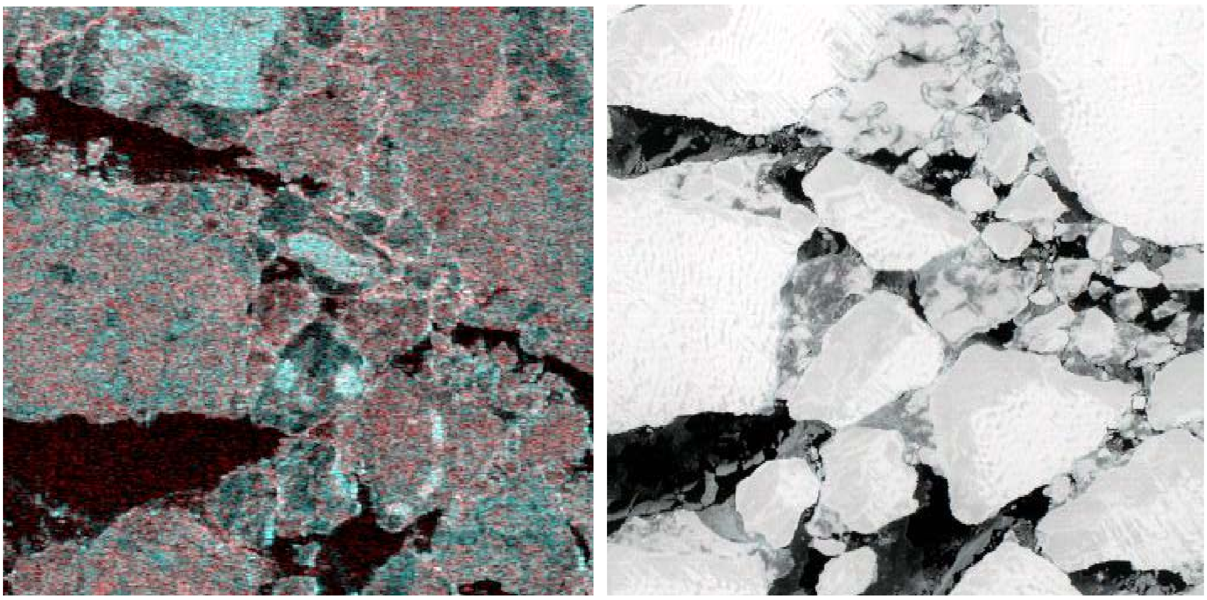

Young ice floes, image width 525 m

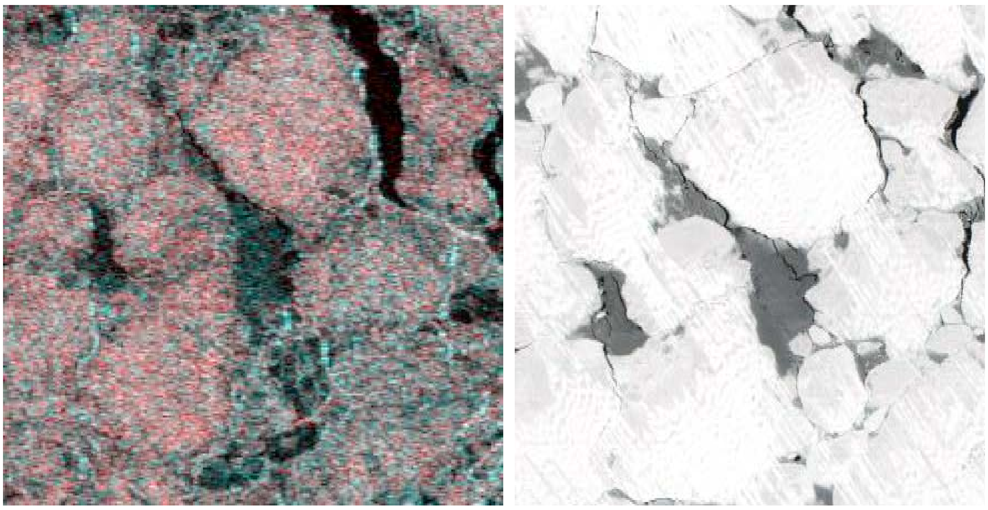

New ice imbedded in young ice, image width 375 m

Figure 2b. Different ice types observed in the area of Storfjord on March 16. Radar images are C-band data (R:HV, G: HH, B:HH).

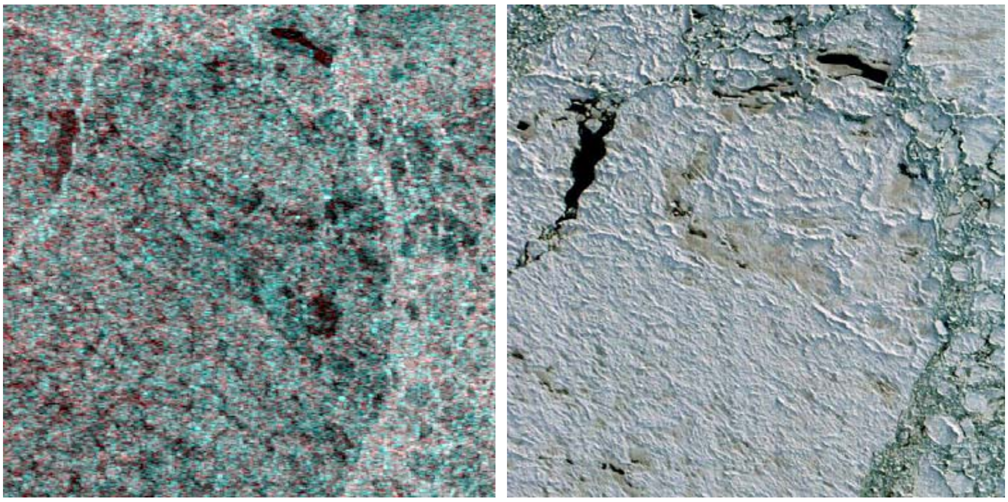

Level ice floe, young / FY ice, image width 525 m

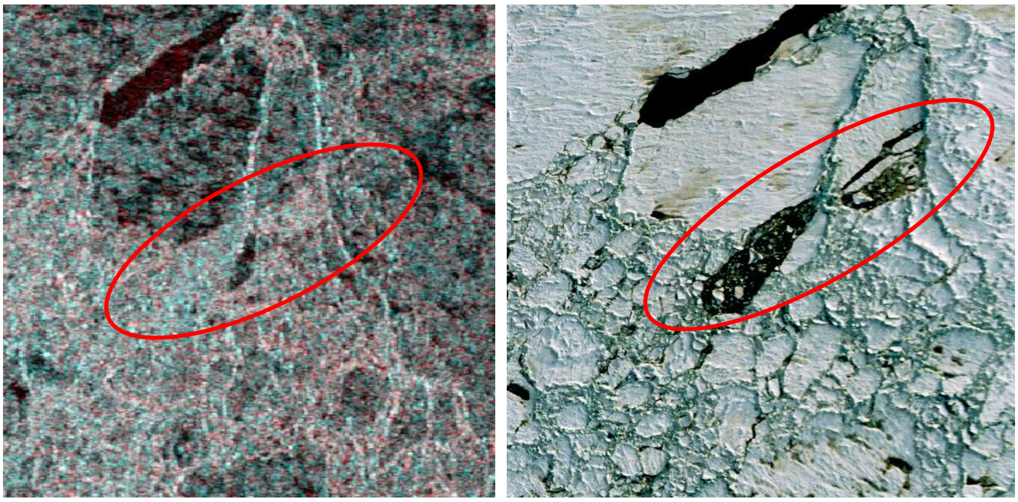

Broken and brash, young ice floes, open water, image width 525 m (note the appearance of the brash-filled open water patches in the SAR image, marked by the ellipse)

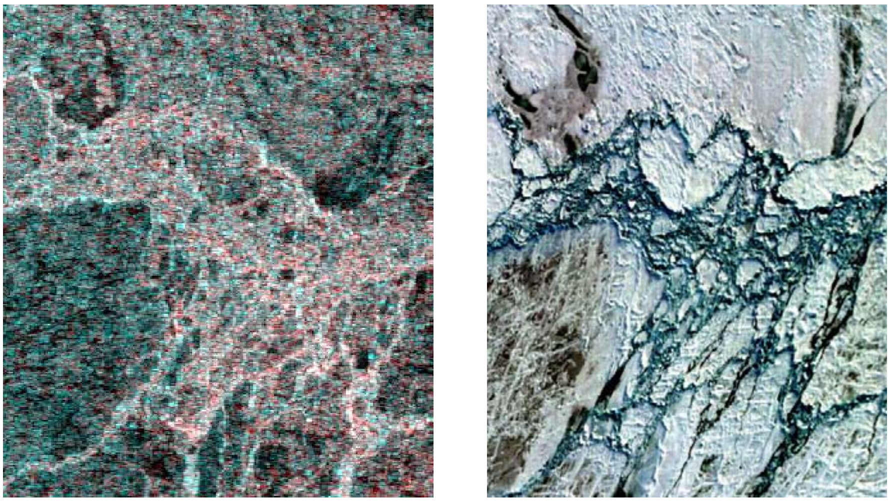

Broken and brash ice, image width 525 m

Figure 3a. Different ice types observed in the area of the Barens Sea on March 18. Radar images are C-band data (R:HV, G: HH, B:HH).

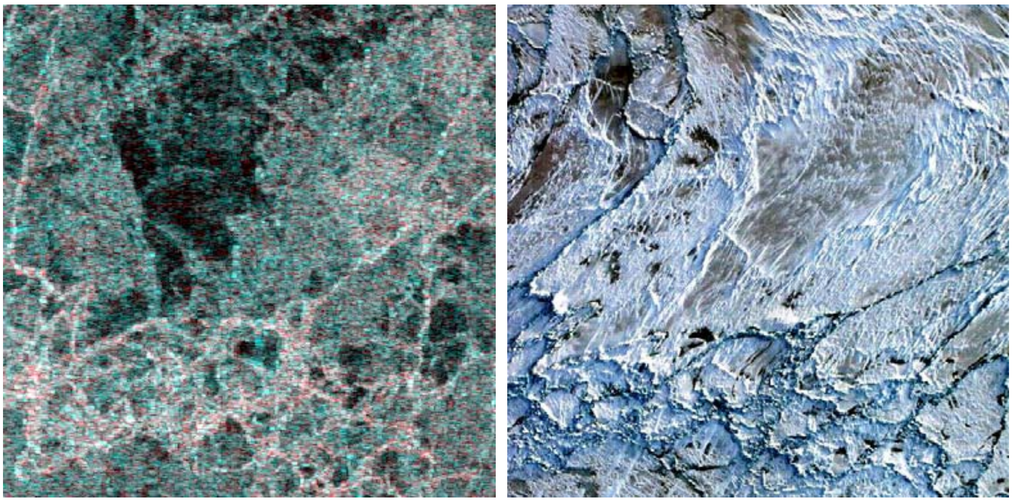

New or young ice and broken/ridged ice, image width 525 m (the radar image indicates that the snow cover influenced the radar signature; the distortions in the optical image are due to abrupt motions of the air plane caused by the strong wind during the flight)

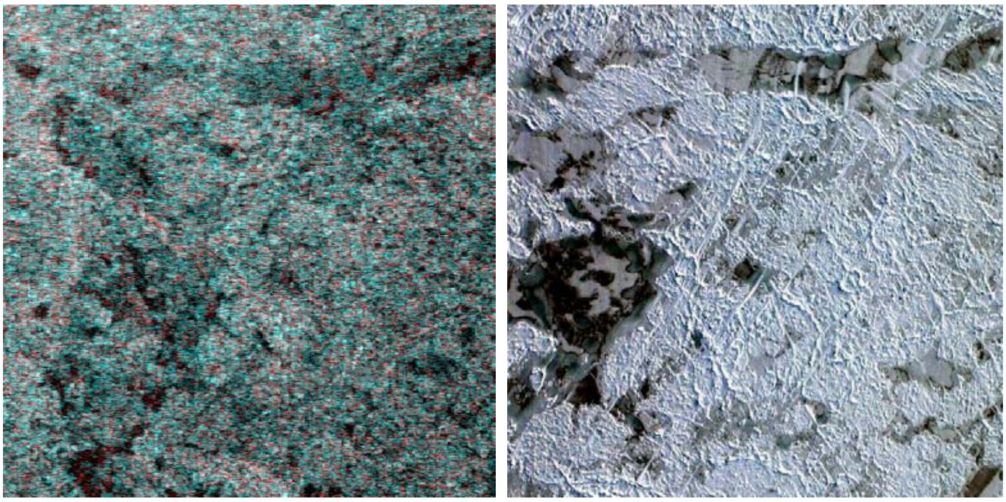

Young ice with moist snow cover, image width 600 m

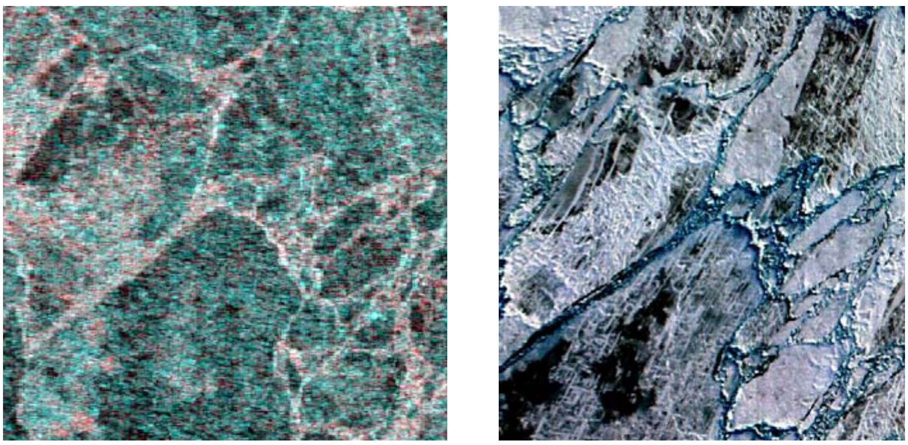

New / young ice, image width 525 m

Figure 3b. Different ice types observed in the area of the Barents Sea on March18. Radar images are C-band data (R:HV, G: HH, B:HH).

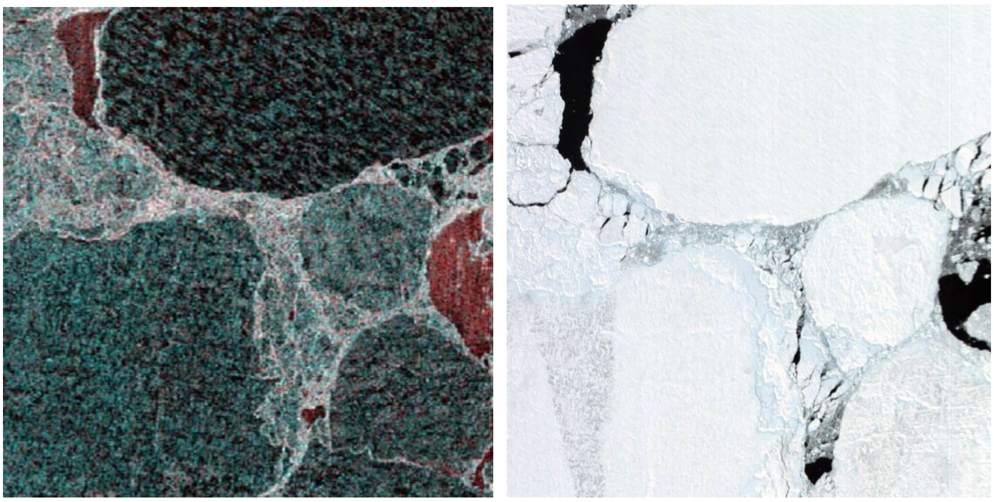

Smooth and rough young ice, brash ice and open water, image width 900 m

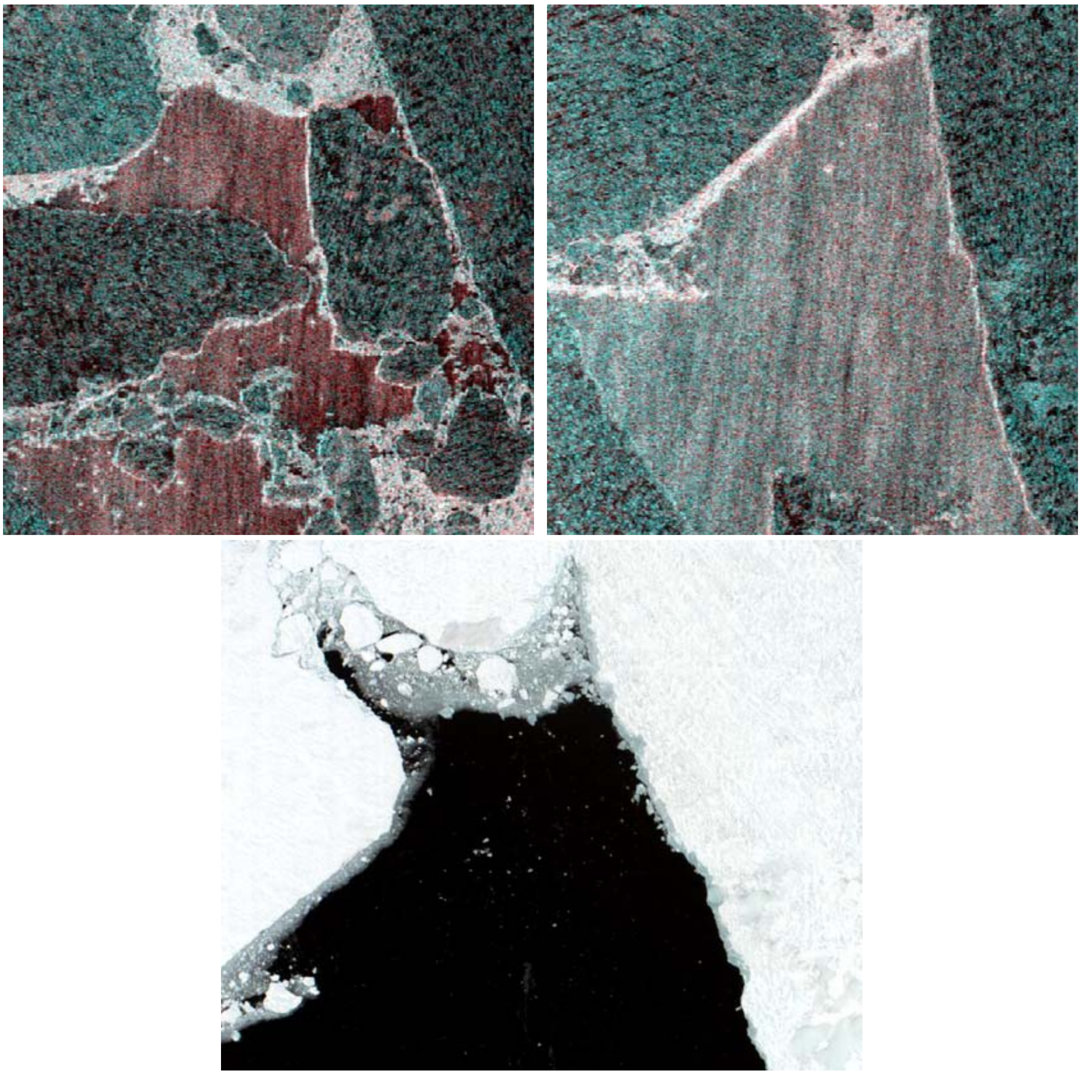

Area of open water, image width 975 m (the ice cover in this area changed considerably within one hour)

Figure 3c. Different ice types observed in the area of the Barents Sea on March 18. Radar images are C-band data (R:HV, G: HH, B:HH).

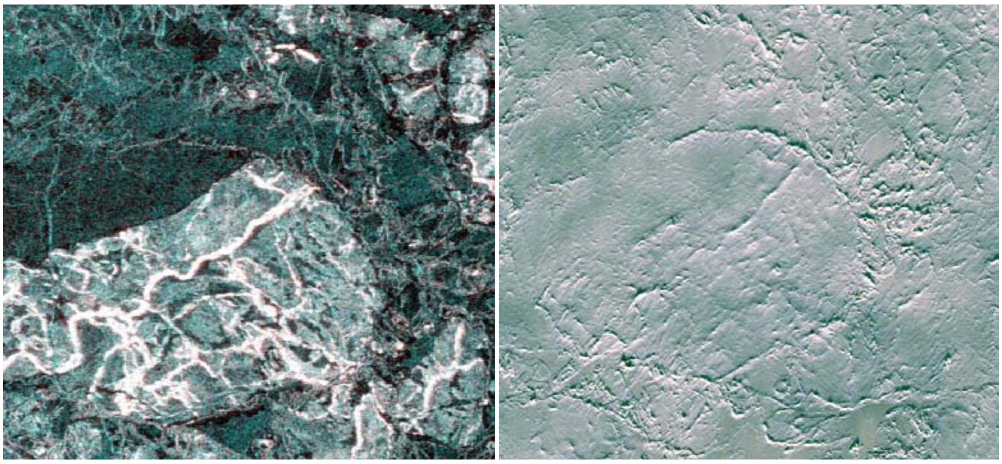

Young and old ice, ridges, image width 1025 m

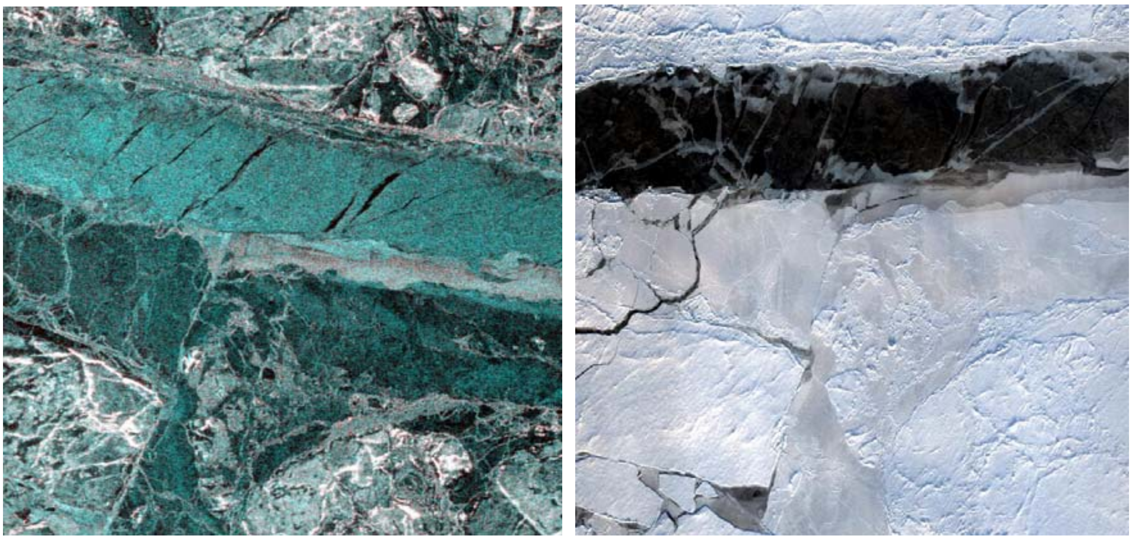

Lead ice, young ice, old ice, image width 1425 m

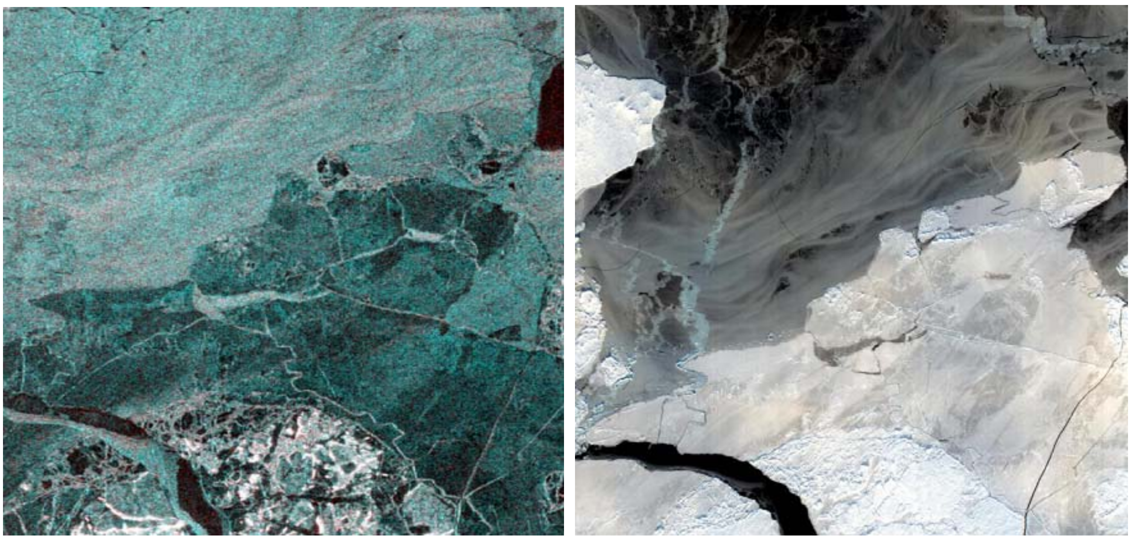

Lead ice and new ice, image width 1425 m

Figure 4a. Different ice types observed in the area of Fram Strait on March 19 and 20. Radar images are C-band data (R:HV, G: HH, B:HH).

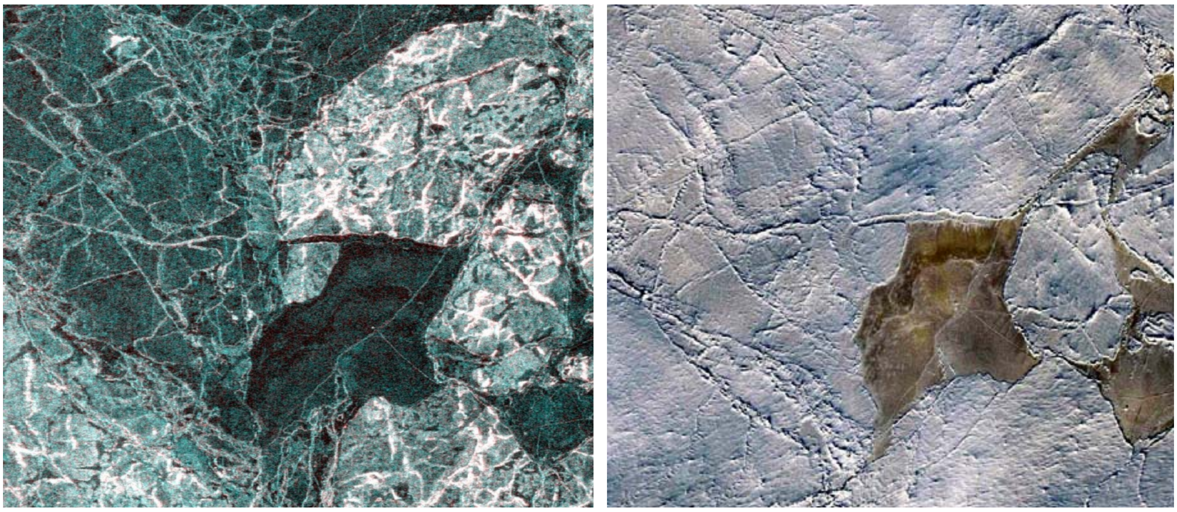

Smooth new ice imbedded in ridged young and/or old ice, image width 1500 m

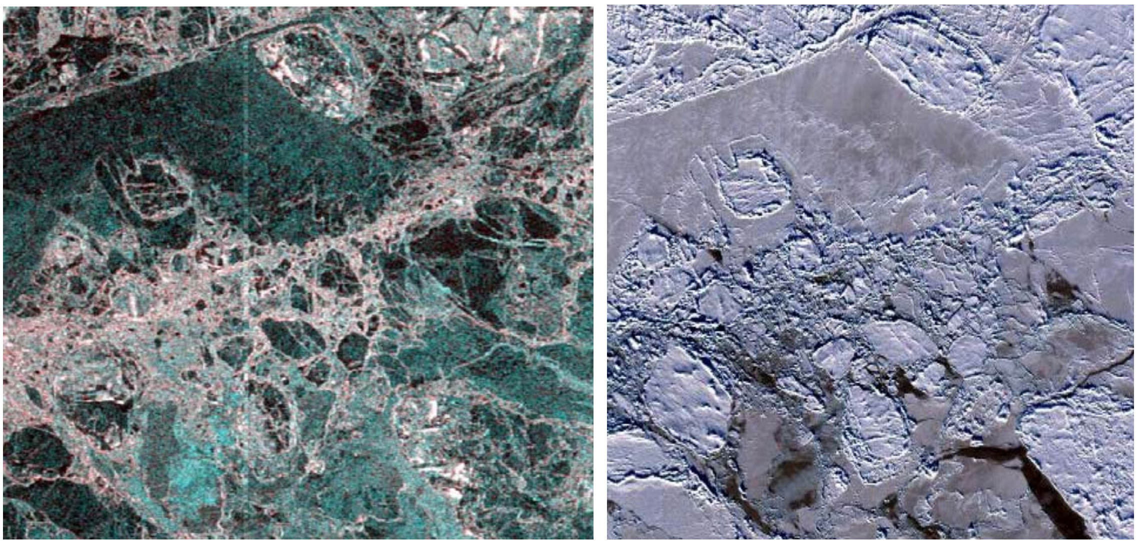

Brash and broken ice, image width 1500 m

Figure 4b. Different ice types observed in the area of Fram Strait on March 19 and 20. Radar images are C-band data (R:HV, G: HH, B:HH).

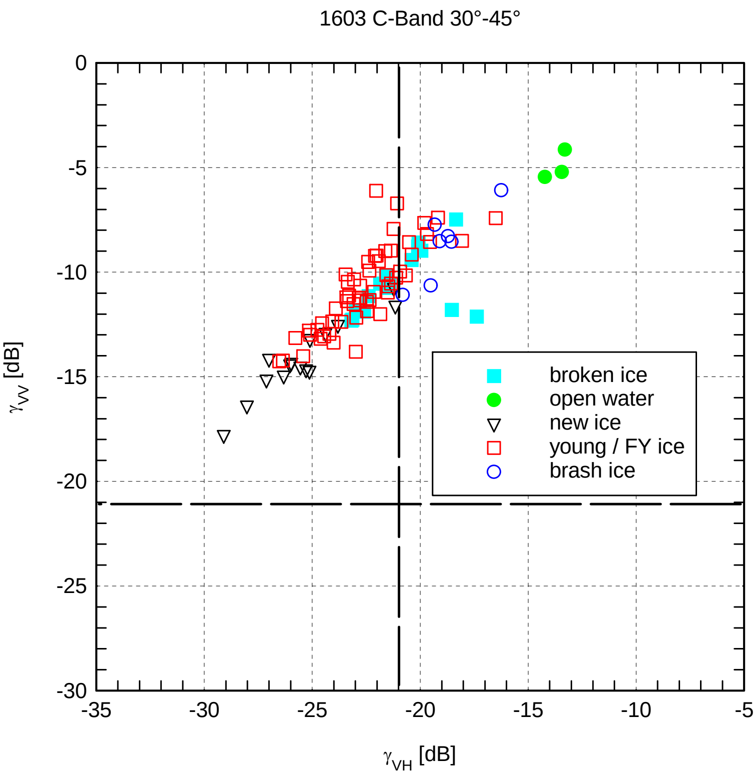

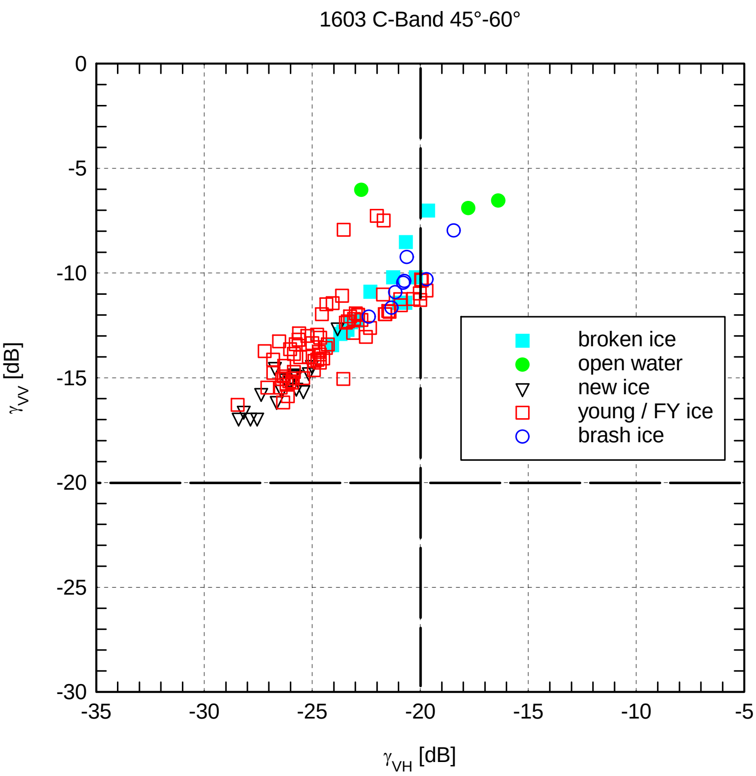

Figure 5a. Backscattering coefficients (γ) at C-band VH- and VV-polarization, for two different incidence angle intervals (i. e. two different areas), measured on March 16 over the Storfjord test site. Dashed lines indicate SAR noise level of the Sentinel-1 mission.

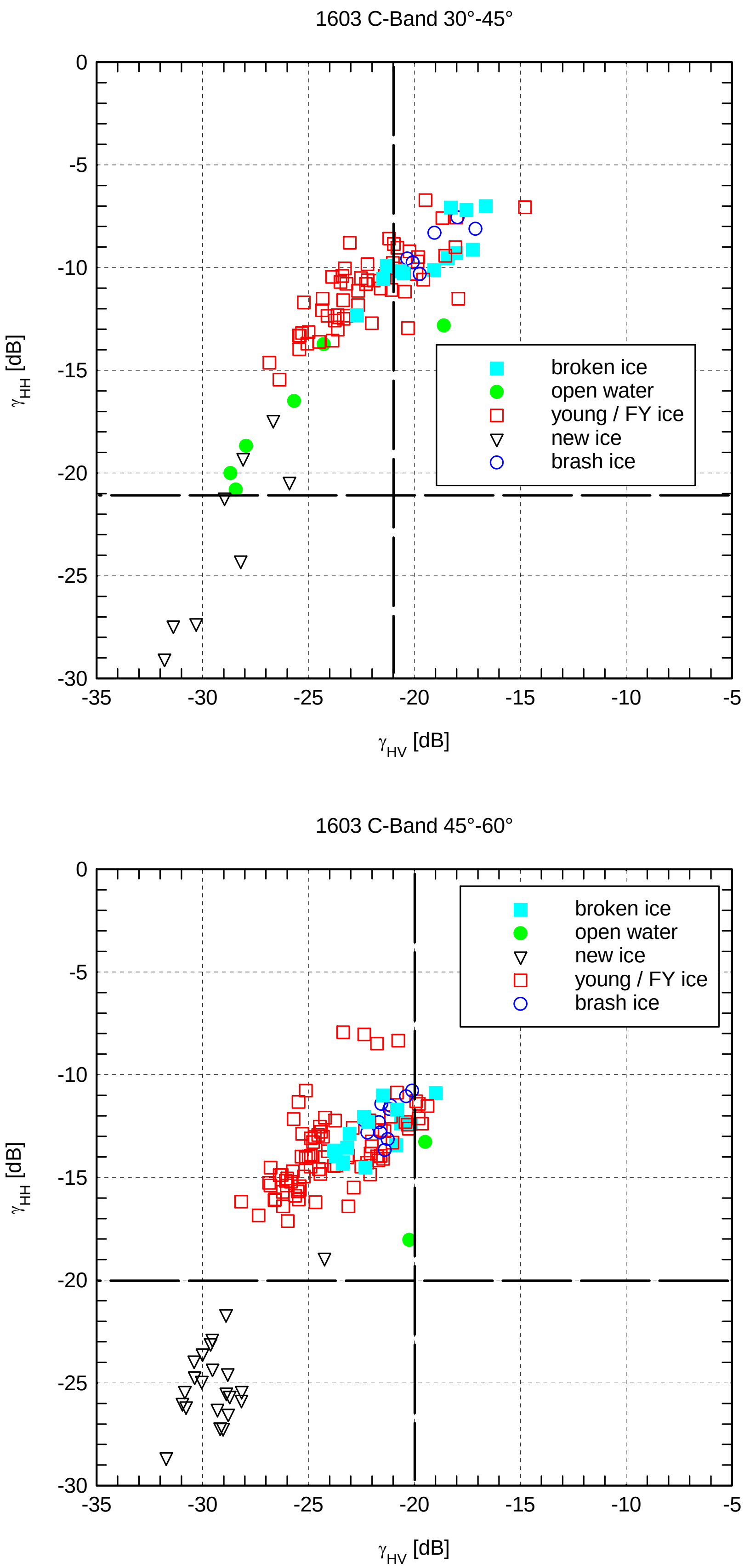

Figure 5b. Backscattering coefficients (γ) at C-band HV- and HH-polarization, for two different incidence angle intervals, measured on March 16 over the Storfjord test site. Dashed lines indicate SAR noise level of the Sentinel-1 mission.

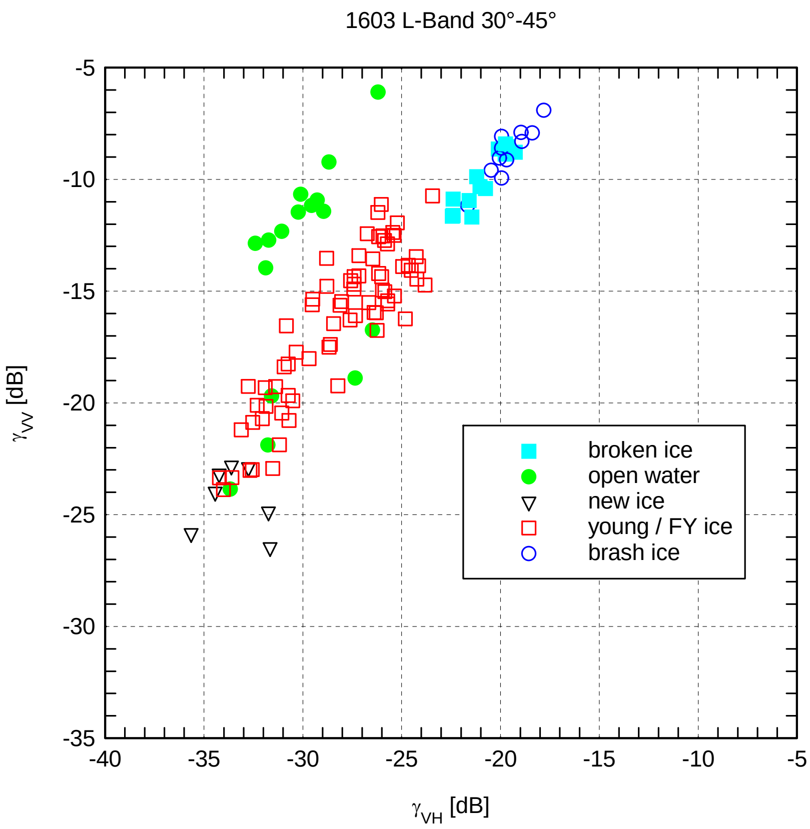

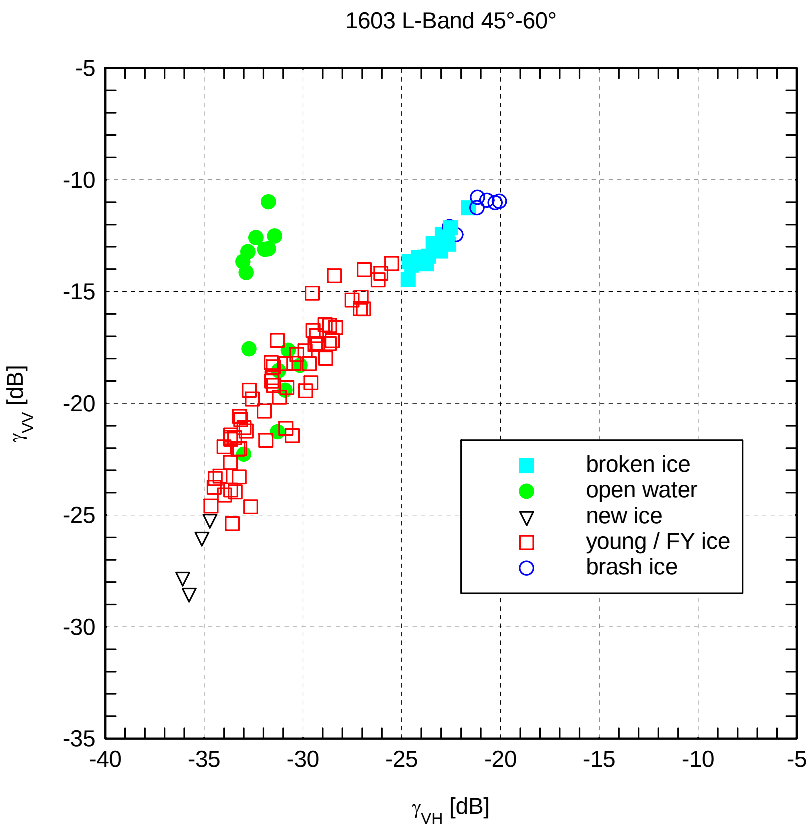

Figure 5c. Backscattering coefficients (γ) at L-band VH- and VV-polarization, for two different incidence angle intervals, measured on March 16 over the Storfjord test site.

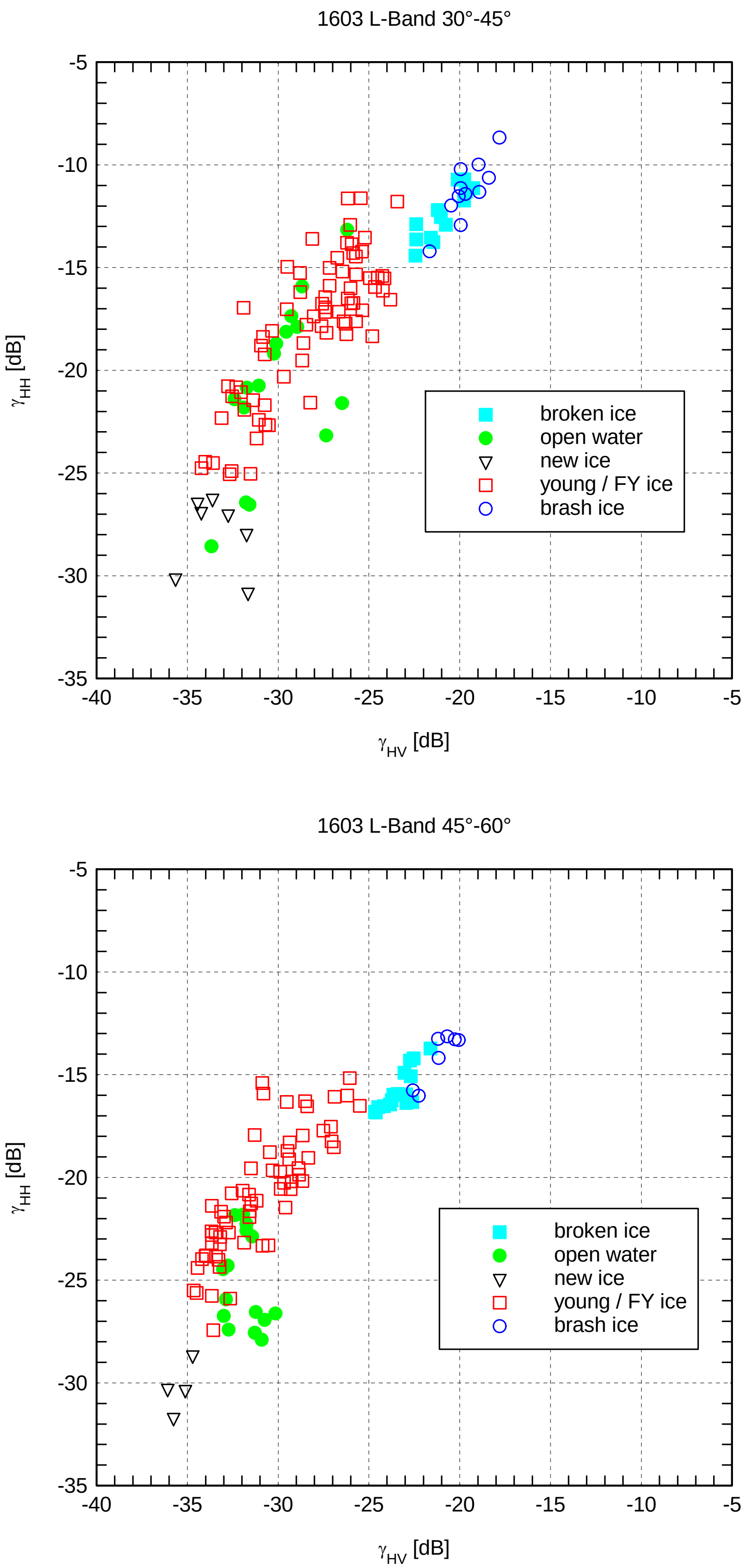

Figure 5d. Backscattering coefficients (γ) at L-band HV- and HH-polarization, for two different incidence angle intervals, measured on March 16 over the Storfjord test site.

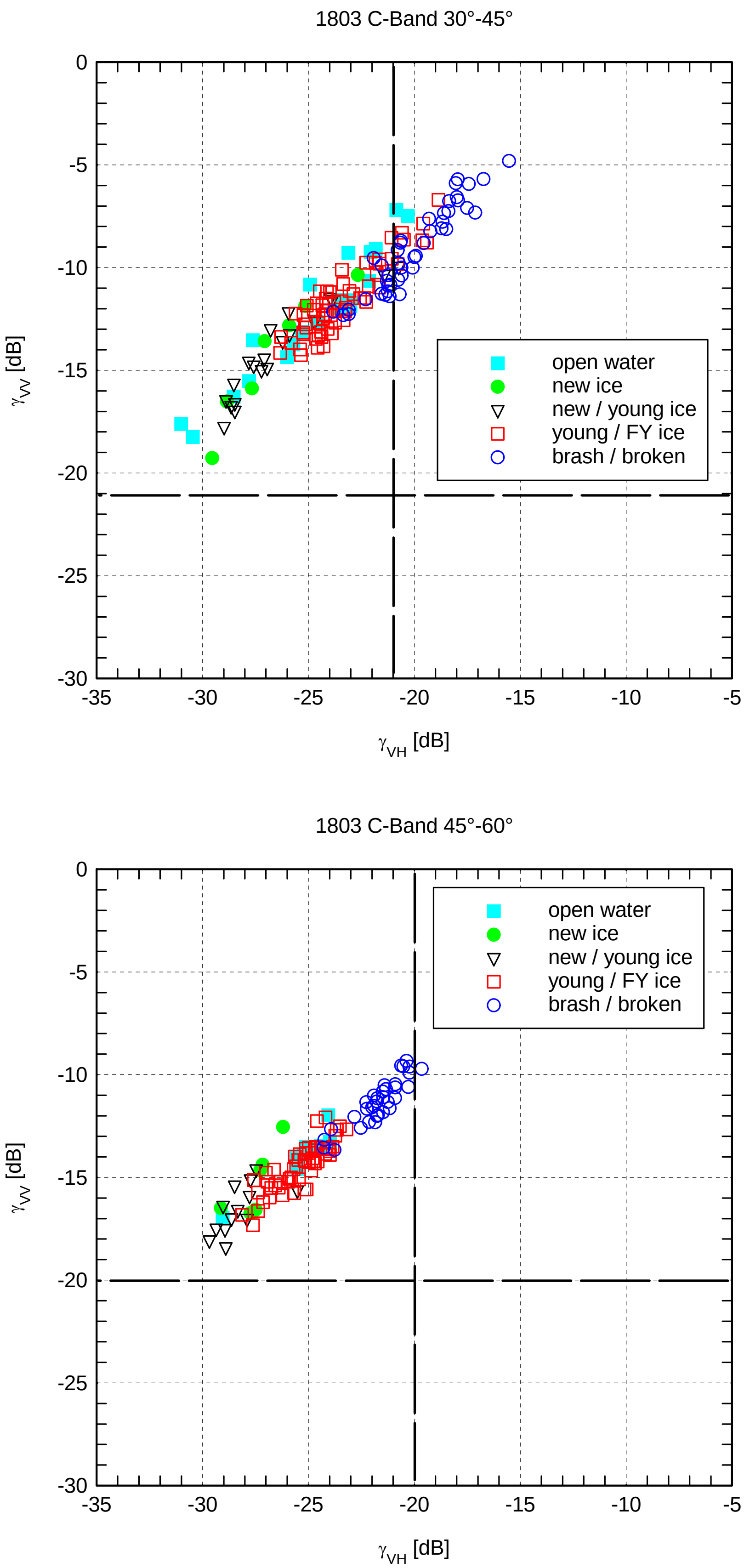

Figure 6a. Backscattering coefficients (γ) at C-band VH- and VV-polarization, for two different incidence angle intervals, measured on March 18 over the Barents Sea test site. Dashed lines indicate SAR noise level of the Sentinel-1 mission.

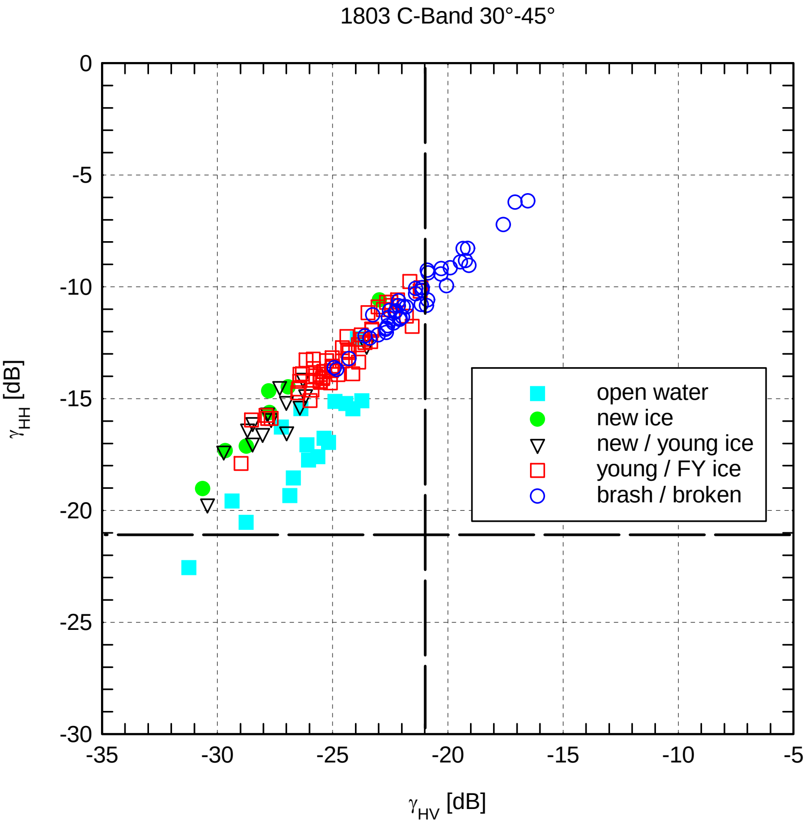

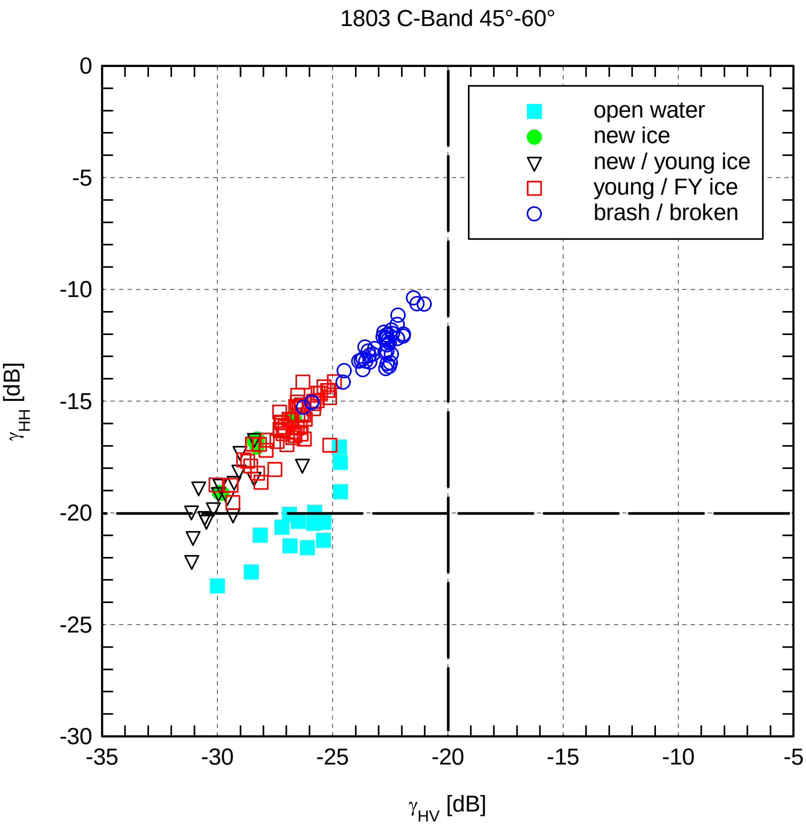

Figure 6b. Backscattering coefficients (γ) at C-band HV- and HH-polarization, for two different incidence angle intervals, measured on March 18 over the Barents Sea test site. Dashed lines indicate SAR noise level of the Sentinel-1 mission.

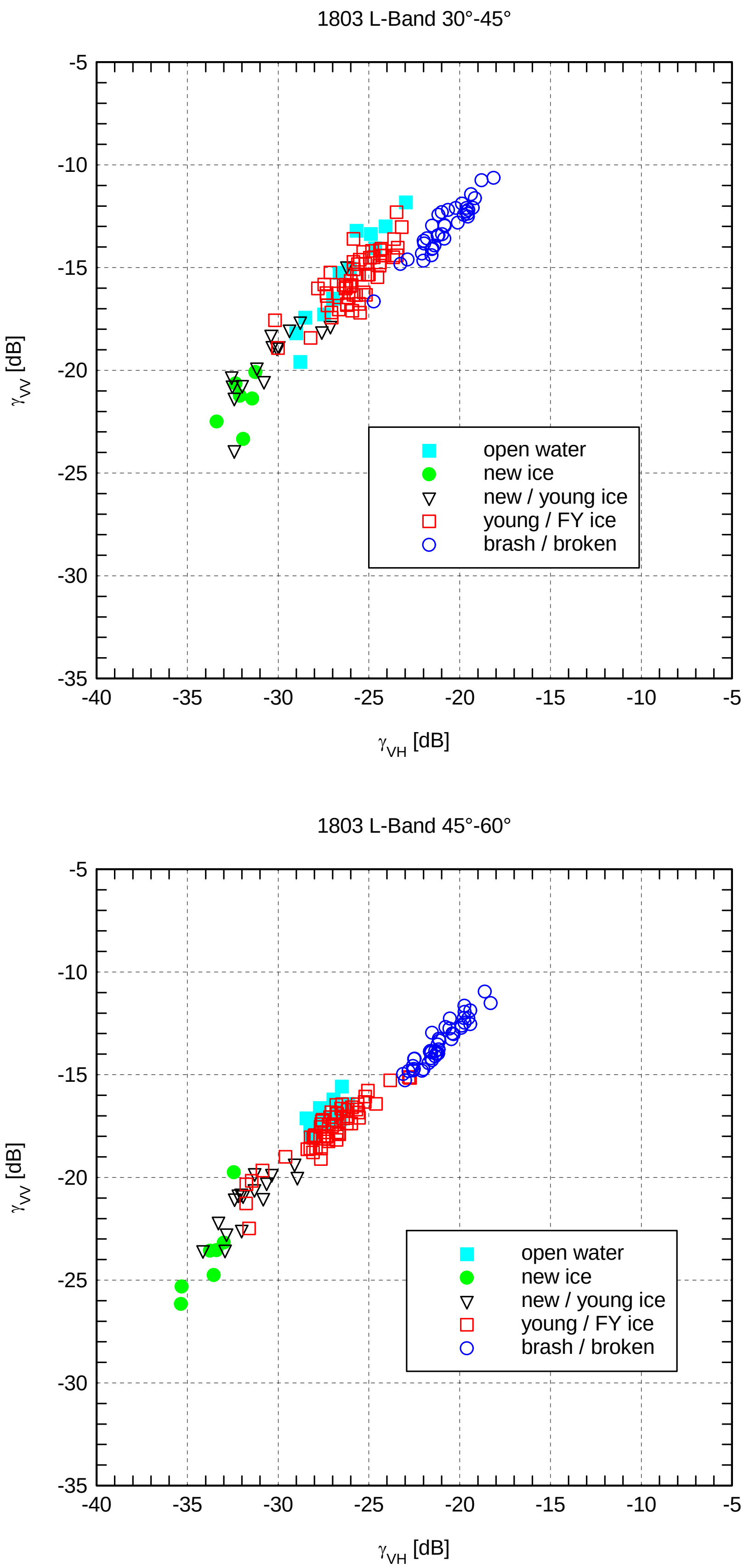

Figure 6c. Backscattering coefficients (γ) at L-band VH- and VV-polarization, for two different incidence angle intervals, measured on March 18 over the Barents Sea test site.

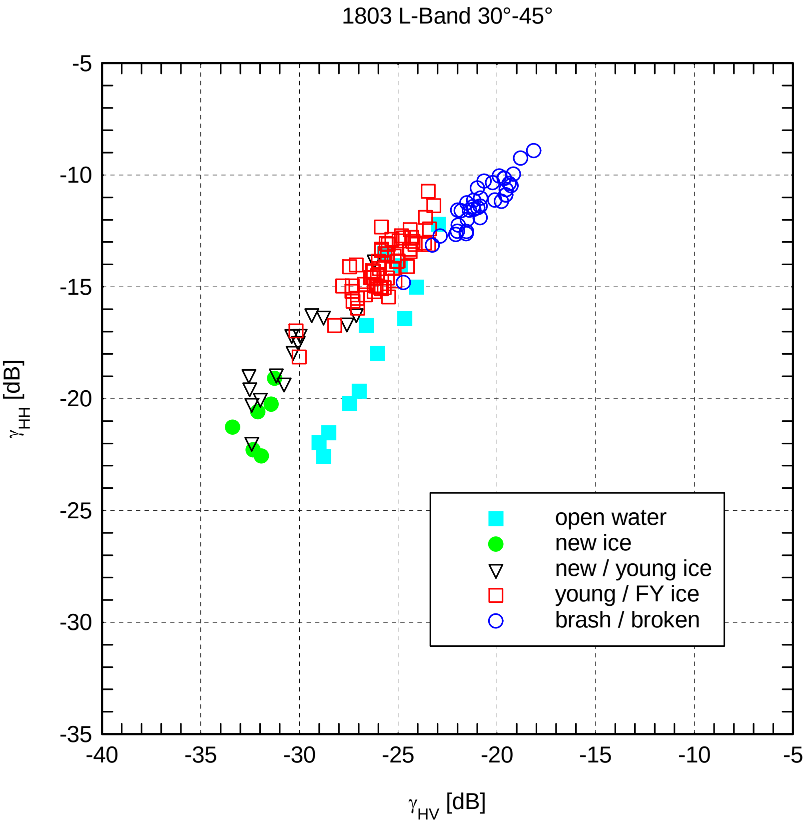

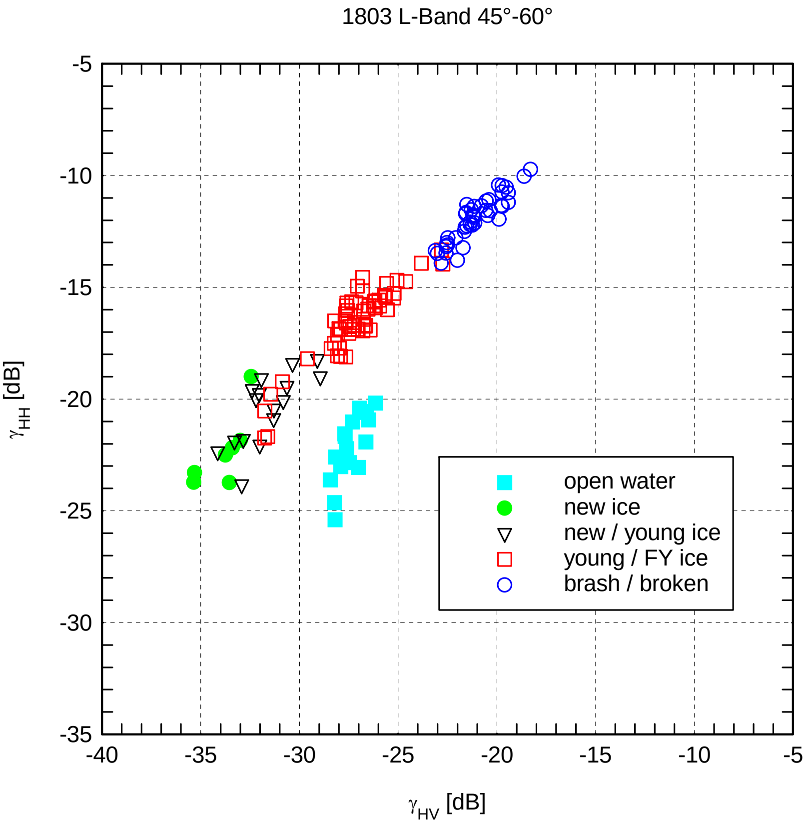

Figure 6d. Backscattering coefficients (γ) at L-band HV- and HH-polarization, for two different incidence angle intervals, measured on March 18 over the Barents Sea test site.

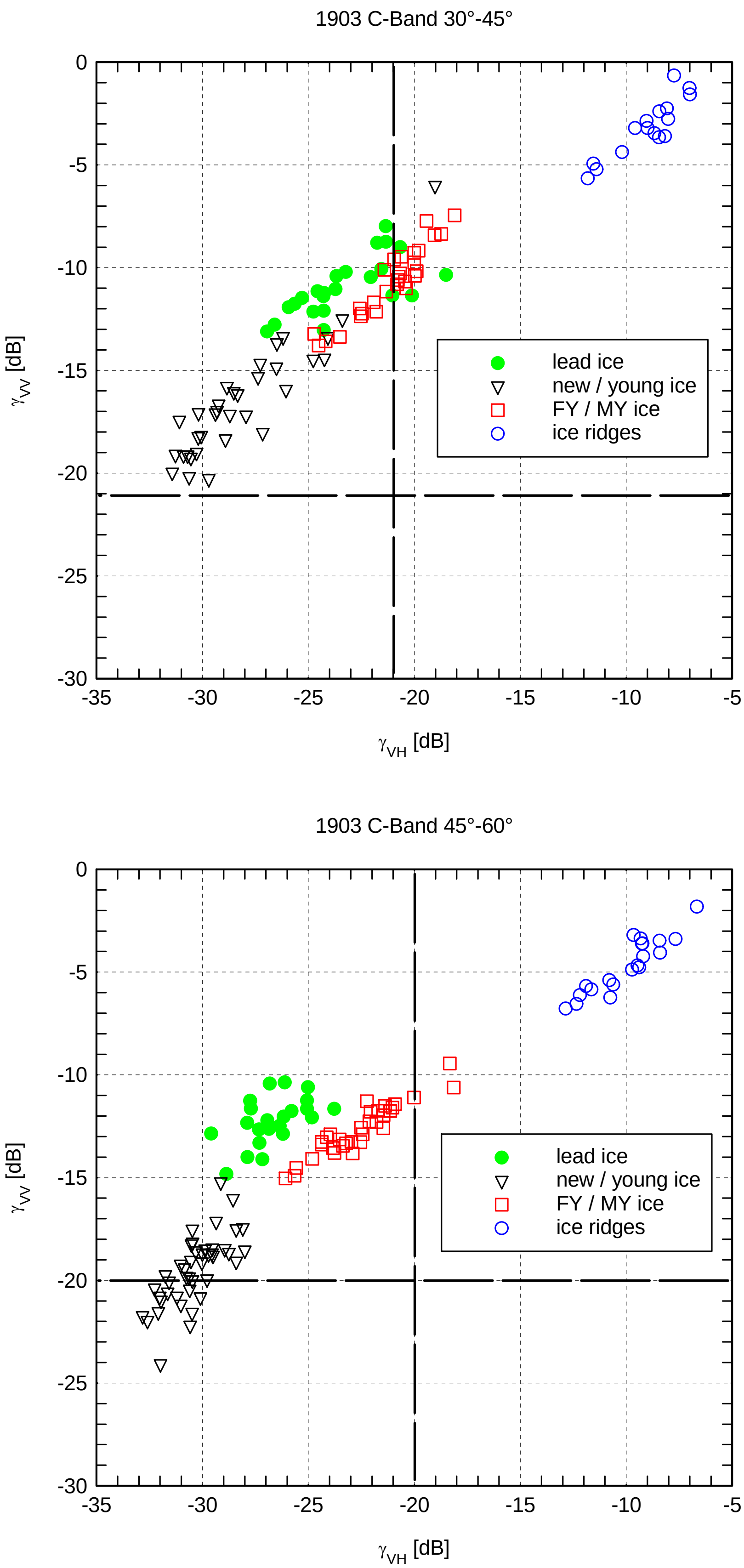

Figure 7a. Backscattering coefficients (γ) at C-band VH- and VV-polarization, for two different incidence angle intervals, measured on March 19 over the Fram Strait test site. Dashed lines indicate SAR noise level of the Sentinel-1 mission.

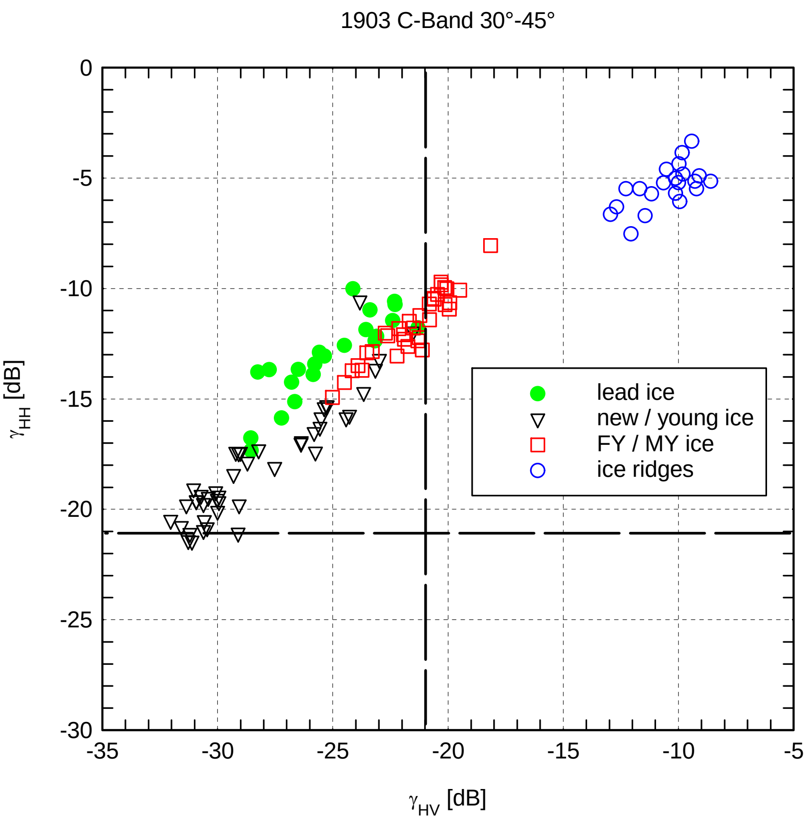

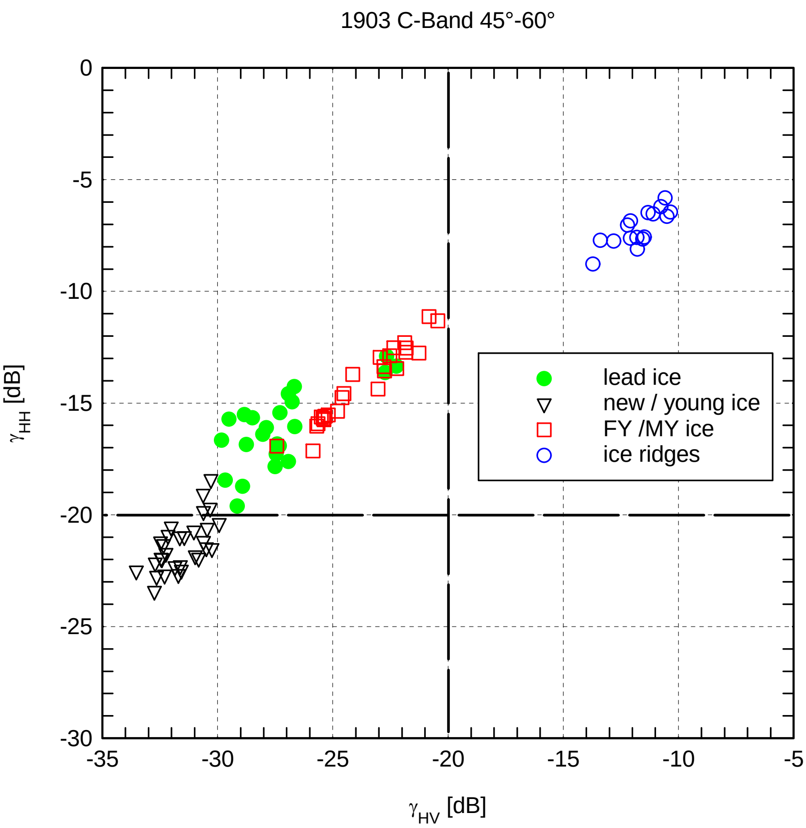

Figure 7b. Backscattering coefficients (γ) at C-band HV- and HH-polarization, for two different incidence angle intervals, measured on March 19 over the Fram test site. Dashed lines indicate SAR noise level of the Sentinel-1 mission.

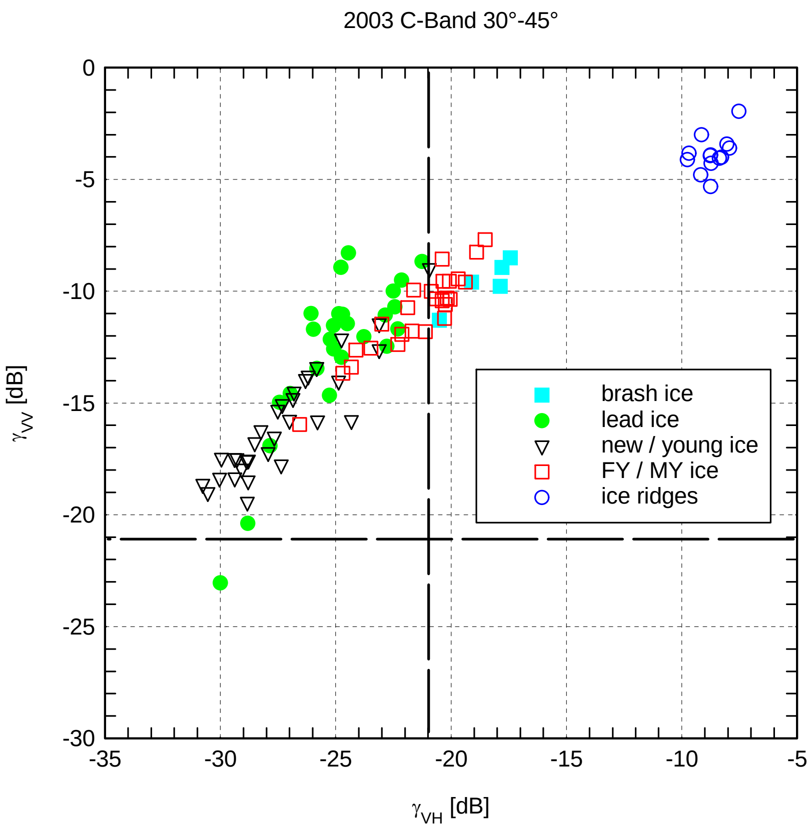

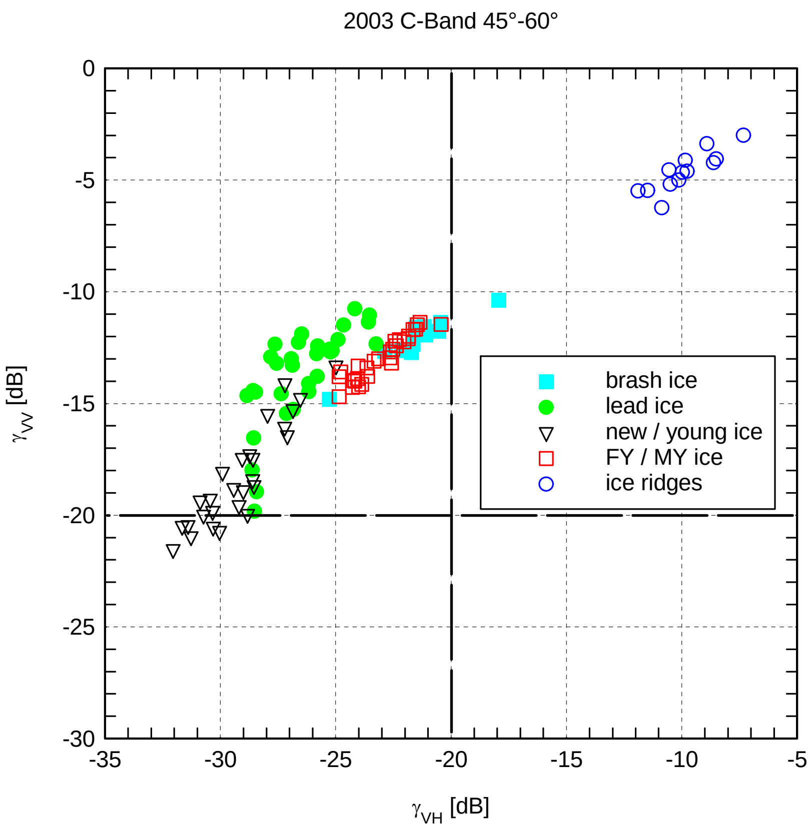

Figure 8a. Backscattering coefficients (γ) at C-band VH- and VV-polarization, for two different incidence angle intervals, measured on March 20 over the Fram Strait test site. Dashed lines indicate SAR noise level of the Sentinel-1 mission.

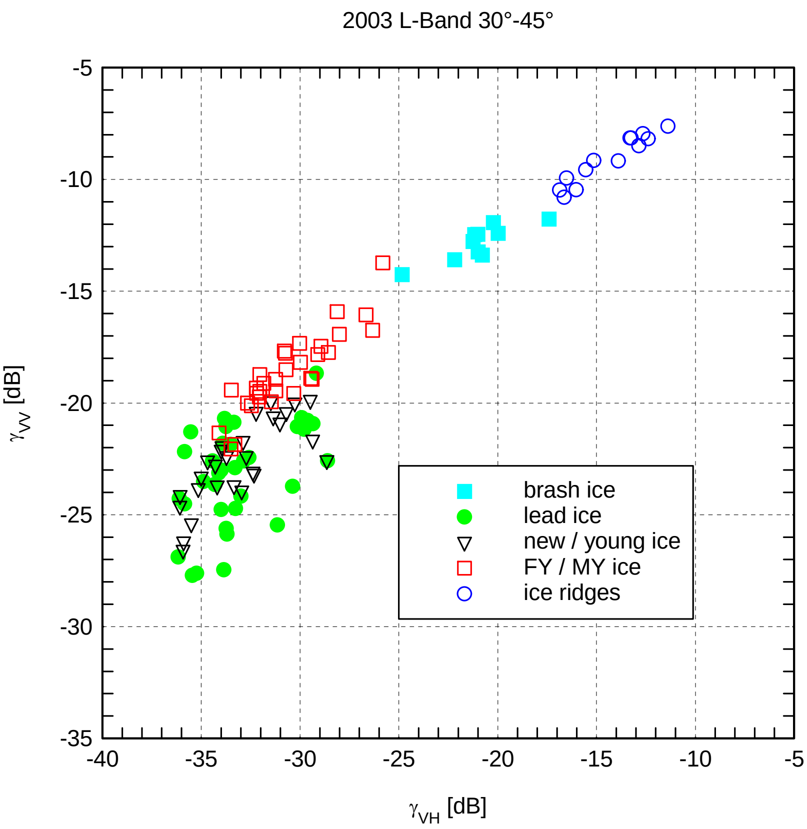

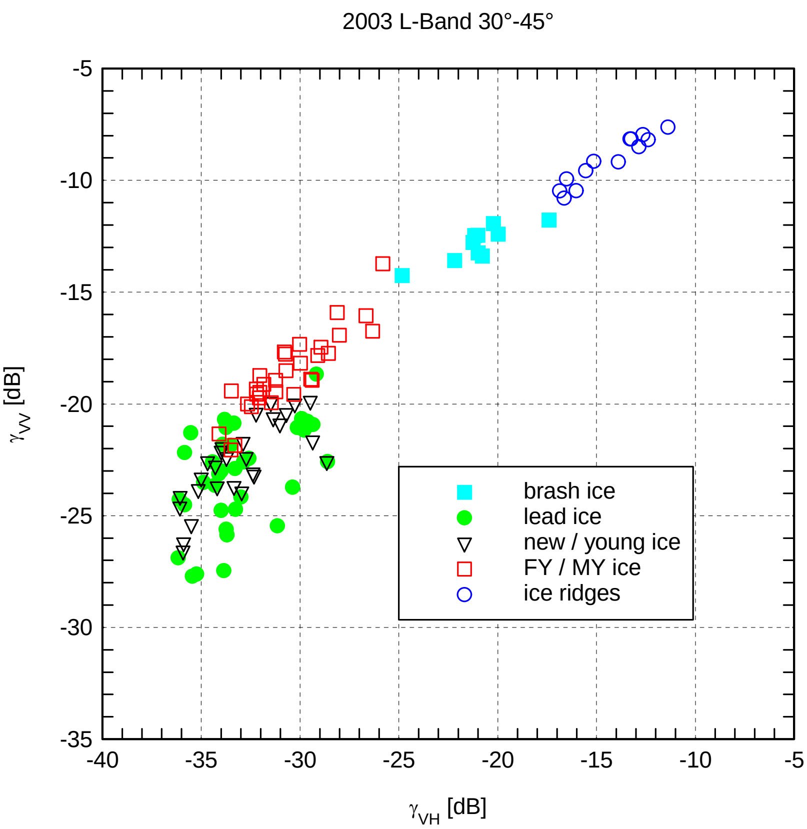

Figure 8b. Backscattering coefficients (γ) at L-band VH- and VV-polarization, for two different incidence angle intervals, measured on March 20 over the Fram Strait test site.

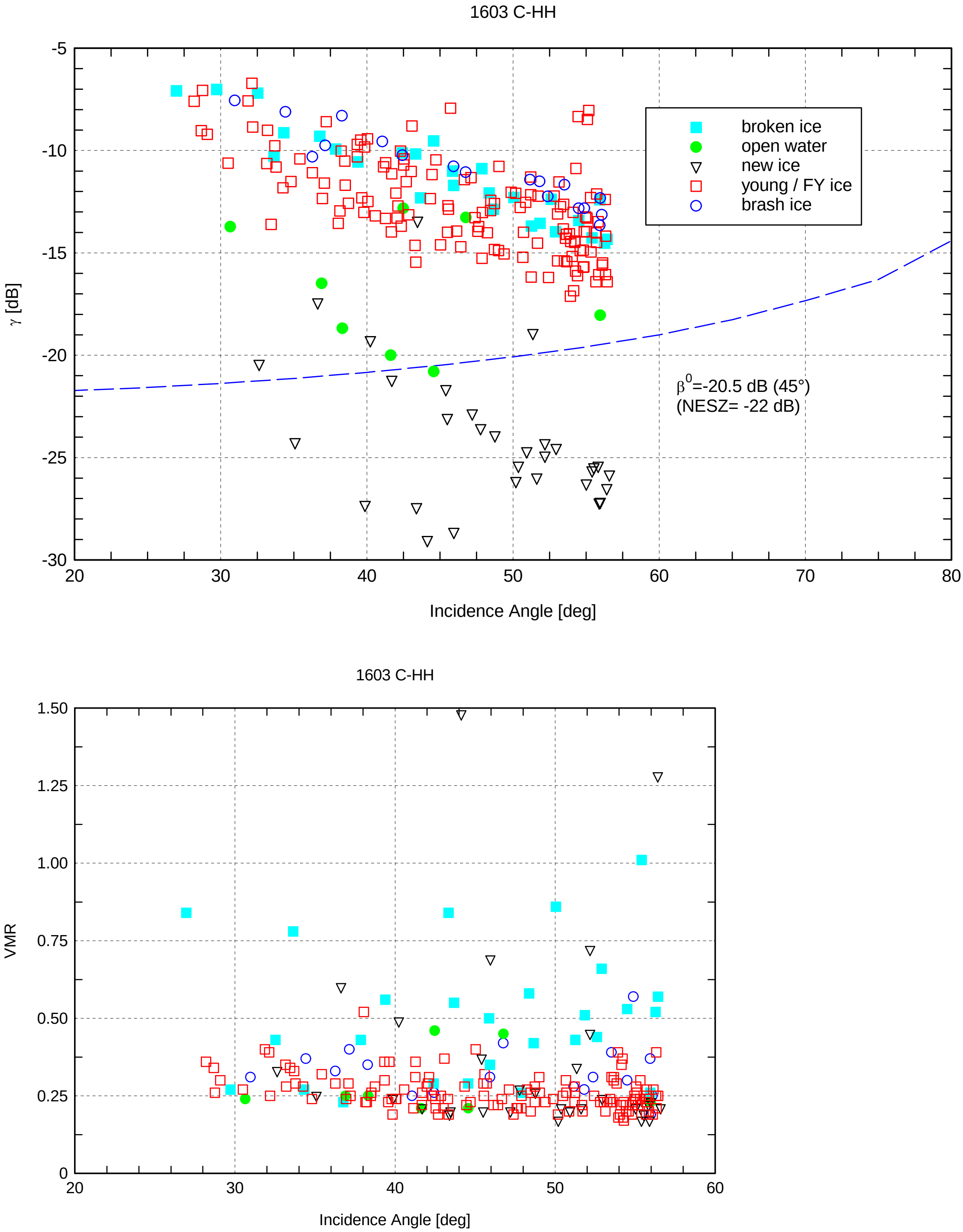

Figure 9a. Radar backscattering coefficient (γ) and variance-to-squared mean ratio (VMR) at C-band HH-polarization as a function of incidence angle measured on March 16 over the Storfjord test site.

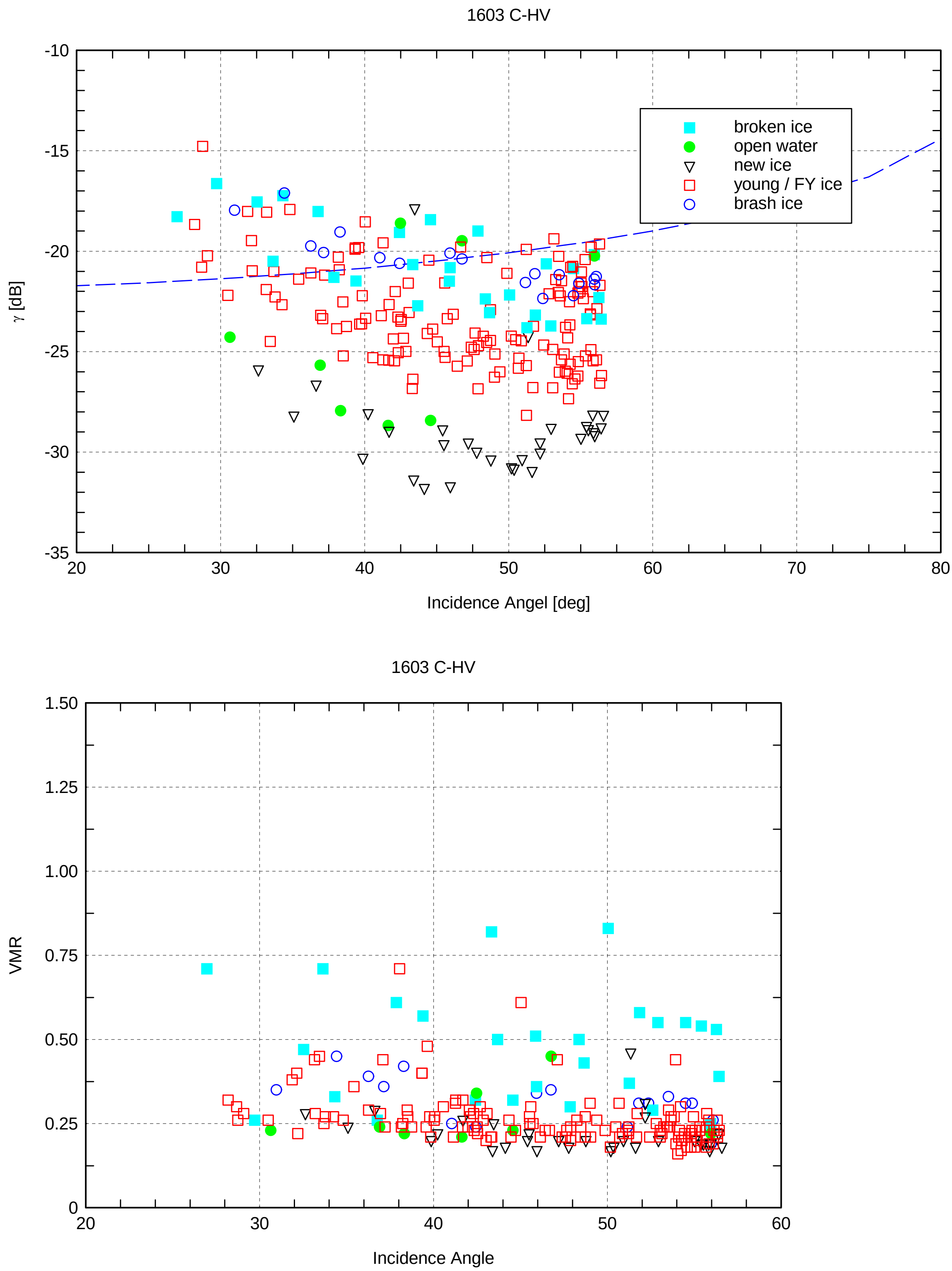

Figure 9b. Radar backscattering coefficient (γ) and variance-to-squared mean ratio (VMR) at C-band HV-polarization as a function of incidence angle measured on March 16 over the Storfjord test site.

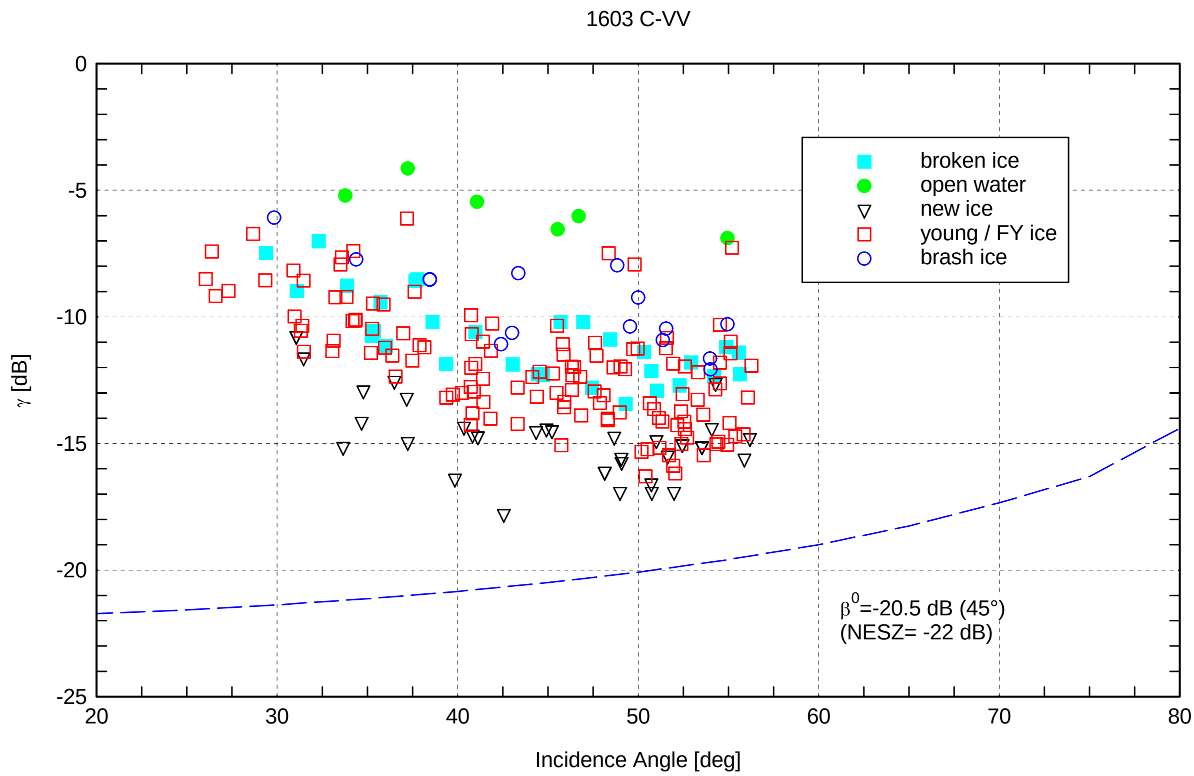

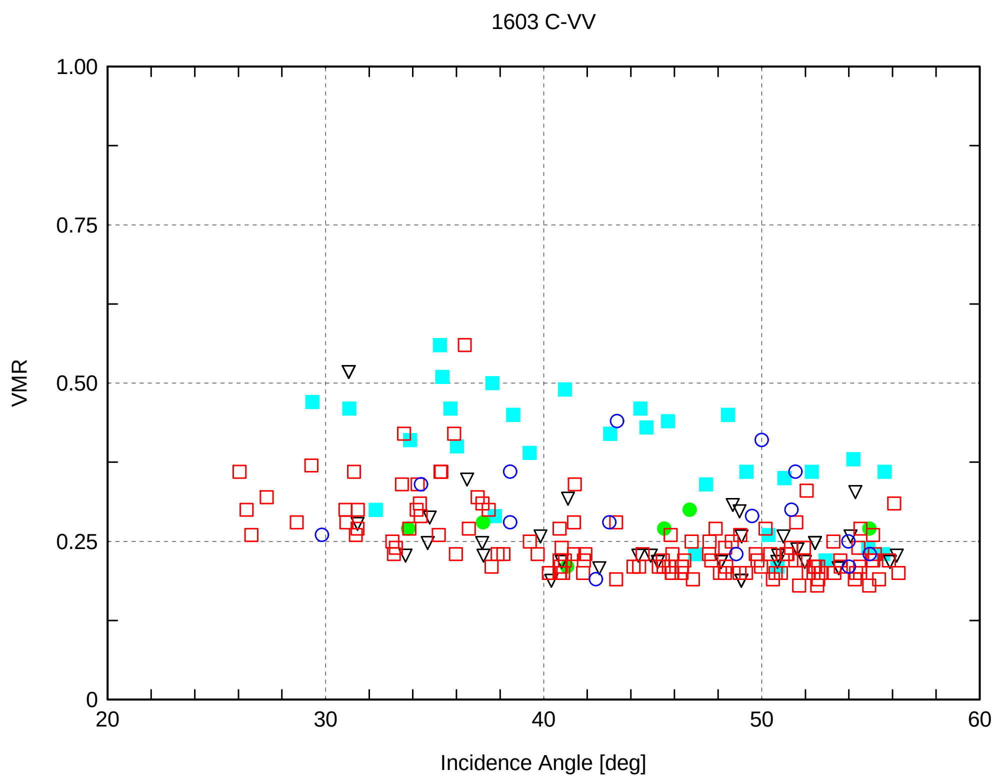

Figure 9c. Radar backscattering coefficient (γ) and variance-to-squared mean ratio (VMR) at C-band VV-polarization as a function of incidence angle measured on March 16 over the Storfjord test site.

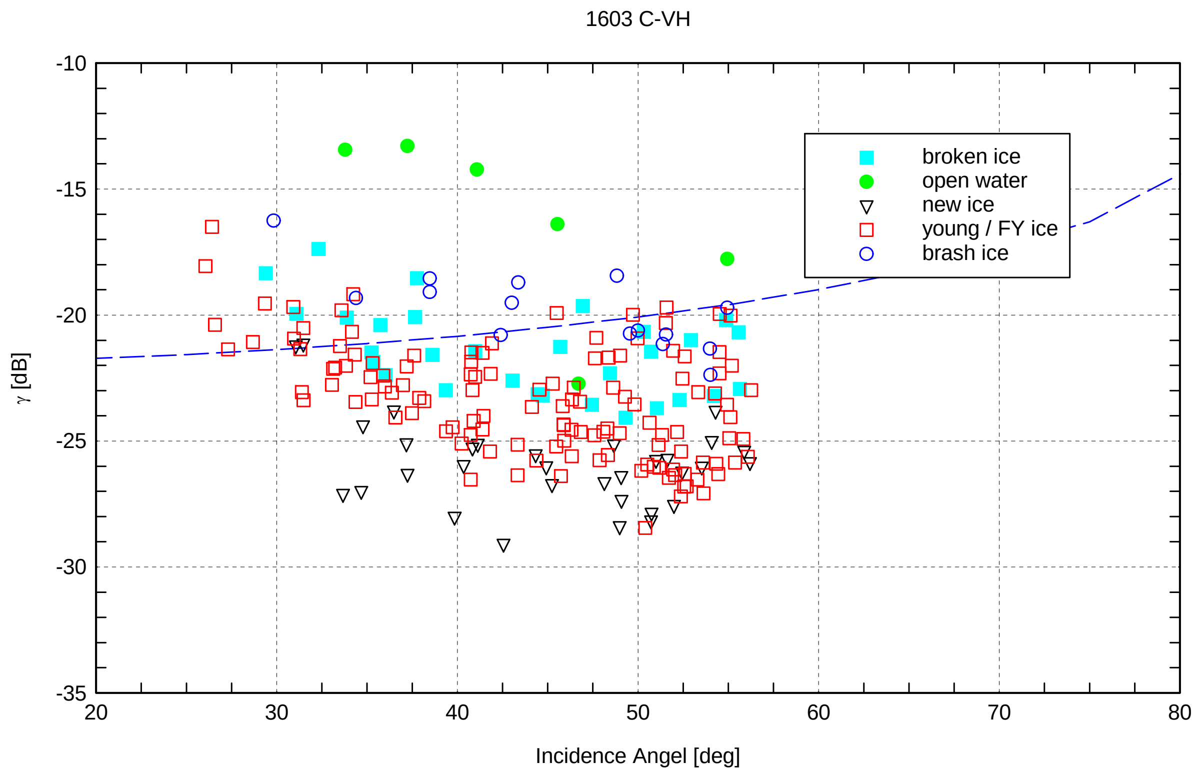

Figure 9d. Radar backscattering coefficient (γ) at C-band VH-polarization as a function of incidence angle measured on March 16 over the Storfjord test site.

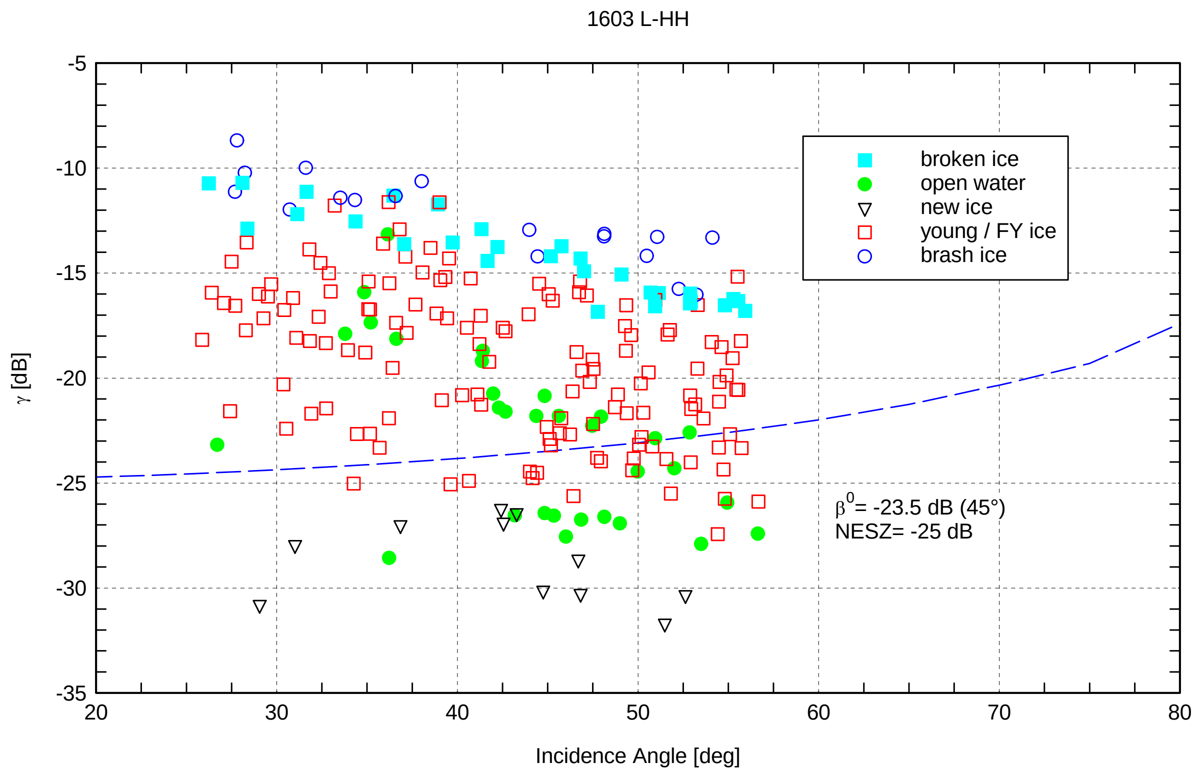

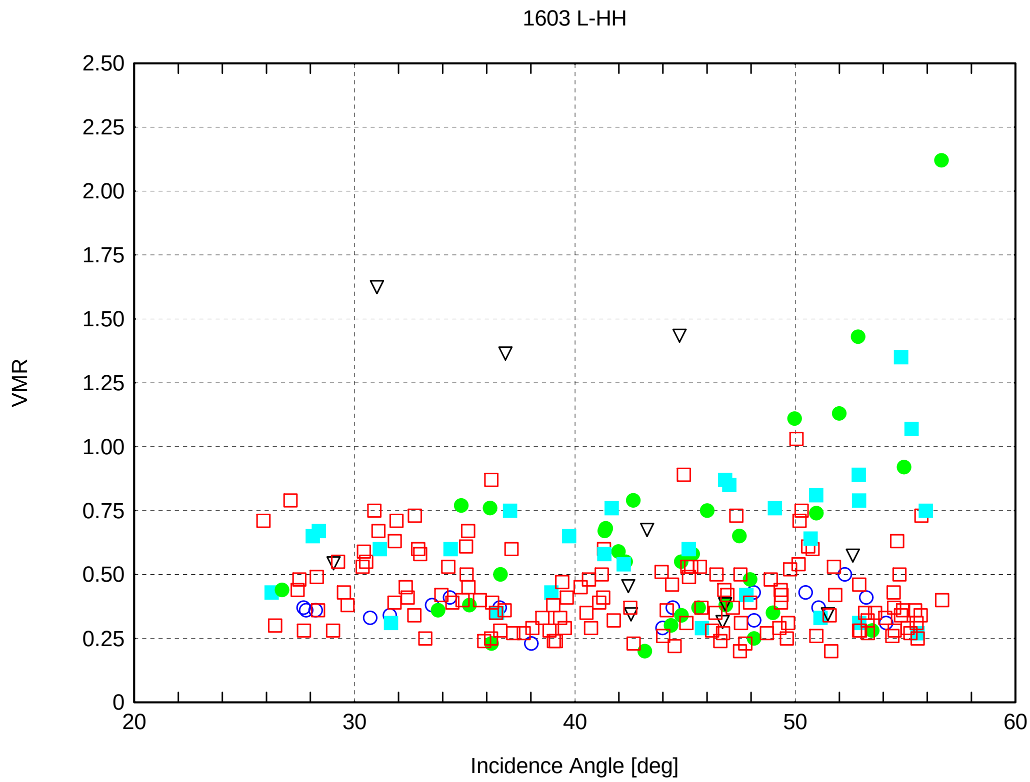

Figure 9e. Radar backscattering coefficient (γ) and variance-to-squared mean ratio (VMR) at L-band HH-polarization as a function of incidence angle measured on March 16 over the Storfjord test site.

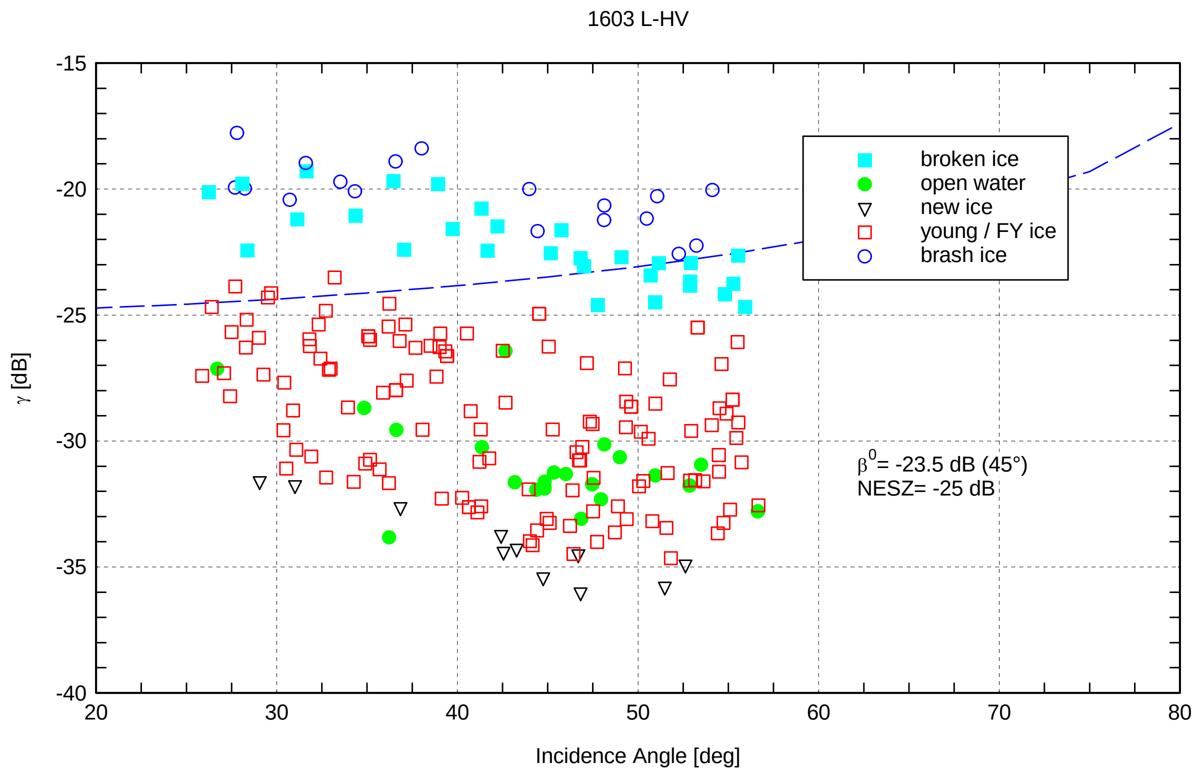

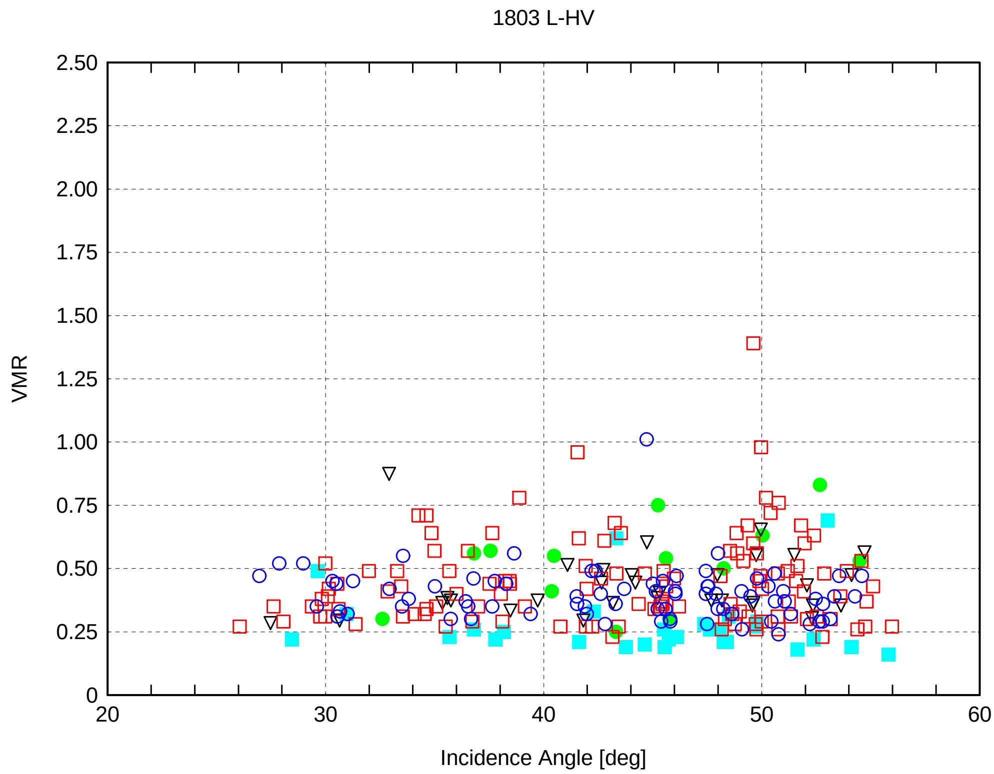

Figure 9f. Radar backscattering coefficient (γ) and variance-to-squared mean ratio (VMR) at L-band HV-polarization as a function of incidence angle measured on March 16 over the Storfjord test site.

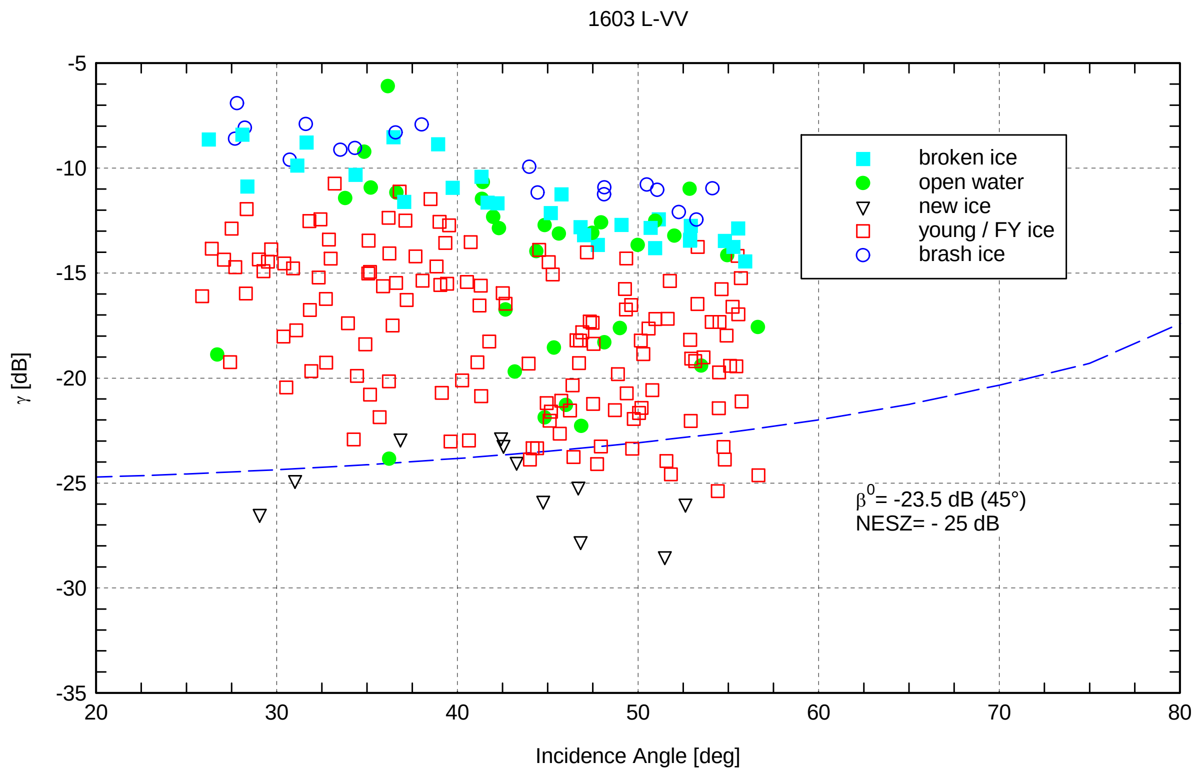

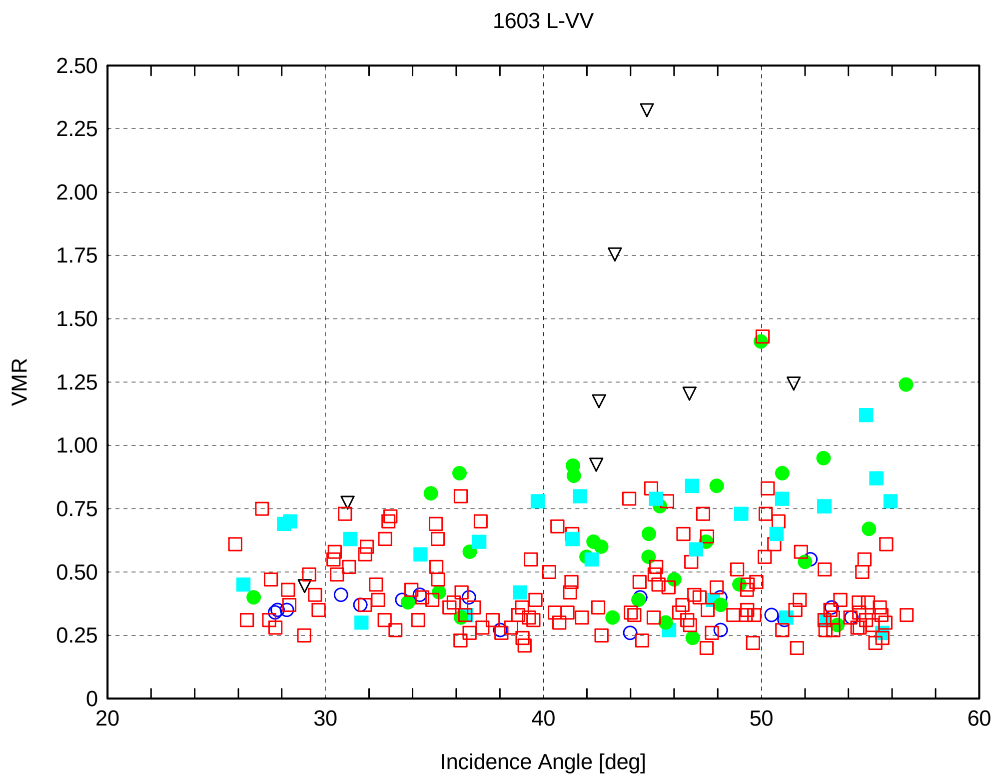

Figure 9g. Radar backscattering coefficient (γ) and variance-to-squared mean ratio (VMR) at L-band VV-polarization as a function of incidence angle measured on March 16 over the Storfjord test site.

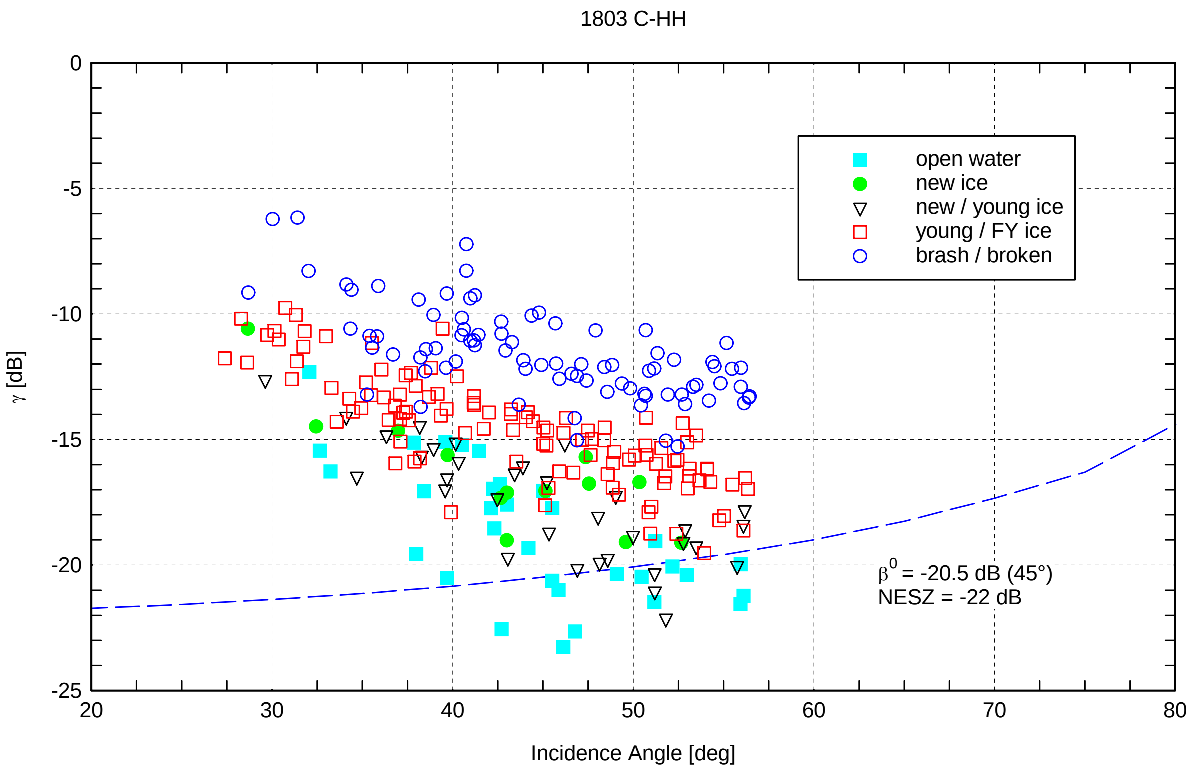

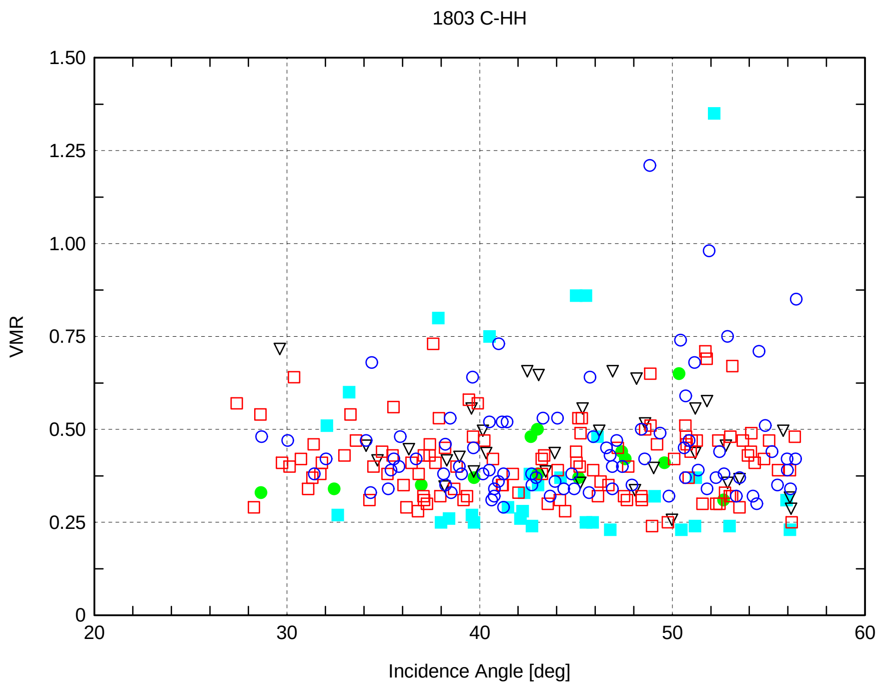

Figure 10a. Radar backscattering coefficient (γ) and variance-to-squared mean ratio (VMR) at C-band HH-polarization as a function of incidence angle measured on March 18 over the Barents Sea test site.

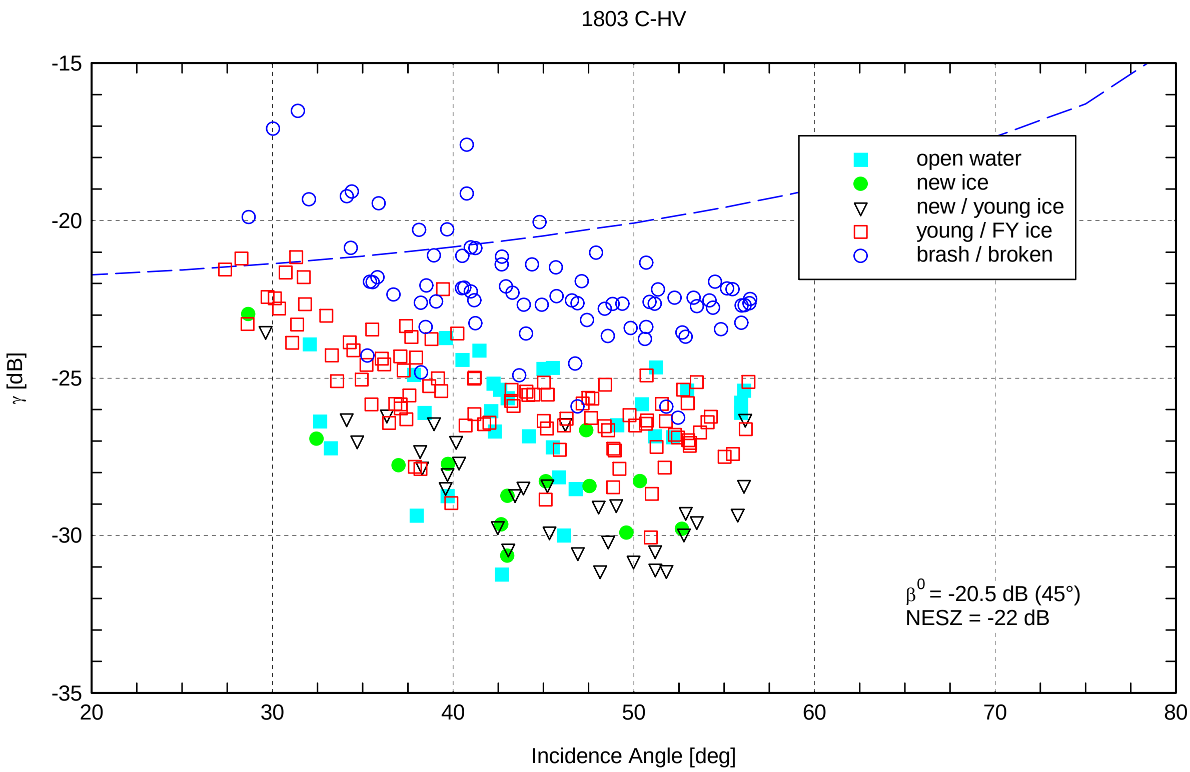

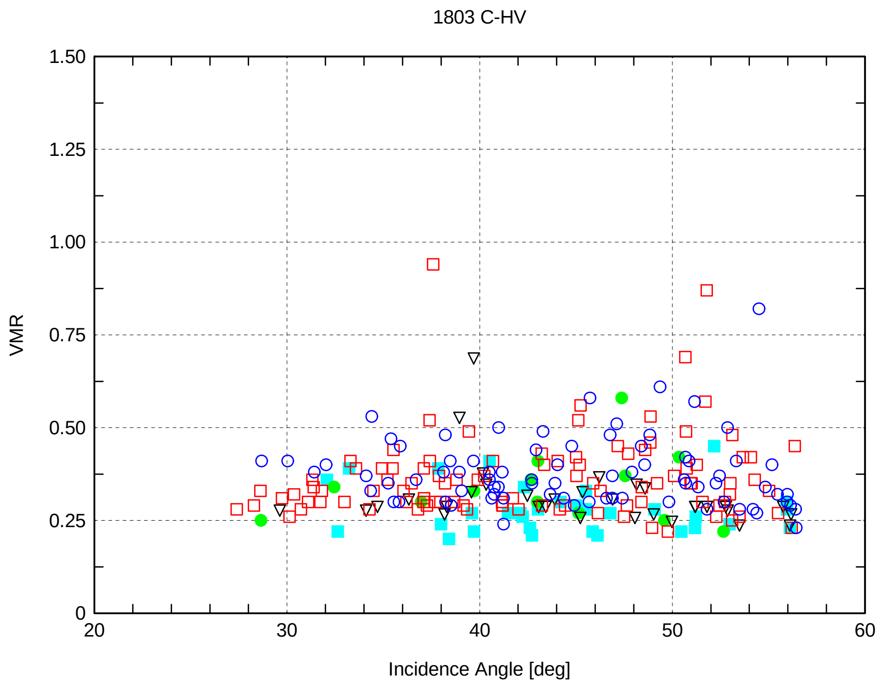

Figure 10b. Radar backscattering coefficient (γ) and variance-to-squared mean ratio (VMR) at C-band HV-polarization as a function of incidence angle measured on March 18 over the Barents Sea test site.

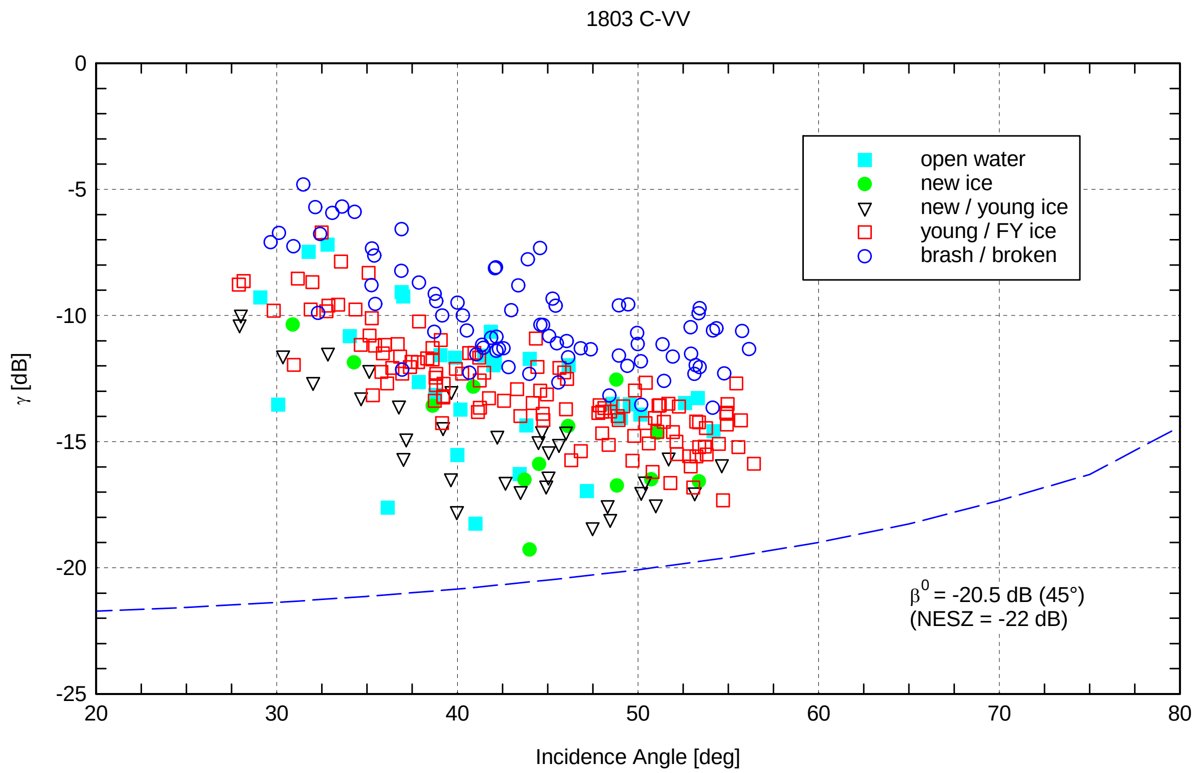

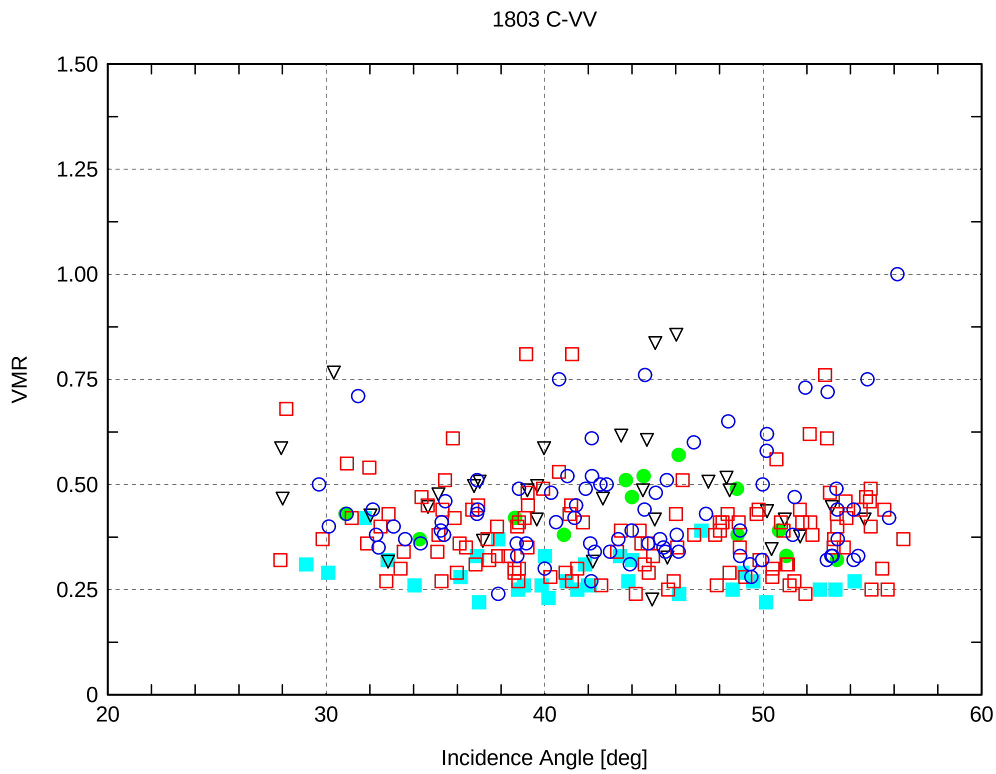

Figure 10c. Radar backscattering coefficient (γ) and variance-to-squared mean ratio (VMR) at C-band VV-polarization as a function of incidence angle measured on March 18 over the Barents Sea test site.

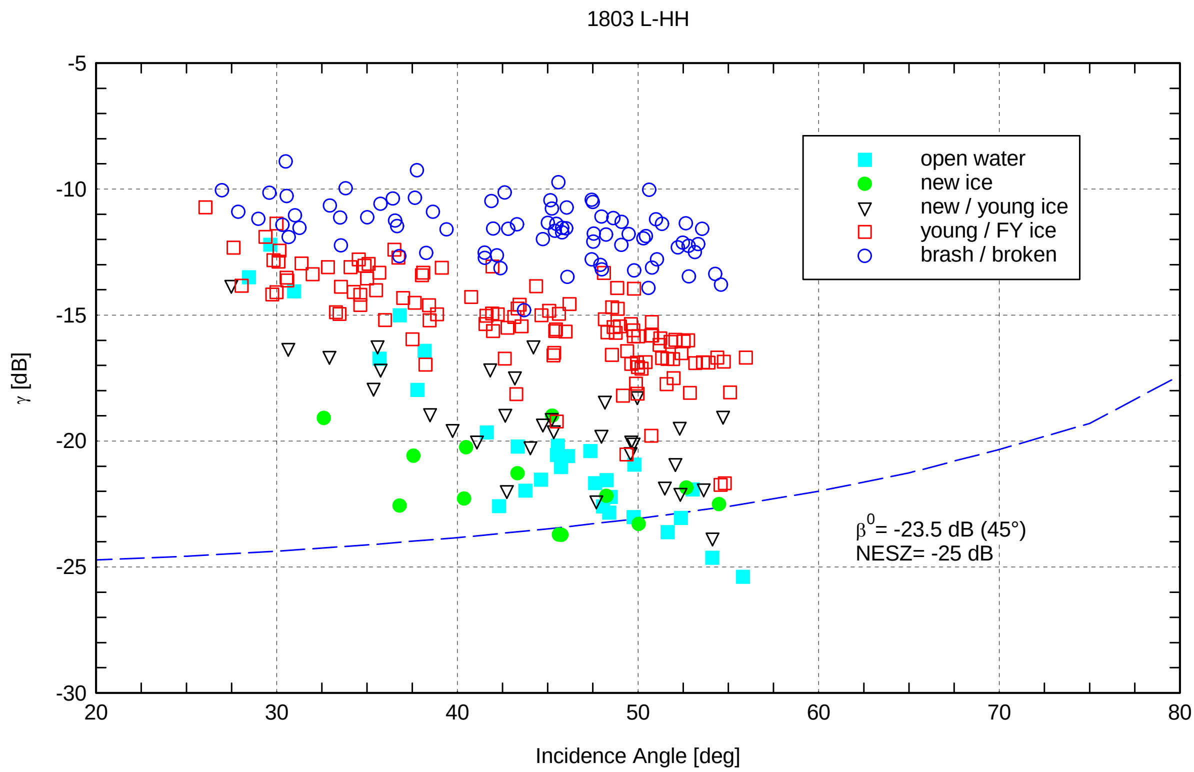

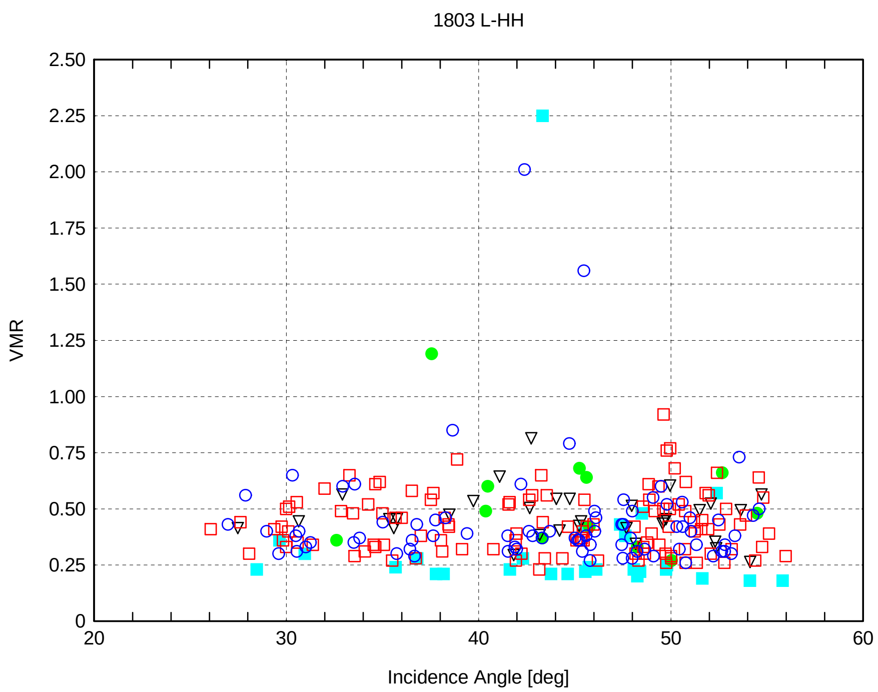

Figure 10d. Radar backscattering coefficient (γ) and variance-to-squared mean ratio (VMR) at L-band HH-polarization as a function of incidence angle measured on March 18 over the Barents Sea test site.

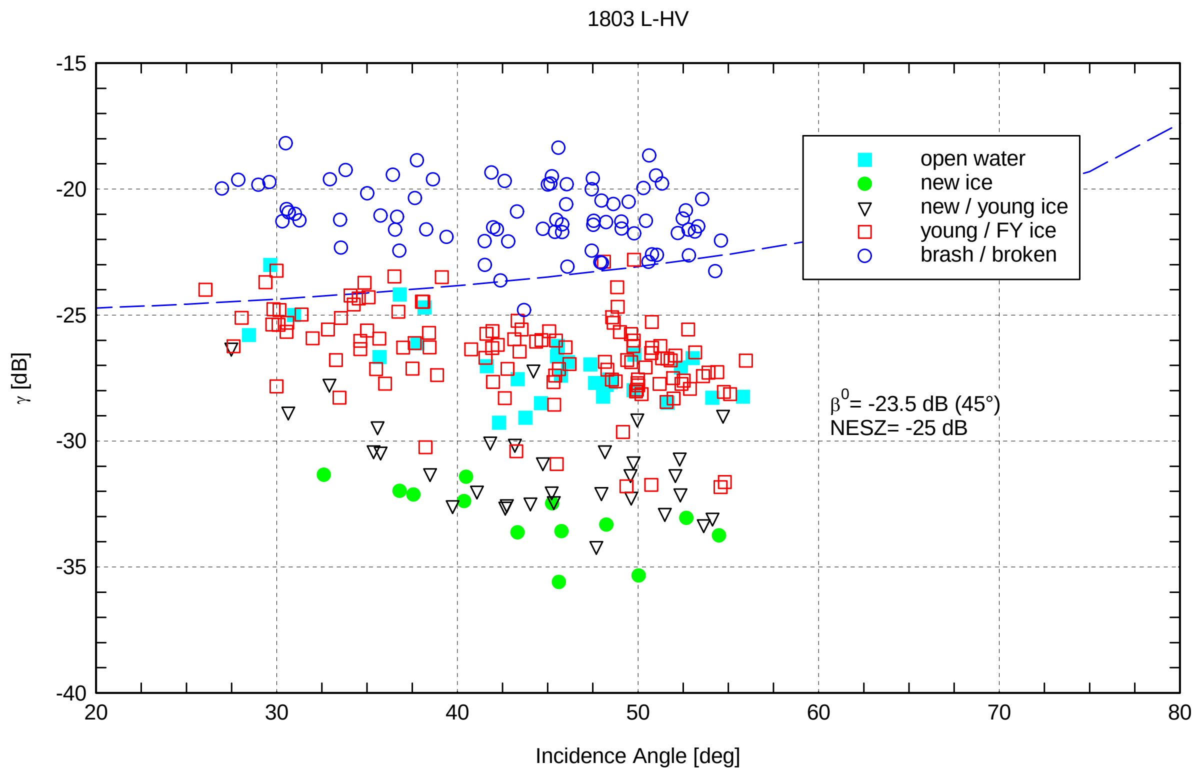

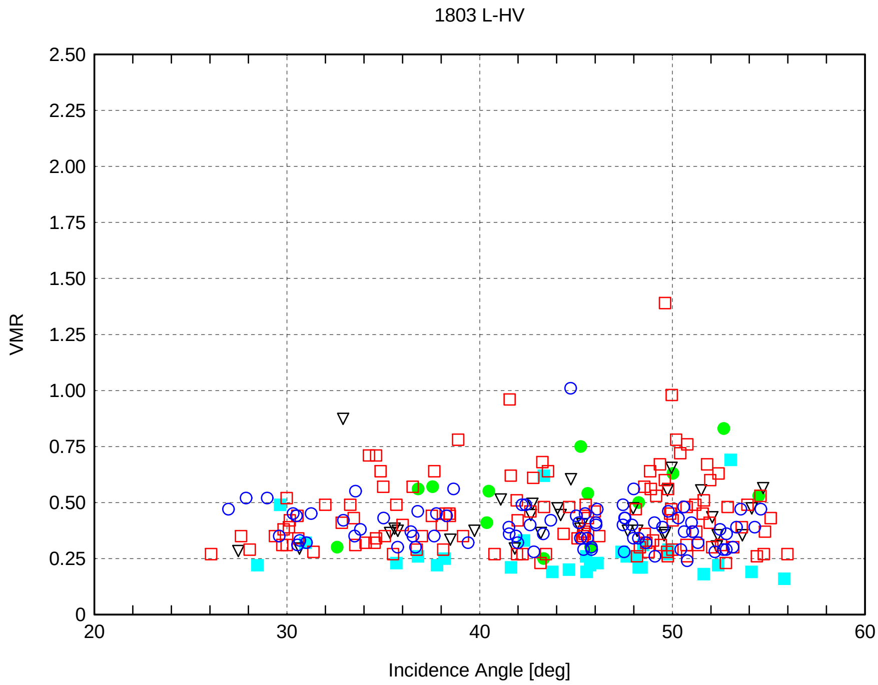

Figure 10e. Radar backscattering coefficient (γ) and variance-to-squared mean ratio (VMR) at L-band HV-polarization as a function of incidence angle measured on March 18 over the Barents Sea test site.

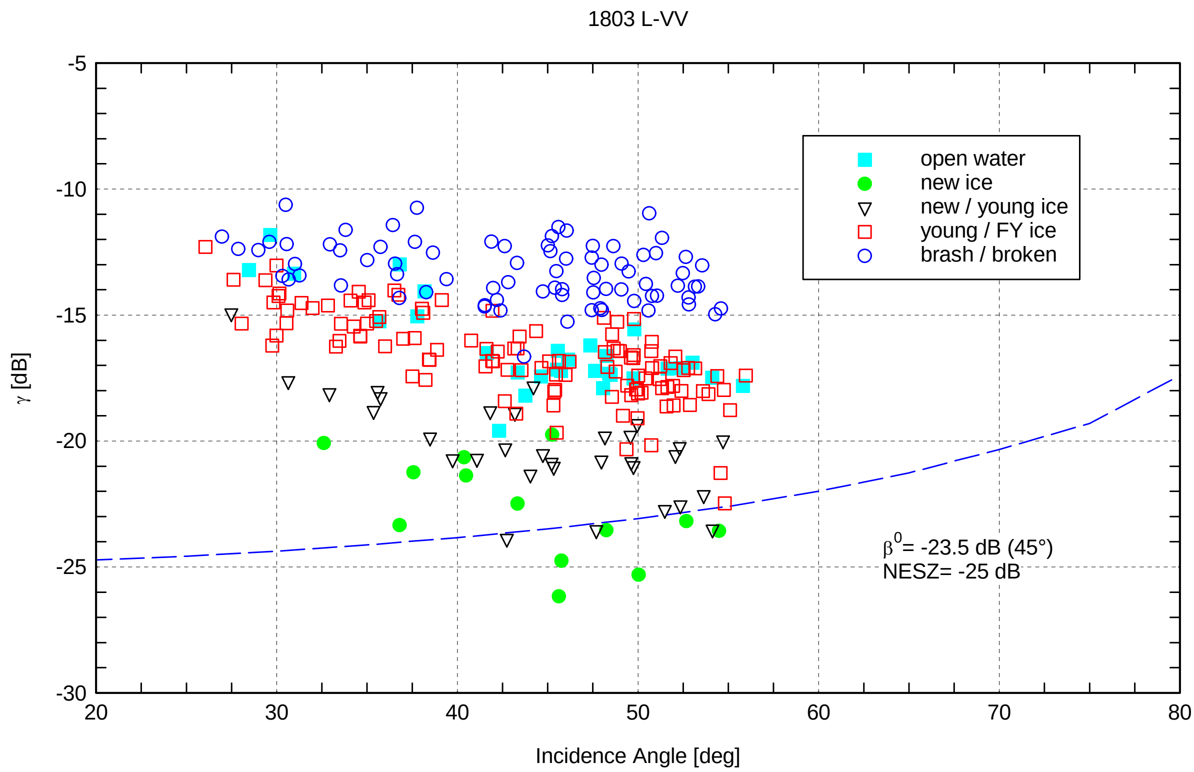

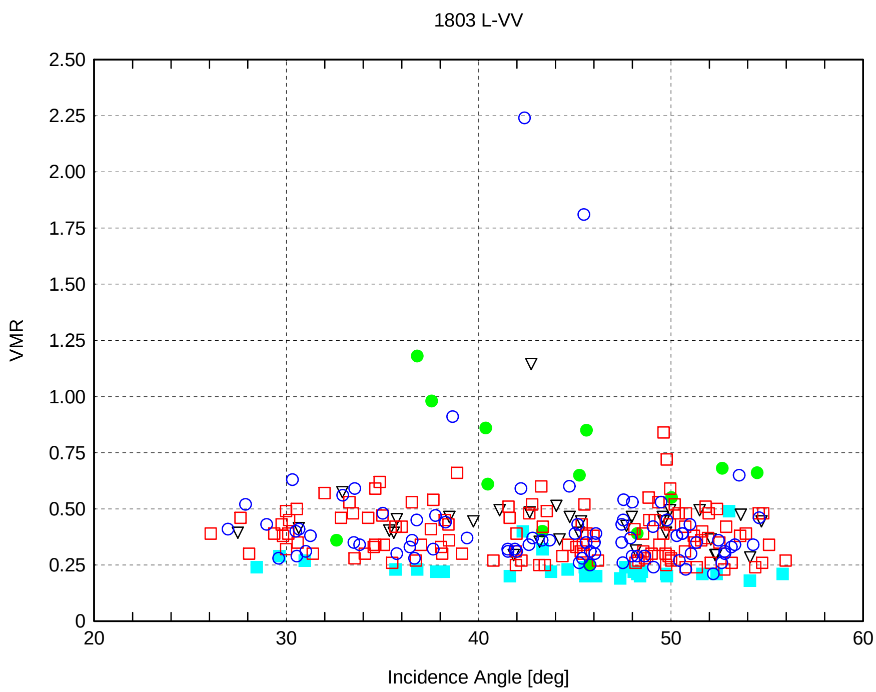

Figure 10f. Radar backscattering coefficient (γ) and variance-to-squared mean ratio (VMR) at L-band VV-polarization as a function of incidence angle measured on March 18 over the Barents Sea test site.

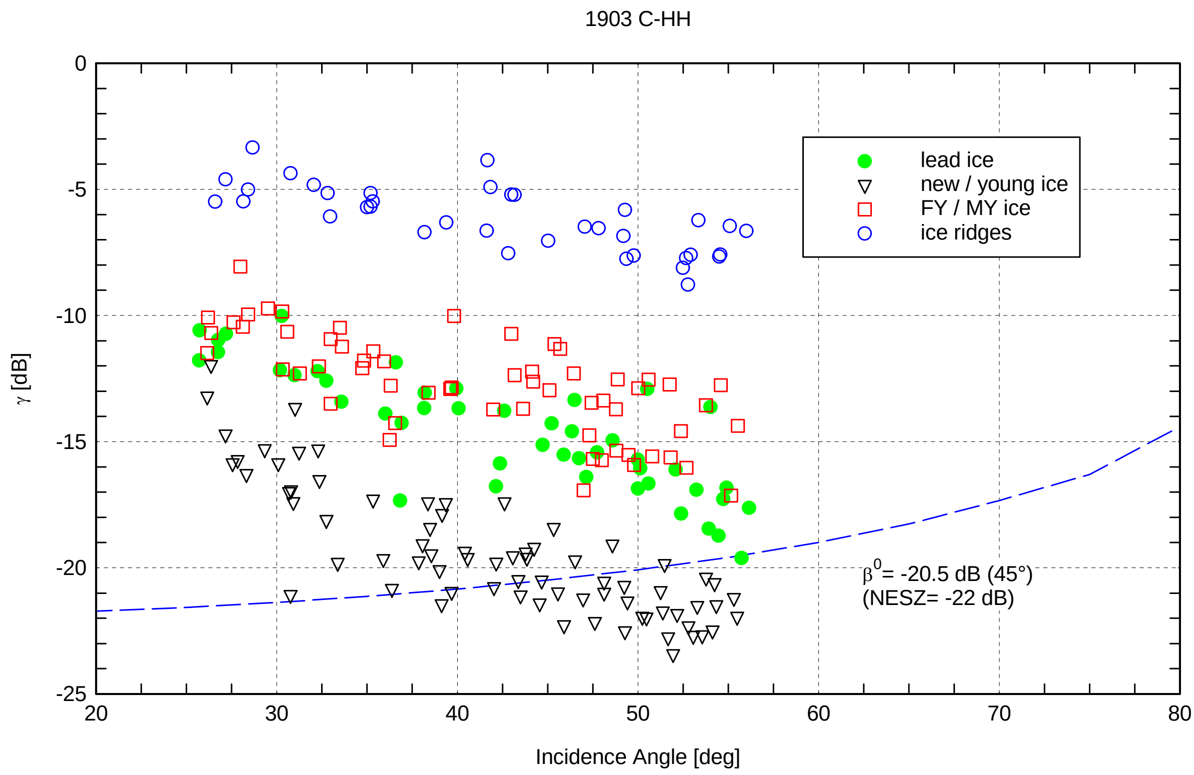

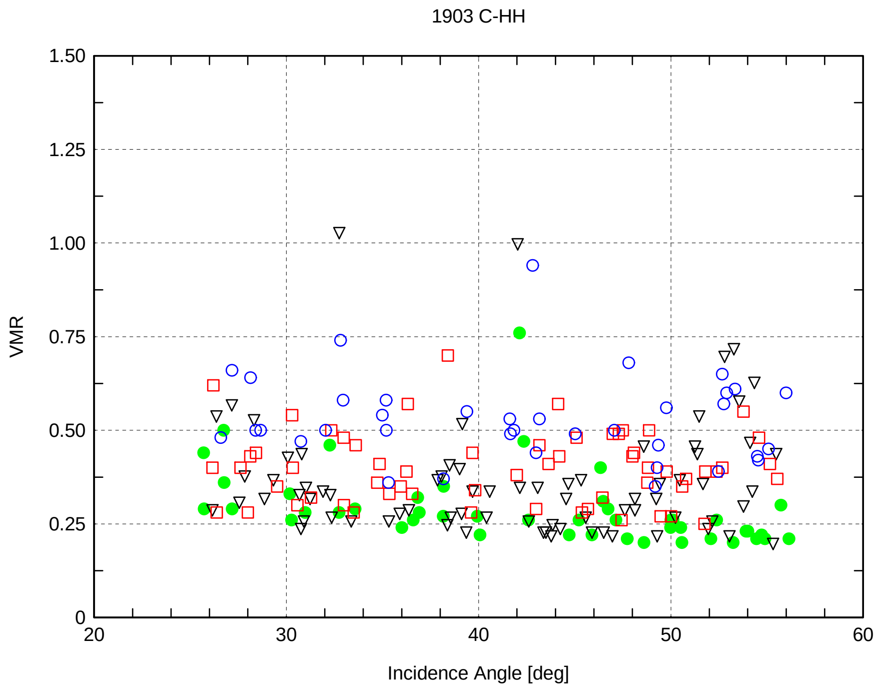

Figure 11a. Radar backscattering coefficient (γ) and variance-to-squared mean ratio (VMR) at C-band HH-polarization as a function of incidence angle measured on March 19 over the Fram Strait test site.

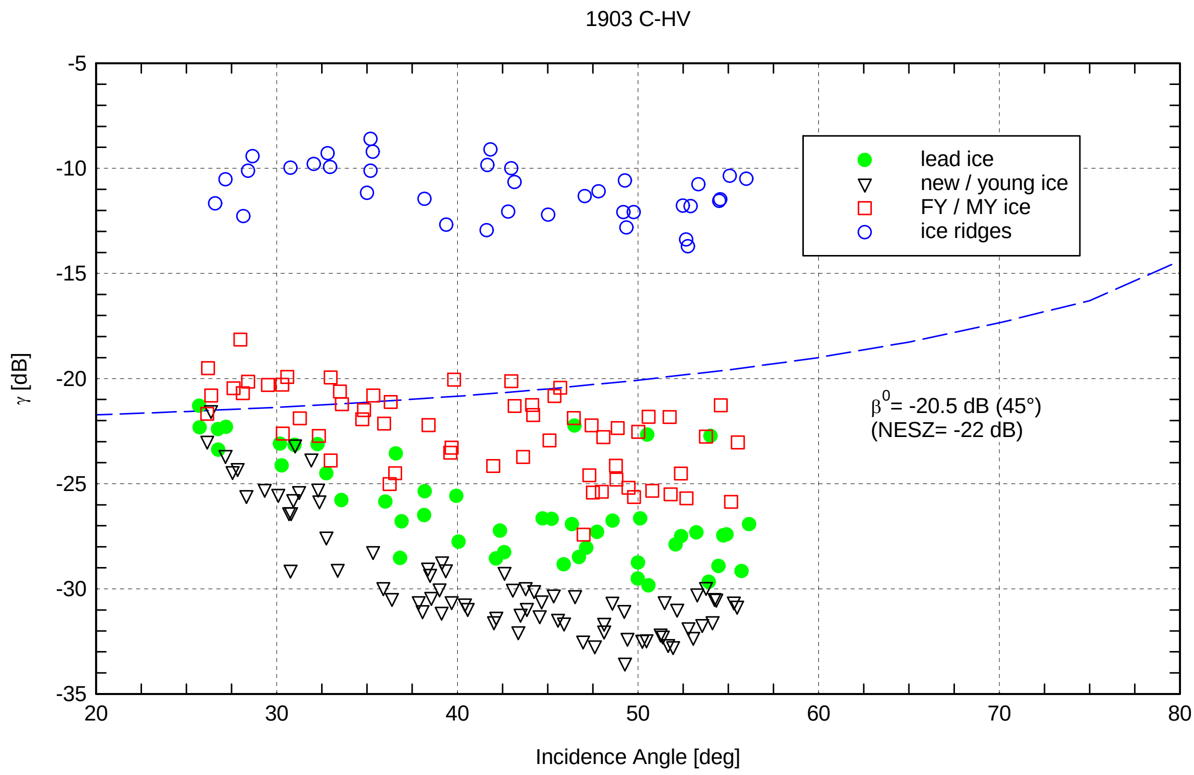

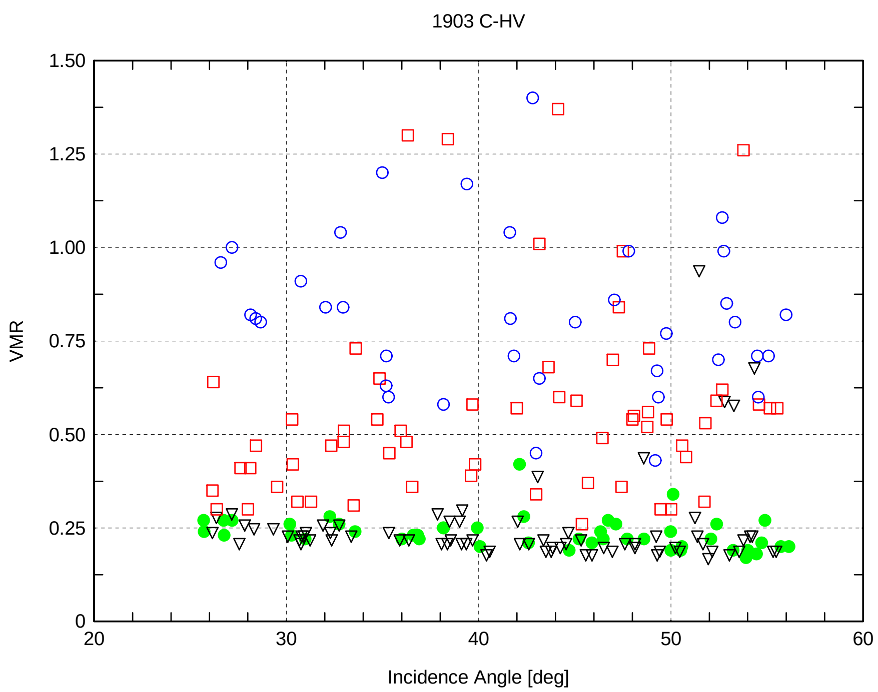

Figure 11b. Radar backscattering coefficient (γ) and variance-to-squared mean ratio (VMR) at C-band HV-polarization as a function of incidence angle measured on March 19 over the Fram Strait test site.

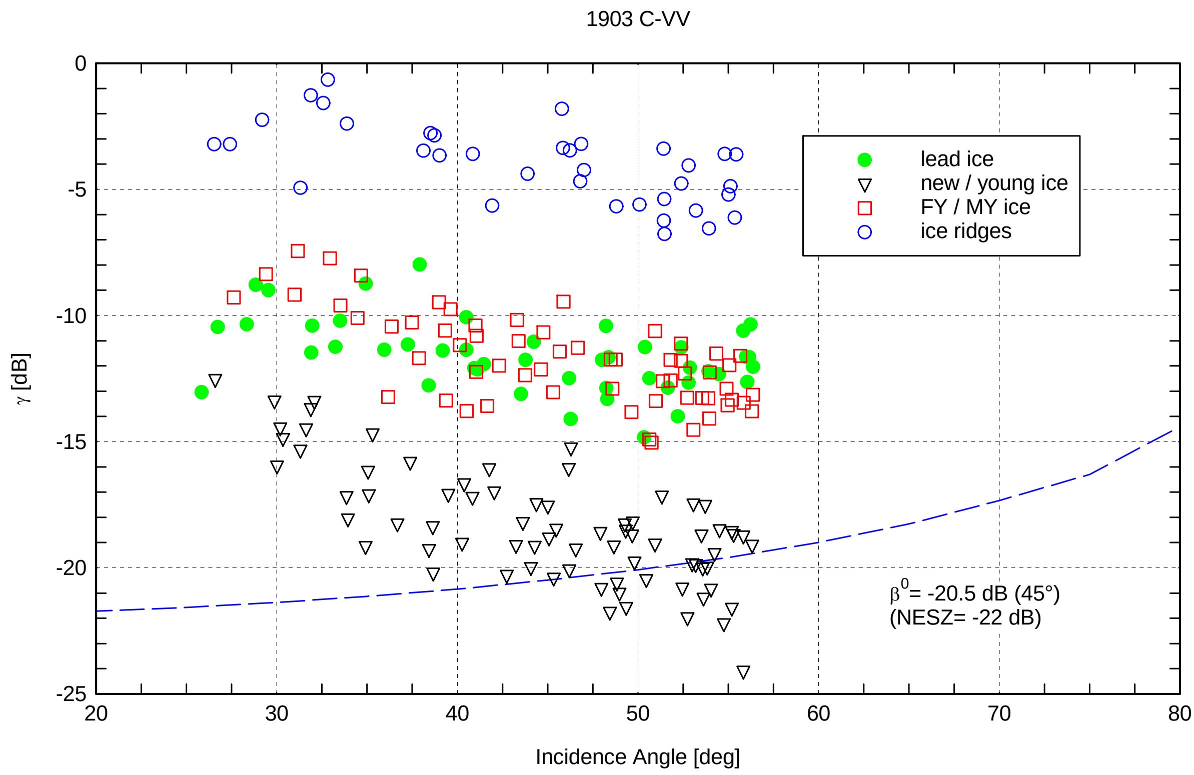

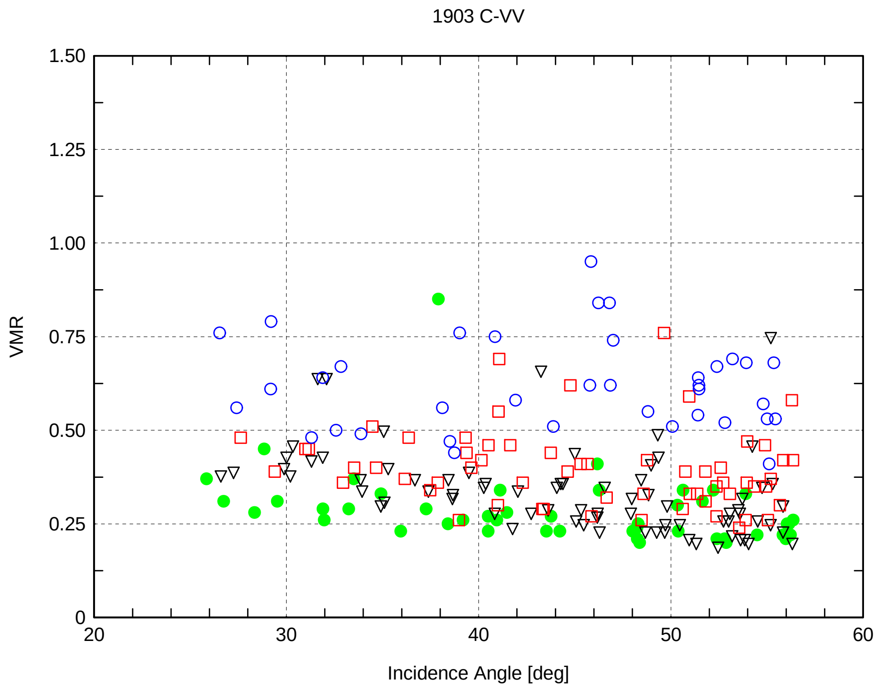

Figure 11c. Radar backscattering coefficient (γ) and variance-to-squared mean ratio (VMR) at C-band VV-polarization as a function of incidence angle measured on March 19 over the Fram Strait test site.

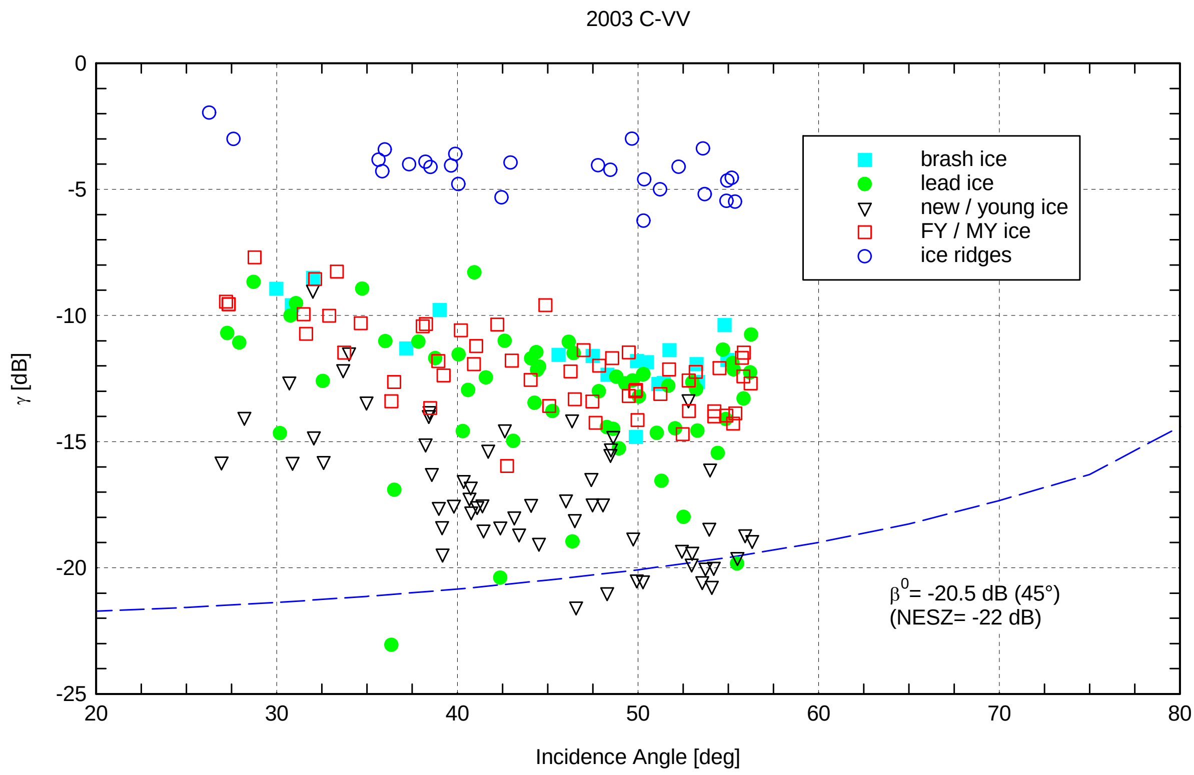

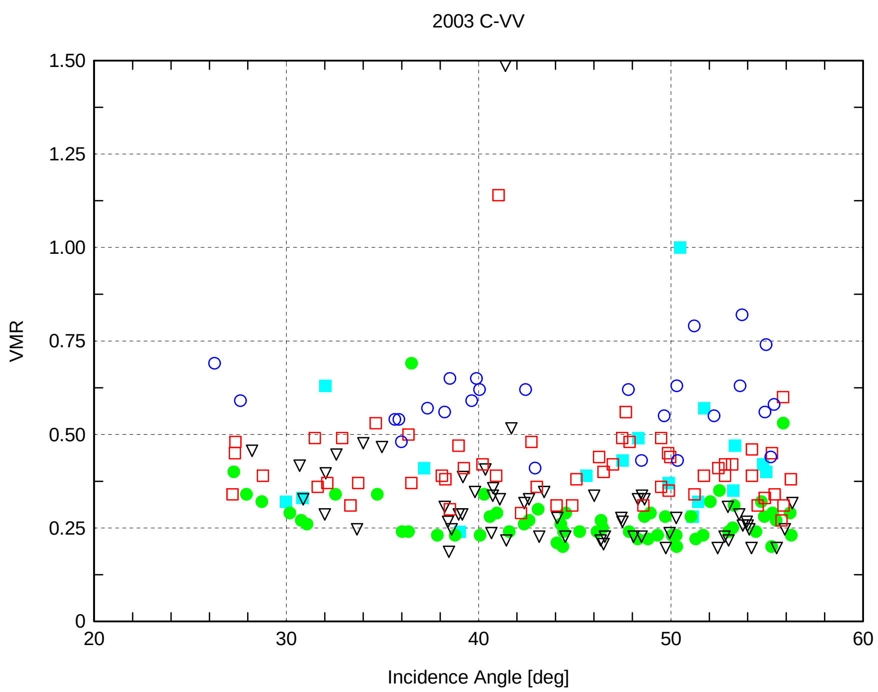

Figure 12a. Radar backscattering coefficient (γ) and variance-to-squared mean ratio (VMR) at C-band VV-polarization as a function of incidence angle measured on March 20 over the Fram Strait test site.

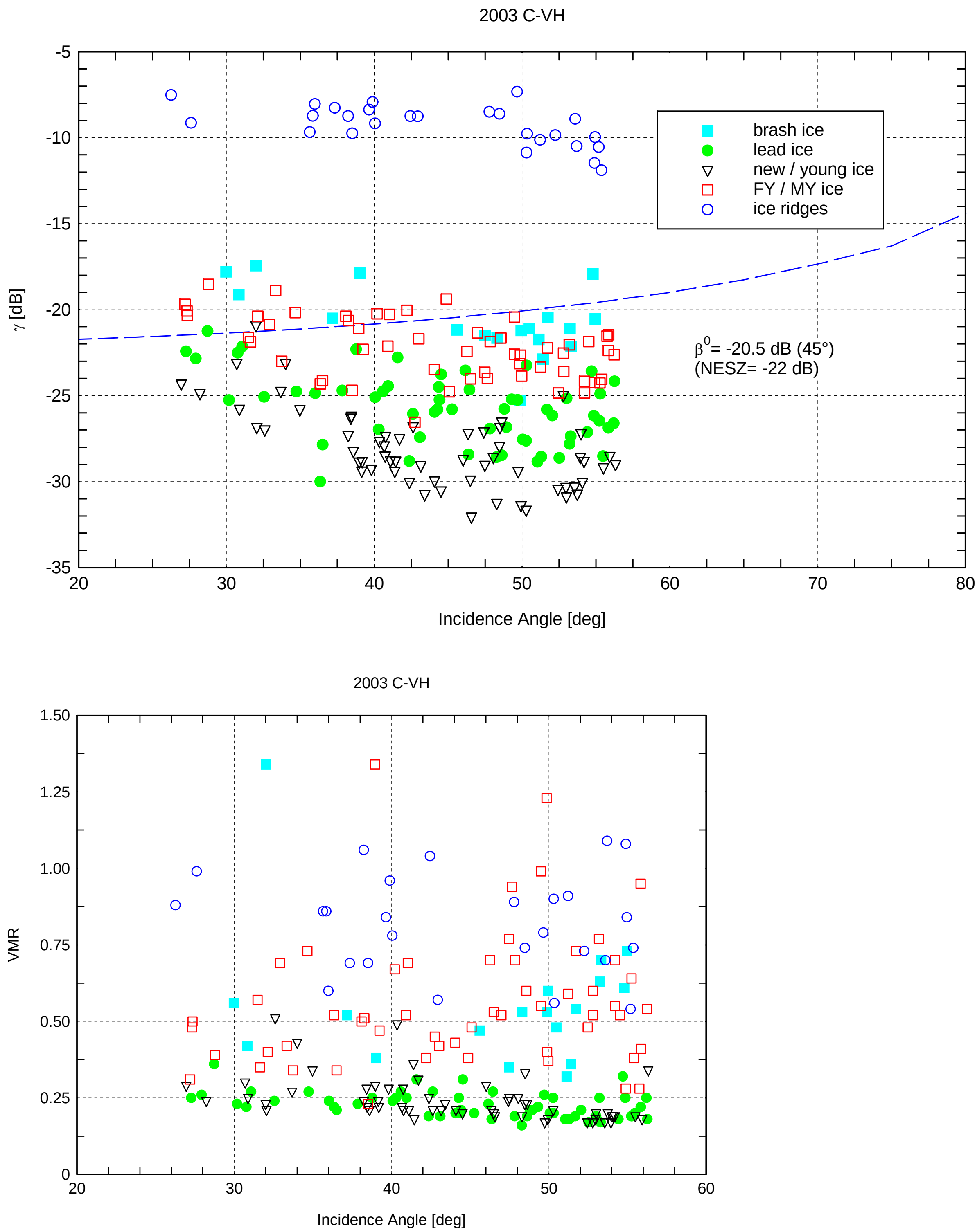

Figure 12b. Radar backscattering coefficient (γ) and variance-to-squared mean ratio (VMR) at C-band VH-polarization as a function of incidence angle measured on March 20 over the Fram Strait test site.

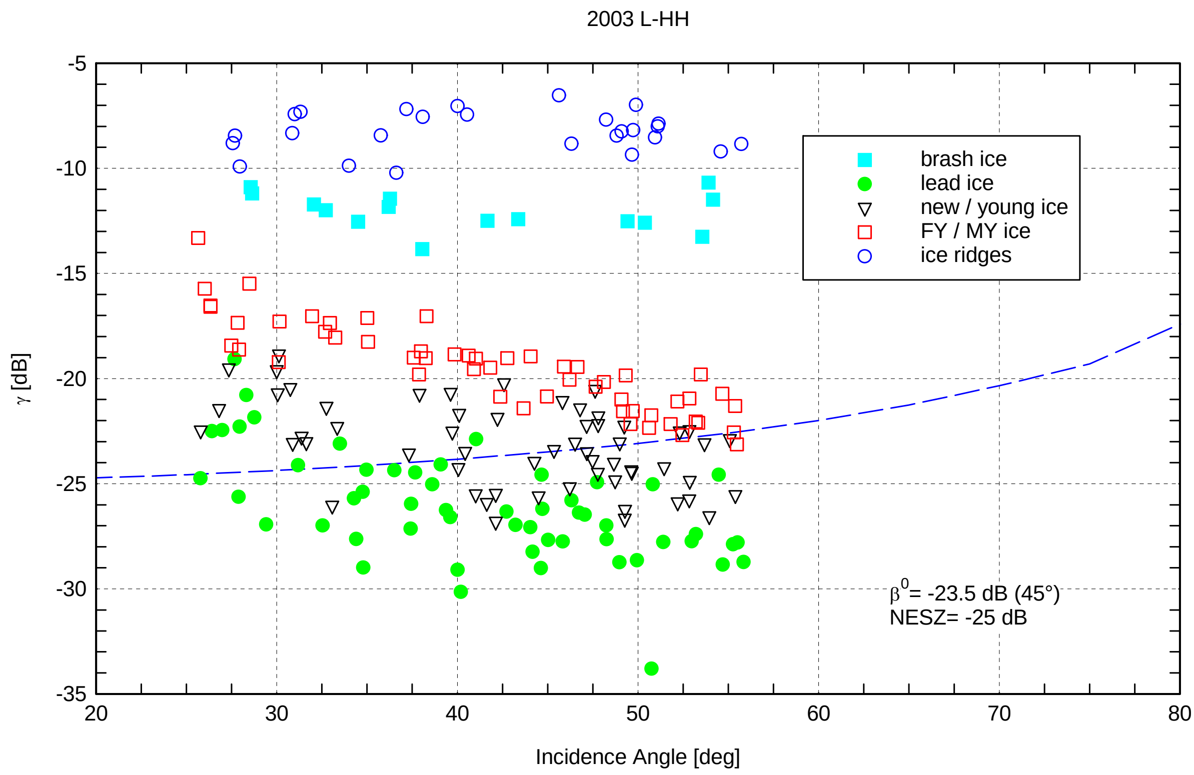

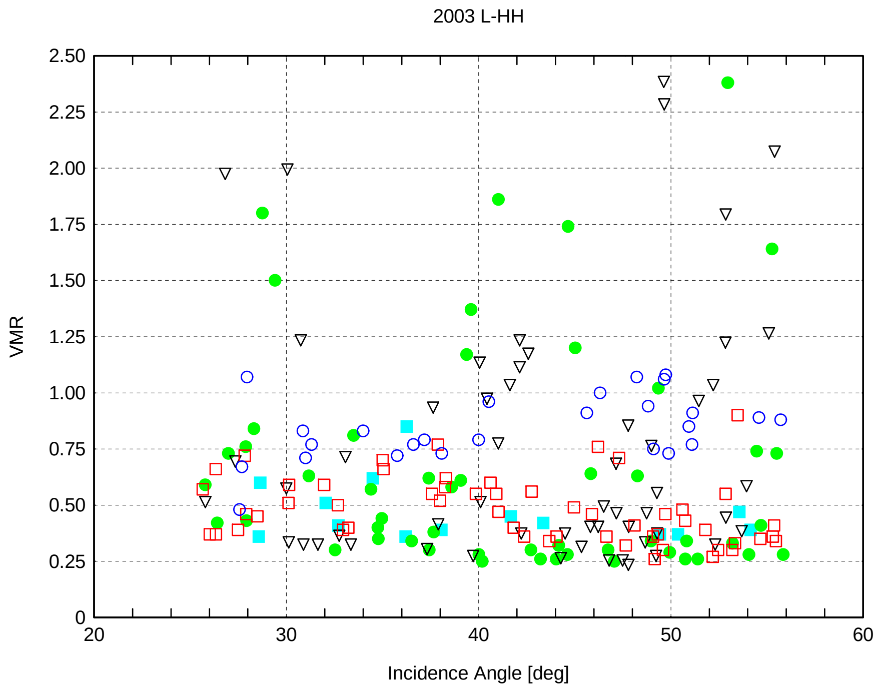

Figure 12c. Radar backscattering coefficient (γ) and variance-to-squared mean ratio (VMR) at L-band HH-polarization as a function of incidence angle measured on March 20 over the Fram Strait test site.

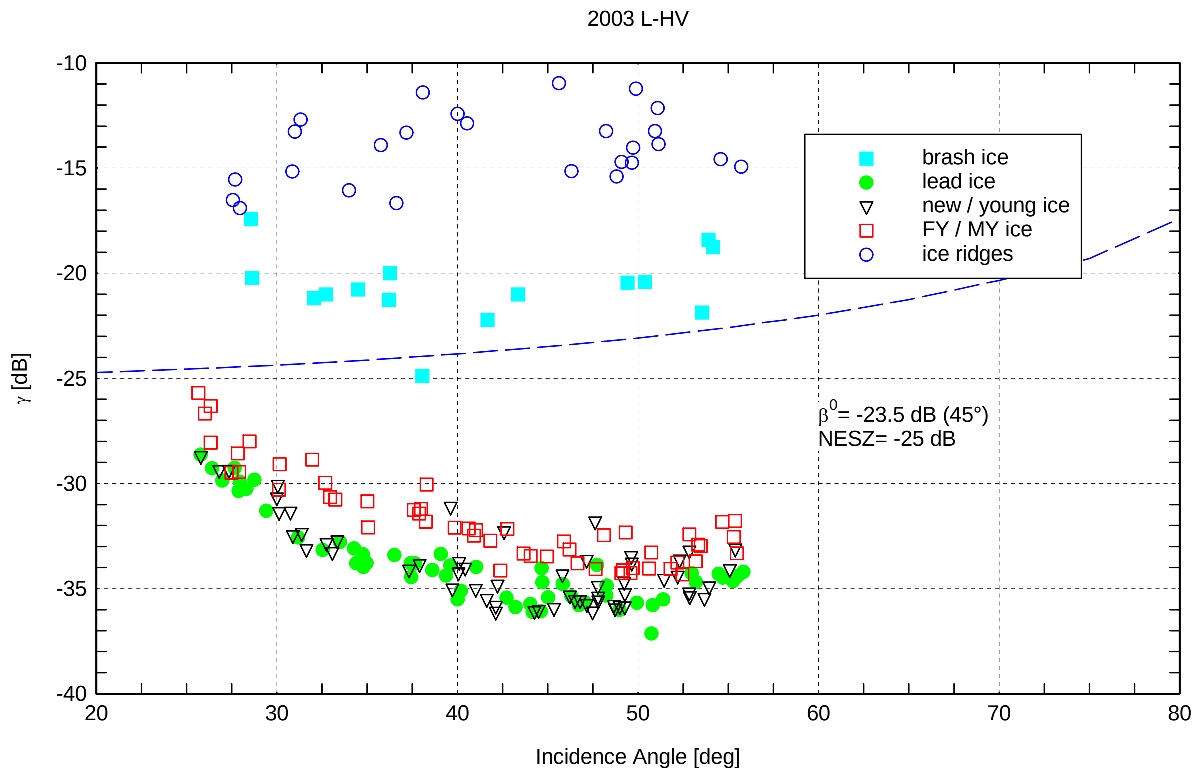

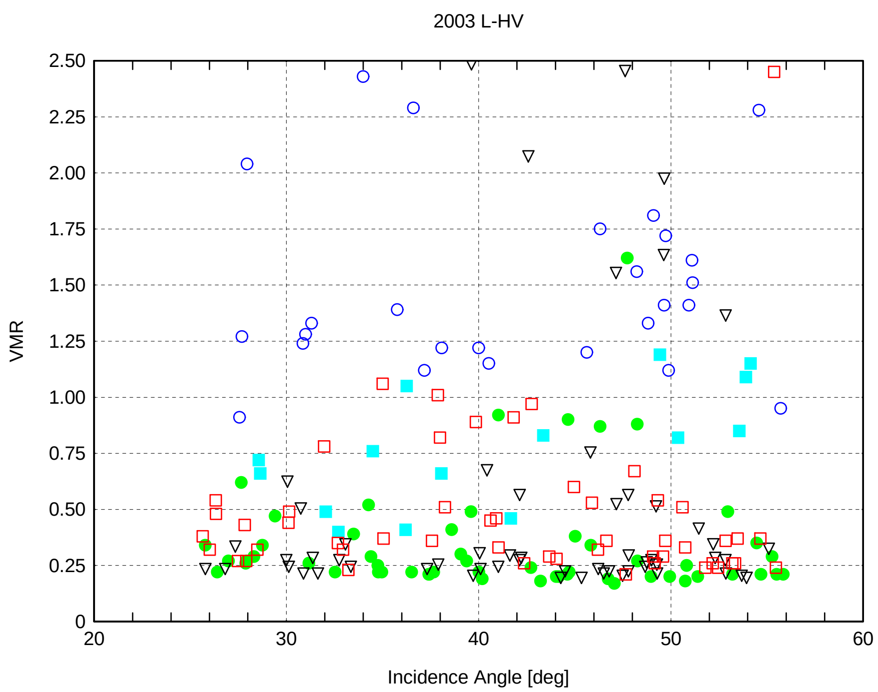

Figure 12d. Radar backscattering coefficient (γ) and variance-to-squared mean ratio (VMR) at L-band HV-polarization as a function of incidence angle measured on March 20 over the Fram Strait test site.

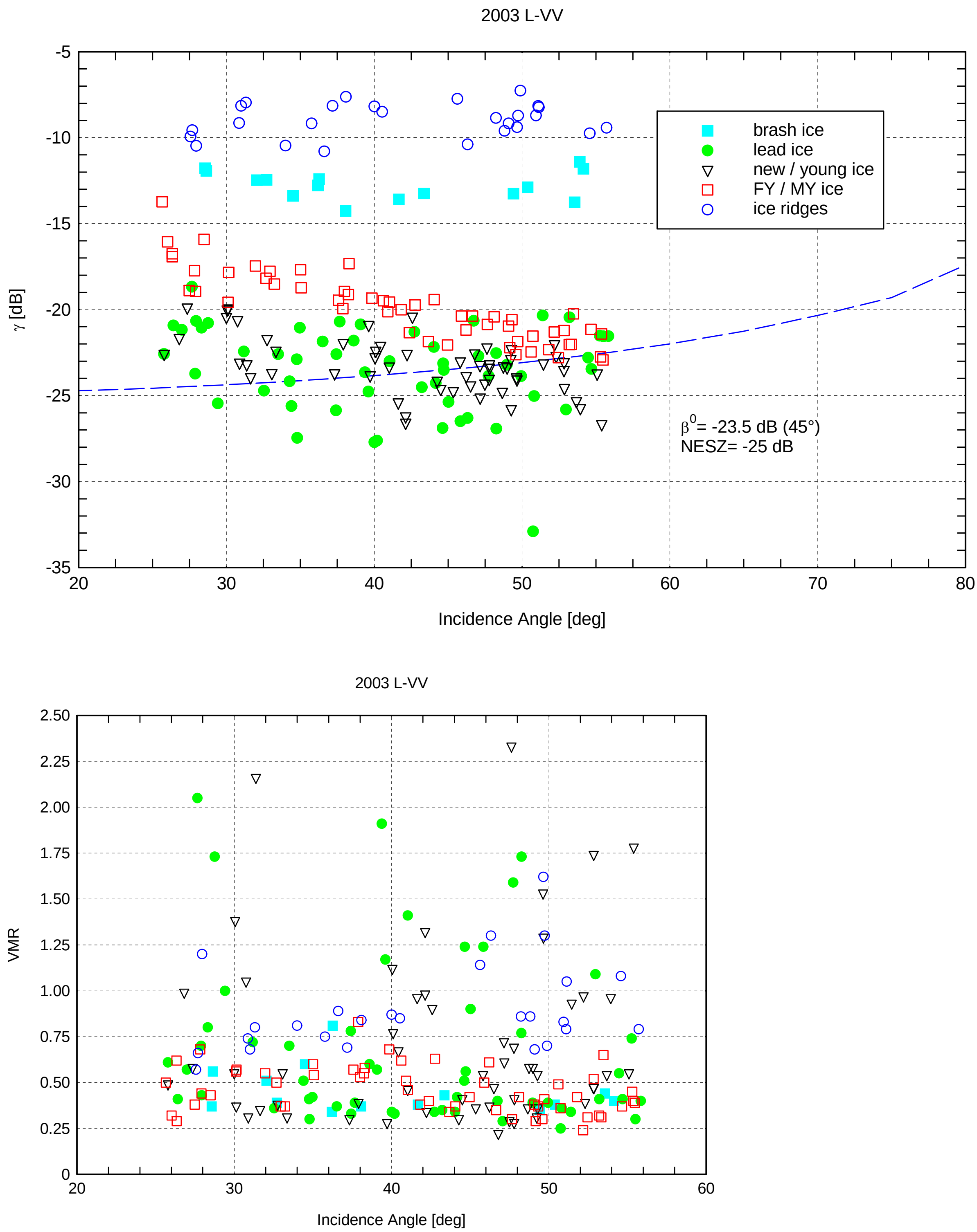

Figure 12e. Radar backscattering coefficient (γ) and variance-to-squared mean ratio (VMR) at L-band VV-polarization as a function of incidence angle measured on March 20 over the Fram Strait test site.

Section 2: Simulation of Sentinel-1 SAR Images

Not only the noise level but also the spatial resolution is an important factor for sea ice classification because it determines which ice cover characteristics typically utilized for an assessment of the ice conditions can still be recognized. For example, single ridges, narrow cracks, and rafting zones in thin ice are difficult to identify at spatial resolutions larger than 20 to 30 m. It is hence useful to have a possibility for simulating the image products of planned satellite missions in order to assess their information content. This can be achieved on the basis of high-resolution low-noise airborne SAR images.

For this study, the original ESAR data were re-processed to image products with 1.5 m and 20 m pixel size, respectively. The former resemble the original ESAR image, the latter are simulations of the interferometric wide-swath mode (IWSM) of the Sentinel-1 SAR. Both images types were processed without spectral weights for side-lobe suppression (see below). To the high-resolution product, no noise was added, for the coarse resolution simulation, the noise level was adjusted corresponding to an NESZ of -22 dB. The number of independent looks was about 4 to 5 in the high-resolution and about 5 to 7 in the coarse-resolution case. The high-resolution products were used for analyzing the radar intensities of different ice types (see Section 1 above). One fundamental difference between real satellite and airborne SAR data is the much larger decrease of the incidence angle from near- to far-range in the latter case. Hence, the coarse resolution images evaluated from airborne data cannot be perfect matches of satellite images. Another issue is that the area covered by airborne measurements is typically much narrower across-track than the satellite swath (3 km for ESAR versus 250 km for the IWSM of the Sentinel-1 SAR). The interpretation of satellite SAR images focuses usually on larger scales on the order of a few kilometres, since variations of ice cover properties can only be assessed by utilizing image segment (windows) that cover a sufficient number of resolution cells.

In order to simulate SAR images with a degraded spatial resolution, it is not sufficient to average over a group of adjacent pixels in the high-resolution airborne imagery, since this operation increases the effective number of looks and, hence, reduces the speckle. Neither can the image just be sub-sampled, because this would change the correlation between adjacent pixels, which, in turn, would impact the effective number of looks resulting from subsequent multi-looking (spatial averaging).

The computer programme that was available for this study is named CSRS (Coarse Spatial Resolution Simulator) and needs the ESAR SLC images as input. An overview of the processing chain is provided in Fig. 13. The single processing steps are indicated in the black boxes. The lines and columns of the image are separately Fourier-transformed, multiplied by functions for spectral weight removal and/or low-pass filtering, and then inverse Fourier-transformed. In the original ESAR images, spectral weighting functions were used for side-lobe suppression. The removal of these weights offers the opportunity to apply different spectral windows when simulating a specific satellite SAR processor. In the recent study, spectral windows for side-lobe suppression were not used. A slant range to ground range projection is carried out before low-pass filtering in range direction in order to end up with a resolution and an equivalent number of looks which are both range independent. As low-pass filter a simple boxcar function was applied. The width of the boxcar function is inversely proportional to the selected pixel size. Finally, the degraded data are power-detected, multilooked and decimated. In practice the last two operations are combined by computing the output of a spatial low-pass filter on a regular ground range grid determined by the pre-defined pixel spacing.

Since the NESZ of the ESAR system is lower than the one of the planned Sentinel-1 SAR, noise was added to the original images. To this end, circular symmetric Gaussian white noise was generated and added to the real and imaginary part of the measured radar signal at a given polarization. (Note: real and imagery part were treated independently from one another.) The noise injection is carried out after the spectral weighting functions in the original EMISAR data are removed, and before low-pass filtering (see Fig. 13). In Fig 14a, the effect of spectral weight removal is depicted, in Fig. 14 b the effect of low-pass filtering.

Critical for the investigations, in particular for the assessment of the noise level, is the stability of the backscattering intensity during the processing steps sketched in Fig. 13. In order to control the stability, a reference ROI is placed on an ice floe in each original SLC-image. Each selected ice floe was characterized by an apparently homogenous radar signature in the intensity image and a had sufficient size, covering several hundred pixels. The mean backscattering coefficient (β) is computed for each step of the processing chain (one step corresponds to one black-framed box in Fig. 13). In Fig. 15, the backscattering coefficients of the original SLC image are compared to the corresponding values in the final 1.5 m pixel product. In this case, no noise was added. If both backscattering coefficients are identical, the corresponding data mark is positioned on the continuous red line. The dashed lines indicate negative and positive deviations from the ideal case by 2 dB. (The same check is also applied when the 20 m pixel image is processed. In this case, however, the ROI in the final coarse resolution product comprises a considerably smaller number of pixels so that mean value, variance, and number of independent looks calculated for the ROI have a larger statistical uncertainty.) Fig. 15 reveals that the backscattered intensity remains rather stable for L-band images from March 16, at C-band on March 18, and at L-band on March 20. In the other cases, deviations larger than 2 dB occur for a number of reference ice floes. A systematic analysis of reasons for larger deviations was not carried out, but the variation of the radar intensity adjacent to the respective reference floe seems to have some influence. The major question is whether the application of the CSRS distorts the assessments concerning the choice of the noise level presented in Section 1. Since both positive and negative deviations occur between original and re-processed data products, and since the difference between the intensities averaged over all original and simulated images is at maximum about 1 dB, it can be assumed that the effect of re-processing the data is negligible.

Simulations of Sentinel-1 imagery are presented in Figs. 16 to 18. The first comparison of a high-resolution low noise image with a simulated IWSM image is from the Storfjord (March 16). Floes larger than 100 m can still be recognized as distinct features, although their edges appear blurred. Narrow cracks and smaller floes are extremely difficult to identify. Compared to the distribution of intensity values in the high resolution low noise image, the histogram of the simulated Sentinel-1 image at like-polarization is only slightly affected. At cross-polarization, however, the difference at the lower values is significant due to the noise level of -21.5 to -19 dB (given as γ, dependent on the incidence angle, see Fig. 9 above). An example from the Barents Sea is shown in Fig. 17. Here, the like- and cross-polarized layers are treated separately in order to demonstrate the loss of information at cross-polarization (Fig. 17b). The corresponding histogram is dominated by noise. The perceptibility of individual floes is lost over large parts of the coarse resolution image. The increase of the noise-γ at larger incidence angles is clearly visible. Due to the noise floor of the IWSM product, the low intensity of these smooth level ice floes is raised to a level corresponding to the backscattered intensity of the brash and broken ice that is found between the level ice floes. The combined effect of a relatively high noise level and a coarse resolution makes the cross-polarized image almost useless for ice classification, whereas the major ice cover characteristics are sufficiently clear recognized in the like-polarized image (Fig. 17a). The last example is from Fram Strait (Fig. 18). Here, the visual information loss in the coarse-resolution IWSM image is almost negligible in comparison to the airborne image. Although the histogram over the backscattering coefficients at cross-polarization indicates a significant decrease of the imaged intensity range at the given noise level, most ice cover characteristics can be more or less easily recognized (not shown). The reason is the large intensity contrast between the different ice classes/features (which were thicker level ice floes, new and young ice, lead ice covered by hoar frost, and ridges in the Fram Strait scenes).

Another possibility to study the effect of coarser spatial resolutions is to compare airborne imagery with corresponding satellite data if available. This requires that the time difference between the measurement flight and the satellite overpass is only small (the acceptable number of hours depends on the ice and wind conditions which affect the ice drift and deformation). Under normal conditions, satellite images have to be ordered at least two weeks in advance. They may cover only limited regions (dependent on the mode chosen) and are acquired at fixed times. Measurements with an airplane can only be carried out if weather and light conditions permit. The distance that can be flown is limited. Hence, often it is a matter of luck whether airborne measurements are sufficiently close to a satellite overpass in time and space.

In Figure 19, zoom-ins of an Envisat ASAR image acquired over the Storfjord on March 16 are compared with corresponding scenes from ESAR. The ESAR image values are backscattering coefficients (γ) in dB-scale, and the ASAR zoom-ins are shown as signal amplitudes in linear scale. (The ASAR image was also converted to intensity in logarithmic scale. The visual appearance did not differ significantly compared to the amplitude image). Intensity stretches of both images were not adjusted to one another. The pixel size of the ASAR image is 12.5 m (APP-mode, number of independent looks is about 2). The image resulting from averaging two adjacent pixels in the original ASAR data matches more closely the characteristics of the Sentinel-1 IWSM product. Since the results of the visual interpretation do not change when using the averaged image, the original ASAR data are shown in Fig. 19.

Relative to the satellite overpass over the Storfjord on March 16, the ESAR flight took place about three hours later. Due to the ice drift, the position of identifiable floes and the shape of open water and thin ice patches between the thicker floes changed within these three hours, particularly in the broken ice zone covered by the image shown in Fig. 19a. Here, the individual ice fragments cannot be identified in the satellite image, and it is extremely difficult to separate zones of small fragments from patches of larger level ice floes. This is caused both by the coarser resolution and the higher noise level which is -22 dB (NESZ) for the Envisat ASAR swath mode IS6. The identification of individual larger level ice floes improves if the radar intensity contrast of the particular floe is large relative to the adjacent ice. Hence, the magnitude of radar signature changes characterizing variations of the ice cover properties is a another important factor affecting the perceptibility of individual ice features. An advantage of the satellite image zoom-ins shown in Fig. 19 is the very narrow incidence angle interval over the image width (only 0.2 deg) in comparison to the airborne case (ESAR: 30 deg), which means that changes of the backscattering coefficient from near- to far range are unambiguously related to changes of ice properties.

In Fig. 20, a comparison between a zoom-in from an ASAR WSM-image and the corresponding ESAR scene is presented. Because the contrast in radar intensity is large for the thicker ice floes and the thinner, young ice patches between them, it is possible to separate this two ice types also in the WSM image. However, many details visible in the airborne image are lost in the ASAR zoom-in, e. g. the rafting and ridging in the new and young ice areas, and the narrow lead running across-track through the middle of the ESAR image (the latter may have closed between the two different data acquisitions, but since the time difference was only one hour and wind speed was low, this is not very probable). In general, the individual ice characteristics that are used for ice type classification in high-resolution images often cannot be recognized in the WSM data products of ASAR. For example, a WSM image acquired over the Barents Sea on March 18 Sea at 18:31 UTC (see Appendix 2, Fig. A2.23) was compared to airborne C- and L-band data from the ESAR flight carried out on the same day between 14:40 and 15:48 UTC. None of the features visible in the airborne imagery could be identified with sufficient certainty in the satellite image. The major reason is presumably the comparatively low radar intensity contrast between adjacent ice features. But also the high wind speed (35-40 kts) , which caused a significant ice drift and deformation, may have to be considered.

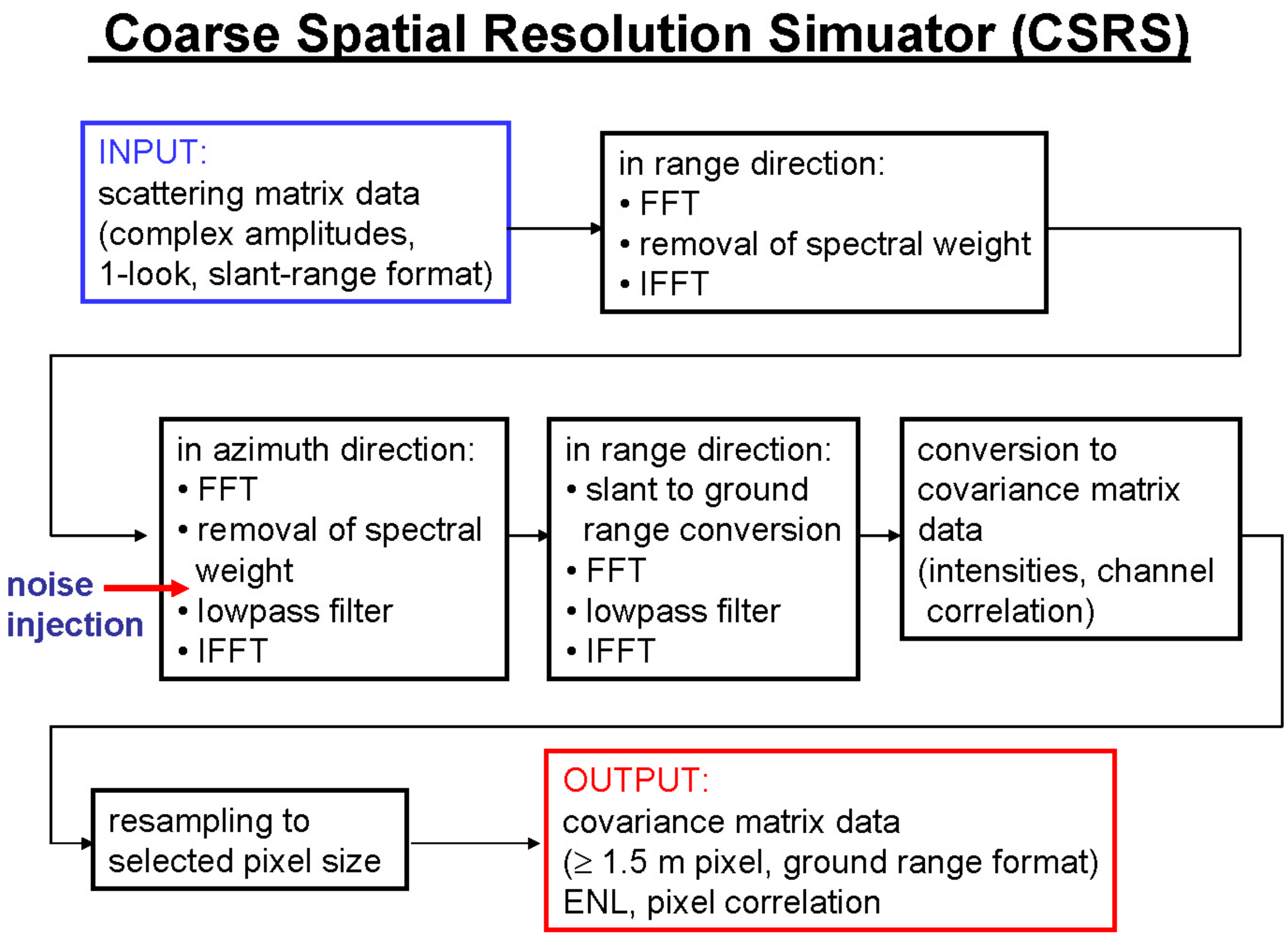

Figure 13. Computer operations for simulation of satellite images from airborne data

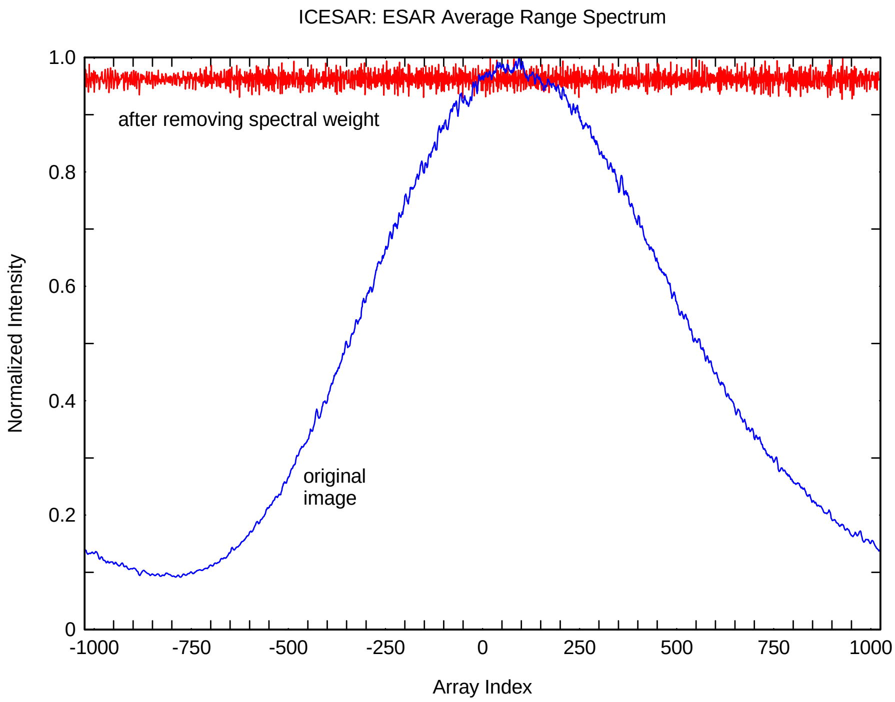

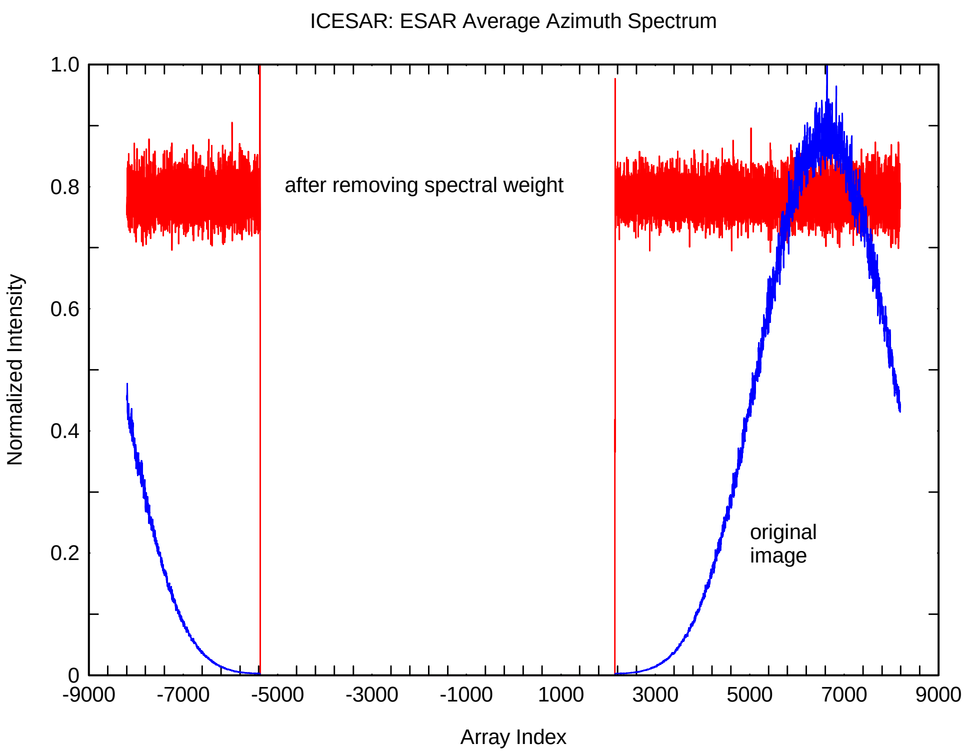

Figure 14a. Power spectra of the original ESAR image (with weighting function) and of the simulated images used in this study (weighting function removed), averaged over all lines in the image (range spectrum, upper graph) and all columns (azimuth spectrum, lower graph), respectively. On the x-axis, the array index is plotted which is determined by the number of lines and columns in the image. In order to avoid numerical artifacts, values in the azimuth spectra were set to zero if the spectral power was below a given threshold.

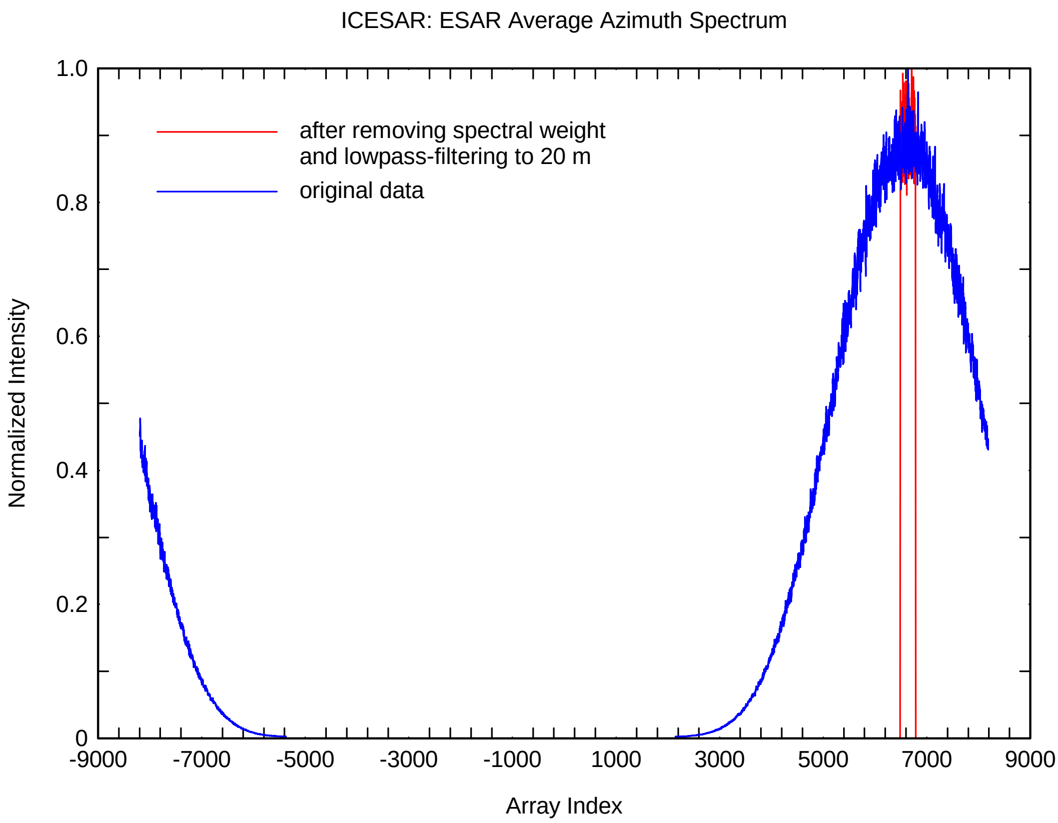

Figure 14b. Spectral information content for a 20 m pixel image (red curve) in comparison to the 1.5 m pixel product (blue curve).

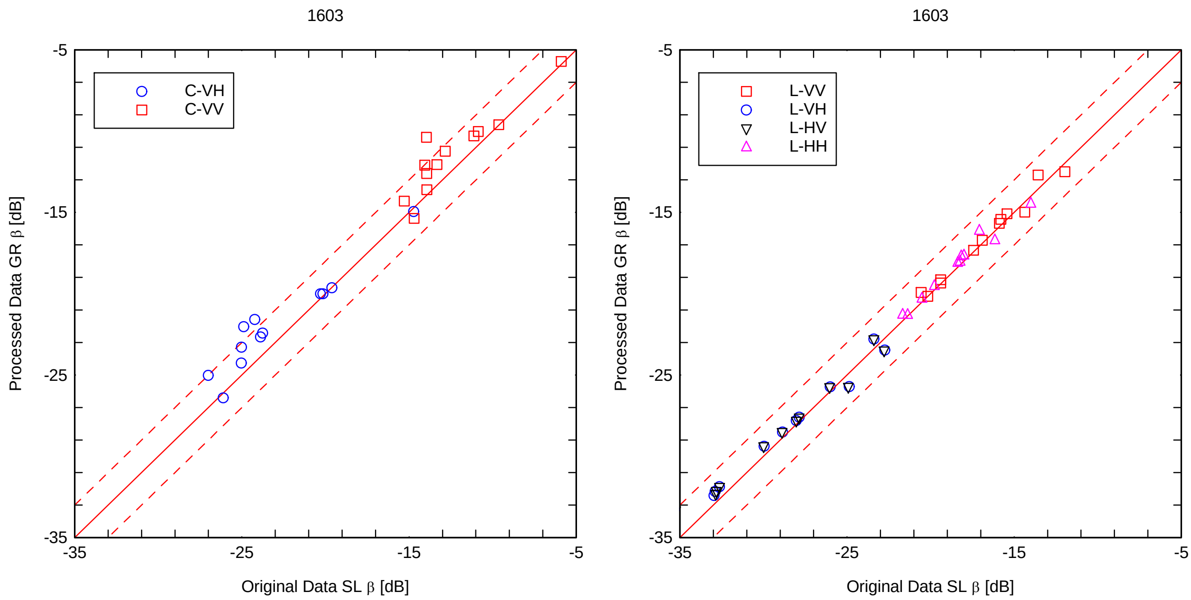

Figure 15. Backscattering coefficients β for the reference ROI in each processed image from the Storfjord area. The value from the original ESAR SLC-data determines the position of a data mark on the x-axis. The position on the y-axis is fixed by the value after processing the image to ground-range format (inclduing removing of spectral weights).

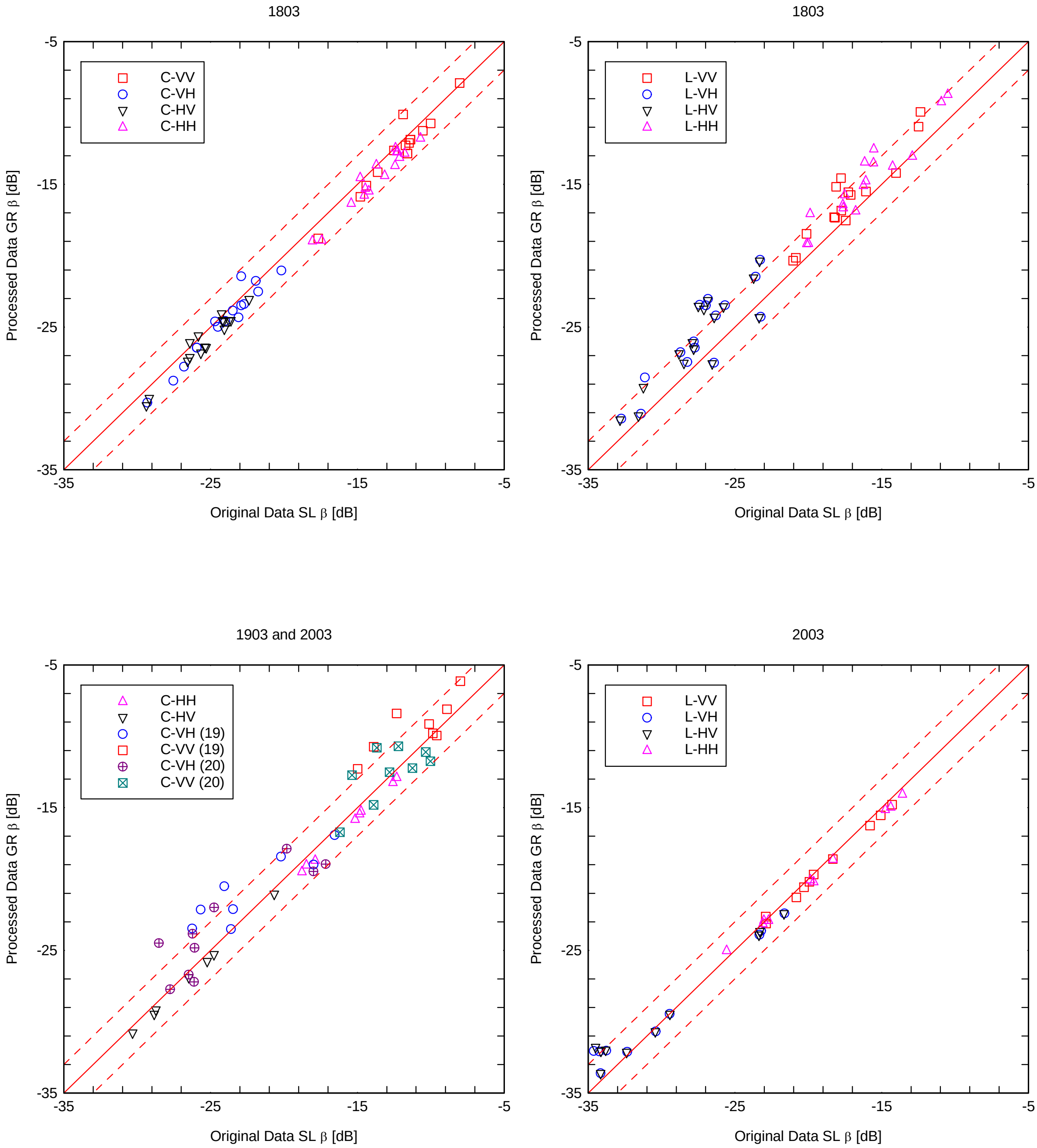

Figure 15. (continued). Results shown are for the Barents Sea (upper graphs) and Fram Strait (lower graphs).

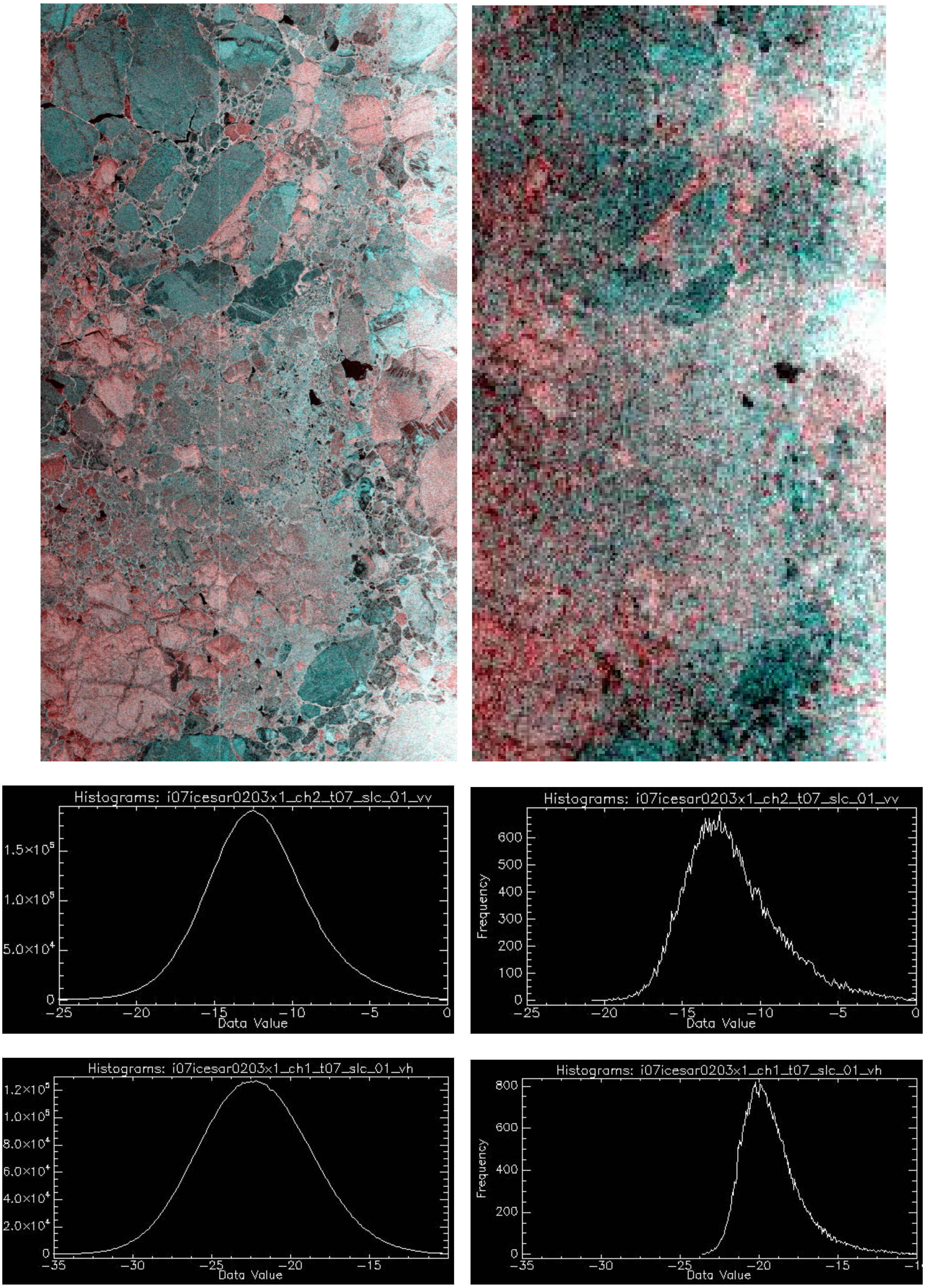

Figure 16. Simulated Sentinel-1 IWSM image (right) in comparison to a 1.5 m pixel image for Storfjord (R-VH, G-VV, B-VV, image width 3 km). Corresponding histograms of the backscattering coefficients γ are shown in the lower part of the figure (upper row: VV-, and lower row: VH- polarization).

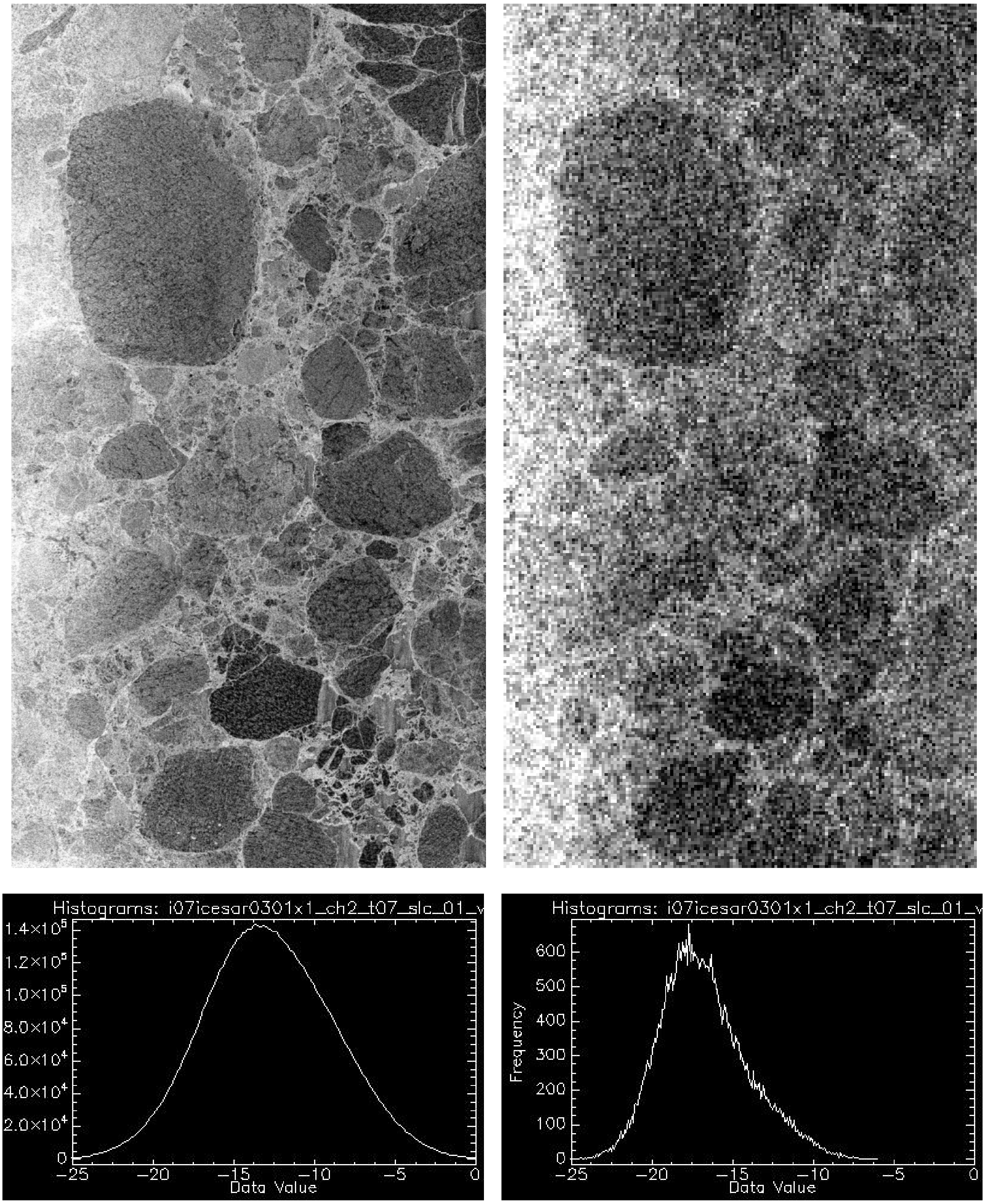

Figure 17a. Simulation of 20 m pixel image product (right) at VV-polarization in comparison to the 1.5 m pixel image for the Barents Sea. Image width is 3 km. Histograms of the backscattering coefficients γ are shown in the lower part of the figure for the 1.5 m pixel image (left) and the 20 m pixel image (right).

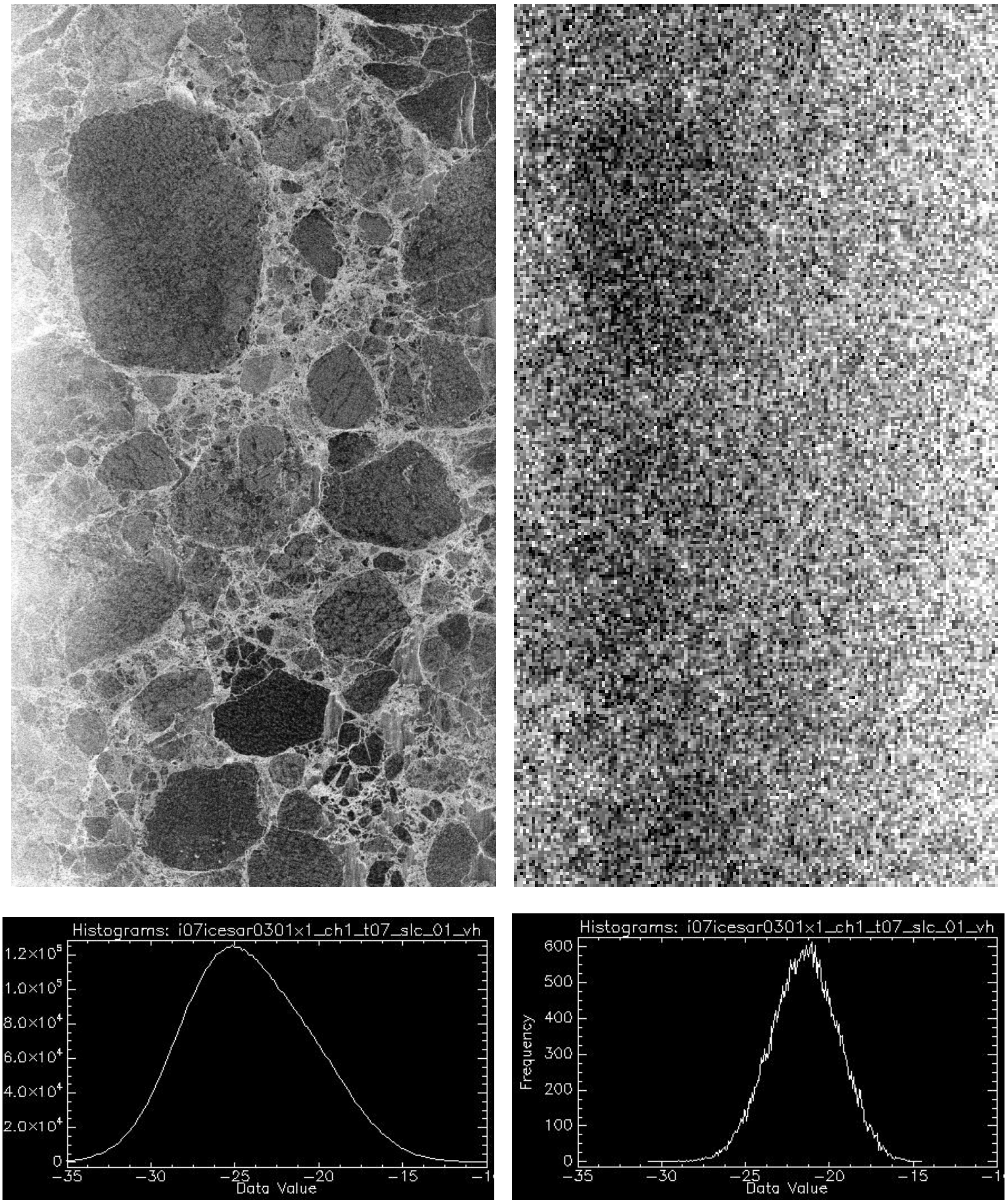

Figure 17b. Simulation of 20 m pixel image product (right) at VH-polarization in comparison to the 1.5 m pixel image for the Barents Sea. Image width is 3 km. Histograms of the backscattering coefficients γ are shown in the lower part of the figure for the 1.5 m pixel image (left) and the 20 m pixel image (right). Note the strong effect of noise which increases at larger incidence angles (right side of the SAR images).

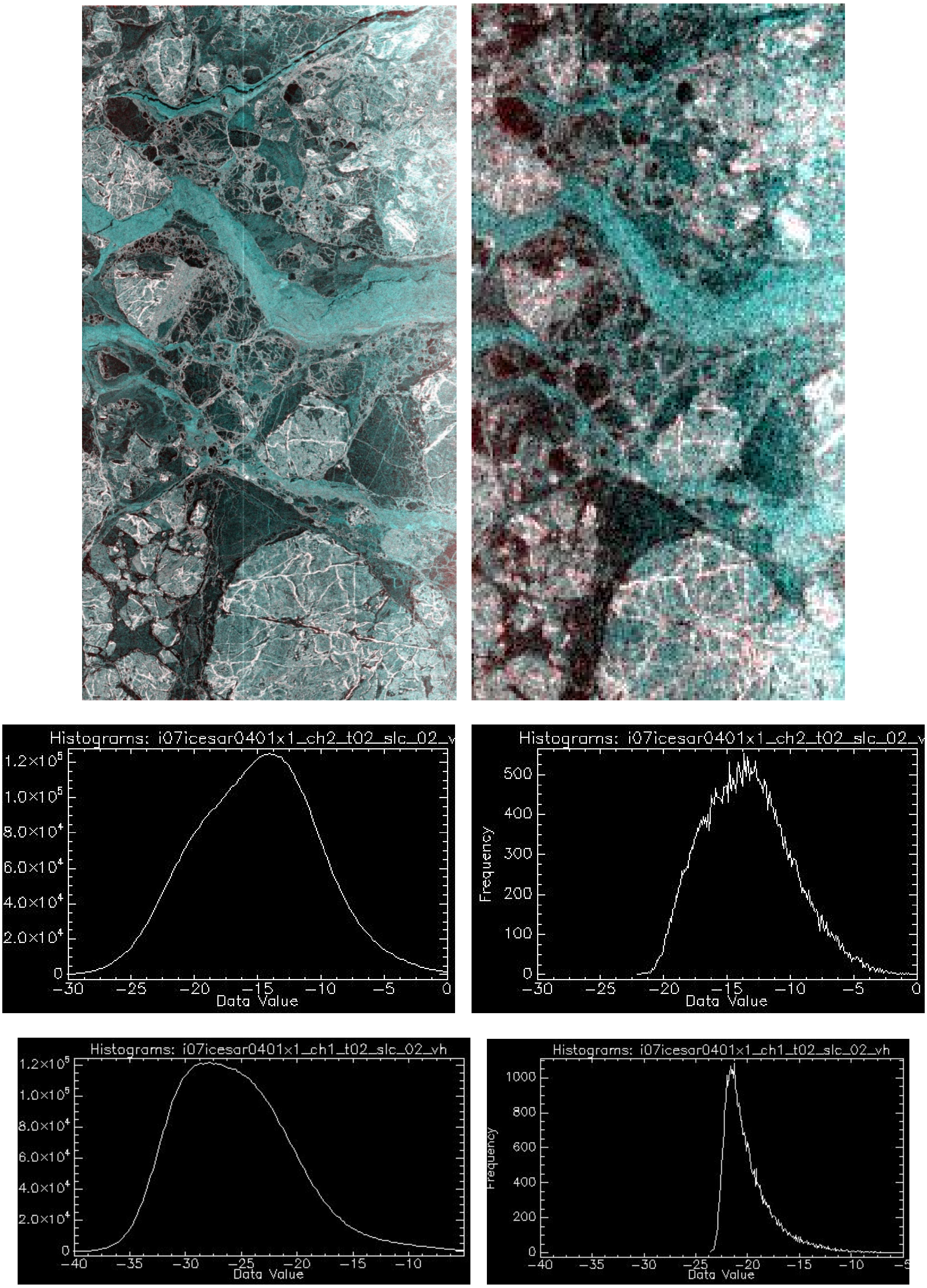

Figure 18. Simulation of 20 m pixel image (right) in comparison to the 1.5 m pixel image for Fram Strait (R-VH, G-VV, B-VV, image width: 3 km). Histograms of the backscattering coefficients γ are shown in the lower part of the figure for the 1.5 m pixel image (left) and the 20 m pixel image (right). Upper row: VV-, and lower row: VH- polarization.

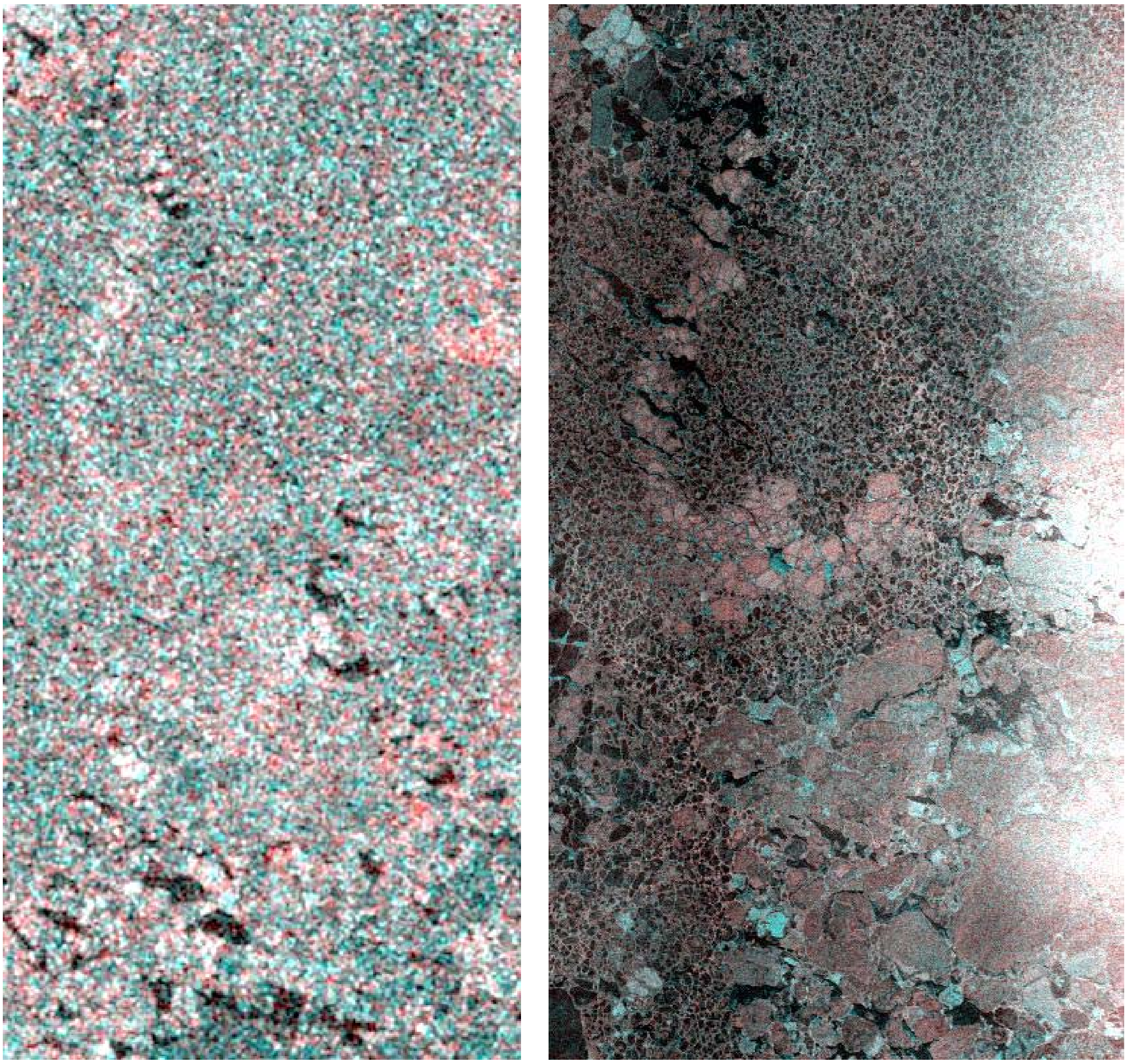

Figure 19a. Left: Zoom-in from Envisat ASAR APP image, acquired on March 16 at 09:37 UTC over the Storfjord (R-VV, G-HH, B-HH). The pixel size is 12.5 m, the incidence angle range over the image width 40.4 to 40.6 deg. Right: ESAR C-band image acquired at12:30 UTC (R-VH, G-HH, B-VV).

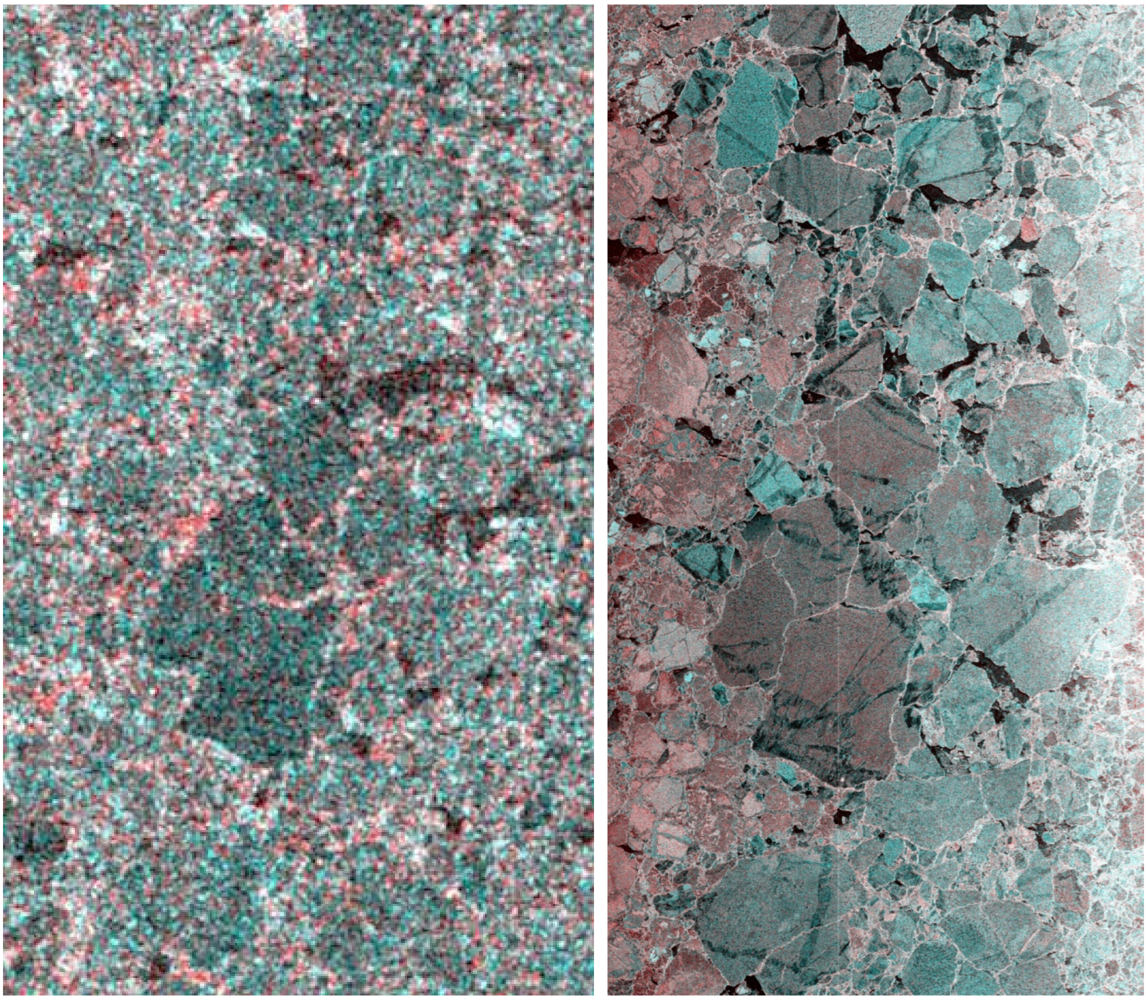

Fig. 19b. Left: Zoom-in from Envisat ASAR APP image, acquired on March 16 at 09:37 UTC over the Storfjord (R-VV, G-HH, B-HH). The pixel size is 12.5 m, the incidence angle range over the image width 40.4 to 40.6 deg. Right: ESAR C-band image acquired at 12:30 UTC (R-HV, G-HH, B-HH).

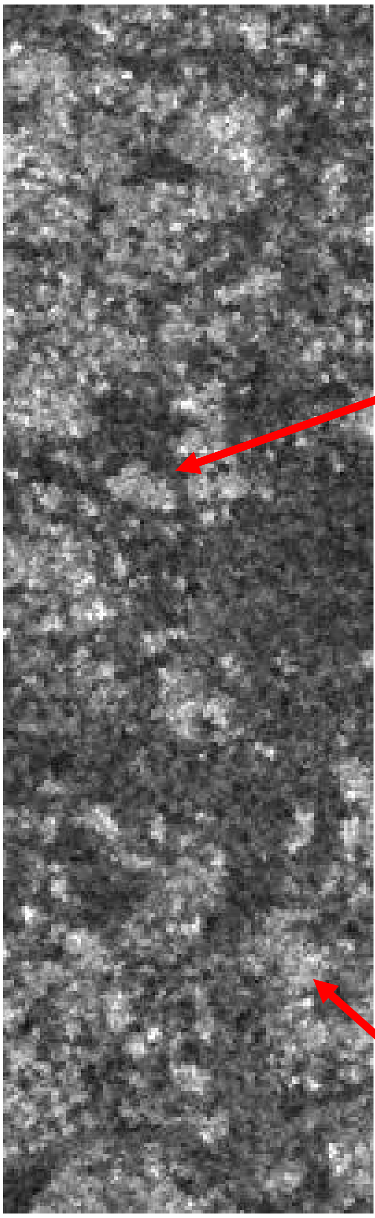

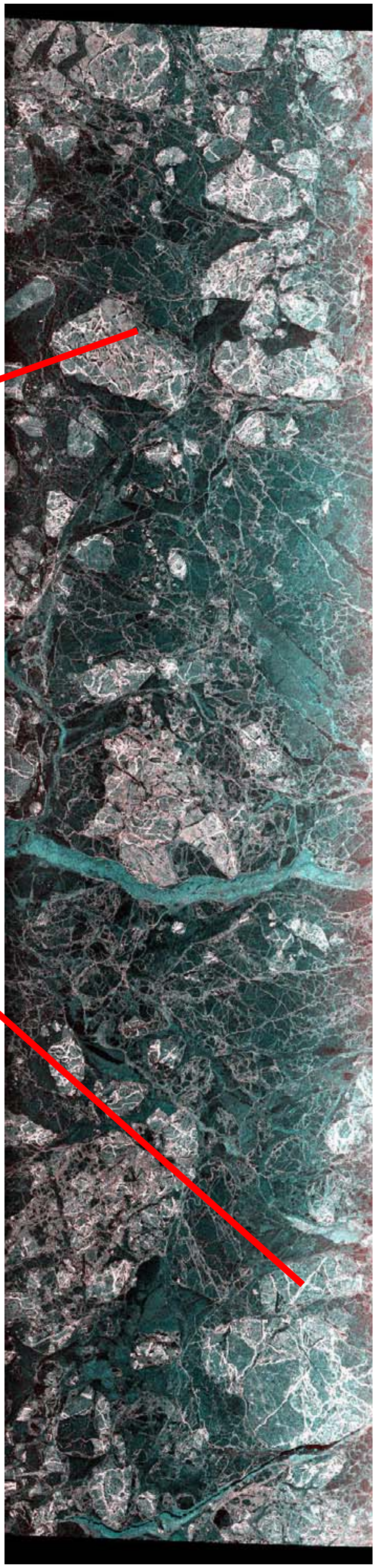

Figure 20. Upper: ASAR WSM image at HH-polarization, incidence angle 26 deg, acquired on March 19 at 1122 UTC over Fram Strait. Left: ESAR image (R-VH, G-VV, B-VV) from 12:26 UTC.

Section3: Assessment of Sentinel-1 SAR configuration for sea ice monitoring

In order to provide a wider basis for the assessment of the Sentinel-1 SAR configuration with regard to sea ice observation and mapping, this section is started with a presentation of selected sea ice studies carried out during the last years. The criterion for choosing a specific study was that it complements the ICESAR data analysis by either focusing on different geographical regions or by adding further information about sea ice conditions and SAR ice signatures around Svalbard.

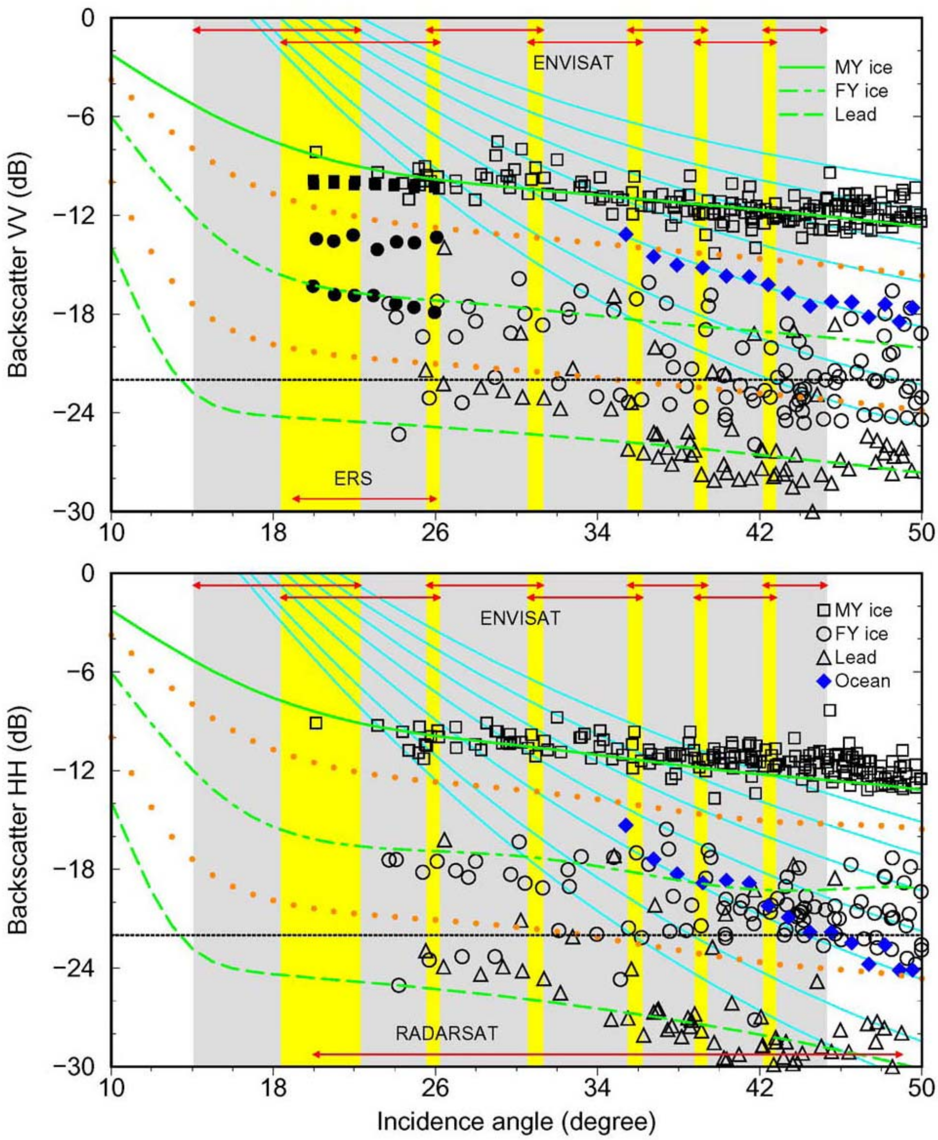

Figure 21a. Backscattering coefficients σ^o of sea ice and open water at VV- and HH-polarization from SAR data (symbols) and from model results (continuous curves). From Nghiem and Bertoia (2001). Explanations are given in the text.

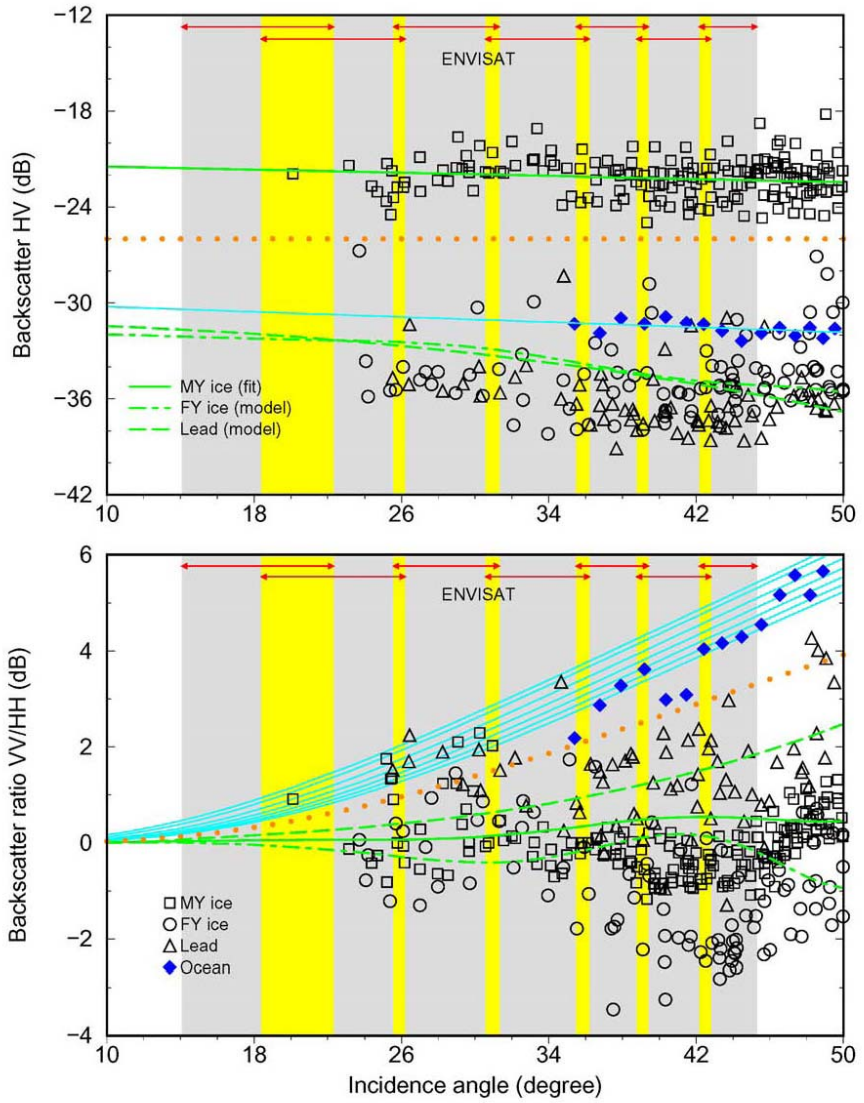

Figure 21b. Backscattering coefficients σ^o at HV-polarization and copolarization ratio of sea ice and open water from SAR data (symbols) and from model results (continuous curves) From Nghiem and Bertoia (2001). Explanations are given in the text.

Nghiem and Bertoia (2001) compiled measured backscattering coefficients of different and supplemented these data by results of theoretical models for sea ice scattering (Fig. 21). The test sites were located in the Beaufort Sea (airborne measurements with AIRSAR) and in the Canadian Arctic Archipelago (satellite data from ERS-1). The measurements were carried out in winter. The sea ice types include deformed and undeformed multi-year and first-year ice, and lead ice of various growth stages. Backscattering values for open water are also depicted in Fig. 21. The corresponding theoretical curves (cyan in Fig. 21) were obtained using the empirical CMOD3-H1 model at neutral wind conditions with speeds of 2 m/s, and 4 m/s to 24 m/s in steps of 4 m/s. Orange dots indicate thresholds between different ice types. Red double arrows mark the ranges of incidence angles for the Envisat, RADARSAT-1, and

ERS SARs. The grey strips denote the incidence angle range of the seven swath modes of ASAR, and the overlap between adjacent swaths is indicated by yellow strips. The black dotted line marks an NESZ of -22 dB.

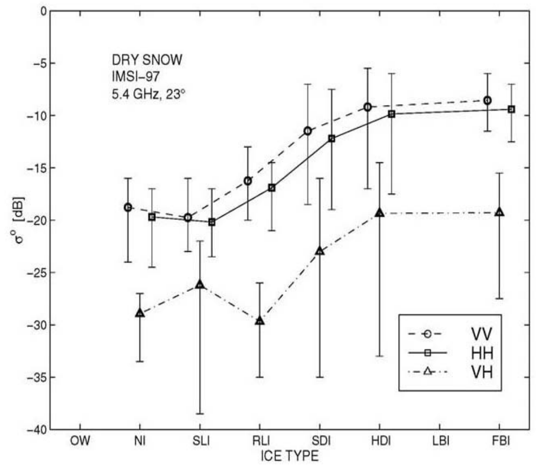

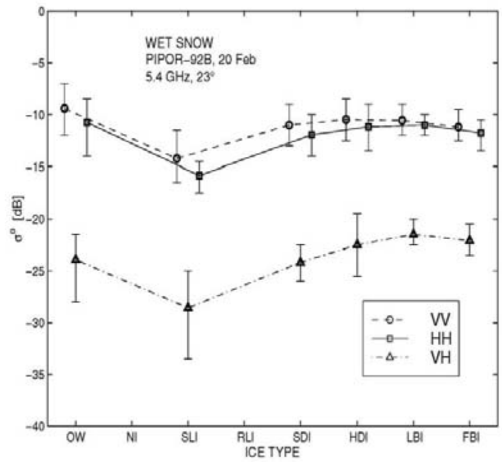

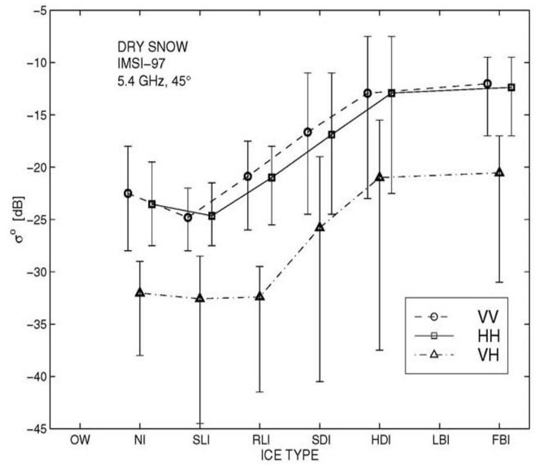

Table 3. Baltic Sea ice type classes assigned for HUTSCAT data.

Main Group	Sub Group	Abbr.	Effect to Ship Navigation
Open water leads	None	OW	None
Nilas	None	NI	None
Level ice	Smooth level ice Rough level ice	SLI RLI	Depends on thickness
Deformed ice	Slightly deformed ice	SDI	Slows down or blocks navigation
	Highly deformed ice	HDI	Usually blocks navigation
Brash ice	Loose brash ice Frozen brash ice	LBI FBI	Depends on thickness

Figure 22. Mean and 90% confidence intervals of σ^o at C-band for various ice types found in the Bay of Bothnia under freezing and melting conditions. Abbreviations of ice types used on the x-axis are explained in the table. From Mäkynen and Hallikainen (2004).

The results presented in Fig 22 are from a study by Mäkynen and Hallikainen (2004) for sea ice found in the Bay of Bothnia. Data were acquired with an airborne scatterometer between 1992 and 1997, mainly under winter conditions. Short periods with temperatures around freezing point characterized by moist or wet snow on the ice were included in the data analysis. The ice in the Bay of Bothnia is only first-year ice, and it is characterized by a much lower salinity than Arctic first-year ice.

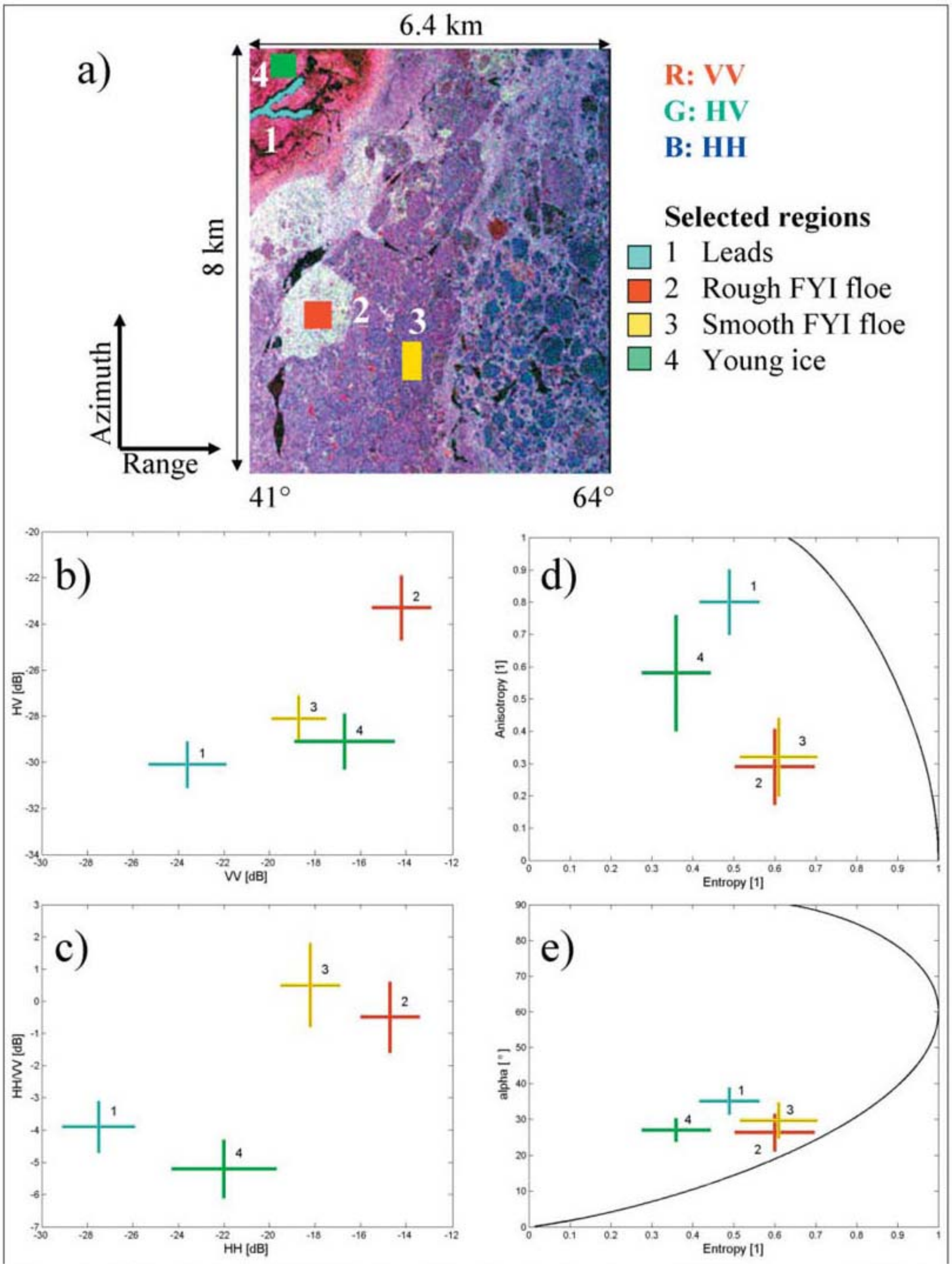

Figure 23. (a) Simulated RADARSAT-2 fully-polarimetric data (based on a CV-580 airborne data acquisition in Northumberland Strait. (b-e) Spatialy averaged (6 ×6 pixels) and selected two-dimensional lots for areas 1-4. The black lines in (d) and (e) indicate the bounds for the respective space. From Scheuchl et al. (2004).

Scheuchl et al. (2004) investigated the potential of RADARSAT-2 for sea ice mapping, using polarimetric C-band SAR data from an airborne campaign in Eastern Canada (see Fig. 23). In their analysis, they focused on new, young, and first-year ice.

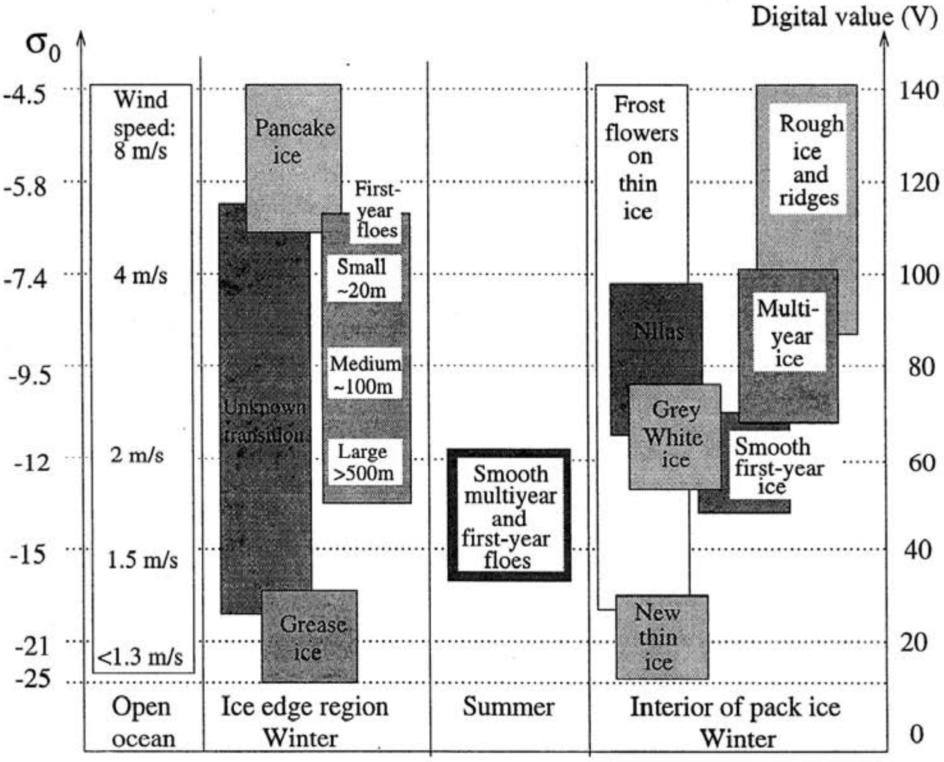

Figure 24. Schematic diagram summarizing SAR backscatter coefficients σ^o at VV-polarization for different ice types in the Barents Sea east of Svalbard. From Sandven et al. (1999).

From a validation campaign for ERS-1, the variations of radar signatures at C-band VV-polarization were determined for various ice classes in the Barents Sea east of Svalbard (Sandven et al., 1999). The ranges of σ^o shown in Fig. 24 are for an incidence angle interval from 20 deg to 26 deg. The situation found in the Barents Sea during ICESAR corresponds to the column "Ice edge region" in Fig. 24, the situation in Fram Strait to "Interior of pack ice". It was found, for example, that the average size of ice floes in a given area determines the intensity retrieved from the ERS-1 image, which is in line with the results of ICESAR presented in Section 1. The thin ice radar intensity may increase drastically when frost flowers appear on the ice. It is noted that the radar incidence angles for which the results of Sandven et al (1999) were obtained are smaller (ERS-1: 20-26 deg) than the ESAR incidence angle range configured during ICESAR. At the lowest incidence angles of the ESAR, the interval of measured radar intensities (Fig. 10c) compares well with Fig. 24, column "Ice edge region" (note: at an incidence angle of 26 deg, the γ-values shown in Fig. 10c are about 0.5 dB higher than σ^o). The radar intensities found in the ESAR images of Fram Strait at C-band VV-polarization for the incidence angle interval from 20 to 30 deg (Figs. 11c, 12a) compare satisfactorily with the values indicated in Fig. 24, column "Interior of pack ice". However, the observed maximum intensities are higher in the ESAR images which can be explained as follows: The cross section of individual ridges usually extends over a few pixels in the high-resolution airborne imagery. Hence, ROIs can be placed such that they cover only the ridge area. This is not possible in the ERS-imagery with its coarser spatial resolution. The intensity evaluated from an ROI is usually from a mixture of ridges and adjacent level ice, i.e. it is lower than the typical intensity from a ridge alone.

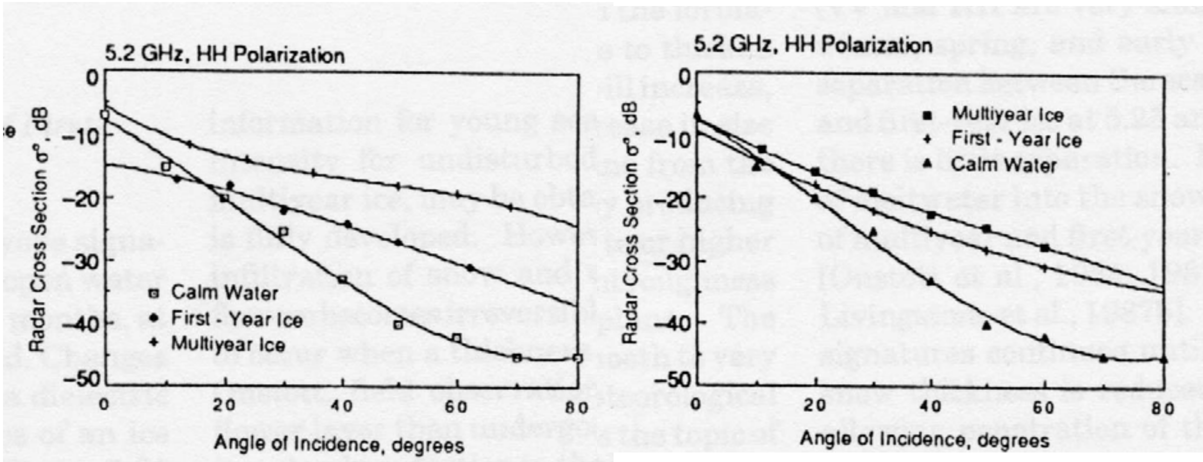

Figure 25. Radar backscattering coefficient for sea ice and water during winter (left) and summer (right). From Onstott (1992).

In the last reference utilized data source on C-band radar signatures of sea ice (Onstott, 1992, see Fig. 25), no information is provided about the location of measurements. Most probably, these data were gathered in the Canadian Arctic by means of a ground-based scatterometer.

Table 2: Ice types affected by the given noise level (θ is incidence angle)

Reference	NESZ = -25 dB	NESZ = -22 dB
Nghiem and Bertoia, 2001	HH, VV: thin and smooth lead ice X-pol.: same + first-year ice	HH, VV: thin lead ice and first-year ice X-pol.: same + low intensity multi-year ice floes
Mäkynen and Hallikainen, 2004	HH, VV: thin ice X-pol.: thin ice, smooth and rough level ice, at larger values of θ even slightly deformed ice	HH, VV: thin and smooth level ice X-pol.: all ice types (with dry and wet snow cover)
Scheuchl et al., 2004	none at VV-pol., lead ice at HH-pol. X-pol.: lead and young ice, and smooth first-year ice	VV-pol.: lead ice, HH-pol.: lead and young ice X-pol.: all ice types
Sandven et al., 1999 (only VV-pol.)	none	new thin ice and grease ice
Onstott, 1992 (only HH-pol.)	none for θ < 50 deg	HH-pol.: first-year ice at θ > 30 deg, multi-year ice at θ > 40 deg under summer conditions

Regarding the effect of the SAR noise level, the findings from the studies presented above are summarized in Table 2. Listed are those ice types for which intensities are observed that lie below the given noise level. Note that for a specific ice type, also samples with intensities above noise level may be found. Interesting additional findings are: The like-polarization ratio VV/HH is ≥ 2 dB between sea ice and open water at incidence angles > 30 deg, but it is much smaller between different ice types (about 0 dB for multi-year ice, slightly > 0 dB for thin lead ice, and ≤ 0 dB for first-year ice) (Nghiem and Bertoia, 2001). The cross-polarization ratios VV/VH and HH/HV are better suited to distinguish ice of different roughness and deformation stages than the like-polarization ratio (Mäkynen and Hallikainen, 2004).

In order to provide an assessment of the Sentinel-1 SAR configuration with respect to sea ice mapping, the data gathered during ICESAR are utilized in two different ways. In Fig. 26a, the widths of the intensity distributions averaged over all images for a given day and polarization are evaluated. The idea behind this representation is that the observed intensity range depends on the noise level and the spatial resolution of the imagery. In the latter case, high intensity spots in a high-resolution image are smeared out over adjacent areas of lower intensity at coarse resolution. Hence the intensity of the larger pixel is lower. The highest and lowest two percent of the area covered by the intensity distribution function are excluded from the analysis in order to alleviate the effect of outliers. The results from the high-resolution low noise images (used for the analysis presented in Section 1) serve as reference (blue and black bars in Fig. 26a). The simulated Sentinel-1 IWSM-scenes (red and cyan bars) reveal the influence of the system noise which ranges from -21.5 to -20.5 dB (γ) for incidence angles between 30 and 45 deg, and from -20.5 to -19 dB between 45 and 60 deg. The effect of noise is obviously severe at cross-polarization, in particular if the ice cover is relatively young as it was the case in Storfjord (March 16) and in the Barents Sea (March 18). At like-polarization, the low intensity values are also affected by the noise floor. In the interpretation, however, it has to be considered that the noise level is not necessarily represented by the lower two-percent limit of the intensity distribution. The bars assigned to cross-polarization coarse resolution for March 18, e. g., represent more or less the width of the noise distribution, as can also be seen in Fig. 26b. At like-polarization, the noise reshapes the left-hand side of the full-resolution distribution function (Fig. 26b, upper two graphs).

The decrease of the maximum intensity values (top ends of the bars) found in the Sentinel-1 simulations is only small in comparison to the airborne reference images. Hence, in a 20 m pixel image product such as the Sentinel-1 IWSM the effect of the reduced spatial resolution on the overall intensity distribution is still negligible. At cross-polarization, the maximum radar intensities are very low for the Barents Sea (March 18), so that the addition of noise in the simulation of the Sentinel-1 imagery causes an increase of the maximum relative to the high-resolution images. The red and cyan bars in Fig. 26a assigned to coarse-resolution imagery demonstrate that the modification of the original radar intensity of a scattering object due to noise may be more complex than the simple threshold lines for the (average) noise level in Figs. 9-12 indicate.

The second presentation (Fig. 27) shows for each measurement site the differences between the observed intensity maximum and minimum (black bar), between the mean intensities of deformed and level ice (green), and between the mean intensities of level and new ice (blue), dependent on polarization and incidence angle interval. These results were obtained on the basis of the ROIs placed on different ice types over all high-resolution low noise reference images. The corresponding results from the simulated Sentinel-1 images are depicted as red bars next to the respective reference bar. They were determined by considering the noise level. That is, the observed reference minimum or the mean intensity of ice classes “deformed”, “level”, and “new” was replaced by the noise intensity if the latter was larger. Dependent on the measurement site, class “deformed” comprises broken ice, brash ice, and ridges, class “level” young, first-year, and multi-year ice, and class “new” nilas and young ice. Hence, the deviations of the mean intensities of new and deformed ice relative to the mean intensity of level ice are not universal measures, but they reflect the intensity contrasts to be expected for a given ice regime. The graphs of Fig. 27 show the magnitude of the respective differences but not the absolute positions relative to the intensity axis such as in Fig. 26.

The black bars include only intensity values from the ROIs. This explains, e. g., the larger difference between the black bars of VV- and HH-polarization on March 16 (Fig. 27) which cannot be observed in Fig. 26 (see also Figs. 9a, 9c). The magnitude of all bars depends generally on the ice regime. For example, the intensity contrast between deformed and level ice was only small for the ice in Storfjord (March 16) but relatively large in Fram Strait (March 19 and 20). The comparison of the red bars (Sentinel-1 IWSM image simulation) with the corresponding reference bars reveals that the intensity contrast between deformed and level ice and between level and new ice is not affected by a noise level of NESZ = -22 dB at like-polarization. In Sentinel-1 cross-polarization images, this level is too high relative to the average new ice intensity. Even the contrast between mean intensities of deformed and level ice is reduced in all cases except for the Fram Strait data (March 19 and 20) at lower incidence angles. This means the noise level is higher than the mean level ice intensity. In the Storfjord and Barents Sea data (March 16 and 18), the average intensities of deformed ice are even lower than the noise floor. One should, however be careful to interpret such finding as “the separation of ice types X and Y is impossible”, since the bars in Fig. 27 are calculated from mean values. In limited areas of an image, the actual intensity contrast between adjacent ice types may be large enough to make a separation possible. In the right-hand scene shown in Fig. 28, which is a Sentinel-1 image simulation at cross-polarization, larger level ice floes (corresponding to young/first-year ice in Figs. 9b+d) are visible in the upper part. The actual radar intensities scattered back from these floes are below the noise level of -22 dB (NESZ), but the intensities of the adjacent areas are considerably higher so that noise addition only decreases the intensity contrast, but the floes can still be well delimited from their neighborhood. This example demonstrates that also image simulations are required to gain a realistic impression concerning the visual interpretation of coarse-resolution images with relatively high noise levels. The results shown in Figs. 26a and 27, on the other hand, provide sort of more general “benchmarks” in order to compare different radar systems.

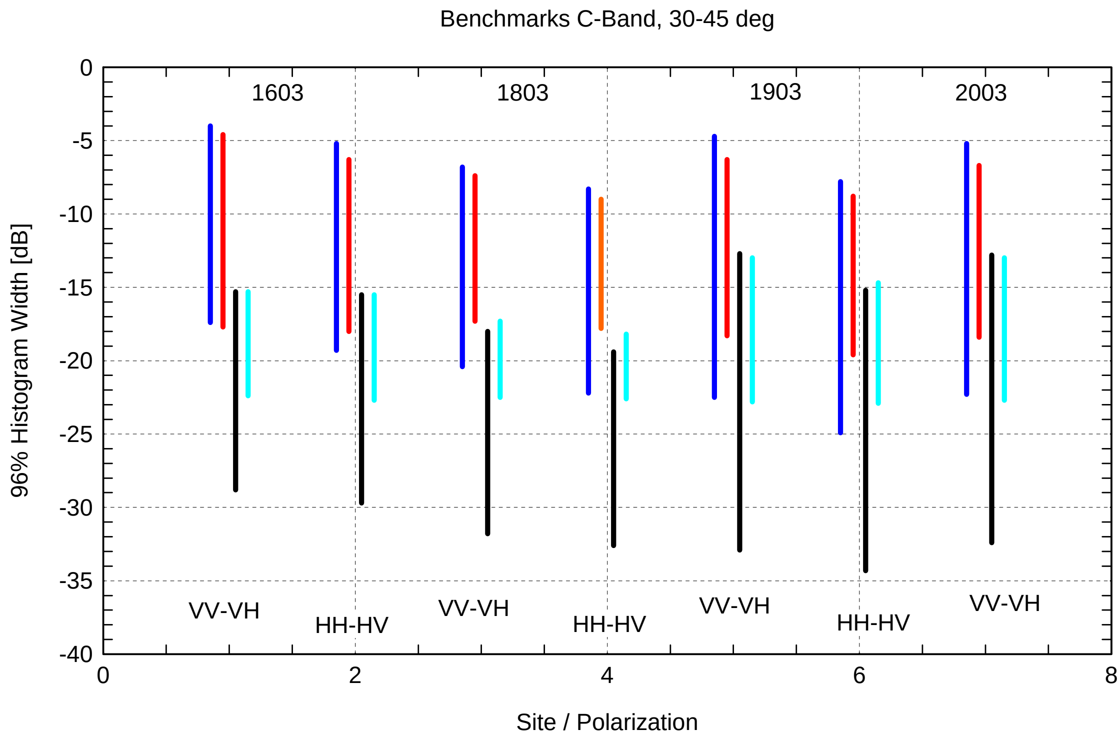

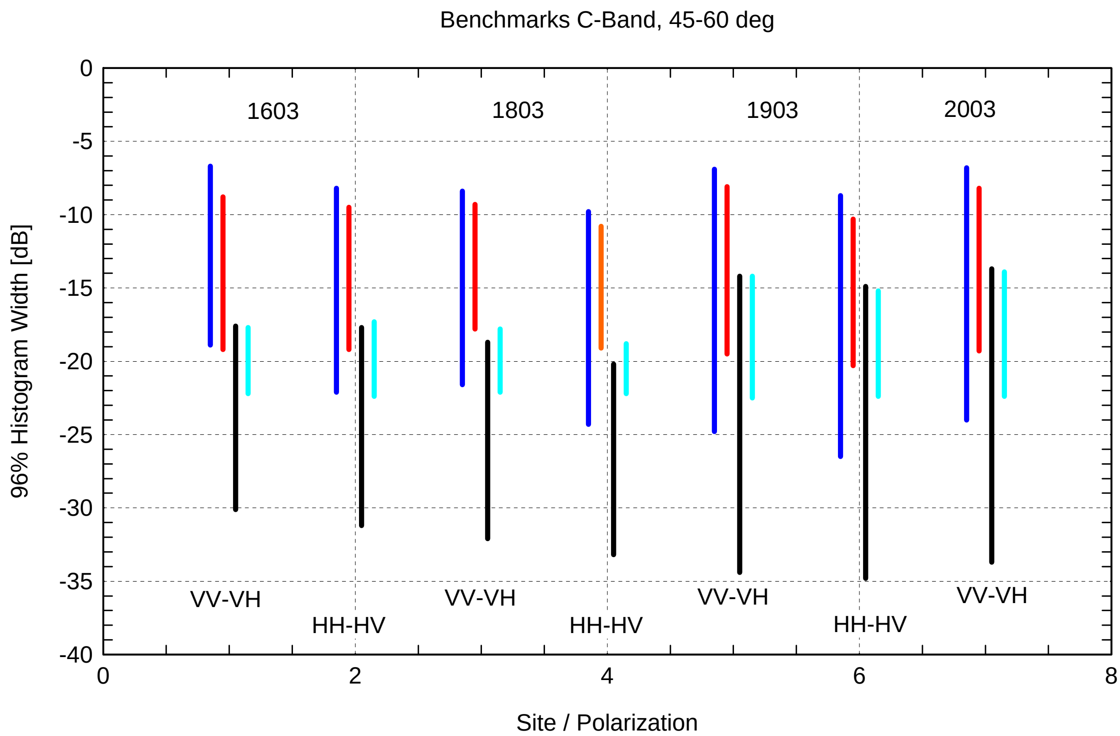

Fig 26a. 96% widths of radar intensity distributions for the investigated ICESAR images. High-resolution low noise data are indicate by blue (like-pol.) and black (cross-pol.) bars, simulated Sentinel-1 images by red (like-pol.) and cyan (cross-pol.) bars. The upper graph shows results for incidence angles between 30-45 deg, the lower graph for 45-60 deg.

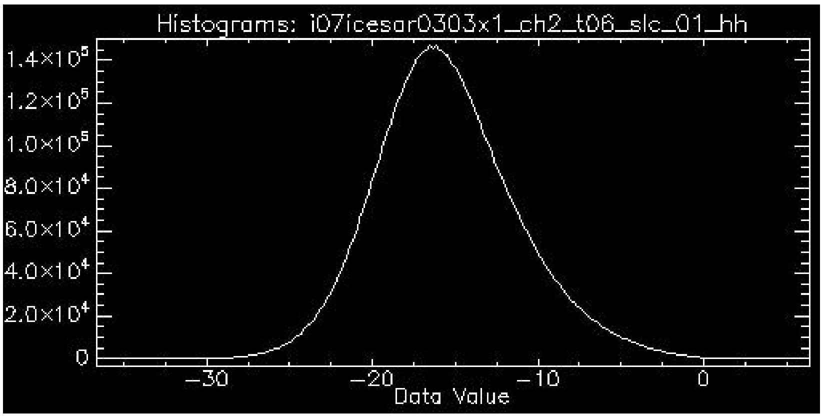

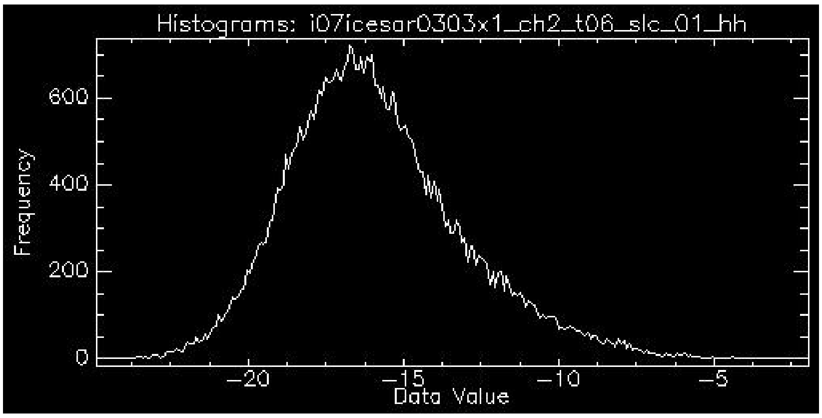

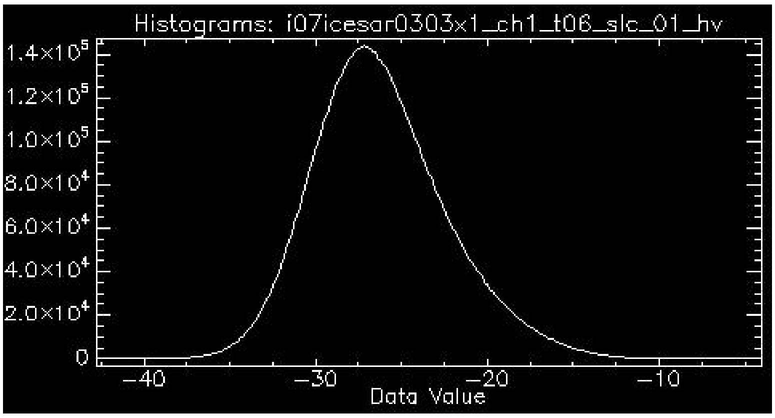

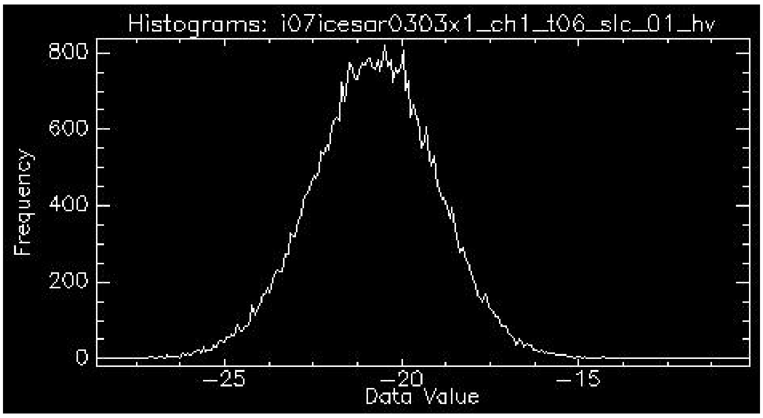

Figure 26b. Histograms of backscattering coefficients (γ) for one image from March 18. From top to bottom: like-polarization full-resolution, like-polarization coarse-resolution, cross-polarization full-resolution, cross-polarization coarse-resolution.

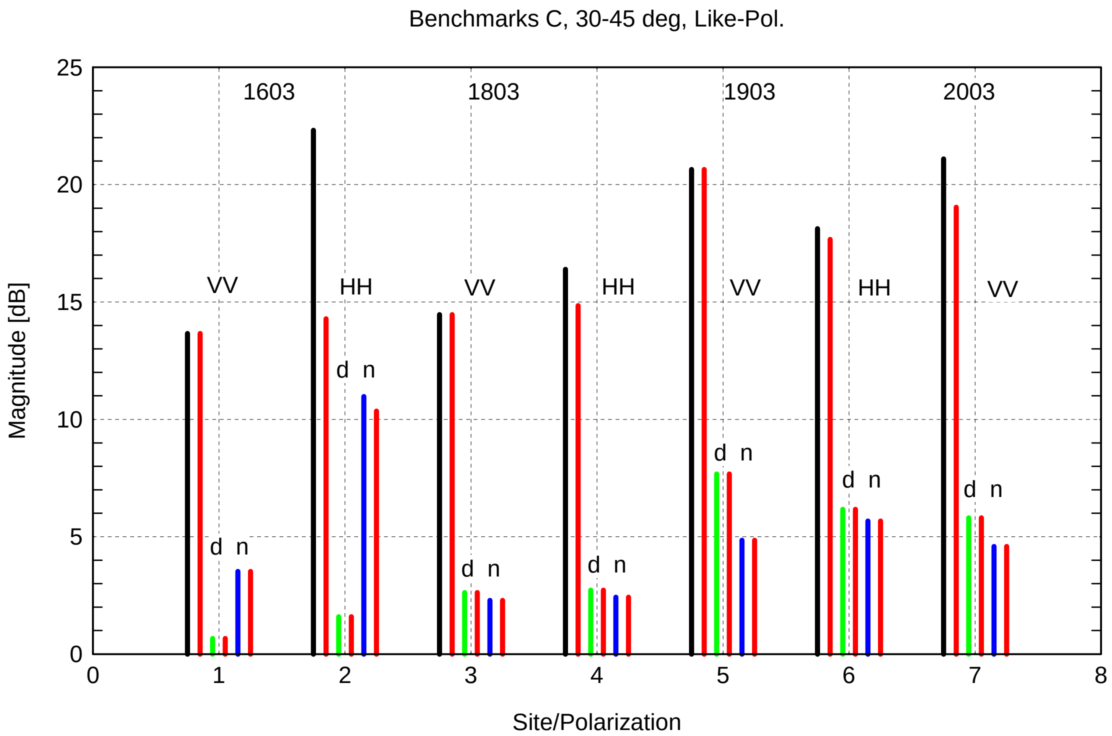

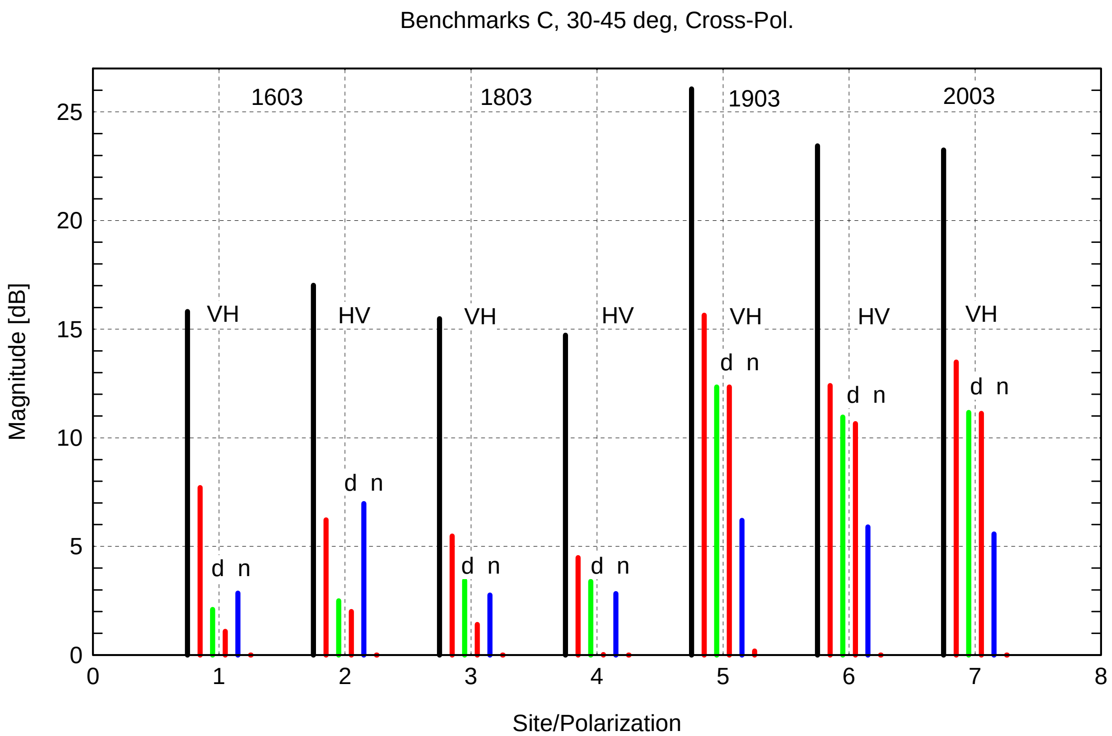

Figure 27 a. Bars showing difference between intensity minimum and maximum (black), between mean intensities of deformed and level ice (green), and between mean intensities of level and new ice (blue). Results are from high-resolution low noise images used in Section 1. Corresponding results for Sentinel-1 image simulations are depicted as adjacent red bars, respectively. Valid for the incidence angle range from 30 to 45 deg. Unlike in Fig. 26a, only the intensity values assigned to the ROIs are considered here.

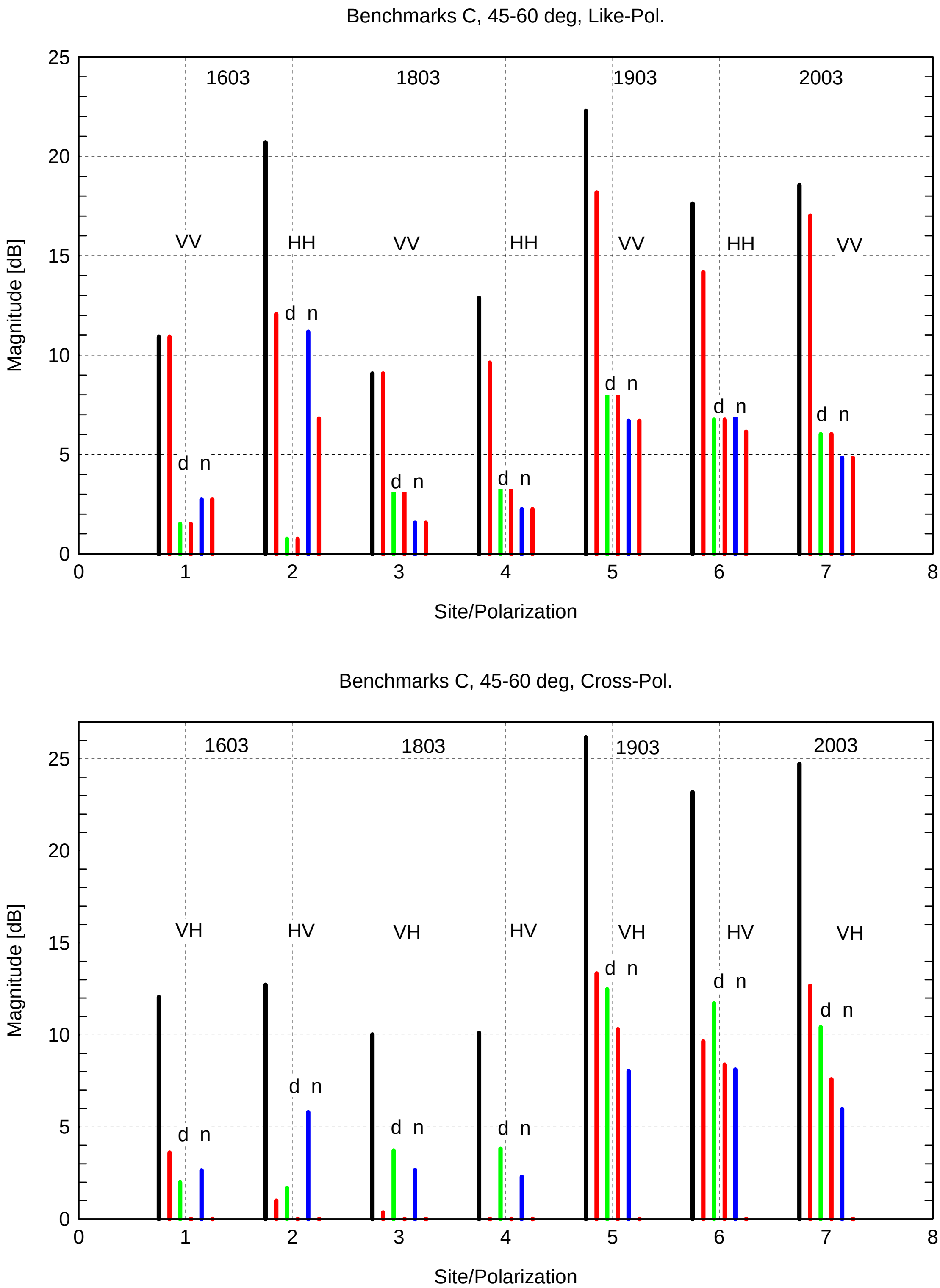

Figure 27b. Same as Fig. 27a, but for incidence angle range between 45 and 60 deg.

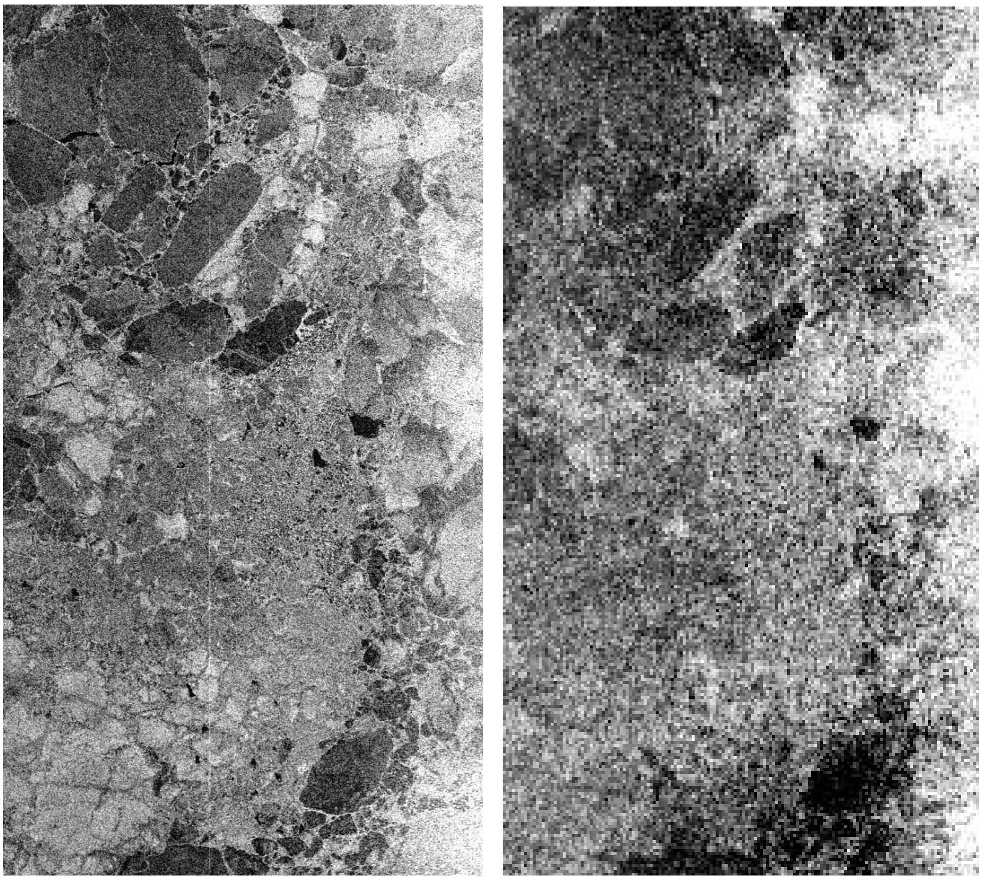

Figure 28. Cross-polarized SAR images from Storfjord (March 16, see also Fig. 16). Left: full-resolution low-noise image, right: Sentinel-1 IWSM simulation. Far-range (i. e. position of larger incidence angles) is on the left edge of the images.

Section 4: Conclusions

Airborne SAR measurements were carried out in winter 2007 over different ice covered ocean regions around Svalbard. Test sites were located in Storfjord, the Barents Sea, and Fram Strait (Fig. 1). Radar data were acquired at C- and L-band at different polarizations. The high-resolution low-noise images were either used to simulate coarse-resolution products with higher noise levels similar to the interferometric wide swath mode of the planned Sentinel-1 SAR mission, or were compared to Envisat ASAR imagery. The major findings regarding the objectives of this study (as listed in the introduction) are as follows:

- **Noise level (C-band)**: Radar intensities at different polarizations were determined for various ice types as a function of incidence angle (Figs. 9-12). To this end, the high-resolution low-noise airborne data were used. Additional, measured radar intensities are provided from a number of studies reported in the literature. The results were utilized to assess the effect of the SAR system noise level on ice type separation. In case of the Sentinel-1 mission the NESZ will be at -22 dB.

  In order to cover the full intensity range of sea ice types observed in the different studies, the ideal values for the NESZ are -25 to -30 dB at like polarization and -35 to -40 dB at cross-polarization, as Figs. 9, 10, 11, 12, 21 , 22 and 23 indicate. The respective lower noise figure is for larger incidence angles (> 30-40 deg). Such noise levels are required, e. g., in order to separate thin ice types or to determine their thickness in studies of the heat flux through the ice.

For operational sea ice mapping, however, it is sufficient to distinguish deformed and level ice and to identify zones of open water and thinner ice without separating different stages of the initial ice growth. In this case, -22 dB are just acceptable at like-polarization, but a noise level of -25 dB, as for the ERS missions, is preferable, in particular at HH-polarization and/or at larger incidence angles (Fig. 26). The decrease of the intensity range in images acquired at cross-polarization with a NESZ of -22 dB is severe in many cases, as was demonstrated in the preceding sections (Figs. 9b+d, 10b, 11b, 12b, 17b, 21b, 22, 23, 26, 27). Only in some images parts it may be possible to retrieve some properties of the ice cover, if the magnitude of intensities and the spatial distribution of ice types/features is favorable (Fig. 28).

- **Spatial resolution:** The effect of a coarser spatial resolution on the sea ice classification is difficult to evaluate quantitatively. One possibility is to simulate coarse resolution products from airborne imagery. Another method is to compare almost simultaneously acquired satellite and airborne SAR imagery. Both approaches were used in this study.

  The spatial resolution provided by the interferometric wide swath mode of the Sentinel-1 mission (here simulated with 20 m pixel size) is still sufficient to identify most ice features (such as ridges, leads, cracks) and ice types unambiguously (Figs 16, 17, 18, 19, 26). It was found that the intensity contrast between different ice types/features and its spatial distribution in the image are important for the perceptibility of ice cover properties at larger pixel sizes (in particular for image products with spatial resolutions ≥ 100 m).
- **Polarization (C-band):** Significant differences occur only in special cases. In the Storfjord images, new ice is better separated from young and first-year ice at HH-polarization (Figs. 9a+b+c). The Fram Strait data reveal that the intensity contrast between distinct ice ridges and level ice is largest at cross-polarization (Figs. 11a+b+c 12a+b). The advantage of the VV polarized channel is that the observed minimum radar intensities are larger than at HH-polarization. This means that a smaller part of the actual intensity distribution function falls below the noise level of -22 dB (Figs. 5a+b, 6a+b, 7a+b).
- **Comparison of C and L band:** The separation of deformed and level ice is easier at L-band in many cases (e. g. Figs 5a-d, 6a-d, 8a+b: brash ice). The intensity contrast between new ice and thicker level ice is slightly larger at C-band in some cases (Figs. 5a-d, 8a+b). From other studies it is known that multi-year and first-year ice can be better distinguished from one another at C-band. Whether C-or L-band images are better suited for sea ice mapping depends on the specific task and on the ice conditions. Further examples can be found in Dierking and Busche (2006) and Dierking and Dall (2007, 2008).
- **Incidence angle (C-band):** The ICESAR data do not indicate any significant incidence angle sensitivities of intensity contrasts between ice types. Only in some cases, the separation of deformed and level ice may improve (Figs. 6a+b).

References

Armstrong, T., B. Roberts, and C. Swithinbank, Illustrated Glossary of Snow and Ice, 2nd Edition, Scott Polar Research Institute, Cambridge, 1973

Dierking, W., and H. Skriver, Change detection for thematic mapping by means of airborne multitemporal polarimetric SAR Imagery, IEEE Trans. Geosc. Remote Sensing, Vol. 40, No. 3, 618-636, March 2002

Dierking, W., and T. Busche, Sea ice monitoring by L-band SAR: An assessment based on literature and comparisons of JERS-1 and ERS-1 imagery, IEEE Trans. Geosc. Remote Sensing, Vol. 44, No. 2, 957-970, April 2006

Dierking, W., and J. Dall, Sea ice deformation status from synthetic aperture radar imagery – Part 1: Comparison of C- and L-band and different polarizations, IEEE Trans. Geosc. Remote Sensing, Vol. 45, No. 11, 3610-3622, Nov. 2007

Dierking, W., and J. Dall, Sea ice deformation status from synthetic aperture radar imagery – Part 2: Effects of spatial resolution and noise level, IEEE Trans. Geosc. Remote Sensing, Vol. 46, No. 8, 2197-2207, Aug. 2008

Oliver, C. J., and S. Quegan, Understanding SAR Images, Boston: Artech House, 1998

Ulaby, F. T., R. K. Moore, and A. K. Fung, 1982, Microwave Remote Sensing, Vol. 2:…, Artech House, Dedham, MA, 1982

Rignot, E., and R. Kwok, Characterization of spatial statistics of distributed targets in SAR data, Int. J. Remote Sensing, Vol. 14, No. 2, pp. 345-363, 1993

Nghiem, S. V., and C. Bertoia, Study of multi-polarization C-band backscatter signatures for Arctic sea ice mapping with future satellite SAR, Can. J. Rem. Sensing, Vol. 27, No. 5, pp. 387-402, 2001

Mäkynen, M., and M. Hallikainen, Investigation of C- and X-band backscattering signatures of Baltic Sea ice, Int. J. Remote Sensing, Vol. 25, No. 11, pp. 2061-2086, 2004

Scheuchl, B., D. Flett, R. Caves, and I. Cumming, Potential of Radarsat-2 data for operational sea ice monitoring, Can. J. Remote Sensing, Vol. 30, No. 3, pp. 448-461, 2004

Sandven, S., O. M. Johannessen, M. W. Miles, L. H. Pettersson, and K. Kloster, Barents Sea seasonal ice zone features and processes from ERS-1 synthetic aperture radar: Seasonal Ice Zone Experiment 1992, J. Geophys. Res., Vol. 104, No. C7, pp. 1584315857, 1999

Onstott, R., SAR and Scatterometer Signatures of Sea Ice, in: Carsey, F. (ed.), Microwave Remote Sensing of Sea Ice, Geophysical Monograph 68, American Geophysical Union, pp. 73-104, 1992

Appendix 1: SAR and optical imagery

This appendix provides information about the available images from the ESAR and the Color Line Scanner (CLS). A few ESAR scenes were not considered for the analysis. For these ones, no complementary SAR images measured at the different mode and/or from the CLS were available. The images are grouped according to the test sites from which they originate. For each test site, the original ESAR images at C- and L-band are shown together as they were provided by DLR. On March 19, L-band images were not acquired. C-band data were measured in dual-polarization mode, L-band data in quad-polarization mode. The colour layer scheme used is either R:HV, G:HH, B:HH or R:VH, G:VV, B:VV at C-band and R:X-pol., G:HH, B:VV for L-band imagery. On March 20, C-band HH-HV data were not acquired. The colour stretch was carried out separately for each image according to the standard setting of the ENVI software package, which was utilized for image analyses. The standard setting results in large image contrasts excluding outliers. Hence, the visual perceptibility of details is optimal, but the colour stretches of all images are not normalized relative to one another. Following each pair or triplet of original DLR images, two C-band image segments resulting from re-processing the data (as described in section 2 of the report) are shown together with the corresponding optical data. The CLS images were delivered in segments of 2048 x 5000 pixels. In order to match their geometry approximately with the SAR images they had to be compressed in across-track direction (by a factor of 0.1 to 0.2 for March 16 because of the low flight altitude, and by 0.7 to 0.8 for the other days). Note that the compressed versions of the optical data are only utilized for this appendix. The colour stretch is also fixed individually for each CLS segment. Occasionally, geometric distortions are visible in the optical images, which were not removed. The edge positions of the area covered by the CLS scanner is indicated by white solid lines in the ESAR images for March 18, 19, and 20. The assignment of selected spots in the optical images to the corresponding positions in the SAR images is provided by arrows if it is difficult to match both image types visually. This may be the case if the time difference between image types (optical/SAR) is large which often means that the ice drift and the resulting changes of the ice cover are not negligible. The times at which optical and SAR data were measured are listed in Table A1.

Table A1: Acquistion times of ICESAR imagery over sea ice

Mode / Date	16/03	18/03	19/03	20/03
C-VV-VH	12:17 12:32 S to N	14:40 14:57 SSW to NNE	12:21 12:30 S to N	11:57 12:07 S to N
C-HH-HV	13:32 13:46 S to N	15:30 15:48 SSW to NNE	12:37 12:47 N to S	
L-QUAD	12:56 13:10 N to S	15:06 15:23 NNE to SSW		12:14 12:26 N to S
Optical	11:40 12:22 S to N	14:32 15:23 SSW to NNE	12:09 12:27 S to N	12:26 12:41 S to N

Date: March 16, Location: Storfjord (from N to S)

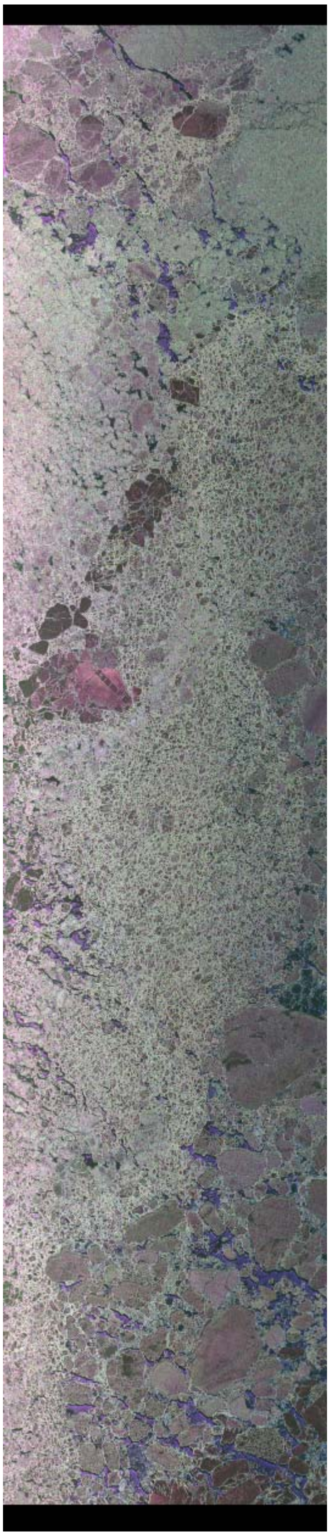

icesar0202x1_t01 (L-Band)
(L-Band Quad-Pol.)

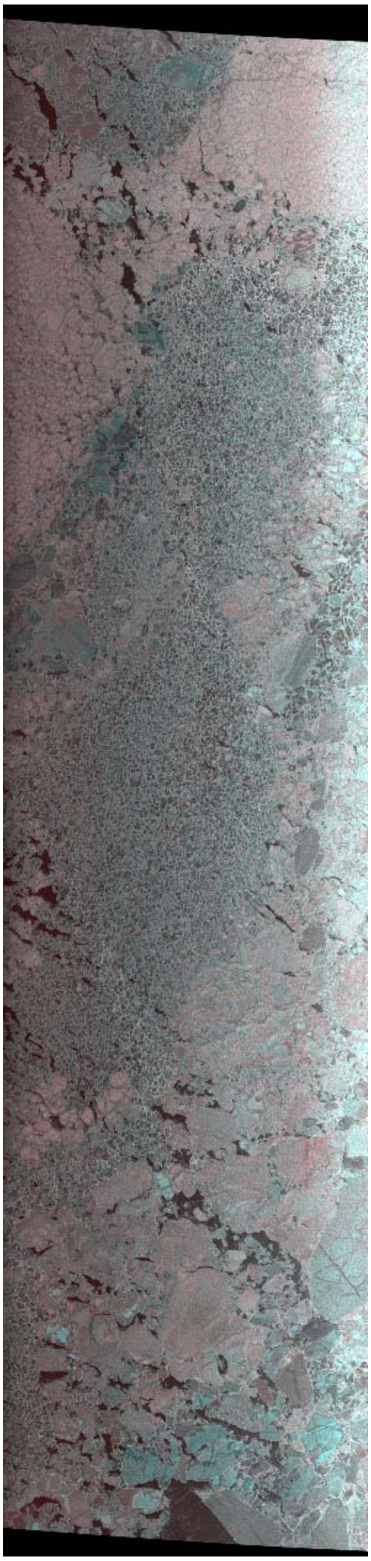

icesar0203x1_t04
(C-Band HH, HV)

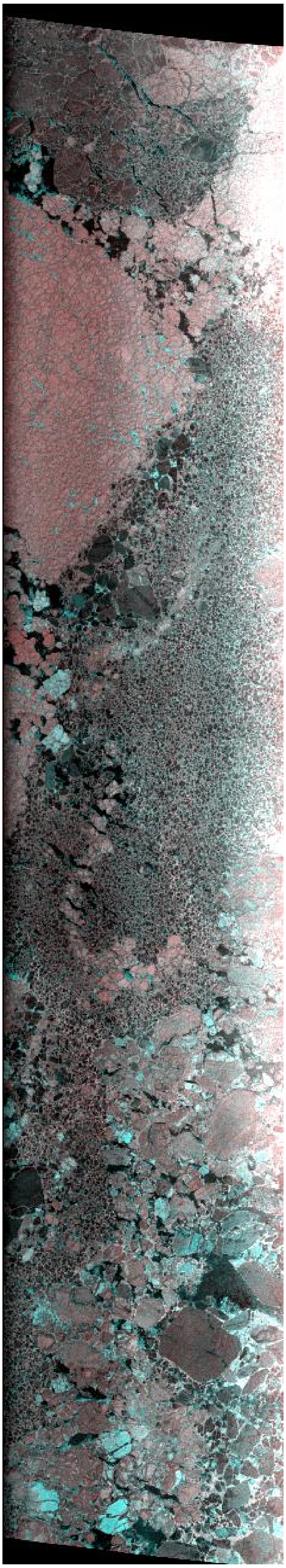

icesar0201x1_t01
(C-Band VV, VH)

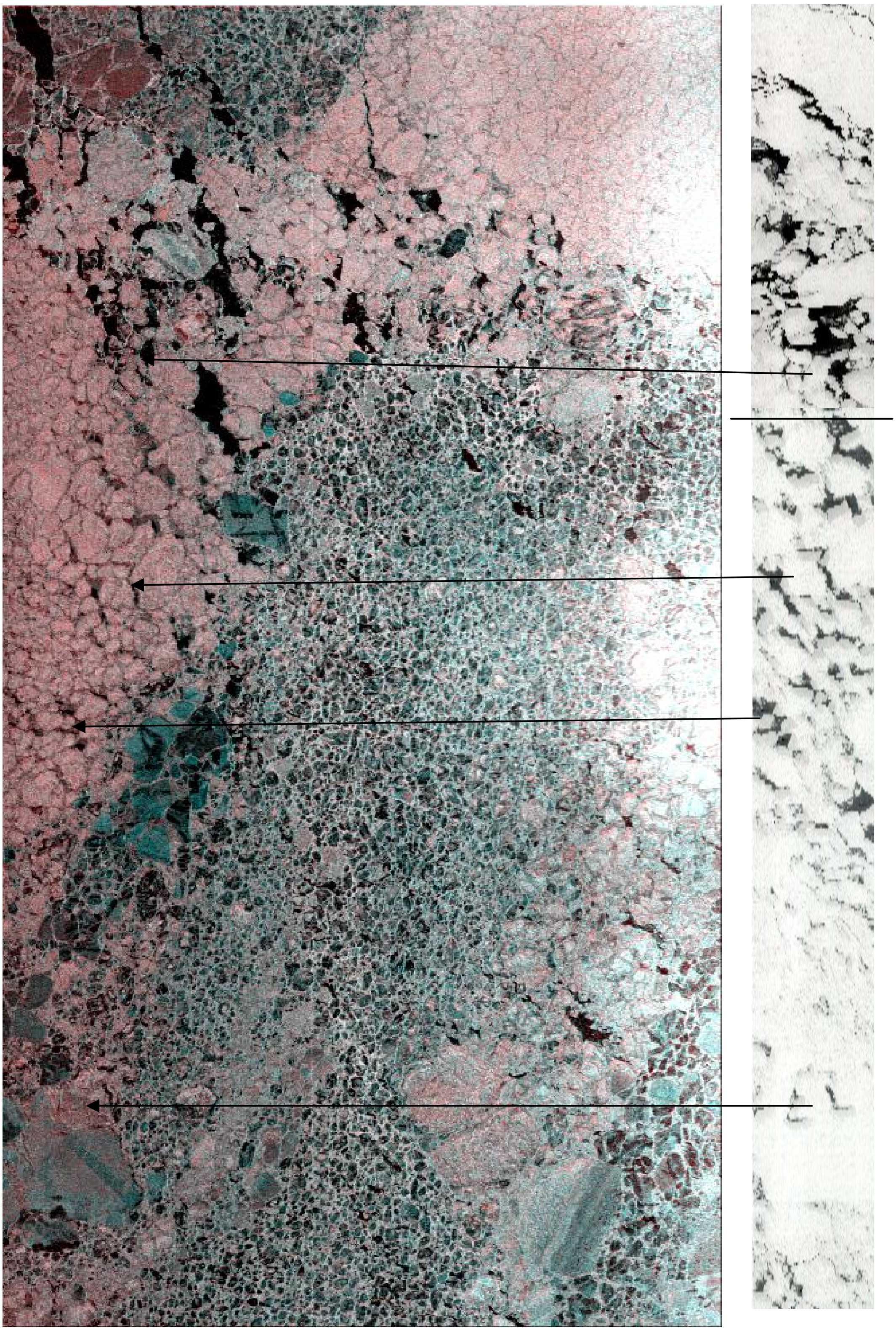

1603CH1_S2, VIS: upper1603_VIS_25, lower 1603_VIS_24

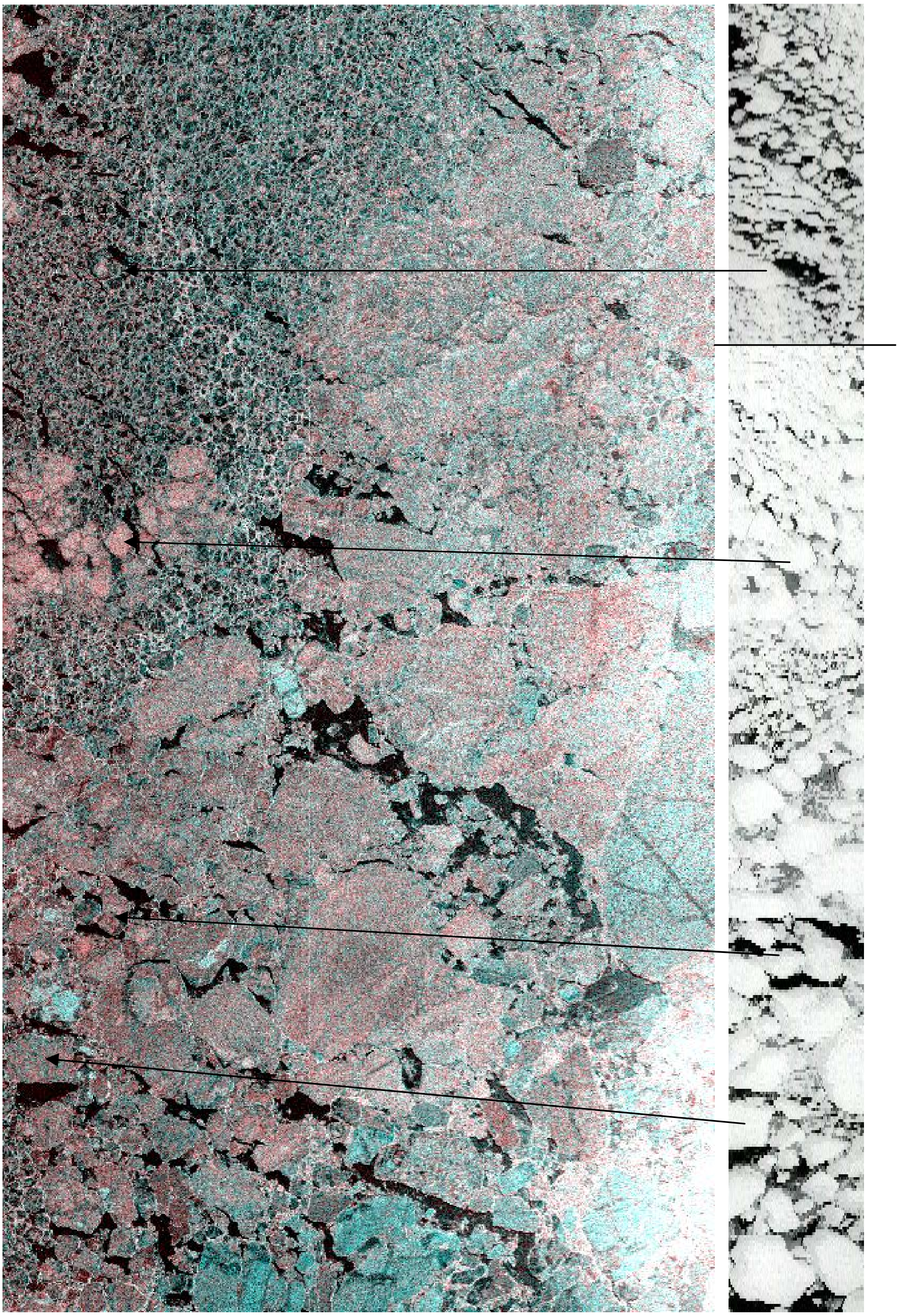

1603CH1_S1, VIS: upper 1603_VIS_24,lower 1603_VIS_23

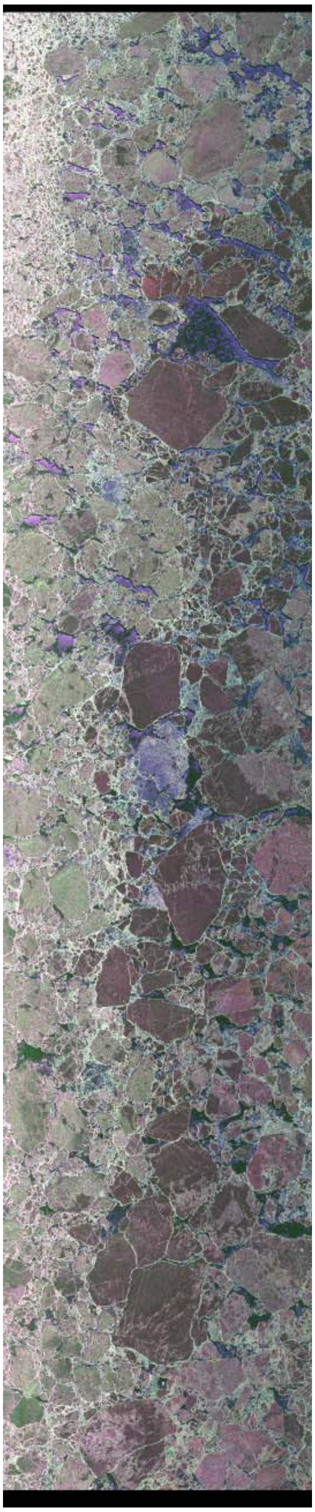

icesar0202x1_t02
(L-Band Quad-Pol.)

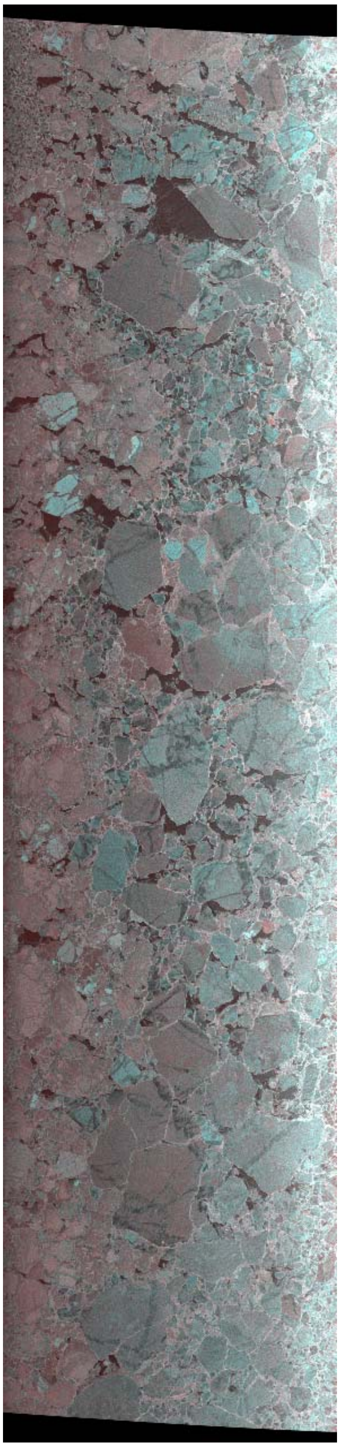

icesar0203x1_t05
(C-Band HH, HV)

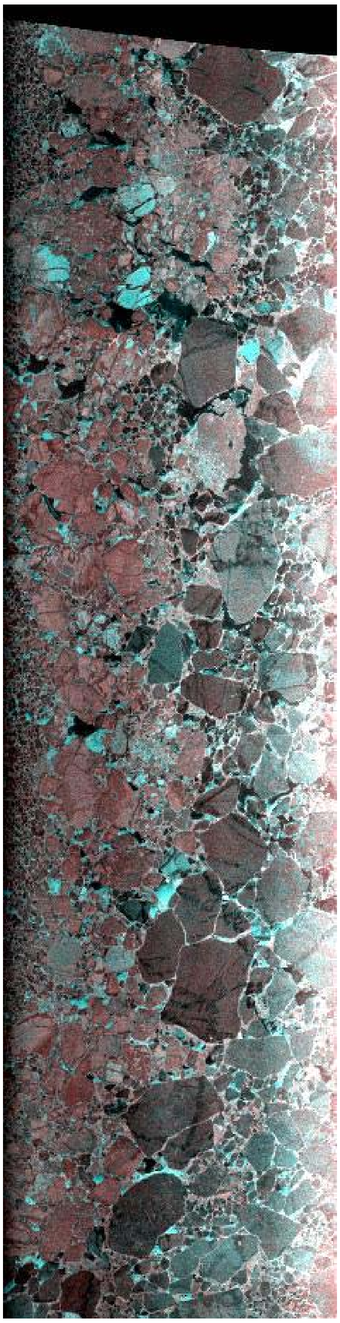

icesar0201x1_t02
(C-Band VV, VH)

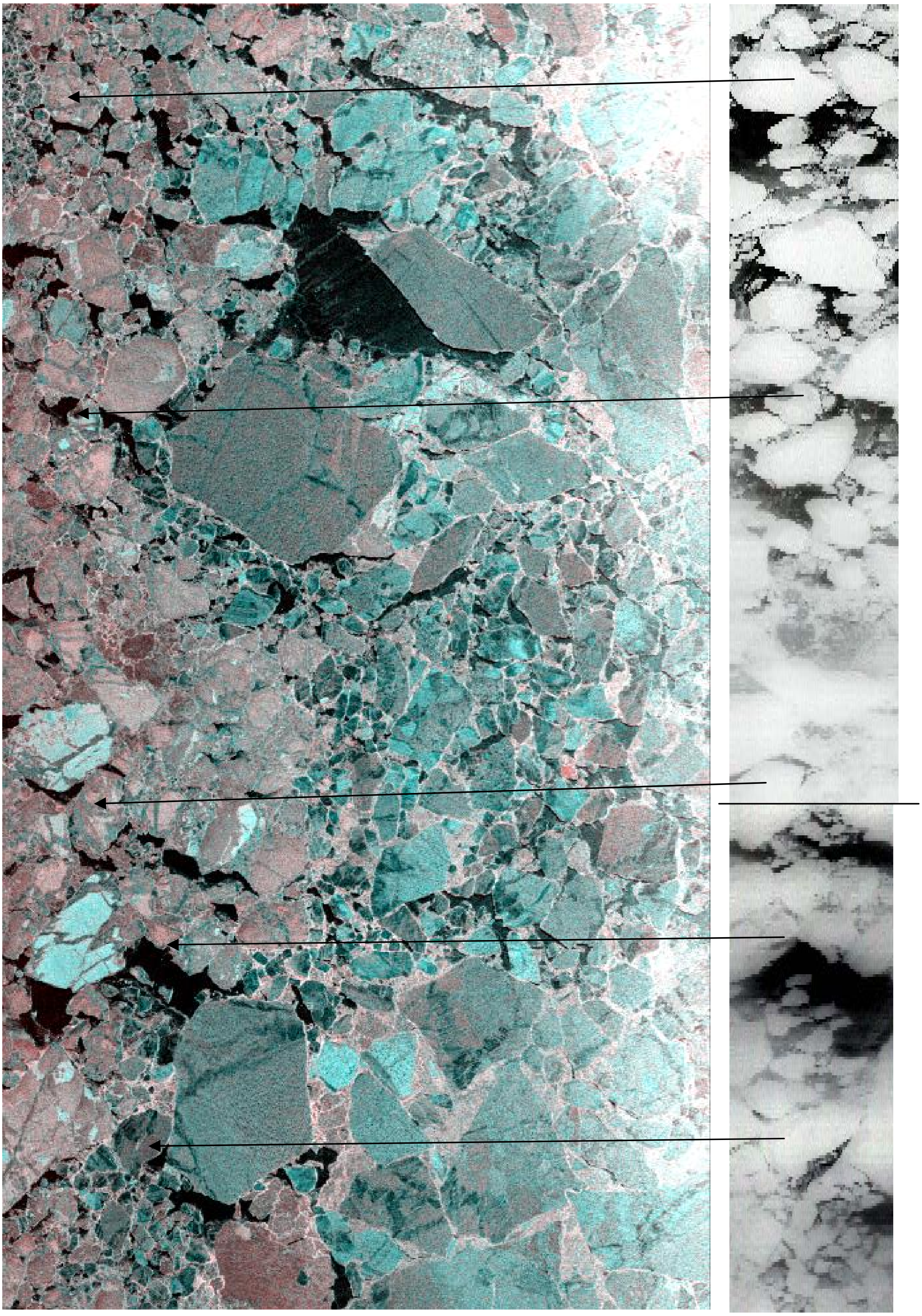

1603CH2_S2, VIS: upper 1603_VIS_23, lower 1603_VIS_22

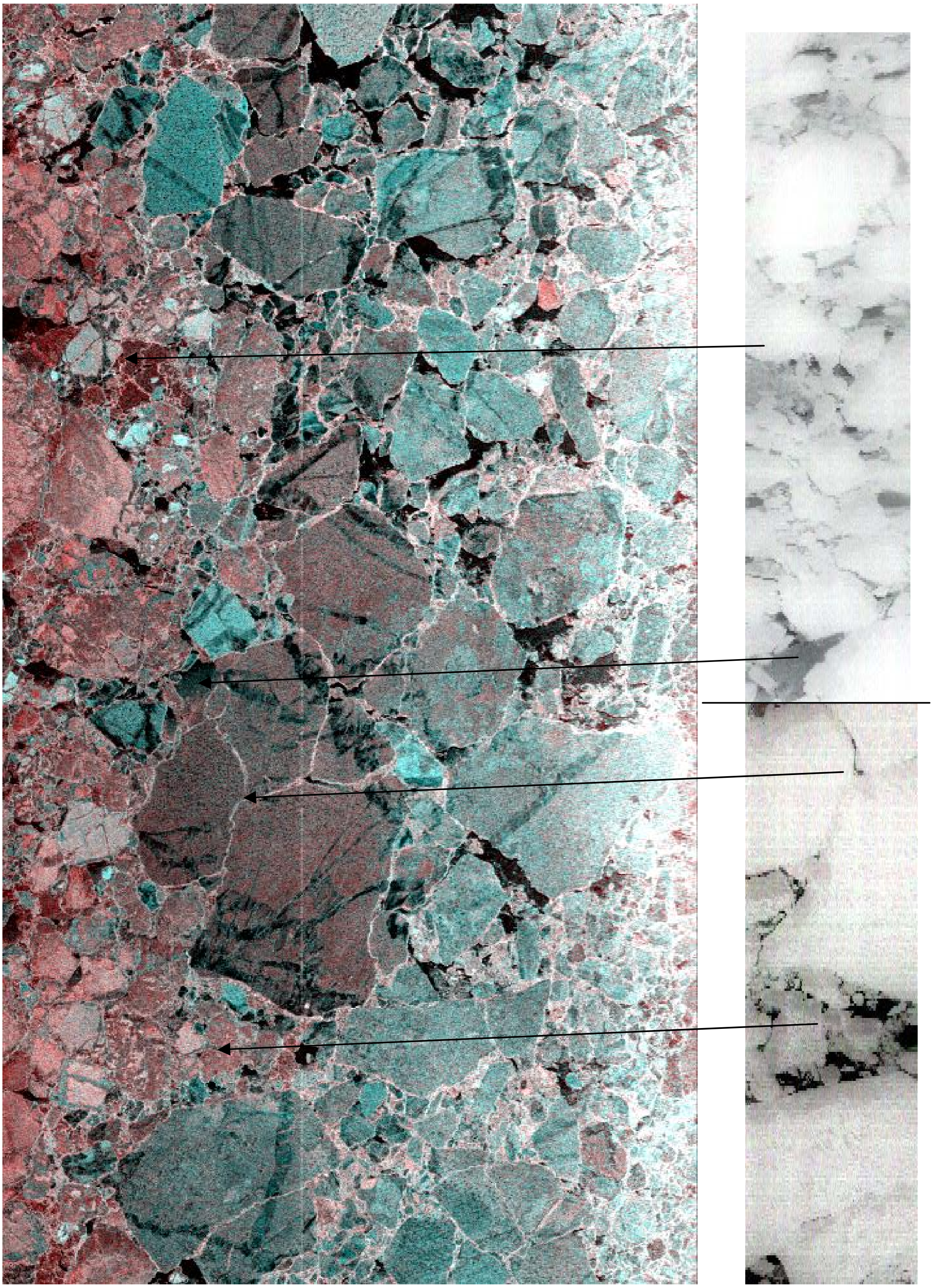

1603CH2_S1, VIS: upper 1603_VIS_22, lower 1603_VIS_21

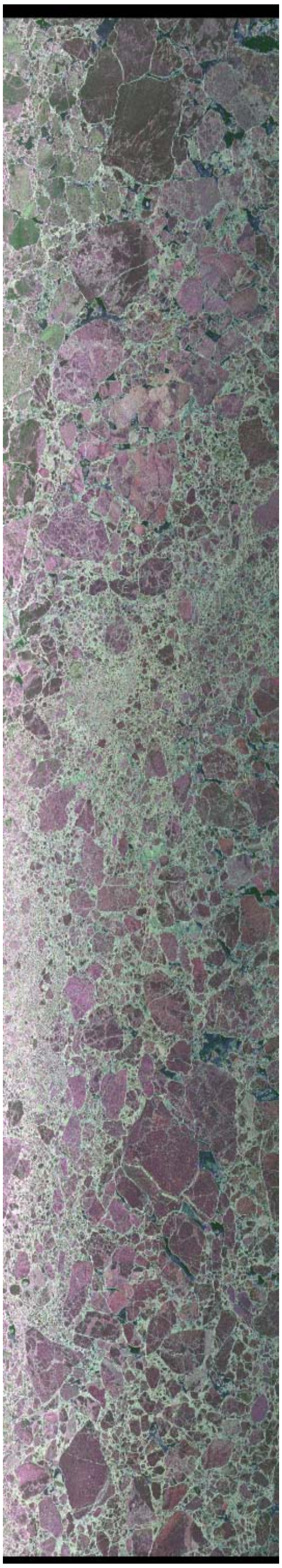

icesar0202x1_t03
(L-Band Quad-Pol.)

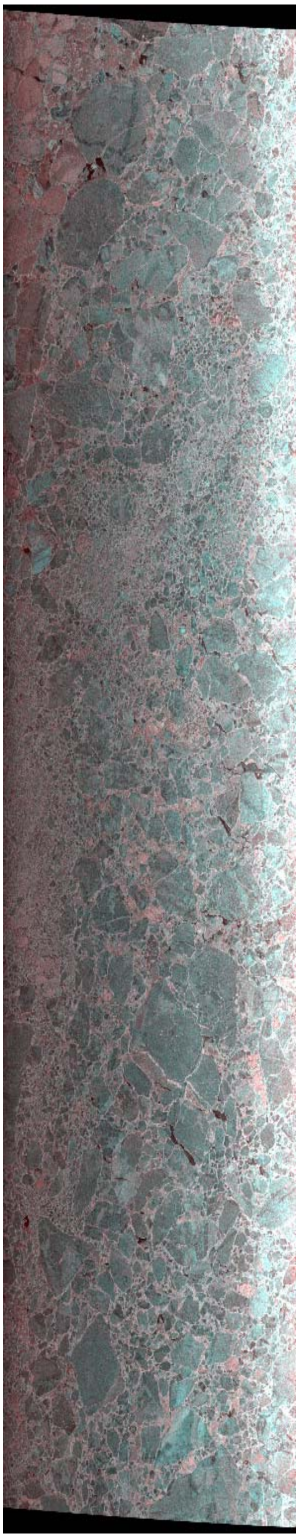

icesar0203x1_t06
(C-Band HH, HV)

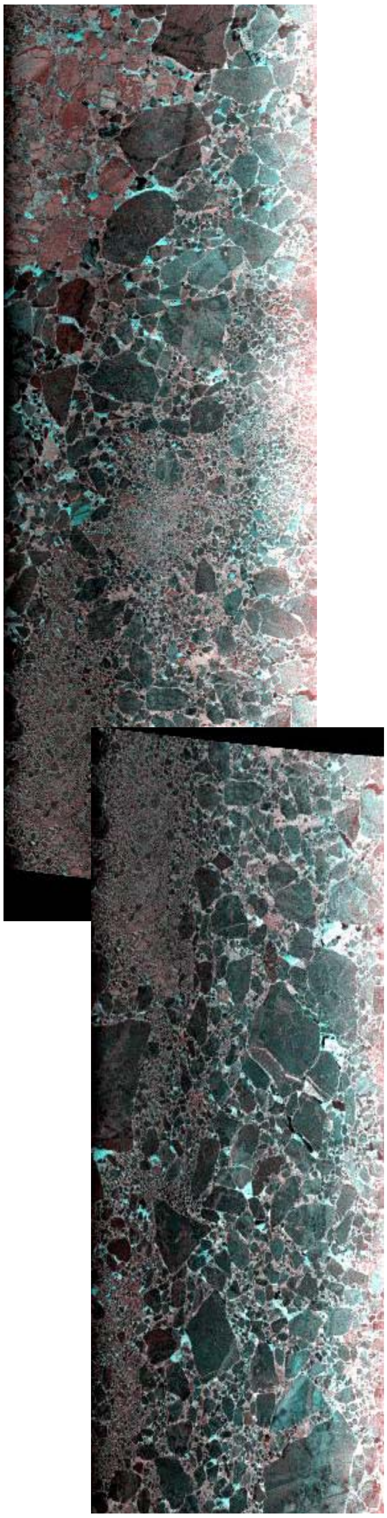

icesar0201x1_t02 (upper)
icesar0201x1_t03 (lower)
(C-Band VV, VH)

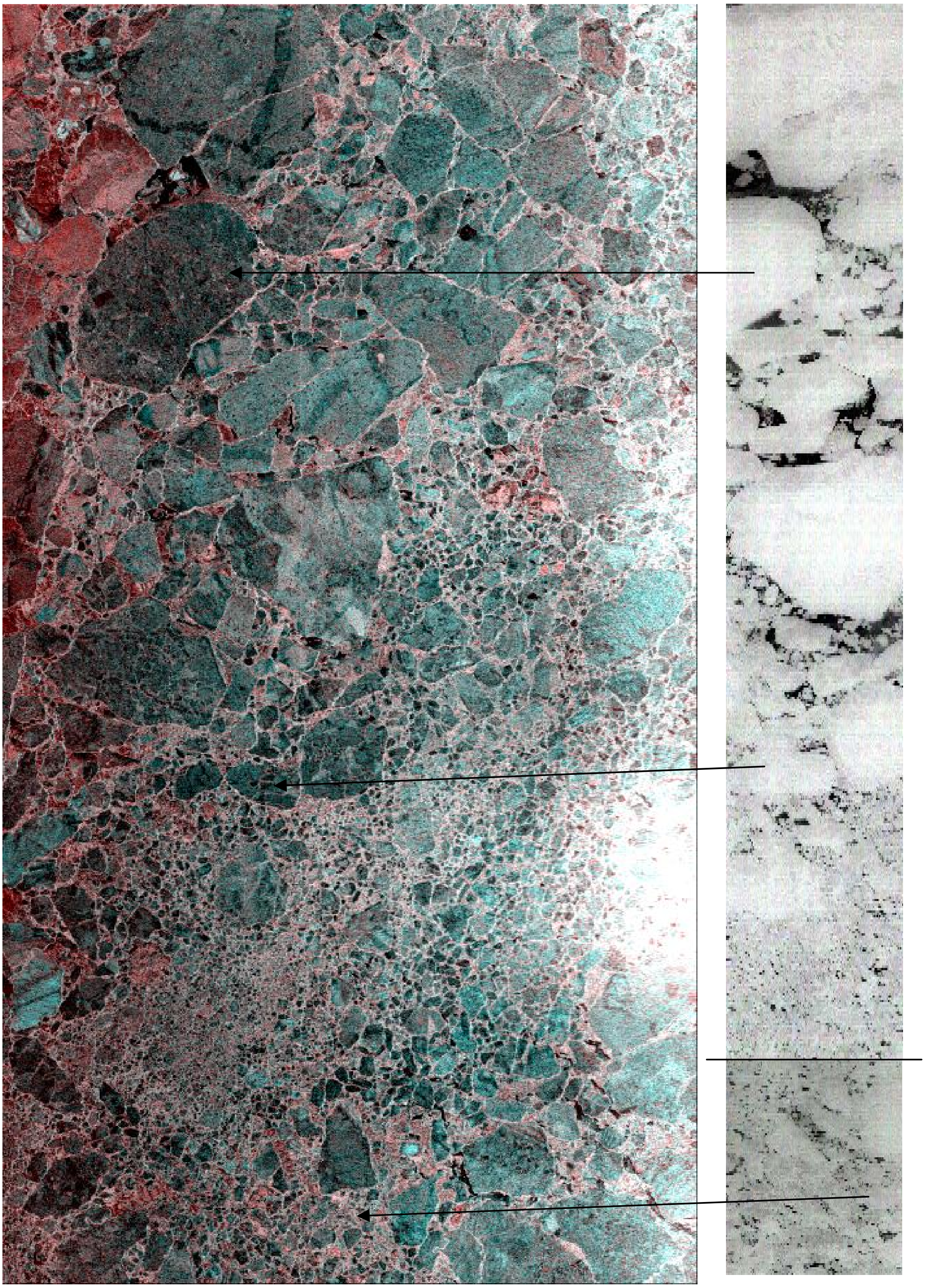

1603CH3_S2, VIS: upper 1603_VIS_21, lower 1603_VIS_20

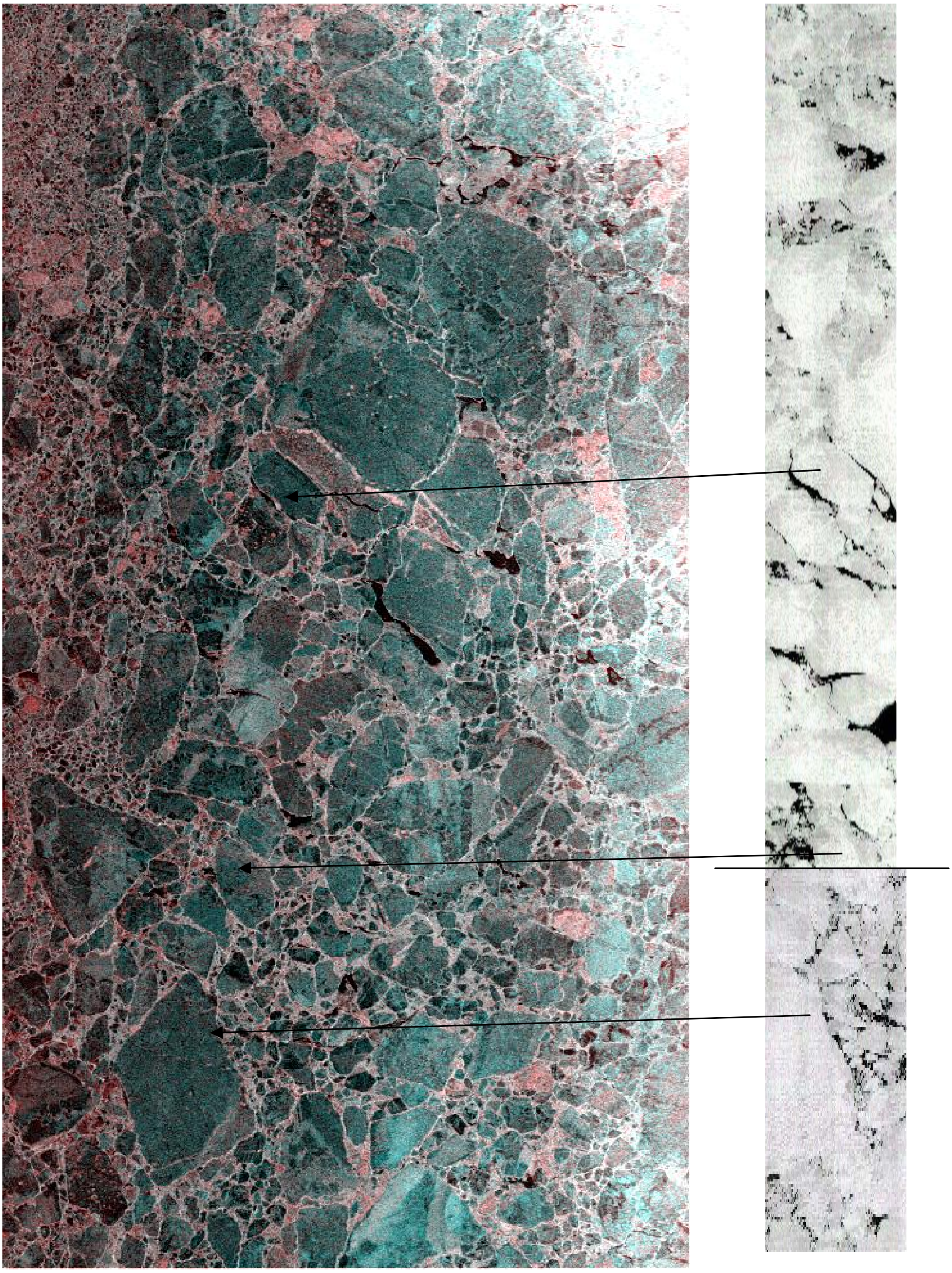

1603CH3_S1, VIS: upper 1603_VIS_20, lower 1603_VIS_19

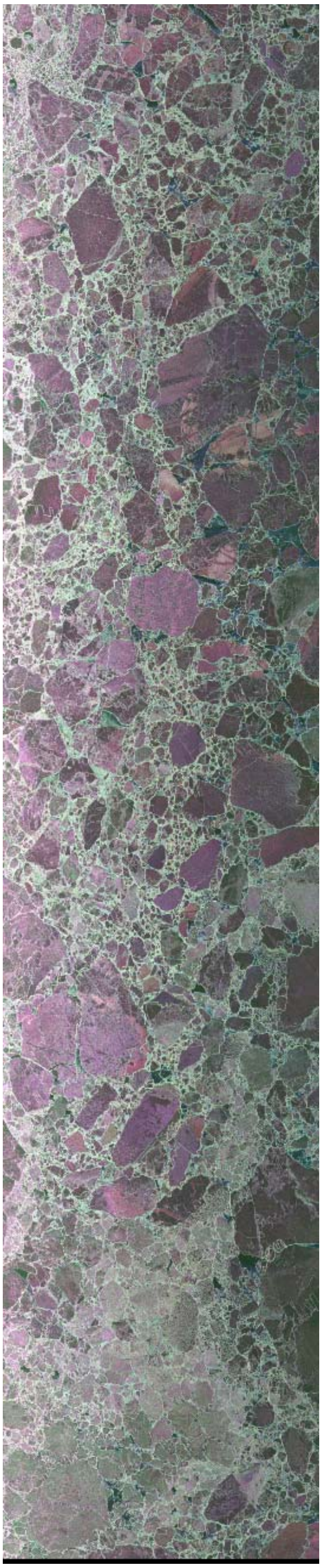

icesar0202x1_t04
(L-Band Quad-Pol.)

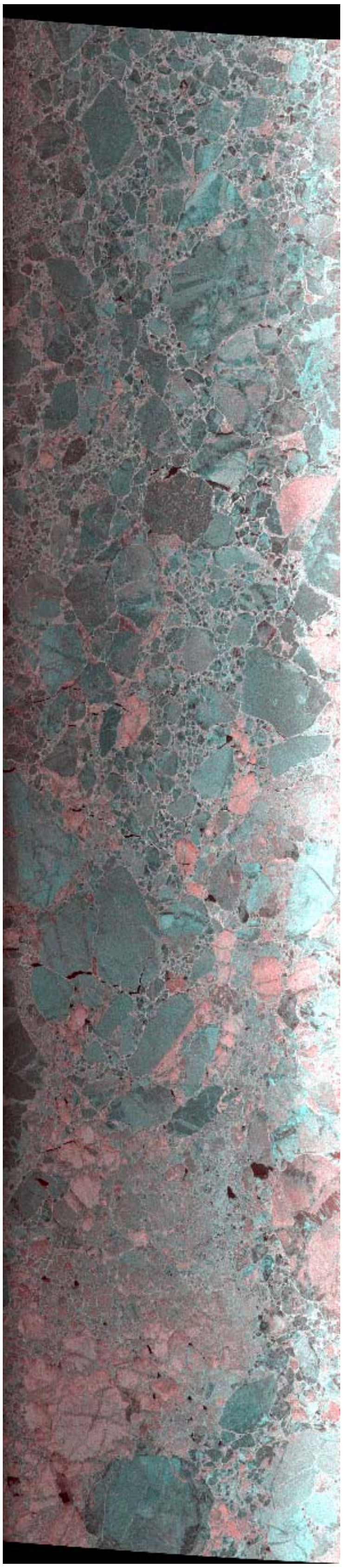

icesar0203x1_t07
(C-Band HH, HV)

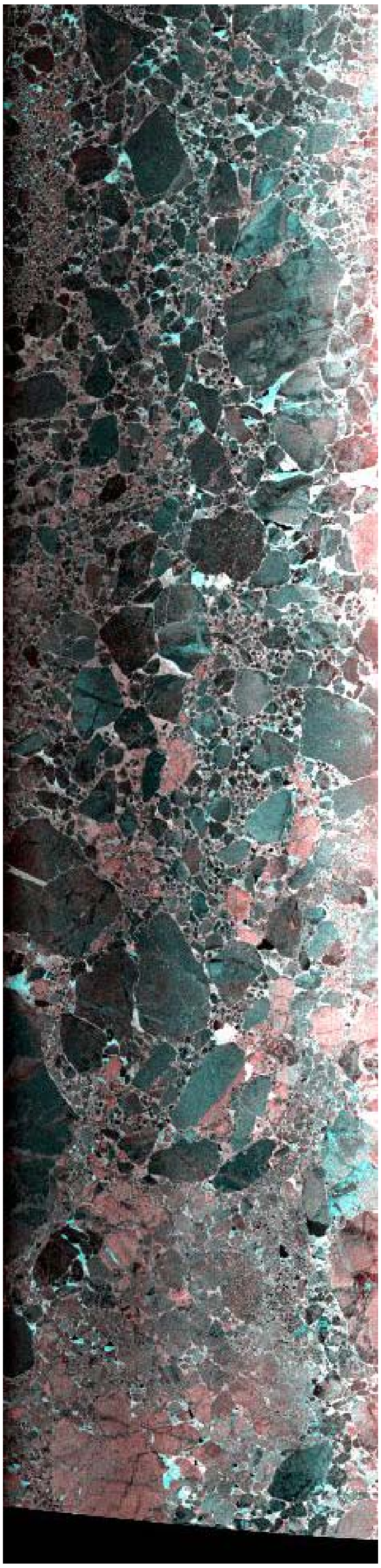

icesar0201x1_t03
(C-Band VV, VH)

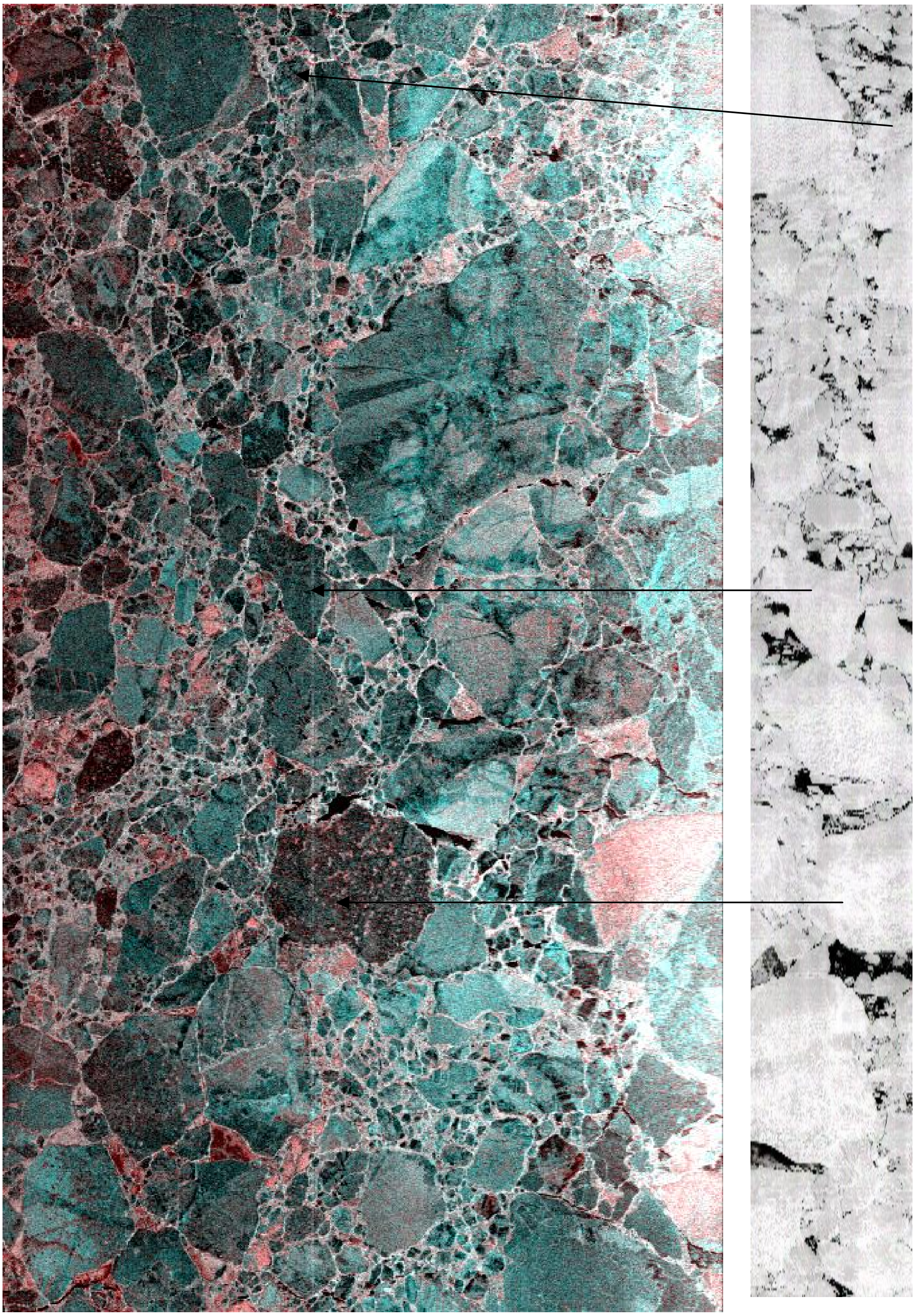

1603CH4_S2, VIS: 1603_VIS_19

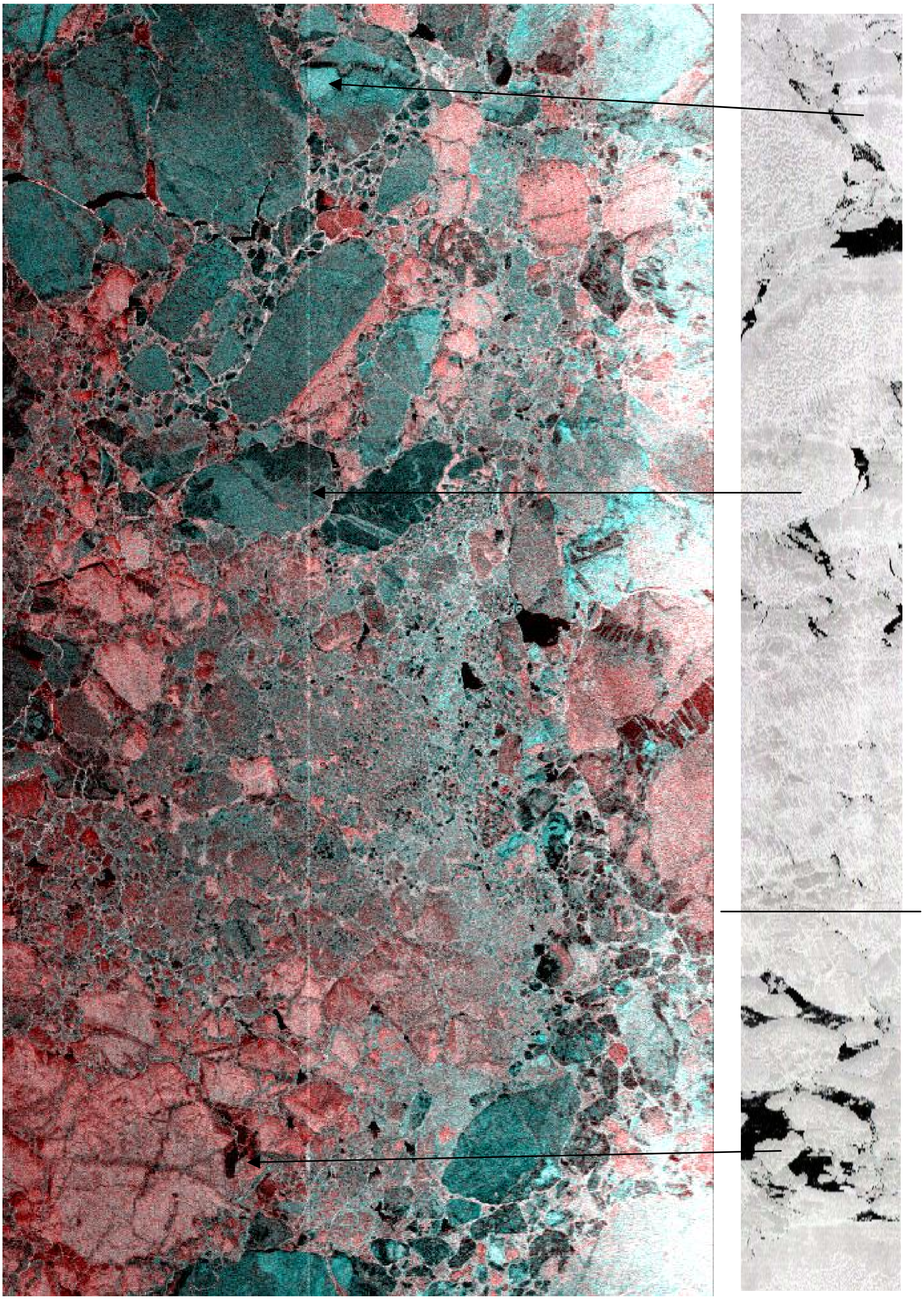

1603CH4_S1, VIS: upper 1603_VIS_18, lower 1603_VIS_17

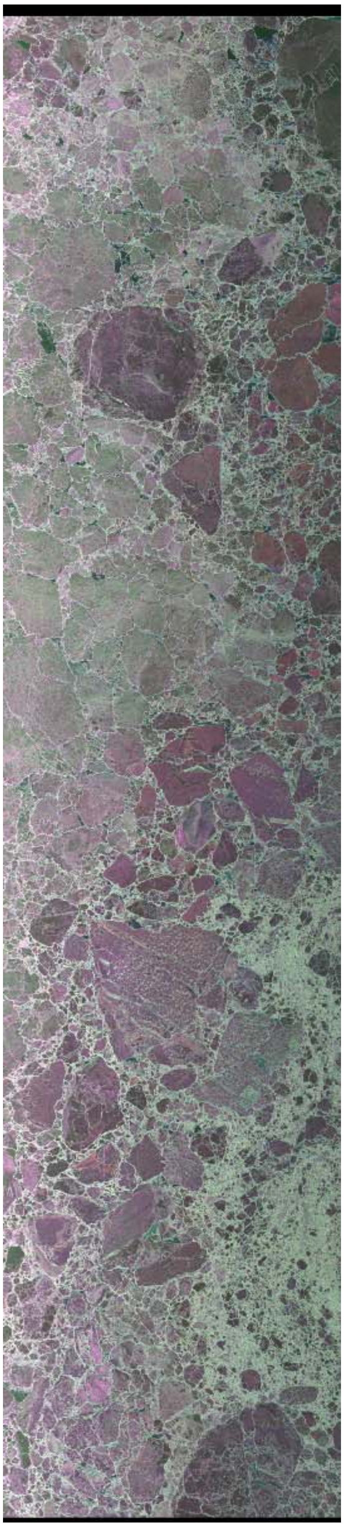

icesar0202x1_t05
(L-Band Quad-Pol.)

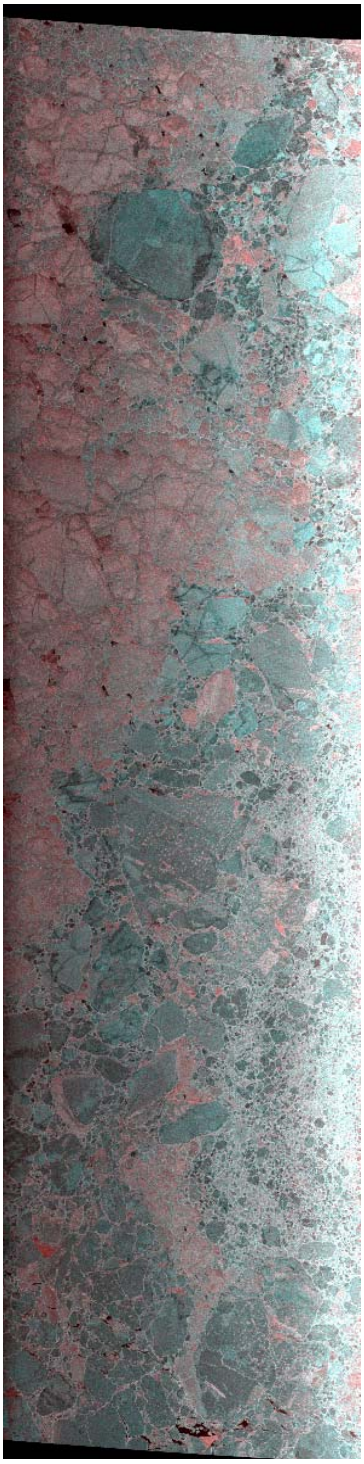

icesar0203x1_t08
(C-Band HH, HV)

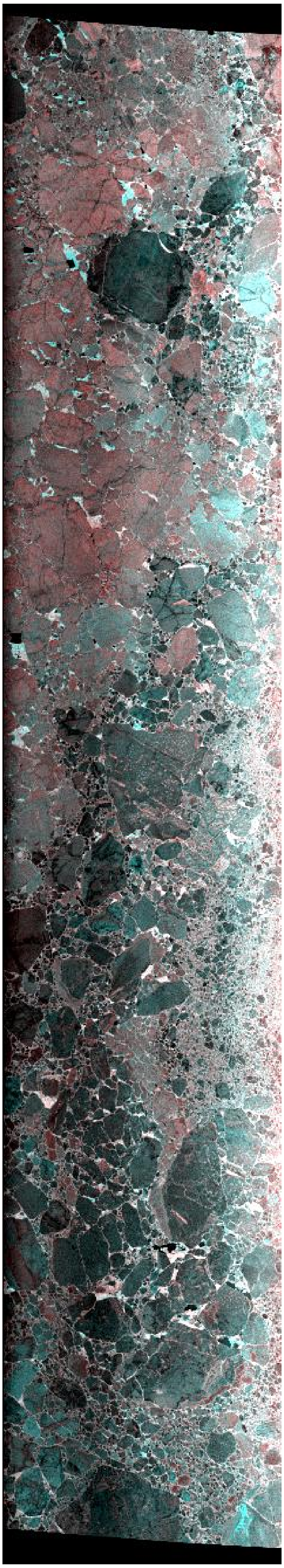

icesar0201x1_t04
(C-Band VV, VH)

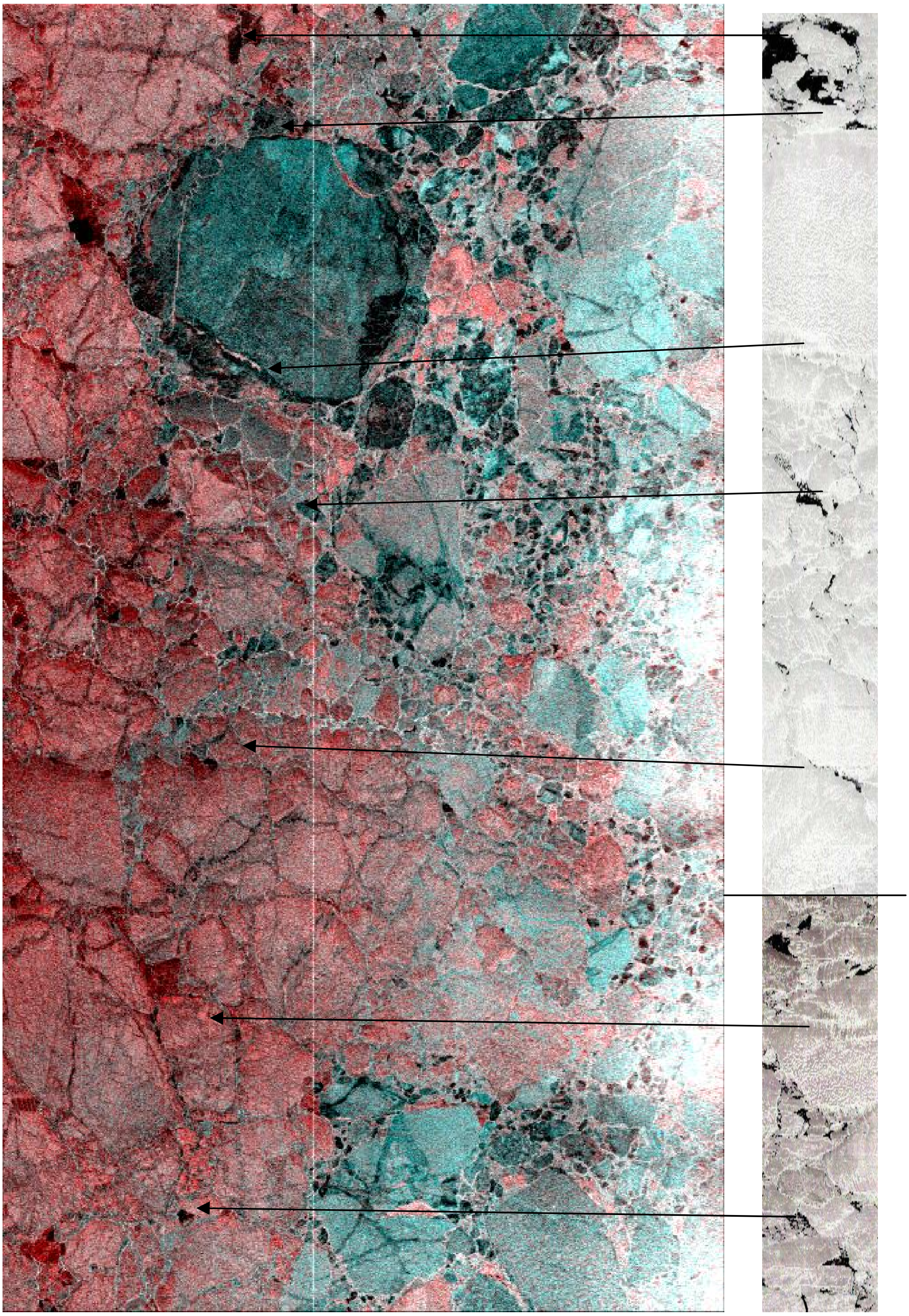

1603CH5_S2, VIS: upper 1603_VIS_17, lower 1603_VIS_16

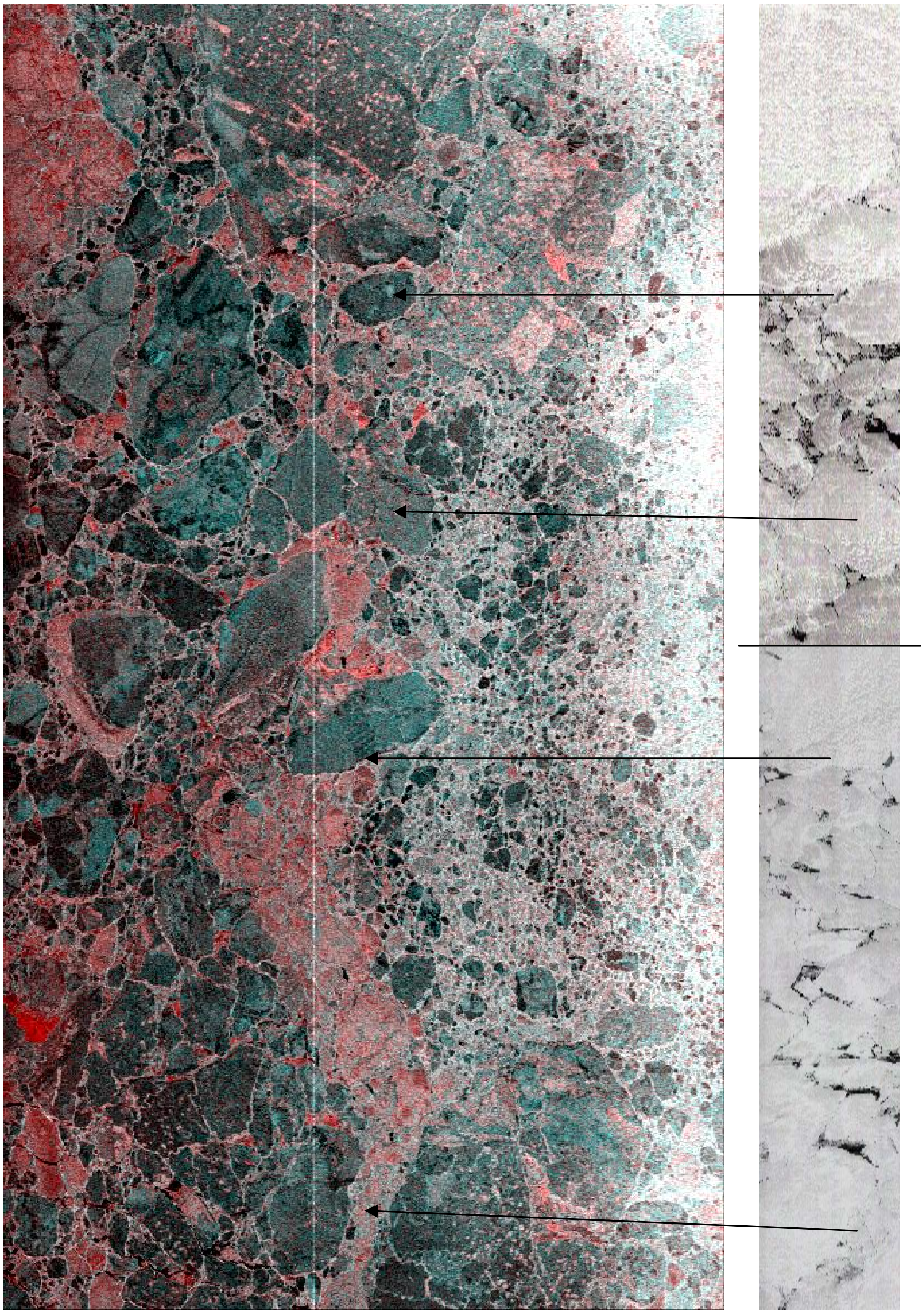

1603CH5_S1, VIS: upper 1603_VIS_16, lower 1603_VIS_15

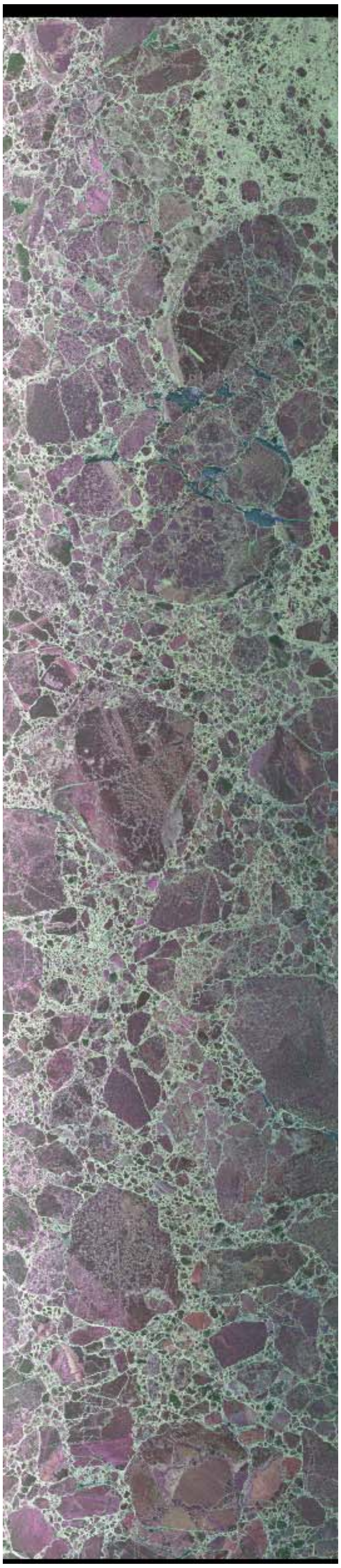

icesar0202x1_t06
(L-Band Quad-Pol.)

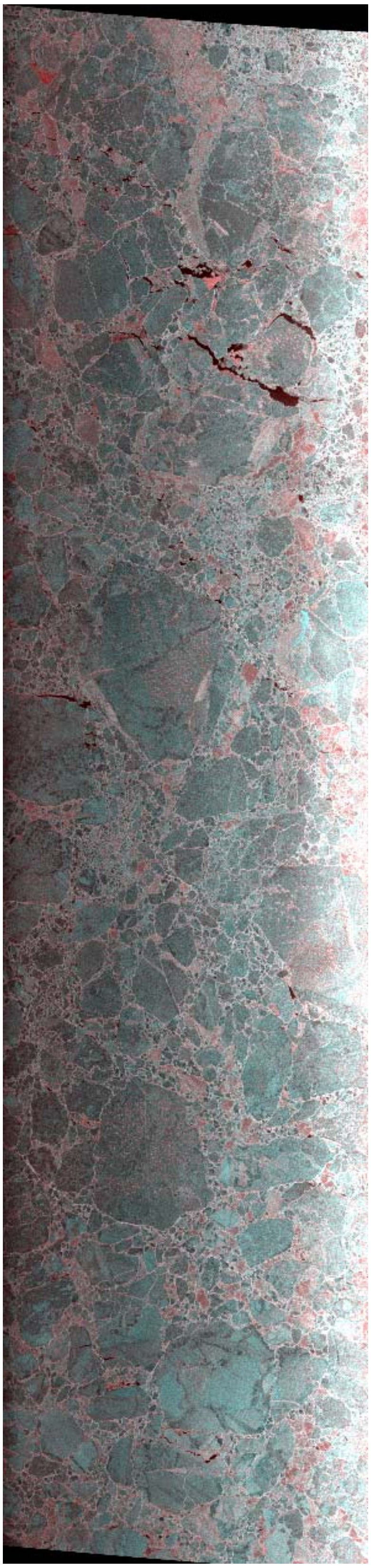

icesar0203x1_t09
(C-Band HH, HV)

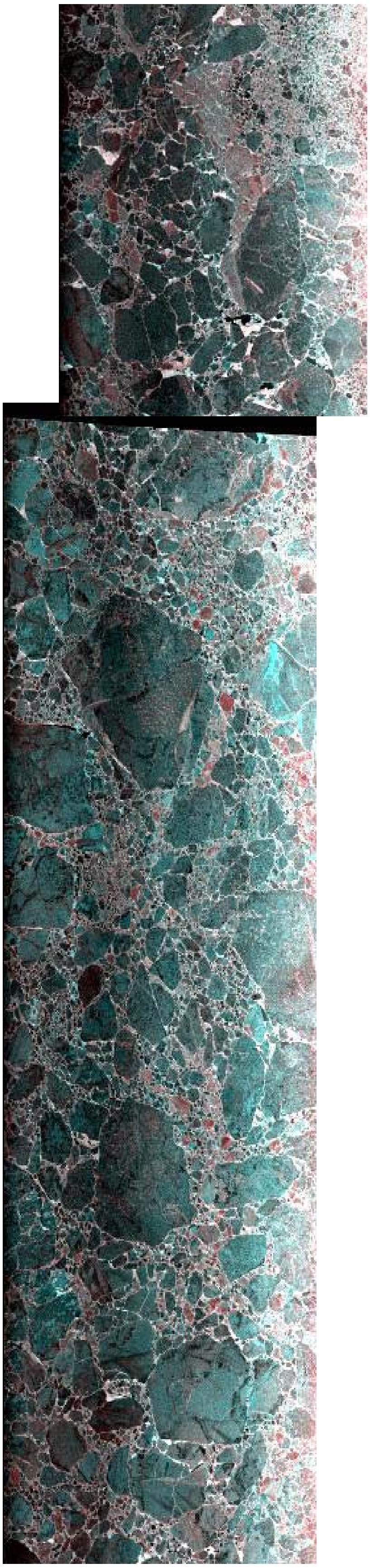

icesar0201x1_t04 (upper)
icesar0201x1_t05 (lower)
(C-Band VV, VH)

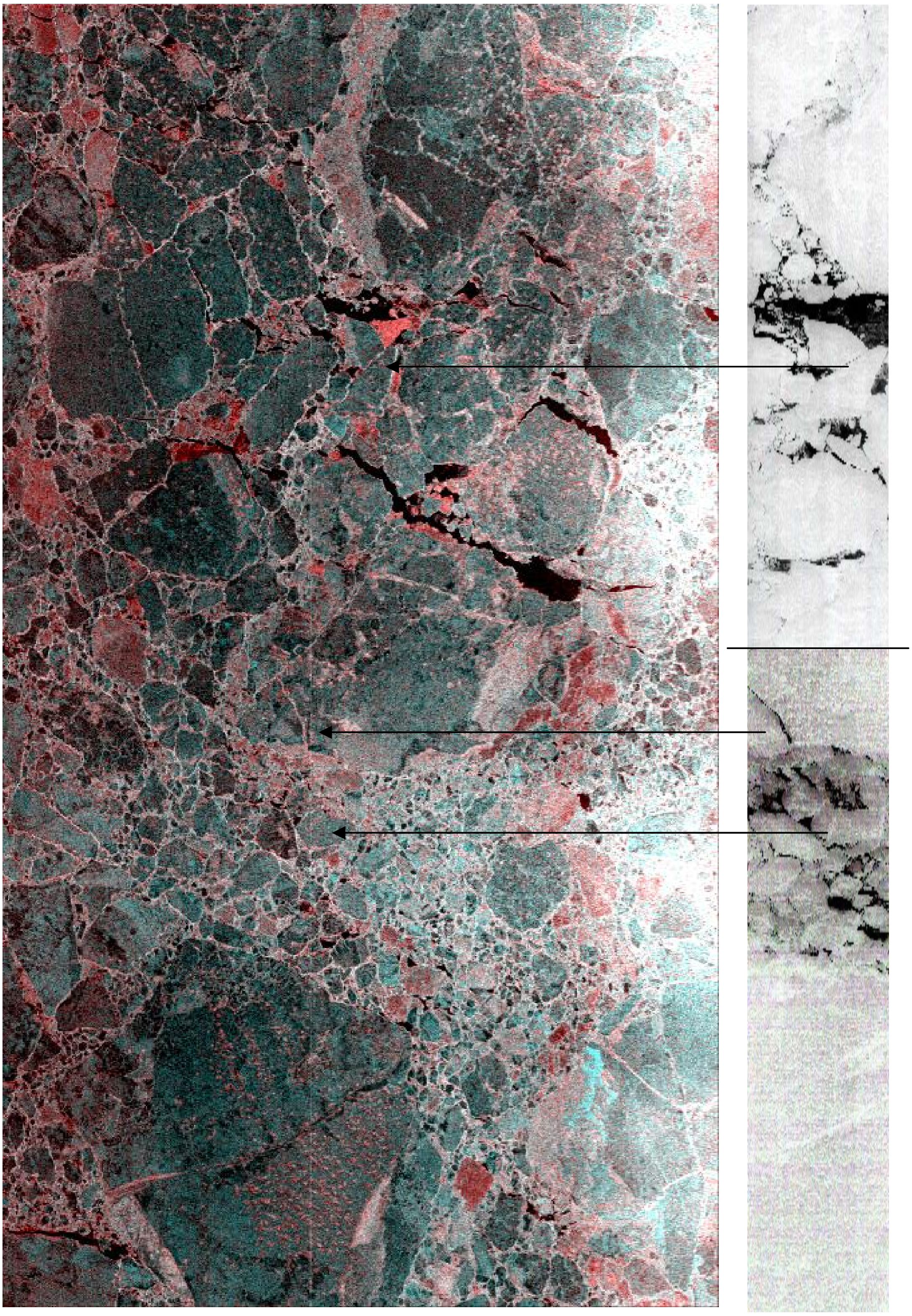

1603C6_S2, VIS: upper 1603_VIS_15, lower 1603_VIS_14

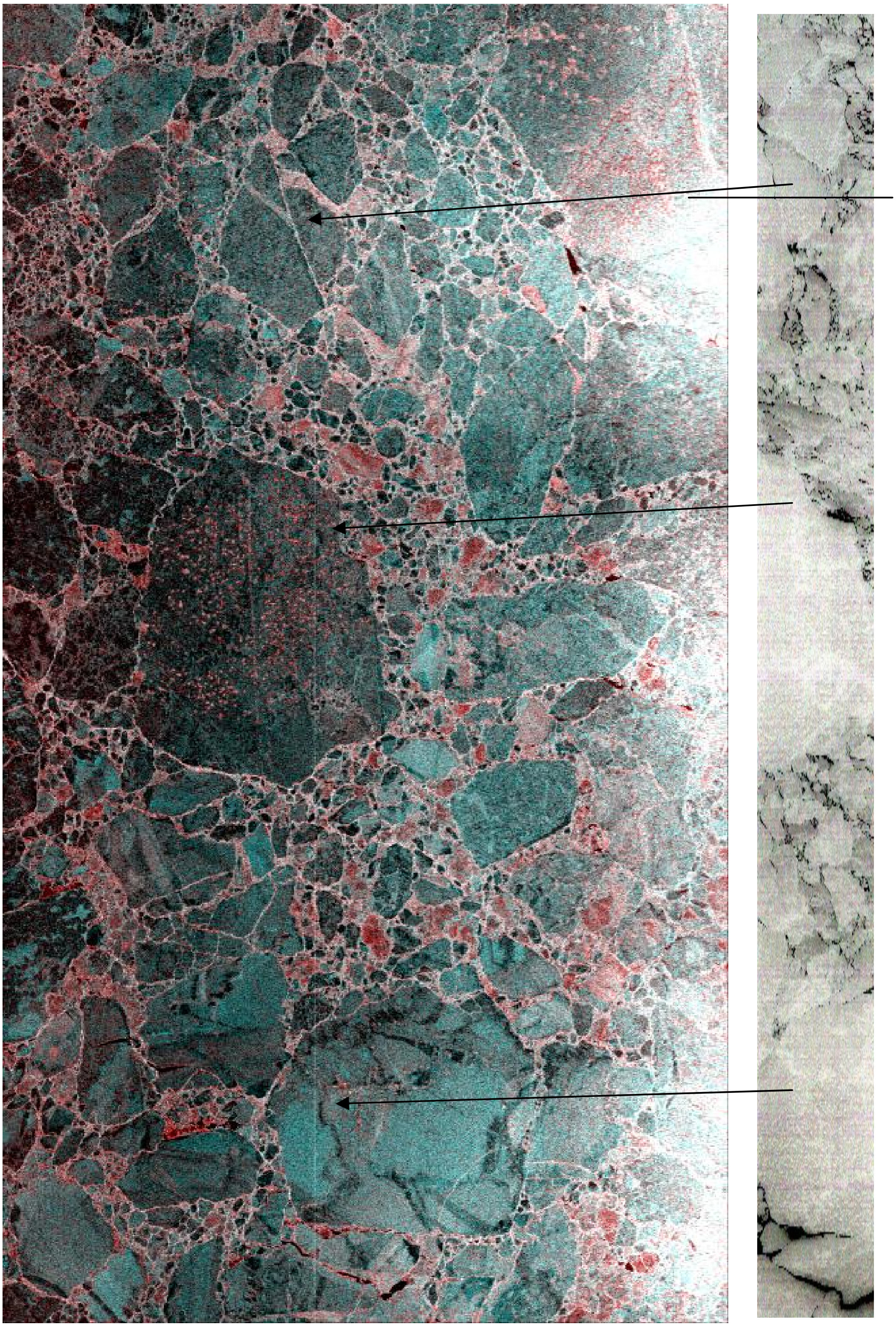

1603C6_S1, VIS: upper 1603_VIS_14, lower 1603_VIS_13

Date: March 18, Location: Barents Sea (from SSW to NNE)

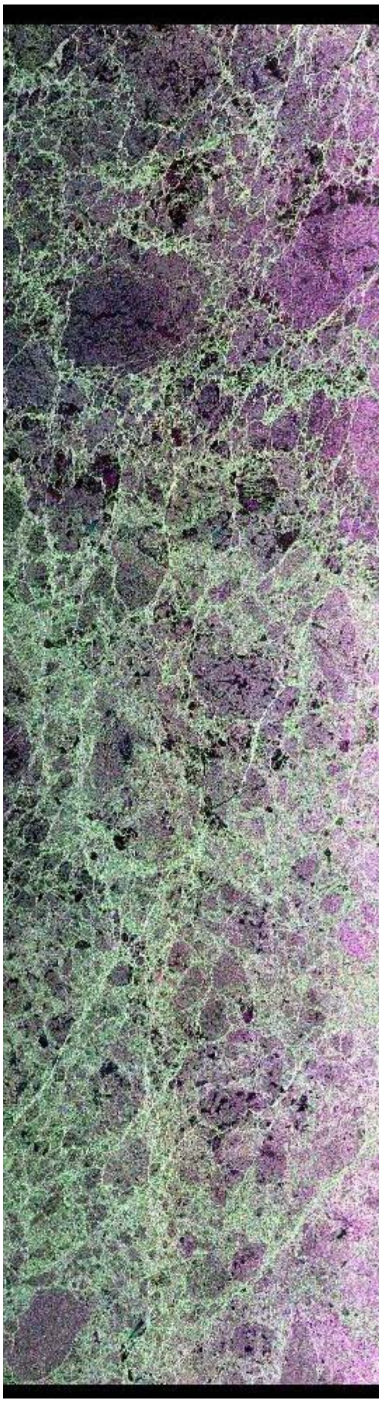

i07icesar0302x1_t01
Upper image edge: NNE
Lower image edge: SSW

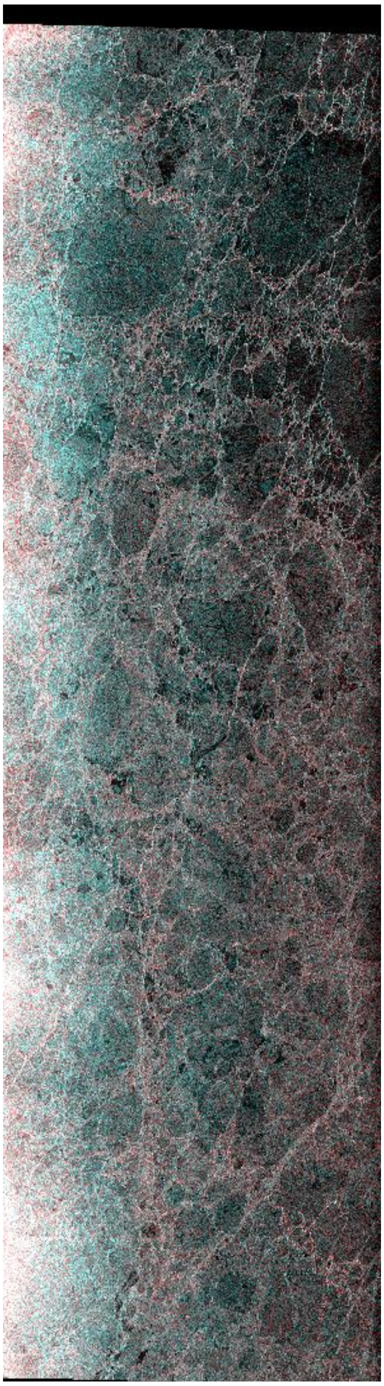

i07icesar0301x1_t01

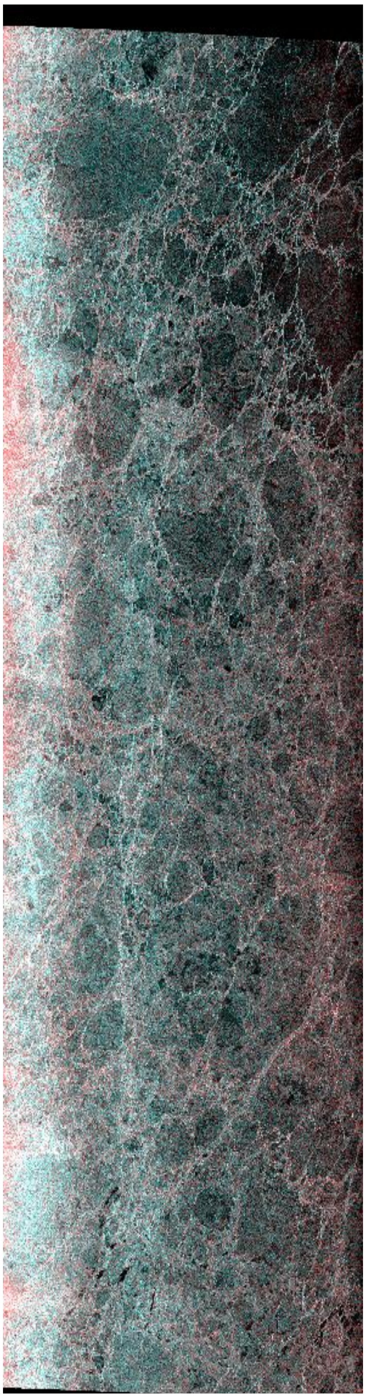

i07icesar0303x1_t01

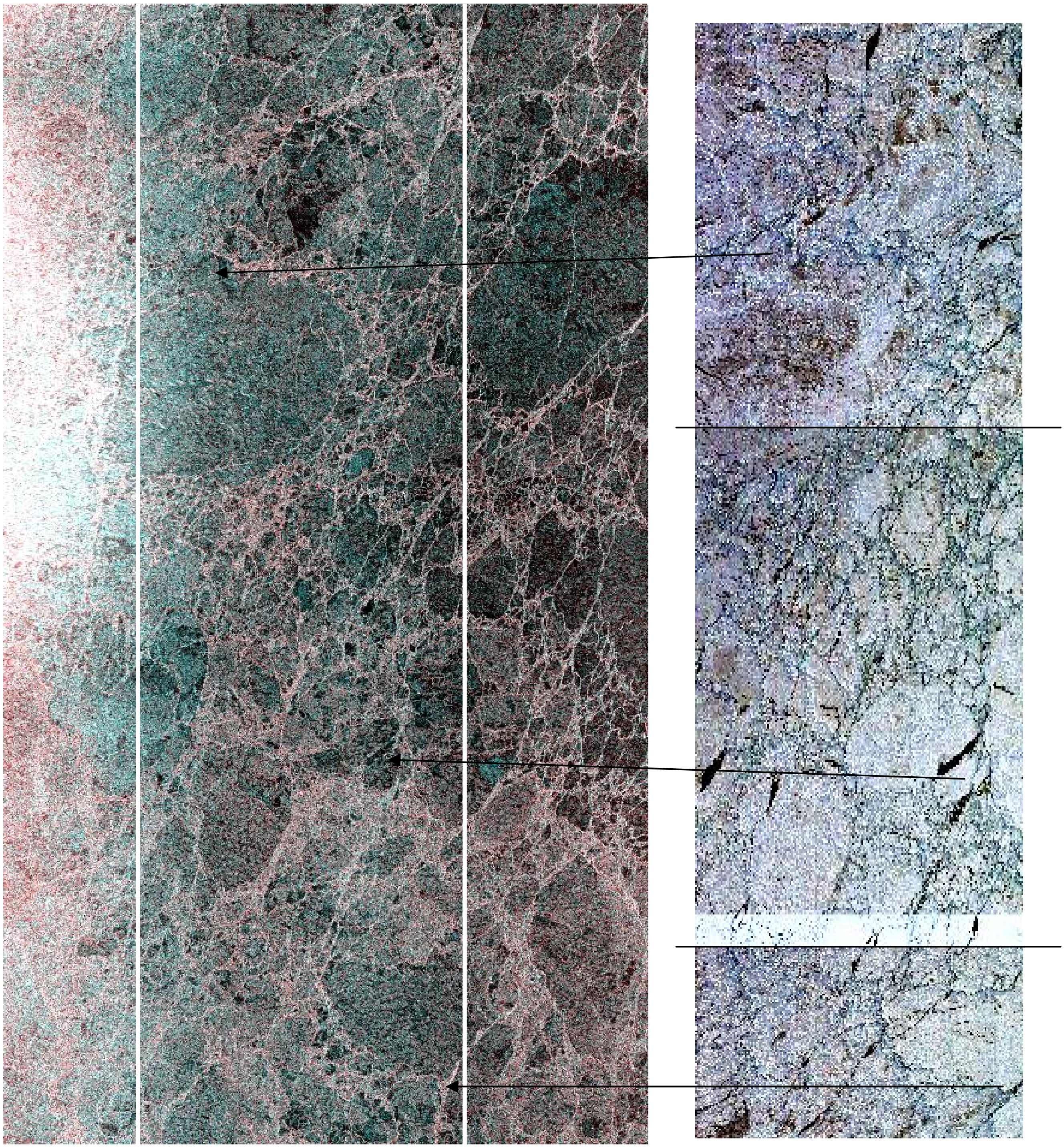

1803CV1_S1, VIS: lower 1803_VIS_07a, middle 1803_VIS_07b, upper 1803_VIS_06

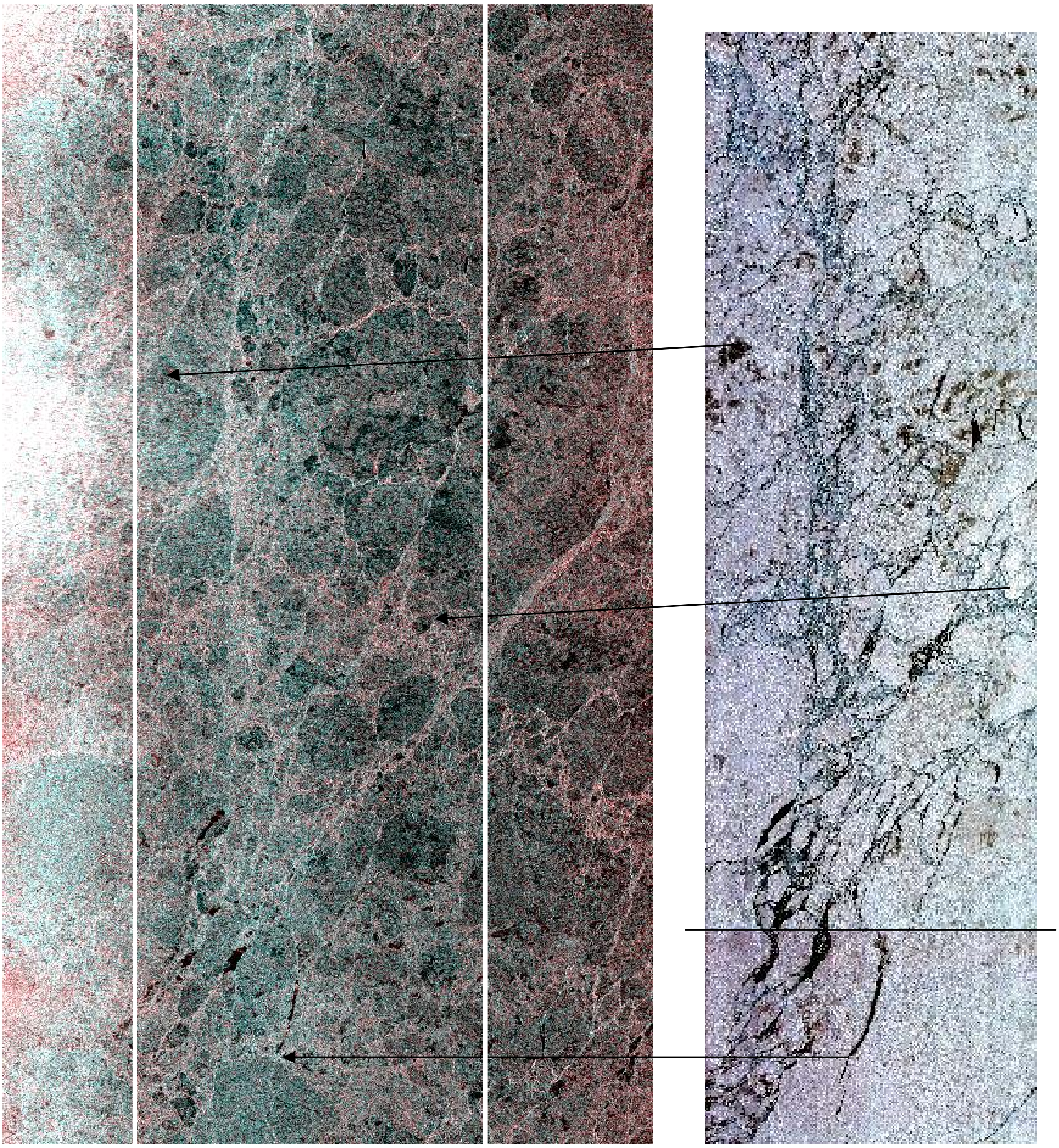

1803CV1_S2, VIS: lower 1803_VIS_9, upper 1803_VIS_08

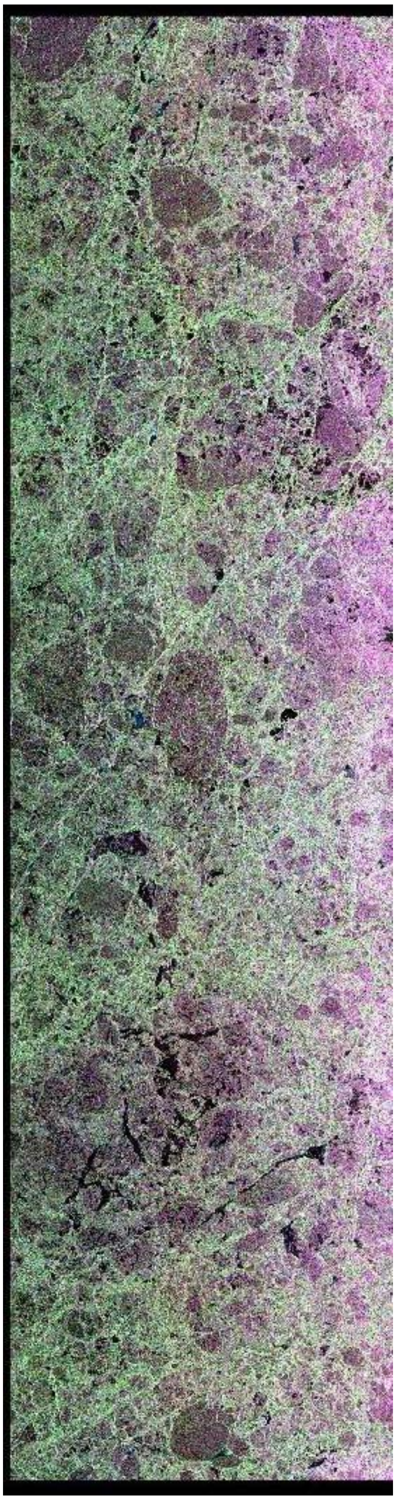

i07icesar0302x1_t02

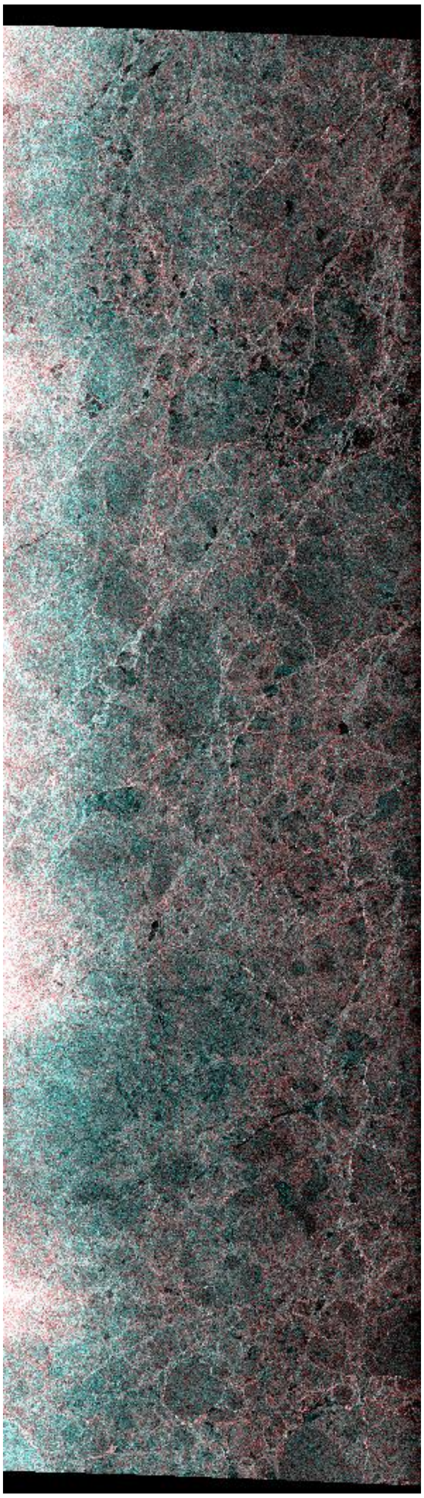

i07icesar0301x1_t02

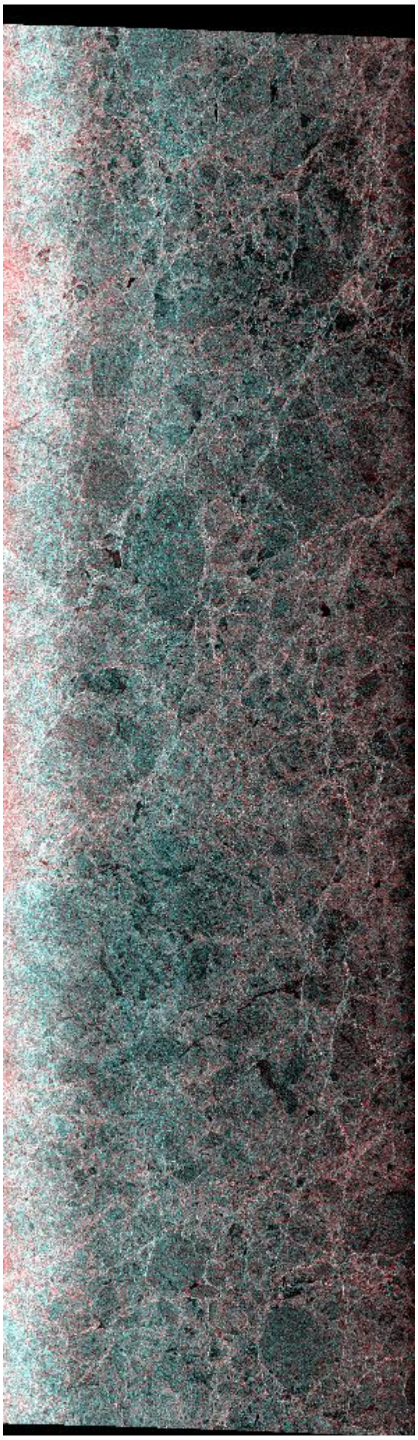

i07icesar0303x1_t02

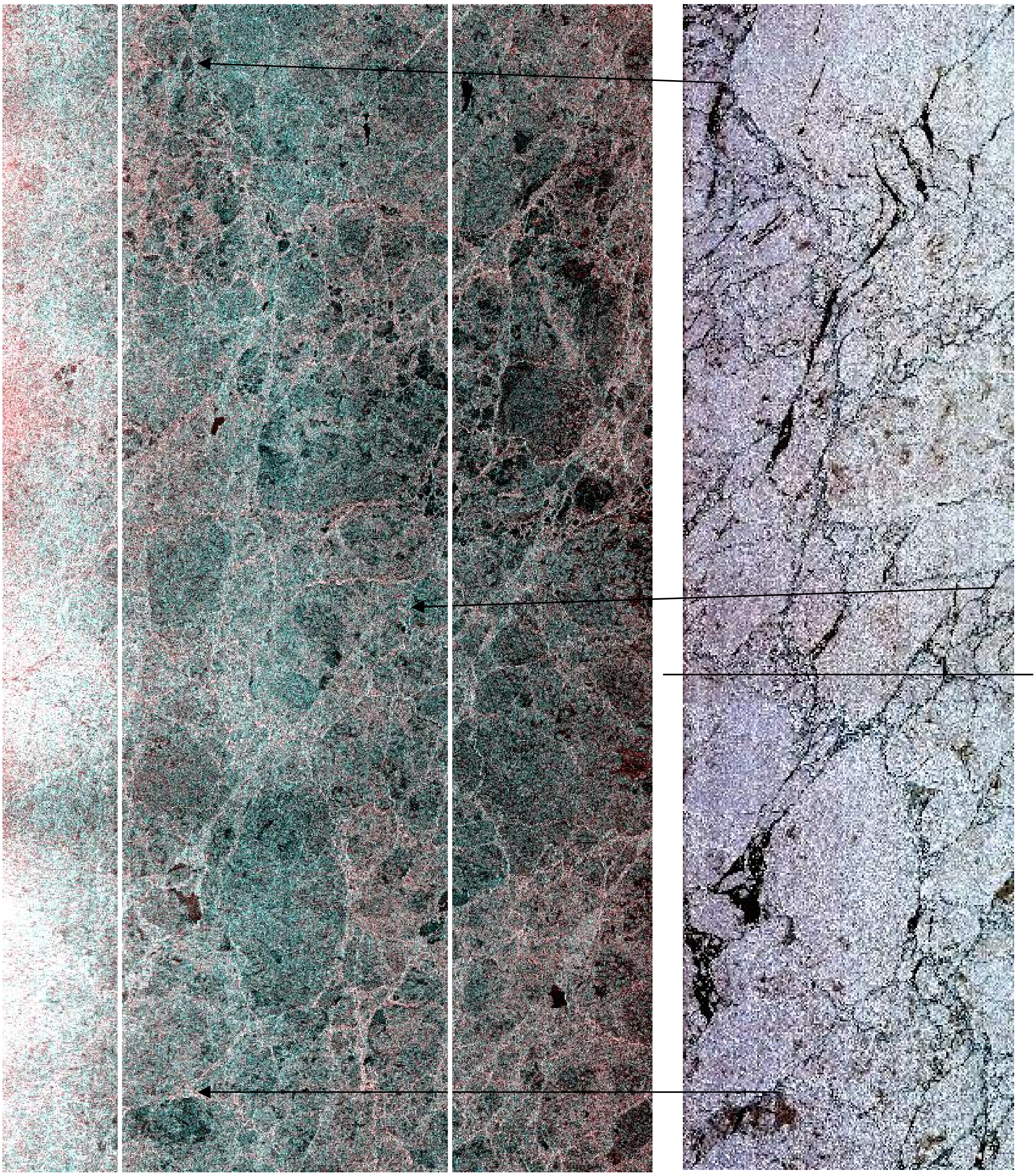

1803CH2_S1, VIS: lower 1803_VIS_10, upper 1803_VIS_09

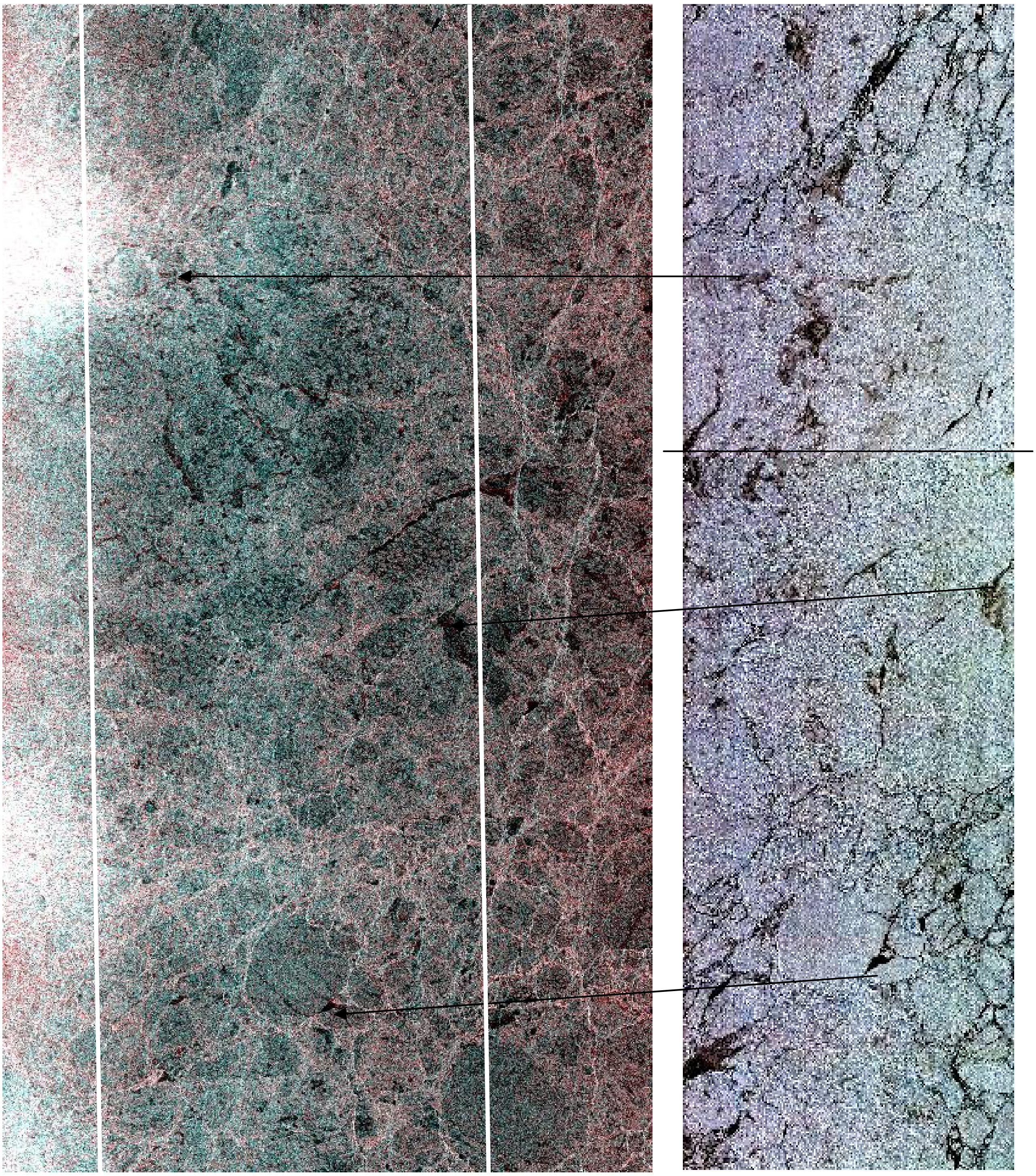

1803CH2_S2, VIS: lower 1803_VIS_11, upper 1803_VIS_10

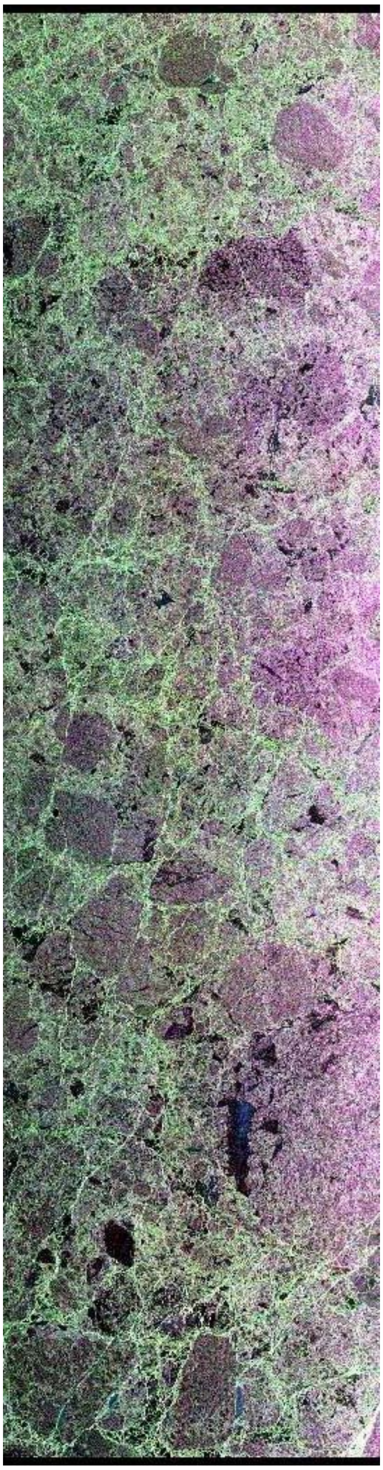

i07icesar0302x1_t03

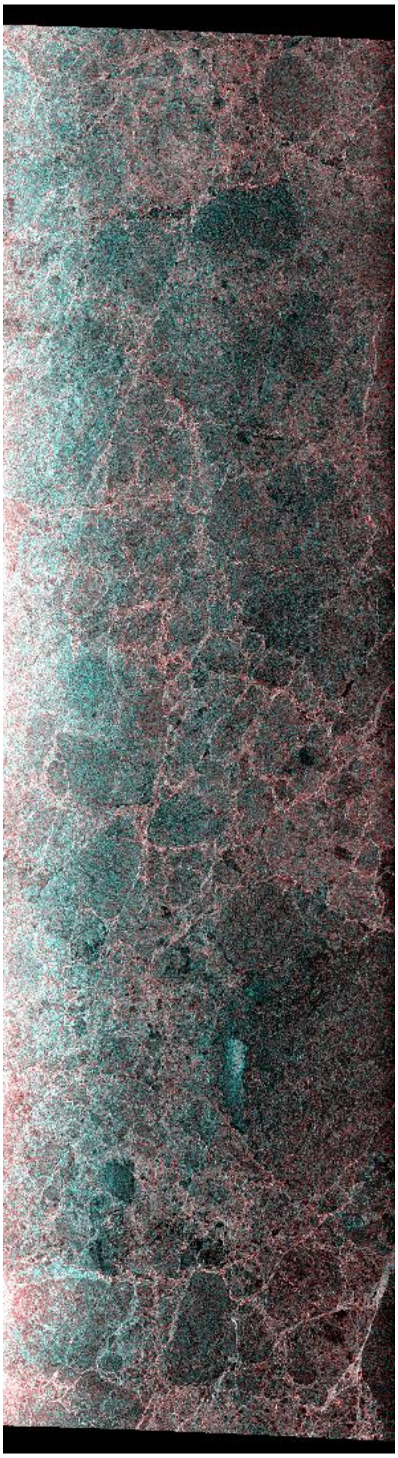

i07icesar0301x1_t03

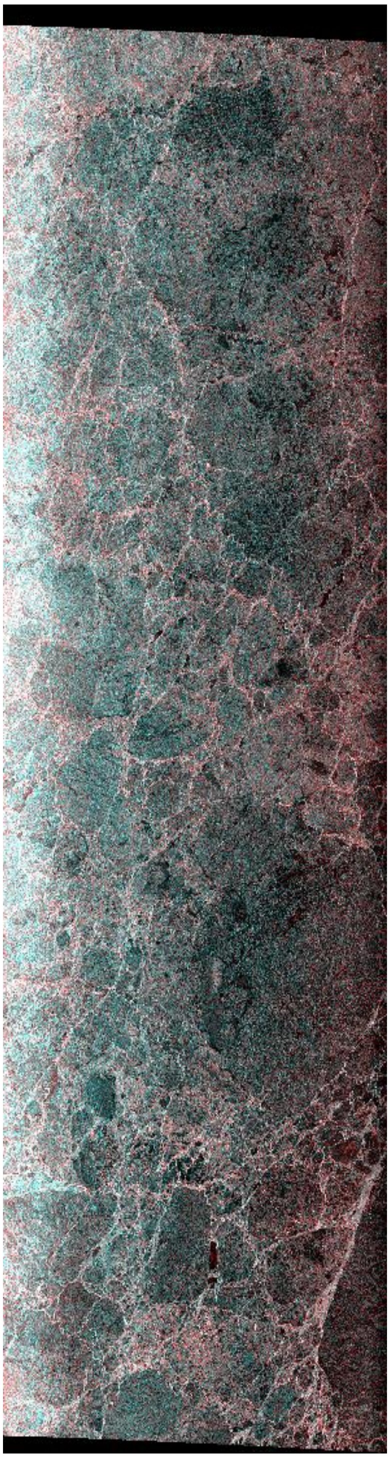

i07icesar0303x1_t03

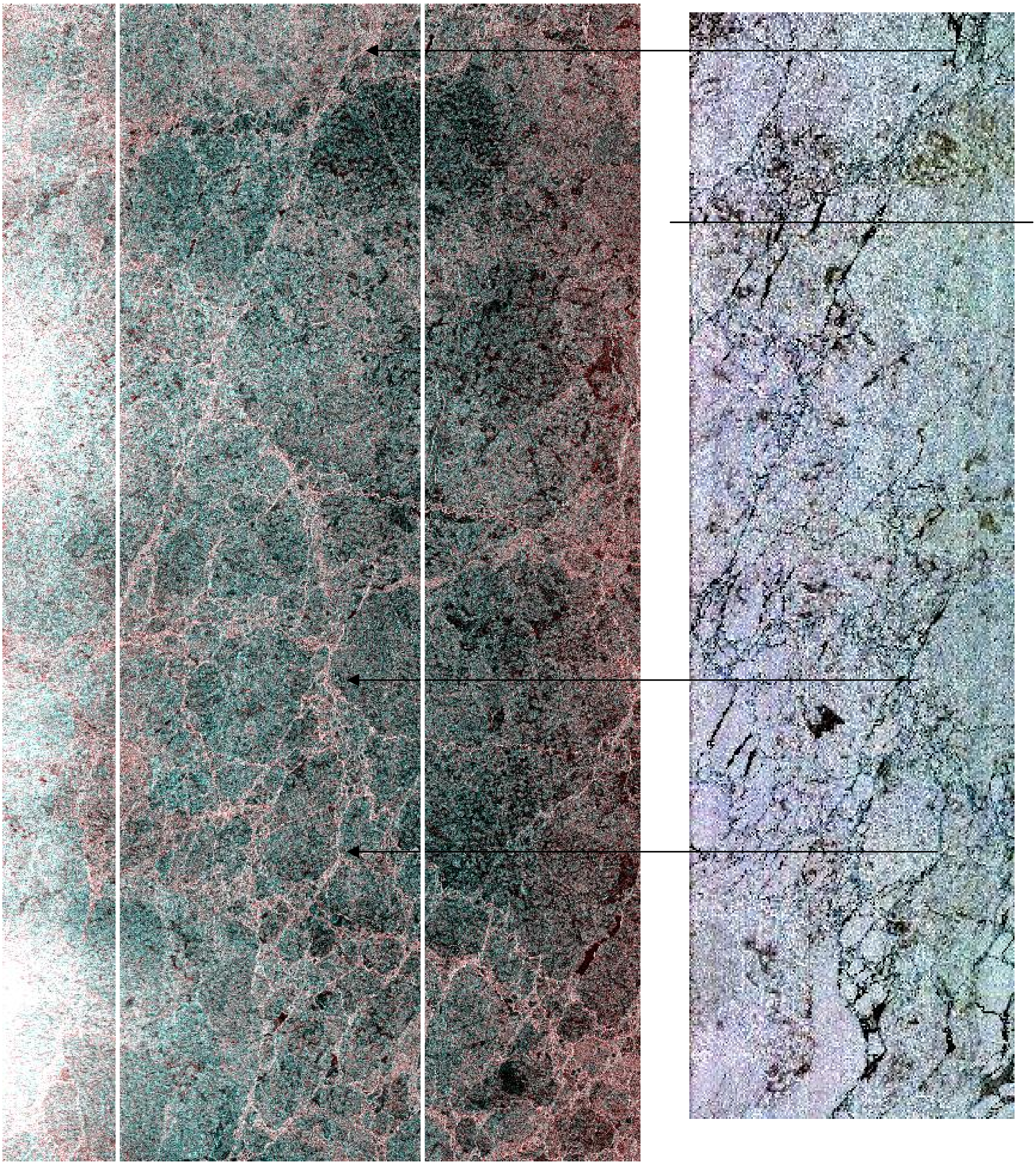

1803CH3_S1, VIS: lower 1803_VIS_12, upper 1803_VIS_11

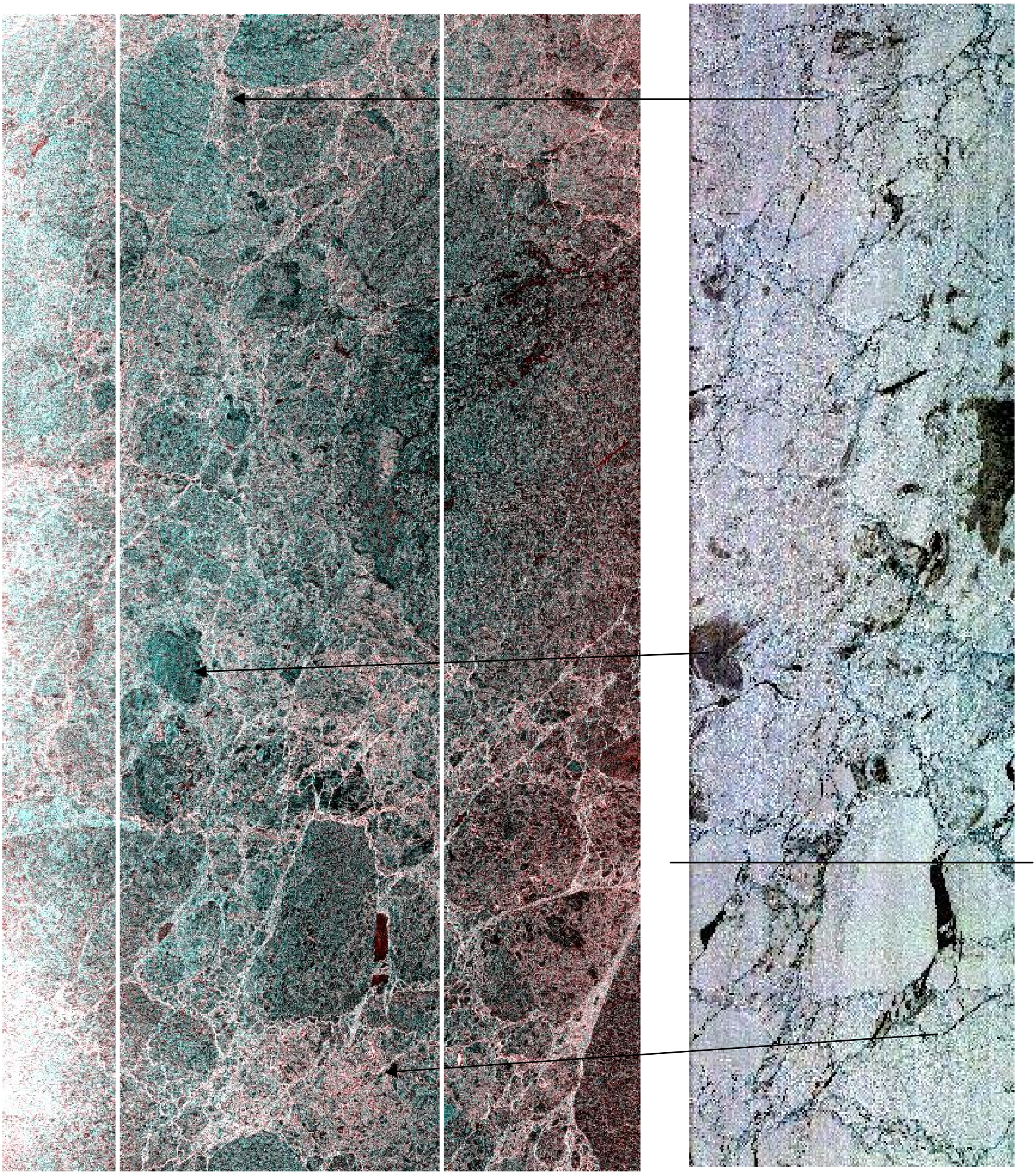

1803CH3_S2, VIS: lower 1803_VIS_14, upper 1803_VIS_13

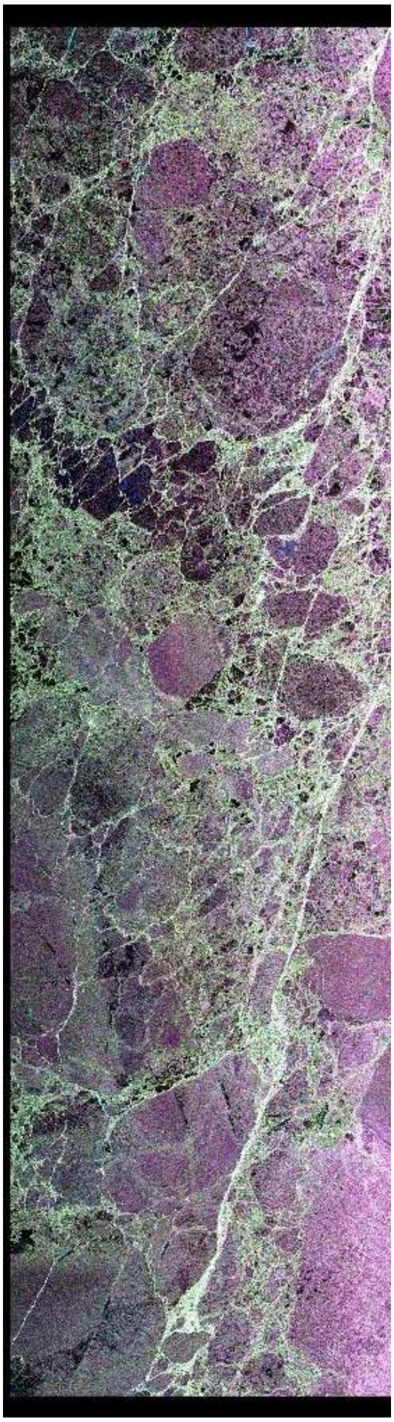

i07icesar0302x1_t04

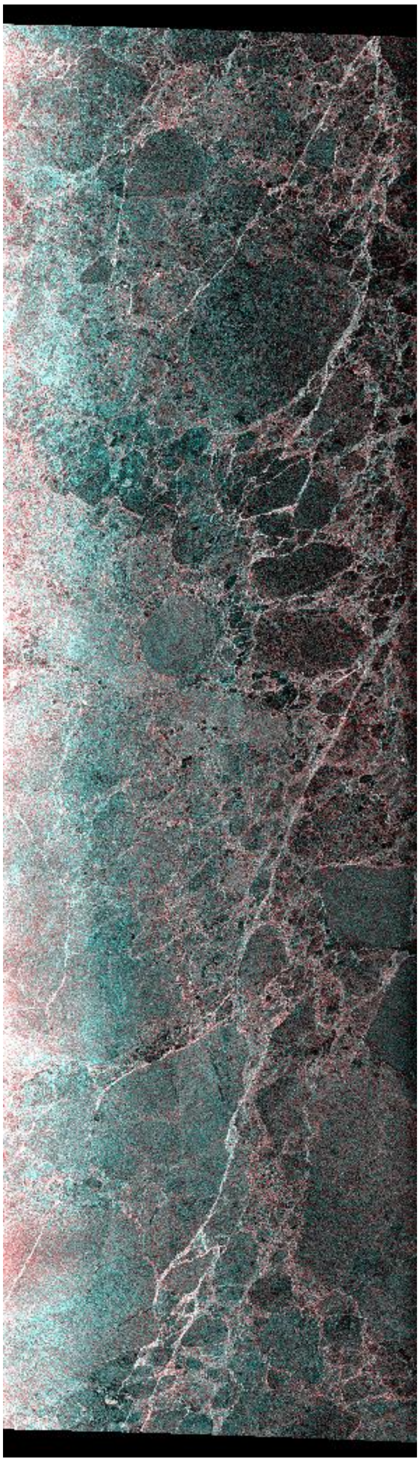

i07icesar0301x1_t04

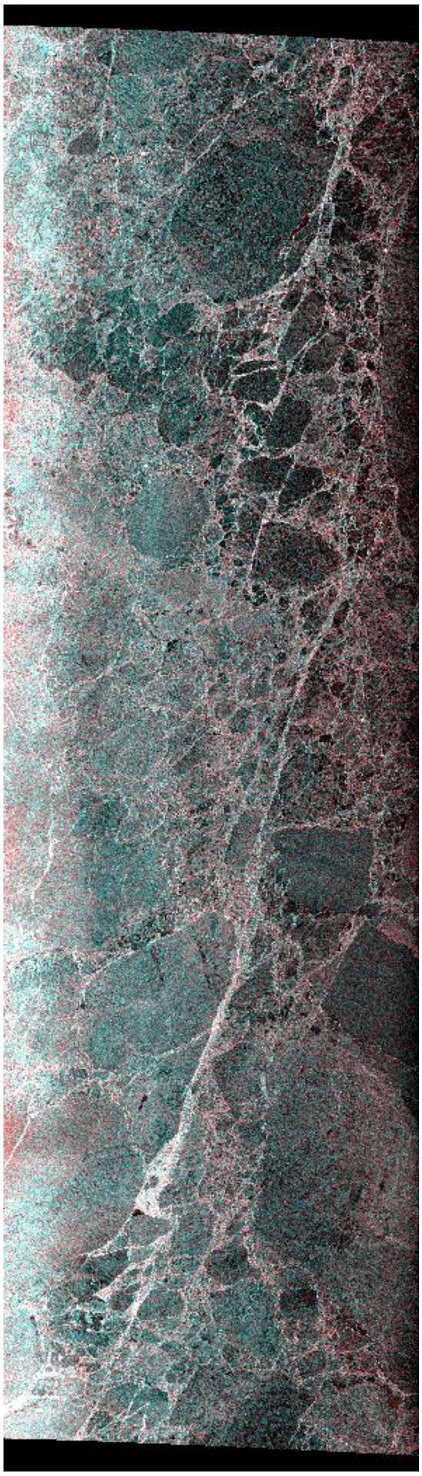

i07icesar0303x1_t04

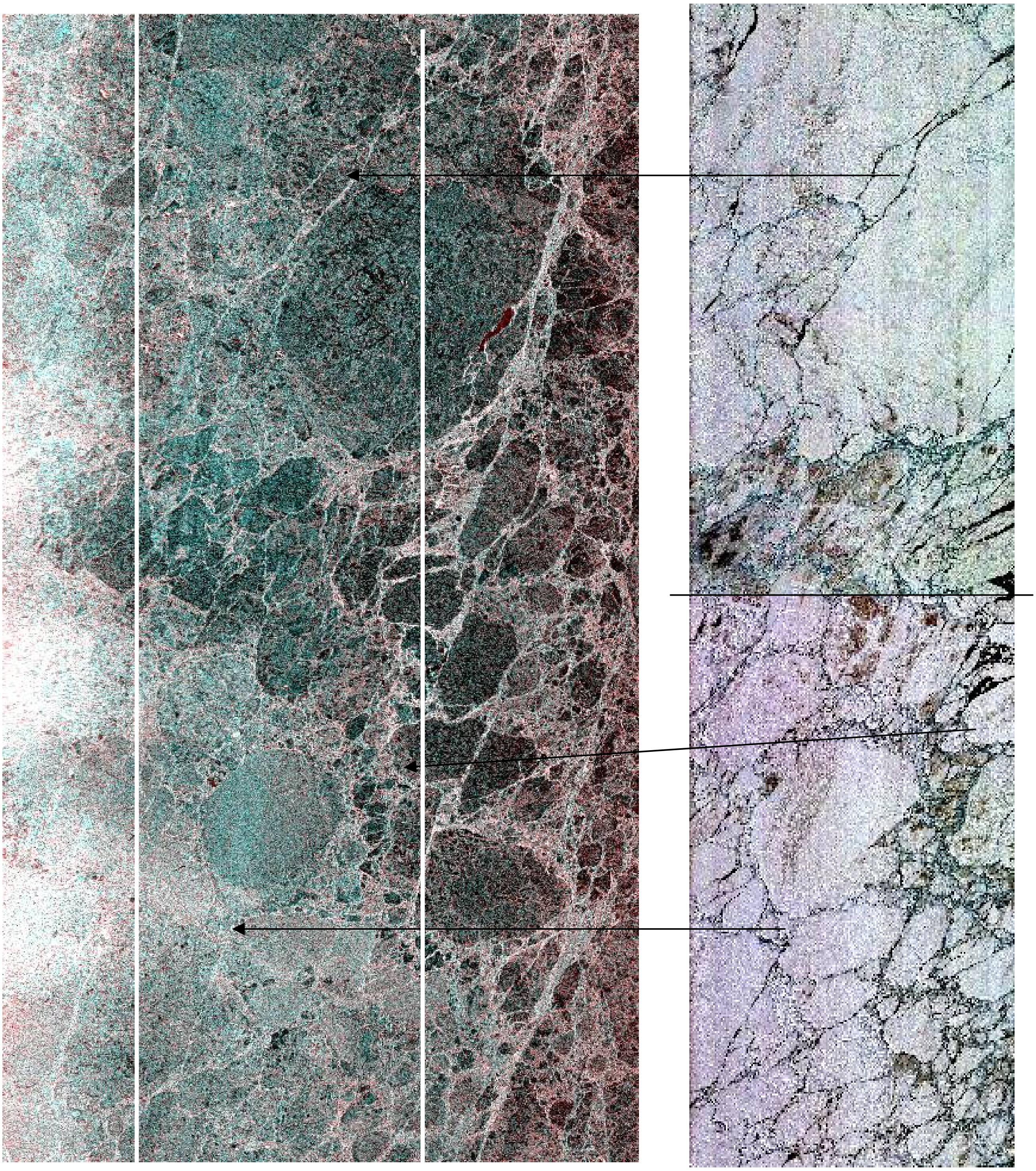

1803CH4_S1, VIS: lower 1803_VIS_15, upper 1803_VIS_14

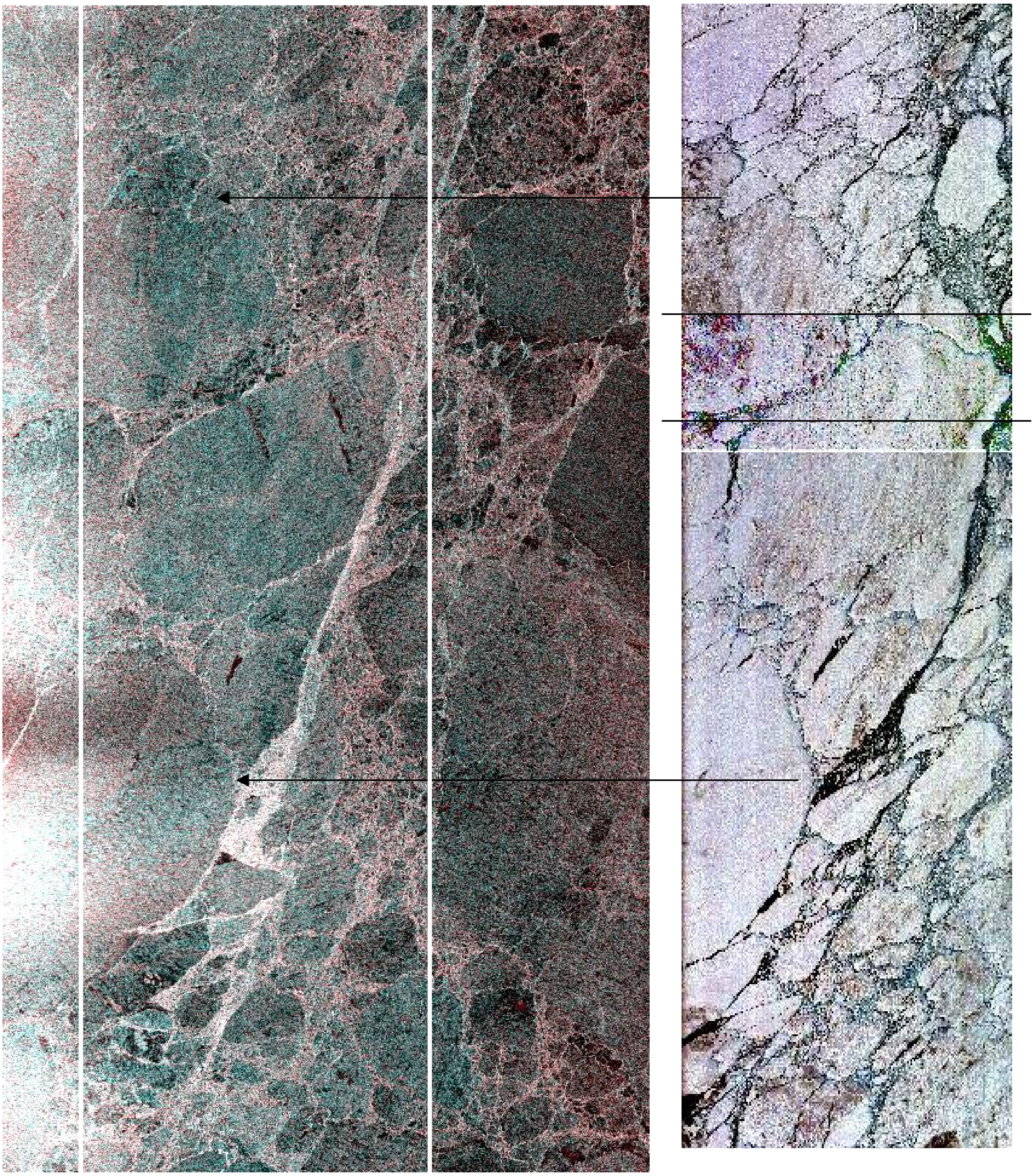

1803H4_S2, VIS: lower 1803_VIS_16a, middle 1803_VIS_16b, upper 1803_VIS_15

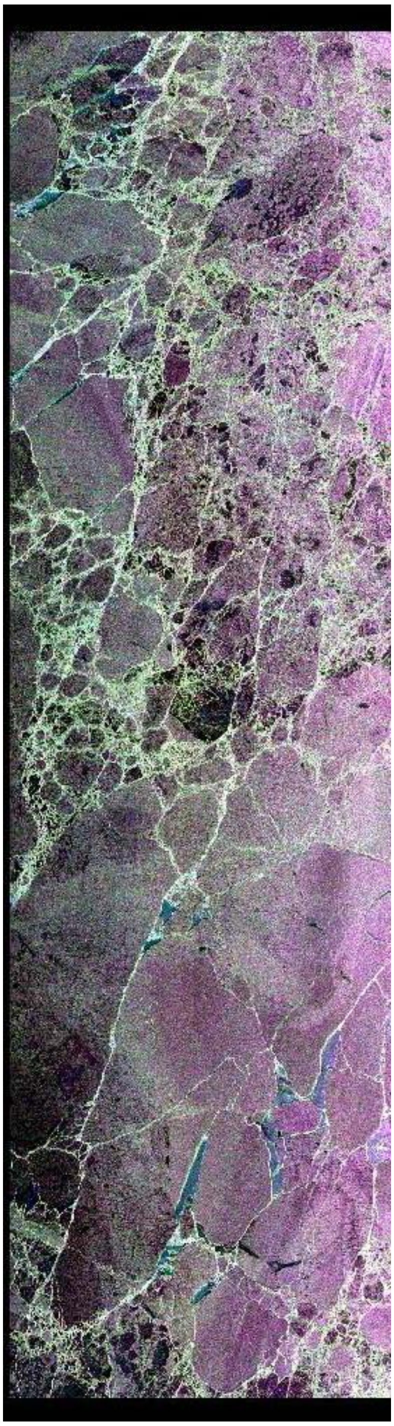

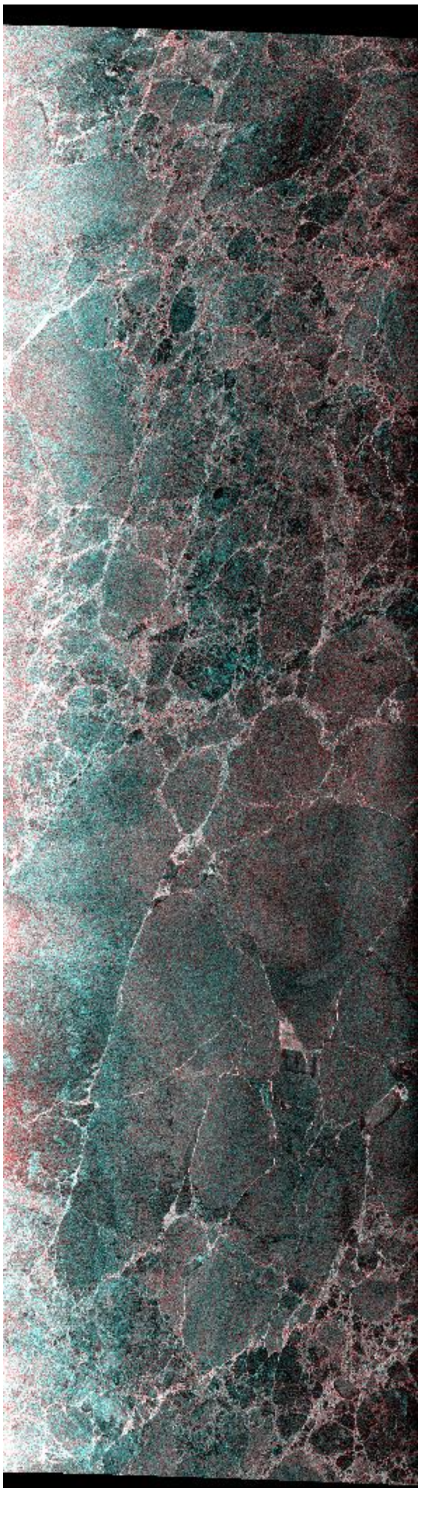

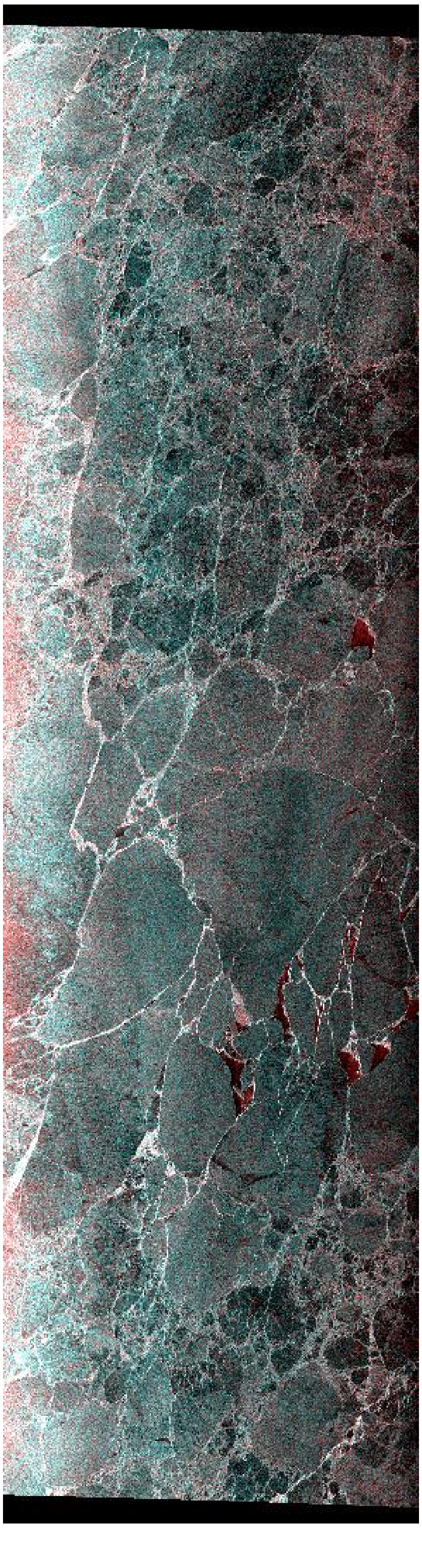

i07icesar0302x1_t05 i07icesar0301x1_t05 i07icesar0303x1_t05

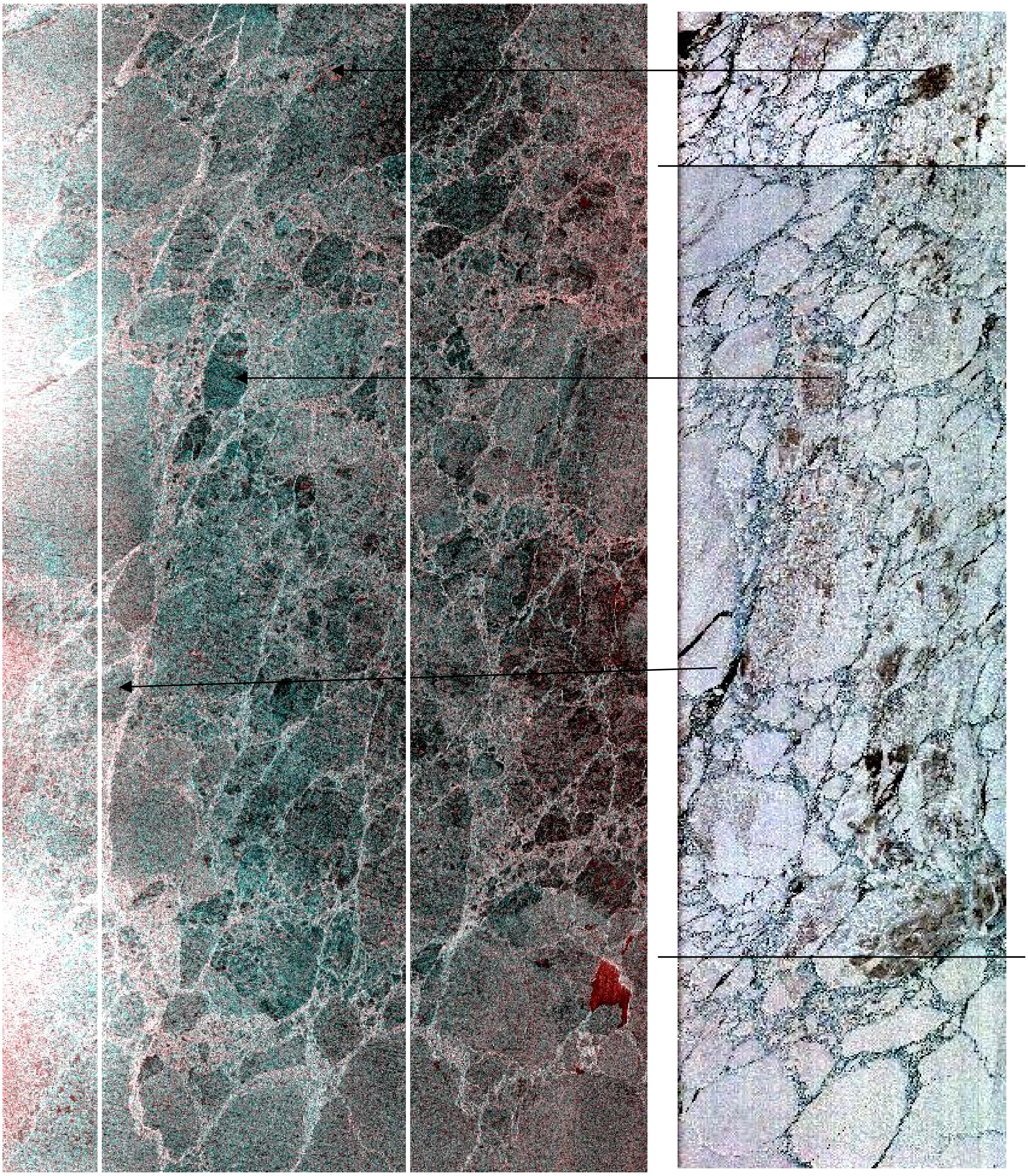

1803CH5_S1, VIS: lower 1803_VIS_18, middle 1803_VIS_17, upper 1803_VIS_16a

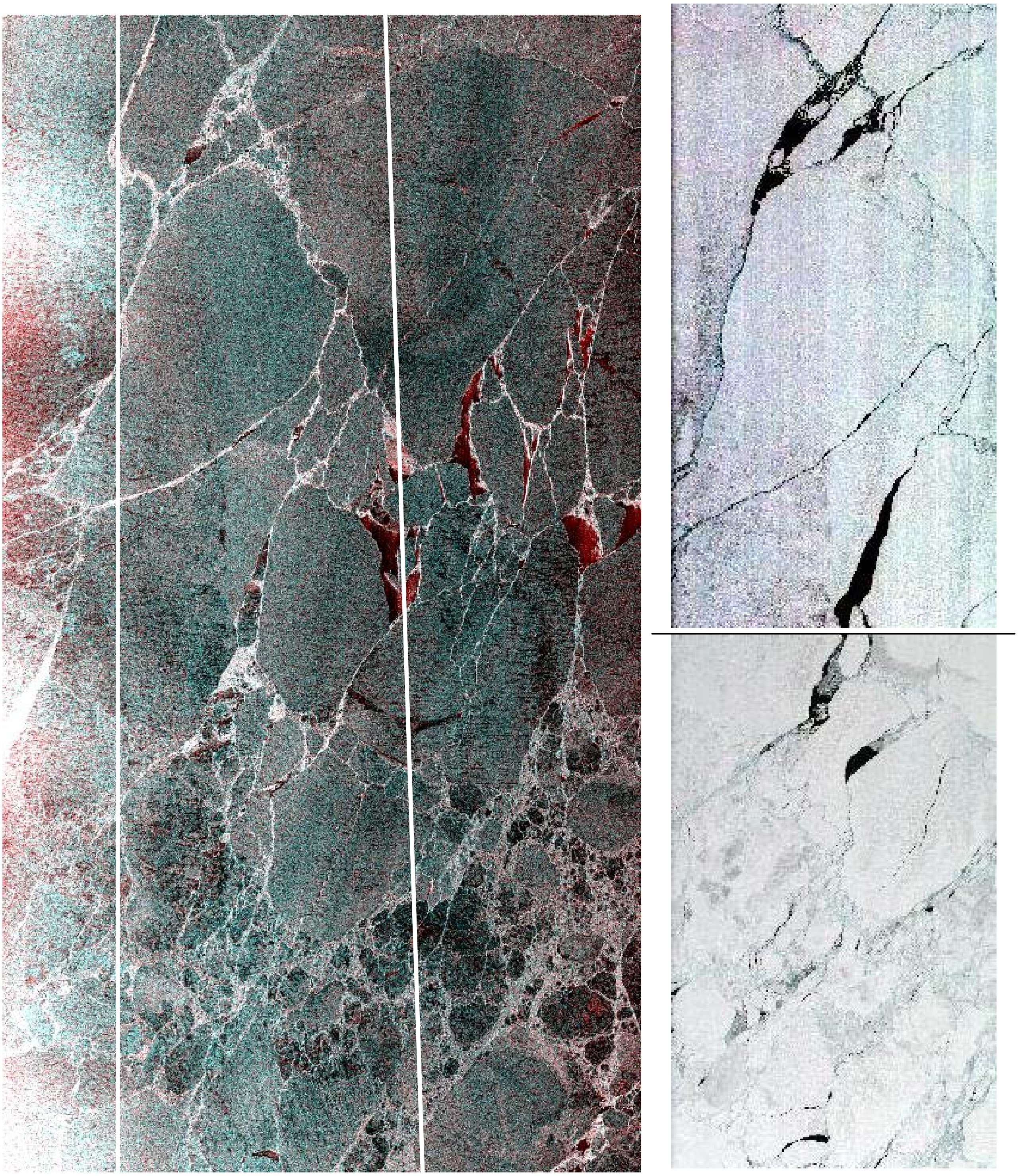

1803CH5_S2, VIS: lower 1803_VIS_19, upper 1803_VIS_18

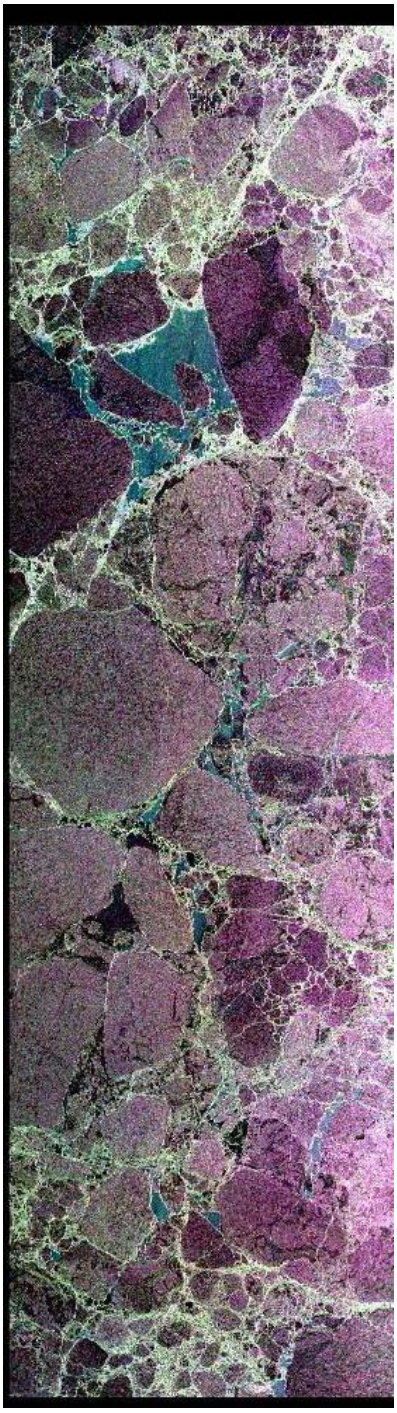

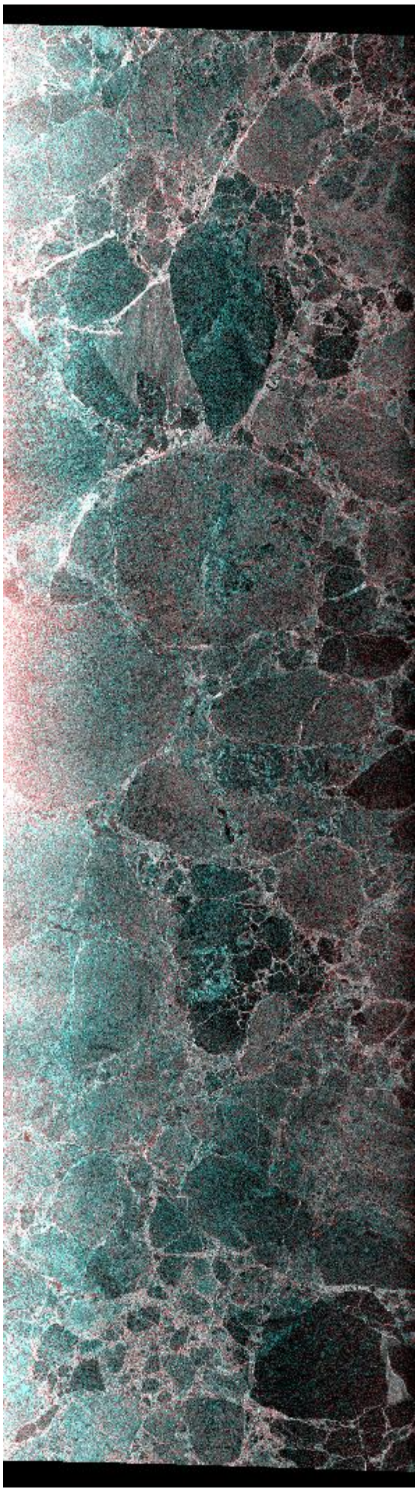

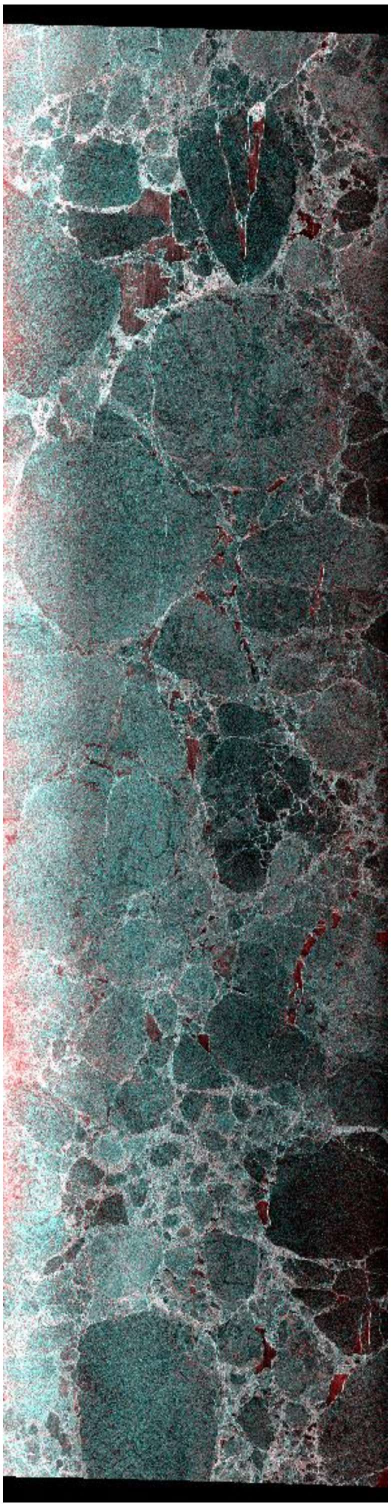

i07icesar0302x1_t06 i07icesar0301x1_t06 i07icesar0303x1_t06

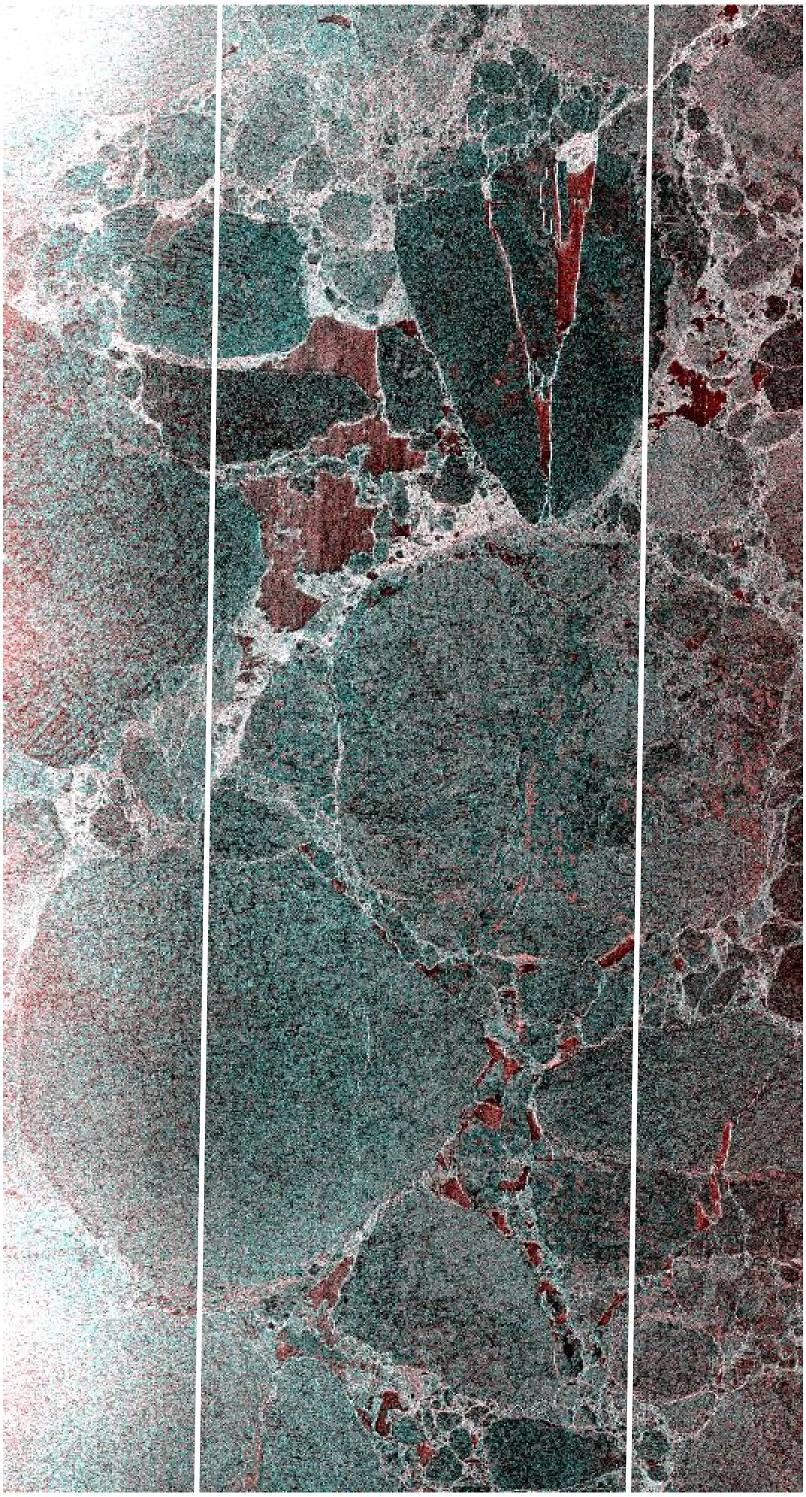

1803CH6_S1, VIS: lower 1803_VIS_20, upper 1803_VIS_19

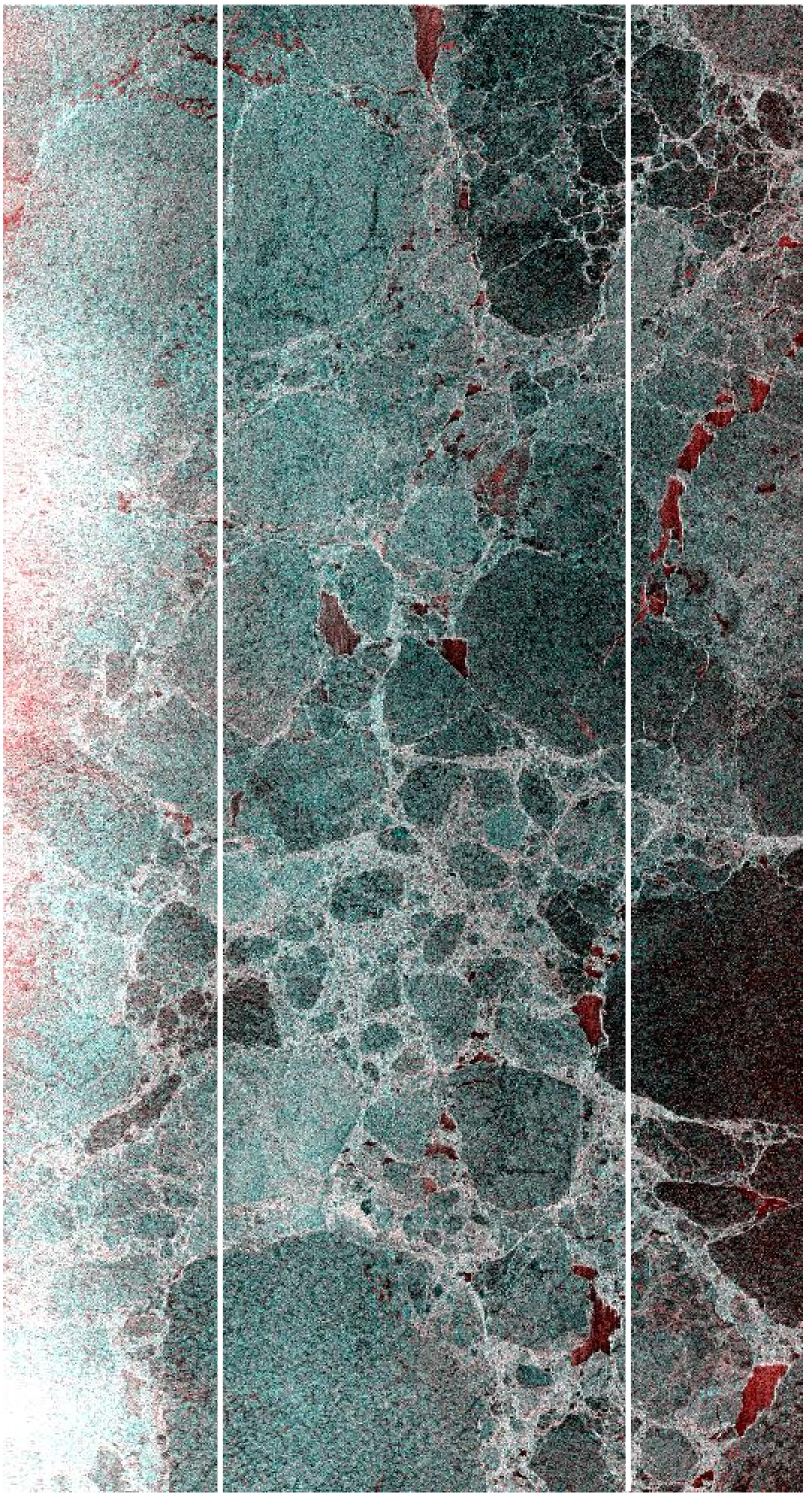 

1803CH6_S2, VIS: lower 1803_VIS_22, upper 1803_VIS_21

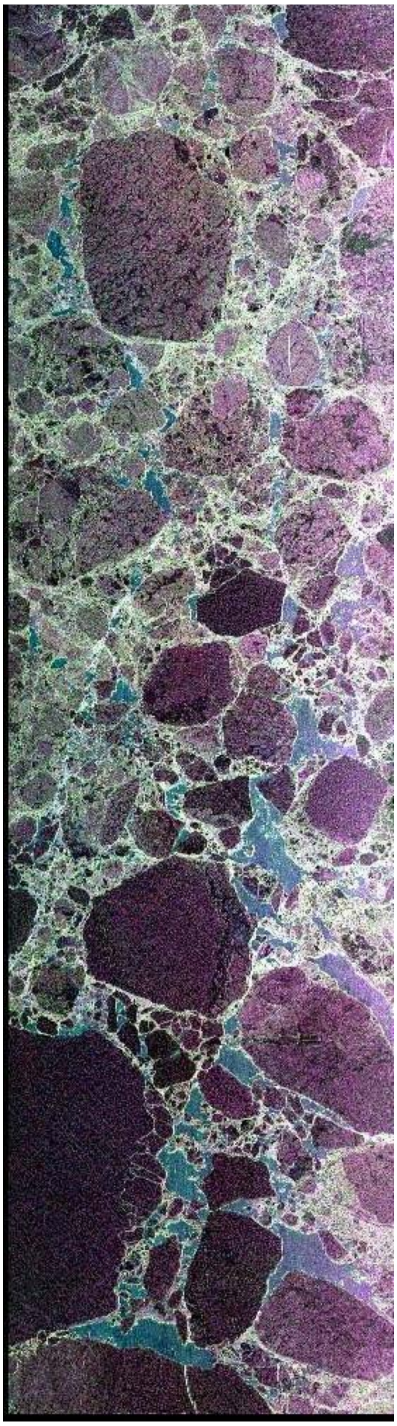

i07icesar0302x1_t07

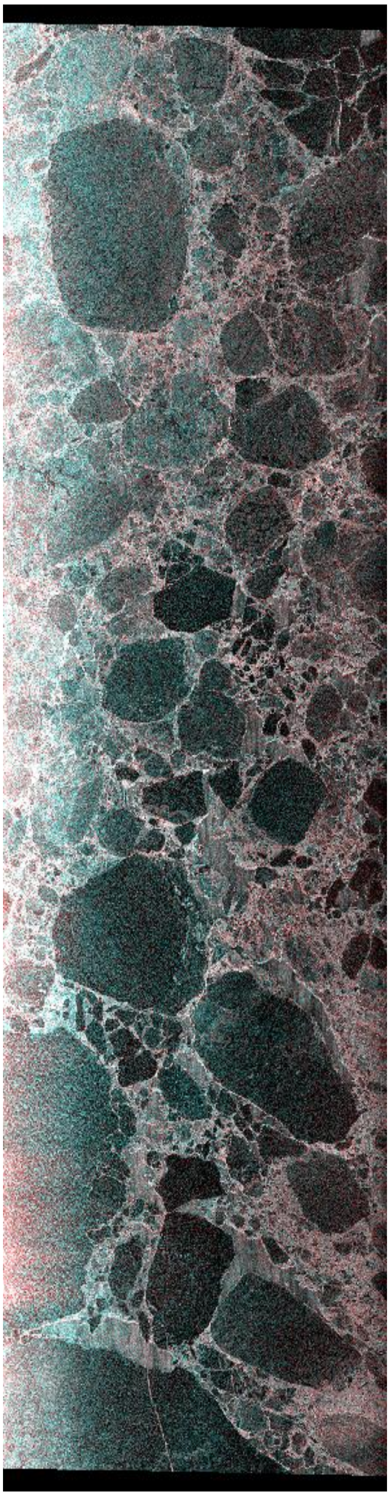

i07icesar0301x1_t07

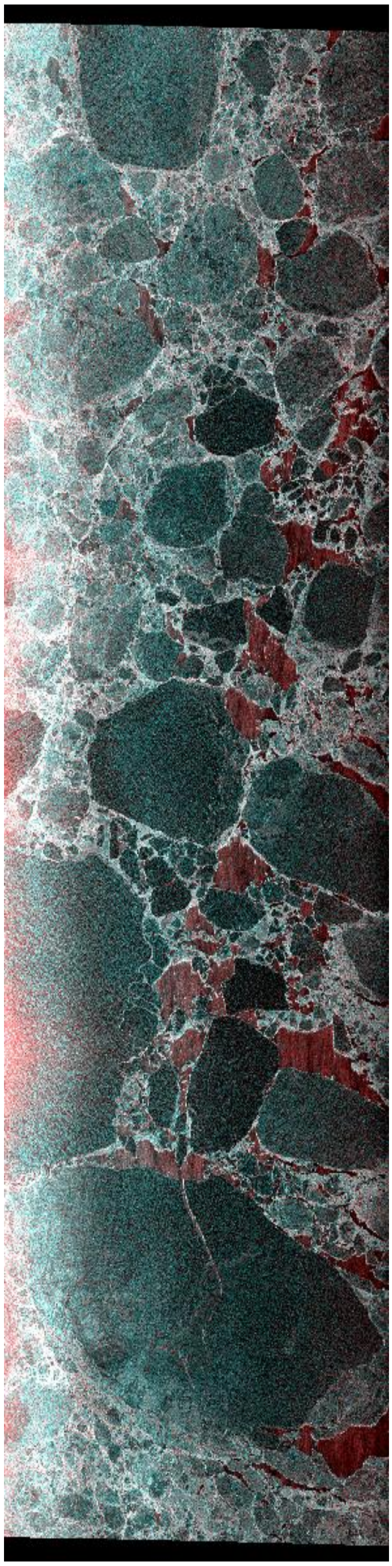

i07icesar0303x1_t07

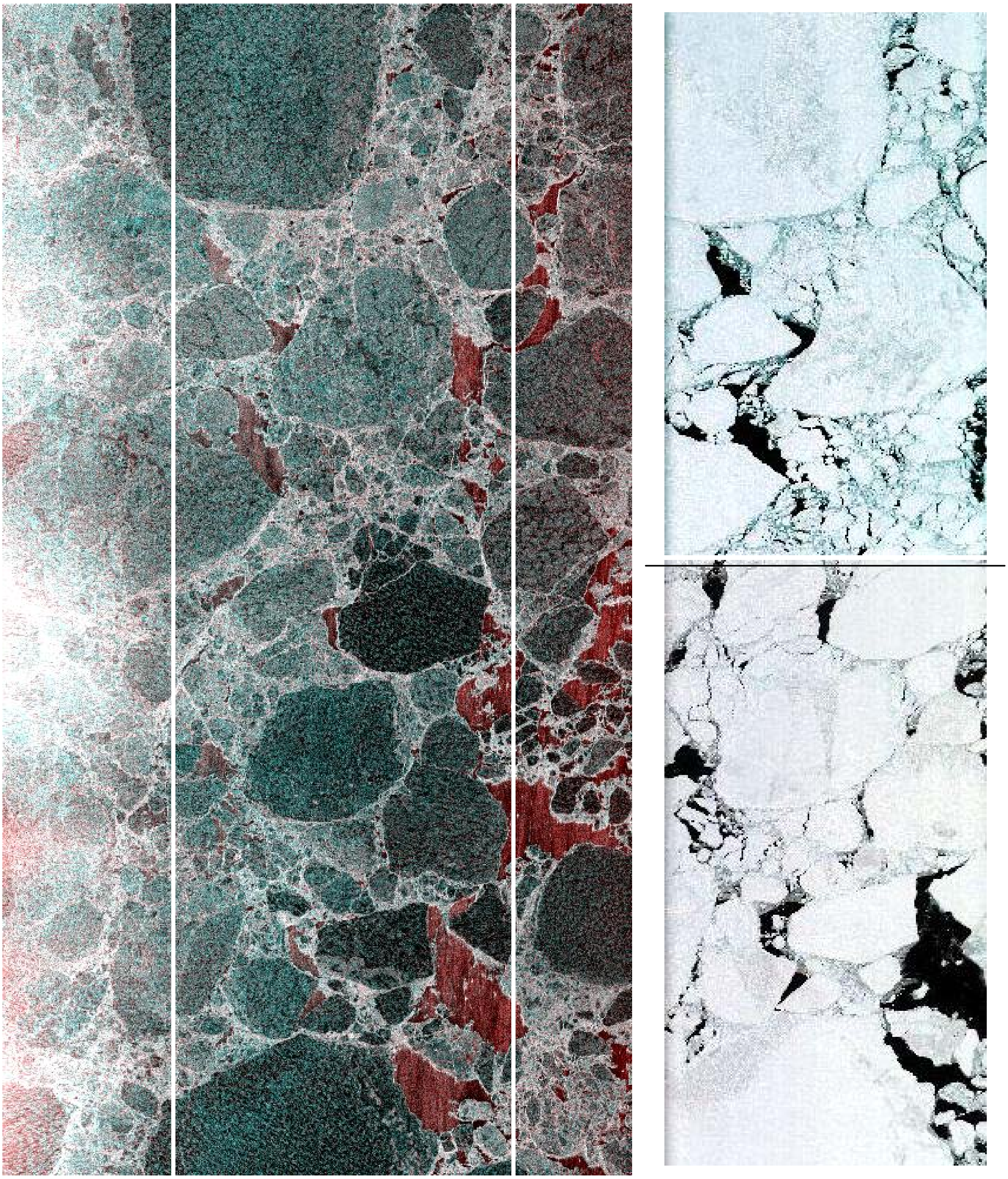

1803CH7_S1, VIS: lower 1803_VIS_23, upper 1803_VIS_22

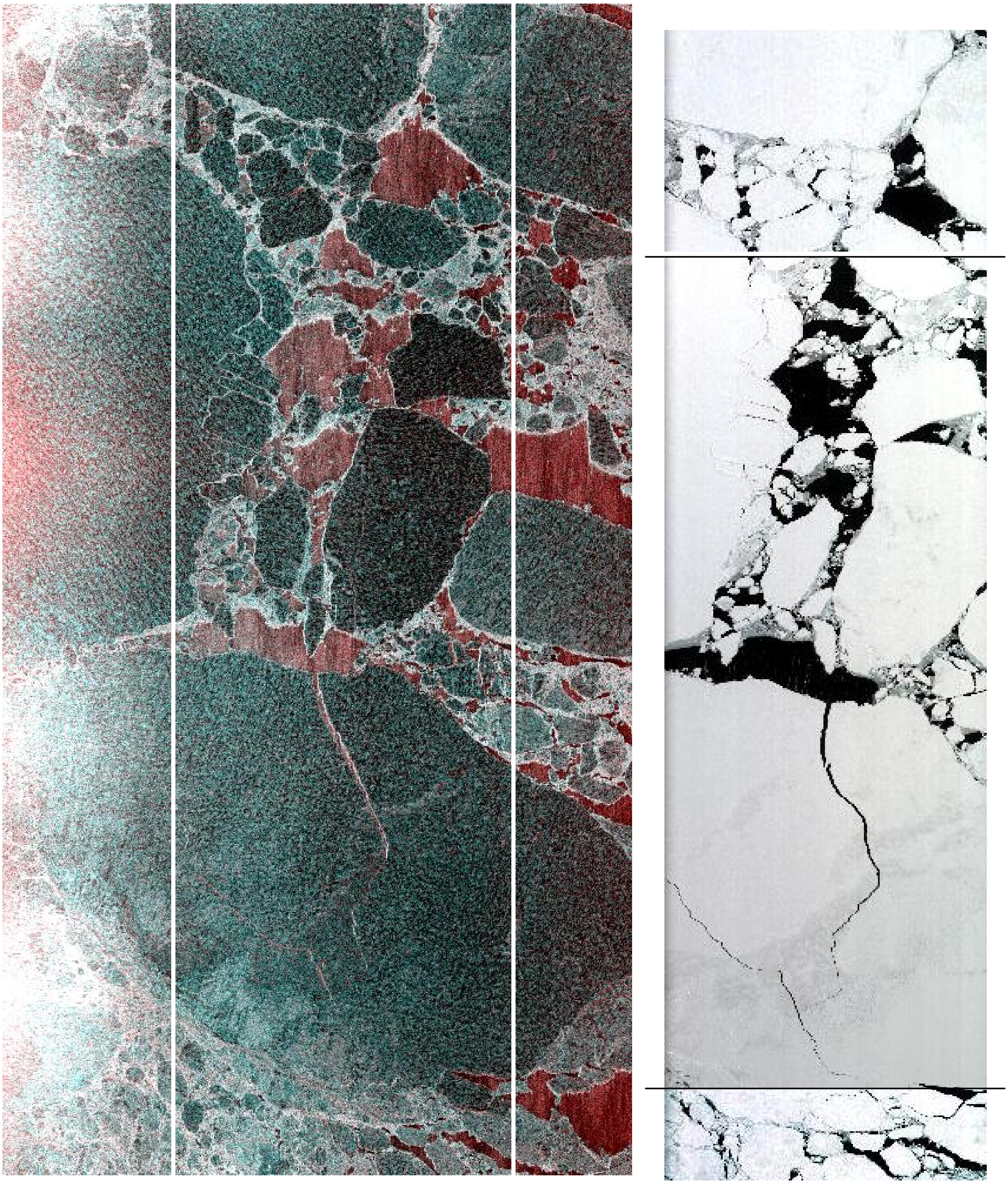

1803CH7_S2, VIS: lower 1803_VIS_25, middle: 1803_VIS_24, upper 1803_VIS_23

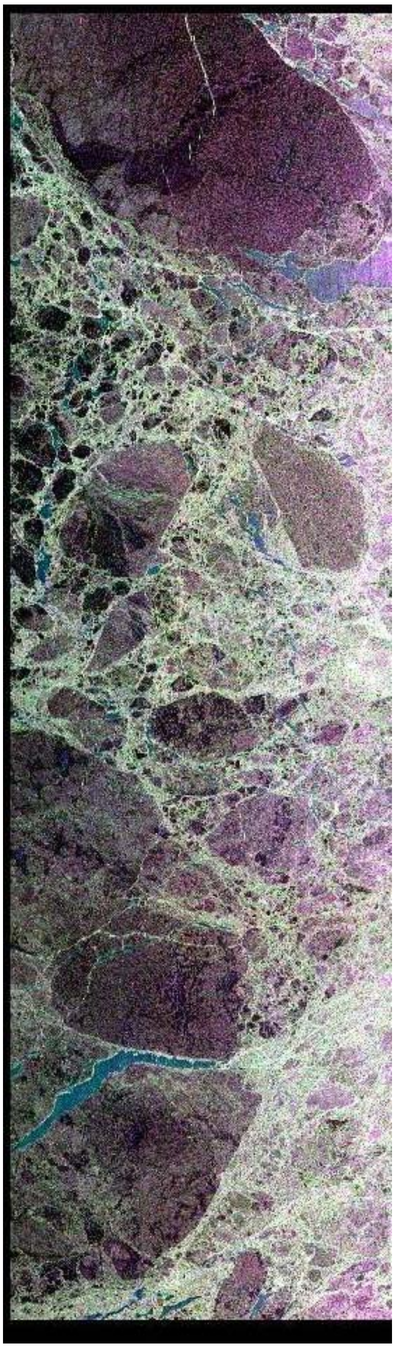

i07icesar0302x1_t08

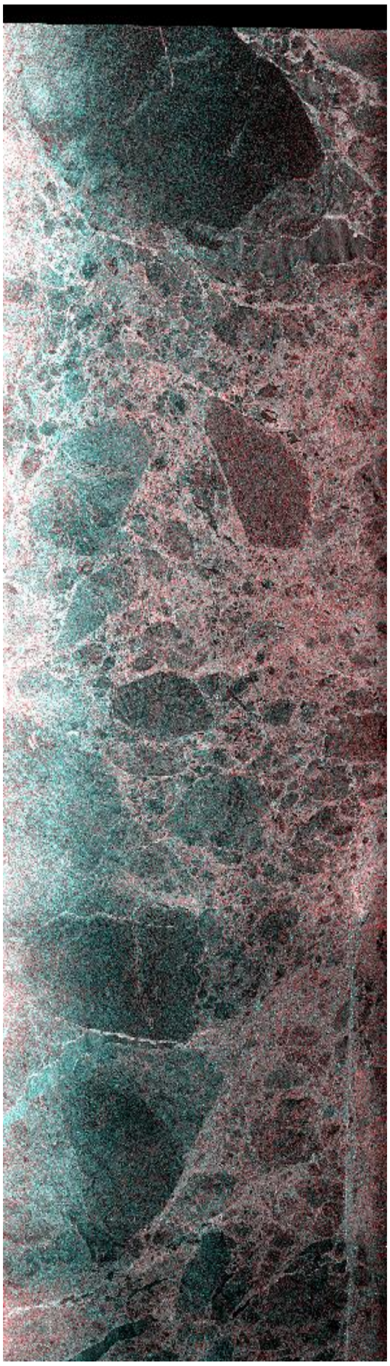

i07icesar0301x1_t08

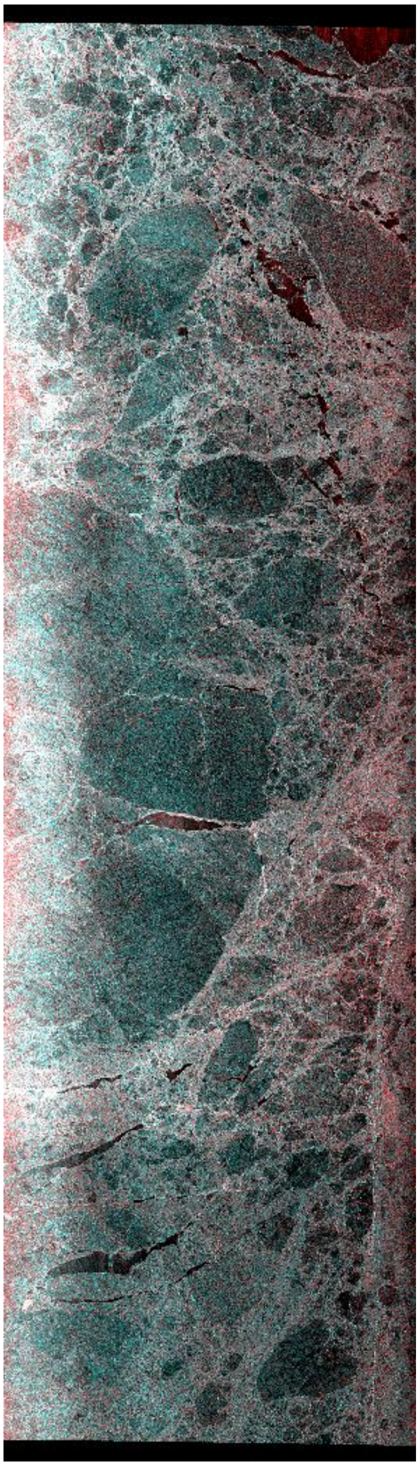

i07icesar0303x1_t08

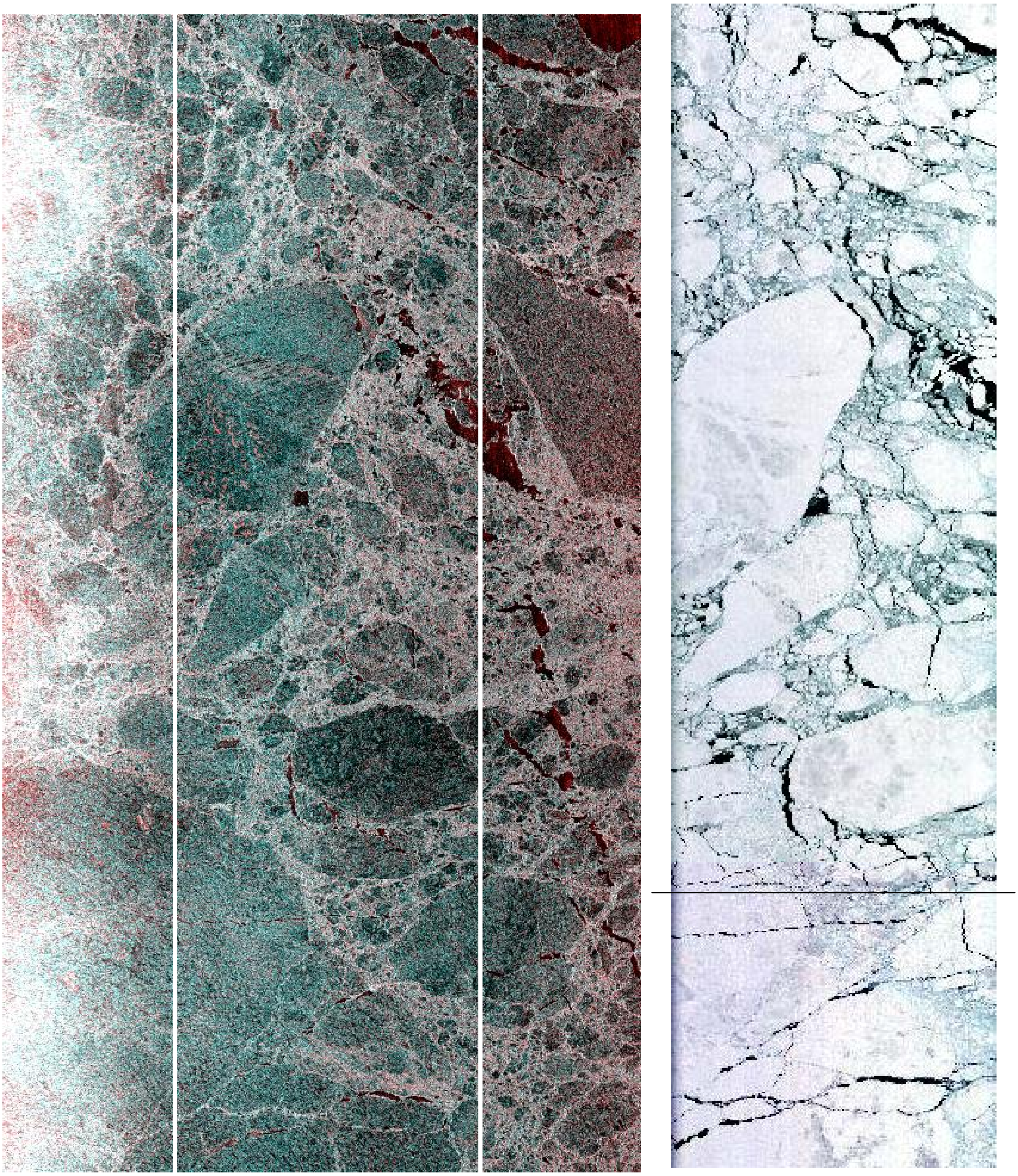

1803CH8_S1, VIS: lower 1803_VIS_26, upper 1803_VIS_25

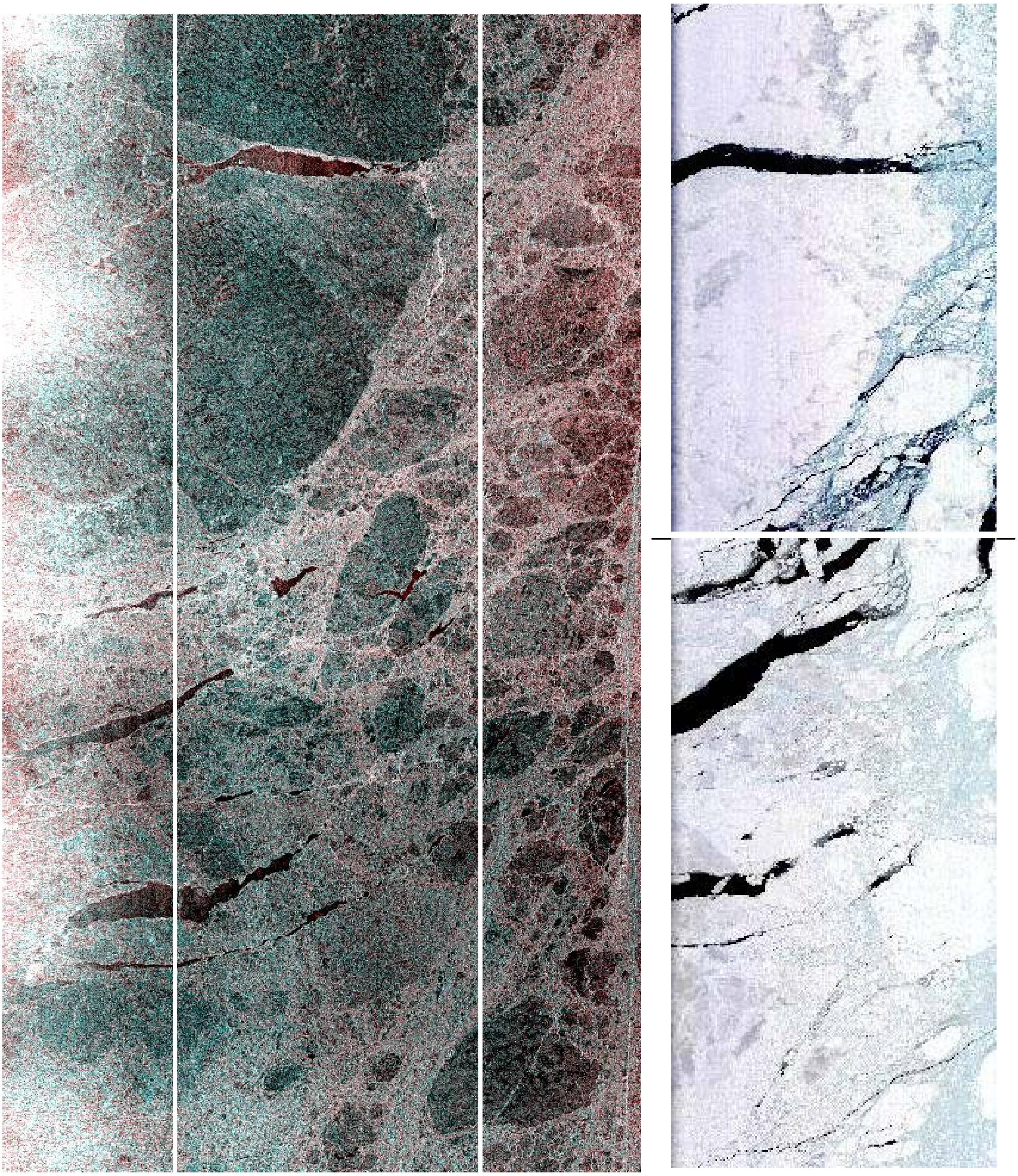

1803CH8_S2, , VIS: lower 1803_VIS_27, upper 1803_VIS_26

Date: March 19, Location: Fram Strait (S to N)

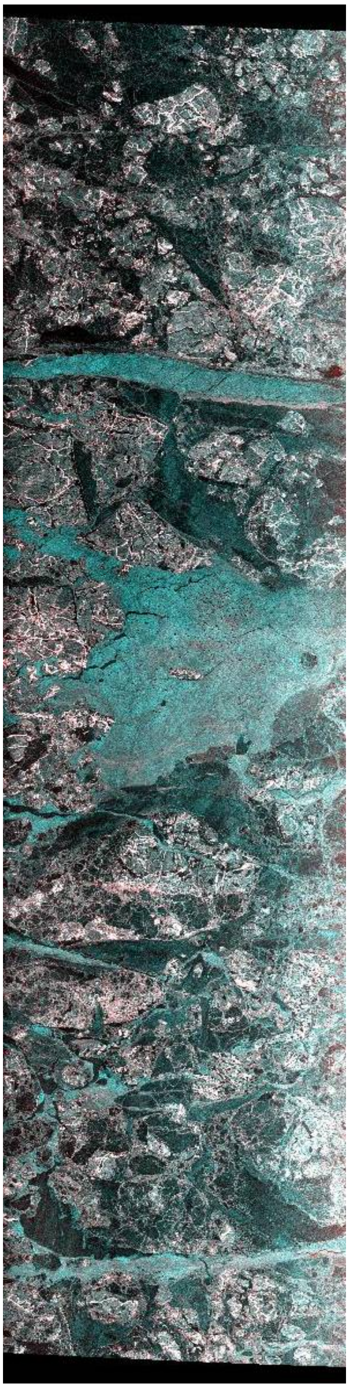

i07icesar0401x1_t01

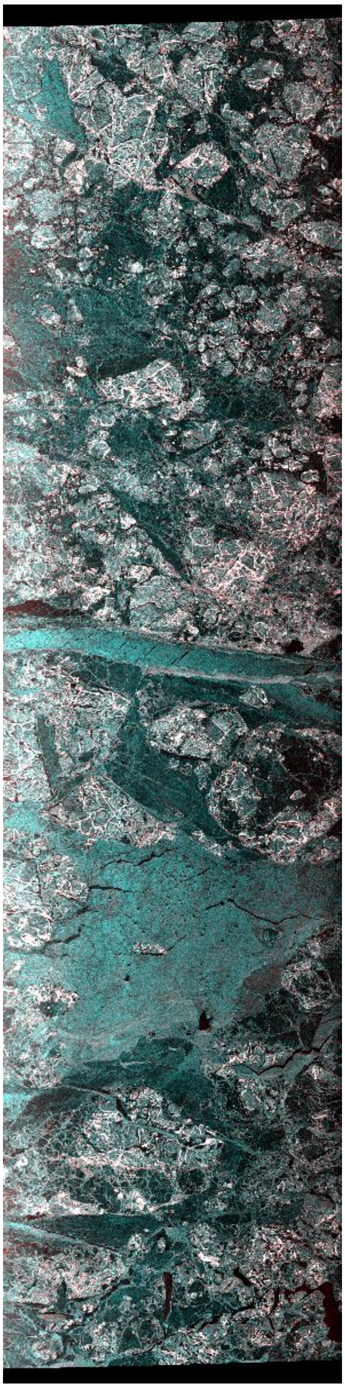

Upper image edge: North
Lower image edge: South

i07icesar0402x1_t01

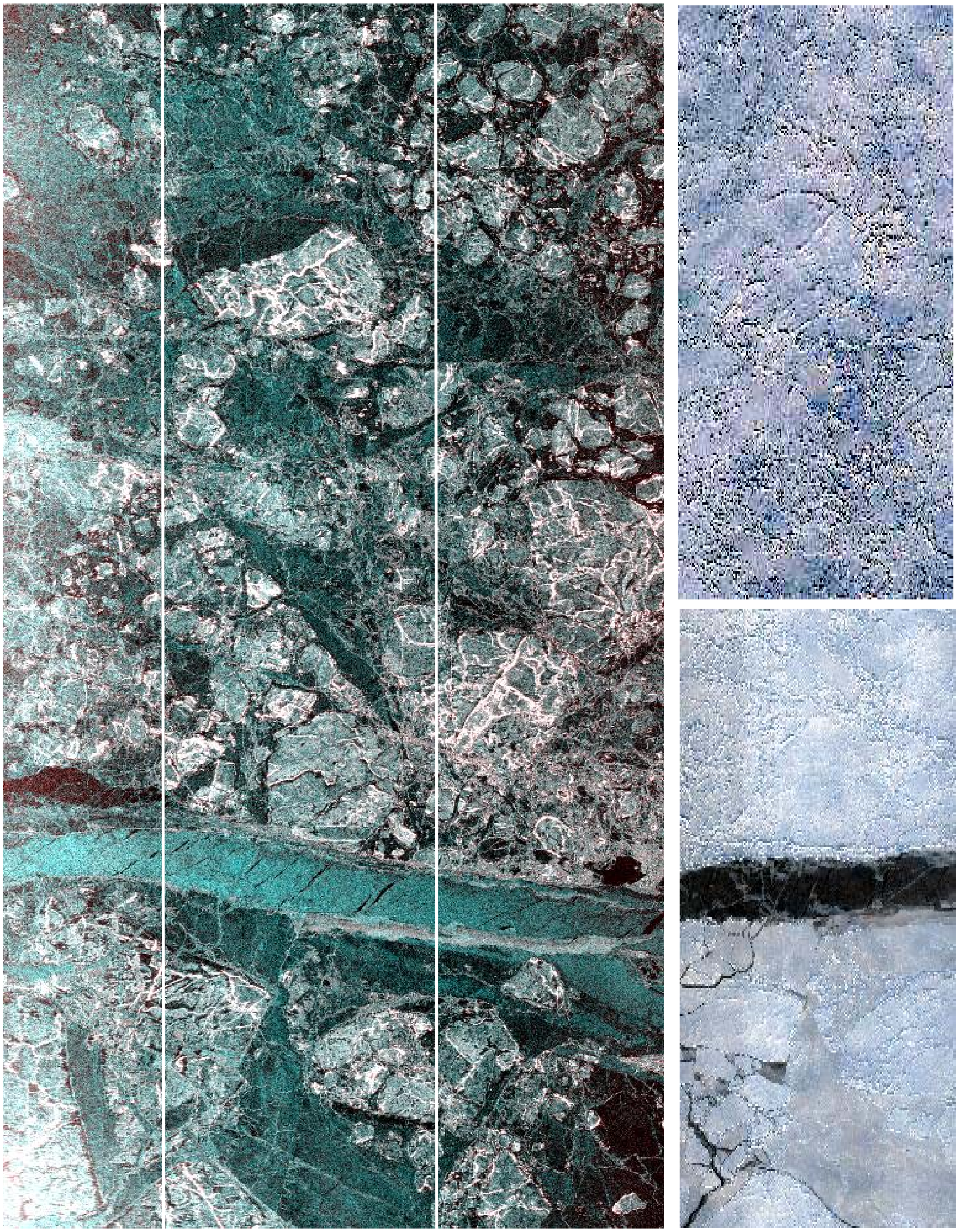

1903CH1_S1, VIS: lower: 1903_VIS_08, upper: 1903_VIS_09

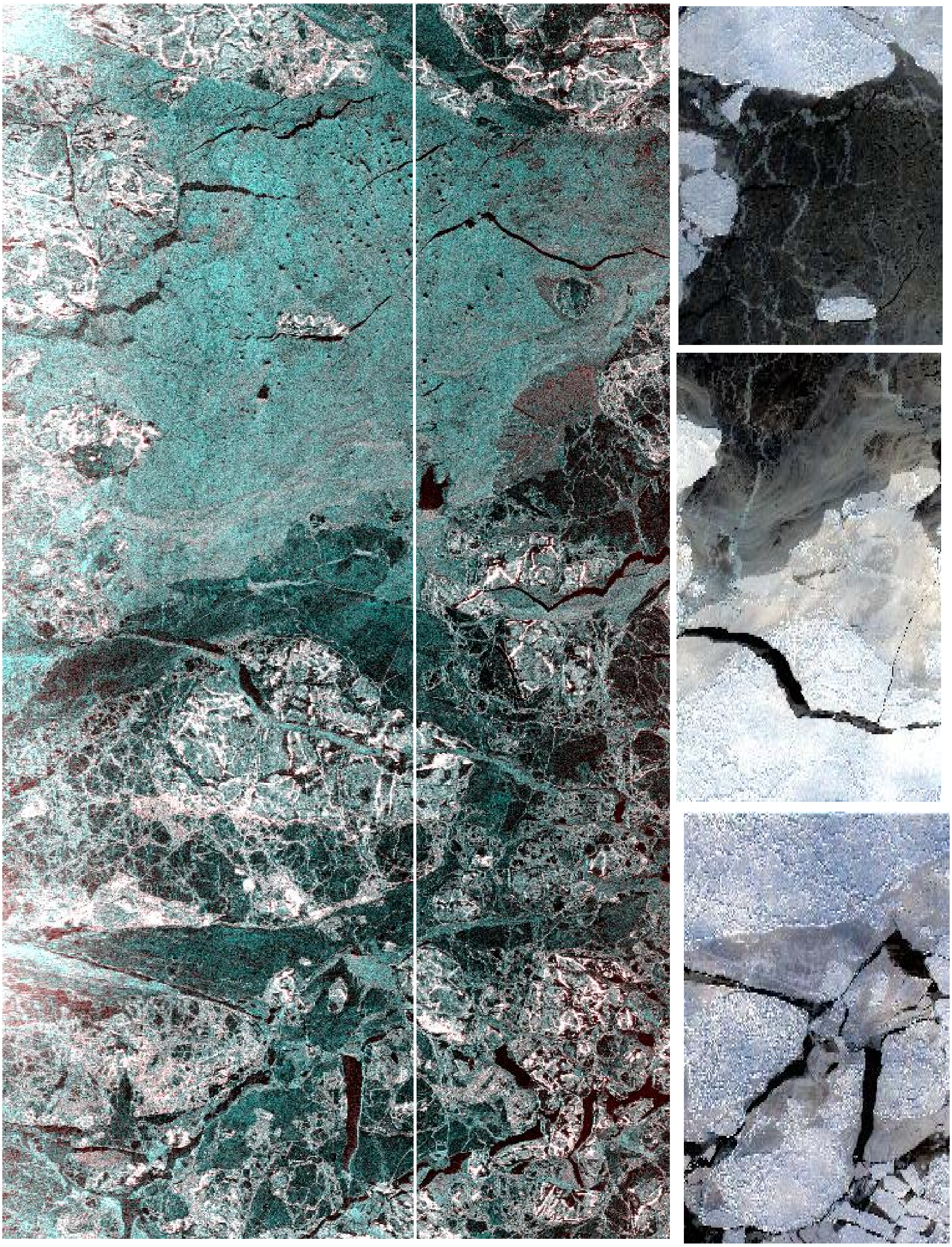

1903CH1_S2, VIS: lower: 1903_VIS_07b, middle: 1903_VIS_07a, upper: 1903_VIS_08

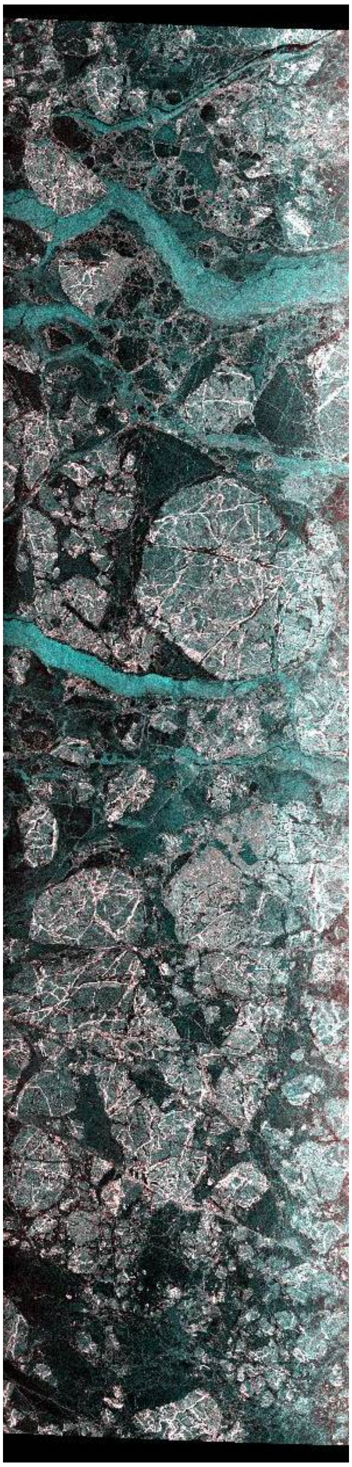

i07icesar0401x1_t02

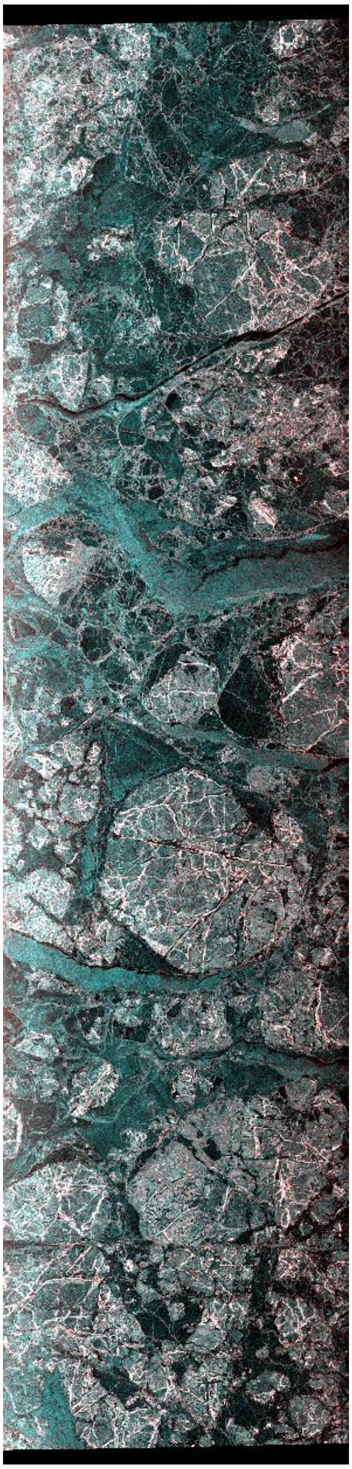

i07icesar0402x1_t02

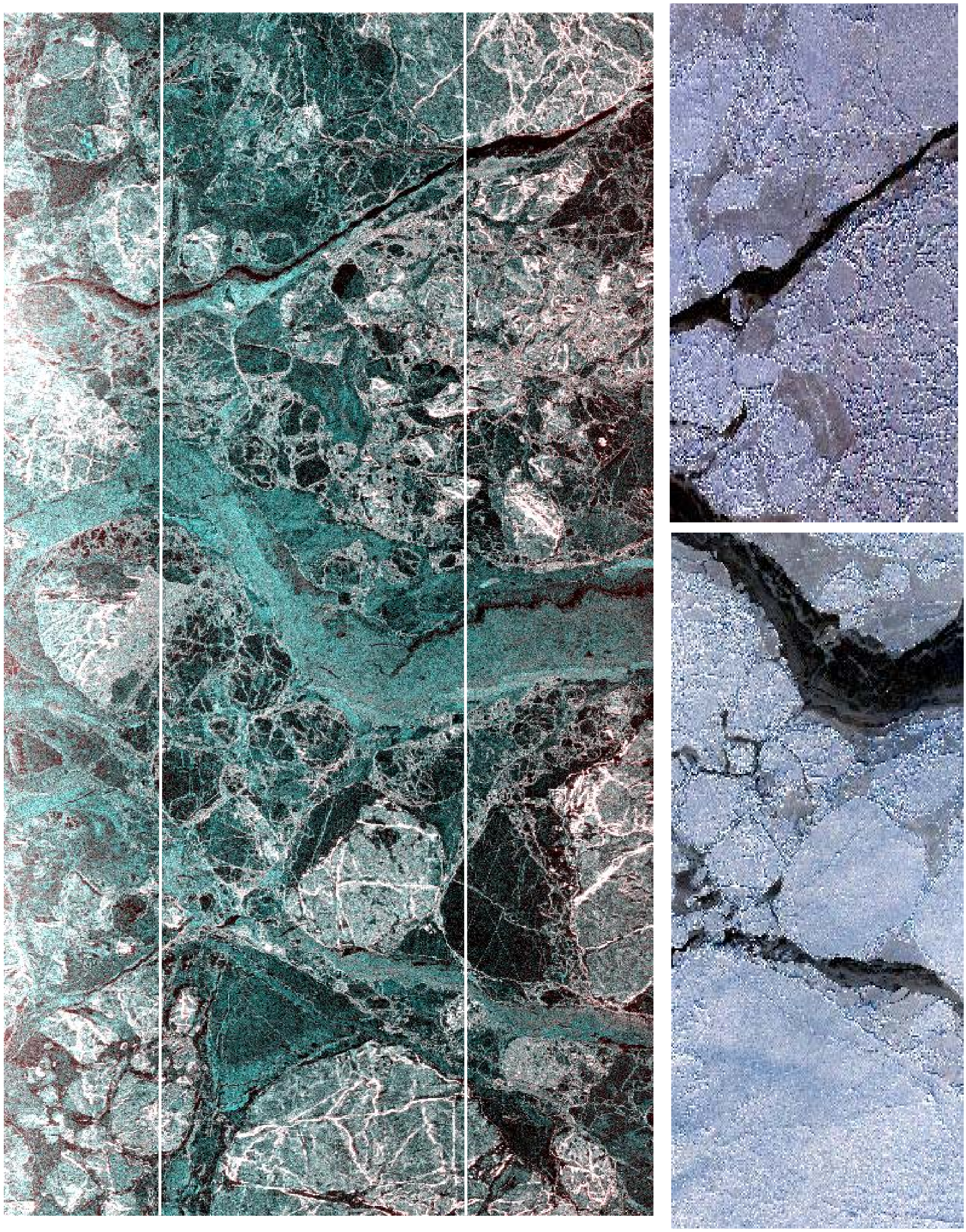

1903CH2_S1, VIS: lower 1903_VIS_11, upper 1903_VIS_12

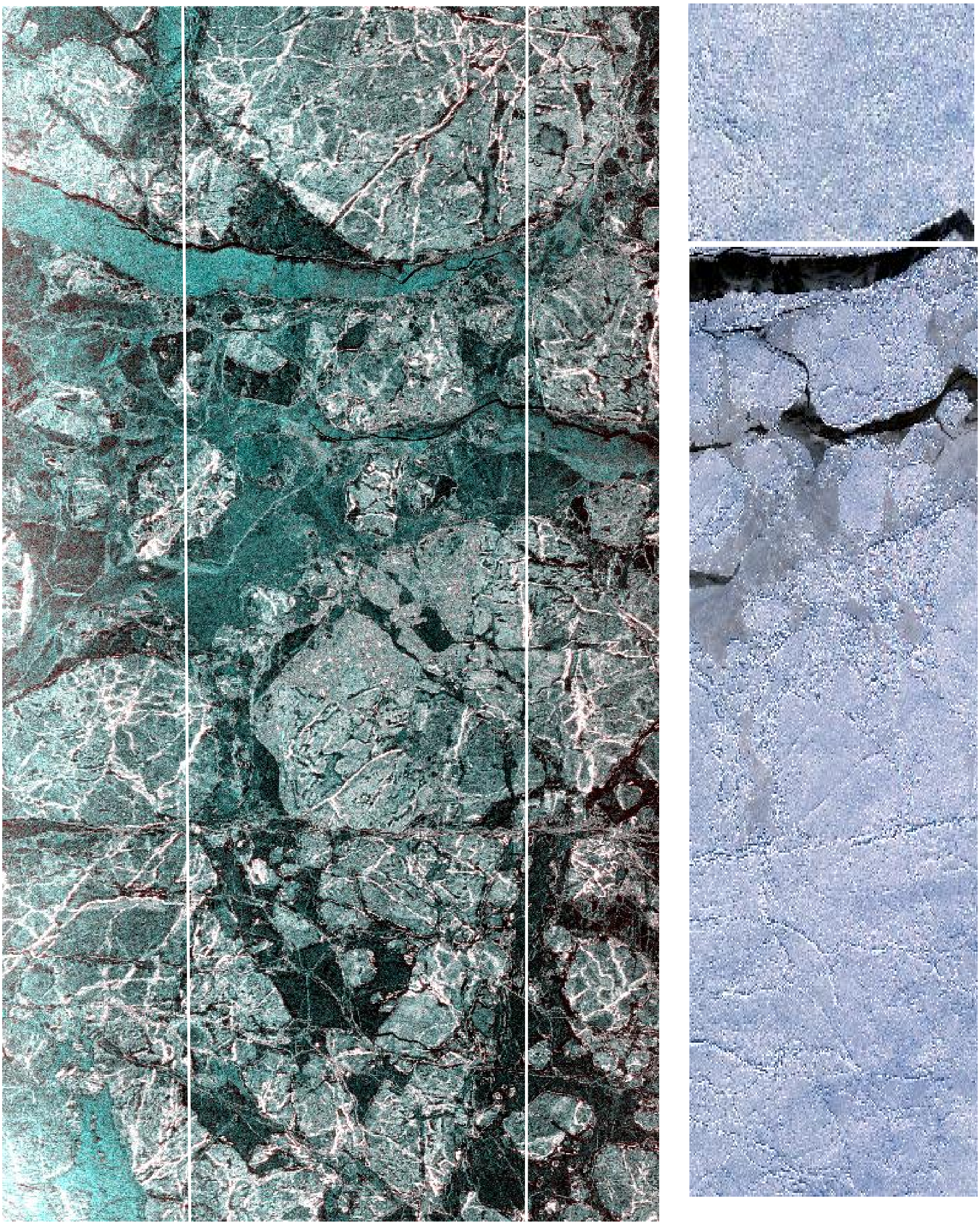

1903CH2_S2, VIS: lower 1903_VIS_10, upper 1903_VIS_12

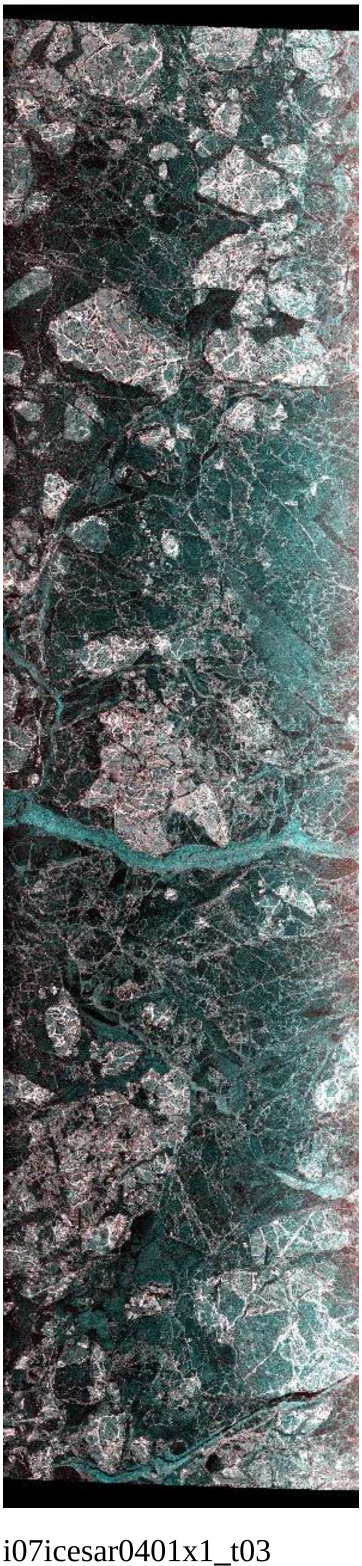

i07icesar0401x1_t03

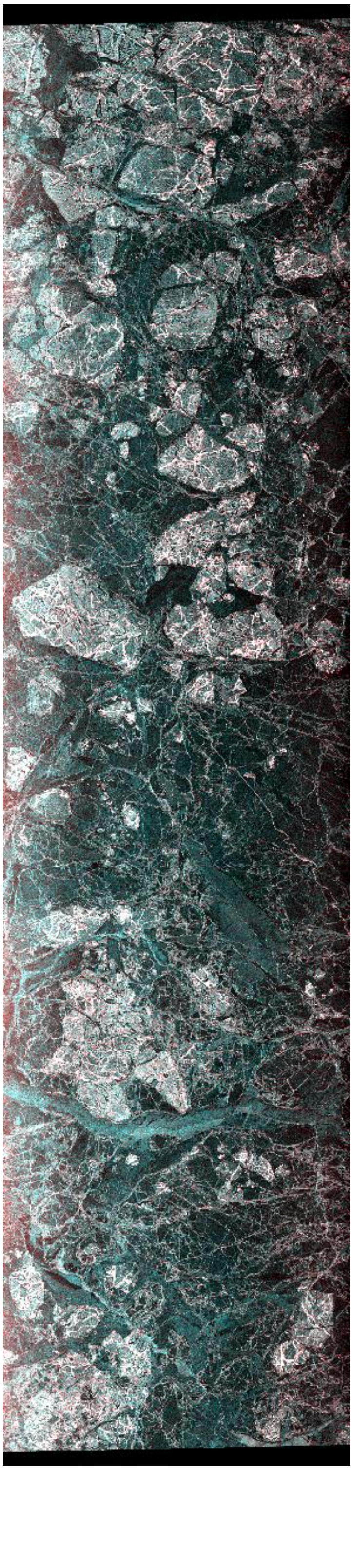

i07icesar0402x1_t03

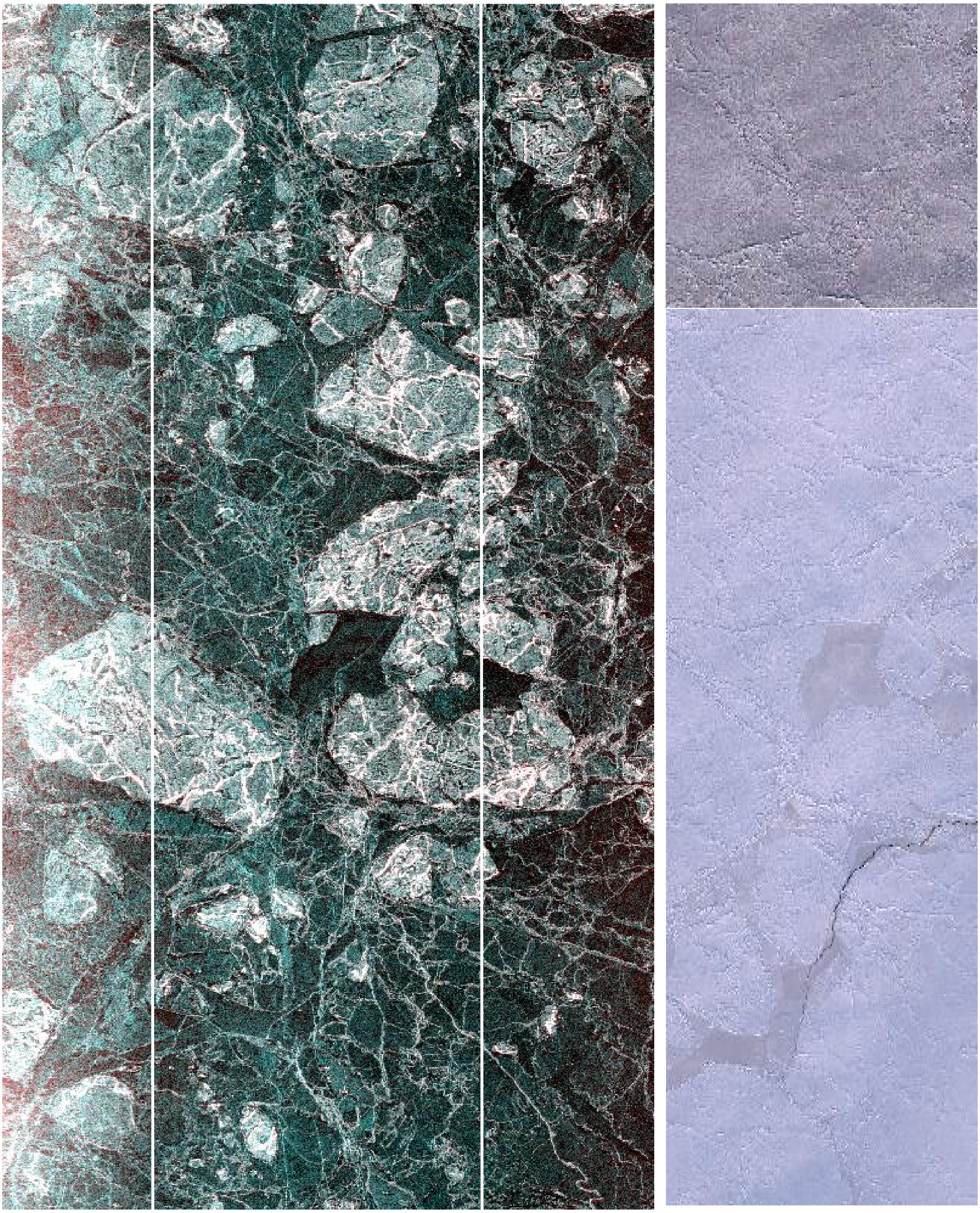

1903CH3_S1, lower 1903_VIS_14, upper 1903_VIS_15

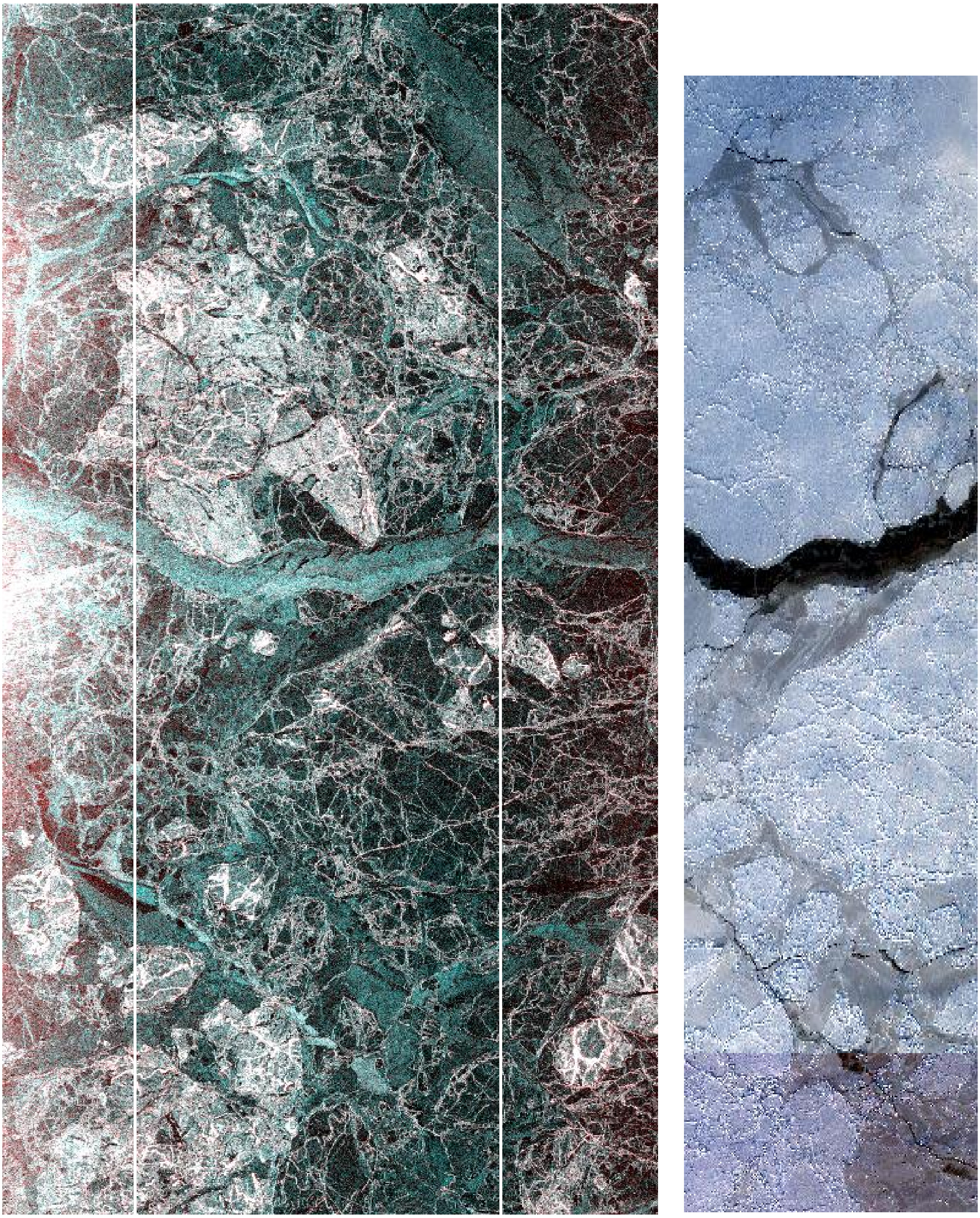

1903CH3_S2, VIS: upper 1903_VIS_13, lower 1903_VIS_12

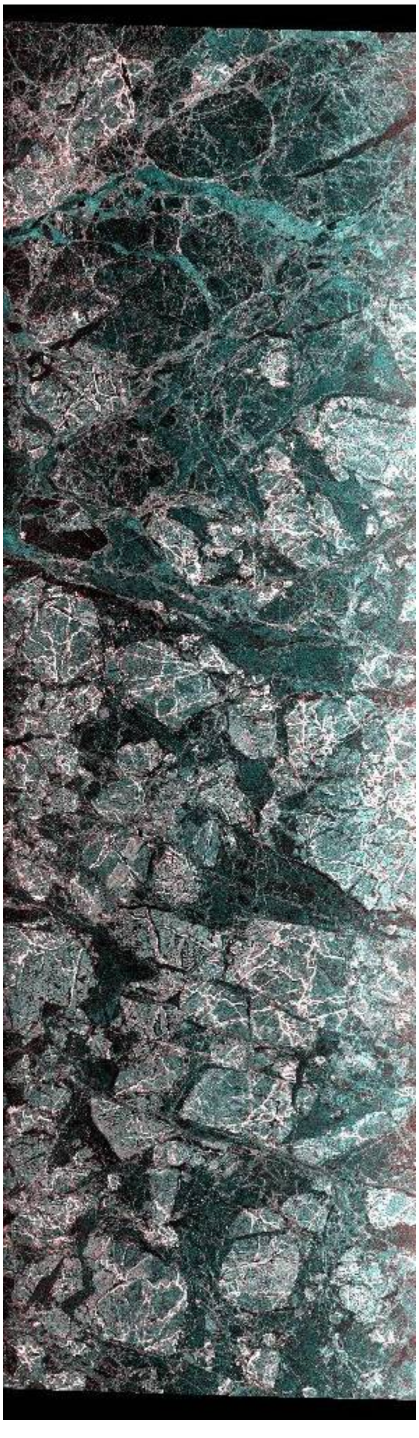

i07icesar0401x1_t04

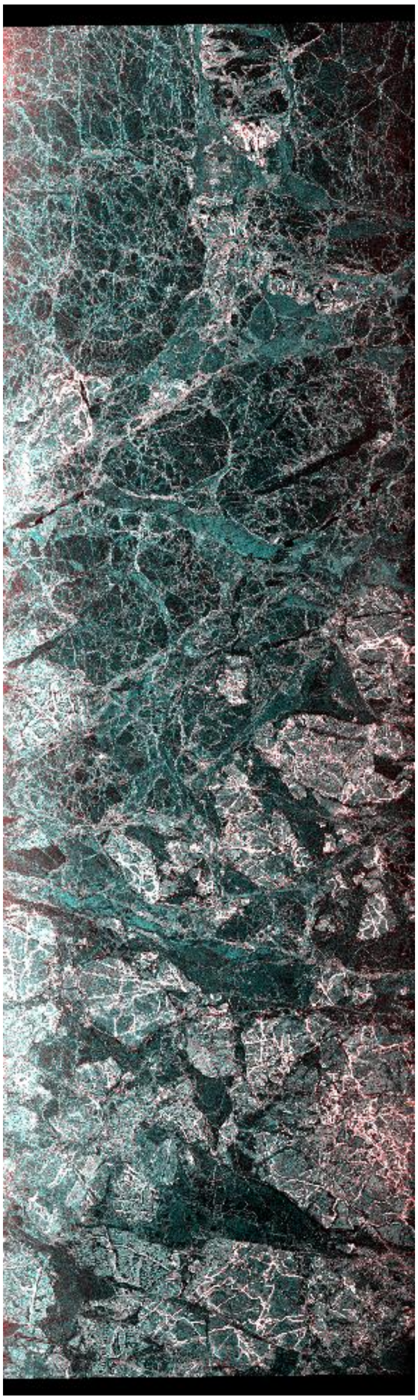

i07icesar0402x1_t04

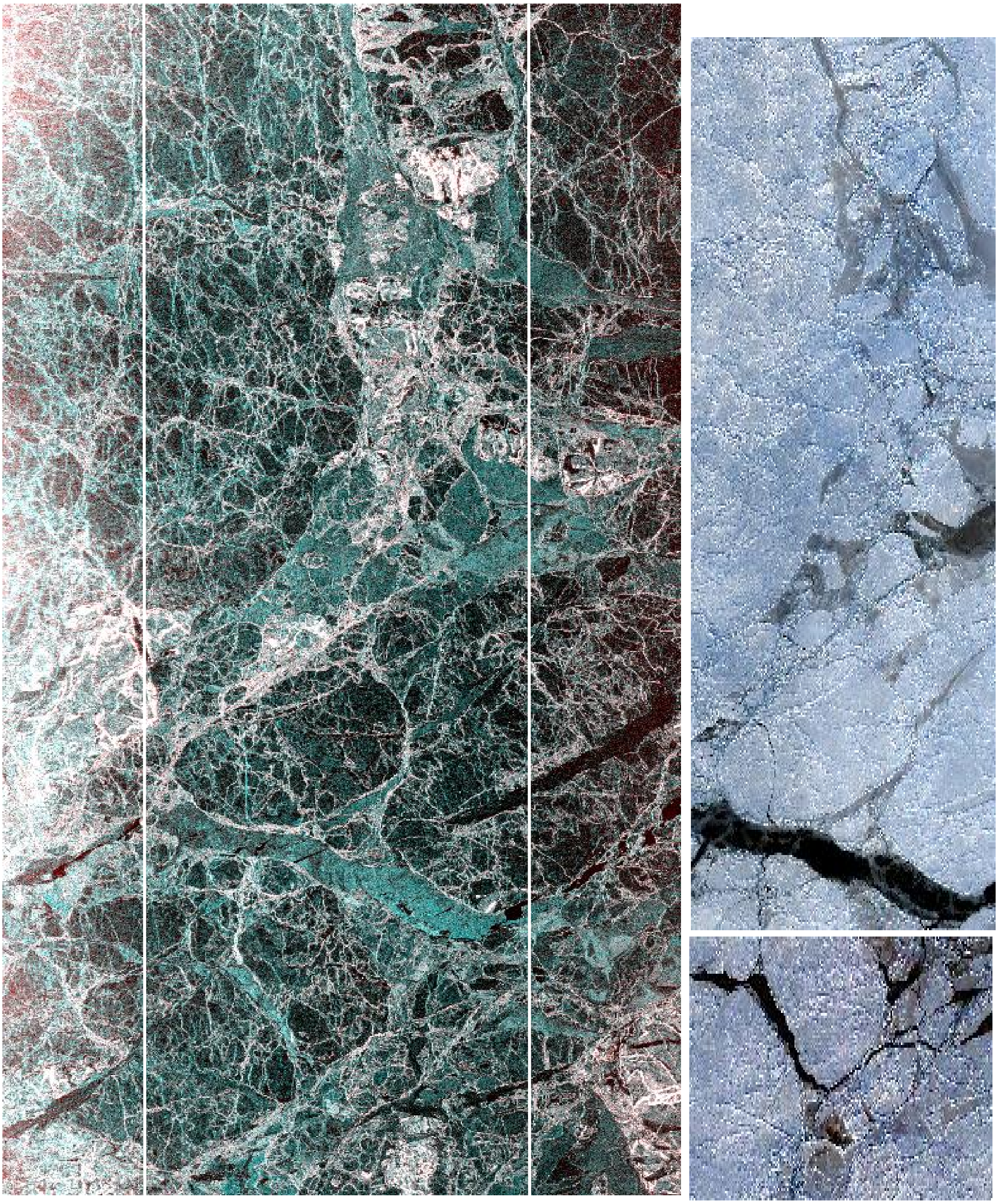

1903CH4_S1, VIS: upper 1903_VIS_17, lower 1903_VIS_16

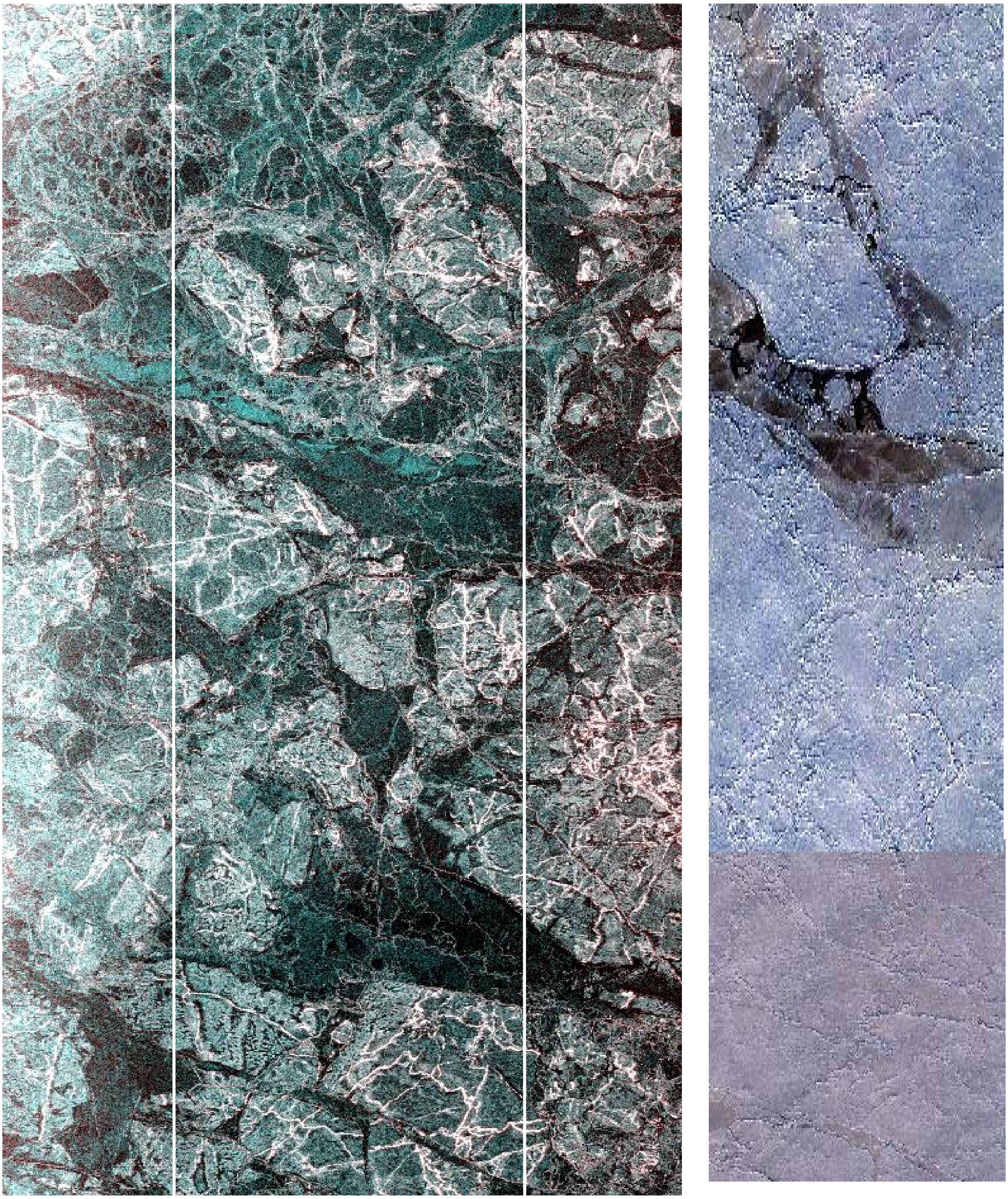

1903CH4_S2, VIS: lower 1903_VIS_15, upper 1903_VIS_16

Date: March 20, Location: Fram Strait (S to N)

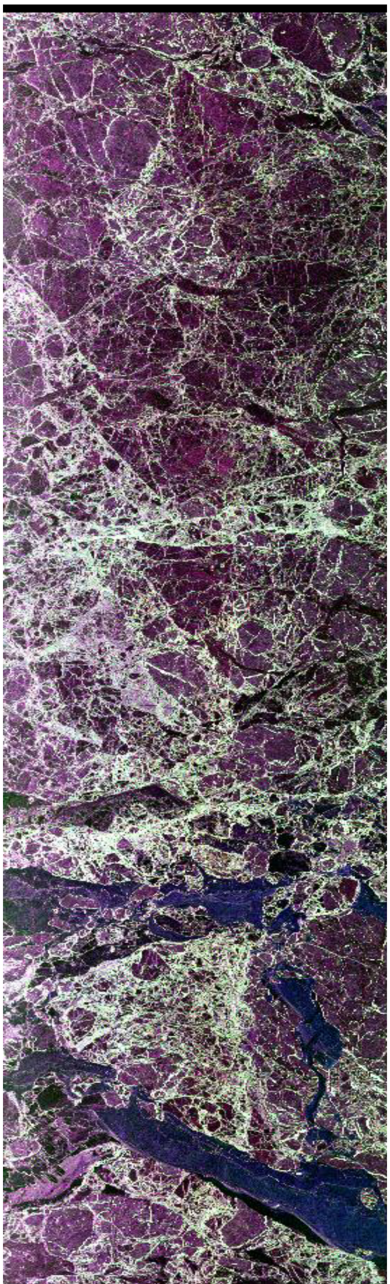

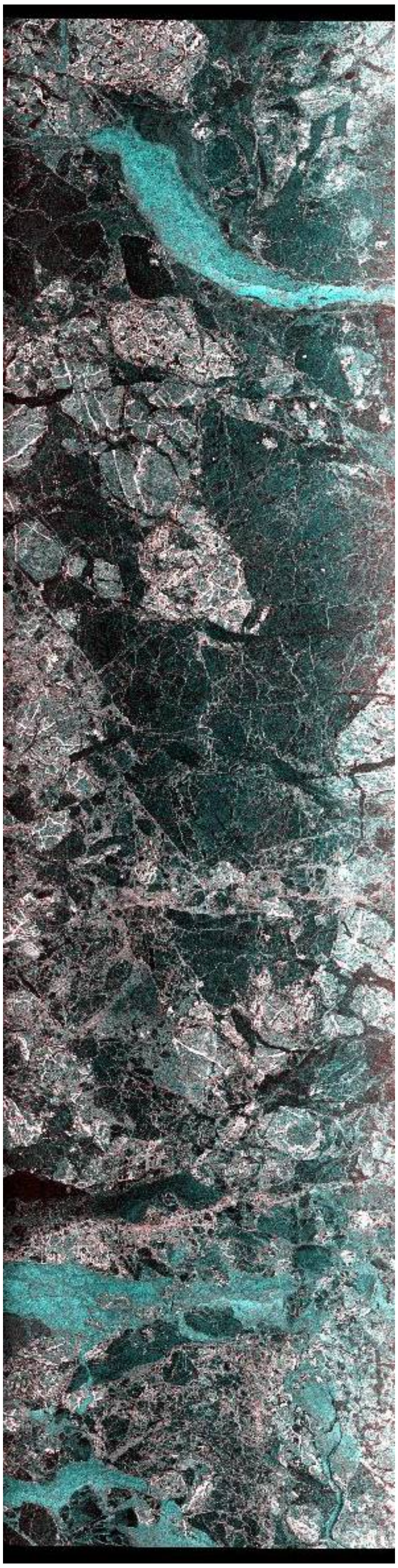

Upper image edge: North
Lower image edge: South

i07icesar0502x1_t01

i07icesar0501x1_t01

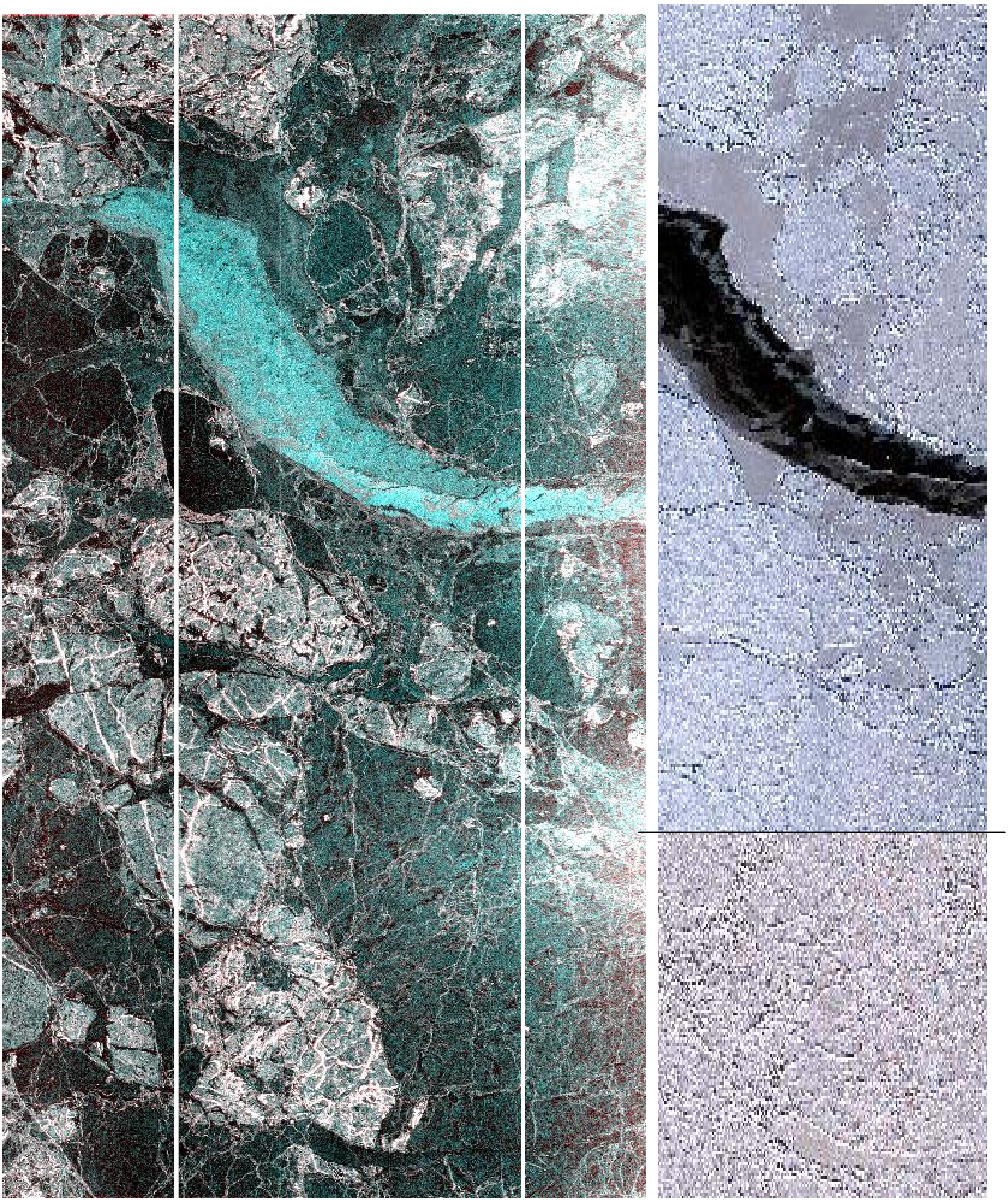

2003C1_S2, VIS: upper 2003_VIS_07,lower 2003_VIS_06

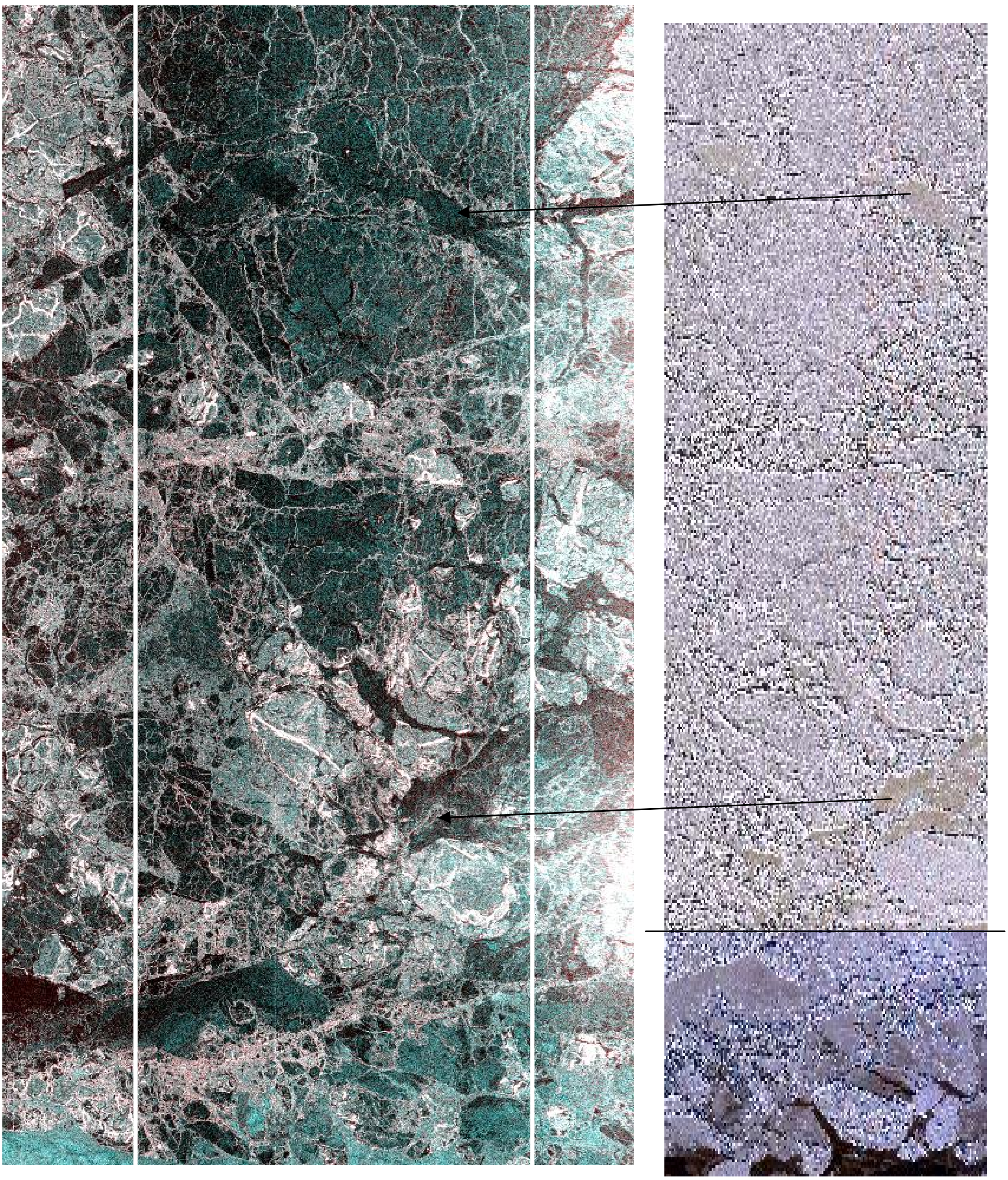

2003C1_S1, VIS: upper 2003_VIS_06, lower 2003_VIS_05

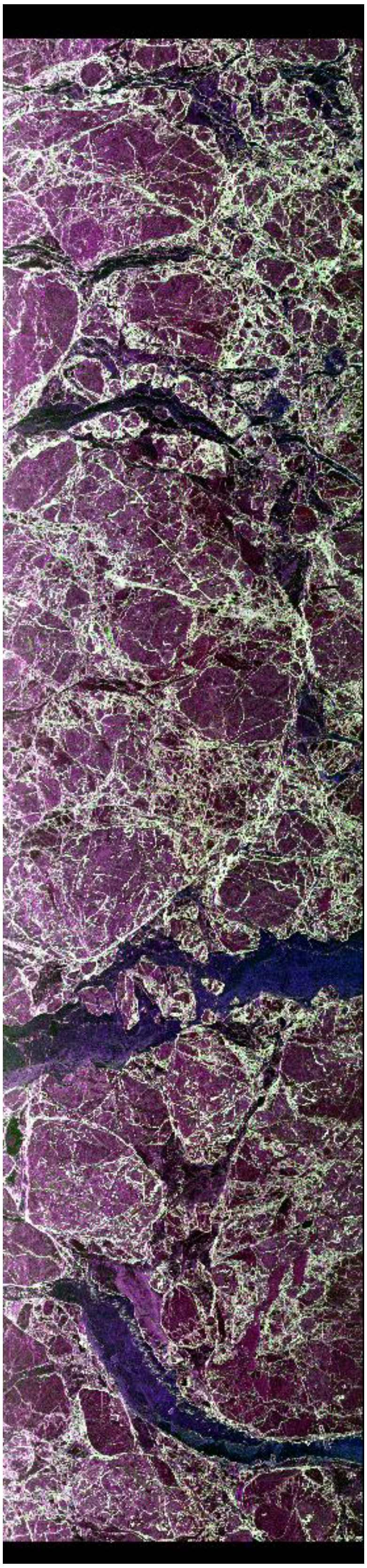

i07icesar0502x1_t02

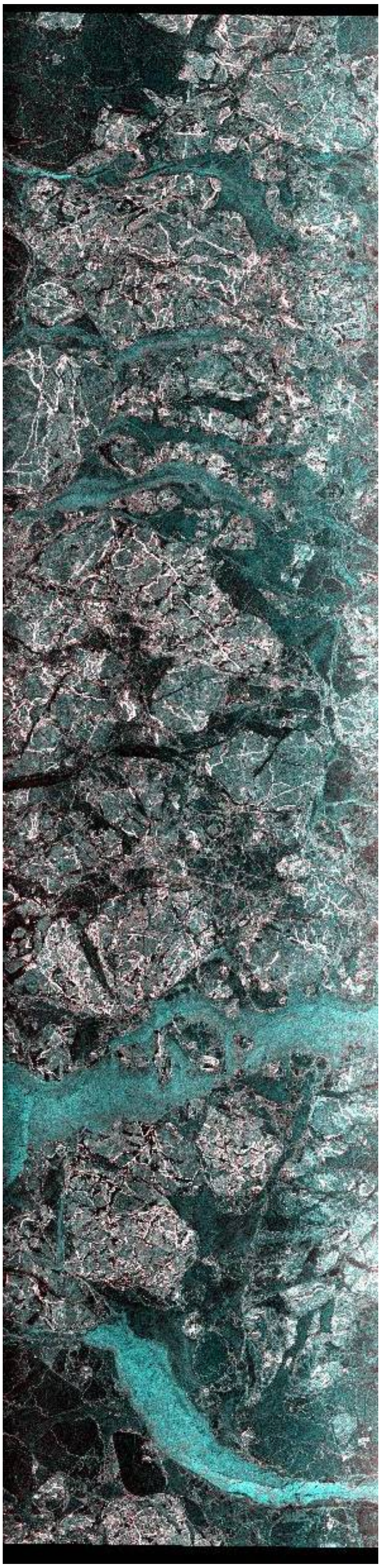

i07icesar0501x1_t02

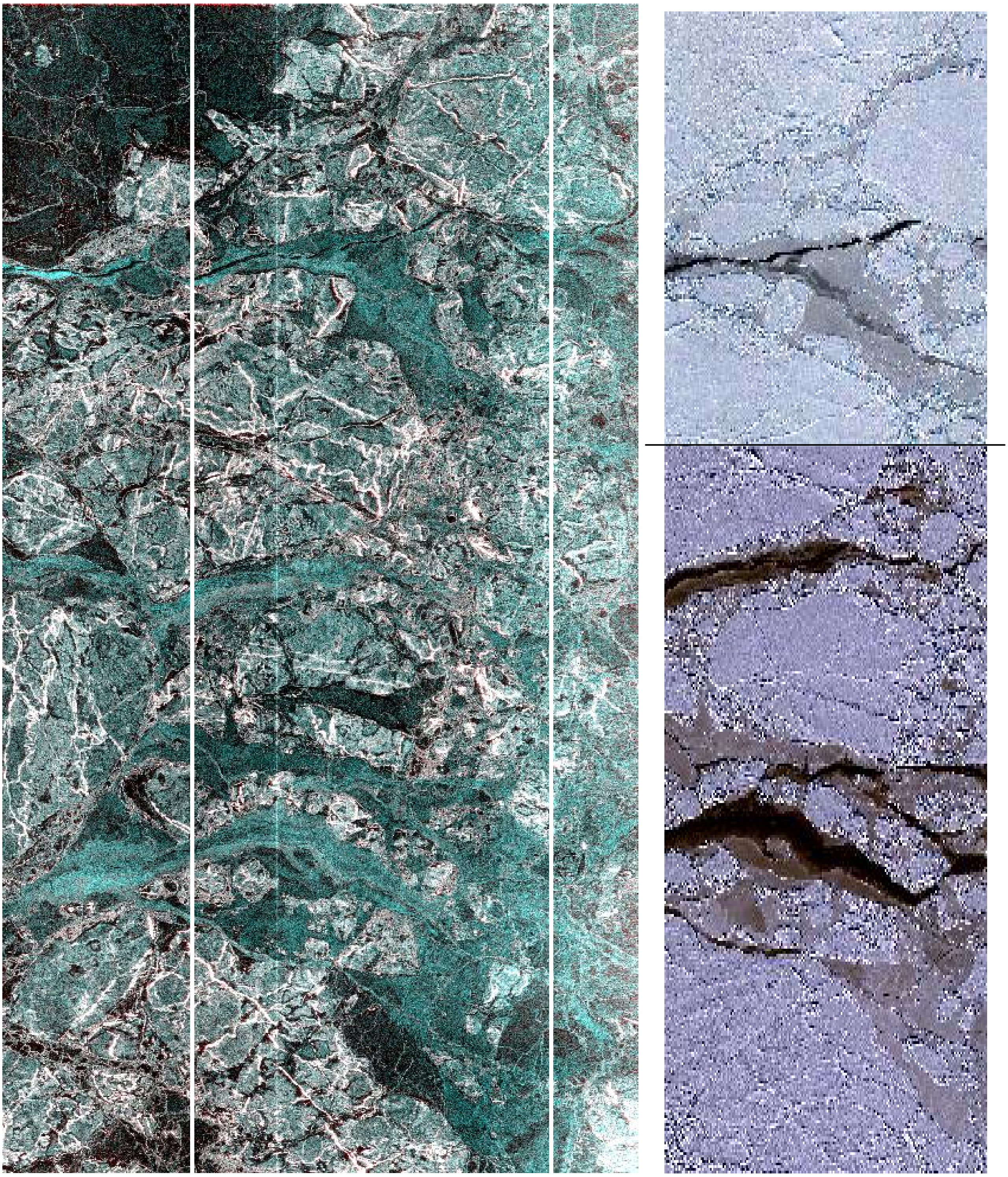

2003C2_S2, VIS: lower 2003_VIS_08, upper 2003_VIS_09

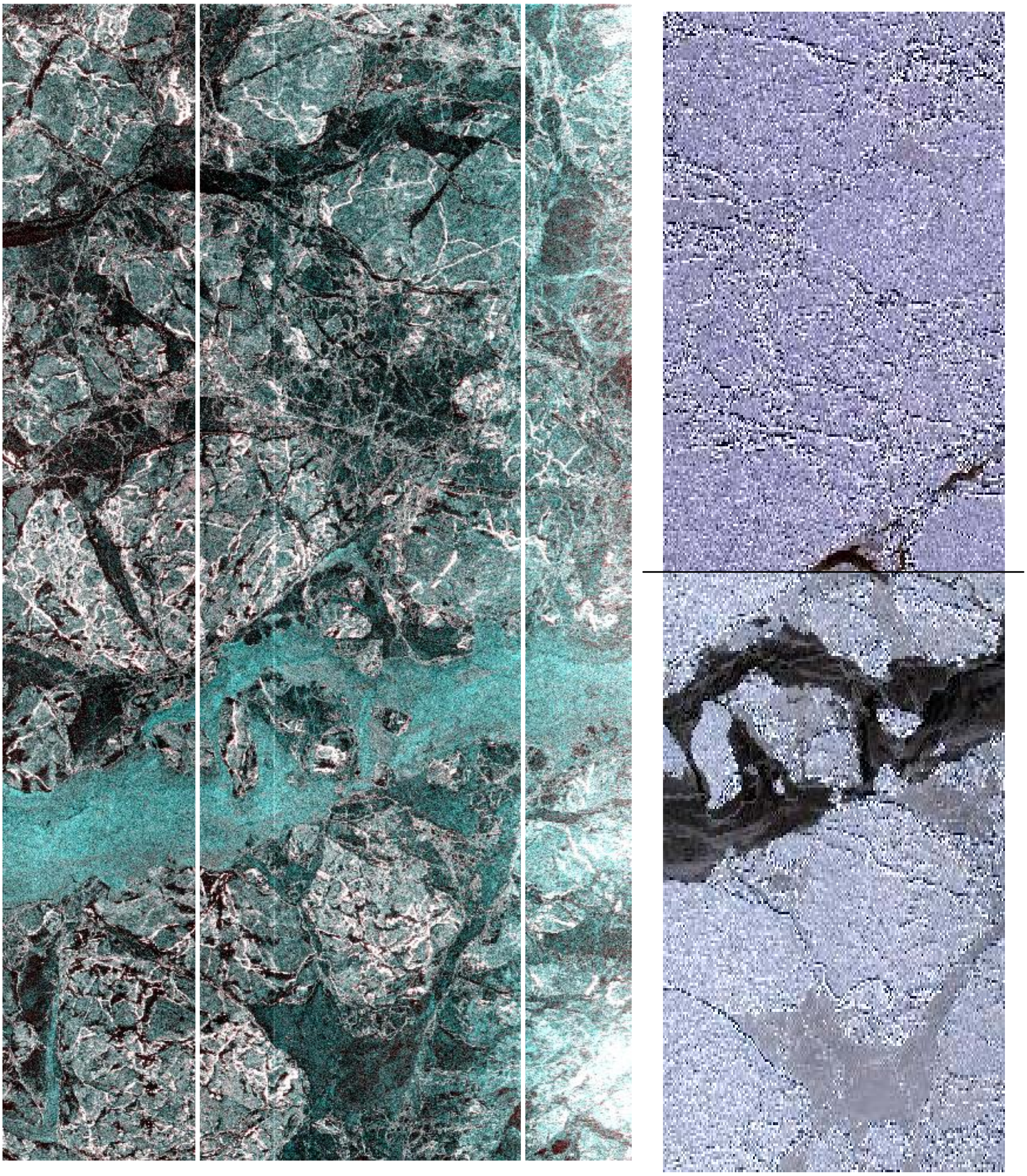

2003C2_S1, VIS: lower 2003_VIS_07, upper 2003_VIS_08

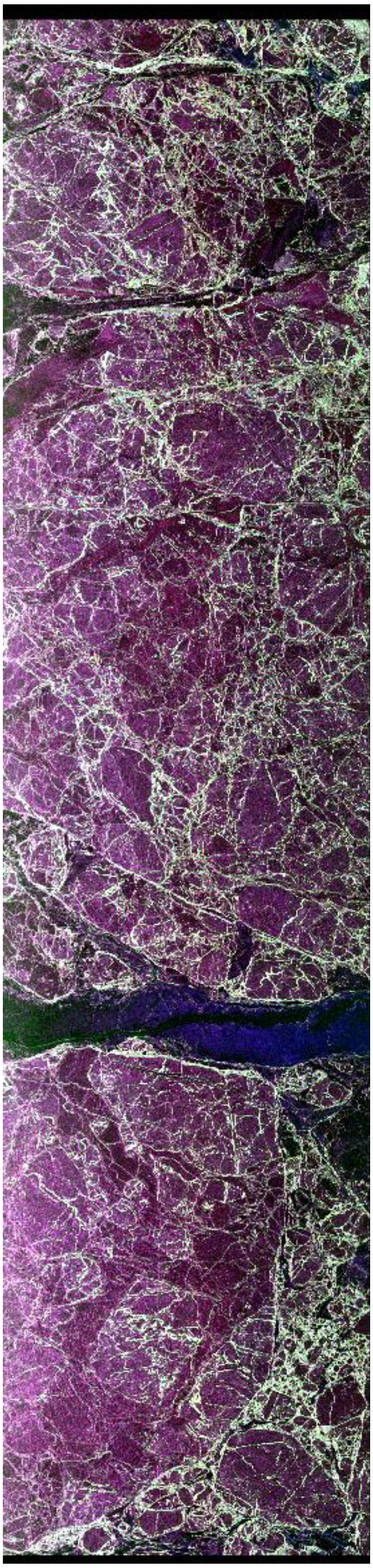

i07icesar0502x1_t03

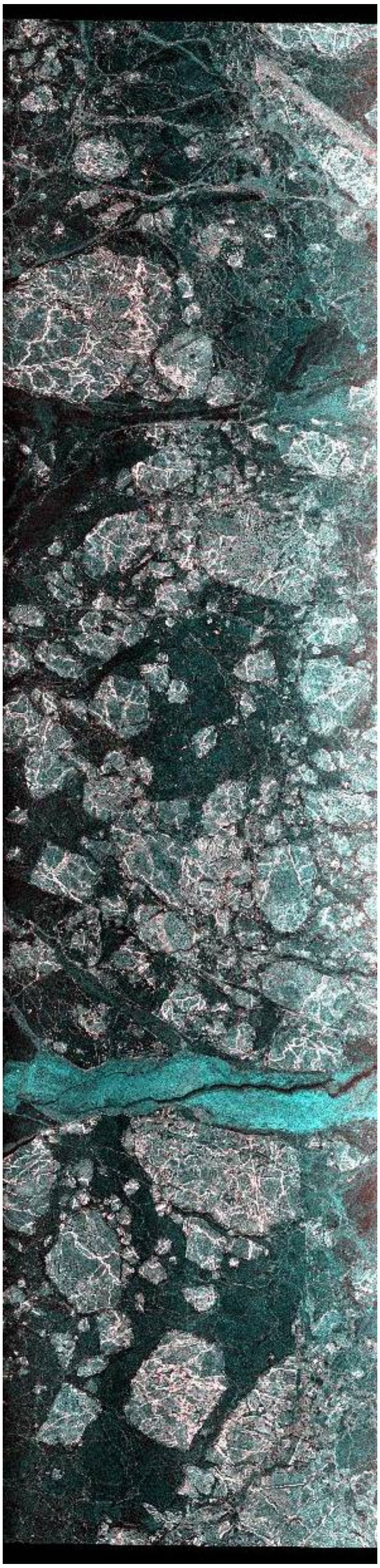

i07icesar0501x1_t03

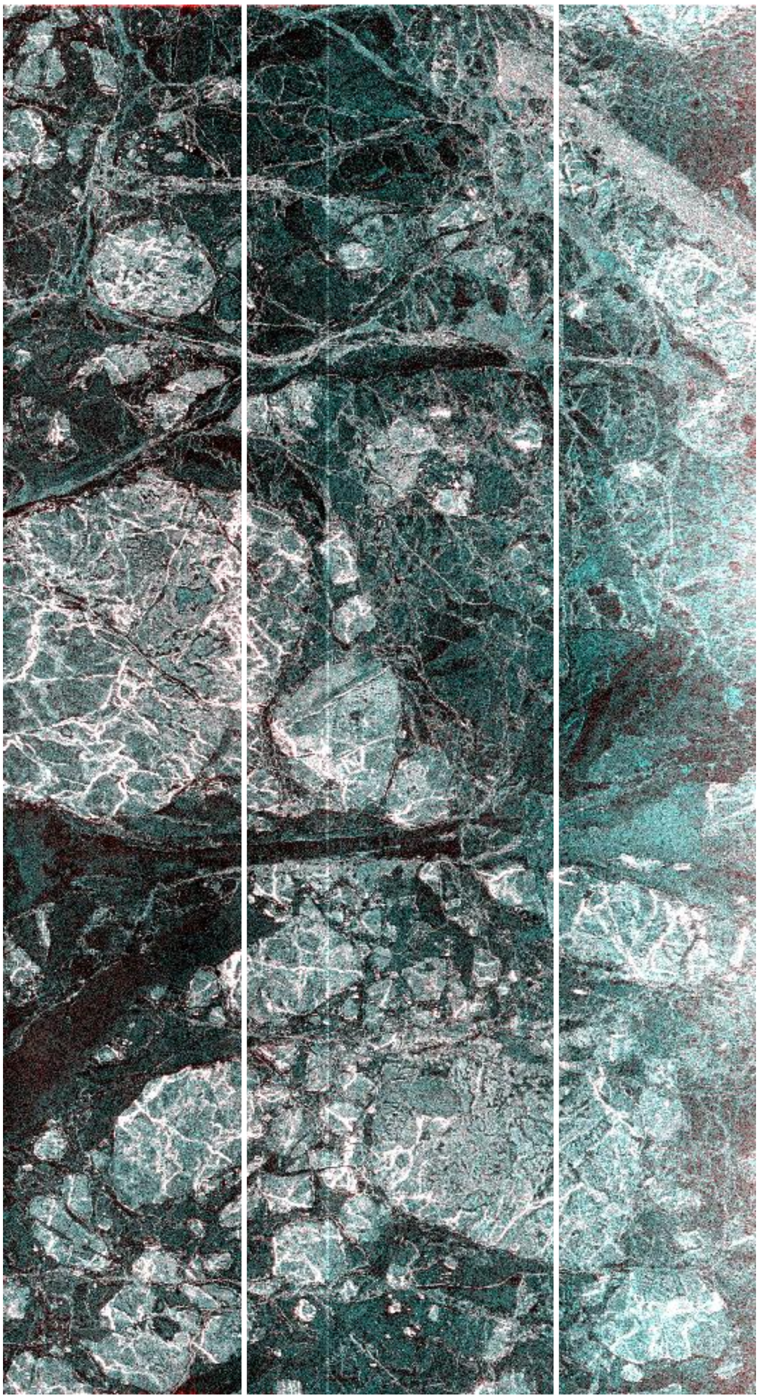

2003C3_S2, lower 2003_VIS_10, upper 2003_VIS_11

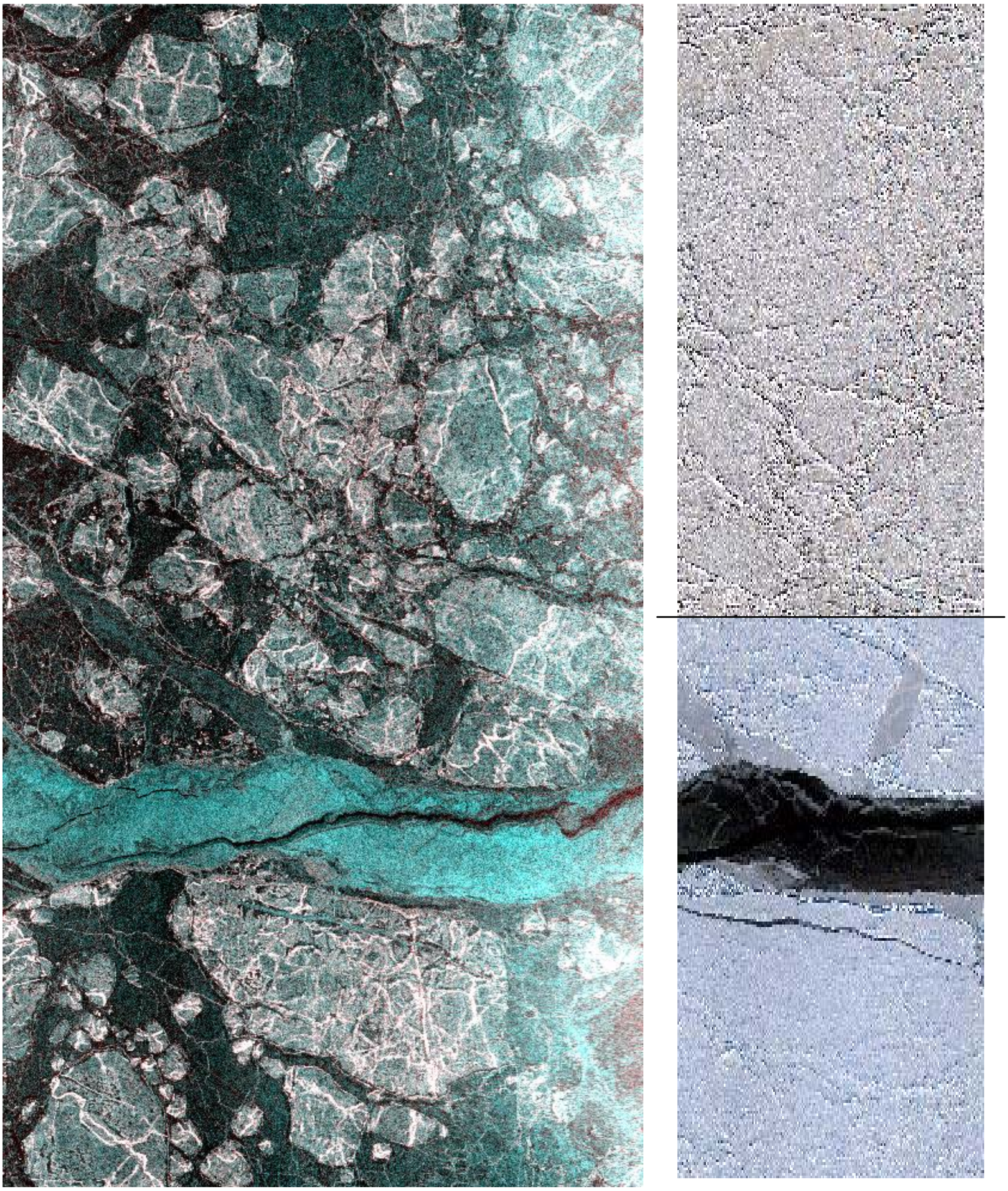

2003C3_S1, lower 2003_VIS_09, upper 2003_VIS_10

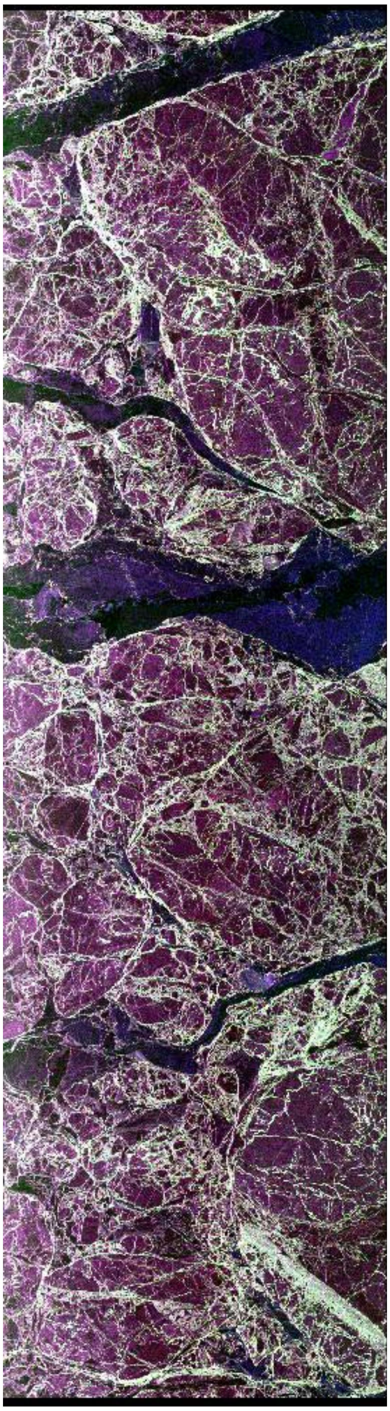

i07icesar0502x1_t04

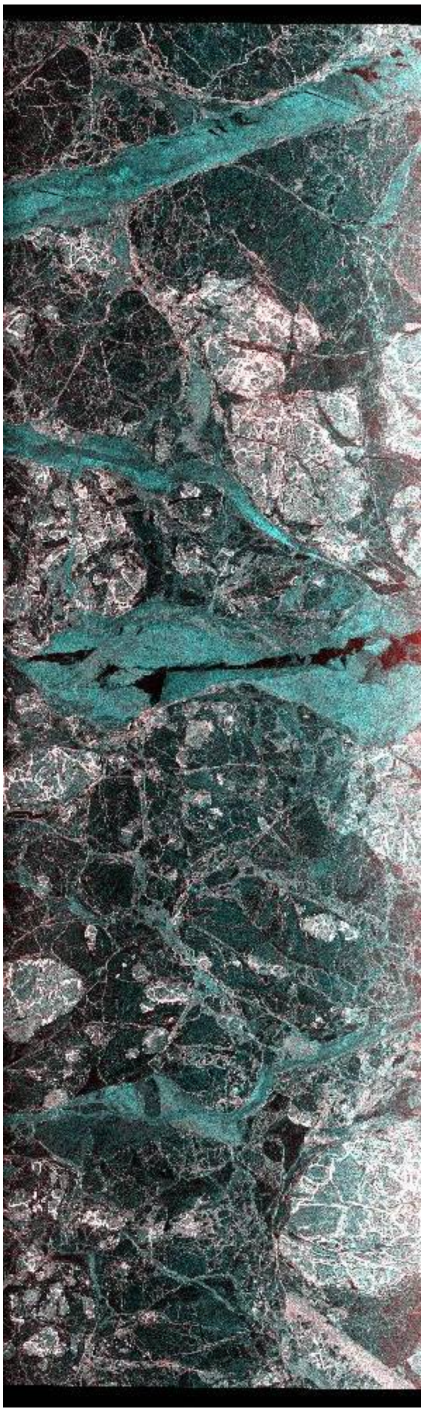

i07icesar0501x1_t04

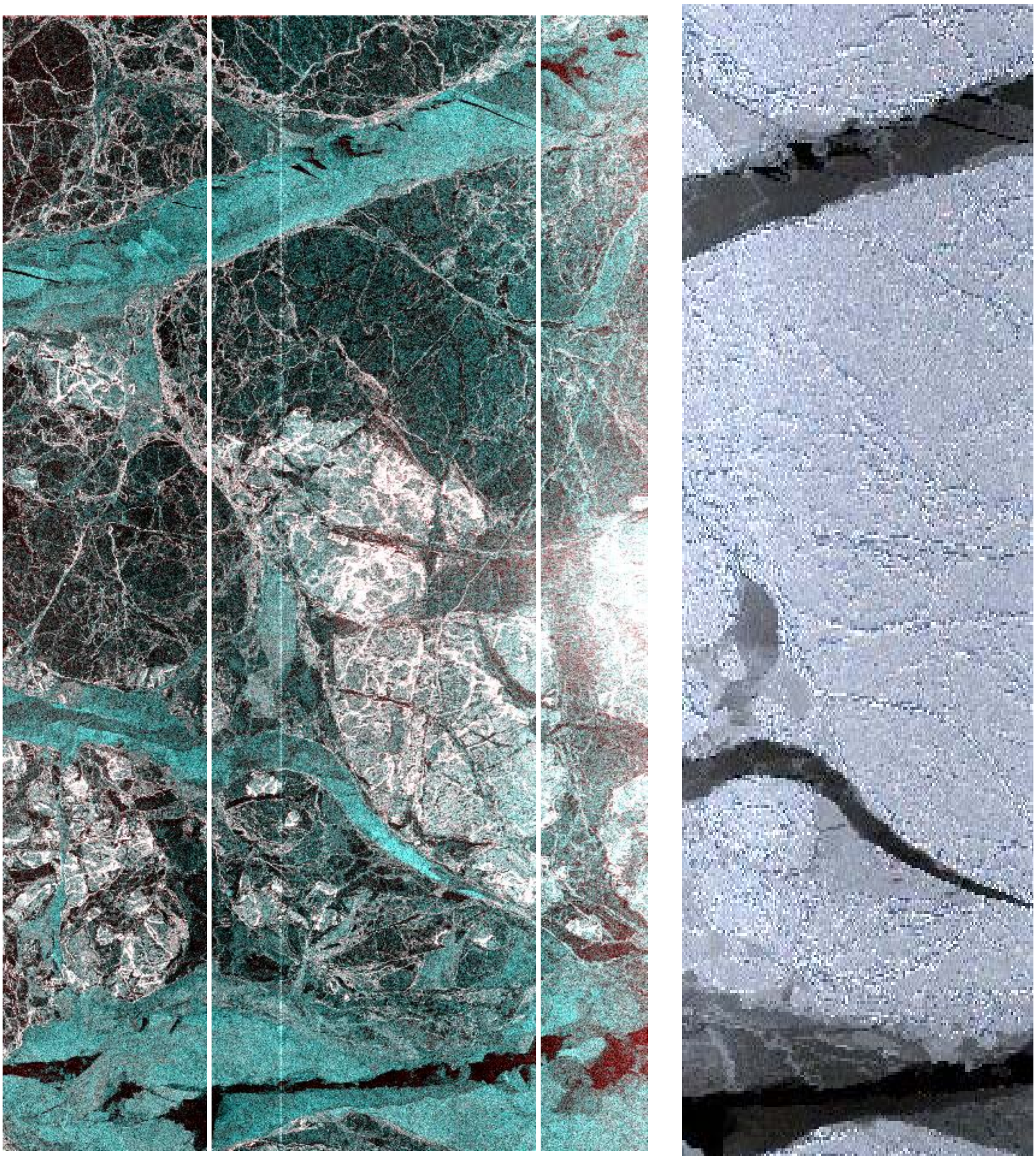

2003C4_S2, 2003_VIS_12

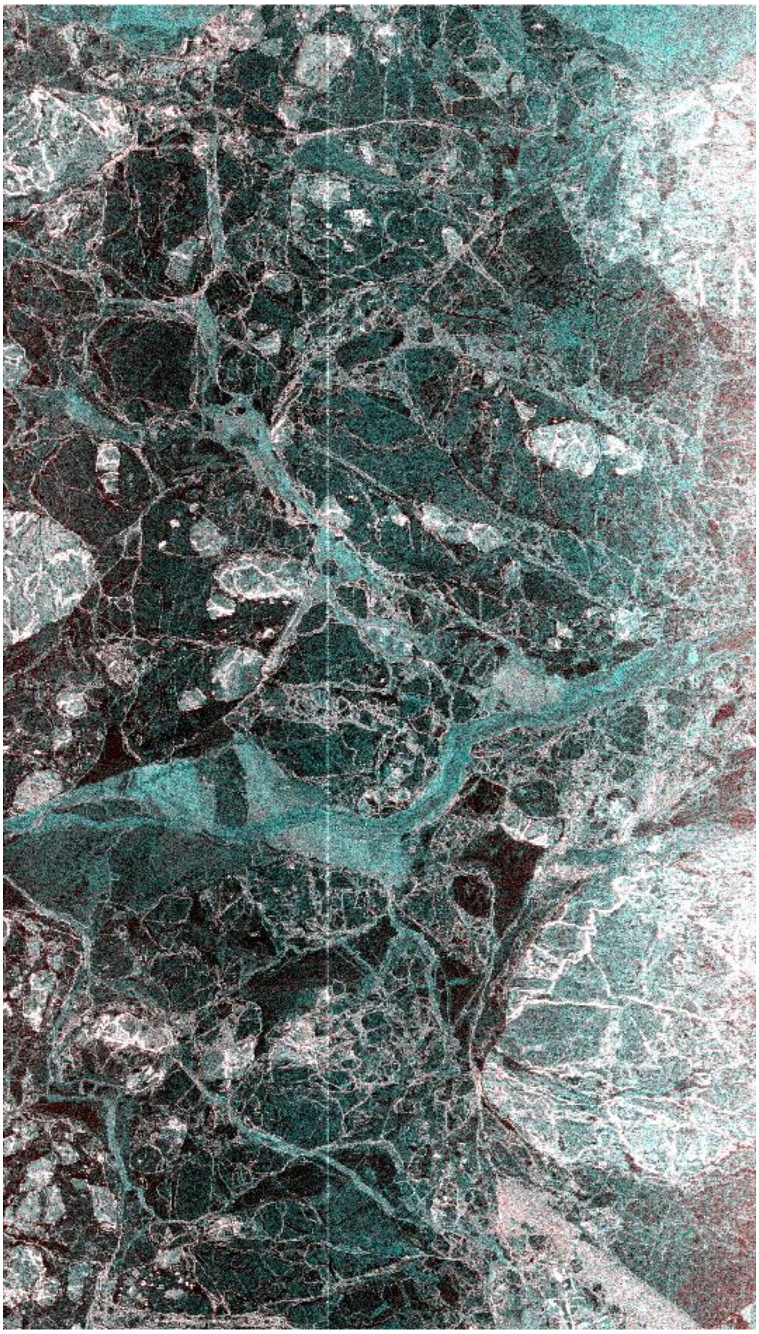

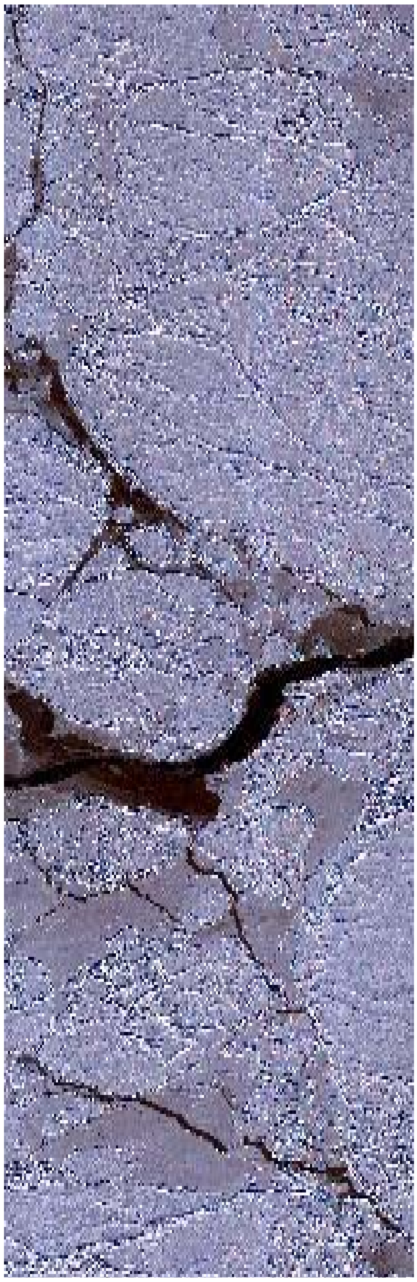

2003C4_S1, 2003_VIS_11

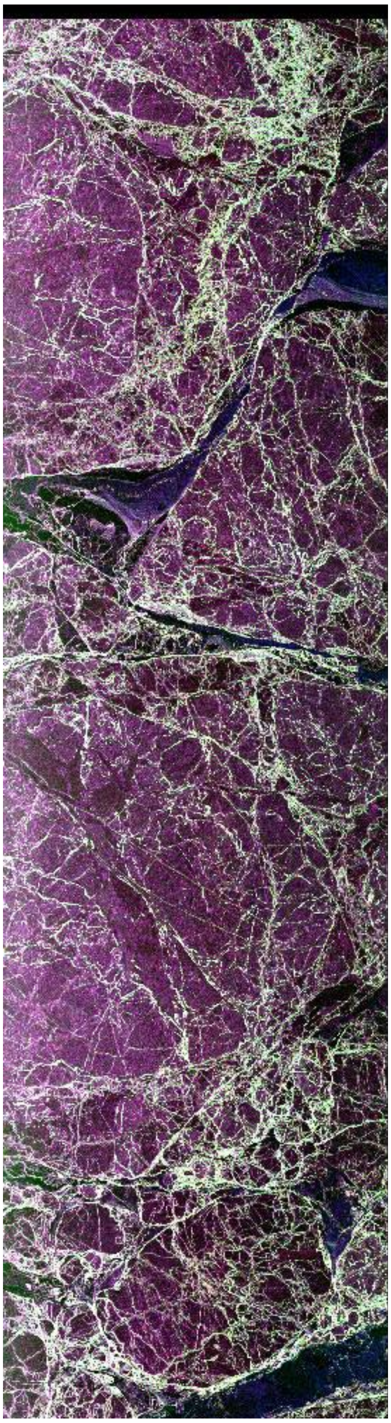

i07icesar0502x1_t05

i07icesar0501x1_t01

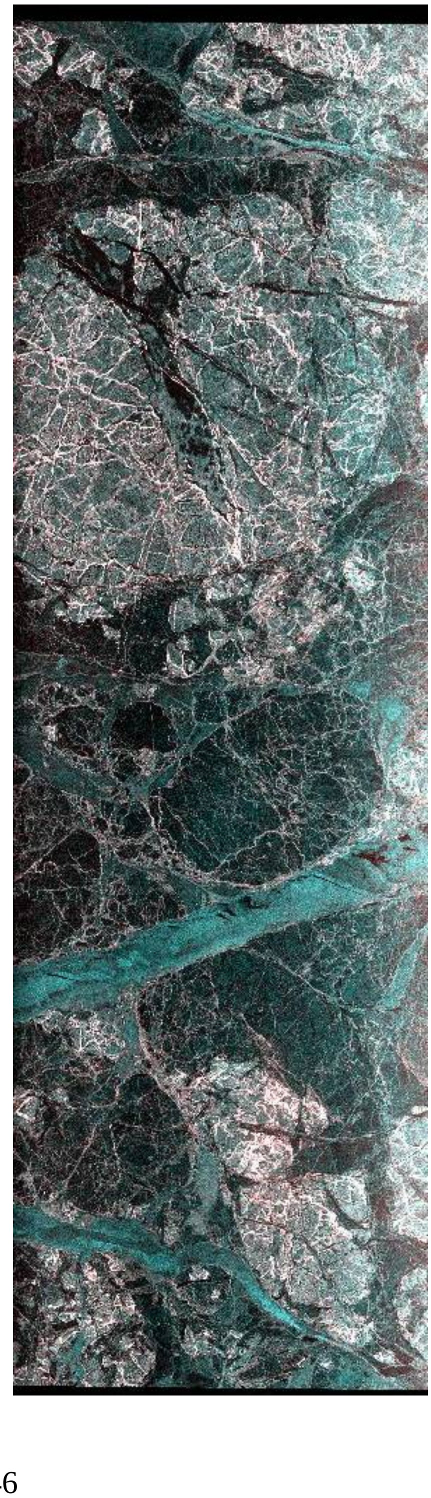

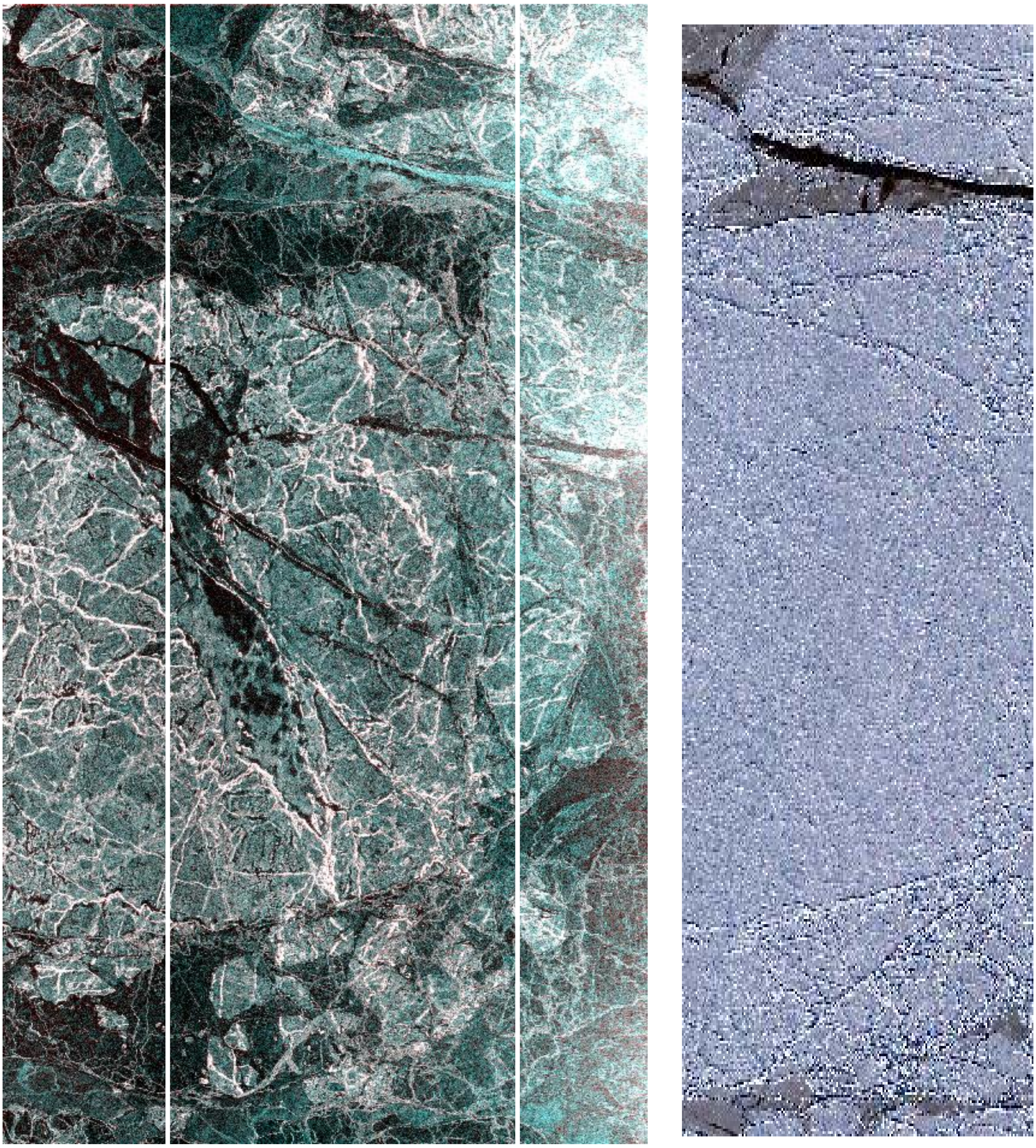

2003C5_S2, 2003_VIS_13

Appendix 2: Polar-2 Data Acquisitions

A2.1 Introduction

The flight operations of Polar-2 were planned according to the three major tasks defined for the ICESAR campaign, namely

(1) to gather data for verification of the Sentinel-1 mission concept for ice services;

(2) to assess the potential of different radar frequencies and polarizations; and

(3) to measure atmospheric turbulence and heat fluxes in the atmospheric boundary layer for different ice conditions.

The objective of the task 3 is to improve algorithms for calculations of the atmospheric drag coefficient as a function of ice surface roughness. The drag coefficient is needed in simulations of atmosphere – sea ice interactions.

This appendix focuses on airborne radar and optical imagery acquired for tasks 1 and 2. In addition, supplementary images are available from satellite SAR, and weather conditions are documented from measurement reports of different meteorological stations in the Svalbard region. The data sets of the optical scanner, the satellite SARs, and the weather stations are described in more detail in the sections below

The instruments mounted on the AWI-aircraft (a Dornier Do228-101, “D-CAWI”, “Polar 2”) during the ICESAR campaign are detailed in Table A2.1 below. The sea ice surface temperature and the atmospheric parameters measured by the Meteopod sonde are only partly described in this appendix. Wind speed and direction and air temperature at flight altitude were monitored during the flights. The radiation thermometer data may provide useful additional information for evaluating the ice classification performance of the radar sensors when the temperature is close to or above freezing point.

Figure A2.1a. Polar-2 aircraft

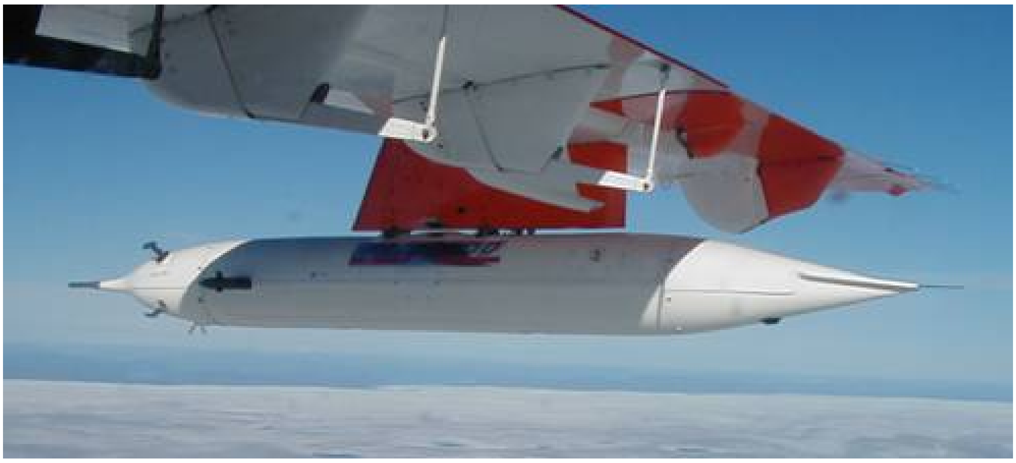

Figure A2.1b: Meteopod

A2.2 Flight Operations of Polar-2

During the campaign, four joint flights of Polar-2 and the DLR-airplane were carried out in the period from March 16 to March 20. Timing and location are shown in Table 2.2 below. The flight protocols can be found in the appendix. Besides these flights which were part of the data acquisition program in preparation of ESA's Sentinel-1 mission, three additional meteorological flights of Polar-2 took place from March 21 to March 25 in the framework of AWI's boundary layer studies (on 21, 23, and 25 of March). These flights do not include linescanner imagery gathered at larger altitudes. Photographs of the ice situation and information about weather conditions during the flights, however, are available to support the analysis of some of the satellite SAR images acquired during that period.

Table A2.1: Polar-2 Instruments

Instrument	Purpose	Technical Configuration
Color Line Scanner (CLS)	Optical image acquisitions during sea ice flights	Bands used: 410-470 nm, 500-570 nm, 580-680 nm Effective resolution at 1000 m altitude and 150 knots (= 77.1 m/s) speed over ground (with 24mm lens, 2048 pixels per line, scan time 20 ms) across-track: 0.5 m along-track: 1.5 m
Laser profiler	Measurements of ice surface elevation along the flight track	Spot diameter: 0.1m (for flight altitude 30m) Horizontal resolution 0.1 m Vertical accuracy 0.02 m Sample rate 2000 Hz
Radiation Thermometer	Measurements of the ice surface temperature on a profile along-track	Opening angle 0.6° Response time 0.1s Sample rate 10 Hz
Meteopod	Probe attached to the wing for measuring the wind vector components, air pressure, humidity, and temperature at flight altitude	Sample rate 100 Hz Accuracy of wind measurements: ±0.5 m absolute, ±0.1 m relative Accuracy of turbulent heat flux measurements: ±5 W/m^2

Over sea ice test sites, Polar-2 and E-SAR carried out their measurements in almost the same time interval. In general, the profiles were flown parallel to the wind direction (however, highly variable wind directions were observed during the March 16 flight, see protocol). The optical data that are required for comparison with the radar imagery were gathered on profiles between 50 and 150 km long, at altitudes between 250 and 915 m and speed-over ground values of 45 - 65 m/s, dependent on wind conditions and visibility (see Table A2.2). Additionally, three legs were flown at each test site at low altitude (about 30 m) for measurements of wind turbulence (Meteopod), surface roughness (laser), and ice surface temperature (radiation thermometer). At the beginning and the end of each leg, the airplane went up to larger altitudes for acquiring vertical temperature profiles. On certain occasions, vertical temperature profiles were measured flying sawtooth patterns over one leg (on March 18 and 20, see figures below). While the aircraft flew over the profile, photos of the ice conditions were taken with a hand-held camera (see protocols at the end of this appendix).

Over the test sites, the DLR airplane flew at an altitude of 3000 m, acquiring C-band dual polarisation (VV-VH or HH-HV) and L-band polarimetric data. The time difference between acquisitions of optical data and the radar images was planned as small as possible. For any point in the images, it is less than 2 hours (see Table 1 in Appendix 1). In order to gather data over different ice conditions, joint flights were carried out over the Storfjord, in the Barents Sea, and in the Fram Strait region northwest of Svalbard (see Figs. A2.2 – A2.5). Because of the larger distance between the airport and the Fram Strait test site, the profile length over which data could be collected were shorter (50-60 km, see Table A2.2).

The plots shown in Figures A2.2-A2.5 include also information on altitude variations during the flights.

Table A2.2: Joint flights of Polar-2 and DLR-airplane, O. D. A. = Optical Data Acquistion

Date	Departure/Arrival Polar-2 (UTC)	Profile Length	O. D. A. Altitude	O. D. A. Speed over Ground	Test Site Region
16/03/07	10:45 – 14:55	150 km	245-305 m	60 m/s	Storfjord
18/03/07	12:15 – 16:45	140 km	915 m	46 m/s	Barents Sea
19/03/07	10:50 – 15:40	50 km	915 m	48 m/s	Fram Strait (NNW Svalbard)
20/03/07	10:40 – 15:45	59 km	915 m	63 m/s	Fram Strait (NNW Svalbard)

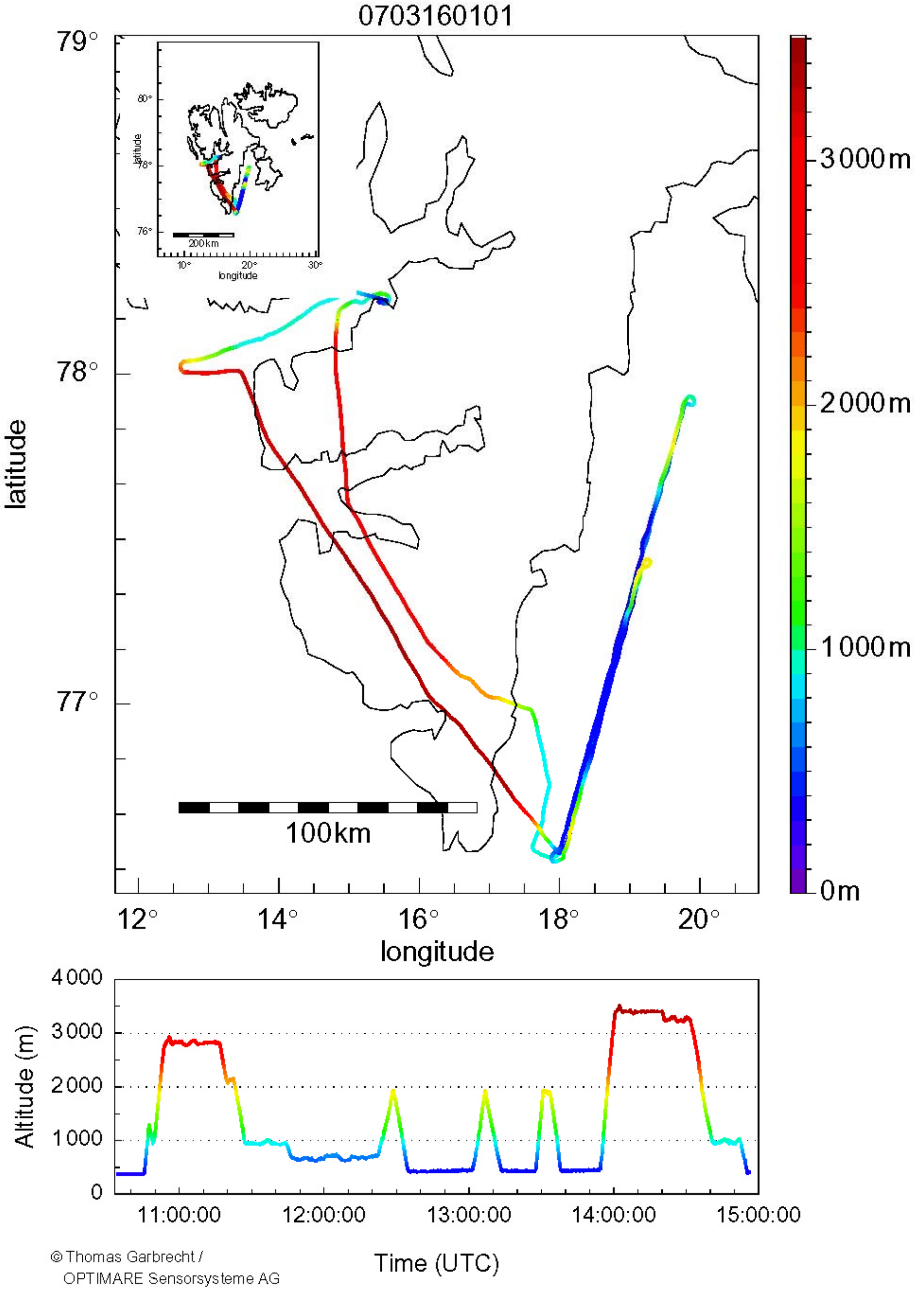

Figure A2.2: Flight pattern of Polar-2 on March 16 in the Storfjord.

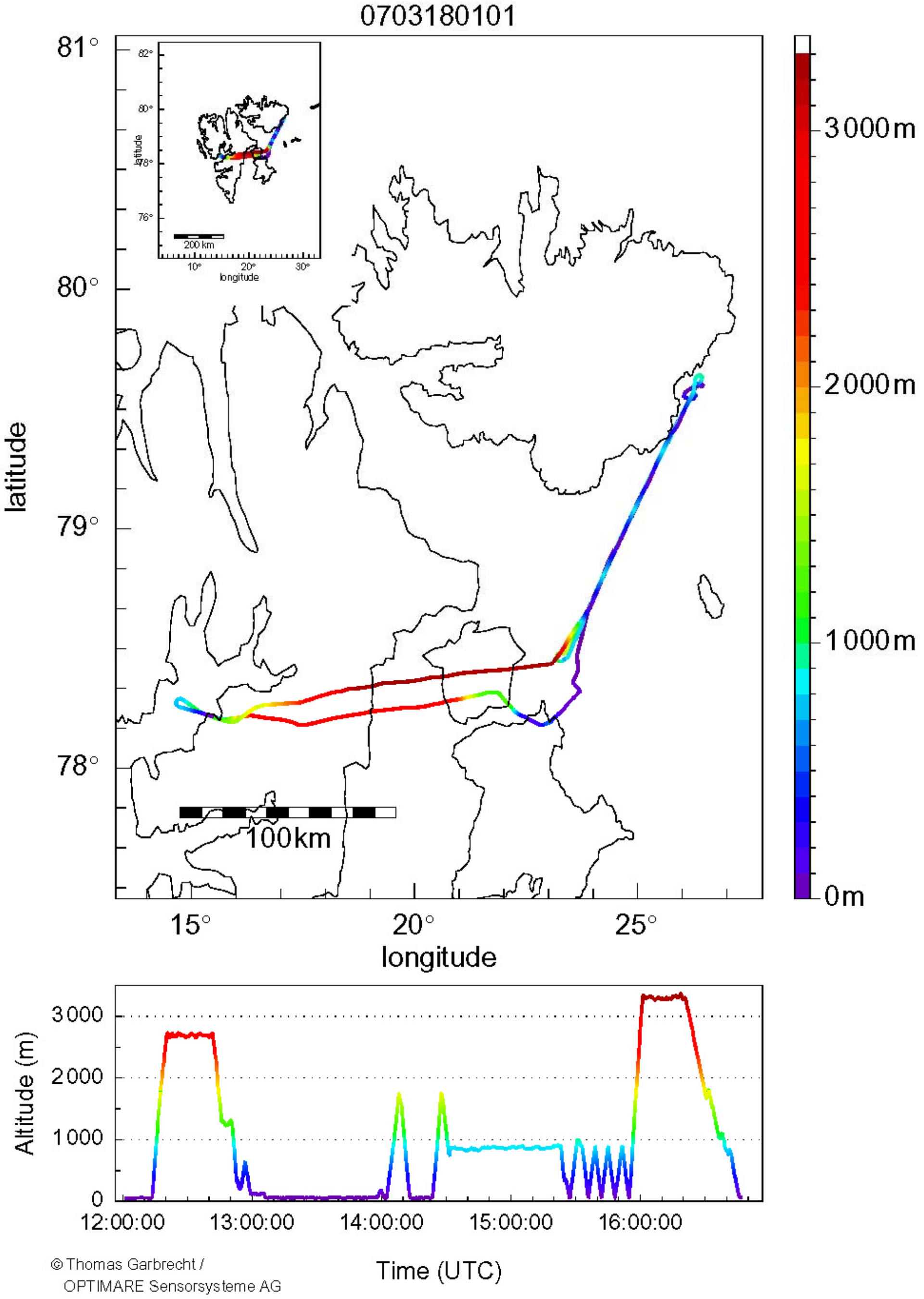

Figure A2.3: Flight pattern of Polar-2 on March 18 in the Barents Sea.

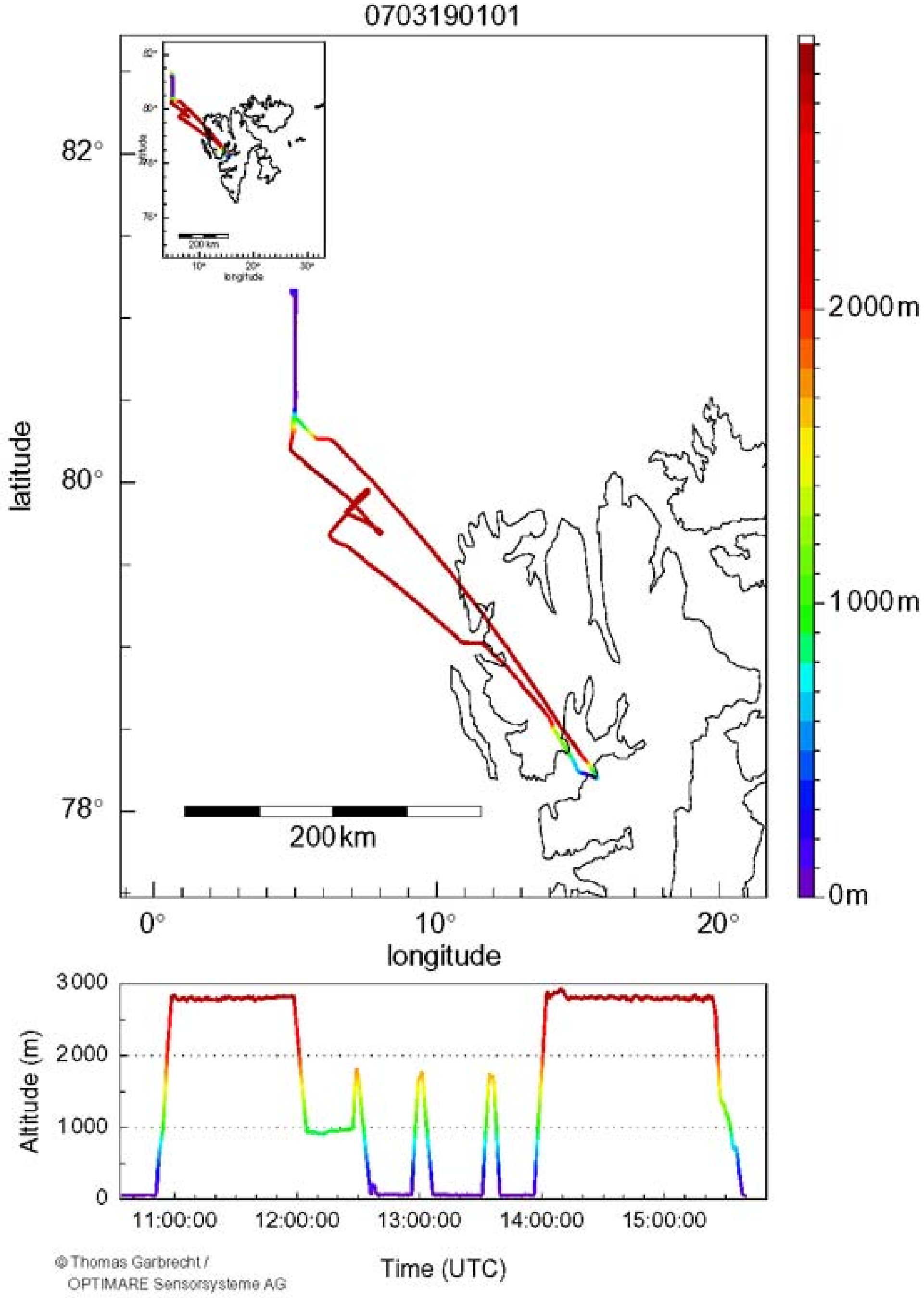

Figure A2.4: Flight pattern of Polar-2 on March 19 in the Fram Strait. Special patterns at high altitude were flown for the calibration of the Meteopod-sonde.

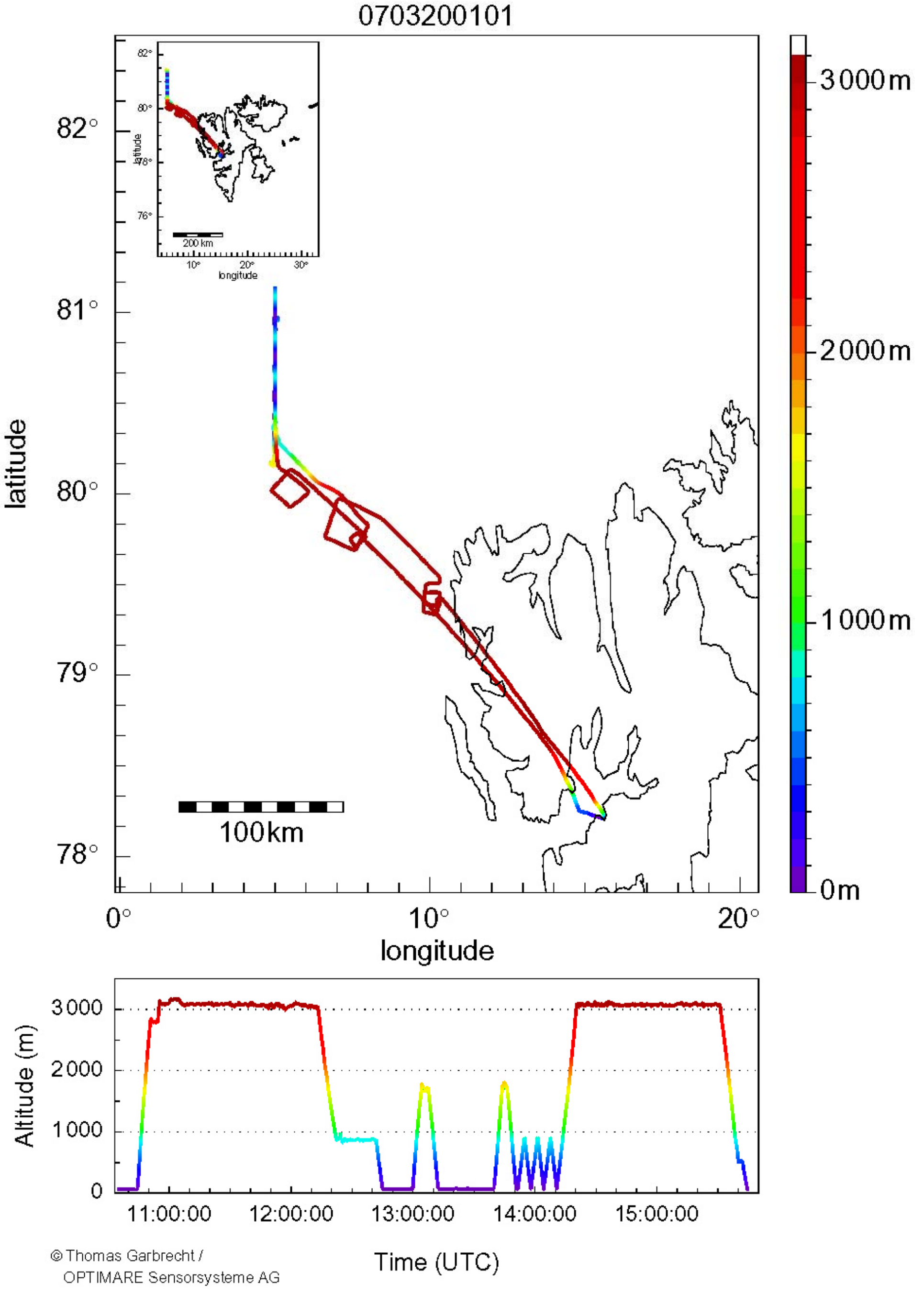

Figure A2.5: Flight pattern of Polar-2 on March 20 in the Fram Strait. On the ferry flights, special patterns were flown for the calibration of the Meteopod-sonde.

A2.3 General Weather Situation

Air temperatures and wind data measured at different weather stations in the Svalbard area are depicted in the graphs Figs. A2.7-A2.9. The position of each station is shown in Figure A2.6. These data give an indication of the average weather conditions and the regional variability in the Svalbard land and coastal area. Meteorological conditions at the measurement locations, observed by the airplane instruments, were partly different. The station data are useful for the interpretation of the satellite SAR data and for assessment of the temporal evolution of weather conditions. Of interest are, for example, temperature rises or falls crossing zero degrees. The scattering signatures in the images are different for “warm” (above freezing point) and wet conditions and for “cold” (below freezing point) and dry conditions. In the former case, the radar signal is scattered back only from the wet snow or ice surface, in the latter case, the radar waves penetrate into the snow and ice which means that the measured radar signal includes contributions from the ice surface and the volume. At L- and C-band, the scattering contribution of a dry snow cover can in general be neglected, but compared to a snow-free ice surface the radar incidence angle on the snow-ice interface is changed, dependent on the dielectric properties of the snow (which are a function of density if the snow is cold and dry).

Figure A2.6: Meteorological stations in the Svalbard Region, from which data were used for the graphs shown below. (Source: http://eklima.met.no)

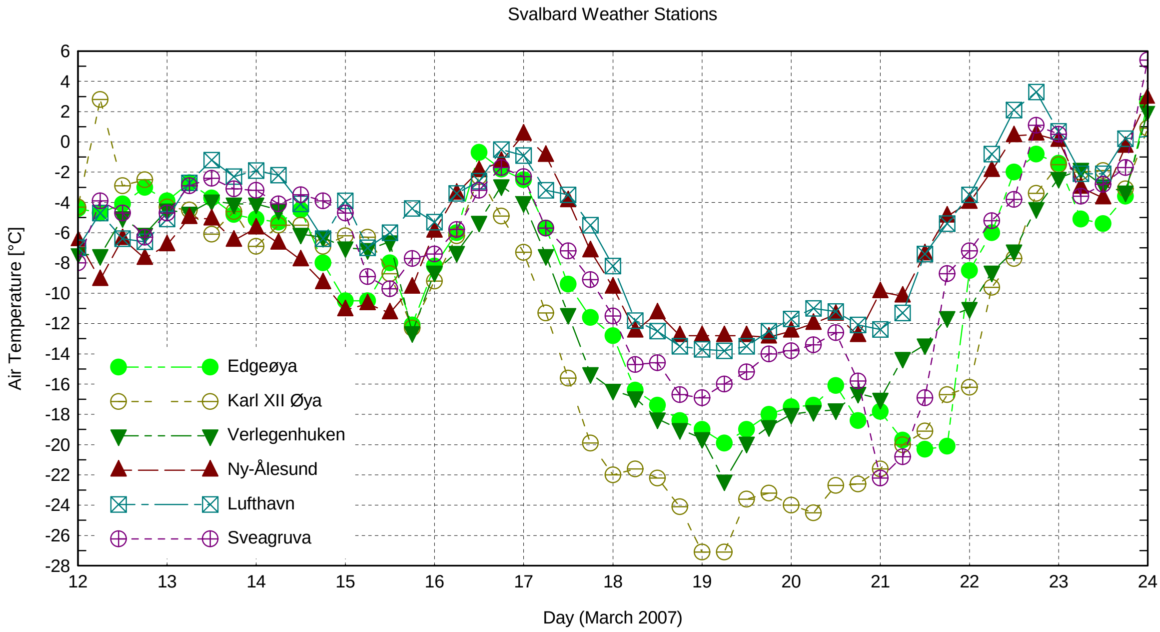

Figure A2.7: Air temperatures measured at different weather stations in a 12-days interval including the dates of the joined sea ice flights.

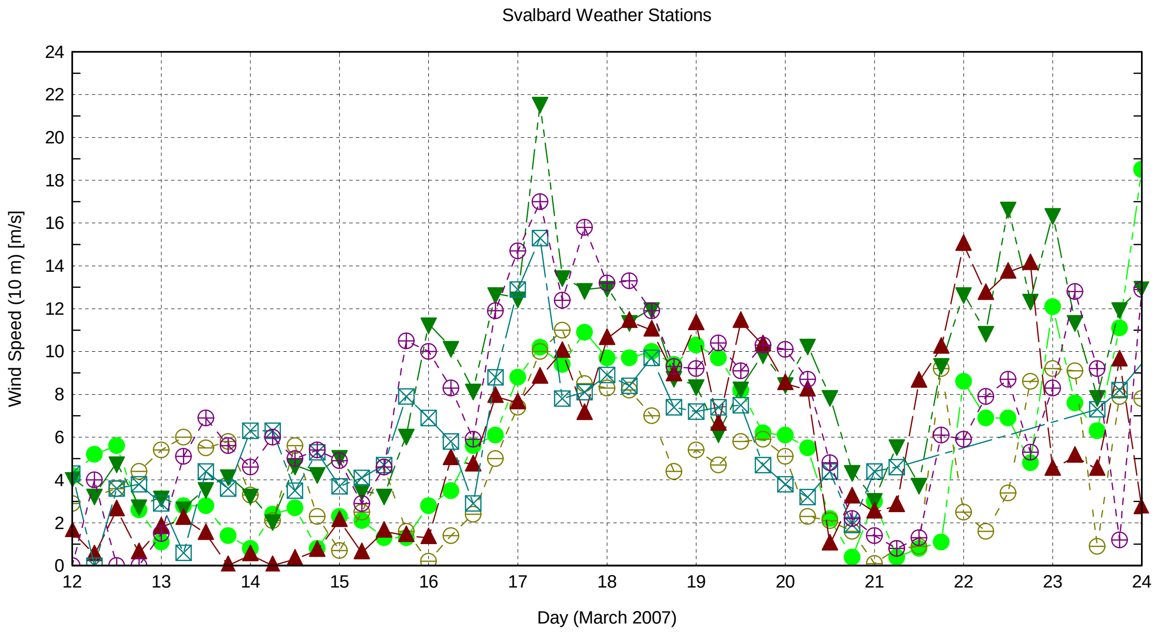

Figure A2.8: Wind speed at 10 m height measured at different weather stations in a 12-days interval including the dates of the joined sea ice flights.

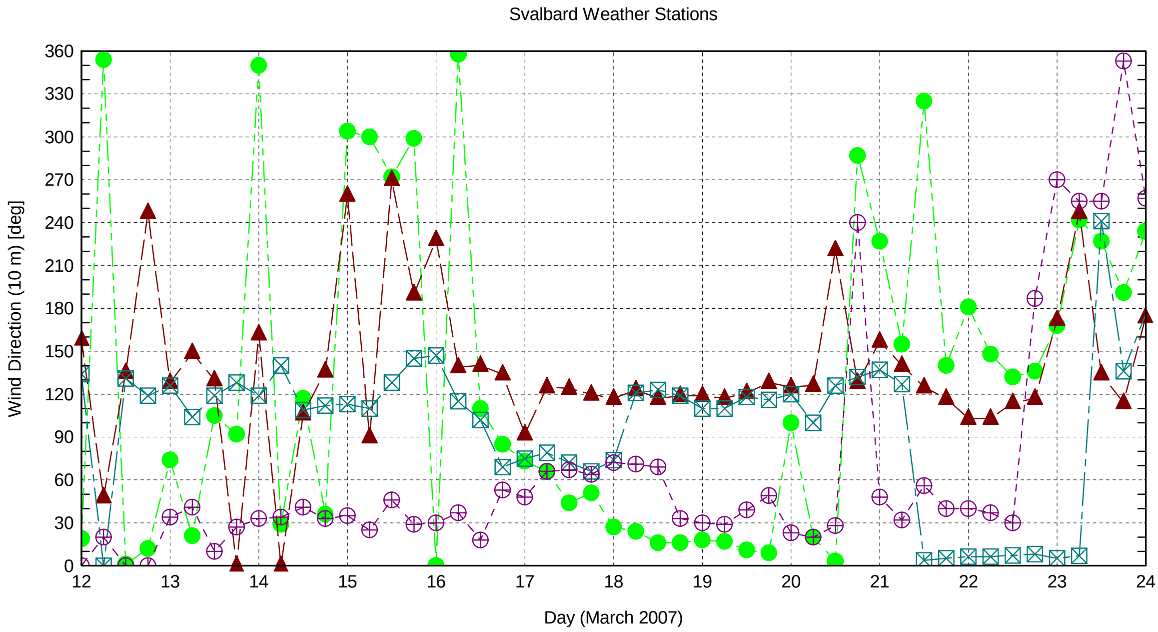

Figure A2.9: Wind direction at 10 m height measured at different weather stations in a 12-days interval including the dates of the joined sea ice flights.

On March 16, during early afternoon, the station air temperatures varied between -6°C and 0°C, the wind speed was between 2 and 8 m/s and the direction between 20 and 140° relative North. During the flight over the Storfjord, the air was about 0 - 2°C at flight altitude 30 m and between -2° and -4°C on the ice surface. Wind speed was about 7 – 15 m/s from north on the southern profile end. Cross-wind conditions prevailed on the northern end.
On March 18, station data at noon time were (air) -22 to -11°C, and (wind) 7 – 12 m/s from 20 – 120°. The corresponding airplane data from the Barents Sea flight are -14°C and 18 – 20 m/s from 20 – 50°. Also on March 19, conditions were cold and dry in the measurement area north of Svalbard (airplane data: -27°C, 8 – 13 m/s, 10 – 25°). The stations registered air temperatures between -24°C and -13°C, and winds at 6 – 12 m/s from 10 – 120° at noon. The next day (March 20), when the second flight in the northern test site took place, air temperature was again low (-27°C), wind was weaker (5-7 m/s from north). Station data varied between -23°C and -11°C, 1-8 m/s from 0-210°. During the period from March 16 to March 20, the precipitation measured at station Ny Ålesund was zero
For the interpretation of the sea ice signatures in the radar images, the effect of a moist snow surface may have to be considered on March 16 (Storfjord flight). The other data were taken under typical winter conditions (i. e. dry snow). The wind around Svalbard was regionally variable in speed and direction during the time interval presented in the graphs above (which needs to be considered for the assessment of possible ice drift magnitude and direction).

A2.4 Color Line Scanner Images

Except on March 16, the light conditions were good to excellent for the acquisition of optical images using the airplane mounted Color Line Scanner (CLS). Two examples are shown in Figs. A2.10 and A2.11. These images are used for the interpretation of the radar images, in particular to separate open water, thin ice (“grey” ice) and snow covered ice. The latter may consist of different ice classes. A separation of these classes is – to a certain degree – possible from the deformation patterns (i. e. size, form and thickness of ice blocks forming the ice ridges). It is noted that in case of a snow-covered ice surface, the separation of ice classes is

easier in the radar imagery if the data are acquired under cold and dry conditions, when the radar signal is only slightly attenuated by the snow.
The average values for swath width, cross-track and along-track resolution are determined from the flight altitude and speed over ground, from the scan time, and from the optical picture angle which is 84 deg for the 24 mm lens used (hence, the swath width of the optical images is $1.8 \times h$, h – height over ground).

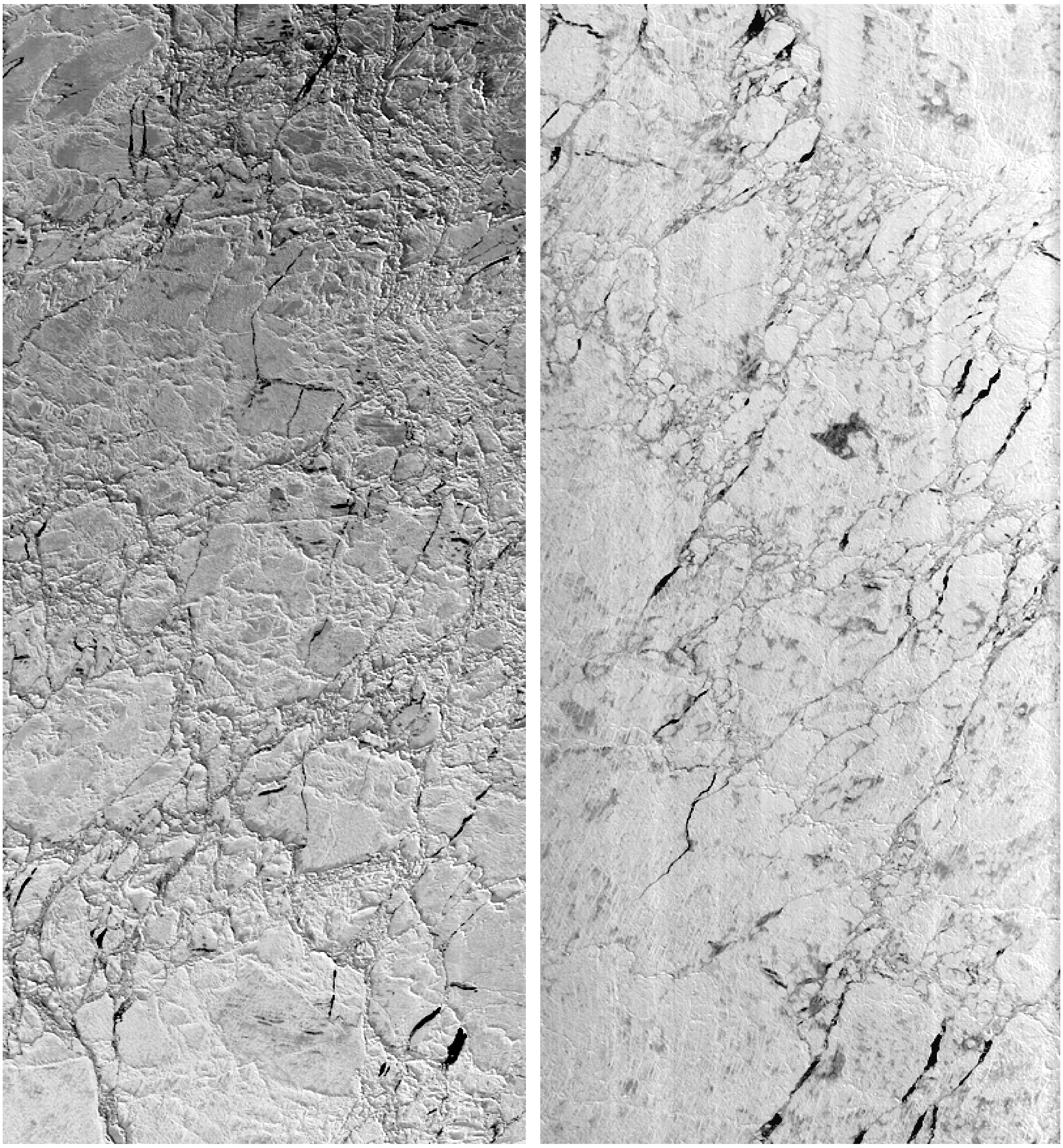

Figure A2.10: Raw CLS data from the Barents Sea. Width of strip is roughly 1700m. Left: segment 3 (close to southwest profile end), right: segment 12. Vignetting effect (across the strip) is already removed.

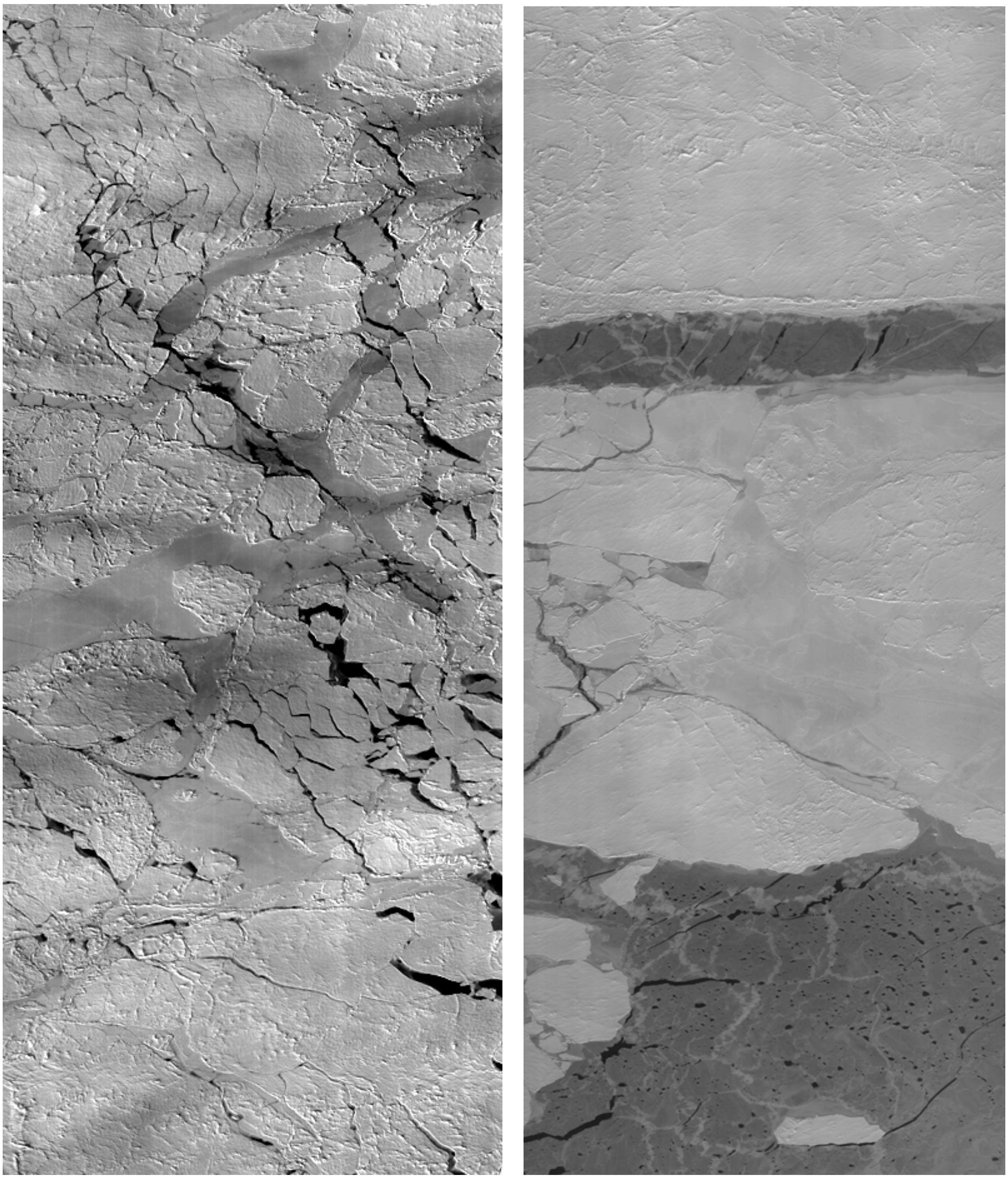

Figure A2.11: Raw CLS data from the northern test area. Left: segment 4, right: segment 8. Vignetting effect is removed. Width of strip approximately 1700 m. Dark patterns on the left strip are from clouds (which were present at the ice margin).

Table A2.3: CLS Data Acquistion, Image Characteristics

Date	Area	Swath width [m]	Number of Segments	Segment Length [km]	Effective Cross-Track Resolution [m]	Effective Along-Track Resolution [m]
16/03/07	Storfjord	440 - 550	32	6	0.2 – 0.3	1.2
18/03/07	Barents Sea	1650	31	4.6	0.45	0.9
19/03/07	Fram Strait	1650	17	4.8	0.45	1.0
20/03/07	Fram Strait	1650	14	6.3	0.45	1.3

Number of segments: The image strips include also parts of the approach to the starting point of the measurement profile.

The CLS images were corrected for the vignetting effect. They are divided into segments of 5000 lines and 2048 columns. Each image consists of three layers (red, green, blue, wavelengths are given in Table "Instrument Data"). The characteristics of the CLS images for the four joint flights are summarized in Table A2.3 above. The CLS data can be geo-registered to the radar images by selecting a larger number of ground control points (GCPs) along ice structures recognizable in both image types. For optimally taking into account the non-linear geometrical distortions in the imagery, it is recommended to use Delaunay triangulation that fits triangles to the irregular spaced GCPs in the CLS images and interpolates pixel values to the output grid.

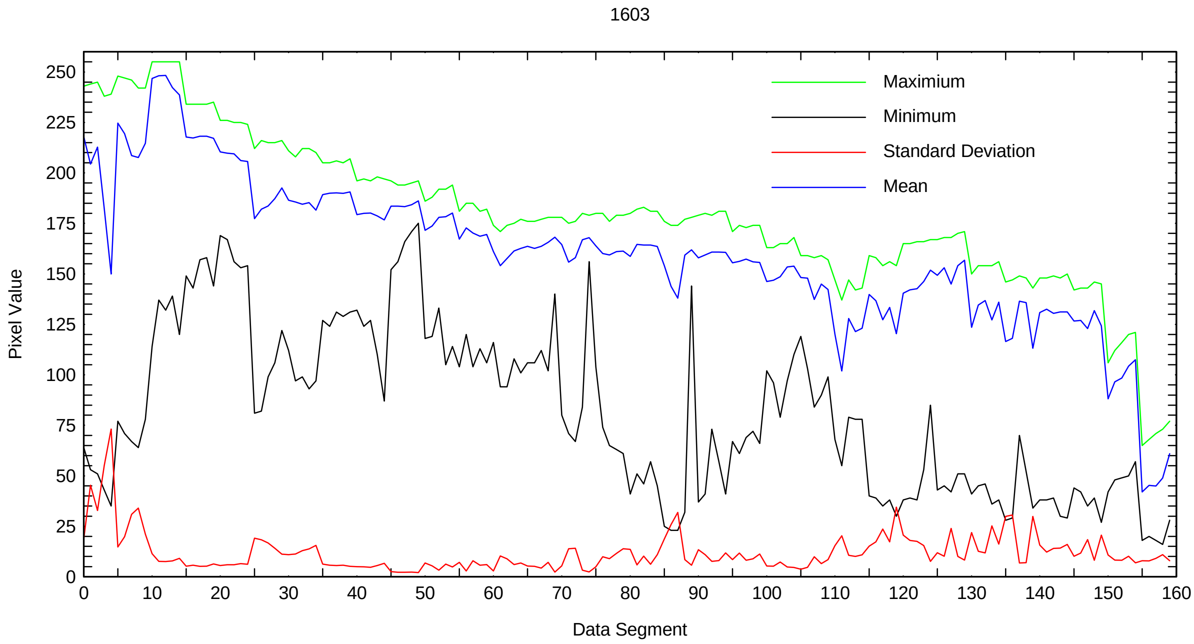

Figure A2.12: Pixel value variations along-track in CLS image sub-segments (1000 lines), blue channel, for flight on March 16 (Storfjord).

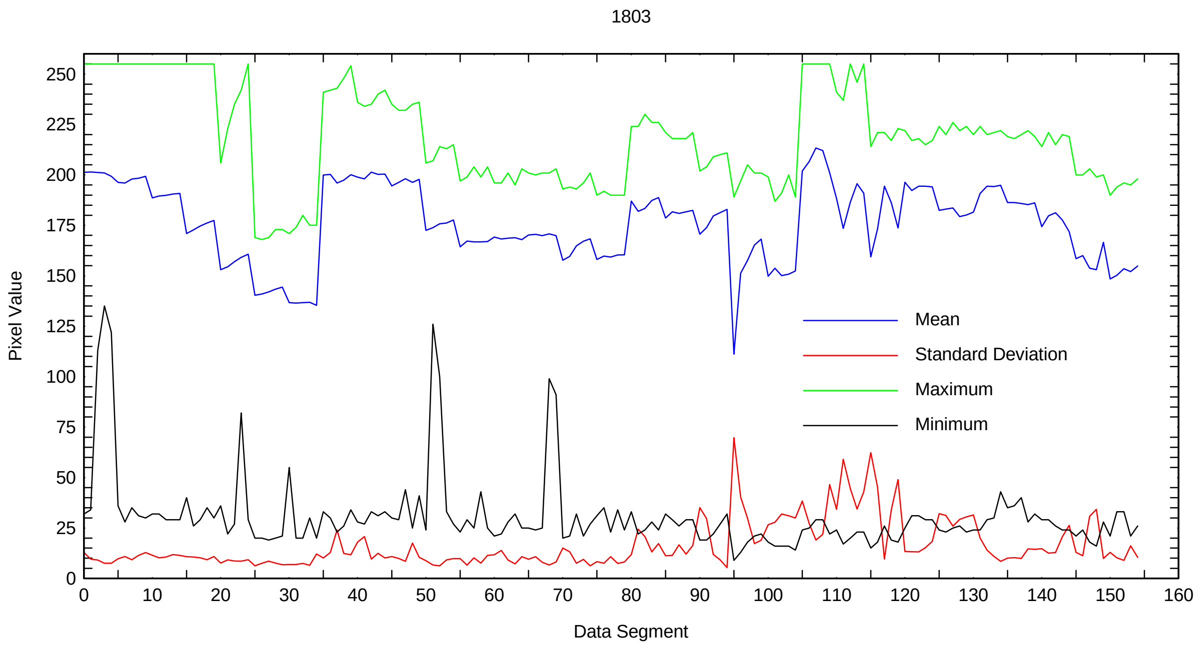

Figure A2.13: Pixel value variations along-track in CLS image sub-segments (1000 lines), blue channel, for flight on March 18 (Barents Sea).

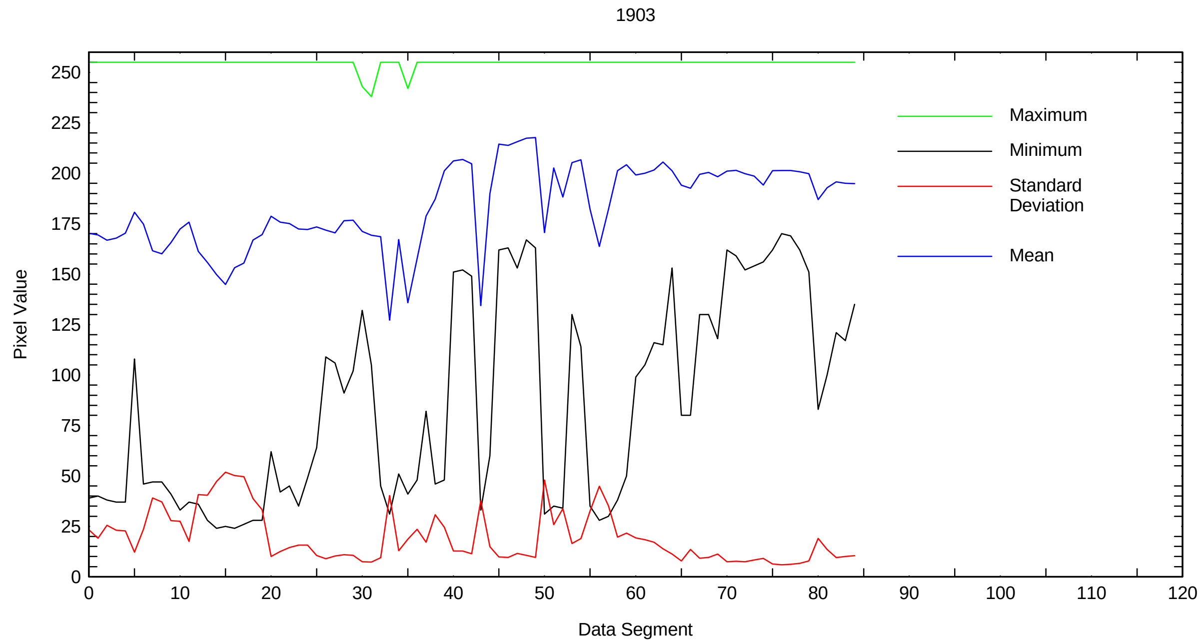

Figure A2.14: Pixel value variations along-track in CLS image sub-segments (1000 lines), blue channel, for flight on March 19 (Fram Strait).

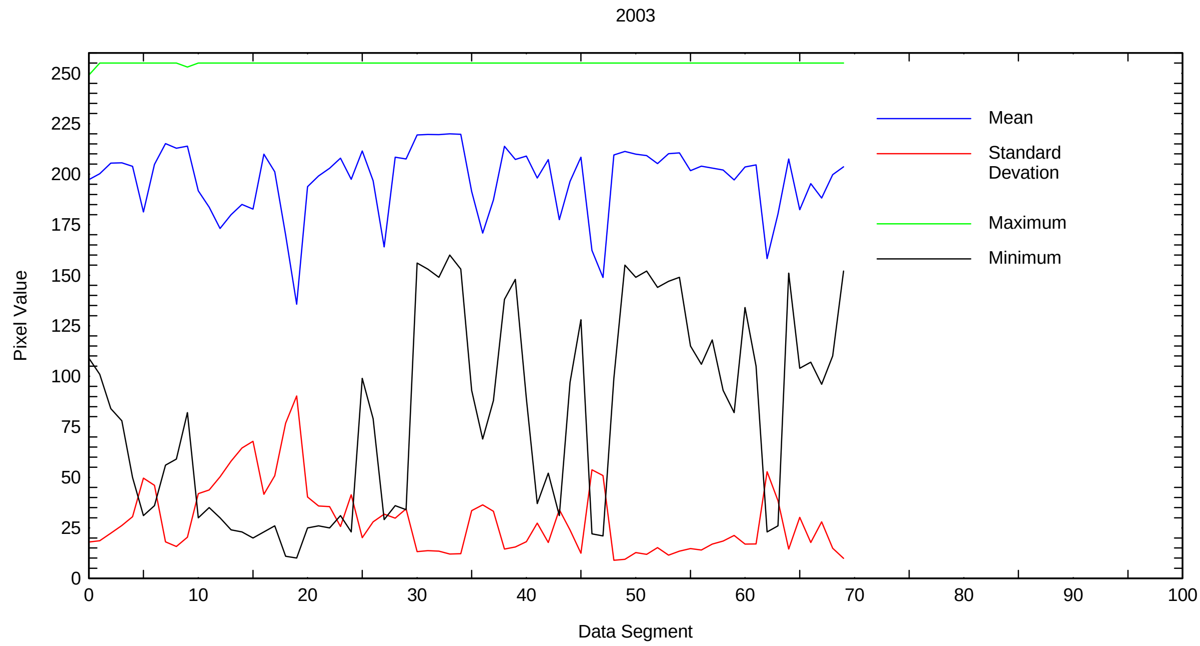

Figure A2.15: Pixel value variations along-track in CLS image sub-segments (1000 lines), blue channel, for flight on March 20 (Fram Strait).

Besides the image properties listed in Table A2.3 and visual inspection, the quality of the CLS data was assessed using the average pixel intensity over segments of 1000 lines and 2048 columns, together with standard deviation and maximum and minimum value. Results are shown in Figs. A2.12 – A2.15 for the blue channel intensities. The CLS uses 8-bit to recode the data. Discontinuities in the curves indicate cases at which the lens aperture was adjusted, or cases where the profile crossed borders between “dark” and “white” ice types or between shadows of clouds and cloud-free zones. Gradual variations are due to slowly changing light conditions. A large standard deviation indicates sufficient dynamic range of grey tones. In all, the data quality is sufficient to excellent. Relative to the other images, the Storfjord data are of lowest quality. They cover only smaller swath widths (see Table A2.3). Because of the finer resolution in cross-track direction, coupled with a relatively coarse resolution along-track, they appear slightly blurred. All images reveal a sufficient dynamic range of grey tones. The aperture had to be adjusted during flights over Storfjord and the Barents Sea. Light conditions got worse along the Storfjord profile. Figure A2.16 shows a comparison between the different colors (channels). Intensities are largest at the blue channel. They differ only slightly between the green and the red channel.

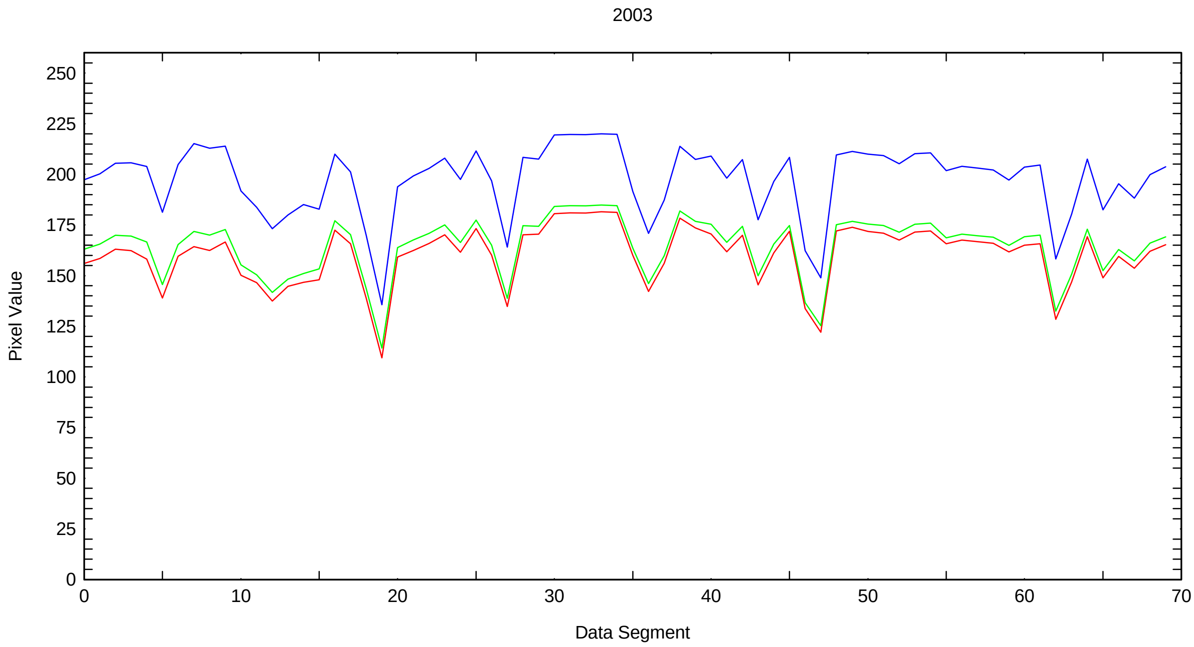

Figure A2.16: Pixel value (intensity) variations along-track in CLS image segments (1000 lines), blue, green, and red channel, for flight on March 20 (Fram Strait). The differences are similar also for the images acquired on March 16, 18 and 19.

Finally, the overlap between the optical images and the radar imagery was checked for two examples. The ESAR images available were from the Barents Sea (March 18) and the Fram Strait (March 19), acquired at C-band VV- and VH-polarization. For the comparison, the blue channel of the CLS data was used. The overlap is excellent, the CLS image strip matches perfectly into the radar swath (see Figs. A2.17 and A2.18).

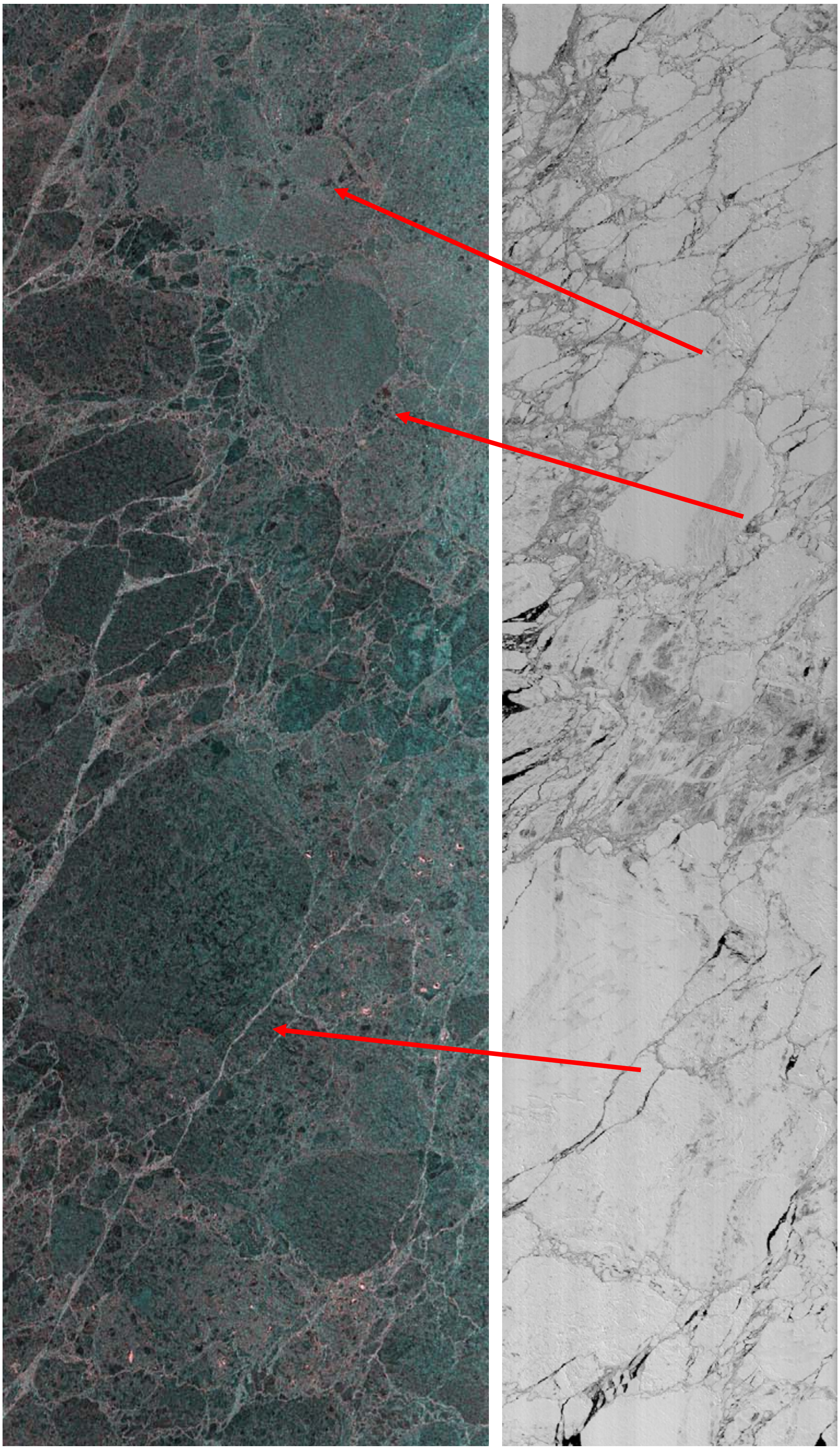

Figure A2.17. ESAR C-band image (R: VH- G:VV- B:VV-polarization) and CLS image (blue channel). The width of the ESAR image section is 2500 m and of the CLS image 1700 m. Red arrows connect matching points. This example demonstrates that some structures are easier to identify in the radar data, other ones in the optical data.

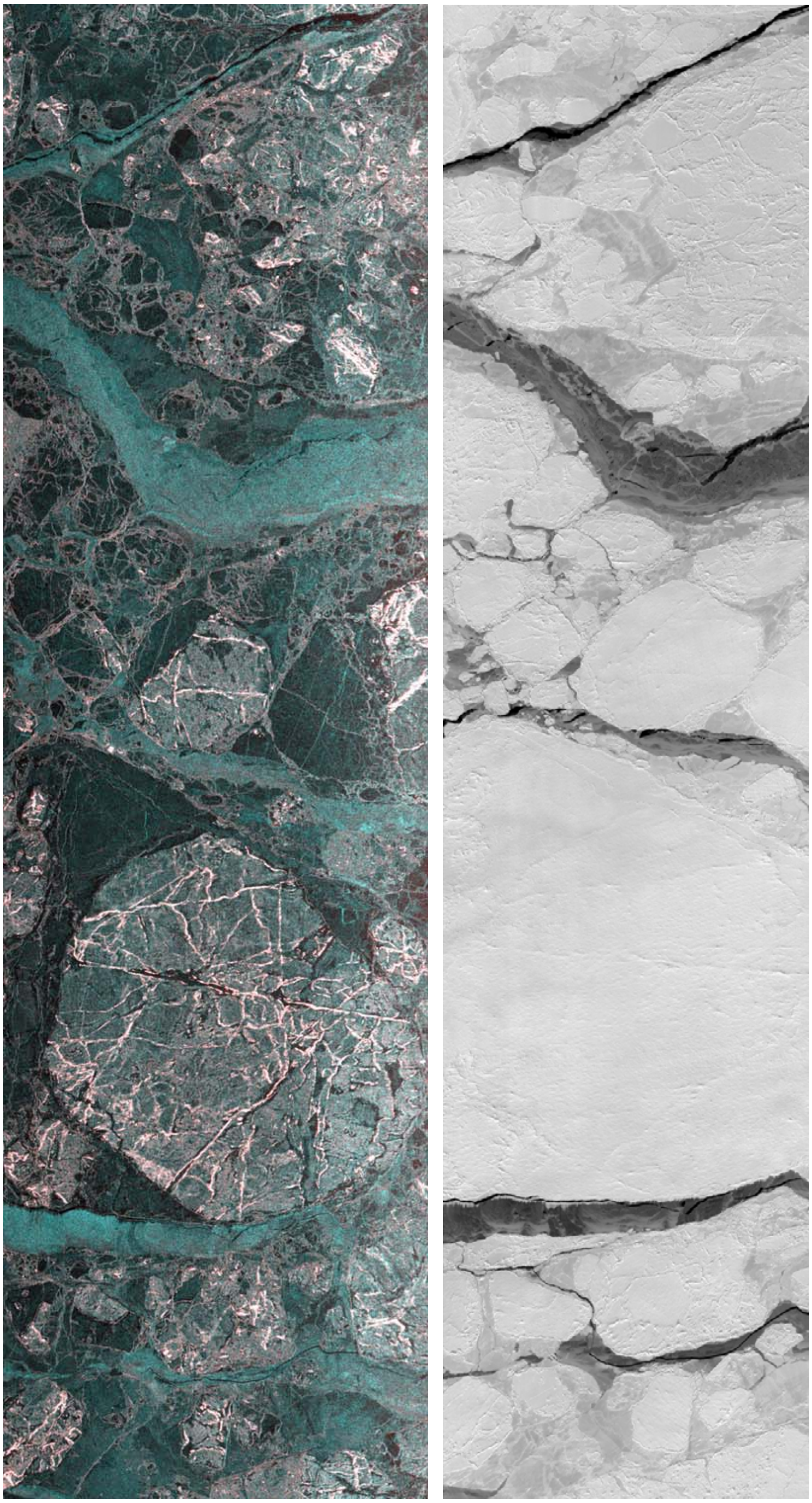

Figure A2.18. ESAR C-band image (R: VH- G:VV- B:VV-polarization) and CLS image (blue channel). The swath width of the ESAR image section is 2000 m and of the CLS image 1700 m. In particular the leads (grey ice and open water) can easily be identified in both images. The structure of floes is much easier to recognize in the radar images.

A2.5 Satellite Data Acquistions

On the basis of ice conditions observed during the Svalex Campaign in 2005 (with similar objectives as ICESAR) and monitored by satellite in the following year, the probability that flights over sea ice northwest of Svalbard would be carried out together with the DLR airplane were initially regarded as low, since the ice edge was relatively far from the northwest tip of Svalbard (the main island), and the maximum distance that can be flown by the DLR airplane with full radar equipment is shorter than for Polar-2. Therefore, higher-resolution APP-products from ENVISAT ASAR were ordered only over Storfjord and the Barents Sea. (During ICESAR, it WAS possible to collect data over sea ice northwest of Svalbard.) Wide-swath mode imagery from ASAR (swath width 400 km, spatial resolution 150 m) and WB1-images from ALOS PALSAR (swath width 250-350 km, resolution 100 m) are available over all test sites visited during ICESAR. Image properties are listed in Table A2.4.

Most of the ASAR data are already received. On the following pages, ASAR browse images from EOLISA are shown together with the position of corresponding swath in the Svalbard region. For PALSAR frames, only a few browse images are available from JAXA's archive.

However, the PALSAR L-band data were not utilized in this study specifically aiming at an assessment of the Sentinel-1 mission with regard to sea ice mapping.

The satellite SAR images reveal variable signatures characteristics dependent on ice and weather conditions ("wet" and "dry"). For open water surfaces, the backscattered intensity varies with wind speed and wind direction relative to the radar look direction. The ASAR APP images are acquired at different incidence angle ranges. The angle change over the swath width is about 8 deg at mode IS1 (15.0-22.9 deg) and about 3 deg at mode IS7 (42.5-45.2 deg). The WSM images cover a much broader incidence angle range (17-43 deg). At larger incidence angles (>25 deg), the contrast between ice types may be enhanced (dependent on ice conditions and radar polarization), and leads and deformation structures such as ridges are easier to identify.

Table A2.4a: Satellite Data

Date	Area	Imaging Mode	Start	Stop	Remark
13.03.	Svalbard East	ASAR WSM HH	09:30:48	09:32:25	Overview of ice conditions
13.03.	Svalbard West	ASAR WSM HH	19:28:26	19:30:13	
14.03.	Storfjord	ASAR APP HH/HV, IS1	10:40:12	10:40:51	initial conditions in Storfjord for flight on 1603; PALSAR frame over same area
14.03.	Storfjord and Barents Sea	ALOS PALSAR WB1, HH	10:12:34	10:13:24	(yet not listed in JAXA's archive, status Aug. 2008)
14.03.	Barents Sea	ASAR APP HH/HV, IS4	18:56:57	18:57:37	
16.03.	Storfjord	ASAR APP HH/VV, IS6	09:37:23	09:38:02	joint flight over same area, a few hours later
17.03.	Barents Sea	ASAR APP HH/HV, IS1	10:45:27	10:46:08	
17.03.	Barents Sea and Fram Strait	ASAR WSM HH	19:02:36	19:04:30	flights in the Barents Sea on 1803 and north of Svalbard on 1903, overlap with PALSAR frame
17.03.	Barents Sea, Storfjord	ALOS PALSAR WB1, HH	10:35:30	10:36:21	
18.03.	Storfjord	ASAR APP HH/HV, IS1	10:14:31	10:15:10	northeast part of strip includes starting point of profile of Barents Sea flight
18.03	Barents Sea	ASAR WSM HH	18:30:59	18:32:02	

Table A2.4b: Satellite Data

Date	Area	Imaging Mode	Start	Stop	Remark
19.03.	Barents Sea	ASAR APP HH/VV, I4	9:42:37	9:43:17	includes parts of profile from Barents Sea flight on 1803
19.03.	Fram Strait	ASAR WSM HH	11:22:12	11:23:48	covers flight north of Svalbard
19.03.	Barents Sea	ASAR APP HH/HV, I1	17:59:53	18:00:27	
20.03.	Barents Sea	ASAR APP HH/HV, I7	9:11:08	9:11:47	
21.03.	Barents Sea	ASAR APP HH/HV, I2	10:19:46	10:20:25	overlap with PALSAR frames, meteoro-logical flight over Storfjord
21.03.	Fram Strait	ASAR WSM	11:59:56	12:00:39	covers flight profile 2003 in the north, overlap with PALSAR frames
21.03.	Storfjord	ASAR APP HH/HV, I1	18:36:58	18:37:36	
21.03.	Barents Sea	ALOS PALSAR WB1 HH	10:01:10	10:02:01	
21.03.	Fram Strait	ALOS PALSAR WB1, HH	11:39:12	11:40:03	
21.03.	Fram Strait	ALOS PALSAR WB1, HH	11:39:53	11:40:44	
21.03.	Storfjord	ALOS PALSAR WB1 HH	19:47:19	19:48:10	(yet not listed in JAXA's archive, status Aug. 2008)
22.03.	Barents Sea and Storfjord	ASAR WSM HH	9:48:33	9:49:39	overlap of ASAR APP and WSM, also overlap with PALSAR frames
22.03.	Barents Sea	ASAR APP HH/HV I1	18:05:30	18:06:09	
22.03.	Storfjord	ASAR APP HH/VV I6	19:45:38	19:46:11	
22.03.	Barents Sea and Storfjord	ALOS PALSAR WB1 HH	10:41:57	10:42:47	
22.03.	Storfjord	ALOS PALSAR WB1 HH	10:42:38	10:43:28	
22.03.	Fram Strait	ALOS PALSAR WB1 HH	12:19:59	12:20:50	
23.03.	Fram Strait	ASAR WSM	10:56:31	10:57:32	
23.03.	Barents Sea	ASAR APP HH/HV I6	19:14:06	19:14:45	
23.03.	Barents Sea	ALOS PALSAR WB1 HH	9:44:41	9:45:32	(yet not listed in JAXA's archive, status Aug. 2008)
23.03	Fram Strait	ALOS PALSAR WB1 HH	11:22:02	11:22:53	

March 13, 2007

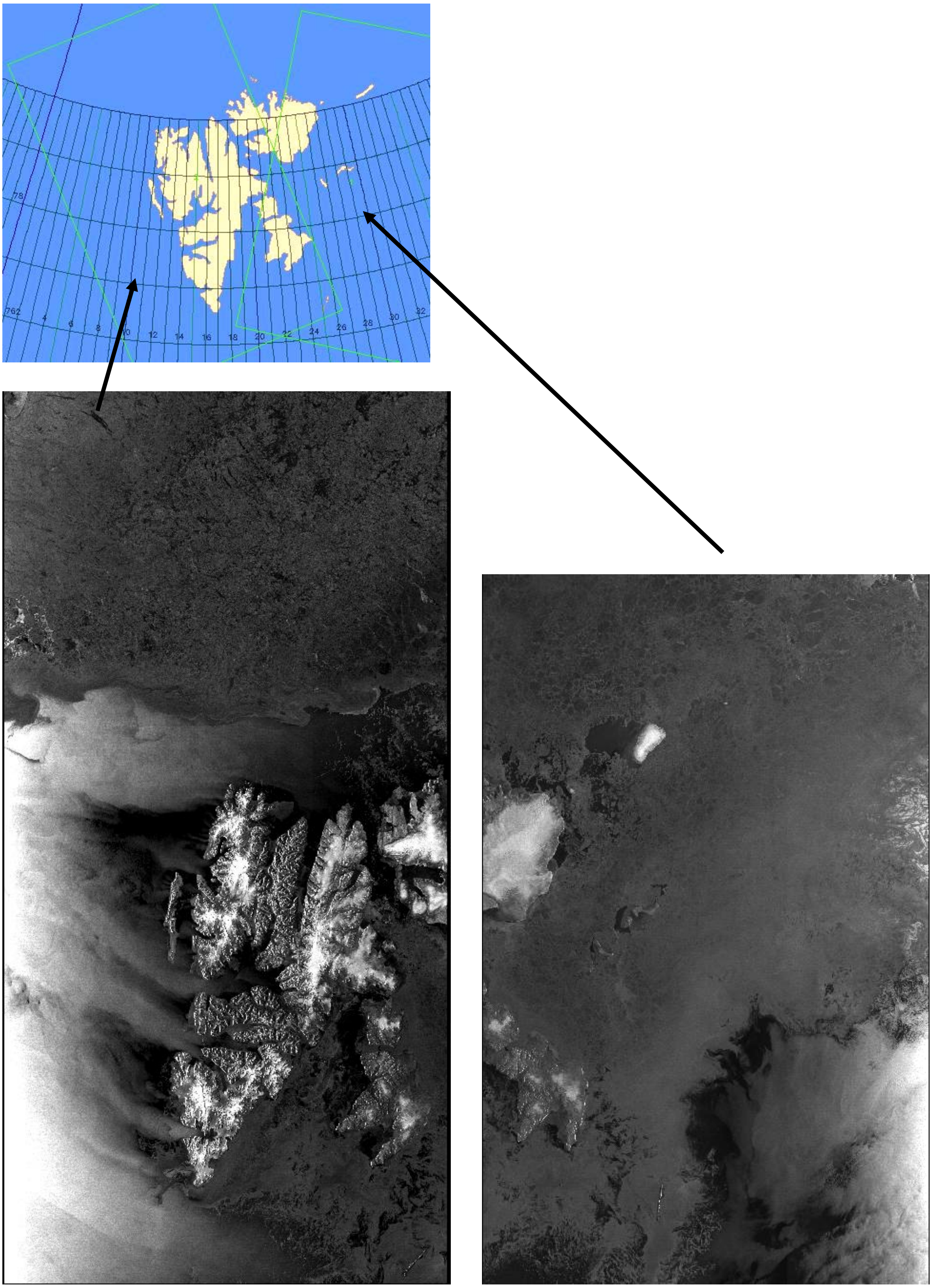

ASAR 1303 1928

ASAR 1303 0930

Figure A2.19. Satellite imagery for March 13

March 14, 2007

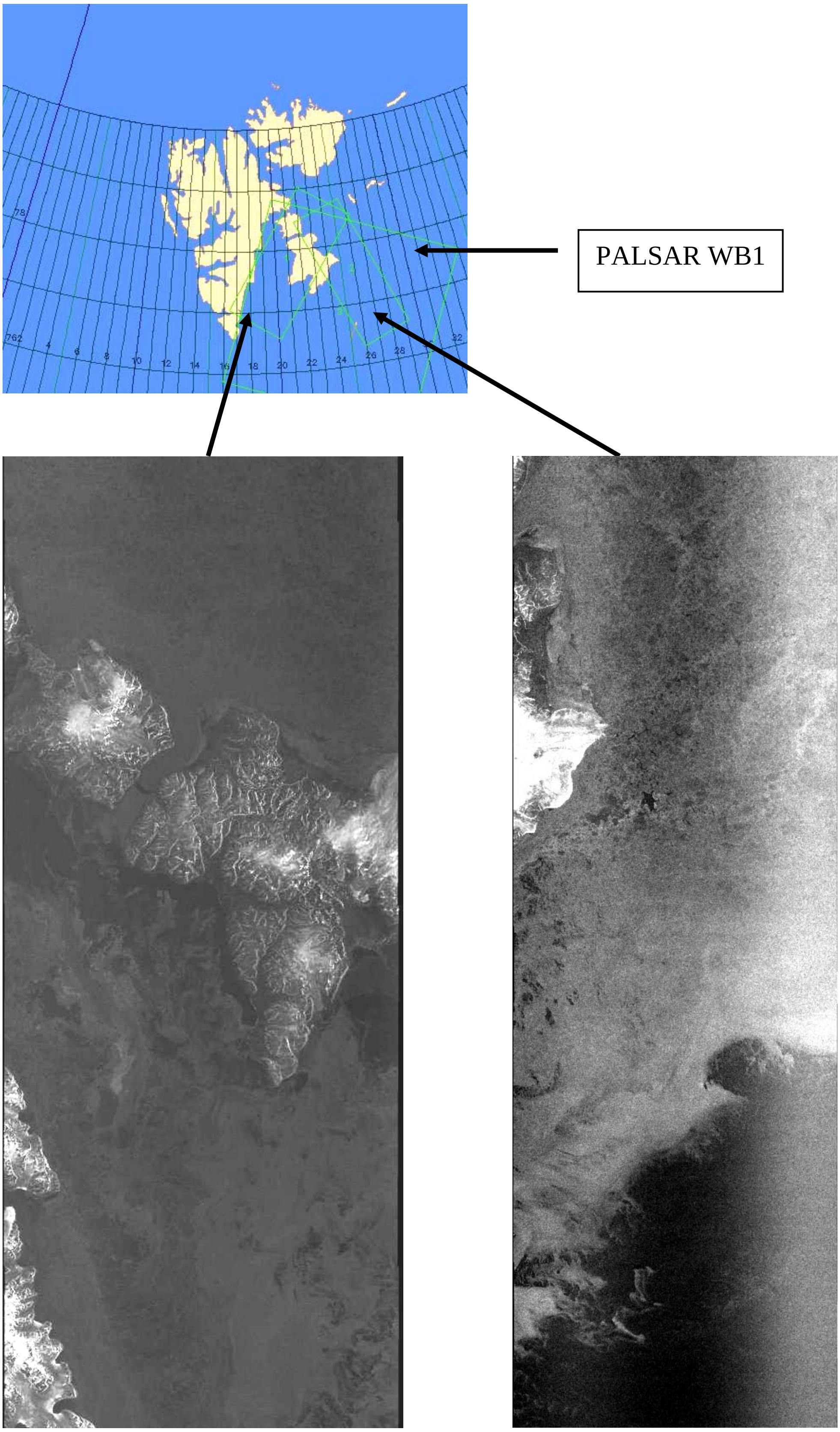

ASAR 1403 1040 ASAR 1403 1856

Figure A2.20. Satellite imagery for March 14

March 16, 2007

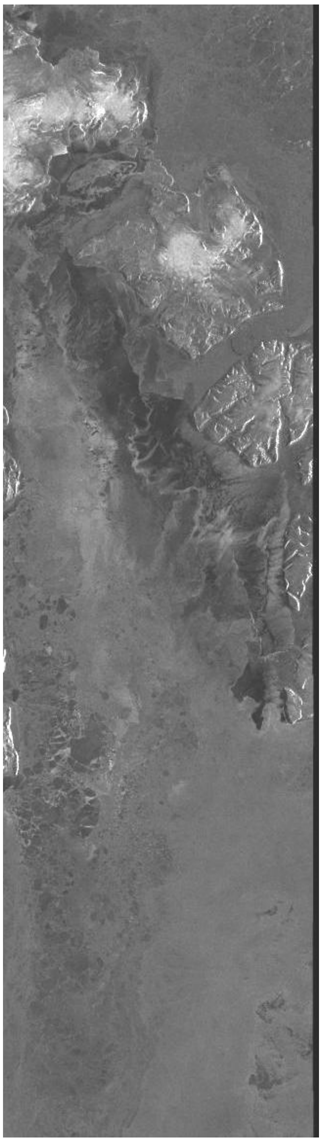

ASAR 16030937

Figure A2.21. Satellite imagery for March 16

March 17, 2007

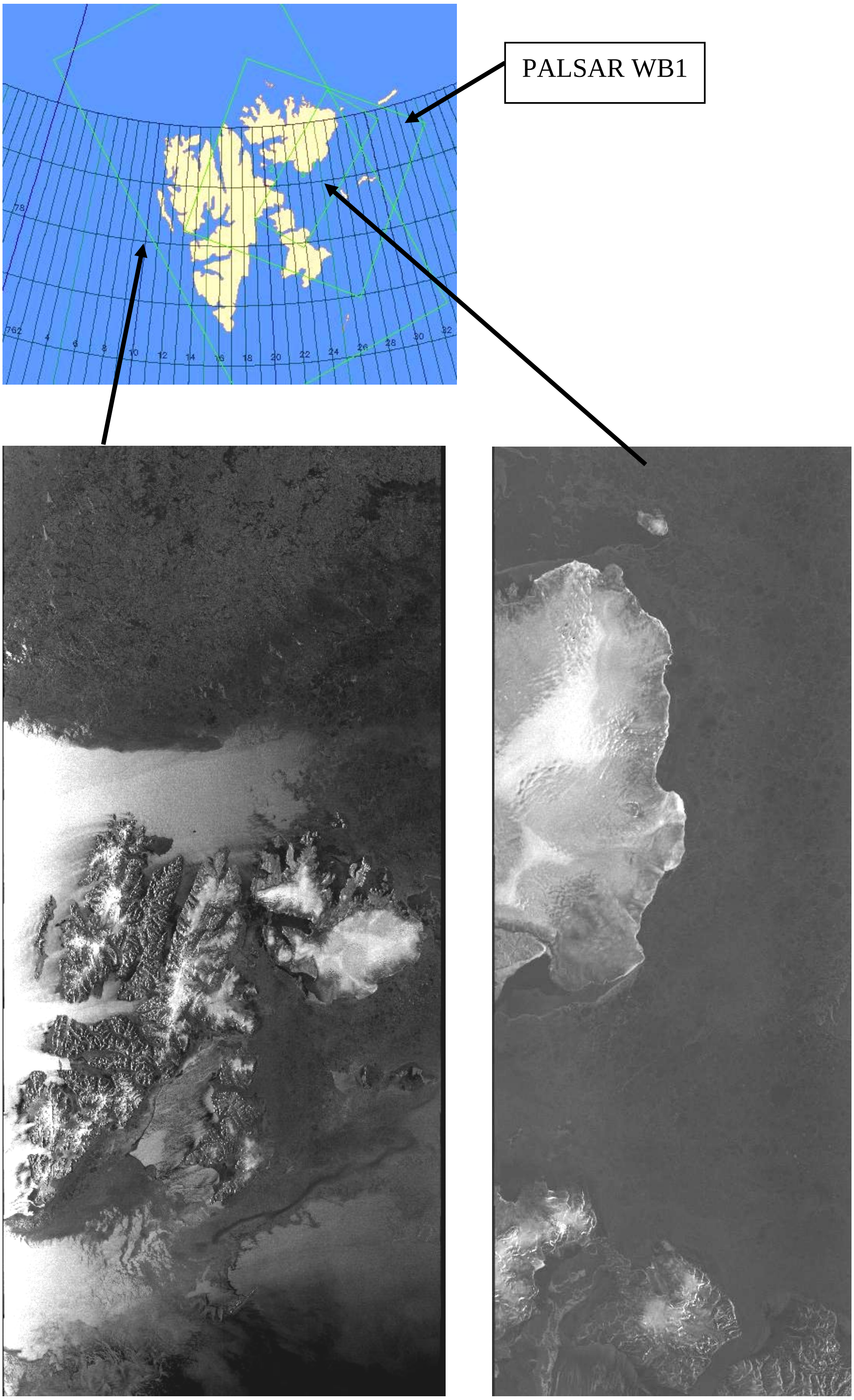

ASAR 17031902

ASAR 17031045

Figure A2.22. Satellite imagery for March 17

March 18, 2007

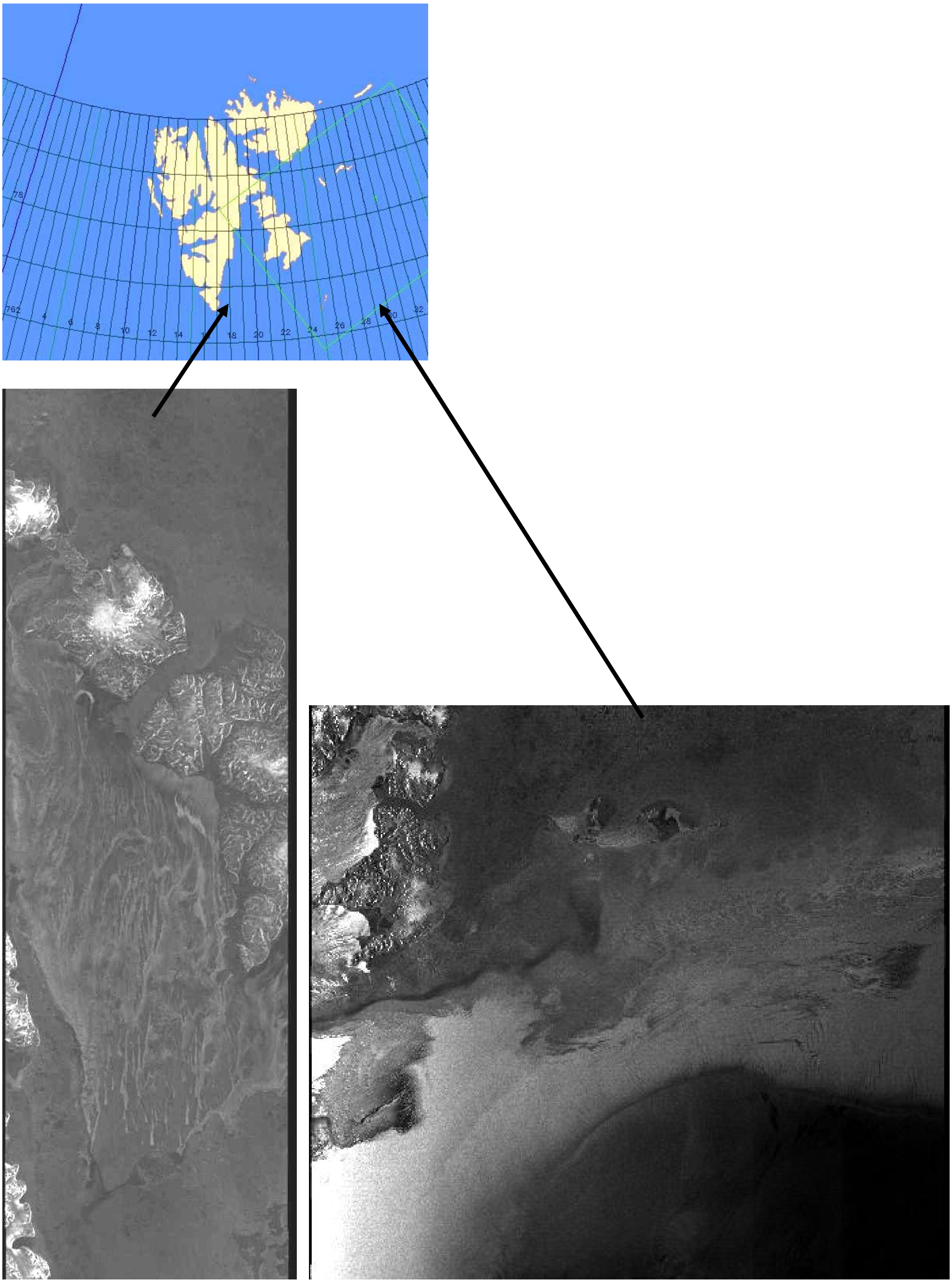

ASAR 18031014 ASAR 18031831

Figure A2.23. Satellite imagery for March 18

March 19, 2007

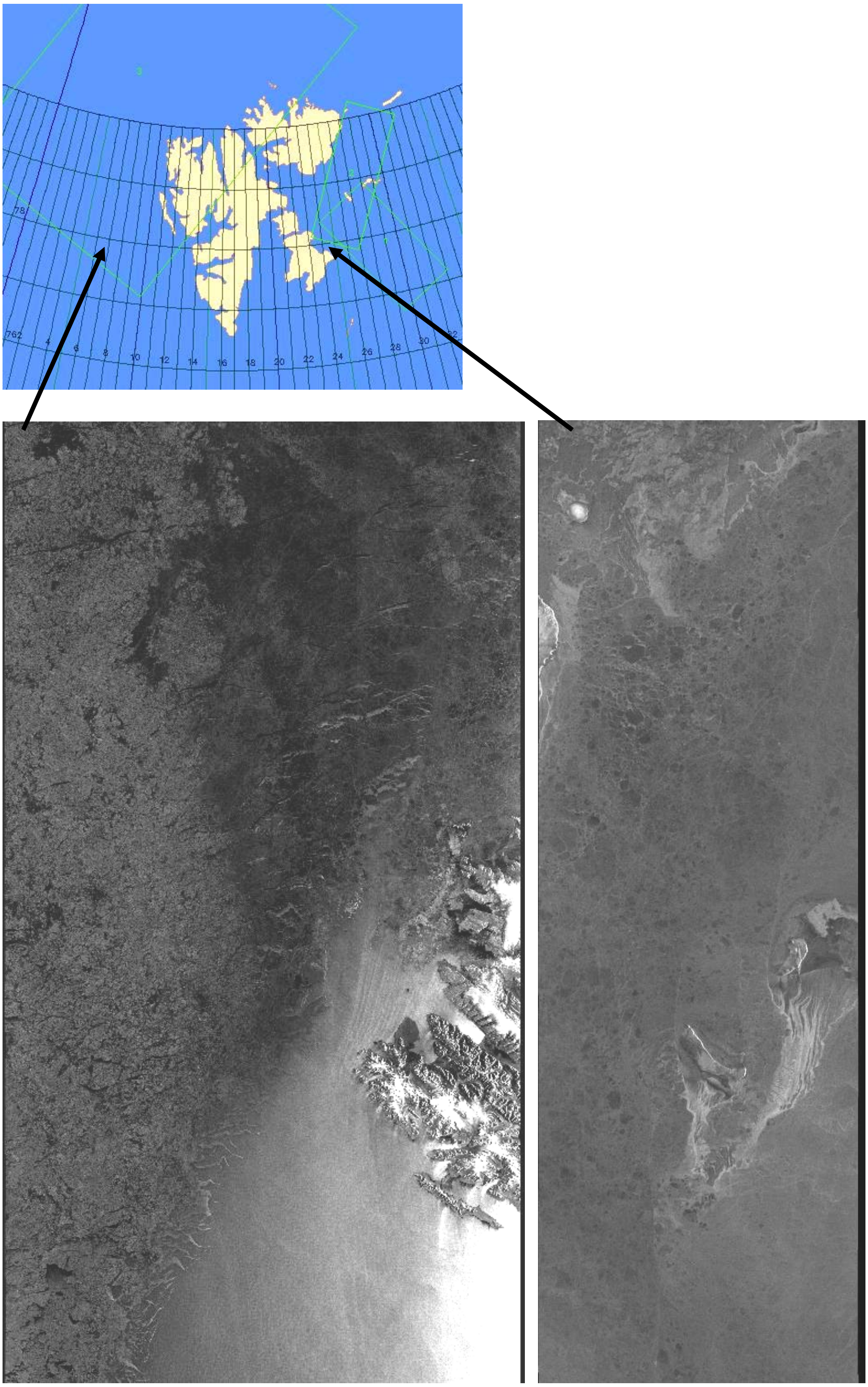

ASAR 19031122 ASAR 19030942

Figure A2.24. Satellite imagery for March 19

March 20, 2007

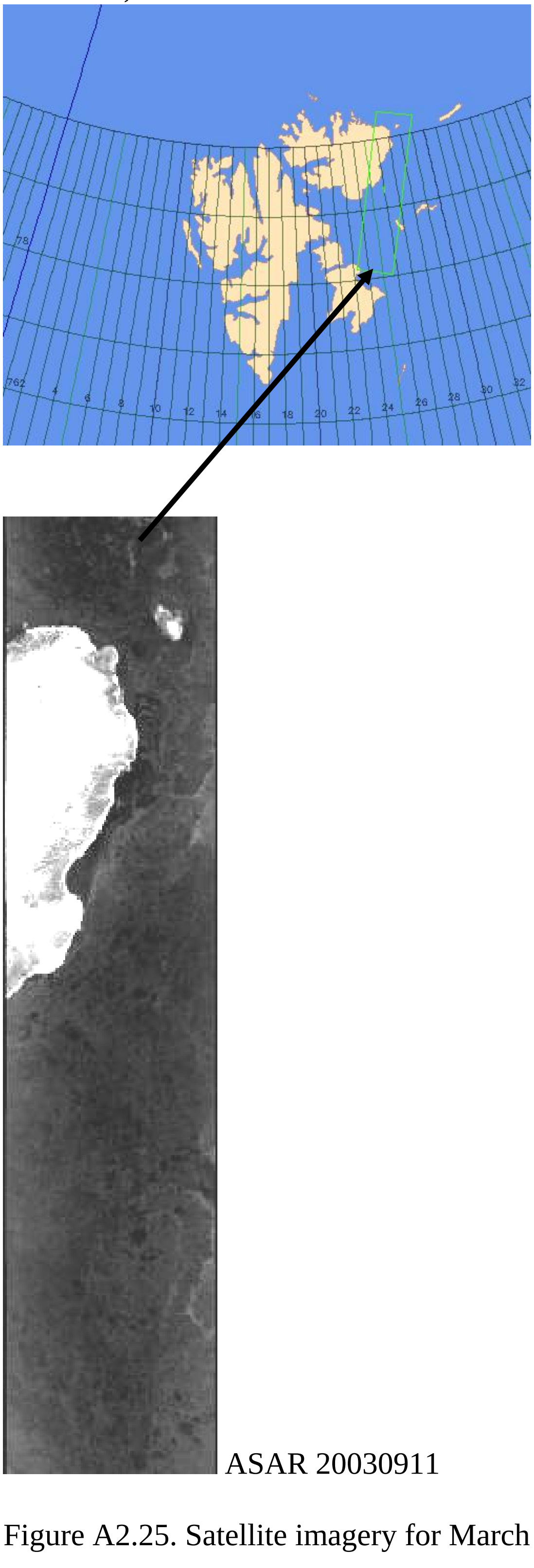

ASAR 20030911

Figure A2.25. Satellite imagery for March 20

March 21, 2007 (A)

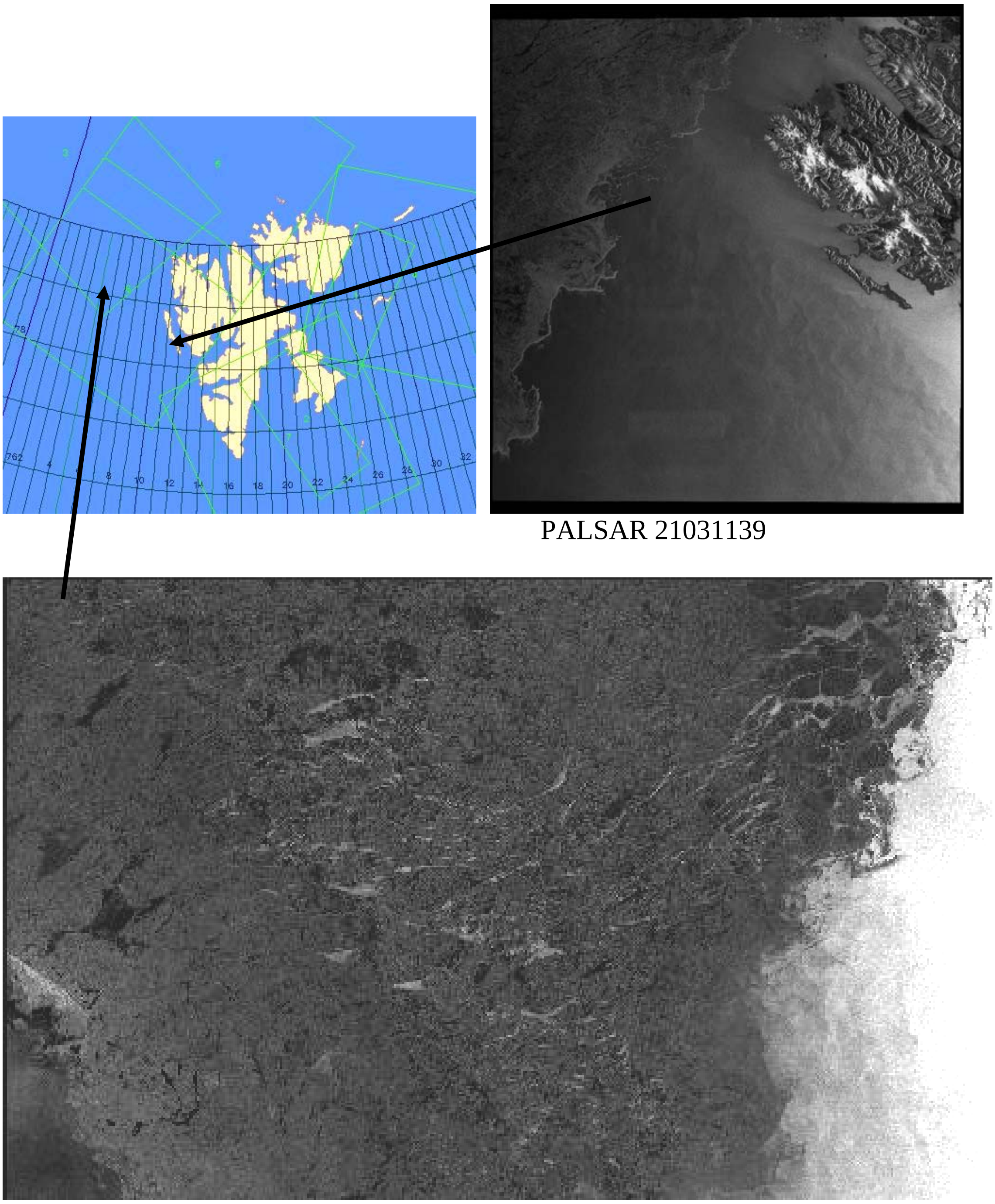

PALSAR 21031139

ASAR 21031159

Figure A2.26a. Satellite imagery for March 21

March 21, 2007 (B)

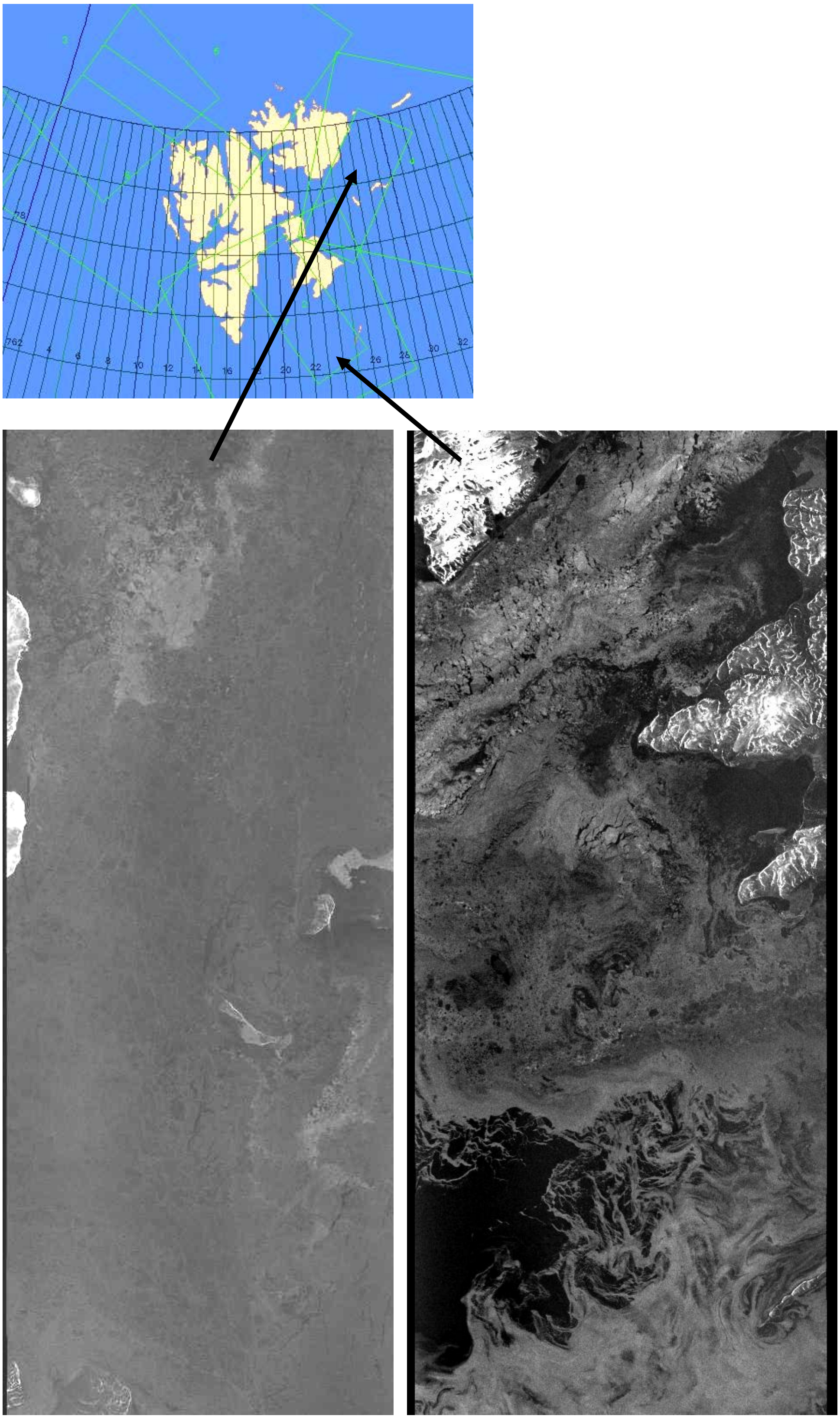

ASAR 21031019 ASAR 21031836

Figure A2.26b. Satellite imagery for March 21

March 22, 2007(A)

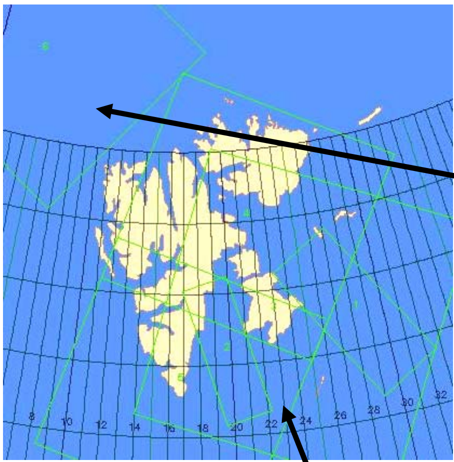

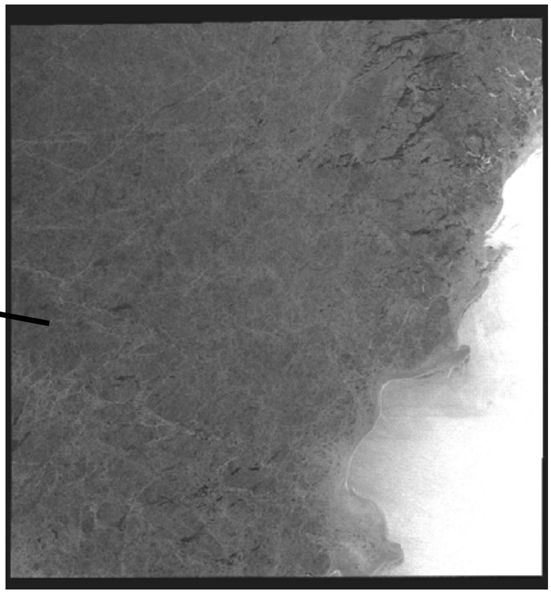

PALSAR 22031219

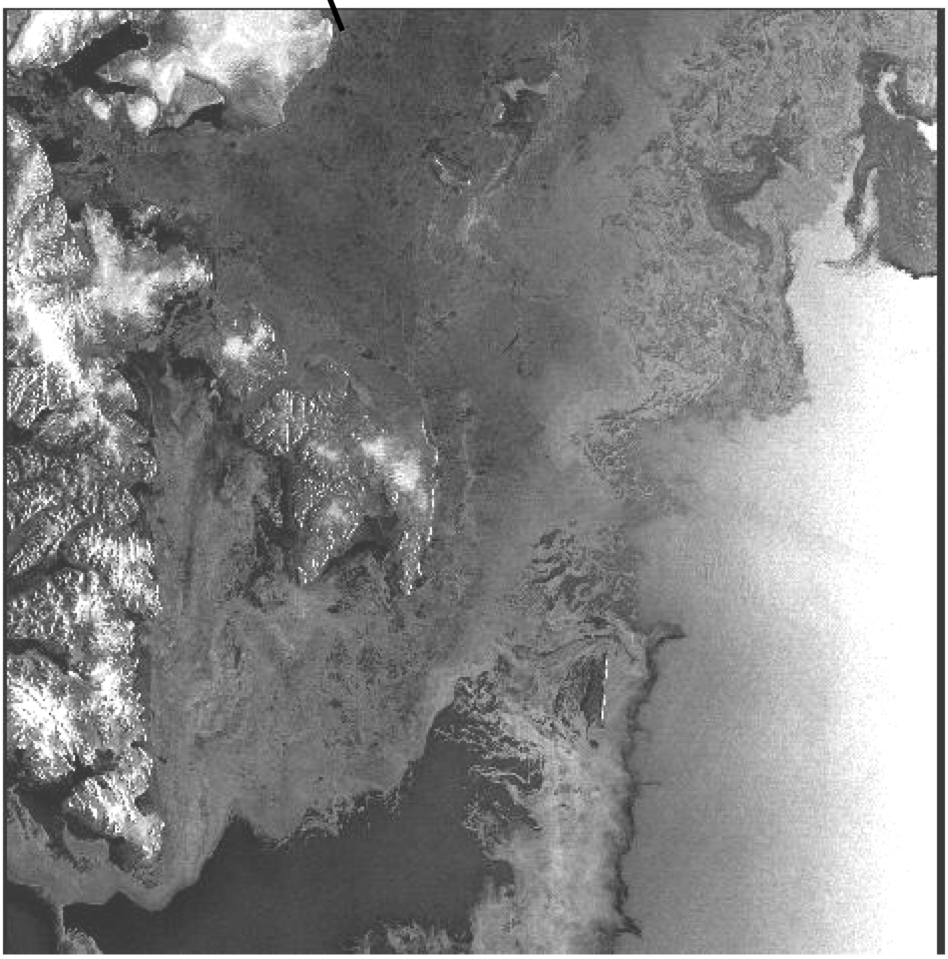

ASAR 22030948

Figure A2.27a. Satellite imagery for March 22

March 22, 2007(B)

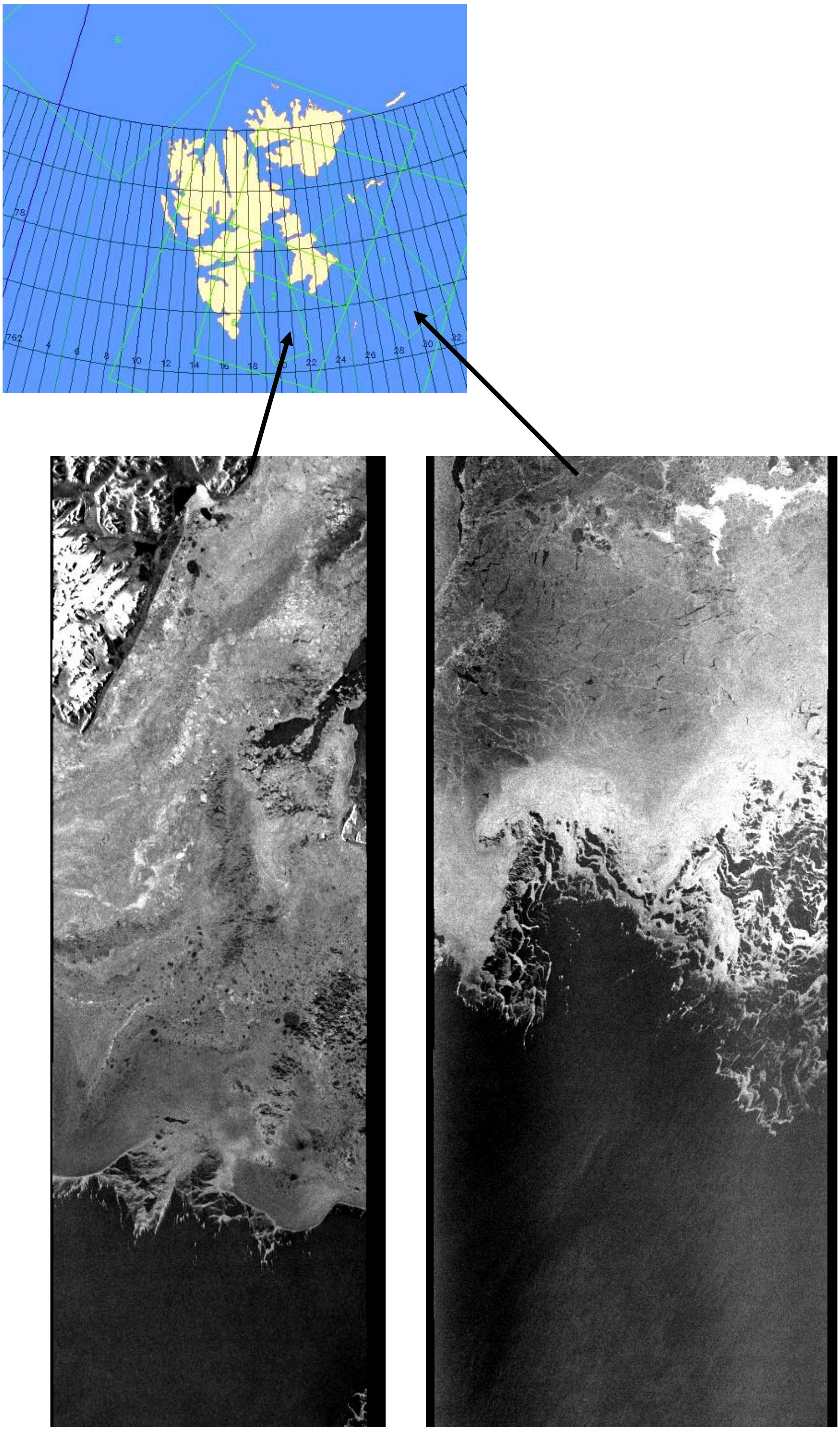

22031945 22031805

Figure A2.27b. Satellite imagery for March 22

March 23, 2007

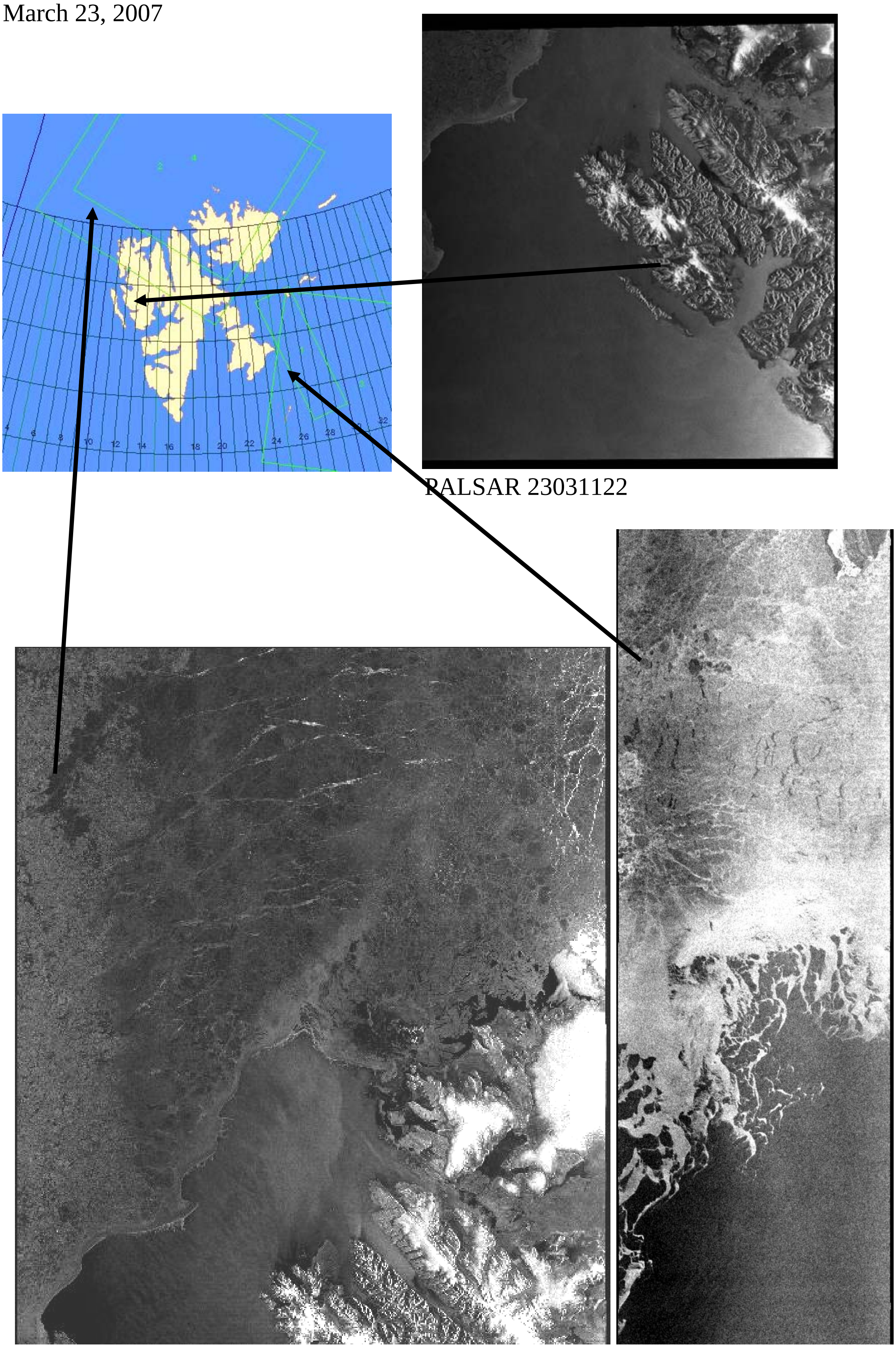

PALSAR 23031122

ASAR 23031056

ASAR 23031914

Figure A2.28. Satellite imagery for March 23

A2.6 Flight Protocol Storfjord, Polar 2

Date: 16 March 2007
Take-off: 10:45 UTC Touchdown: 14:55 UTC
Crew: Andreas Hahn and Jens Heider (pilots), Thomas Garbrecht, Wolfgang Dierking

Test site: Storfjord, profile from 77.8388N, 19.7509E and 76.5478N, 18.0612E

Flight pattern: 4 legs, the first at 800-1000 ft altitude ("linescan-track"), legs 2-4 ("turbulence-tracks") at 100 ft. Leg 1 started from southern waypoint. Legs 3 and 4 covered only half of the profile length, starting from the southern waypoint. At the end of each leg, "temps" (vertical temperature profiles) were measured up to 5000 ft. The altitude of the linescan track had to be fixed at low level because of low visibility. Leg 1: 11:40:20 to 12:22:12. Leg 2: 12:35:20 to 13:01:20. Leg 3: 13:14:30 to 13:27:35 (leg finished on mid of profile). Leg 4: 13:38:00 to 13:54:20 (all UTC).

Weather: Wind speed varied between 15 and 30 kts. On the southern part of the flight track, the wind direction was almost parallel to the flight direction, on the northern part, cross-wind conditions prevailed. The air temperature at flight altitude 100 ft was slightly above freezing point, the ice surface temperature slightly below (-2 to -4°C). Cloud cover was 100 percent, cloud base at about 1000 ft, cloud top higher than 10000 ft (which was the flight altitude of the DLR airplane).

Technical: Flight altitude changes of linescan track: southern waypoint 11:40:20 – 1000 ft; 11:44:00 begin descent from 1000 ft to 800 ft; 12:00:00 1000 ft; 12:05:50 800 ft, 12:10:34 begin ascent to 1000 ft. These variations were necessary because of cloud conditions. Hand-held photographs were taken to the left side from flight direction.

Ice cover: At the southern end, the ice was broken into floes with diameters on the order of 100 m (sizes can be later evaluated from ESAR images) (Fig.A2.29). Moving northward, the ice floes became larger, with patches of open water and new ice between the floes (Fig. A2.30), followed by a zone of small broken ice floes (Fig. A2.31) Later, the ice cover was less disturbed though some cracks were present (Fig. A2.32), and at some places the cracks opened indicating divergent ice motion (Fig. A2.33). On the mid-section of the profile and northwards, smaller and larger leads with patches of open water and new ice were observed (Figs A2.34 and A2.35). Close to the northern profile end, water saturated snow or water patches appeared on the ice surface (Fig. A2.36). At the northern profile end, rafted grey ice was found (Fig. A2.37).

Problems: The linescanner time was +2 seconds compared to the time on the meteorology rack when profile 4 was finished. The date on the linescanner data files was 15 of March instead of 16. The bad visibility required changes in altitude on the linescanner track which are also marked in the data editor file. Image contrast in linescanner data is low.

Fig. A2.29. Ice situation at southern end of the flight track. (leg 4, time ca. 13:52 UTC, 100 ft)

Fig. A2.30: Ice situation a few minutes (< 10) after passing southern waypoint, leg 1 flight altitude 800ft.

Fig. A2.31. Zone of broken ice, located between ice cover types Fig. 2 and Fig. 4 (leg 1, flight altitude 800 ft)

Fig. A2.32.Large areas of almost undisturbed ice cover (partly with cracks) (12:59 UTC on leg 2, flight altitude 100 ft).

Fig. A2.33. Divergent ice situation roughly at mid profile position (leg 1, altitude 800 ft).

Fig. A2.34. Leads at roughly mid profile, with wind streaks on open water and broken grey ice on downwind side (leg 2, altitude 100 ft).

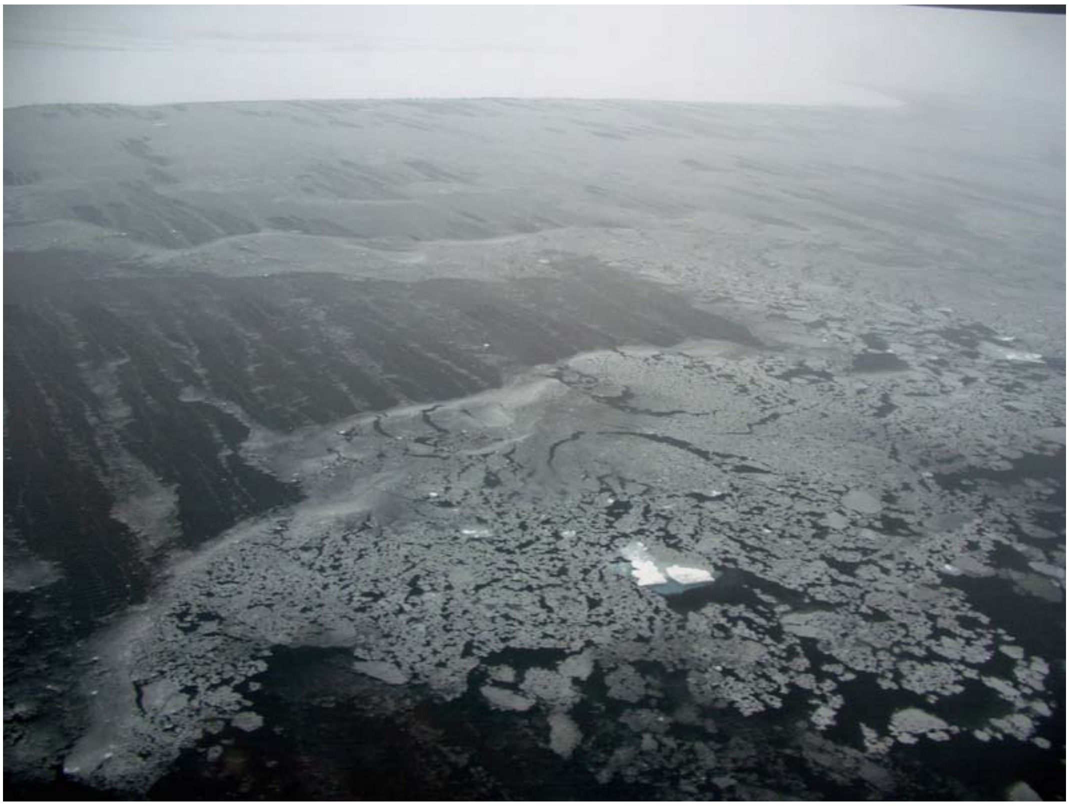

Fig. A2.35. Large lead (leg 2, time 12:40 UTC, altitude 100 ft)

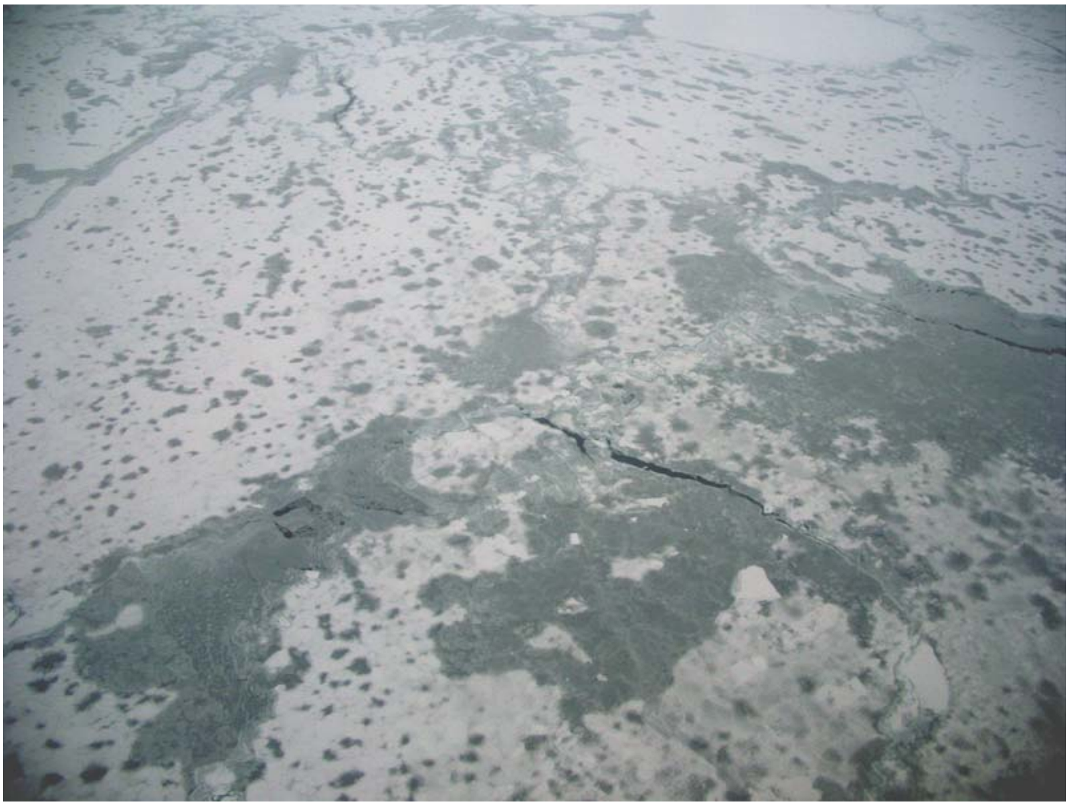

Fig. A2.36. Wet ice surface close to northern end of profile (leg 1, altitude 1000 ft)

Fig. A2.37. Northen end of profile, during temp-ascent (leg 1, > 1000 ft)

Additonal information:

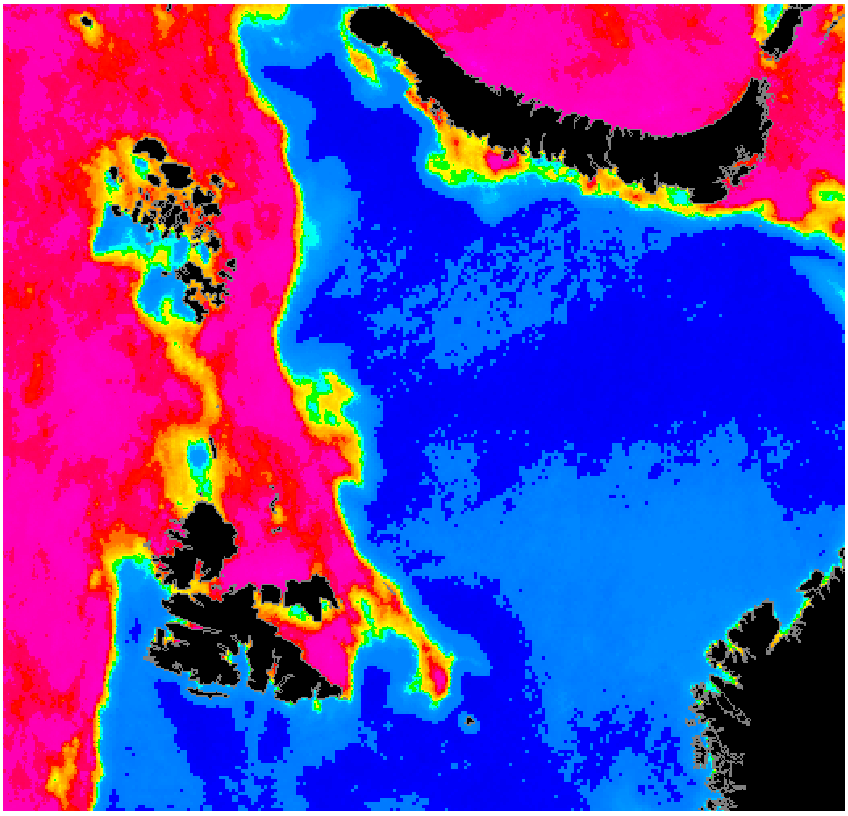

Fig. A2.38. Sea ice concentration on March 16 from passive microwave data. Source: www.seaice.dk

A2.7 Flight Protocol Barents Sea, Polar 2

Date: 18 March 2007
Take-off: 12:13 UTC Touchdown: 16:46 UTC
Crew: Andreas Hahn and Jens Heider (pilots), Thomas Garbrecht, Wolfgang Dierking

Test site: Barents Sea, profile from 78°41.8'N, 23°53.5'E and 79°36.4'N, 26°15.4'E

Flight pattern: 4 legs, first and second leg at 100 ft altitude ("turbulence-track"), leg 3 ("linescan-track") upwind at 3000 ft, leg 4 ("sawtooth-track" for vertical temperature profiles) between 100 and 3000 ft. Leg 1 started from south-west waypoint. At the end of each leg, "temps" (vertical temperature profiles) were measured up to 6000 ft, at the end of leg 4 up to 10000ft. Leg 1: 13:06 to 13:59. Leg 2: 14:13 to 14:23. Leg 3: 14:32 to 15:23. Leg 4: 15:32 to 15:54 (all UTC).

Weather: Wind speed was about 35 to 40 kts. Wind direction between 20 and 50°. The air temperature at flight altitude 100 ft and the ice surface temperature were at about -14°C. Thin clouds with patches of blue sky now and then. Later low haze on the ice.

Technical: Aperture was opened stepwise from the beginning to the end of the profile. Hand-held photographs were taken to the left side from flight direction. Linescan track: speed over ground at profile start 90 kts.

Ice cover: First-year ice. Southwest: almost closed, lots of ice ridges. Northeast: more open water patches, ice still rough, but more variable, different floe sizes from a few 100 meters to brash ice (fragments < 1m).

Problems: After arriving at the planned profile start (78°23,0'N 23°28,3'E), the wind direction was at about 10° which meant a very short profile before reaching the coast of Nordaustlandet. However, after a while, the wind direction changed to 20-30°, and the profile was adjusted accordingly (new start and the end point are given above). The FU did not fly over the whole profile length. Very rough flight (rough ice, high wind speed).

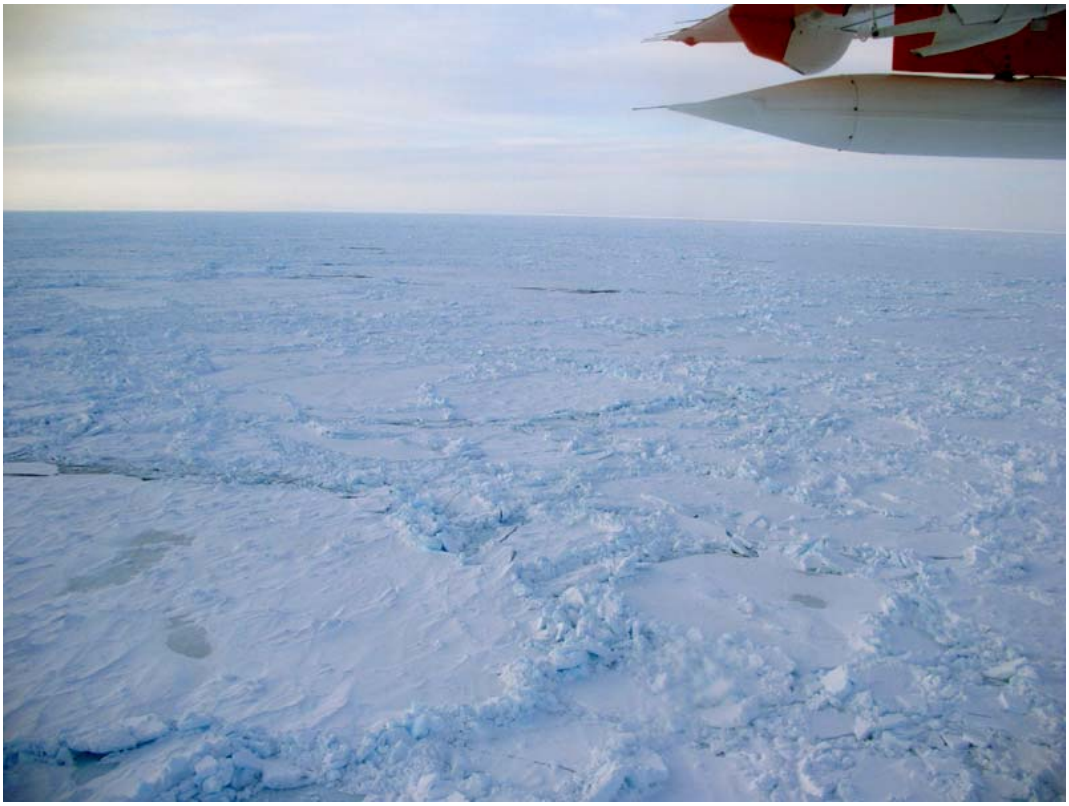

Figure A2.39. Close to southeastern WP (13:20 UTC, 100ft altitude)

Figure A2.40. 13:23 UTC, 100ft


Figure A2.41. 13:39:40 UTC, 100ft


Figure A2.42. 13:43:00 UTC 100ft

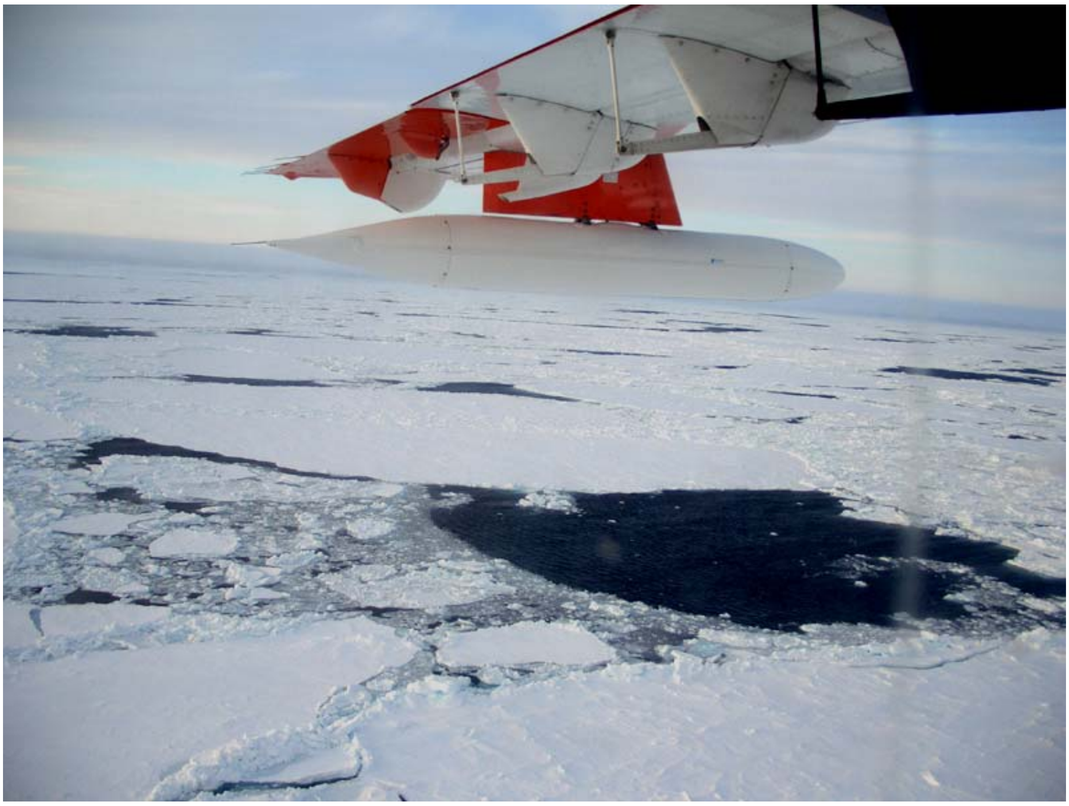
Figure A2.43. 13:45:20 UTC, 100ft


Figure A2.44. 13:49:00 UTC, 100ft

Figure A2.45. 13:56:00UTC, 100ft

Figure A2.46. Open water at the end of the profile, 13:58 UTC 100ft

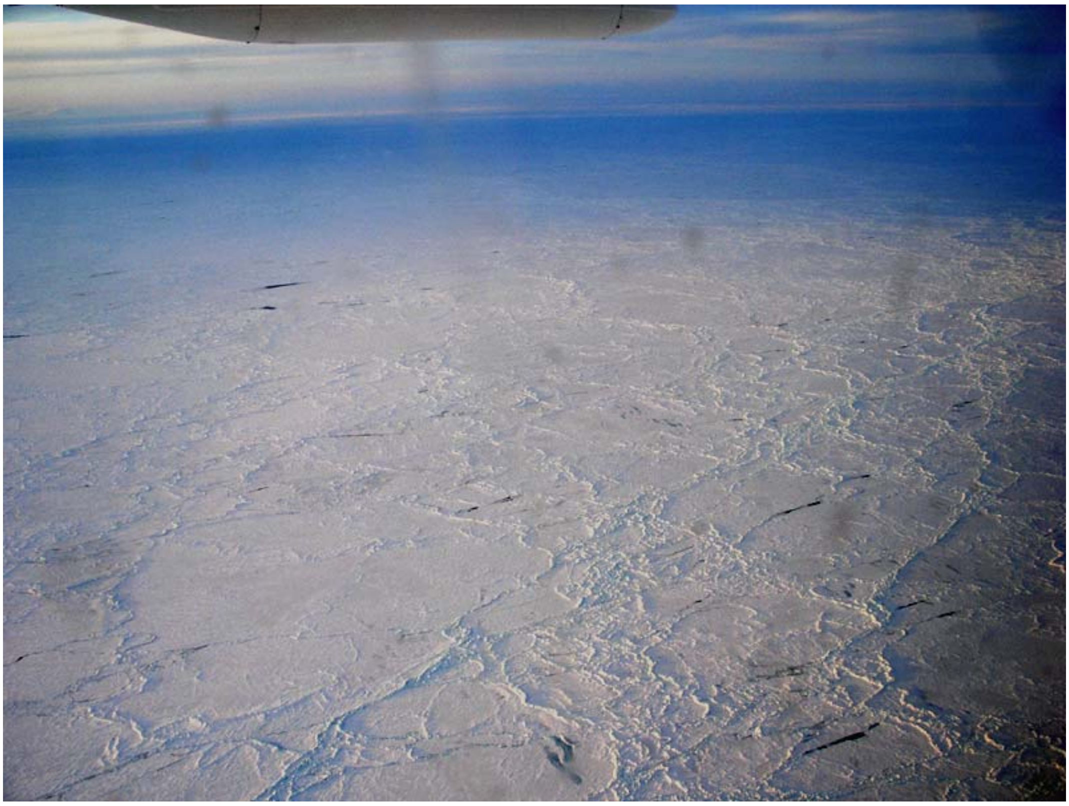
Figure A2.47. Approaching southwest WP (profile start). 14:37 UTC, 3000 ft altitude

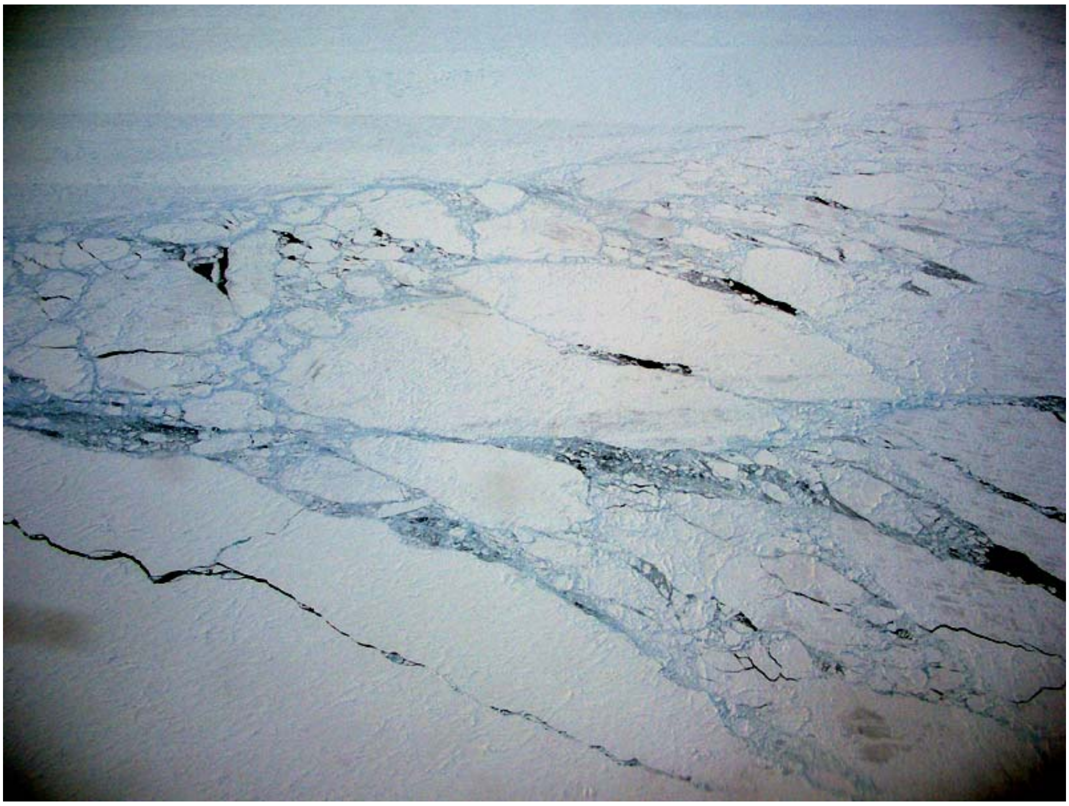
Figure A2.48. 15:56:10 UTC, 3000ft

Figure A2.49. 15:02:10 UTC, 3000ft

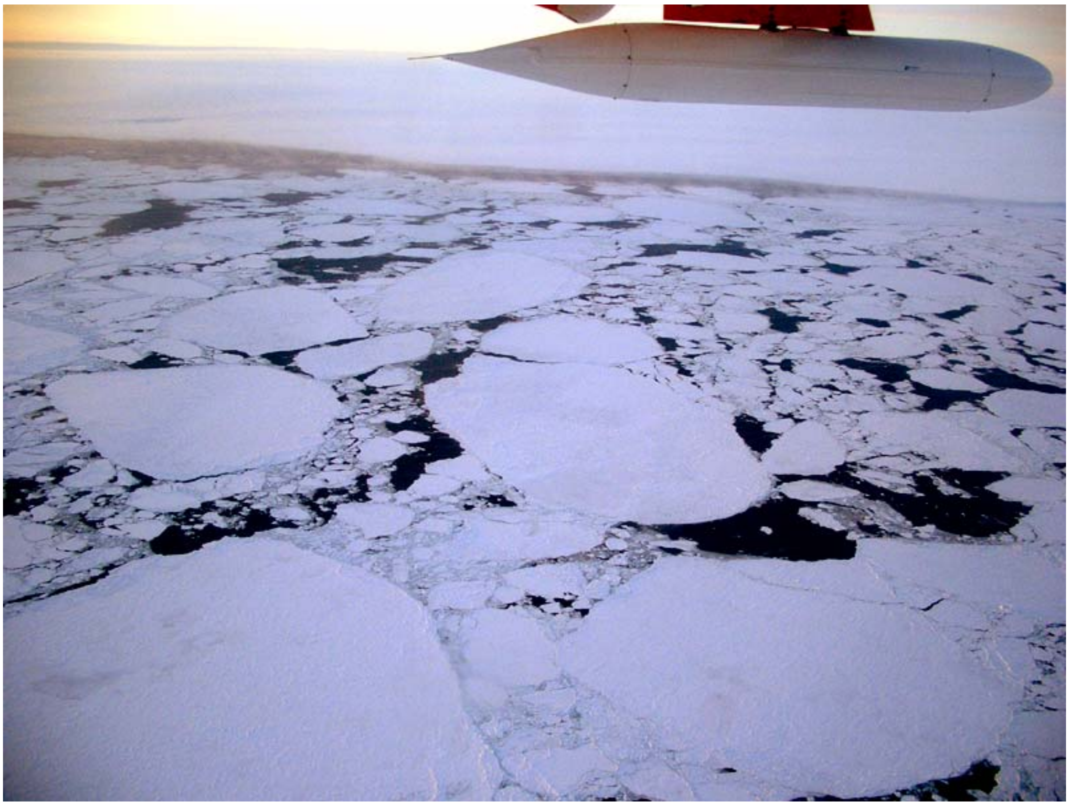

Figure A2.50. 15:09:30 UTC, 3000ft, edge of glacier in the background (Nordaustlandet)

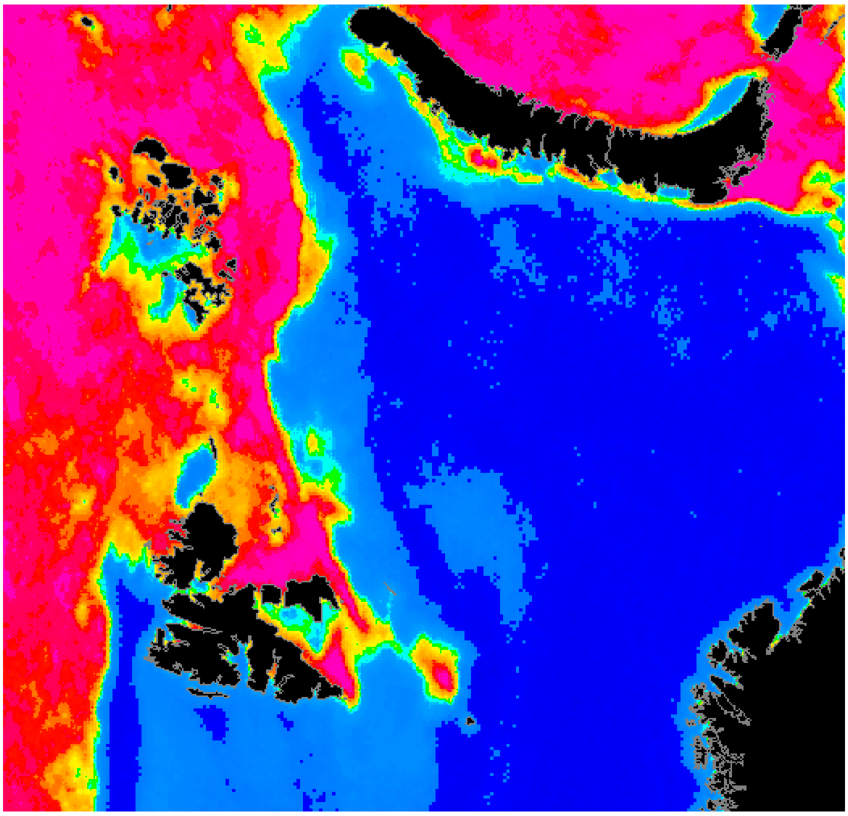

Figure A2.51. Sea ice concentration on March 18 from passive microwave. Source: www.seaice.dk

A2.8 Flight Protocol Fram Strait (1), Polar 2

Date: 19 March 2007
Take-off: 10:51 UTC Touchdown: 15:39 UTC
Crew: Andreas Hahn and Jens Heider (pilots), Thomas Garbrecht, Wolfgang Dierking

Test site: Fram Strait, profiles 1+2 between 80°30.0'N, 5°0.0'E to 80°56.9'N, 5°0.0'E, profiles 3+4 between 80°30.0'N, 5°0.0'E to 81°11'N, 5°0.0'E

Flight pattern: 4 legs, leg 1 ("linescan-track") upwind at 3000 ft, 27 nm long, leg 2 downwind at 100 ft altitude ("laser-track"), legs 3 and leg 4 ("turbulence-tracks") at 100ft. Leg 1 started from southern waypoint. At the end of each leg, "temps" (vertical temperature profiles) were measured up to 6000 ft, at the end of leg 4 up to 10000ft. Leg 1: 12:09 to 12:27. Leg 2: 12:44 to 12:55. Leg 3: 13:06 to 13:30. Leg 4: 13:39 to 13:56 (all UTC).

Weather: Wind speed was between 15 and 25 kts. Wind direction between 10 and 25°. The air temperature at 100 ft was about -27°C and the ice surface temperature at about -21°C. Clouds only at the ice margin, over most parts of the profile clear sky.

Technical: Aperture was kept constant. Hand-held photographs were taken to the left side from flight direction. Linescan track was flown with about 94 kts over ground.

ESAR imagery acquired only at C-band. DLR-FU arrived about 10 minutes later at southern profile start.

Ice cover: Thick FY ice (end-winter ice, thickness was presumably > 1 m for some floes) with grey ice between the floes. Floes sizes variable between a few meters and a few hundred meters. The older ice was snow-covered, snow was partly more than 30 cm thick. Because of the northern wind, the ice edge was divergent, with ice floes drifting southwards (Figs. 1 and 2).

Problems: none.

Figure A2.52. Close to the ice edge, 11:45 UTC, 10000ft altitude

Figure A2.53. Already behind the ice edge, approaching southern WP (10000ft altitude), photo taken between 11:50 and 11:57.

Figure A2.54. Profile start. 12:10:30, 3000ft altitude

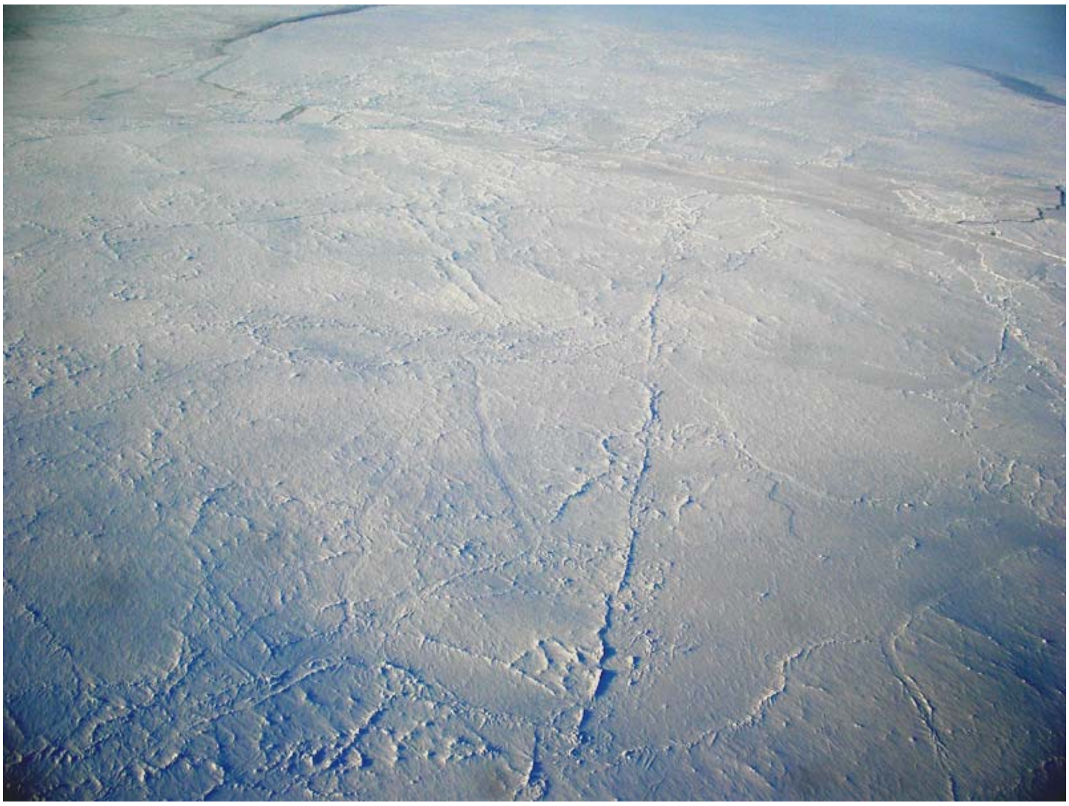
Figure A2.55. 12:13:30 UTC, 3000ft


Figure A2.56. 12:15:30 UTC, 3000ft

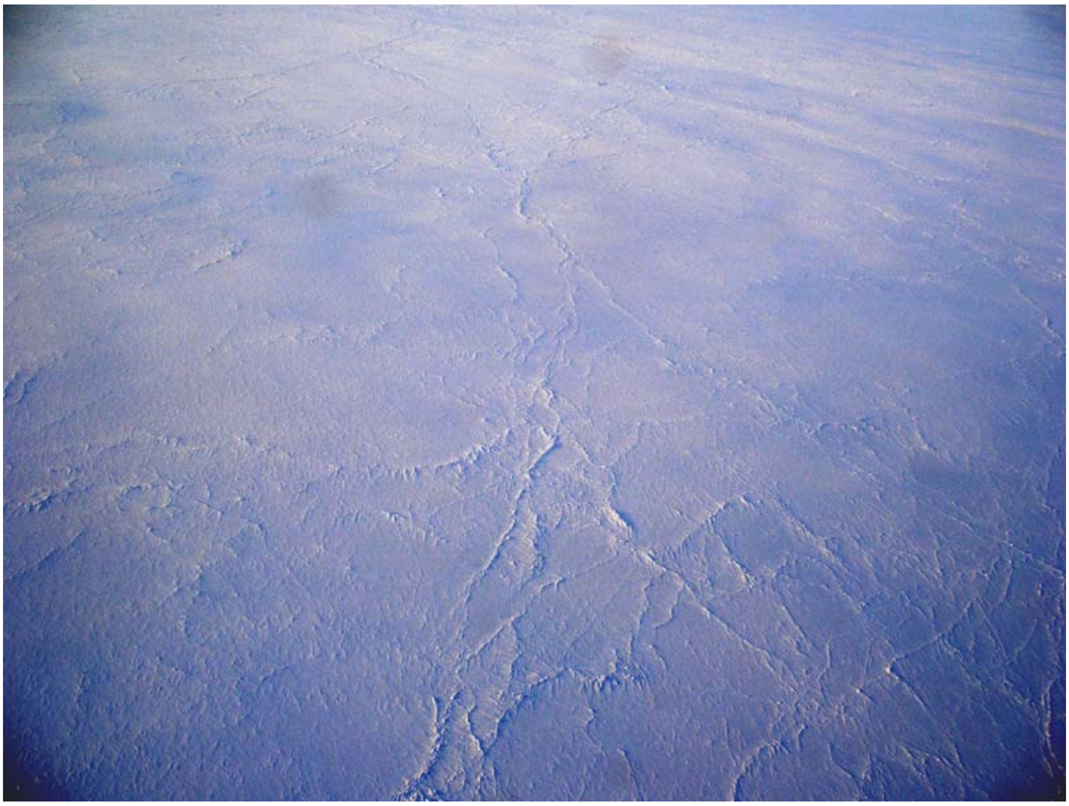

Figure A2.57. 12:21:40 UTC, 3000ft

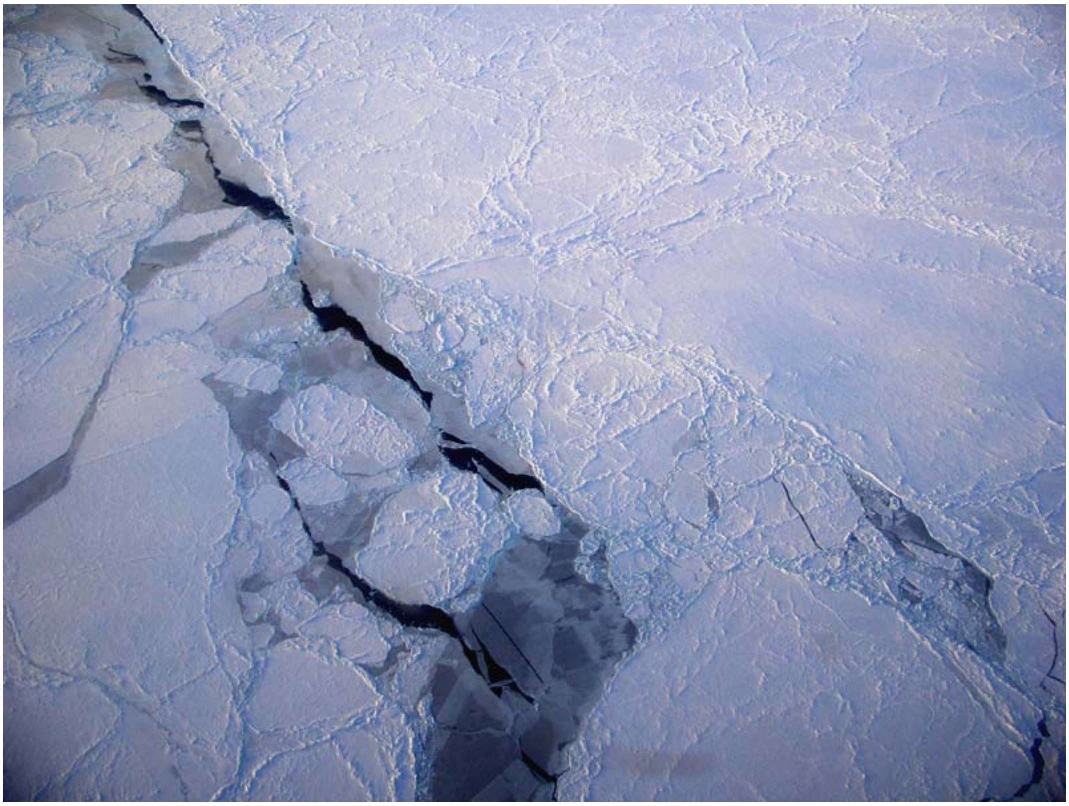

Figure A2.58. 12:25:40 UTC, 3000ft, close to profile end

Figure A2.59. 12:44:10 UTC, altitude 100ft, at northern profile end

Figure A2.60. 12:45:48 UTC, 100 ft

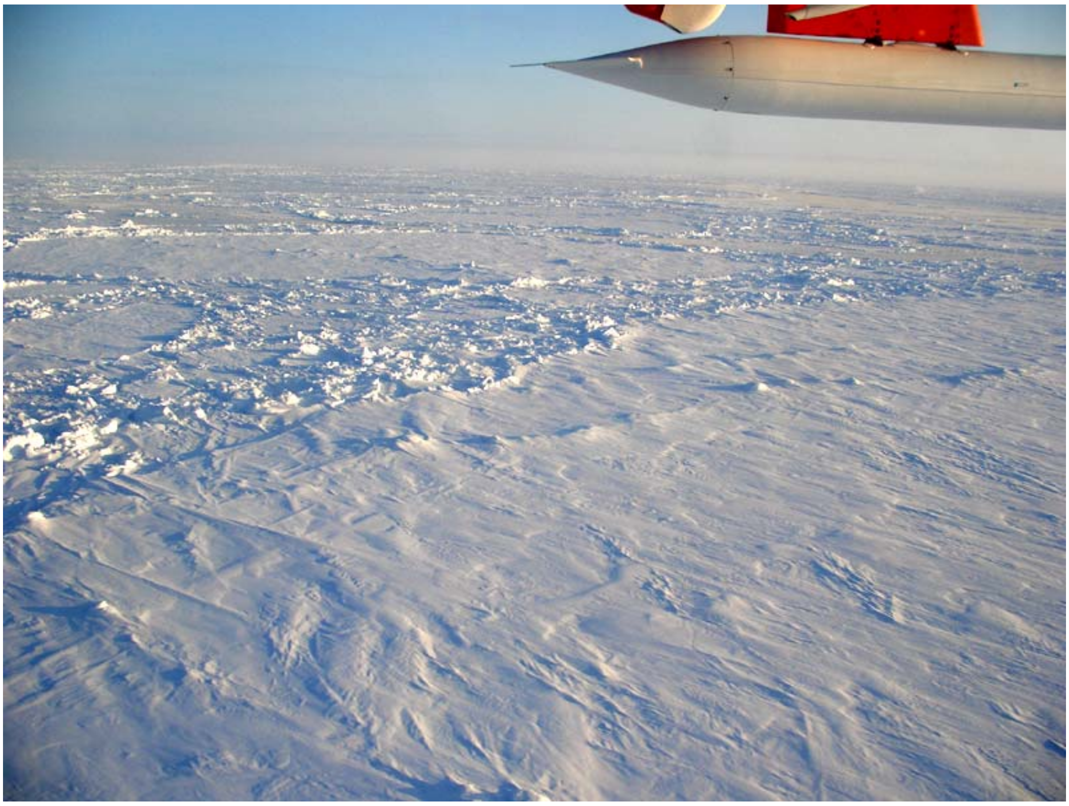
Figure A2.61. 12:47:55 UTC, 100 ft

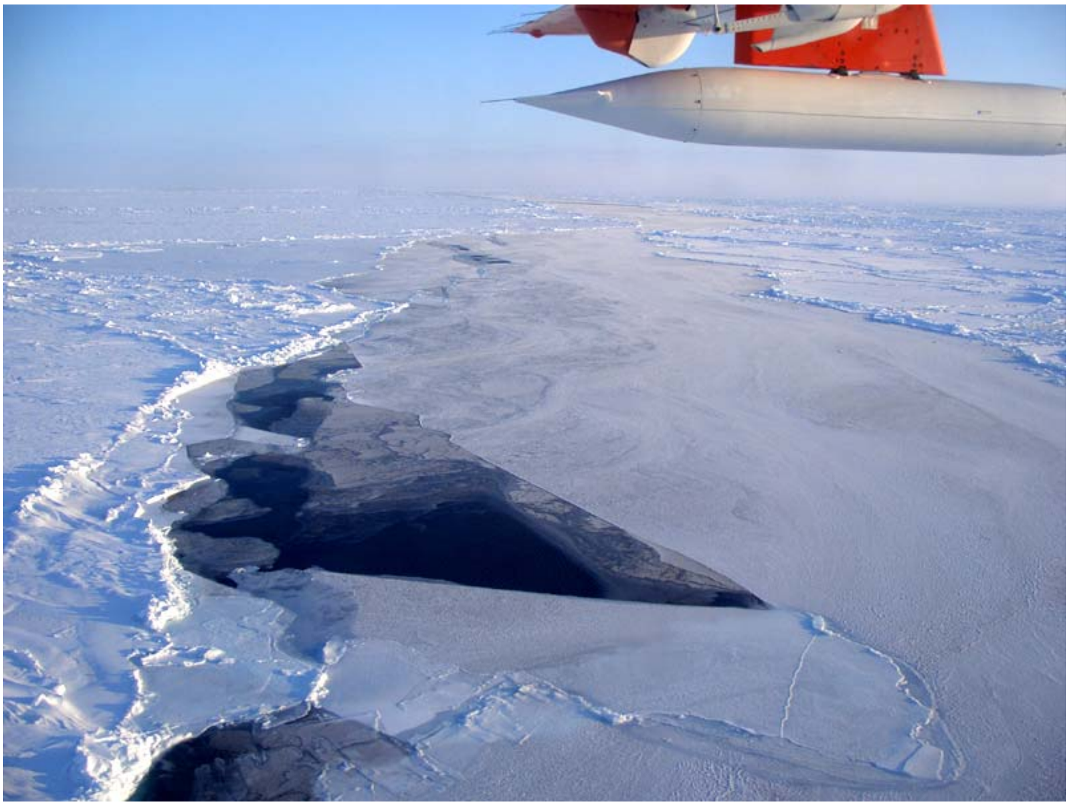
Figure A2.62. 12:47:55 UTC, 100 ft

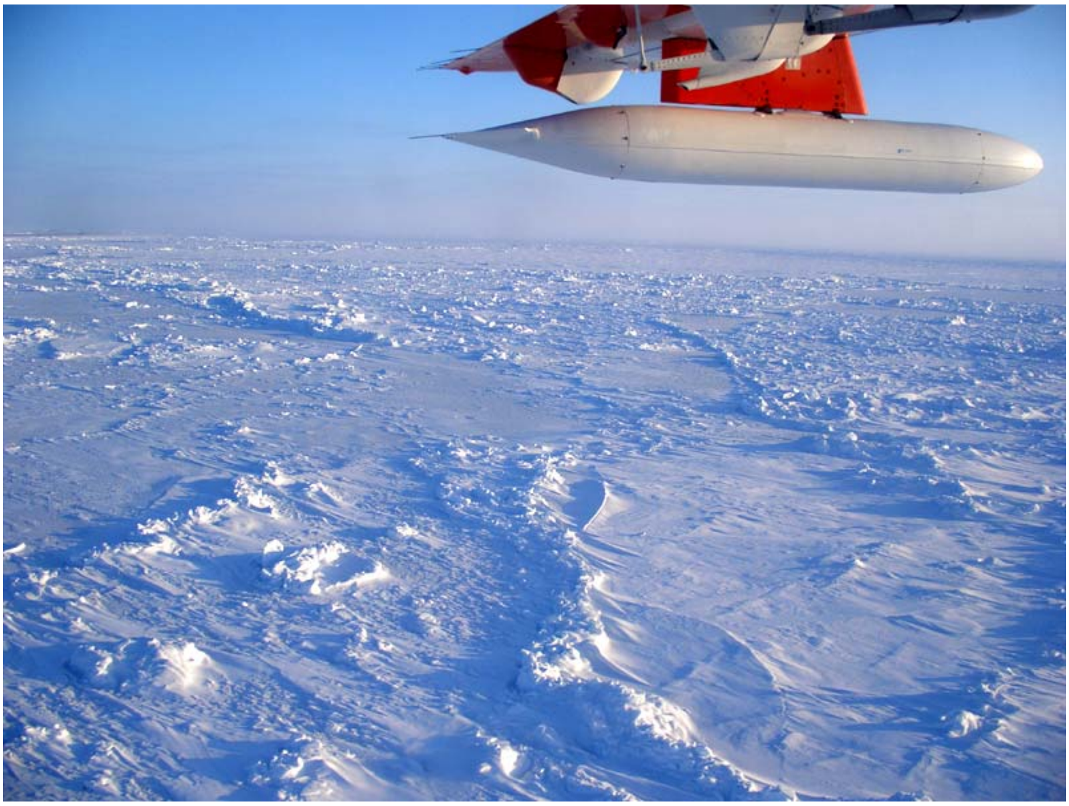
Figure A2.63. 12:51:10 UTC, 100 ft

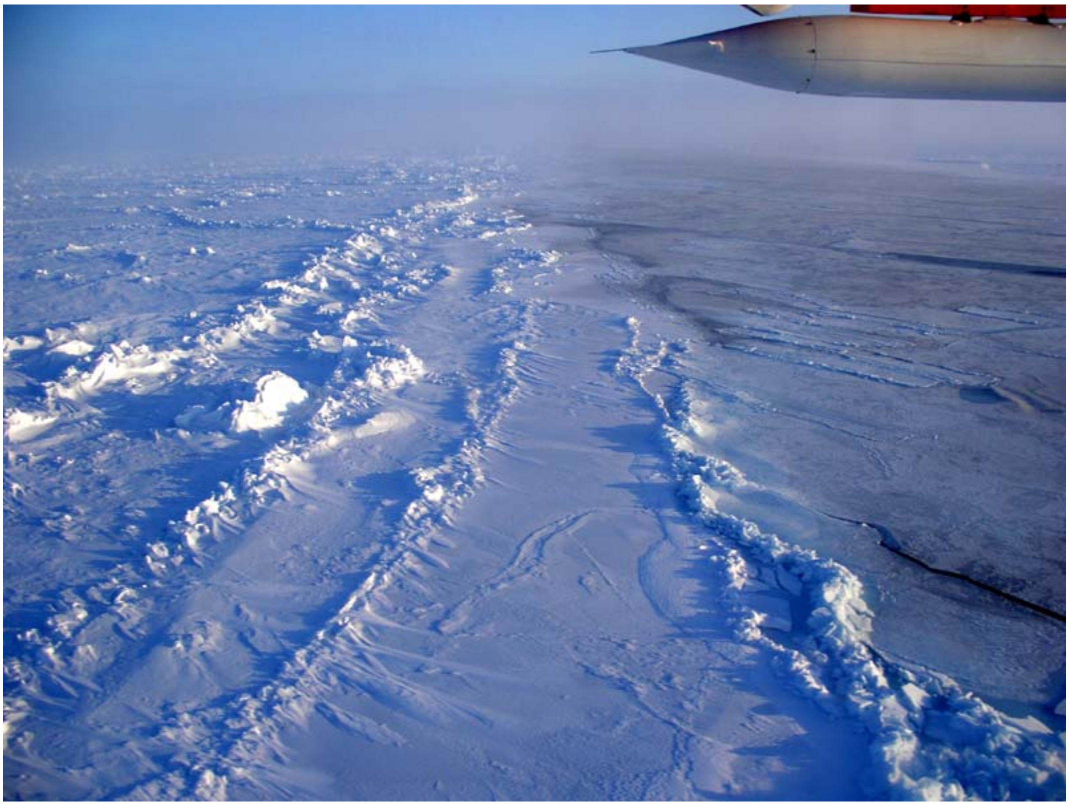
Figure A2.64. 12:53:10 UTC, 100 ft


Figure A2.65. 12:53:45 UTC, 100 ft


Figure A2.66. 12:54:44 UTC, 100 ft, shortly before southern profile end

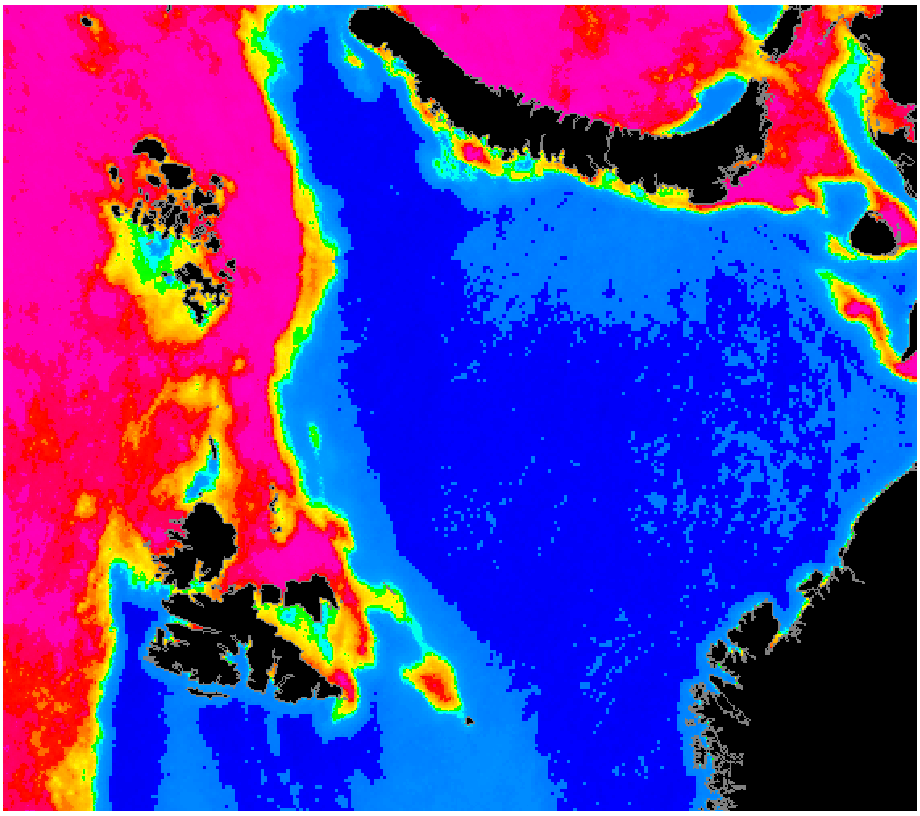

Figure A2.67. Sea ice concentration March 19, from passive microwave. Source: www.seaice.dk

A2.9 Flight Protocol Fram Strait (2), Polar 2 (W. Dierking, 21 March)

Date: 20 March 2007
Take-off: 10:44 UTC Touchdown: 15:45 UTC
Crew: Andreas Hahn and Jens Heider (pilots), Thomas Garbrecht, Wolfgang Dierking

Test site: Fram Strait, profiles 1+2 between 80°25.0'N, 5°0.0'E to 80°56.9'N, 5°0.0'E, profiles 3+4 between 80°25.0'N, 5°0.0'E to 81°14.8'N, 5°0.0'E

Flight pattern: 4 legs, leg 1 ("linescan-track") upwind at 3000 ft, 32 nm long, leg 2 downwind at 100 ft altitude ("laser-track"), leg 3 upwind ("turbulence-track") at 100ft, leg 4 downwind ("sawtooth") between 100ft and 3000ft. Leg 1 started from southern waypoint. At the end of each leg, "temps" (vertical temperature profiles) were measured up to 6000 ft, at the end of leg 4 up to 10000ft. Leg 1: 12:26 to 12:41. Leg 2: 12:44 to 12:59. Leg 3: 13:12 to 13:39. Leg 4: 13:50 to 14:10 (all UTC).

Weather: Wind speed was about 10-15 kts, wind direction at about 0°. The air temperature at 100 ft was about -27°C and the ice surface temperature at about -24°C. Clouds only at the ice margin, over profile clear sky.

Technical: Aperture was kept constant. Hand-held photographs were taken to the left side from flight direction. Linescan track was flown with about 123 kts over ground. ESAR imagery acquired at C-band VV-VH and L-band polarimetric. DLR-FU passed southern WP on their way back about 1 minute before Polar-2 started the linescan-track (i. e. at the end of the linescan profile, the difference was about 25 mintes). Polar-2 flew calibration patterns for the turbulence sonde before entering into and after leaving the test site.

Ice cover: Thick FY ice (end-winter ice, thickness was presumably > 1 m for some floes) with grey ice between the floes. Floes sizes variable between a few meters and a few hundred meters. The older ice was snow-covered, snow was partly more than 30 cm thick. Because of the northern wind, the ice edge was divergent, with ice floes drifting southwards. Comparing linescan tracks from March 20 and 19, one recognizes that different parts of the ice surface were imaged, which is due to the ice drift.

Problems: none.

Figure A2.68. Close to profile start position. Time 12:28:10 UTC, altitude 3000ft

Figure A2.69. Time 12:31:58 UTC, altitude 3000ft

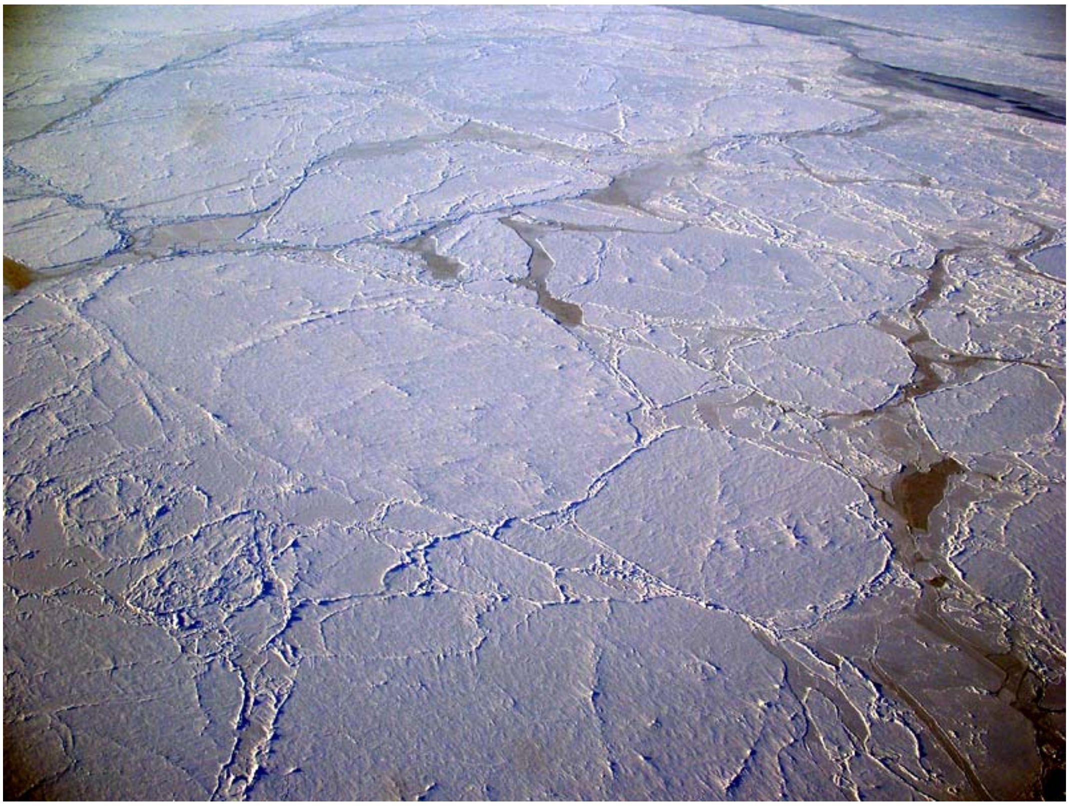

Figure A2.70. Time 12:36:55 UTC, altitude 3000ft

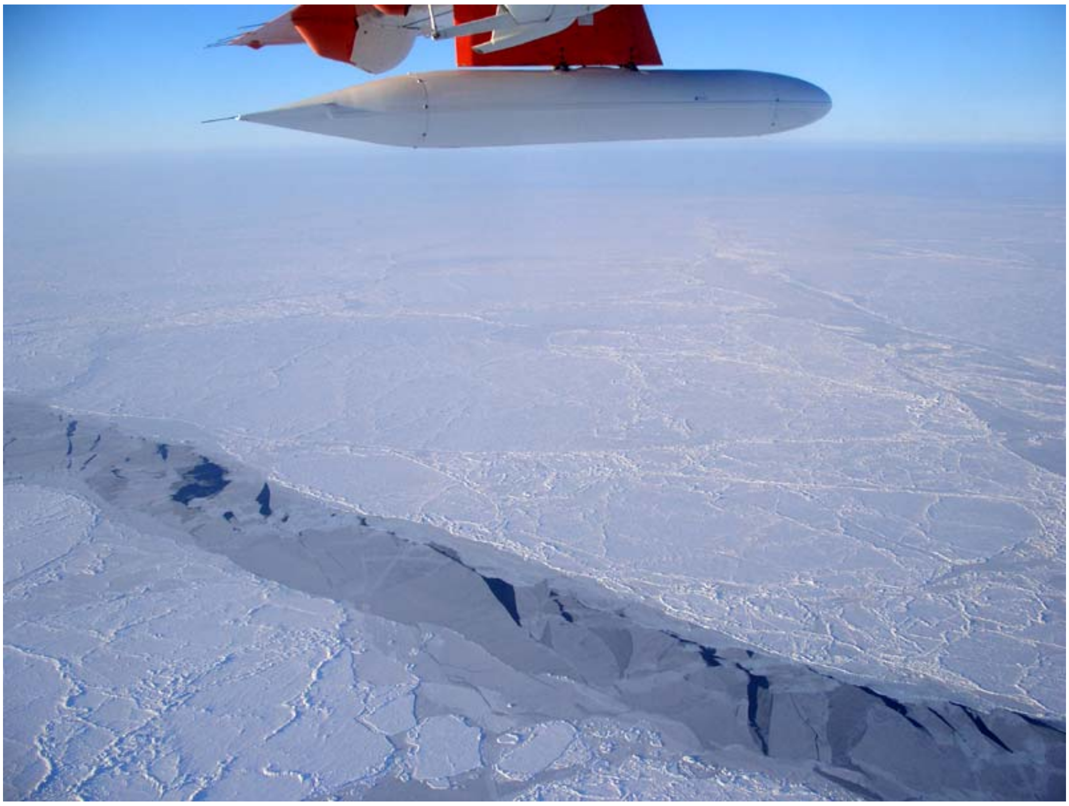

Figure A2.71. Time 12:38:25 UTC, altitude 3000ft

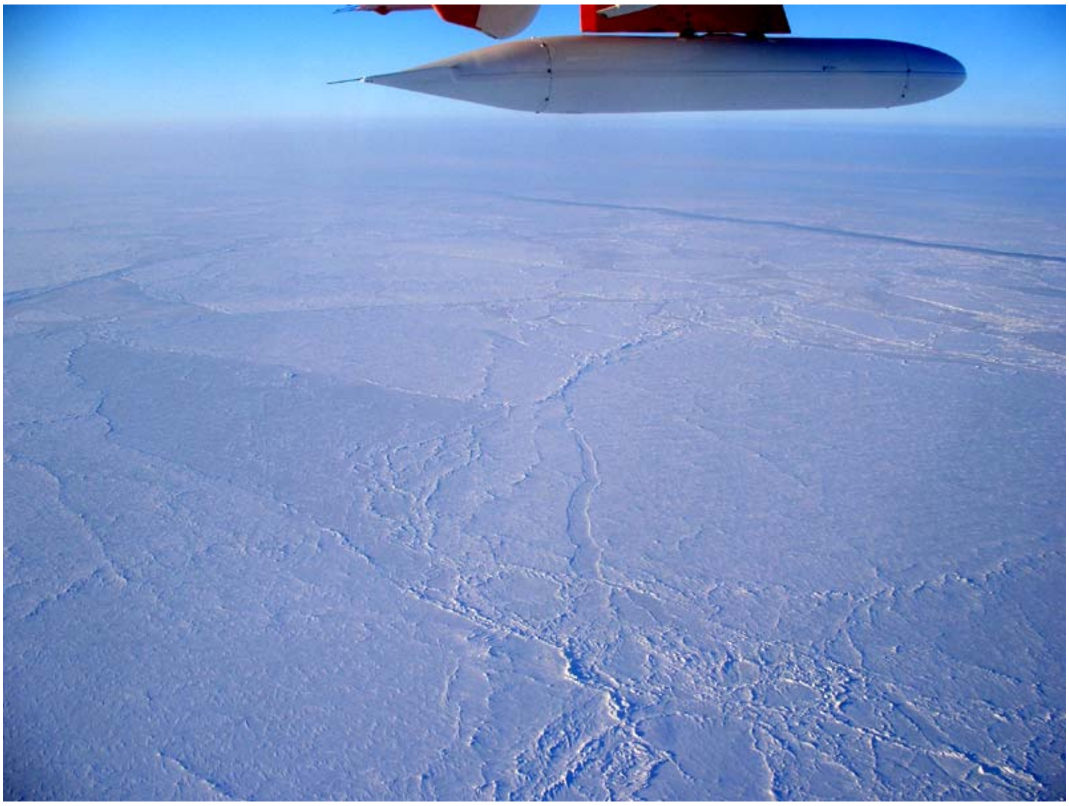

Figure A2.72. Close to end of linescan-track, time 12:41:36 UTC, altitude 3000ft

Figure A2.73. Shortly after flying over end point of linescan track, 12:45:18 UTC, altitude 100ft

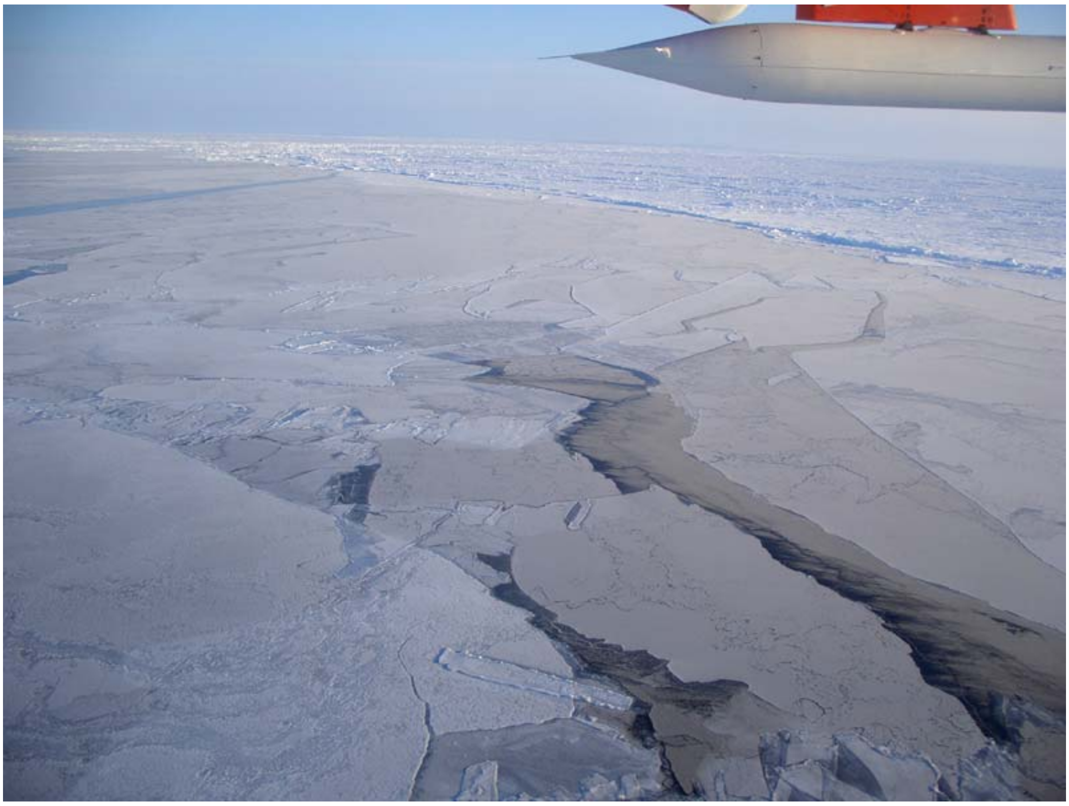

Figure A2.74. Time 12:47:20 UTC, altitude 100ft

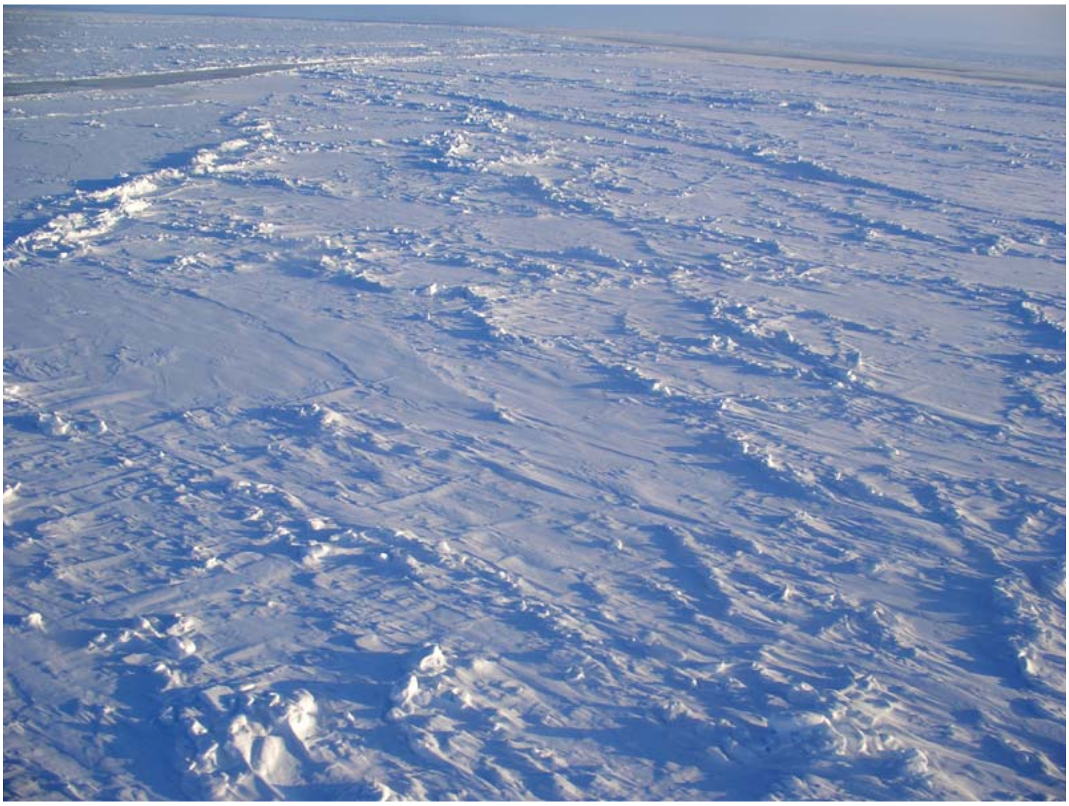
Figure A2.75. Time 12:48:10 UTC, altitude 100ft

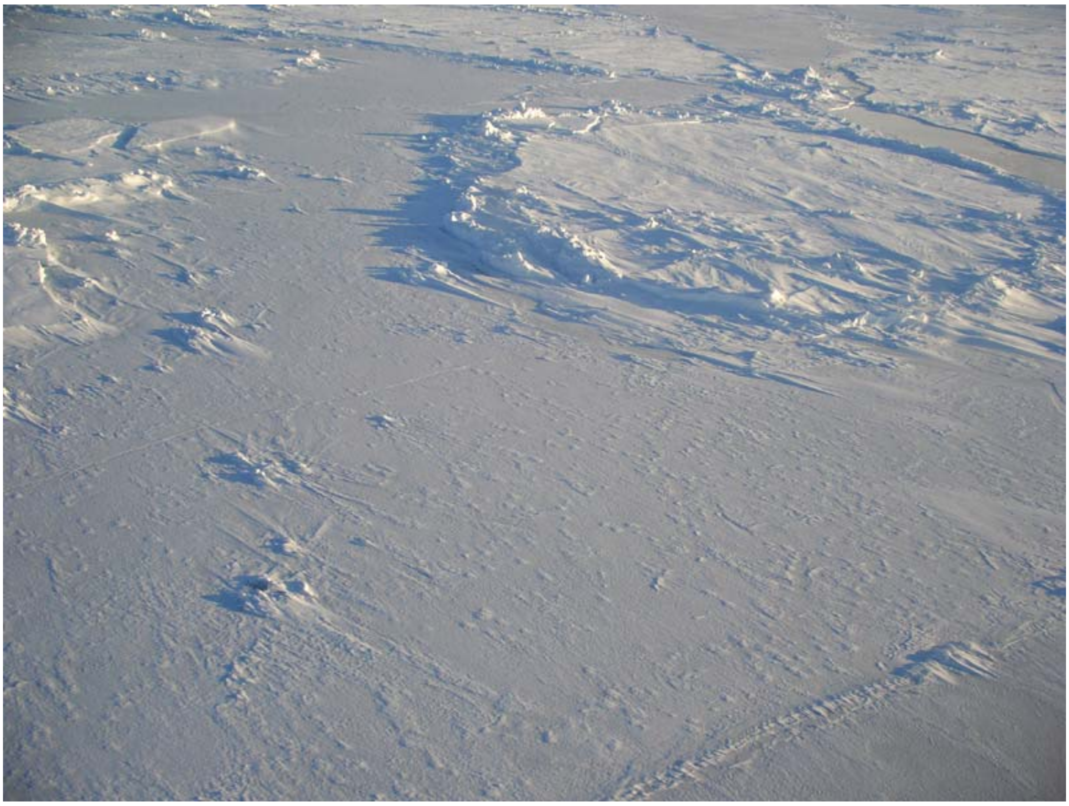
Figure A2.76. Time 12:54:20 UTC, altitude 100ft


Figure A2.77. Time 12:56:08 UTC, altitude 100ft

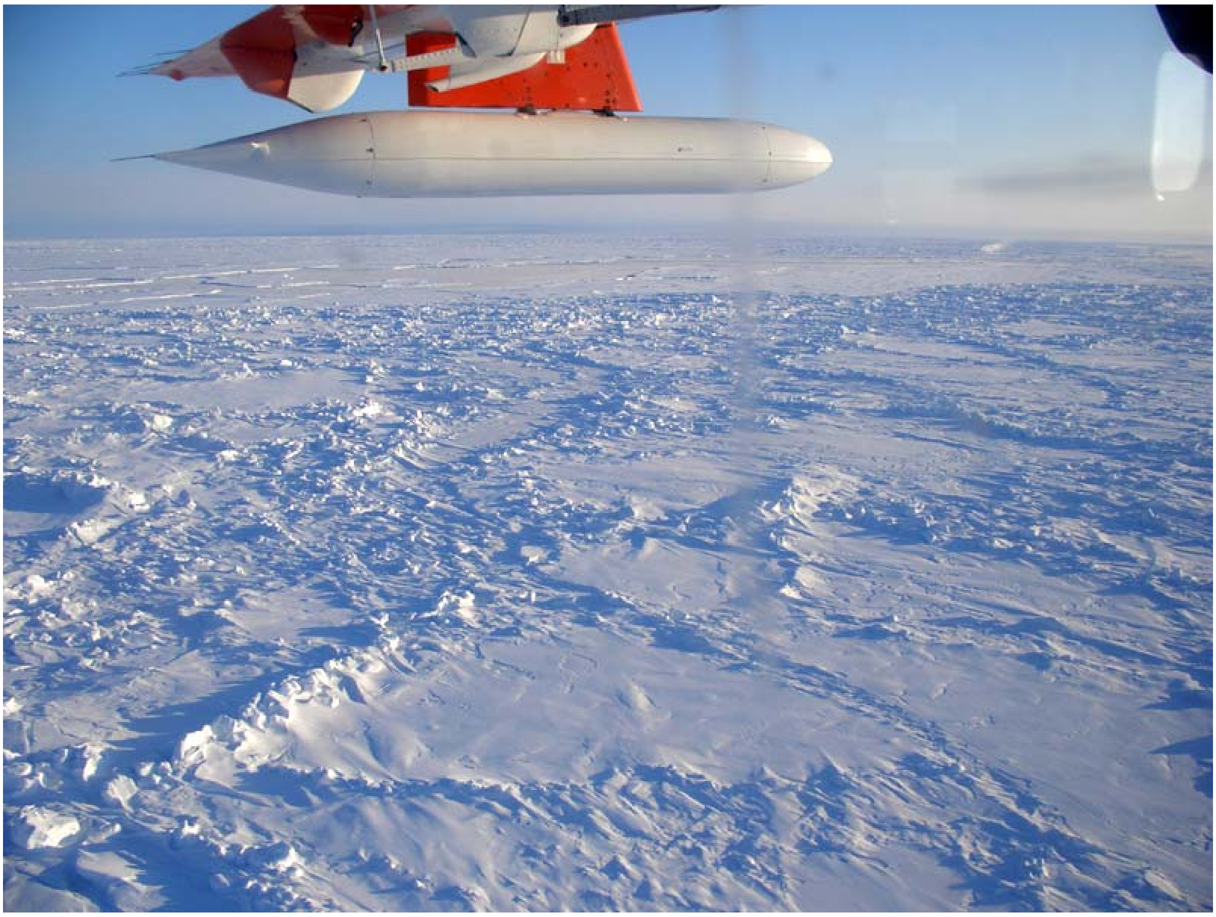
Figure A2.78. Time 12:59:00 UTC, altitude 100ft (at southern WP)

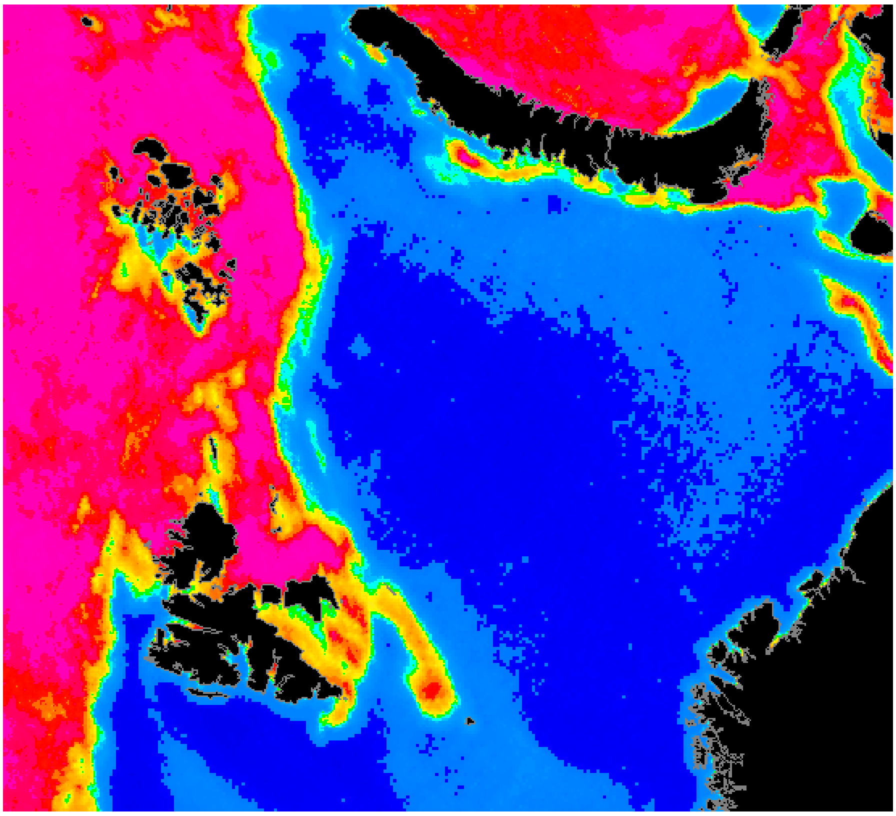

Figure A2.79. Sea ice concentration March 20, from passive microwave. Source: www.seaice.dk